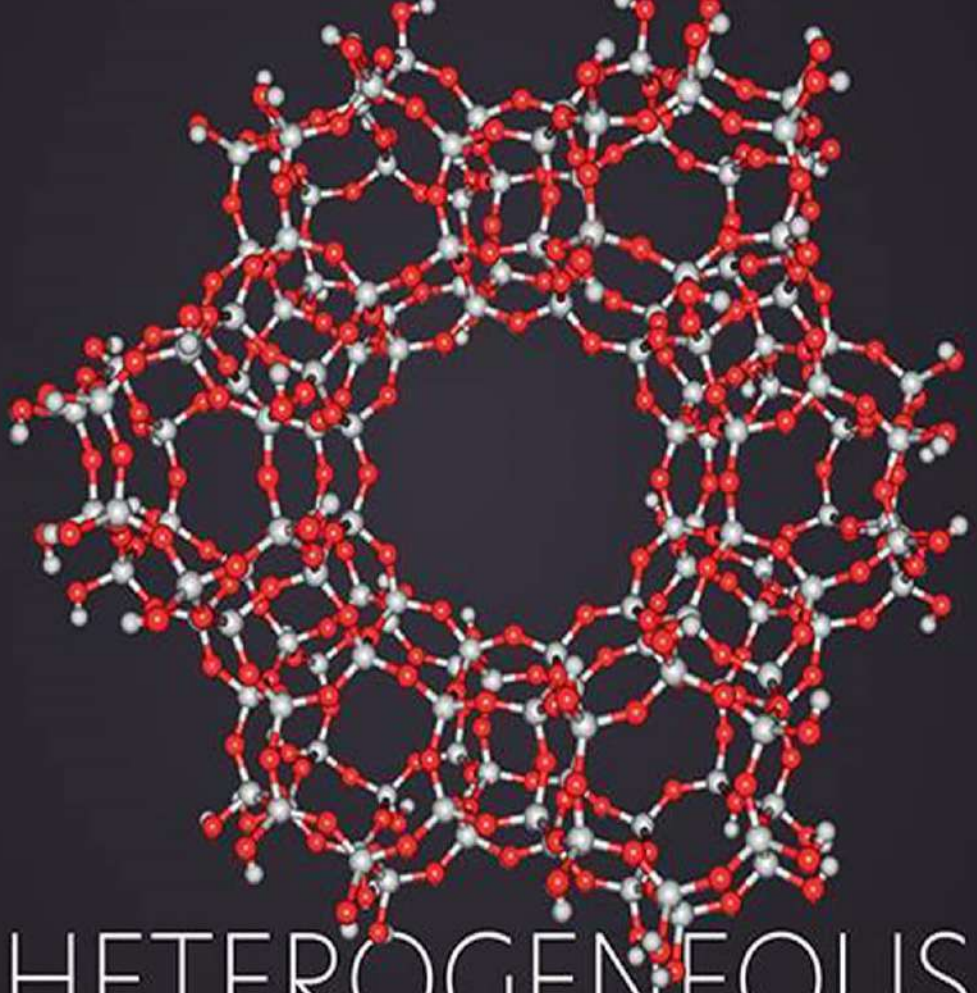

HETEROGENEOUS CATALYSIS

FUNDAMENTALS, ENGINEERING AND CHARACTERIZATIONS

GIOVANNI PALMISANO
SAMAR AL JITAN
CORRADO GARLISI

with accompanying presentation slides and instructor's manual

ELSEVIER

Heterogeneous Catalysis

Heterogeneous Catalysis

Fundamentals, Engineering, and Characterizations (with accompanying presentation slides and instructor's manual)

Giovanni Palmisano

Department of Chemical Engineering, Khalifa University, Abu Dhabi, United Arab Emirates

Samar Al Jitan

Department of Chemical Engineering, Khalifa University, Abu Dhabi, United Arab Emirates

Corrado Garlisi

Luxembourg Institute of Science and Technology, Luxembourg

ELSEVIER

Elsevier
Radarweg 29, PO Box 211, 1000 AE Amsterdam, Netherlands
The Boulevard, Langford Lane, Kidlington, Oxford OX5 1GB, United Kingdom
50 Hampshire Street, 5th Floor, Cambridge, MA 02139, United States

Notices

Knowledge and best practice in this field are constantly changing. As new research and experience broaden our understanding, changes in research methods, professional practices, or medical treatment may become necessary.

Practitioners and researchers must always rely on their own experience and knowledge in evaluating and using any information, methods, compounds, or experiments described herein. In using such information or methods they should be mindful of their own safety and the safety of others, including parties for whom they have a professional responsibility.

To the fullest extent of the law, neither the Publisher nor the authors, contributors, or editors, assume any liability for any injury and/or damage to persons or property as a matter of products liability, negligence or otherwise, or from any use or operation of any methods, products, instructions, or ideas contained in the material herein.

British Library Cataloguing-in-Publication Data
A catalogue record for this book is available from the British Library

Library of Congress Cataloging-in-Publication Data
A catalog record for this book is available from the Library of Congress

ISBN: 978-0-323-89845-4

Publisher: Susan Dennis
Editorial Project Manager: Maria Elaine D. Desamero
Production Project Manager: Bharatwaj Varatharajan
Cover Designer: Matthew Limbert

Typeset by MPS Limited, Chennai, India

Contents

Preface

Heterogeneous catalysis is a multidisciplinary subject of relevance to a large number of students, scholars, practitioners, and industries, touching in different ways chemical engineering, chemistry, and materials science. Its significance is evident looking at the current applications in the industrial synthesis of a wide range of commodities and fine chemicals, as also at the continuous efforts in the scientific activities targeting the preparation of more efficient catalysts followed by characterizations aimed at the understanding of their performance, along with the investigations on novel catalytic processes and reactors.

In the last decades, a number of textbooks and scientific books have appeared dealing with specific aspects of catalysis or trying to achieve a more holistic presentation of the fundamentals and applications.

Unlike other disciplines, heterogeneous catalysis does not allow for a straight and rigorous theoretical development of its principles to justify observed phenomena, since an all-embracing theory has not been developed to date, due to the complexity of the mechanisms behind it.

For this reason, former authors have usually covered only a few fundamental aspects of catalysis, moving forward to discuss the implications in terms of applications and materials' characterizations.

This book presents an overview of the fundamentals of heterogeneous catalysis in Chapter 1, Introduction, and Chapter 2, Fundamentals of the Adsorption Process, covering the basic concepts and quantities for the less experienced reader with few examples of industrial catalytic processes, followed by the adsorption theory starting with the molecular orbital approach. The thermodynamics and kinetics of adsorption/desorption are described with graphical exemplifications for a better understanding. A handful of examples taken for literature are also provided to guide the reader through the complex interpretation of the catalysts' features. The *Focus* sections in these two chapters report case studies on how the configuration and the supports of catalysts can affect their electronic properties and activity, and present a number of solved numerical examples.

Chapter 3, Adsorption Models, Surface Reaction, and Catalyst Architectures, describes the traditional adsorption models with an overview on recent developments covered in the *Focus* sections, which are found throughout the book and point mostly to the correlation between materials preparation/properties and catalytic performance, along with numerical examples. The chapter ends with the models for surface reaction and the role of cocatalysts and supports.

Chapter 4, Surface Area and Porosity, deals with the assessment of the surface area and porosity, with insights on the old and more recent hysteresis classifications and models to estimate porosity and pore size distribution. This chapter presents a significant number of examples taken from recent literature that are intended to develop the reader's skills on the interpretation of isotherms with hysteresis loops and pore size distributions. *Focus* sections describe the working principles and the equipment used for the assessment of the textural properties of catalysts, numerical examples on the BET equation, tortuosity and diffusivity, along with a case study on the design of catalysts for the enhancement of diffusion.

Overall, the first four chapters give a unique overview of the fundamentals of catalysis, inclusive of all the kinetic and thermodynamic aspects related to adsorption/desorption, followed by a detailed and updated presentation on the assessment of surface area and porosity.

Chapter 5, Catalytic Reaction Engineering, covers the reaction engineering topics of heterogeneous catalysts, particularly useful for readers without a background in chemical engineering who did not study catalytic reaction engineering and reactor modeling. The *Focus* sections describe different types of catalytic reactors, the modeling of diffusion and transport in porous catalysts, the design and preparation of catalyst pellets for fixed bed reactors, and they also include solved reaction engineering problems.

Chapter 6, Green Heterogeneous Catalysis, is a survey on green catalysis, ranging from electrocatalysis to photocatalysis and the catalytic conversion of biomass to biofuel. The chapter is focused on the applications after a quick introduction to the principles of these three green approaches. *Focus* sections cover the preparation aspects of recently developed catalysts and the connection between catalyst properties and activity/selectivity.

To conclude, the most popular characterization techniques used for solid catalysts are discussed in Chapter 7, Characterization Techniques, where the fundamentals of all techniques are explained followed by examples of their applications. This chapter is approachable by both a newcomer and a more expert reader who would like to be introduced to a characterization technique he/she is not familiar with and analyze few data describing catalysts reported in the literature. The application of in-situ techniques, the characterization of catalysts during their synthesis, and the description of a synchrotron facility are among the topics covered in the *Focus* sections.

The book, which is reader friendly and accessible to a heterogeneous readership ranging from senior undergraduate students up to Master's and PhD level students, along with experienced scholars and practitioners, is supplemented with *Presentation Slides* for each chapter, useful for classes, seminars, workshops. An *Instructor's Manual* is also available upon request with the answers to the proposed questions and problems. Case studies addressing materials preparation among other topics and numerical examples can be found in the *Focus* sections of each chapter. End of chapter *Questions and Problems* are proposed for self-tests and as a reference for assignments/exams to be arranged by instructors.

The authors are thankful to Mr. Mujeeb Oladipupo Kareem for his contribution to the Instructor's Manual and his useful suggestions.

Giovanni Palmisano
Samar Al Jitan
Corrado Garlisi

To access the Instructor's Manual including answers to proposed questions and problems please go to the following website and register to use: https://textbooks.elsevier.com/web/Login.aspx?MREDIR=../web/Manuals.aspx?isbn=9780323898454

CHAPTER 1

Introduction

Catalytic reactions are subdivided into two distinct categories depending on the phases of both the catalyst and the reacting mixture. If the catalyst is in solution with at least one of the reactants, then the process is defined as *homogenous catalysis*. On the contrary, if the process involves more than one phase (e.g., solid catalyst with reactants in the liquid or gas phase), then it is defined as *heterogeneous catalysis*. Of these two types, heterogeneous catalysis is more common. This is mainly attributed to the simple and complete separation of the reaction products from the solid catalyst. Catalysts are quite valuable and their reuse is in high demand. Hence, the possibility of catalyst recycling makes heterogeneous catalysis economically much more attractive.

Today, heterogeneous catalysis plays a key role in many important industrial processes, since it involves c. 80% of the industrial chemical conversions. As such, it is applied in (1) the production of organic and inorganic chemicals, (2) crude oil refining and petrochemistry, (3) environmental protection, and (4) energy-conversion processes. Heterogeneous catalysis takes place through surface reactions, with adsorption of at least one of the reactants on the catalyst surface as the initial step.

A *catalyst* is defined as a substance that increases the rate of a chemical reaction without itself undergoing a chemical change. A good catalyst must possess high activity, the desired selectivity, and long-term stability. The activity of a catalyst may be assessed via different parameters, including its *turnover frequency* (TOF), *conversion*, *yield*, and, most importantly, *selectivity*. These fundamental catalysis terms will be thoroughly defined and explained within this chapter after a historical account of heterogeneous catalysis.

1.1 Historical background

The Swedish chemist Jöns Jacob Berzelius has been credited with coining the term *catalysis* (from the Greek *kata-*, "down," and *lyein*, "loosen") in 1835. In an attempt to connect a series of observations made by other scientists in the late 18th and early 19th centuries, Berzelius concluded that in addition to affinity, there was a further force, namely, the catalytic force, able to trigger decomposition in bodies and form new compounds. Some of the most significant studies that served as a background for Berzelius to formulate the

Heterogeneous Catalysis.
DOI: https://doi.org/10.1016/B978-0-323-89845-4.00001-1

concept of catalysis were the transformation of starch to sugar by acids observed by Gustav Kirchhoff, the enhanced combustion of a variety of gases in the presence of platinum observed by Humphry Davy, and the oxidation of alcohol to acetic acid in the presence of fine platinum powder [1].

In 1834 Michael Faraday observed the catalytic action of platinum that catalyzed the spontaneous combustion of hydrogen and oxygen in water electrolysis. He was the first to introduce the concept of what we know as adsorption and hypothesize that catalytic reaction occurs on the catalyst surface following the simultaneous adsorption of the reactants involved in the process [2]. Presently, water electrocatalysis is being widely applied in the industrial production of high-purity hydrogen [3].

An important contribution to catalysis as we know it now was given by Wilhelm Ostwald in 1897, who defined a catalyst as a material that *modifies the reaction rate without appearing in the final products*, thereby recognizing catalysis as a kinetic phenomenon for the first time [4]. In the same years, Paul Sabatier investigated the hydrogenation reaction catalyzed by metals, such as nickel, other than platinum. He proposed the formation and decomposition of intermediate complexes with the surface catalysts, resulting in a lowering of the Gibbs energy of the system [5].

A fundamental step in catalysis occurred in 1909, when the chemist Fritz Haber discovered that a significant amount of *ammonia* could be generated from hydrogen and nitrogen in the presence of osmium and uranium catalysts. The potential for industrial application of these processes could be increased by working at high pressure, and to that end, the Haber's laboratory apparatus was converted to a high-pressure large-scale industrial apparatus by Carl Bosh. Afterward, Badische Anilin und Soda Fabrik (BASF) started a large program to develop a cheaper and effective catalyst. Alvin Mittasch, together with his colleagues, Wolf and Stern, identified magnetite (Fe_3O_4) as the best candidate for ammonia production [6]. In the wake of these results, in 1923, BASF also developed the first plant for the synthesis of methanol from syngas produced from coal in the presence of ZnO/Cr_2O_3 catalysts operating at c. 400°C and 200 bar [7].

In 1938 Fischer and Tropsch studied the *conversion of syngas* to hydrocarbons and alcohols catalyzed by metals such as cobalt and iron (i.e., Fischer–Tropsch synthesis) [8].

In the early 20th century, a greater understanding of the mechanisms behind the catalytic processes was gained thanks to the studies conducted by Irving Langmuir on *adsorption* and Hugh Stott Taylor on surface *active sites*. The latter especially focused on the heterogeneity of the catalyst surface, which usually presents vacancies, kinks, terraces, ledges, etc., being hosting sites where metal atoms have different coordination numbers and thus catalytic activities [2]. Meanwhile, Stephen Brunauer, Paul Hugh Emmett, and Edward Teller explained the physical adsorption of gas molecules on a solid surface; Eric Rideal,

Mikhail Temkin, Michel Boudart, and many others provided a valuable contribution to a greater understanding of the kinetics of catalytic reactions [9].

In the 1930s catalytic cracking was introduced in the petroleum refining industry. This process allowed to break the C−C bonds in large petroleum molecules, converting them into high-octane fuels using an aluminum chloride catalyst (i.e., Friedel−Crafts catalysts). Yet, the foundation of modern petroleum refining was established in 1942 with the commercialization of *fluid catalytic cracking* (FCC). These processes enabled to maintain the catalyst particles in suspension by a stream of vaporized hydrocarbons blown through the reactor and successively passed through the regenerator [7].

An important landmark was the advent of synthetic *zeolites*, aluminosilicate catalysts, in the 1960s, when amorphous silica−alumina catalysts used in FCC were gradually replaced by synthetic faujasites (zeolites X and Y) (Fig. 1.1). The zeolite catalysts were orders of magnitude more active than the conventional ones and ensured a much higher yield of gasoline, the key product in FCC plants. This type of catalyst, characterized by a broad variety of structures, rapidly found applications in further processes in petroleum refining and basic petrochemistry. Fig. 1.1 shows some of the typical structures, along with the distinctive micropore systems and dimensions of zeolites. Among these, the synthetic zeolite ZSM-5 is one of the most used industrially, being the prototype of shape-selective catalysts and finding application in the synthesis of ethylbenzene, conversion of methanol to gasoline, and isomerization of xylenes [10].

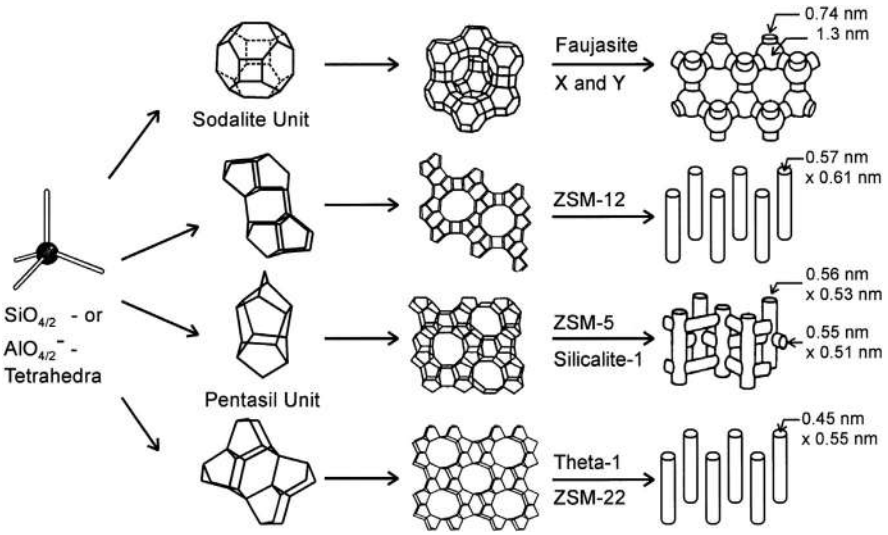

Figure 1.1
Four examples of zeolite structures with their micropore system and dimensions. *Source: Reproduced from [10].*

From the 1960s, the evolution of the transportation industry, the increase in industrial activity, and the severe rise in air-born pollutants have led to the establishment of new laws that regulate vehicle and stationary emissions [11]. Driven by these regulations, global attention and widespread interest in environmental catalysis grew substantially. *Environmental catalysis* addresses problems relating directly to emission control, NO_x removal, volatile organic compound conversion, and waste treatment. Presently, the research focus of environmental catalysis has expanded from pollutant abatement to include pollutant prevention. Accordingly, new catalytic routes have been explored for the synthesis of value-added products without the formation of undesirable pollutants and for the production of new clean fuels with low sulfur content [12].

The engineering of semiconductors, especially of titanium oxide, has led to growing attention toward heterogeneous photocatalysis during the 20th century, which nowadays is a hot topic in applied catalysis for the possibility to efficiently degrade any organic pollutants and produce alternative clean fuels by the irradiation of a catalyst. The earliest reference on photocatalysis dates back to 1911, when Alexander Eibner studied the effect of the illumination of ZnO on the bleaching of Prussian blue. However, in the absence of practical applications, these processes remained a curiosity for much of the 20th century. In the 1970s Akira Fujishima and Kenichi Honda [13] observed the *electrochemical photolysis of water* in a cell consisting of an ionically conducting separator and a rutile TiO_2 electrode irradiated by near-UV light and connected to a platinum counter electrode via an electrical load (Fig. 1.2). The Honda–Fujishima effect attracted the attention of the whole scientific

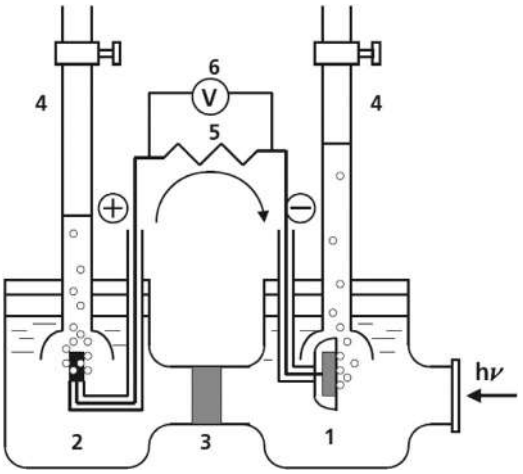

Figure 1.2
Schematic of the electrochemical cell employed by Fujishima and Honda for the photolysis of water: (1) rutile electrode, (2) platinum counter electrode, (3) ionically conducting separator, (4) gas burette, (5) load resistance, and (6) voltmeter. *Source: Reproduced from [14].*

community because of its potential to overcome the dependence on petroleum by producing clean hydrogen from abundant and inexpensive water and sunlight.

Energy-efficient catalytic processes such as those that utilize renewable energy sources have also seen a very fast development [12]. One example is the industrial production of hydrogen through renewable energy-powered water electrocatalysis in a process known as a power-to-gas (PtG). Fig. 1.3 shows the main components of a PtG system in which electricity is converted into hydrogen by water electrocatalysis. The produced hydrogen is stored to be later reconverted back into electricity either through fuel cells or hydrogen combustion engines. Other applications of hydrogen are presented in Fig. 1.3. Solar and wind energy are the most commonly applied renewable energy sources in PtG systems. Due to strong fluctuations in supply, however, renewable power is frequently coupled with public electricity from the grid. As of 2013, 12 pilot-scale PtG systems have utilized solar energy as a source of renewable power for water electrocatalysis, while wind energy has been applied in nine other pilot-scale plants of the same [15].

The application of automotive catalysts as principal emission-control tools in the detoxification of exhaust gases has seen unqualified success. Here, hydrocarbons and carbon monoxide are oxidized into CO_2 and water, while NO_x is reduced to N_2 and O_2. Shortly following their positive implementation in US vehicles of the model year 1975, automotive catalysts were also later adopted in Japan and Europe sometime in the 1980s [16]. Initially, Pt and Pd, in different proportions, were chosen as catalysts for the oxidation reaction. However, after exhibiting a significantly enhanced activity in the catalytic reduction of nitrogen oxides, Rh was also later introduced into the *automotive catalytic system* [17]. Currently, Pd, Pd/Rh, Pt/Rh, and Pt/Pd/Rh catalysts are all in commercial use.

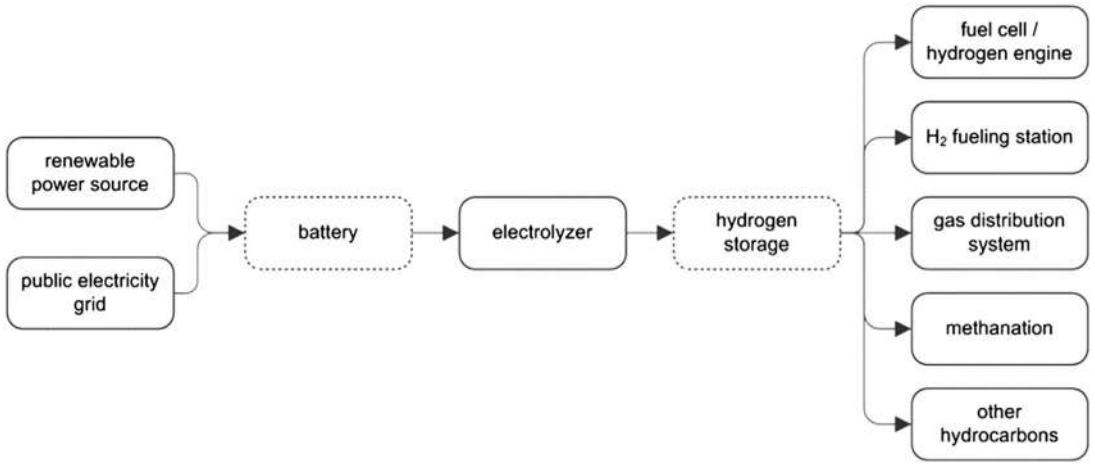

Figure 1.3
The main components of a power-to-gas system and the various types of applications for it.
Source: Reproduced from [15].

In the 21st century, *catalytic asymmetric synthesis* methods, developed by Knowles, Noyori, and Sharpless, have seen great significance in the industrial production of pharmaceuticals and agro-chemicals [18]. Catalytic asymmetric synthesis refers to catalytic methods in which one of the enantiomers is formed in preference to the other. Here, a chiral catalyst is used to produce large quantities of an optically active compound from a precursor that may be chiral or achiral. On this basis, many organic chemists have recently developed numerous methods that convert prochiral substrates into chiral products with high enantioselectivity.

Pd-catalyzed carbon–carbon bond-forming reactions, developed by Heck, Negishi, and Suzuki, have also had a huge influence on synthetic organic chemistry during the 21st century [19]. A large number of natural products and biologically active compounds in the fine chemical and pharmaceutical industries are presently being synthesized by these Pd-catalyzed *cross-coupling reactions*. This is mainly attributed to the mild reaction conditions and the tolerance of a wide range of functional groups. In Pd-catalyzed cross-coupling reactions, two molecules assemble on Pd via the formation of metal–carbon bonds. The carbon atoms bound to Pd are, therefore, in very close proximity to one another. Accordingly, the two carbon atoms couple together and a new carbon–carbon single bond is formed.

Focus 1.1: Effect of Zn:Cr ratio on the structure and reactivity of ZnO/Cr_2O_3 catalysts for methanol synthesis

Advances on the ZnO/Cr_2O_3 catalyst developed by BASF in 1923 for the synthesis of methanol from syngas have been recently achieved by Song et al. [20] who studied the effect of different Zn:Cr ratios—from 100:0 to 0:100—on the catalytic performance. The catalysts with ratios from 65:35 to 55:45 consisted of $ZnCr_2O_4$ spinel with a low degree of crystallinity and high surface area. In particular, the sample with 65:35 exhibited the highest reactivity due to the optimum Zn:Cr ratio corresponding to that of the hydrotalcite-like precursor $Zn_4Cr_2(OH)_{12}CO_3$. This precursor, formed during the synthesis of the catalysts by coprecipitation, decomposed during calcination to the nonstoichiometric Zn–Cr spinel, which is the active phase of ZnO/Cr_2O_3 in methanol synthesis. On the other hand, the lower activity of Cr-rich catalysts was mainly ascribed to the formation of chromates during the calcination, having a detrimental impact on methanol synthesis.

Density functional theory calculations showed that (100) surface of the spinel has favorable oxygen vacancy formation energies. Fig. 1.4 displays the calculated local structure for the spinel with excess 60% Zn content (26.66% doping). The nonstoichiometric surface is terminated by an amorphous-like thin layer of ZnO, which is the active phase for methanol production, since it possesses a low oxygen vacancy formation energy, as well as not too strong adsorption of hydrogen and carbon monoxide.

(*Continued*)

Focus 1.1: Effect of Zn:Cr ratio on the structure and reactivity of ZnO/Cr_2O_3 catalysts for methanol synthesis (Continued)

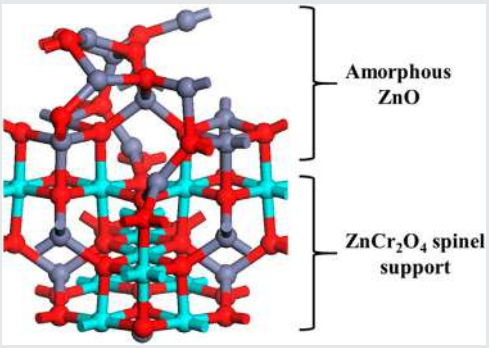

Figure 1.4
Local structure for the spinel structure with 26.66% Zn doping. *Source: Reproduced from [20].*

1.2 Fundamental concepts and quantities in catalysis

1.2.1 Fractional coverage

The extent of surface *fractional coverage* θ indicates the portion of catalytic sites occupied by an adsorbed species (adsorbate) and it can be defined in the following way:

$$\theta = \frac{\text{Number of adsorption sites occupied}}{\text{Total number of adsorption sites}} \tag{1.1}$$

This quantity is usually calculated from the volume of adsorbate adsorbed (V) by $\theta = V/V_m$, where V_m is the volume of adsorbate corresponding to a complete *monolayer* (i.e., a single layer of atoms or molecules adsorbed on the surface of a catalyst). The volumes V and V_m are of the free gas measured in the same conditions of temperature and pressure [21]. When θ reaches the value of 1, the surface catalytic sites are completely occupied, and adsorption of further layers is possible only on top of the first one (multilayer adsorption), as it will be widely discussed in the following chapters.

1.2.2 Catalytic activity

The catalytic activity is related to the ability of a catalyst to change the reaction rate, which, in turn, can be defined in many ways depending on the reaction system. In general, the *reaction rate* (R) is a function of temperature and partial pressure or concentration of the reactants. It can be

expressed as the product of an apparent coefficient (k) and a function (f) of the partial pressure (gas−solid system) or concentration (liquid−solid system) of the reactant i:

$$R = kf(p_i) \text{ (gas−solid system)} \tag{1.2}$$

$$R = kf(c_i) \text{ (liquid−solid system)} \tag{1.3}$$

where p_i and c_i are the partial pressure and concentration of the reactant i, respectively. The reaction rate expresses a change in the number of moles (of a reactant or product) per unit time per unit mass (or surface) of a catalyst. The *rate constant* can be expressed through the Arrhenius equation:

$$k = Ae^{-\left(\frac{E^*}{RT}\right)} \tag{1.4}$$

where A is the preexponential factor not changing with temperature, R is the universal gas constant, T is the absolute temperature, and E^* is the apparent *activation energy*. E^* is usually different from the true activation energy since the concentration of the reactant at the catalyst surface may be temperature dependent, although the catalyst structure may not be affected by temperature changes. To avoid resorting to the activation energy, most of the time catalytic activity is expressed in terms of *TOF*, which is defined as the number of molecular reactions or catalytic cycles (n) per active site of the catalyst per unit time. Being a reaction rate, *TOF* depends on the reaction conditions including temperature and composition of the reacting system. In general, *TOF* can be expressed as:

$$TOF = \frac{1}{S}\frac{dn}{dt} \tag{1.5}$$

where t stands for reaction time and S indicates the number of active sites. For the most relevant heterogeneous catalytic reactions in industry, TOF is in the range of 10^{-2}–10^{2} s^{-1}. The main difficulty in determining TOF lies in counting active sites. Moreover, sites may not be all identical. In such situations, S is usually replaced by the total exposed area, mass, or volume of the catalyst [7].

Fig. 1.5 presents the results of a study conducted on the catalytic gas-phase hydrogenation of *p*-nitrobenzonitrile (*p*-NBN) to *p*-aminobenzonitrile (*p*-ABN) using a series of oxides as support for the catalyst consisting of gold (Au) particles with a mean size 3−8 nm. Different supports resulted in different Au nanoparticle sizes, impacting the hydrogen chemisorption (Fig. 1.5A) and *TOF* (Fig. 1.5B). The variation of the *TOF* with the mean Au size coincided with that observed for H_2 uptake, indicating a strong correlation between the hydrogenation rate and H_2 dissociation capacity. The reduced *TOF* at small Au size (<3 nm) is due to the semiconducting properties of the catalysts to the detriment of the metallic ones [22].

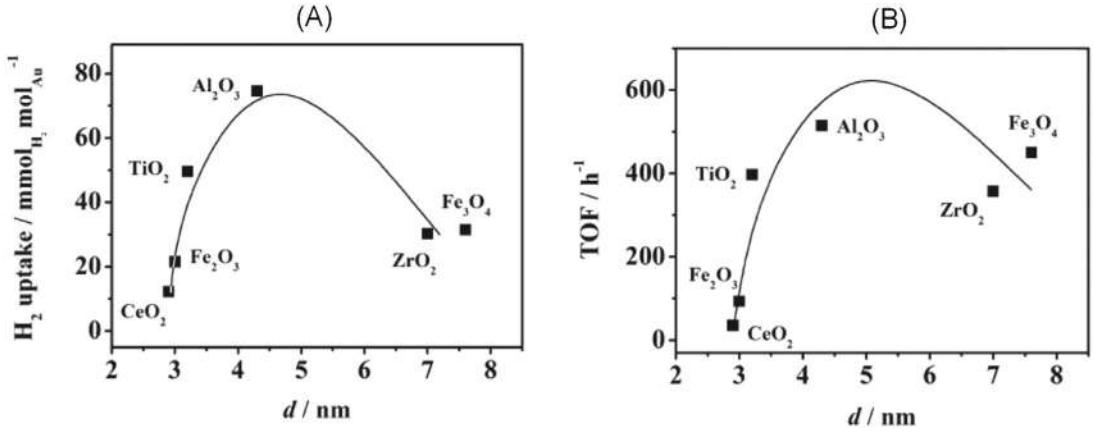

Figure 1.5
Variation of (A) H_2 uptake and (B) TOF of p-NBN with metal particle size for the hydrogenation of p-nitrobenzonitrile over Au catalysts supported on various oxides. *Source: Reproduced from [22].*

Focus 1.2: Single-atom catalysis for hydrogen evolution reaction

Single-atom catalysis has been a hot topic in research over the last few years. Given the high cost of many catalytic materials, especially noble metals, reducing the nanostructures to atomically distributed metal centers supported on a suitable catalyst can considerably decrease metal usage and maximize atom efficiency. A recent study in this area reports the enhanced catalytic activity of a single-atom Pt supported on nanoporous (np) nonstoichiometric cobalt selenide (denoted as Pt/np-$Co_{0.85}Se$) catalyst [23]. The atomic engineering of np-$Co_{0.85}Se$ by single Pt atoms doping is an effective strategy to produce a robust electrocatalyst for hydrogen evolution reaction (HER), ensuring a TOF much higher than those achieved by np-$Co_{0.85}Se$ alone and many reported catalysts.

Fig. 1.6 depicts the schematic of the HER mechanism over Pt/np-$Co_{0.85}Se$ in neutral media. The water molecules are selectively adsorbed on the Co sites. Later on, H_2O is dissociated into intermediate H_{ads} and OH_{ads} by Co sites. The formed H_{ads} can be adsorbed on a nearby empty Co site or Pt site and be finally converted into H_2.

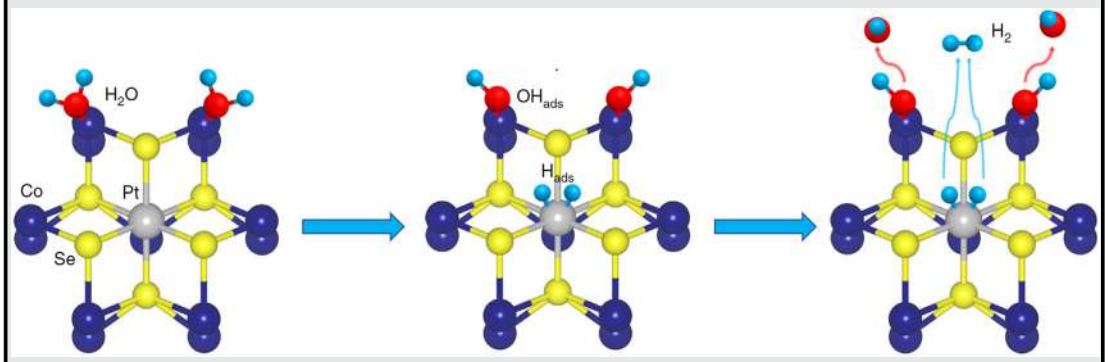

Figure 1.6
Schematic illustration of the HER mechanism over np-$Co_{0.85}Se$ catalyst. *HER*, Hydrogen evolution reaction. *Source: Readapted from [23].*

The stability of the reaction intermediates formed at the surface of the catalyst plays a significant role in determining the rate of a catalytic reaction. According to *Sabatier*'s idea, the intermediate should be stable enough to be formed but not too stable, as it must decompose and evolve into the products. This principle can be represented graphically by *volcano-shaped plots* that were first introduced by Baladin. In these diagrams, a measure of the catalytic activity such as the reaction rate, *TOF*, temperature at a fixed conversion/ reaction rate, etc. is plotted against a measure of the *stability of the reaction intermediate* such as its enthalpy of formation.

Fig. 1.7A shows the typical volcano plot for the metal-catalyzed decomposition of formic acid, where the temperature for a specific reaction rate is plotted against the heat of formation (ΔH_f) of the reaction intermediate, namely, metal formate, at a fixed conversion (Section 1.2.3) [24]. At low ΔH_f, the rate of adsorption is low and rate-limiting due to the little predisposition of the metal formate to form. On the other hand, at high ΔH_f, the low rate of desorption becomes rate-limiting. The peak of the volcano, namely, the highest catalytic activity, is observed for platinum group metals, which are characterized by intermediate values of ΔH_f, for which the two conflicting effects are balanced and the resulting reaction rate is a combination of the rate of adsorption and rate of desorption.

Fig. 1.7B displays the volcano plot for the electrocatalytic HER on various catalysts [25]. The current density J_0 (i.e., rate of oxidation and reduction at an equilibrium electrode) is plotted versus the Gibbs free energy for hydrogen adsorption ΔG_{H^*}, which is a good descriptor of the intrinsic activity of a metal catalyst for this reaction. The catalysts to the left of Pt bind hydrogen atoms too strongly, blocking the active sites and failing to give rise

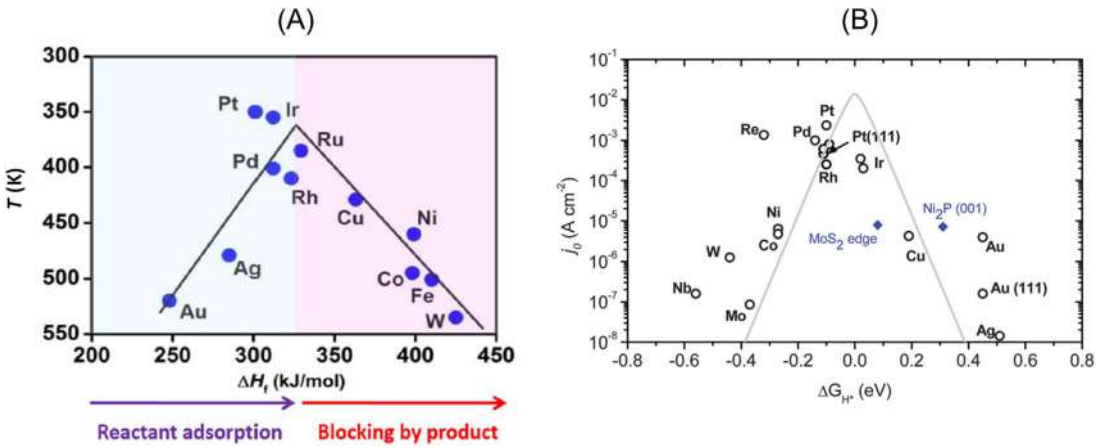

Figure 1.7

Volcano plot for (A) decomposition of formic acid on various transition metals and (B) hydrogen evolution reaction on different catalysts. *Source: (A) Reproduced from [24]. (B) Reproduced from [25].*

to the development of hydrogen. Conversely, the catalysts to the right of Pt bind hydrogen too weakly, thus not stabilizing the intermediate state and precluding the reaction to occur.

Cocatalysts can be used to boost catalytic activity by acting as further reaction sites, improving the stability of the catalyst or promoting the charge separation and transport, the latter being the case of photocatalytic processes. Here, the loading of the light-harvesting photocatalyst with a metal cocatalyst such as platinum, palladium, and copper is the most popular way to promote the activity, for example, in the water photosplitting. The cocatalyst can indeed capture the photogenerated electrons and suppress hole−electron recombination, lower the activation energy for H_2 generation, as well as act as a reaction site for the reduction of protons [26]. Cocatalysts can also serve as initiators of polymerization reactions. For instance, cocatalysts such as methylaluminoxane (MAO) act as activating species for the catalyst in metal-catalyzed polymerization processes [27].

Catalyst support also plays an integral part in the catalytic performance, primarily because it brings out the capability of the supported catalyst to act as an active center for the target reaction. The support may be inert or participate in the catalytic process. Typical materials for catalyst supports include alumina, titania, graphite, activated carbon, and silica, which exhibit a high surface area, chemical and mechanical stability, and ability for dispersing catalyst particles over the surface [28]. The reader is referred to Section 3.4 for more details on cocatalysts and supports.

1.2.3 Conversion, yield, and selectivity

The progress of a heterogeneous reaction can be characterized by three main quantities: conversion, yield, and selectivity.

The *conversion* designates the consumption of the reactant(s). It can be defined as the ratio of the number of moles of the reactant A consumed to the number of moles of A fed. At a constant fluid density, the conversion of A at the time t ($X_A(t)$) can be calculated by the following equation:

$$X_A(t) = \frac{C_A^0 - C_A(t)}{C_A^0} \tag{1.6}$$

where C_A^0 is the initial concentration and $C_A(t)$ is the concentration at the time t. If density changes, concentrations must be replaced by molar quantities in batch reactors or by molar flows in flow reactors. In the presence of multiple reactants charged in nonstoichiometric amounts, the conversion is calculated with respect to the limiting reactant.

The *yield* refers to the product formations. The yield of a product B at a time t ($Y_B(t)$) can be expressed as the ratio of the number of the limiting reactant A converted to B to the initial number

of moles of the limiting reactant A. At a constant density, for the reaction ν_A A$\rightarrow\nu_B$ B, where ν_A and ν_B are the relevant stoichiometric coefficients, the yield of B can be calculated as follows:

$$Y_B(t) = \frac{C_B(t) - C_B^0}{C_A^0} \quad \frac{\nu_A}{\nu_B} \tag{1.7}$$

The *selectivity* of a catalyst is indicative of its ability to direct the reaction to yield a particular product, while inhibiting the formation of others. A catalyst affects the selectivity of a reaction, resulting in reaction pathways, and thus products, which are not possible in the same noncatalytic system. At constant fluid density, the selectivity of the product B at a time t ($S_B(t)$) can be calculated as:

$$S_B(t) = \frac{C_B(t) - C_B^0}{C_A^0 - C_A(t)} \quad \frac{\nu_A}{\nu_B} \tag{1.8}$$

The selectivity can also be defined in relation to the reaction rates. In the case of parallel reactions, the reactant A can react to give two products, B and C, at rates R_1 and R_2, respectively, over the same catalyst (Eqs. 1.2–1.3). During the reaction, B can also react to give C at a rate R_3. The situation is depicted in Scheme 1.1.

The selectivity S to product B can be expressed as:

$$S = \frac{R_1 - R_3}{R_1 + R_2} \tag{1.9}$$

If B is not converting to C ($R_3 = 0$), the selectivity to B becomes:

$$S = \frac{R_1}{R_1 + R_2} \tag{1.10}$$

The formation of the desired product can be thus accelerated by using an appropriate catalyst able to modify the reaction kinetics accordingly, although the formation of undesirable products may be thermodynamically favored. A catalyst thereby changes the ratio of the rates by selectively increasing the rate at which the targeted reaction proceeds with respect to the other competing reactions.

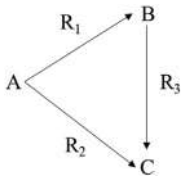

Scheme 1.1
Schematic of parallel reactions in which one of the two products can evolve to the other.

It is clear that *a catalytic reaction can proceed differently depending on the catalyst employed*. One important example is the reaction of carbon monoxide and hydrogen which can lead to the formation of different products using different catalytic systems. A nickel catalyst can selectively favor the formation of methane [29]. On the other hand, when copper-based and/or a mixture of zinc oxide and chromium oxide ($ZnO-Cr_2O_3$) is used as a catalyst, methanol is the main product [30]. Still, formaldehyde is the selective product in the aqueous phase in the presence of a catalyst consisting of a mixture of ruthenium and nickel–alumina ($Ru-Ni/Al_2O_3$) [31].

$$CO(g) + 3H_2(g) \xrightarrow{Ni} CH_4(g) + H_2O(g) \tag{1.11}$$

$$CO(g) + 2H_2(g) \xrightarrow{Cu-based,ZnO/Cr_2O_3} CH_3OH(g) \tag{1.12}$$

$$CO(l) + H_2(l) \xrightarrow{Ru-Ni/Al_2O_3} HCHO(l) \tag{1.13}$$

Another example concerns the selective oxidation of hydrocarbons. The noncatalytic process yields the two most thermodynamically favored products, namely, CO_2 and H_2O. Nevertheless, selective catalytic oxidation can give rise to the corresponding aldehydes and/or ketones, by selective insertion of oxygen, or alkenes, by selective removal of hydrogen [32]. Finally, in the automotive three-way converters, NO reacts with CO and is reduced to the desired product, namely, N_2, over rhodium catalyst, while it can be converted to a pollutant, that is, NH_3, if the reaction is catalyzed by Pt catalyst [11].

It is important to note that the product *selectivity can be controlled and adjusted* in many ways such as the structural, chemical, electronic, compositional, and morphological alteration of the catalyst. Yet, certain catalysts rely on the molecular sieve effect, showing selectivity toward a reactant or product depending on its shape or size of molecules. Two catalysts identical from the chemical standpoint, but with pores of different sizes, may show different selectivities. For instance, zeolites are microporous catalysts with cages of molecular dimension that selectively accept or reject certain reactants or products depending on their pore size. In addition to reactant and product selectivity, they may also present restricted transition-state selective mechanisms, preventing certain reactions due to the restricted space available for the corresponding transition states [33].

Focus 1.3: Enzymes as a source of inspiration for the development of tailor-made catalysts

The way the catalyst interacts with the reacting molecules, and ultimately its activity and selectivity, depends on a number of factors that include experimental setup, operating conditions (e.g., temperature and pressure) and physicochemical properties of the catalyst.

(*Continued*)

Focus 1.3: Enzymes as a source of inspiration for the development of tailor-made catalysts (Continued)

In the rational design of tailor-made catalysts, enzymes (naturally occurring biocatalysts) have acted as a source of inspiration for scientists to tune the physicochemical properties of catalysts [34]. Many enzymes rely on a well-confined space, that is, the cage, around the active centers to ensure the proximity of these to the substrate molecules. Moreover, they can preorganize the substrate in a favorable energy conformation in the cage, which can also destabilize intermediates and reduce the transition state barrier leading to an increased reactivity [35,36]. These concepts have been extremely useful for the development of catalysts such as *zeolites, metal-organic frameworks (MOFs), covalent-organic frameworks (COFs)*, which rely on the so-called confinement effect to govern the activity and selectivity.

MOFs are a relatively novel class of catalysts consisting of two main components, that is, inorganic vertices (metal ions or clusters) and organic linkers arranged in an ordered, highly porous heterogeneous network (Fig. 1.8). The molecular diversity and the tunable character of these building blocks enable an almost infinite variety of MOFs. The main advantage of this type of catalyst is indeed the ease of adjusting their physicochemical properties through modifying their organic ligands, metal centers, active functional groups, or yet by tuning their morphology [37]. Moreover, the confined space of MOFs involves a high surface area with enhanced and monodisperse loading of catalytically active species, which can lead to better performance compared to traditional catalysts.

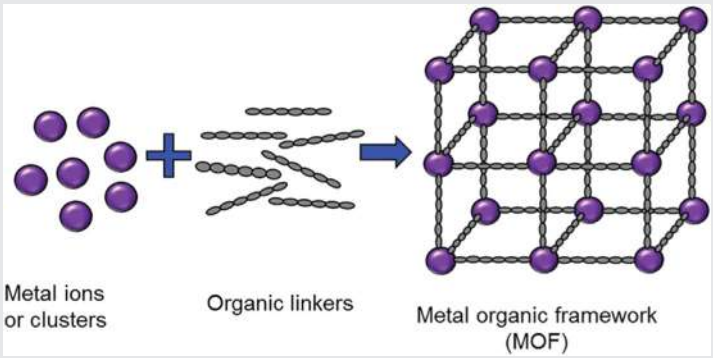

Figure 1.8
Schematic structure of the MOF. *MOF*, Metal-organic framework. *Source: Reproduced from [38].*

Focus 1.4: Numerical examples of fundamental quantities in catalysis

- Surface coverage

The adsorption of O_2 on mesoporous Al_2O_3 leads to the formation of a monolayer with volume $V_m = 60\ cm^3\ g^{-1}$. Calculate the volume V of adsorbed O_2 when $\theta = 0.25$.

(*Continued*)

Focus 1.4: Numerical examples of fundamental quantities in catalysis (Continued)

Solution

By rearranging Eq. (1.1), V can be calculated as:

$$V = \theta V_m = 0.25 \times 60\,\text{cm}^3\,\text{g}^{-1} = 15\text{cm}^3\text{g}^{-1}$$

- Reaction rate and TOF

Consider the following second-order catalytic liquid-phase reaction run at a temperature of 500K:

$$2\text{A} \rightarrow \text{B}$$

A mixture of zinc oxide and iron oxide (ZnO/Fe_3O_4) is used as a catalyst for the reaction. The initial concentration of A (C_{A0}) is 0.12 mol L^{-1}. The preexponential factor A in the Arrhenius equation is 1200 L^2 mol^{-1} g^{-1} s^{-1} and the activation energy E_a is 3.0 kJ mol^{-1}. Knowing that the number of adsorption sites in the catalyst is 0.63 mol g^{-1}, calculate the initial TOF.

Solution

The second-order rate constant can be calculated by the Arrhenius equation:

$$k = Ae^{-\left(\frac{E_a}{RT}\right)} = 1200\text{L}^2\text{mol}^{-1}\text{g}^{-1}\text{s}^{-1} \times \text{e}^{-\left(\frac{3.0\times10^3\ \text{Jmol}^{-1}}{8.314\ \text{Jmol}^{-1}\text{K}^{-1}\times 500\text{K}}\right)} = 583.1\text{L}^2\text{mol}^{-1}\text{g}^{-1}\text{s}^{-1}$$

The initial reaction rate R_0 can be obtained as follows:

$$R_0 = k[C_{A0}]^2 = 583.1\ \text{L}^2\text{mol}^{-1}\ \text{g}^{-1}\text{s}^{-1} \times 0.12^2\text{mol}^2\ \text{L}^{-2} = 8.4\ \text{mol}\ \text{g}^{-1}\text{s}^{-1}$$

The initial TOF per gram of catalyst can be obtained as follows:

$$\text{TOF} = \frac{R_0}{\text{Number of adsorption sites}} = \frac{8.4\ \text{mol}\ \text{g}^{-1}\text{s}^{-1}}{0.63\ \text{mol}\ \text{g}^{-1}} = 13.3\text{s}^{-1}$$

- Conversion, selectivity, yield

A photocatalytic batch reactor is fed with an aqueous solution of toluene (A) having an initial concentration of 0.75 M. Toluene is selectively oxidized to benzaldehyde (B) using a TiO_2 catalyst under UV irradiation. During the photocatalytic process, a small fraction of the formed benzaldehyde is converted to benzoic acid (C). After 30 min of reaction, the product contains the three compounds with the following concentrations: $C_A = 0.21$ M, $C_B = 0.45$ M, $C_C = 0.05$ M. Calculate X_A, S_B, S_C, Y_B, and Y_C.

Solution

$$X_A = \frac{C_{A0} - C_A}{C_{A0}} = \frac{0.75 - 0.21}{0.75} = 0.72$$

$$S_B = \frac{C_B}{C_{A0} - C_A} = \frac{0.45}{0.75 - 0.21} = 0.83 \qquad S_C = \frac{C_C}{C_{A0} - C_A} = \frac{0.05}{0.75 - 0.21} = 0.09$$

$$Y_B = \frac{C_B}{C_{A0}} = \frac{0.45}{0.75} = 0.60 \qquad Y_C = \frac{C_C}{C_{A0}} = \frac{0.05}{0.75} = 0.07$$

Focus 1.5: Synthesis techniques for catalytic materials

The preparation methods of catalytic materials are largely described in the literature [39–41]. Tables 1.1 and 1.2 summarize the main techniques used to synthesize bulk and supported catalysts [42]. It is a common practice to deposit the as-prepared bulk catalysts on support (Section 3.4.1), in the form of nanoparticles or yet as a thin film, that is, materials ranging from fractions of a nanometer to several micrometers in thickness. Thin films can also be deposited directly from solid or gaseous precursors, such as in physical vapor deposition and chemical vapor deposition techniques, without the need to first synthesize bulk catalysts in powder form.

Table 1.1: Main synthesis techniques for bulk catalysts.

Technique	Description
Sol–gel	A colloidal suspension (sol), obtained from liquid solutions of organometallic or inorganic precursors, evolves to a three-dimensional network with a highly viscous material (gel). The removal of the remaining liquid (solvent) phase then occurs via a drying process.
Precipitation/ coprecipitation	A solid phase is formed from a solution by adjusting temperature and pH so that the concentration of the compounds exceeds their solubility.
Hydrothermal/ solvothermal	The catalyst is prepared from high-temperature aqueous solutions at high vapor pressures.
Solid-state reactions	The starting material is a mixture of solids that react at high temperatures. The diffusion of atoms or ions results in a layer of the reaction products which is boosted by chemical reaction with the reactants adjacent to its boundaries.
Spray pyrolysis	Precursor droplets formed by atomization are transported by a gas carrier to a high-temperature zone of the reactor where the droplets are heated and pyrolyzed.

Table 1.2: Main synthesis techniques for supported catalysts.

Technique	Description
Deposition–precipitation	A catalytically active precursor is deposited onto a support suspended in solution by a chemical reaction in the liquid phase. A precipitant is then added slowly under vigorous mixing.
Impregnation	The active precursor is attached to a support. The liquid solvent is then evaporated, followed by calcination to convert the precursor into the desired form.
Wet coating technologies (thin-film preparation)	A liquid precursor is applied to a substrate (glass, silicon) and converted to the desired material by successive post-treatment steps. Typical examples are spin-coating and dip-coating
Chemical vapor deposition (thin-film preparation)	One or more volatile precursors react and/or decompose in the vapor phase in the proximity of or on the heated substrate.
Physical vapor deposition (thin-film preparation)	The source material is changed from the solid phase to the vapor phase and then is deposited on a substrate surface, by returning to a condensed phase. The most common Physical Vapor Deposition processes are evaporation and sputtering.

1.3 Importance of heterogeneous catalysis in today's industry

Heterogeneous catalysis plays a dominant role in today's industry since c. *80% of the industrial processes* rely on catalysis at some production step, spanning from the petroleum industry to the production of commodities (i.e., NH_3 and sulfuric acid) and synthesis of fine chemicals such as pharmaceuticals [43]. In terms of production volumes, the most important industrial processes making use of heterogeneous catalysis are summarized in Table 1.3. The reagents, target products, and used catalysts, typically *metals, metal oxides,*

Table 1.3: Most important industrial processes making use of heterogeneous catalysis.

Process	Catalyst	Reactants	Target products
Ammonia synthesis	Fe_3O_4	N_2, H_2	NH_3
Nitric acid production	Pt or Rh	NH_3, O_2	HNO_3
Sulfuric acid production	V_2O_5	S, O_2, H_2O	H_2SO_4
Methanol production	Cu-based, ZnO/Cr_2O_3	CO, H_2	CH_3OH
Olefin hydrogenation	Ni	Alkenes	Corresponding Alkanes
Olefin metathesis	Re, Mo, Re_2O_7, WO_3 etc.	Alkenes	Alkenes with a different structure upon splitting of the $-C=C-$ bond and exchanging of alkylidene fragments
Catalytic cracking	Zeolite Y	High-boiling and high-molecular-weight hydrocarbons of petroleum crude oils	Monomeric or dimeric aromatics, shorter chain linear, and branched alkane and alkene molecules
Catalytic steam reforming	Ni on Al_2O_3-MgO	CH_4, H_2O	CO, H_2
Catalytic reforming	Pt and/or Re on alumina	Naphthas distilled from crude oil	High-octane liquid products
Ethylene oxide production	Ag on Al_2O_3	C_2H_2, O_2	C_2H_4O
Fischer–Tropsch process	Fe, Co or Ru	CO, H_2	Mixture of gasoline and diesel-range molecules
Polymerization of alpha-olefins	Ziegler–Natta catalysts (i.e., mixtures of halides of transition metals with organic derivatives of nontransition metals)	Alpha-olefins	Polymers of alpha-olefins
Hydrodesulfurization, hydrodenitrogenation	Co/MoS_2 or Ni/WS_2	Crude oil or products of cracking	Crude oil or products of cracking without organic sulfur- and nitrogen-containing components

or zeolites, are also reported in the table. A brief description of some of these processes and their corresponding catalysts are presented in the following.

1.3.1 Ammonia synthesis

After sulfuric acid, ammonia (NH_3) is the most highly produced industrial chemical (c. 146 million tons per year). It is mostly used in the manufacture of fertilizers, but it also plays an important role in the production of plastics, nitric acid, explosives, fibers, and other chemicals such as refrigerants.

Most ammonia is synthesized on a large scale by the *Haber process*, which combines nitrogen from the air with hydrogen from natural gas or, more rarely, naphtha.

Typical ammonia-producing plants rely on more than one catalytic process, showcasing how heterogeneous catalysis is well integrated into the modern industrial chain. In the first step, methane is converted into hydrogen via catalytic steam reforming, while in the second one, the produced hydrogen reacts with nitrogen to form ammonia via the Haber process. The flow diagram of a typical process of ammonia production is shown in Fig. 1.9.

Before steam reforming, the feedstock passes through a desulfurization unit at 300°C–400°C and 30–130 atm in order to remove sulfur compounds that can poison the catalysts used in the following steps. In this process, the organic sulfur compounds are converted to hydrogen sulfide, which is then adsorbed and removed by passing it through beds of zinc oxide. The hydrogenation reaction can be catalyzed by a number of catalysts including *ruthenium disulfide (RuS_2), cobalt-modified molybdenum disulfide (MoS_2)*, or a mixture of cobalt and molybdenum.

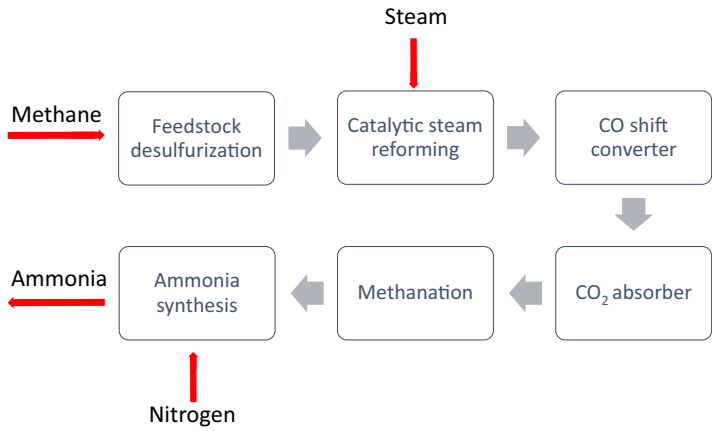

Figure 1.9
Typical flow diagram of an ammonia production plant.

$$H_2(g) + RSH(g) \rightarrow RH(g) + H_2S(g) \quad (1.14)$$

$$ZnO(s) + H_2S \rightarrow ZnS(s) + H_2O(g) \quad (1.15)$$

In the catalytic steam reforming, methane is converted to synthesis gas after reacting with steam over a *nickel* catalyst, finely dispersed on an alumina support. *Cobalt and noble metals* are also active, but more expensive than nickel. Operating temperature and pressure are in the range 495°C–525°C and 5–45 atm, respectively. A secondary reforming unit is normally used to convert the residual methane at the exit of the first unit:

$$CH_4 + H_2O \rightarrow CO + 3H_2 \quad (1.16)$$

The synthesis gas is thus sent to a CO shift converter where CO is converted to CO_2 and additional H_2 over an iron/chromium(III) oxide catalyst at a temperature of 400°C–450°C and pressure 1–85 atm. In a second shift converter, the concentration of CO is further decreased by passing the syngas over a copper oxide/zinc oxide catalyst at a lower temperature (c. 220°C).

$$CO + H_2O \rightarrow CO_2 + H_2 \quad (1.17)$$

Afterward, the CO_2 is removed by scrubbing the gas with a solution of aqueous ethanolamine. At the exit of the scrubber, the residual amounts of CO and CO_2 are removed from the H_2 gas by catalytic methanation in the presence of a nickel catalyst at temperatures and pressures in the range 400°C–600°C and 1–30 atm, respectively.

$$CO + 3H_2 \rightarrow CH_4 + H_2O \quad (1.18)$$

$$CO_2 + 4H_2 \rightarrow CH_4 + 2H_2O \quad (1.19)$$

Hydrogen from the methanator is finally delivered to a fixed bed reactor where it reacts with nitrogen in stoichiometric proportion to form ammonia via the Haber process. The catalyst is Fe_3O_4 with some promoters such as potassium hydroxide. The typical operating temperature and pressures are in the range 330°C–430°C and 100–200 atm.

1.3.2 Sulfuric acid production

Sulfuric acid (H_2SO_4) is the largest volume industrial chemical manufactured in the world (c. 200 million tons per year). It is used to make a broad spectrum of end-use products such as fertilizers, explosives, dyes, inorganic salts and acids, and electrolytes in lead-acid batteries and it is a key chemical in oil refining and mineral processing.

Industrially, it is manufactured by two main methods, namely, the *lead-chamber process* and the *contact process*. The first one allows the production of relatively dilute acid (<78%), mainly intended for the fertilizer sector, while the second process produces a more

concentrated acid. Both processes start from solid sulfur or iron pyrite which are burned in the air at c. 1000°C to produce sulfur dioxide (SO_2). In the lead-chamber process, nitrogen oxide generated from the decomposition of niter (KNO_3) is used as a gaseous catalyst for the production of sulfur trioxide (SO_3) and H_2SO_4 from SO_2 in a series of chambers of sheet lead.

The contact process makes use of a *vanadium oxide catalyst (V_2O_5) on silica* at a temperature of 400°C–450°C and pressure of 1–2 atm, to promote the oxidation of SO_2 to SO_3, whose kinetics are extremely slow in the absence of a catalyst. These catalytic reactions involve two main steps: (1) oxidation of SO_2 into SO_3 by V^{5+}, which is reduced to V^{4+} and (2) catalyst regeneration during which V^{4+} is oxidized back to V^{5+} by O_2. The V_2O_5 catalyst is typically in the form of pellets and contains a promoter such as cesium sulfate to prevent its melting at the operating temperatures. The reactor used for this process is a fixed bed reactor, which usually contains four separate catalytic beds. After the catalytic steps, SO_3 is delivered to an absorption tower where it is made to react with concentrated H_2SO_4 to form oleum (i.e., $H_2S_2O_7$). Finally, oleum is mixed with water in a dilution tank to obtain concentrated H_2SO_4.

1.3.3 Catalytic cracking

Catalytic cracking is one of the most crucial conversion processes employed in the petroleum refining industry. It can be applied to a range of feedstock spanning from gas oil to heavy oil and sand bitumen, which are converted to high-value products including LPG, gasoline, diesel, and slurry oil. Catalytic cracking presents a series of advantages compared to thermal cracking such as lower operating temperature and pressure, more flexibility in terms of product slates, characterized by a higher octane number and higher yields of gasoline, C_4 olefins, and aromatics [44]. Today, FCC units are implemented in about 400 refineries around the world and this process is considered one of the most important industrial achievements of the 20th century.

A typical *FFC unit* is shown in Fig. 1.10A. A small fraction of the feedstock is usually burned in the regenerator, providing the heat required for cracking. On the other hand, the hot catalyst is mixed with the preheated feedstock in the bottom part of the riser reactor at a temperature of about 550°C. The cracking reactions and the formation of gases cause the expansion of the reacting mixture, which reaches the upper part of the reactor at a temperature of c. 500°C. After being separated from the mixture and stripped of the residual products, the catalyst is sent to the regenerator, where the coke is burned off at c. 760°C and finally recirculated back to the riser reactor.

As shown in Fig. 1.10B, the catalyst system includes a series of components, among which a stabilized form of *zeolite Y* is the catalytic one. This zeolite is characterized by microchannels that connect its so-called supercages through 12-ring openings [46]. The acid

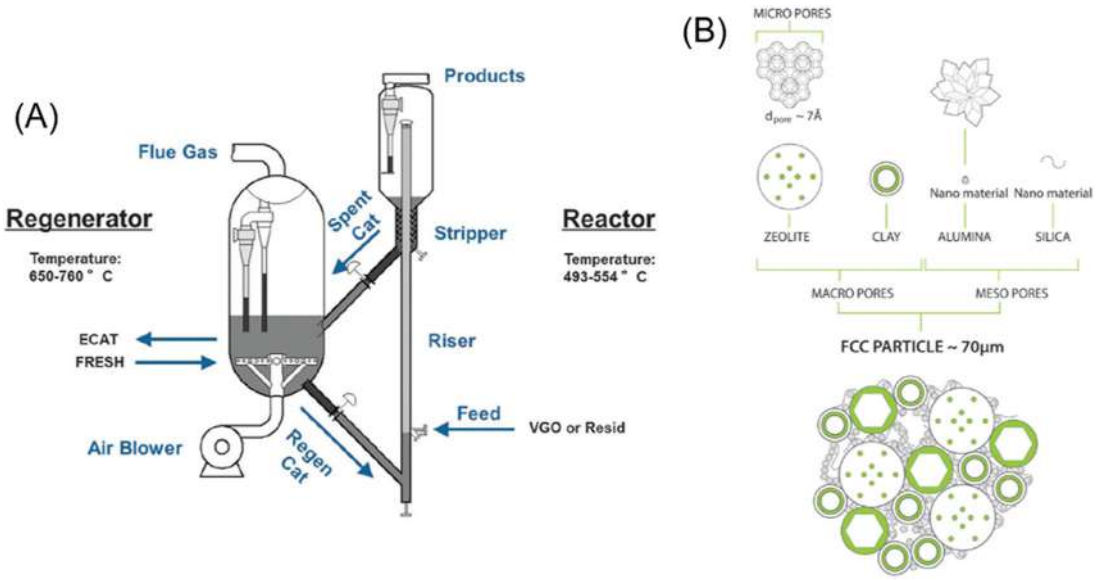

Figure 1.10
(A) Schematic of the FCC process and (B) typical structure of a particle used in the catalytic system of FCC. *FCC*, Fluid catalytic cracking. *Source: (B) Reproduced from [45].*

sites in the internal micropores allow larger molecules to be converted to the desired gasoline range hydrocarbons. The other elements of the catalytic systems are clay which serve as filler, alumina, and silica particles which increase the meso- and microporosity of the matrix, enabling the access and the precracking of the larger hydrocarbons in the feed.

1.3.4 Polymerization of alpha-olefins

Alpha-olefins have a wide range of applications such as comonomers for polyethylene, synthetic lubricants, surfactant intermediates, and oils for synthetic drilling fluids. The fabrication of polymers such as *polyethylene* and *polypropylene* is by far the most important application of this family of organic compounds that are usually polymerized over *Ziegler–Natta catalysts*, named after the two chemists Karl Ziegler and Giulio Natta. These catalysts consist of a mixture of metals and organic derivatives of nontransition metals. Typical examples of Ziegler–Natta catalysts are $TiCl_4 + Et_3Al$ and $TiCl_3 + AlEt_2Cl$. This class of catalysts offers many advantages over the noncatalyzed radical polymerization stymied by lack of control over stereochemistry and formation of allylic radicals that are precursors of undesired branched polymers. On the other hand, Ziegler–Natta catalysts restrict the addition of monomer units to a specific regular orientation (i.e., tacticity), finely control the average molecular weight, and grant narrow distributions of the molecular weights.

The reaction involved in the polymerization process consists of four main steps: *initiation, propagation, transfer, and termination*. The polymerization starts with the alkylation of the transition metal in the catalyst bearing the positive charge and proceeds with the insertion of monomer olefins into the developing chains. The process stops when the formed chain is disengaged from the active center, usually through β-hydride elimination. Afterward, the formed metal hydride can often give rise to a further polymerization reaction (β-hydride transfer reaction) [46]. The molecular weight is controlled through the addition of appropriate quenching agents that deactivate the catalyst. Yet, the stability of the chemisorbed catalytic complex is one of the most important factors affecting stereoselectivity. This usually depends on the defects of the catalysts, surface energy of the crystal lattice, and the radius of the metal species bound to the metal-organic compound.

1.4 Questions and problems

1. Prepare a report on three disrupting innovations in the field of catalysis which took place in 20th century. Look into the last 10-year literature to analyze their current state of the art and assess the development grounds.
2. If the TOF of catalyst A is greater than that of catalyst B for a given reaction, what can you conclude?
3. Can the yield toward a certain product be greater for catalyst A versus catalyst B if the selectivity is greater for B versus A? Why?
4. Study the thermodynamics Eqs. (1.11−1.12) and comment on the spontaneity of these reactions and on the enthalpic effects (run a literature search to collect the needed thermodynamic data). Explain which improvements the introduction of a catalyst can bring about.
5. Explain why the enthalpy of formation for a reaction intermediate on the surface of a catalyst can affect the activity.
6. Perform a literature search on recent studies in which vanadium oxides were used as catalysts, discuss the mechanism of reaction, and assess their performance in comparison with alternative catalysts.
7. The catalytic reaction $2A \rightarrow B + 3C$ has a rate constant of 0.142 $L^2\ mol^{-1}\ g^{-1}\ s^{-1}$ at 298K and 0.556 $L^2\ mol^{-1}\ g^{-1}\ s^{-1}$ at 475K. Calculate the activation energy for the reaction.
8. A catalyst allows to reduce the activation energy of a reaction from 15 to 3 kJ mol^{-1}. Assuming that the preexponential factor in the Arrhenius equation does not change and that the temperature is 325K in both cases, by what factor is the reaction rate accelerated?
9. The initial formic acid decomposition rate at 473K over a Ru/C catalyst follows a first-order kinetics with a kinetic constant of 3.2×10^{-4} L $g^{-1}\ s^{-1}$. The initial

concentration of formic acid is 1.2 mol L^{-1} and the total number of adsorption sites is 5.0×10^{-3} mol g^{-1}. Calculate the initial TOF.

10. Consider the following reactions:

    A → 2B(desired)

    A → C(undesired)

    A batch reactor is fed with 90 mol of A. The final product consists of 8 mol of A, 140 mol of B, and 8 mol of C. Calculate (1) the conversion of A, (2) the yield of B, and (3) the selectivity of B relative to C.

11. Consider the following catalytic first-order liquid-phase reactions:

    A → B(desired)

    A → C(undesired)

    The initial concentration of A is 0.5 mol L^{-1} and the temperature is 400K. The desired reaction has a preexponential factor of 1.0×10^{14} L g^{-1} s^{-1} with an activation energy of 75 kJ mol^{-1}. The undesired reaction has a preexponential factor of 0.2×10^{14} L g^{-1} s^{-1} with an activation energy of 85 kJ mol^{-1}. Calculate the selectivity toward the desired product B.

12. Consider the catalytic liquid-phase reactions between A and B which gives rise to the reaction intermediate C* evolving to the product P:

    $A + 2B \rightarrow C^*_{ads} \rightarrow P$

    The enthalpy of formation of C* (ΔH_{C^*}) is used as a descriptor of the catalytic activity and to build the corresponding volcano plot. The enthalpies of formation of A (ΔH_A) and B (ΔH_B) are 122 kJ mol^{-1} and −226 kJ mol^{-1}, respectively. The table below shows the enthalpy of formation ($\Delta H_{reaction}$) of adsorbed C* obtained using various transition metal catalysts. Demonstrate through calculations which transition metal is the best potential candidate for the target reaction.

Transition metal	$\Delta H_{reaction}$ (kJ mol^{-1})
Cu	850
Ag	1020
Ru	691
Fe	340
Ni	578
Pt	1231
Au	1459
Ir	940
Pd	1100

References

[1] M. Boudart, B.H. Davis, H. Heinemann, Introduction, Handbook of Heterogeneous Catalysis, Wiley-VCH Verlag GmbH, Weinheim, Germany, 2008, pp. 1–48.

[2] M. Piumetti, A brief history of the science of catalysis – I: From the early concepts to single-site heterogeneous catalysts, Chim. Oggi. 32 (2014).
[3] F.M. Sapountzi, J.M. Gracia, C.J. Kee, J. Weststrate, H.O.A. Fredriksson, J.W.H. Niemantsverdriet, Electrocatalysts for the generation of hydrogen, oxygen and synthesis gas, Prog. Energy Combust. Sci. 58 (2017) 1–35.
[4] G. Ertl, W. Ostwald, Founder of physical chemistry and Nobel Laureate 1909, Angew. Chem. Int. Ed. 48 (2009) 6600–6606.
[5] H. Knözinger, K. Krochloefl, Heterogeneous catalysis and solid catalysts, Ullmann's Encyclopedia of Industrial Chemistry, Wiley-VCH Verlag GmbH & Co. KGaA, 2003.
[6] T. Kandemir, M.E. Schuster, A. Senyshyn, M. Behrens, R. Schlögl, The Haber-Bosch process revisited: on the real structure and stability of "ammonia iron" under working conditions, Angew. Chem. Int. Ed. 52 (2013) 12723–12726.
[7] J.M. Thomas, W.J. Thomas, Principles and Practice of Heterogeneous Catalysis, John Wiley Sons, 2015.
[8] B.H. Davis, Fischer-Tropsch synthesis: overview of reactor development and future potentialities, Top. Catal. 32 (2005) 143–168.
[9] J.R.H. Ross, Heterogeneous catalysis – chemistry in two dimensions, Heterogeneous Catalysis, Elsevier, 2012, pp. 1–15.
[10] J. Weitkamp, Zeolites and catalysis, Solid State Ion. 131 (2000) 175–188.
[11] C.H. Bartholomew, R.J. Farrauto, Fundamentals of Industrial Catalytic Processes, John Wiley & Sons, Inc, Hoboken, NJ, United States, 2005.
[12] G. Centi, P. Ciambelli, S. Perathoner, P. Russo, Environmental catalysis: trends and outlook, Catal. Today (2002) 3–15. Elsevier.
[13] A. Fujishima, K. Honda, Electrochemical photolysis of water at a semiconductor electrode, Nature 238 (1972) 37–38.
[14] K. Hashimoto, H. Irie, A. Fujishima, TiO_2 photocatalysis: a historical overview and future prospects, Jpn. J. Appl. Phys., Part. 1 Regul. Pap. Short Notes Rev. Pap. 44 (2005) 8269–8285.
[15] G. Gahleitner, Hydrogen from renewable electricity: an international review of power-to-gas pilot plants for stationary applications, Int. J. Hydrog. Energy 38 (2013) 2039–2061.
[16] M. Shelef, R.W. McCabe, Twenty-five years after introduction of automotive catalysts: what next? Catal. Today 62 (2000) 35–50.
[17] K.C. Taylor, J.C. Schlatter, Selective reduction of nitric oxide over noble metals, J. Catal. 63 (1980) 53–71.
[18] P. Ahlberg, Advanced information on the Nobel prize in chemistry 2001. https://www.nobelprize.org/uploads/2018/06/advanced-chemistryprize2001-1.pdf, 2001 (accessed 05.07.20).
[19] J.-E. Bäckvall, Scientific background on the Nobel prize in chemistry 2010. https://www.nobelprize.org/uploads/2018/06/advanced-chemistryprize2010-1.pdf, 2010 (accessed 05.07.20).
[20] H. Song, D. Laudenschleger, J.J. Carey, H. Ruland, M. Nolan, M. Muhler, Spinel-structured $ZnCr_2O_4$ with excess Zn is the active ZnO/Cr_2O_3 catalyst for high-temperature methanol synthesis, ACS Catal. 7 (2017) 7610–7622.
[21] P. Atkins, J. De Paula, Elements of Physical Chemistry, seventh ed., Oxford University Press, 2016.
[22] Y. Hao, F. Cárdenas-Lizana, M.A. Keane, Gas phase chemoselective hydrogenation of p-nitrobenzonitrile over gold: effect of metal particle size, support and the metal-support interface, Catal. Struct. React. 3 (2017) 165–173.
[23] K. Jiang, B. Liu, M. Luo, S. Ning, M. Peng, Y. Zhao, et al., Single platinum atoms embedded in nanoporous cobalt selenide as electrocatalyst for accelerating hydrogen evolution reaction, Nat. Commun. 10 (2019) 1743.
[24] X. Liu, S. Li, Y. Liu, Y. Cao, Formic acid: a versatile renewable reagent for green and sustainable chemical synthesis, Cuihua Xuebao/Chinese J. Catal. 36 (2015) 1461–1475.
[25] C.G. Morales-Guio, L.A. Stern, X. Hu, Nanostructured hydrotreating catalysts for electrochemical hydrogen evolution, Chem. Soc. Rev. 43 (2014) 6555–6569.

[26] H.L. Chou, B.J. Hwang, C.L. Sun, Catalysis in fuel cells and hydrogen production, New Futur. Dev. Catal. Batter. Hydrog. Storage Fuel Cells, Elsevier B.V., 2013, pp. 217–270.
[27] E.Y.X. Chen, T.J. Marks, Cocatalysts for metal-catalyzed olefin polymerization: activators, activation processes, and structure-activity relationships, Chem. Rev. 100 (2000) 1391–1434.
[28] Y. Sakata, Y. Tamaura, H. Imamura, M. Watanabe, Preparation of a new type of $CaSiO_3$ with high surface area and property as a catalyst support, Stud. Surf. Sci. Catal, Elsevier Inc., 2006, pp. 331–338.
[29] J. Sehested, S. Dahl, J. Jacobsen, J.R. Rostrup-Nielsen, Methanation of CO over nickel: mechanism and kinetics at high H_2/CO ratios, J. Phys. Chem. B 109 (2005) 2432–2438.
[30] M.C. Molstad, B.F. Dodge, Zinc oxide–chromium oxide catalysts for methanol synthesis, Ind. Eng. Chem. 27 (1935) 134–140.
[31] A.M. Bahmanpour, A. Hoadley, A. Tanksale, Formaldehyde production via hydrogenation of carbon monoxide in the aqueous phase, Green Chem. 17 (2015) 3500–3507.
[32] J.R.H. Ross, How does a catalyst work? Heterogeneous Catalysis, Elsevier, 2012, pp. 47–64.
[33] S.M. Csicsery, Shape-selective catalysis in zeolites, Zeolites 4 (1984) 202–213.
[34] V. Mouarrawis, R. Plessius, J.I. van der Vlugt, J.N.H. Reek, Confinement effects in catalysis using well-defined materials and cages, Front. Chem. 6 (2018) 623.
[35] T. Alberi, W.A. Gilbert, D.R. Ponzi, G.A. Petsko, The role of mobility in the substrate binding and catalytic machinery of enzymes, Ciba Found. Symp. 93 (2008), John Wiley and Sons Ltd., pp. 4–24.
[36] D.L. Pompliano, A. Peyman, J.R. Knowles, Stabilization of a reaction intermediate as a catalytic device: definition of the functional role of the flexible loop in triosephosphate isomerase, Biochemistry 29 (1990) 3186–3194.
[37] A.S. Varela, W. Ju, P. Strasser, Molecular nitrogen-carbon catalysts, solid metal organic framework catalysts, and solid metal/nitrogen-doped carbon (MNC) catalysts for the electrochemical CO_2 reduction, Adv. Energy Mater. 8 (2018) 1703614.
[38] I.I. Alkhatib, C. Garlisi, M. Pagliaro, K. Al-Ali, G. Palmisano, Metal-organic frameworks for photocatalytic CO_2 reduction under visible radiation: a review of strategies and applications, Catal. Today 340 (2020) 209–224.
[39] M. Campanati, G. Fornasari, A. Vaccari, Fundamentals in the preparation of heterogeneous catalysts, Catal. Today (2003) 299–314. Elsevier.
[40] F. Pinna, Supported metal catalysts preparation, Catal. Today 41 (1998) 129–137.
[41] J.A. Schwarz, C. Contescu, A. Contescu, Methods for preparation of catalytic materials, Chem. Rev. 95 (1995) 477–510.
[42] M. Bellardita, A. Di Paola, S. Yurdakal, L. Palmisano, Preparation of catalysts and photocatalysts used for similar processes, Heterogeneous Photocatalysis, Elsevier, 2019, pp. 25–56.
[43] P. Schlexer, Computational modeling in heterogeneous catalysis, Reference Module in Chemistry, Molecular Sciences and Chemical Engineering, Elsevier, 2017.
[44] J.G. Speight, Heavy and Extra-Heavy Oil Upgrading Technologies, Elsevier Inc, 2013.
[45] E.T.C. Vogt, B.M. Weckhuysen, Fluid catalytic cracking: recent developments on the grand old lady of zeolite catalysis, Chem. Soc. Rev. 44 (2015) 7342–7370.
[46] R.A. Van Santen (Ed.), Modern Heterogeneous Catalysis, Wiley-VCH Verlag GmbH & Co. KGaA, Weinheim, Germany, 2017.

CHAPTER 2

Fundamentals of the adsorption process

All catalyzed heterogeneous reactions occur on the surface of a solid catalyst. Accordingly, at least one, or all, of the reacting species must come into contact with the surface. Prior to that, however, the reacting species must reach the catalyst surface from the bulk of the fluid. Similarly, after the reaction, the produced species must detach from the surface and then move away from it. In summary, the overall process of heterogeneous catalytic reactions proceeds through a sequence of five individual steps as follows [1,2]:

1. Reactant diffusion to active surface,
2. Reactant adsorption onto surface,
3. Reaction on the surface,
4. Product desorption from surface, and
5. Product diffusion away from surface.

As can be deduced from above, *all surface-facilitated chemical reactions must be preceded by the surface adsorption* of chemical species.

2.1 Physical and chemical adsorption

Adsorption, or the process by which a species (the adsorbate) comes into contact with the surface of another (the adsorbent), may be classified into one of two fundamental modes: physical adsorption (or physisorption) and chemical adsorption (or chemisorption) [2,3]. The difference arises depending on how the chemical species interacts with the adsorbent surface (Table 2.1).

Physisorption describes the adsorption of a species onto a surface through *weak intermolecular forces*, including Van der Waals (such as London dispersion and dipole−dipole) and hydrogen bonding. Consequently, the electron density distribution of both the adsorbate and the adsorbent remains unchanged. In physisorption, *the enthalpy of adsorption is low*, typically in the range of 5−40 kJ mol^{-1} depending on the molecular masses and the polarities of the species involved. Furthermore, physisorption is characterized as a *fast, reversible, nondissociative process* with the possibility of multilayer adsorbate build-up. During the formation of the first layer, the heat of adsorption is almost the same as, but not exactly equal to, the heat of condensation. Conversely, for the formation of the second and subsequent layers, the heat of adsorption represents the heat of

Heterogeneous Catalysis. DOI: https://doi.org/10.1016/B978-0-323-89845-4.00004-7

Table 2.1: Summary of the most important features of physical and chemical adsorption processes.

	Physisorption	Chemisorption
Nature of bond	Weak intermolecular forces	Strong chemical bonds
Adsorption kinetics	Fast	Variable
Nature of adsorption	Reversible, nondissociative	Irreversible, dissociative or not
Uptake	Multilayer	Monolayer
Enthalpy of adsorption	Low (5–40 kJ mol^{-1})	High (40–800 kJ mol^{-1})

liquefaction. Therefore physisorption occurs within temperature ranges near or below the condensation point of the adsorbate. If physisorption took place at a temperature above the condensation point, then it would be confined to a single layer, since the condensation of a second layer onto the first one would not be possible [4].

The term *chemisorption* describes the adsorption of a species onto a surface through the *breakage/formation of ionic or covalent bonds*. As a result, the electron density arrangement is significantly altered. Unlike physisorption, the process of chemisorption typically requires activation and therefore its adsorption kinetics is extremely variable. Moreover, chemisorption, which is *limited to the formation of a monolayer*, is an *irreversible* process that may or may not be dissociative. The *enthalpy of adsorption is high*, usually in the wide range of 40–800 kJ mol^{-1} depending on the strength of the involved chemical bonds. Infrared and photoelectron spectroscopy techniques, along with temperature programmed desorption, which will be later discussed in Chapter 7, Characterization Techniques, are the most definitive methods used to identify a chemisorption process.

The outermost layer of an adsorbent may be rearranged with the formation of the adsorbate monolayer. For example, the surface structure of Rh (110) before and after oxygen adsorption is displayed in Fig. 2.1A and B, respectively. Upon oxygen adsorption, a significant reconstruction of Rh atoms occurs, consequently leading to a (2×1) "missing row" [5]. A (2×1) reconstruction means that the periodicity in one direction is twice the original cell size, while the other remains the same. Therefore the surface of an adsorbent must never be regarded as a rigid structure where exposed atoms are statically fixed at their lattice points. When adsorbate–adsorbent and adsorbate–adsorbate interactions are considerable, the adlayer takes up an ordered structure to minimize the overall free energy by balancing the internal energy and the entropy [6]. In general, the adsorbates will occupy high symmetry and high-coordination sites. The magnitude of adsorbate-induced relaxations and reconstructions vary as a function of the adsorbate coverage. This is mainly attributed to direct and indirect interactions between the adspecies, including for instance electrostatic interactions and adsorbent-mediated interactions [7]. As shown in Fig. 2.1C, hydrogen, at coverages less than or equal to 0.5, adsorbs onto Rh (110) in threefold coordinated sites.

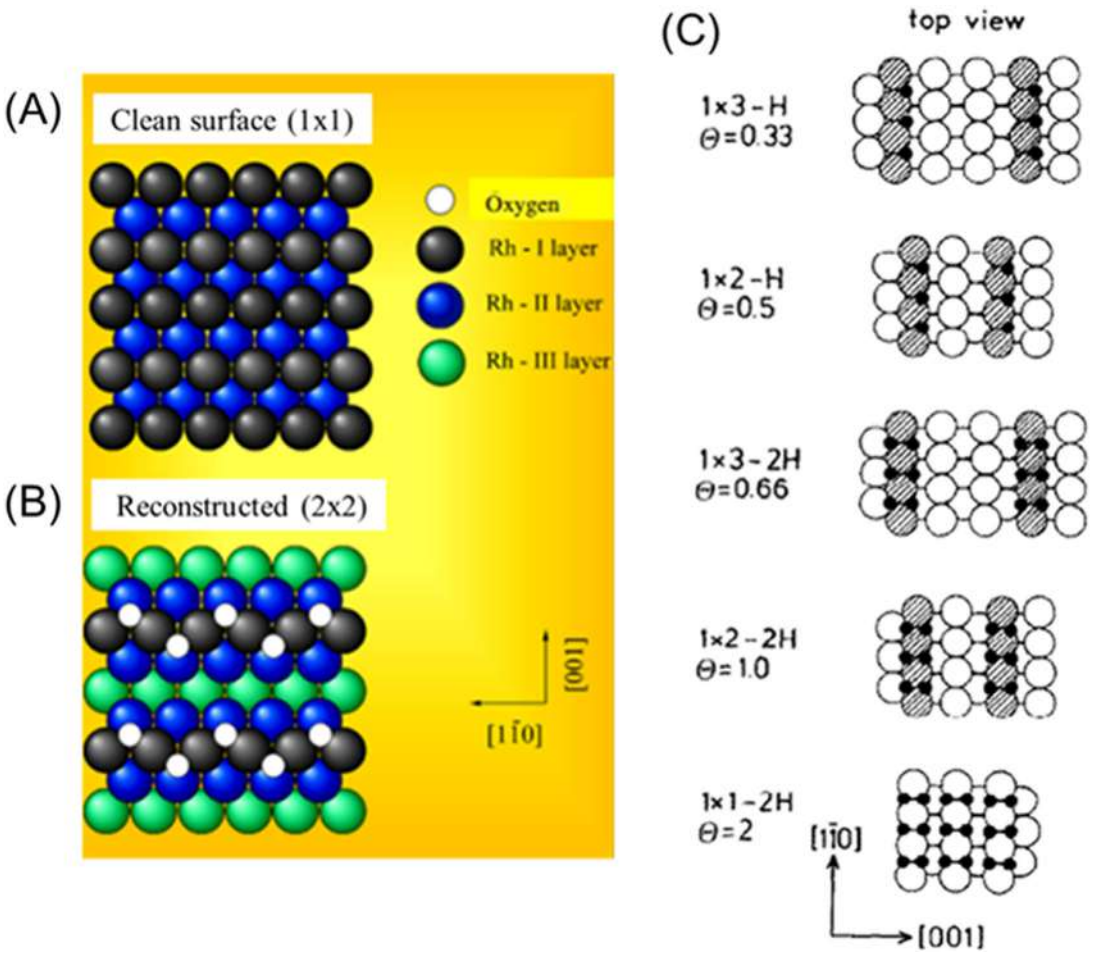

Figure 2.1

(A) Ideal structure of a clean Rh (110) surface and (B) structure of the reconstructed Rh (110) surface after the adsorption of oxygen. (C) Top view of the Rh (110) surface configuration with respect to different hydrogen coverages (θ represents the coverage and is defined as the ratio of the number of adsorbate atoms to the number of adsorbent surface atoms). Black circles represent hydrogen atoms, white circles represent rhodium atoms, and shaded circles represent hydrogen-induced reconstruction of the first rhodium layer. $1 \times 3 - H$ ($\theta = 0.33$), $1 \times 2 - H$ ($\theta = 0.5$), $1 \times 3 - 2H$ ($\theta = 0.66$), $1 \times 2 - 2H$ ($\theta = 1$), and $1 \times 1 - 2H$ ($\theta = 2$) represent the five commensurate phases that result because of hydrogen adsorption [8]. Source: *Reproduced from [5,8].*

However, at a high coverage of 2, the local coordination of the hydrogen atoms changes. To allow for equidistant arrangements in both [110] and [001] directions, the repulsive interactions between neighboring hydrogen atoms move the adatoms up, increasing the bond length to the second layer of Rh atoms [8]. Note that in this case, the coverage is

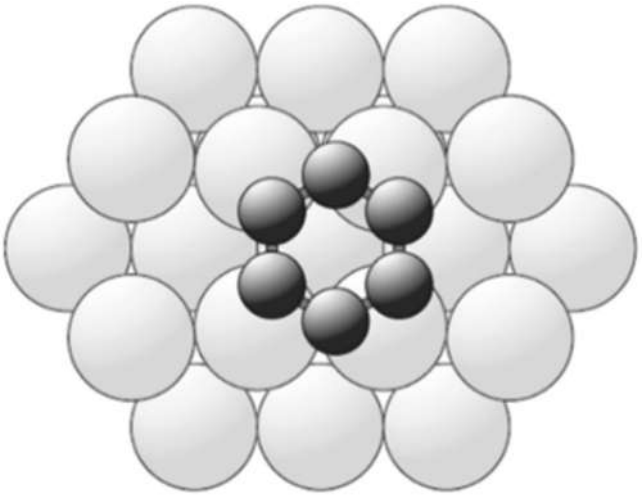

Figure 2.2
Top view of the adsorption of benzene on Ni (110). Darker circles represent the carbon atoms of benzene while lighter circles represent nickel atoms. The hydrogen atoms of benzene have not been included. Source: *Reproduced from [9].*

defined as the ratio of the number of adsorbate atoms to the number of adsorbent (surface) atoms.

The nature of a molecule's binding mechanism, which can be determined via spectroscopic data, may be used for the identification of both the molecule's orientation on the surface and the interatomic bond length [9]. Results from a photoemission study on the adsorption of benzene on Ni (110), for example, show a downward shift in energy for one of the molecule's π-orbitals. This implies that benzene adsorbs on Ni (110) with its molecular plane parallel to the surface, as depicted in Fig. 2.2. Furthermore, a photoelectron diffraction study on the same revealed an increase in the C—C bond distance after adsorption.

Focus 2.1: Special sites at noble and late transition metal catalysts

The bond strength of adsorbates is heavily dependent on the structure of the adsorbent system. Single-crystal metal particles, specifically those with high-index planes, are known to possess a high density of atomic-sized steps that function as strong catalytic sites [10]. According to the *Hammer—Nørskov d-band model* [11], which correlates changes in the energy center of the valence d-band density of states at the surface sites with their ability to form chemisorption bonds, *step-metal atoms* are capable of binding adsorbates more strongly than

(*Continued*)

Focus 2.1: Special sites at noble and late transition metal catalysts (Continued)

surface-metal atoms. This has been attributed to the smaller d-band width of metal atoms at the atomic steps. A smaller d-band width leads to an upshift in the d-band center and, consequently, an upshift of the whole electrostatic potential.

The bond strength may change as a result of modifications in the structure at the reaction site (atomic structure effect) or as a result of changes in the structure elsewhere in the system (electronic structure effect). Both the atomic structure effect and the electronic structure effect contribute to reducing the energy barrier for the dissociation of a diatomic molecule at a stepped metallic surface [11]. As an illustrative example, consider the dissociative adsorption of nitric oxide (NO) on a flat Ru (0001) surface (Fig. 2.3A) in comparison to that on a stepped Ru (0001) surface (Fig. 2.3B and Fig. 2.3C). The reaction energy barrier for the dissociation of NO on a flat Ru (0001) surface is equal to 1.4 eV (Fig. 2.3A). After the introduction of a step elsewhere in the adsorbent system (i.e., not at the reaction site), the barrier reduces to 0.9 eV (Fig. 2.3B). Since the geometric configuration of NO remained the same, the change in the energy barrier is attributed to the local change in the electronic structure produced by the nonlocal change in the adsorbent structure (electronic structure effect). Conversely, after the introduction of a step at the reaction site, the barrier further reduces to 0.2 eV (Fig. 2.3C). In this case, the geometric configuration of NO changes and the reduction in the energy barrier is attributed to the local change in the atomic structure as a result of the local change in the adsorbent structure (atomic structure effect). With this new structure, the NO molecule can effectively interact with more Ru atoms than in the previous configuration and the dissociation is, hence, more favorable.

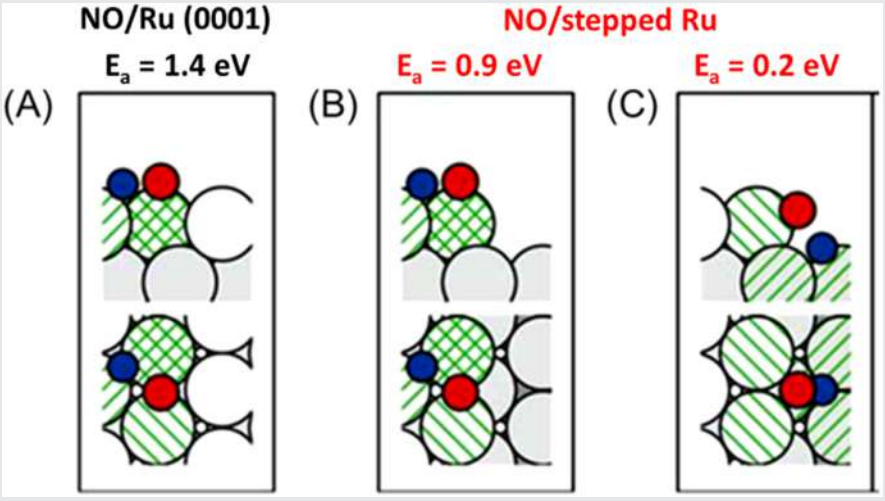

Figure 2.3
Transition state geometries for NO dissociation over: (A) flat Ru (0001), (B) stepped Ru (0001) where NO retains its geometry from the flat surface, and (C) stepped Ru (0001) where NO utilizes the atomic structure of the step. E_a represents the reaction energy barrier.
Source: *Reproduced from [11].*

(*Continued*)

Focus 2.1: Special sites at noble and late transition metal catalysts (Continued)

It is, however, extremely difficult to synthesize metals with high-index facets due to the resulting high surface energy. Crystal growth rates in the direction perpendicular to a high-index plane are typically much faster than those along the normal direction of a low-index plane [12]. Hence, high-index planes are quickly eradicated during particle formation and, consequently, more complex techniques, such as electrochemical treatment and seed-mediated growth, are required for their preparation [12,13]. Nonetheless, transition and noble metals, including those with low-index facets, typically possess multifarious crystal structures. As a result, different types of defects, such as steps, kinks, and corners, are often present on their surfaces. The number and types of defect structure may be controlled by adjusting the synthesis conditions and methods. A more common method currently used for the construction of defects is etching (chemical or physical) [14]. In chemical etching, a certain chemical, usually an acid or a base, reacts with the catalytic material, leading to the formation of special defect sites on the surface. On the other hand, and with physical etching, energetic particles, such as ions, electron beams, or plasma, bombard the material and, depending on the working power and treatment time, different types and different concentrations of surface defects are formed.

Surface chemical bonds, which are broken and formed during the process of chemical adsorption on a catalyst, *may be discussed in terms of simple molecular orbital theory* [15]. Consider two H atoms, each with a positive nucleus and a negative s electron. If the two H atoms move closer to one another, the 2s orbitals will overlap. Using quantum mechanics, the energy diagram presented in Fig. 2.4A may be obtained. By the overlap of the two H atoms, a *bonding orbital* is created with two electrons, which are now more strongly bound to the two nuclei. An *antibonding orbital* is also formed as a result of the overlap. If the overlap between the two atoms increases, then the stabilization increases. In other words, the splitting between the bonding and the antibonding orbitals will increase as illustrated in Fig. 2.4B. A strong bond between two atoms is created when the electrons fill only the bonding orbital. A strong adsorbate bond, however, is not desirable in catalysis since it will be extremely difficult to break. Fig. 2.4C shows the filling of molecular orbitals to form strong, intermediate, and no bond. *An intermediate bond*, as previously discussed in Section 1.2.2, *is preferable* for catalytic processes and is created with a filled bonding orbital and a half-filled antibonding orbital. If all orbitals are filled, no bonds are formed.

In metals, the overlap of atomic orbitals results in the formation of *bands*, contrary to the formation of molecular orbitals in molecules. Electrons occupy the individual levels of the bands according to the building-up principle. The highest occupied level is defined as the *Fermi level,* E_F. Electrons in the Fermi level of a metal can be promoted to a vacuum level, E_{vac}, outside the metal surface. The minimum energy required to remove an electron from a metal to the vacuum is known as the *work function*.

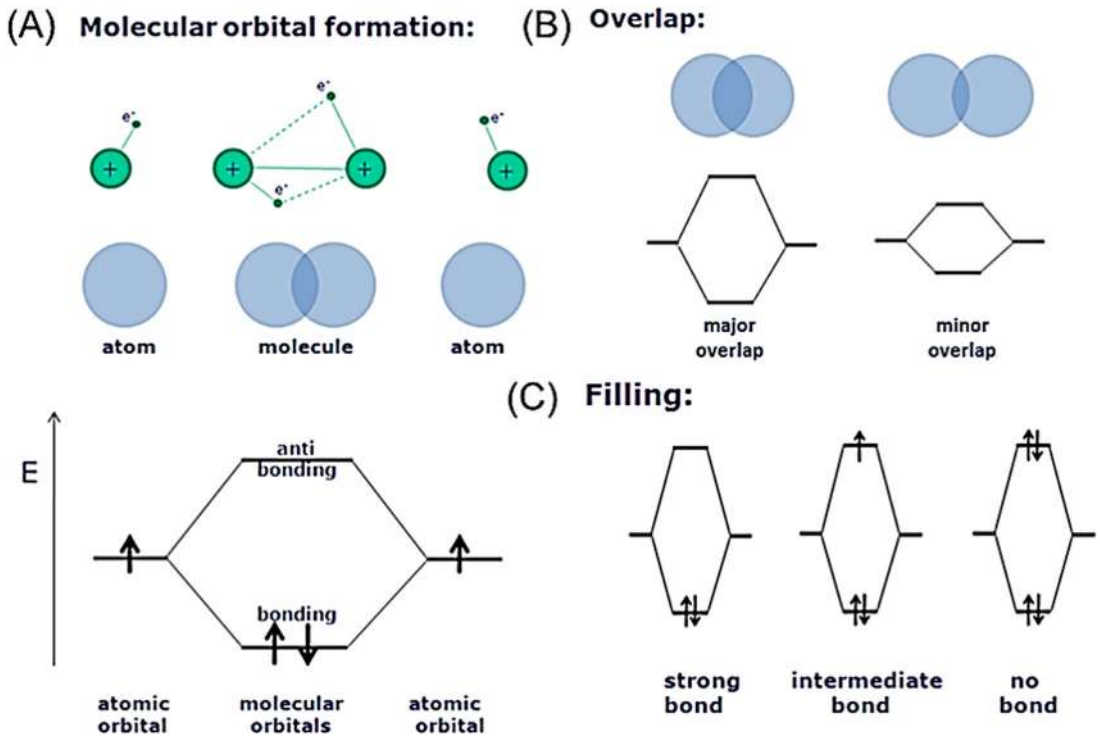

Figure 2.4
The basic principles of molecular orbitals: (A) formation, (B) overlap, and (C) filling. Blue circles represent hydrogen atoms while black arrows represent electrons. Source: *Reproduced from [16].*

Now, consider the adsorption of a free atom on a transition metal (or a d-metal). As the atom adsorbs to the metal surface, a chemisorption orbital is formed, whereby the bonding orbital is completely filled, while the antibonding orbital is completely empty (Fig. 2.5A). This creates a very strong bond, which is characteristic of reactive metals such as Cr. In Fig. 2.5B, another metal with a higher filling of the d-band is presented. Here, a chemisorption orbital with a filled bonding orbital and a partly filled antibonding orbital forms, creating a bond with moderate strength. This is commonly the case with less reactive metals such as Rh. Fig. 2.5C shows the d-metals as presented in a periodic table. Elements on the left display strong atomic adsorption, while elements on the right exhibit weaker adsorption [15].

Next, consider the adsorption of a free molecule on a d-metal (Fig. 2.6). As the molecule approaches the metal surface, both the bonding and antibonding orbitals of the free molecule will interact with the metal. *The occupied bonding orbital of the free molecule (σ) will create adsorption orbitals* with the metal in the same way a free atom does (discussed earlier). Accordingly, the bonding orbital will be filled and the

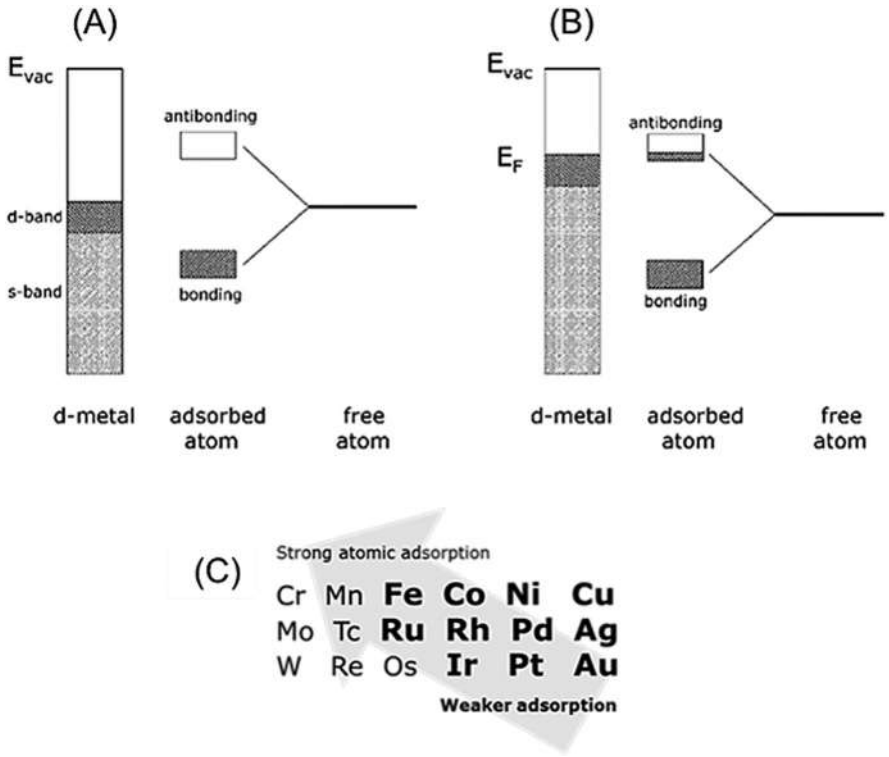

Figure 2.5
Energy diagrams for the adsorption of a free atom on a d-metal, either through (A) a strong chemisorption bond or through (B) a weak chemisorption bond (E_{vac} represents energy of the vacuum level, E_F represents energy of the Fermi level). (C) Strength of atomic adsorption on d-metals. Source: *Reproduced from* [16].

antibonding orbital will be partly filled. A moderate bond from the occupied bonding orbital of the molecule is therefore formed. The empty antibonding orbital of the free molecule (σ^*) will also create adsorption orbitals with the metal. Here, only the bonding orbital is partly filled. A bond between the molecule and the metal will still form. However, since the bond is derived from the antibonding state of the free molecule, the molecule, or more specifically the internal bonds of the molecule, will become weaker. This is strictly related to one of the basic definitions of *a catalyst*, which *should bind to an adsorbate and at the same time weaken its internal bonds*. In the case of dissociative adsorption, a similar approach is followed. However, this time, the bonding orbital created from the empty antibonding orbital of the free molecule (σ^*) will have to be entirely filled. This causes the molecule to break down and completely dissociate [15].

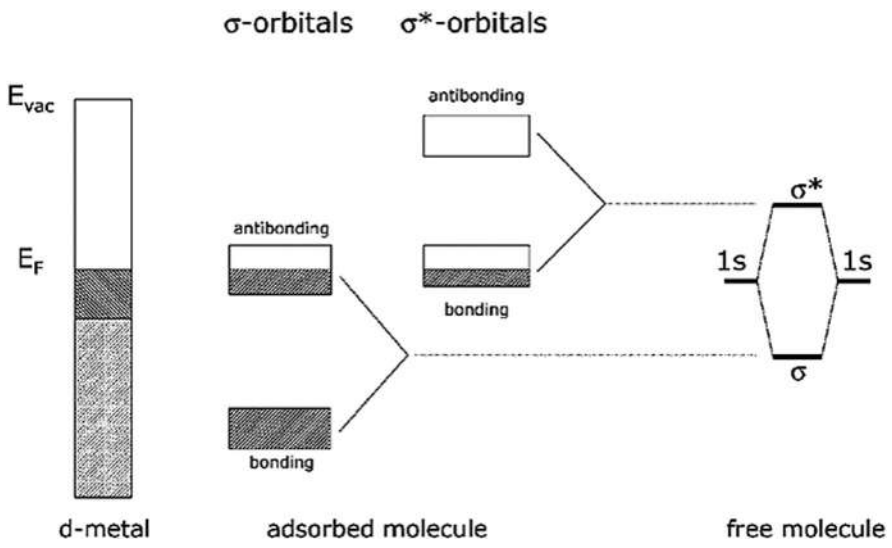

Figure 2.6
Energy diagram for the adsorption of a simple diatomic molecule on a d-metal (E_{vac} represents the energy of the vacuum level, E_F represents the energy of the Fermi level). σ and σ* are the bonding and antibonding orbitals of the free molecule. Source: *Reproduced from [16].*

Focus 2.2: Influence of the support properties on the formation of bonding and antibonding orbitals during adsorption

The properties of the support in supported metal catalysts are known to strongly affect the catalytic activity of the metal [17], as further discussed in Section 3.4.1. In particular, support's properties, such as the presence of protons and the type of charge compensating cations, have been shown to considerably alter the formation of bonding and antibonding orbitals during adsorption. As an illustrative example, consider the adsorption of hydrogen on a platinum catalyst where LTL zeolite is used as a support (Fig. 2.7). The acidity/alkalinity of the LTL zeolite was varied by either impregnating a commercial K-LTL zeolite with KNO_3 or exchanging with NH_4NO_3 to give K/Al ratios ranging from 0.63 to 1.25 [17]. By increasing the K/Al ratio, the alkalinity of the support increases. As a result, the negative charge on the oxygen ion of the LTL support also increases by an amount equivalent to $\delta-$. This shifts the interacting orbitals to a lower binding energy or, in other words, lowers the ionization potential. The atomic 1s orbital remains at the same energy position. The molecular antibonding orbital, however, shifts to a lower energy position with respect to the Fermi level (i.e., the resonance energy, E_{res}, decreases). The decrease in E_{res} as a result of increasing alkalinity is schematically represented in Fig. 2.7 (see transition from a to b). The decrease in the Pt—H bond strength with increasing support alkalinity was verified experimentally using X-ray absorption spectroscopy (see Section 7.3).

(*Continued*)

Focus 2.2: Influence of the support properties on the formation of bonding and antibonding orbitals during adsorption (Continued)

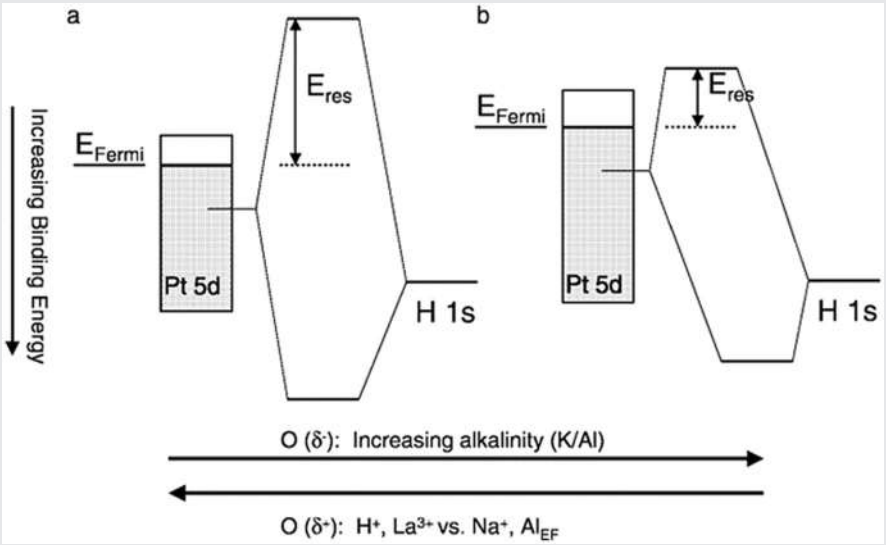

Figure 2.7
Schematic representation of the Pt—H bonding as a function of the support properties, where transition from a to b represents the decrease in E_{res} due to the increase in alkalinity and transition from b to a represents the increase in E_{res} as a result of increasing number of protons or charge of the cations. Source: *Reproduced from [17].*

Conversely, the negative charge on the oxygen ion of the LTL support can decrease by an amount equivalent to $\delta +$. This might be achieved by increasing the number of protons or by increasing the charge of the cations. As a result of the lower negative charge, the interacting orbitals shift to a higher binding energy or, in other words, the ionization potential increases. The molecular antibonding orbital shifts to a higher energy position with respect to the Fermi level (i.e., E_{res} increases and the Pt—H bond strengthens). The increase in E_{res} as a result of an increasing number of protons or charge of the cations is schematically represented in Fig. 2.7 (see the transition from b to a).

2.2 Thermodynamics and energetics of adsorption

As per the basic principles of thermodynamics, *adsorption processes are expected to be exothermic* [2]. Adsorption is a spontaneous process (Gibbs free energy, ΔG, <0), that is always accompanied by a decrease in entropy ($\Delta S < 0$). Therefore, from

$$\Delta G = \Delta H - T\Delta S \tag{2.1}$$

the enthalpy change accompanying adsorption, ΔH, must be negative (exothermic). Although this is true for the vast majority of adsorption processes, there are rare instances where it is not [18]. For example, consider a diatomic gas molecule, A_2, which dissociatively chemisorbs on a solid surface, S, with an A—S bond energy equal to half of that of the A—A bond. If each of the two atoms A possesses two-dimensional mobility, the entropy of the system increases (4 degrees of freedom compared to 3 degrees of freedom for gaseous A_2) and ΔH can be positive without affecting the negative sign of the variation in the Gibbs free energy, which is negative for spontaneous processes.

On the other hand, the natural decrease in entropy of the adsorbate during adsorption may be overcome by the simultaneous increase in the entropy of the adsorbent [2], leading again to the possibility of a positive ΔH provided that and given that $T\Delta S > \Delta H$ to account for the spontaneity of the process.

2.2.1 Heat of adsorption

M.W. Roberts showed that the heat of adsorption of simple diatomic gases on metal surfaces can be estimated from the enthalpy of formation [2,19]. Thereafter, Tanaka and Tamaru expressed the initial *heat of chemisorption,* ΔH_a, in kcal mol^{-1}, as:

$$\Delta H_a = a\left[\left(-\Delta H_f\right) + 37\right] + 20 \tag{2.2}$$

where a is a gas-dependent constant and ΔH_f is the enthalpy of formation [20]. Tables 2.2 and 2.3 list a few examples of the heat of adsorption for different adsorbate/

Table 2.2: Heat of adsorption for different adsorbate/adsorbent systems.

Adsorbate	Adsorbent	Heat of adsorption (kJ mol^{-1})	Reference
CO	Zeolite (NaX)	26	[21]
CO_2	Zeolite (ZIF-8)	16	[22]
	Zeolite (H-ZSM-5)	15.3—28.7	[23]
CH_4	Zeolite (NaX)	20	[21]
	Zeolite (13X)	15.3—19.2	[24]
	Zeolite (ZIF-8)	12	[22]
	Silica gel	11.7—13.7	[24]
	Activated carbon	15.3—22.3	[24]
N_2	Zeolite (NaX)	21	[21]
	Zeolite (13X)	12.8—19.7	[24]
	Activated carbon	12.2—17.4	[24]
H_2	Charcoal	2.9—3.7	[25]
	Carbon nanotubes	2.1—3.7	[25]
	Graphene	0.9—2.9	[25]
Benzene	Zeolite (CaY)	81.7—92.1	[26]
	Zeolite (NaY)	62.8—79.5	[26]

Table 2.3: Enthalpy of formation for different reaction intermediates [27].

Compound	Enthalpy of formation (kJ mol^{-1})	Compound	Enthalpy of formation (kJ mol^{-1})
$H_{2(g)}$	0	$C_2H_{6(g)}$	−85
$O_{2(g)}$	0	$C_2H_{4(g)}$	+ 52
$Br_{2(l)}$	0	$C_8H_{18(l)}$	−269
$C_{(s)}$	0	$NH_{3(g)}$	−46
$H_2O_{(l)}$	−286	$NO_{2(g)}$	+ 34
$H_2O_{(g)}$	−242	$Al_2O_{3(s)}$	−1676
$CO_{2(g)}$	−394	$Fe_2O_{3(s)}$	−826
$CH_{4(g)}$	−75	$KCl_{(aq)}$	−419
$CH_3OH_{(g)}$	−239		

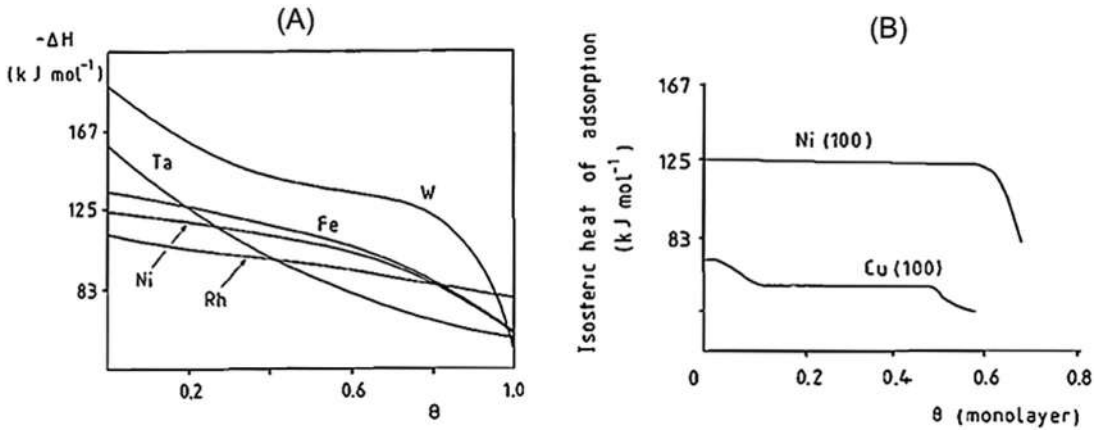

Figure 2.8

(A) Heat of adsorption as a function of coverage, θ, for the adsorption of hydrogen on different polycrystalline metal surfaces. (B) Heat of adsorption as a function of coverage, θ, for the adsorption of carbon monoxide on single-crystal surfaces. Source: *Reproduced from [2].*

adsorbent systems and of the enthalpy of formation for different reaction intermediates, respectively.

For a solid surface with distinct active sites, *the heat of adsorption decreases as the coverage increases* (Fig. 2.8A). This is because the most energetic sites of the solid are occupied first. Conversely, for a surface with uniform sites, the heat of adsorption remains almost constant as the coverage increases (Fig. 2.8B). Nonetheless, after a certain critical coverage has been reached, sharp drops in the heat of adsorption are observed in Fig. 2.8B. This sudden decrease indicates the onset of adsorbate−adsorbate repulsions. More specifically, as coverage increases, dipole−dipole interactions, in addition to the overlapping of atomic and molecular orbitals, become more prominent and, as a result, adsorbates begin to repel each other more strongly [2].

2.2.2 Binding energy of adsorbates

2.2.2.1 Physisorbed species

The *interaction potential, U*, of an isolated species as it approaches a solid surface may be written as:

$$U = U_d + U_r + U_p + U_{fd} + U_{fq} + U_{sp} \tag{2.3}$$

where U_d is the attractive dispersion potential, U_r is the close-range repulsion term, U_p is the polarization energy, U_{fd} is the field−dipole interaction, U_{fq} is the field-gradient-quadrupole interaction, and U_{sp} is the self-potential, which takes into account interactions between adsorbates. In addition to the aforementioned terms, the interaction potential is also a function of the adsorbed species' position, r, with respect to the adsorbent [2]. The first three terms on the right-hand side of Eq. (2.3) are always present. U_{fd} and U_{fq} depend on whether a dipole or a quadrupole is present in the adsorbate. And, finally, U_{sp} is often negligible for small uptakes.

For simple adsorbate−adsorbent systems, the Lennard-Jones equation may be used to estimate the interaction potential as an alternative to Eq. (2.3), which requires the evaluation of complex terms. The interaction potential is expressed by the *Lennard-Jones equation* as:

$$U = \sum_i U(r_i) = \sum_i \left[-\frac{A}{r_i^6} + \frac{B}{r_i^{12}} \right] = 4\varepsilon \sum_i \left[\left(\frac{\sigma}{r_i}\right)^{12} - \left(\frac{\sigma}{r_i}\right)^{6} \right] \tag{2.4}$$

where A and B are the attraction and repulsion constants, ε is the energy of interaction (i.e., depth of potential well), and σ is the distance at which the interparticle potential is zero. Other more applied forms of the Lennard-Jones equation include:

$$U = \sum_i \left[-\frac{A}{r_i^6} + Bexp(-Cr_i) \right] \tag{2.5}$$

$$U = \sum_i \left[-\frac{A}{r_i^6} + Bexp(-Cr_i) + \frac{D}{r_i^8} \right] \tag{2.6}$$

$$U = \sum_i \left[-\frac{A}{r_i^6} + \frac{Bexp(-Cr_i)}{r_i^D} + \frac{K_{q1q2}}{r_i} \right] \tag{2.7}$$

where A, B, C, and D are well-defined parameters with values that can be found in the literature for a wide variety of different systems. Computations based on the Lennard-Jones equation can reveal the energetically most favorable orientation for a species when adsorbed on the surface of a solid [28].

2.2.2.2 Chemisorbed species

D.D. Eley proposed that *when molecules are chemisorbed on metals, localized covalent bonds form* [29,30]. For the dissociative chemisorption of hydrogen, H_2, on a metal, M, he wrote [31,32]:

$$2M + H_2 \rightarrow 2(M - H) \tag{2.8}$$

and he described the heat of adsorption, ΔH, *at zero coverage* as [31,32]:

$$-\Delta H = 2D_{MH} - D_{HH} \tag{2.9}$$

where D_{MH} and D_{HH} are the energies of the M—H and the H—H bonds, respectively. Eley's equation assumes that all M—M bonds remain intact during the adsorption process. To calculate D_{MH}, Eley proposed the use of *Pauling's equation* [31,32]:

$$D_{MH} = \frac{(D_{MM} + D_{HH})}{2} + 23.06(x_M - x_H)^2 \tag{2.10}$$

where x_M and x_H are the electronegativities of the metal and hydrogen, respectively. Eley's model for the heat of adsorption at zero coverage agrees well with experimental data with errors reported to be within c. 10% [2]. This proves the proposition suggested by Eley, which states that the bond formed between H and M is predominantly covalent. Eq. (2.9) may also be used to estimate the heat of adsorption in ionic chemisorption processes. However, for the specific example of hydrogen chemisorption on different metal surfaces, computed values did not agree well with experimental ones [33]. This indicates that the likelihood of ionic bond formation between H and M is very low.

One example of *ionic chemisorption* is the adsorption of sodium on a metal such as tungsten:

$$Na + W \rightarrow Na^+W^- \tag{2.11}$$

The heat of adsorption, ΔH, may be deduced by:

$$-\Delta H = e\phi - eI + \frac{e^2}{4\pi\varepsilon_0(4R)} \tag{2.12}$$

where $e\phi$ is the energy released when an electron is transferred to the lowest unoccupied energy level of the metal, eI is the energy needed to remove an electron from the highest occupied level of an atom, and ε_0 is the free space permittivity. The third term in the right-hand side of Eq. (2.12) represents the electrostatic energy arising from the presence of a positive ion at a distance R from the surface. The difference in energy between an electron at the highest occupied level (i.e., the Fermi level) of a metal and an electron at rest in the vacuum just outside the metal is known as the work function, Φ (Fig. 2.9). In covalent chemisorption, changes in the work function during gas uptake indicate some degree of charge separation. More specifically, the work function increases as the electrons flow from the metal to the adsorbate and decreases when the electrons flow to the metal [2].

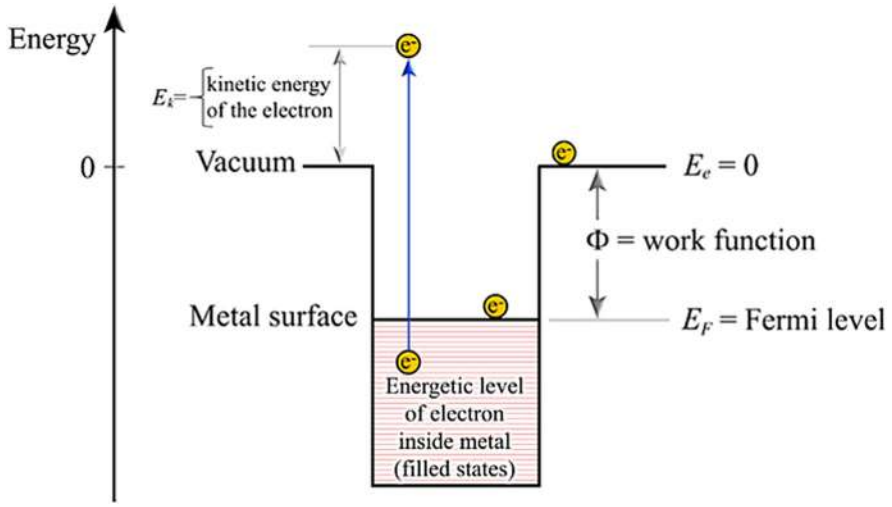

Figure 2.9
The potential well of a metal illustrating the difference in energy between an electron at the Fermi level of a metal and an electron at rest in vacuum, that is, the work function, Φ. The work function corresponds to the minimum amount of energy needed to remove an electron from a metal and is therefore equal to the ionization energy. E_e represents the energy level of the vacuum. Source: *Reproduced from [34].*

Focus 2.3: Numerical example on the estimation of the heat of adsorption from the binding energy of adsorbates

Consider the dissociative chemisorption of hydrogen (H_2) on the surface of tungsten (W). Calculate the heat of adsorption, ΔH, at zero coverage, given that the measured contact potential of a complete monolayer is −1.04 V. Note that D_{HH} is 103.2 kcal mol^{-1}.

Solution
The heat of adsorption may be calculated using Eq. (2.9). First, however, Eq. (2.10) must be used to calculate the binding energy between tungsten and hydrogen. For that, the binding energy between two tungsten atoms must be obtained as per the following equation, where S is the sublimation energy of the metal [31]:

$$D_{MM} = \frac{2}{12}S$$

For tungsten, the heat of sublimation at 298K is 203.5 kcal mol^{-1}. Hence,

$$D_{WW} = \frac{2}{12} \times 203.5 = 33.9 \text{ kcal mol}^{-1}$$

(*Continued*)

Focus 2.3: Numerical example on the estimation of the heat of adsorption from the binding energy of adsorbates (Continued)

Next, the difference in electronegativity between tungsten and hydrogen ($x_W - x_H$) must be evaluated. This term is equal to the dipole moment (μ) of the W—H bond, which may be estimated using the following equation, where V is the measured contact potential of a complete monolayer (in volts) and C_s is the number of sites per centimeter of surface (1.2×10^{15} for tungsten) [31]:

$$x_M - x_H = \mu = \frac{V}{2\pi \times 300 \times C_s}$$

For tungsten,

$$x_W - x_H = \mu = \frac{-1.04}{2\pi \times 300 \times 1.2 \times 10^{15}} = -0.46 \text{ debyes}$$

Substitution into Eq. (2.10) yields:

$$D_{WH} = \frac{(D_{WW} + D_{HH})}{2} + 23.06(x_W - x_H)^2 = \frac{(33.9 + 103.2)}{2} + 23.06(-0.46)^2 = 73.4 \text{ kcal mol}^{-1}$$

Finally, using Eq. (2.9):

$$-\Delta H = 2D_{WH} - D_{HH} = 2(73.4) - 103.2 = 43.6 \text{ kcal mol}^{-1}$$

2.3 Kinetics of adsorption

2.3.1 Adsorption time

The time during which an adsorbate remains adsorbed on a surface is defined as the *residence time*, τ. For a simple molecule adsorbed on a metal surface, Ertl and coworkers found that τ can be expressed as:

$$\tau = \tau_0 exp\left(\frac{E_a^{des}}{RT}\right) \tag{2.13}$$

where τ_0 is the vibrational frequency of the bond formed between the adsorbate and the surface (estimated to be c. 10^{-13} s for the majority of cases), E_a^{des} *is the activation energy of desorption*, R is the universal gas constant, and T is the temperature [35]. Using statistical mechanics, an equivalent expression was theoretically derived in 1924 by the Russian physicist Frenkel [36]:

$$\tau = \tau_0 exp\left(\frac{Q}{RT}\right) \tag{2.14}$$

where Q *is the heat of adsorption* [note that the activation energy of desorption is equal to the heat of adsorption under certain circumstances (see Section 2.3.3)].

Focus 2.4: Numerical example on the estimation of the activation energy of desorption from residence time data

Consider the adsorption of CO on a Pd (111) surface. The residence time at different temperatures was determined from phase lag in modulated molecular beam experiments and the results are listed in the following table. Calculate the activation energy of CO desorption from the Pd (111) surface.

Temperature (K)	Residence time (s)
550	0.05153
575	0.00829
600	0.00341
625	0.00152
650	0.00037
675	0.00018
700	0.00005

Solution

From Eq. (2.13), we can see that a plot of ln τ versus $1/T$ yields a straight line with a slope equal to E_a^{des}/R and an intercept equal to ln τ_0. Hence, for the data above, we obtain the following plot where the slope of the line is 16,911K and the intercept is −33.856.

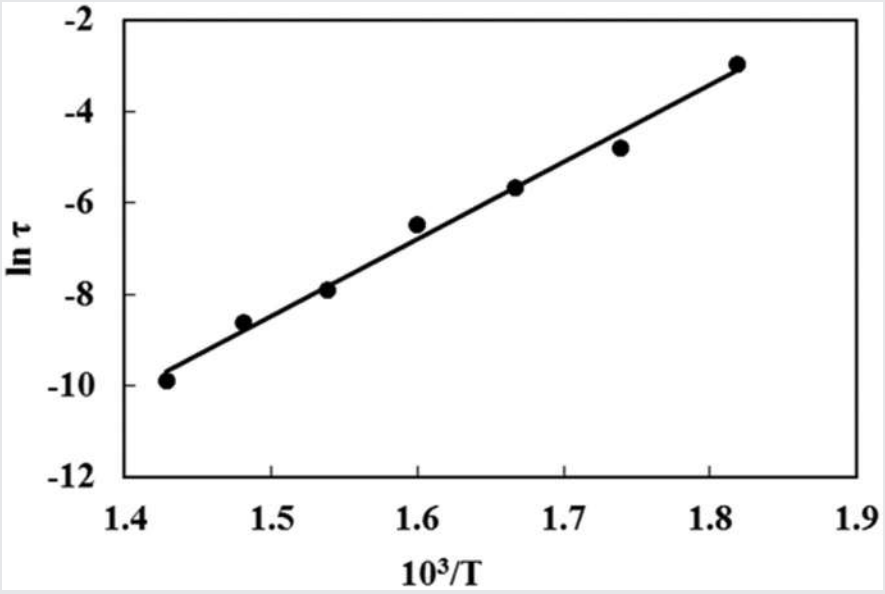

(*Continued*)

Focus 2.4: Numerical example on the estimation of the activation energy of desorption from residence time data (Continued)

Multiplying the slope by the universal gas constant (1.986 cal mol^{-1} K^{-1}) yields an activation energy of desorption equal to 33.6 kcal mol^{-1}. From the value of the intercept, the vibrational frequency of the bond τ_0 is found to be c. 10^{-14} s.

2.3.2 Adsorption rate

The *adsorption rate, r, of a species onto a surface* is expressed as:

$$r = kC^n \tag{2.15}$$

where k is the adsorption rate constant, C is the concentration of the adsorbate in the gas phase, and n is the kinetic order of adsorption. Alternatively, the rate may be expressed in terms of the species' partial pressure, P, as:

$$r = kP^n \tag{2.16}$$

The rate constant, which varies as a function of different reaction conditions including temperature, pressure, and surface concentration, is given by Arrhenius equation as:

$$k = A' exp\left(\frac{-E_a'}{RT}\right) \tag{2.17}$$

where A' is the temperature-independent preexponential factor, E_a' is the apparent activation energy of adsorption, R is the universal gas constant, and T is the absolute temperature. Unlike the true activation energy, the apparent activation energy does not account for temperature-variation effects, such as changes in the catalyst structure, and temperature-dependent factors, like the reactant concentration on the catalyst surface [2]. Substitution gives:

$$r = A'C^n exp\left(\frac{-E_a'}{RT}\right) \tag{2.18}$$

The adsorption rate is dependent on (1) the arrival rate of species at the active surface and (2) the proportion of species that undergoes adsorption [2,3]. Thus it would be more meaningful to express the rate (molecules m^{-2} s^{-1}) as the product of the flux, F, and the sticking probability, S:

$$r = FS \tag{2.19}$$

The flux, in molecules $m^{-2}\,s^{-1}$, is defined by the *Hertz–Knudsen equation* as:

$$F = \frac{P}{(2\pi m k_B T)^{\frac{1}{2}}} \tag{2.20}$$

where P is the gas pressure in $N\,m^{-2}$, m is the mass of the species in kg, k_B is Boltzmann's constant, and T is the temperature in K [37].

The *sticking probability* $(0 < S < 1)$ is defined as the ratio between the adsorption rate and the bombardment rate. It is a function of the adsorbate/adsorbent system and it depends on many factors. Some of these factors include the concentration of prebound species and the activation barrier of adsorption [2,3]. The sticking probability is, therefore, expressed as:

$$S = s' f(\theta) exp\left(\frac{-E_a^{ads}}{RT}\right) \tag{2.21}$$

where s' is the condensation coefficient and $f(\theta)$ is a function of the surface coverage, θ, of the prebound species (Eq. 1.1). As the surface coverage increases, the sticking probability decreases since the number of available sites is smaller [38]. Note that the activation energy of adsorption may itself be a function of the surface coverage. In nondissociative adsorption, the sticking probability is directly proportional to the concentration of vacant sites. Since θ represents the fraction of sites which are occupied, $f(\theta) = (1-\theta)$. In dissociative adsorption, $f(\theta) = (1-\theta)^n$ where n represents the number of parts the molecule disassociates into [2,3]. Substitution into Eq. (2.19) gives:

$$r = \frac{s' f(\theta) P}{(2\pi m k_B T)^{\frac{1}{2}}} exp\left(\frac{-E_a^{ads}}{RT}\right) \tag{2.22}$$

Focus 2.5: Oxygen adsorption on Pt (111): Effect of coverage on both sticking probability and heat of adsorption

The adsorption of oxygen on Pt surfaces is essential for the understanding of catalytic oxidation processes taking place on transition metal surfaces. As can be seen in Fig. 2.10, the heat of adsorption and the sticking probability decrease significantly between 0 and ca. 0.02 ML (ML: monolayers). This abrupt drop can only be indicative of the presence of defect sites (such as steps), which become occupied and saturated first (see Focus 2.1). Fig. 2.10 also shows that the saturation coverage appears to be lower than 0.25 ML. This means that adsorption on neighbor sites (ω_1) and next nearest neighbor sites (ω_2) is not possible [39]. Hence, it may be concluded that the decrease in the heat of adsorption is mainly due to the occupation of third neighbor sites (ω_3). If it were due to ω_1 and ω_2 sites, a closer packing of oxygen atoms on the surface would have taken place, eventually leading to a higher level of coverage.

(*Continued*)

Focus 2.5: Oxygen adsorption on Pt (111): Effect of coverage on both sticking probability and heat of adsorption (Continued)

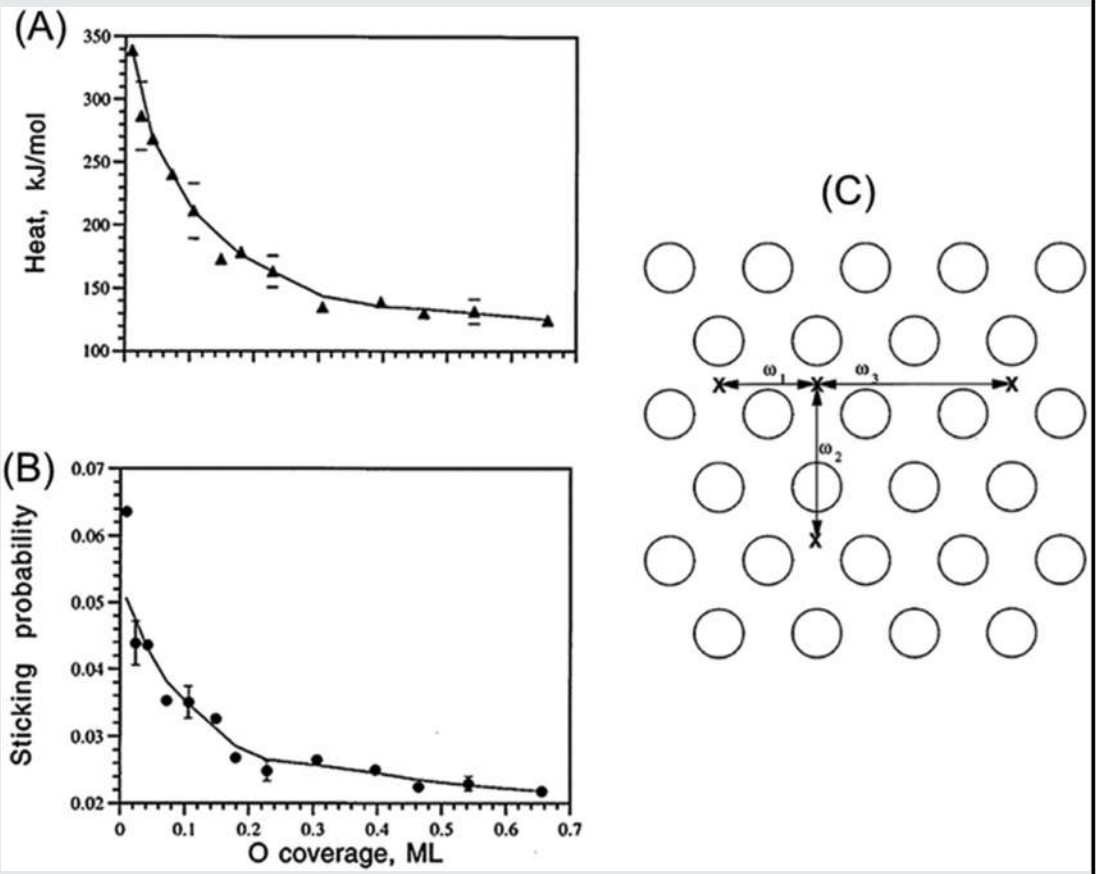

Figure 2.10

(A) Heat of adsorption and (B) sticking probability of oxygen atoms on the clean surface of Pt (111) at 300K. ML represents the monolayers of oxygen (O) adatoms relative to the number of surface Pt atoms. (C) Schematic representation of a clean Pt (111) surface. Circles represent surface Pt atoms while crosses represent possible adsorption sites for the oxygen atoms. ω_1, ω_2, and ω_3 represent next, second, and third nearest neighbor positions, respectively. Source: *Reproduced from [39].*

Focus 2.6: Numerical example on the estimation of the sticking probability from the adsorption rate

Oxygen gas (at 10^{-5} Pa and 300K) dissociatively adsorbs on Ni (100) surface with an initial rate of 1.69×10^{17} molecules $m^{-2}\,s^{-1}$. Calculate the initial sticking probability of oxygen (O_2) on Ni (100).

(*Continued*)

Focus 2.6: Numerical example on the estimation of the sticking probability from the adsorption rate (Continued)

Solution

Using Eq. (2.20), the flux of the oxygen molecules may be calculated:

$$F = \frac{P}{(2\pi mkT)^{\frac{1}{2}}} = \frac{10^{-5}\text{Pa}}{\left(2 \times \pi \times 5.31 \times 10^{-26}\text{kg} \times 1.38 \times 10^{-23}\text{m}^2\ \text{kg s}^{-2}\ \text{K}^{-1} \times 300\text{K}\right)^{\frac{1}{2}}}$$

$$= 2.69 \times 10^{17}\ \text{molecules m}^{-2}\text{s}^{-1}$$

Then, the initial sticking probability of oxygen is computed by application of Eq. 2.19:

$$S = \frac{r}{F} = \frac{1.69 \times 10^{17}\ \text{molecules m}^{-2}\ \text{s}^{-1}}{2.69 \times 10^{17}\ \text{molecules}\ \text{m}^{-2}\ \text{s}^{-1}} = 0.63$$

2.3.3 Potential energy diagrams

The potential energy diagram of an adsorption process represents the *variation of the potential energy of the system* as a function of distance z of an adsorbate from the surface of an adsorbent. This simplistic model accounts for distance as the only parameter influencing the energy of the system and neglects many other factors including the molecule's angular orientation and position relative to the surface plane. It also assumes that the molecule is isolated and interacting with a clean surface [2,3]. Fig. 2.11 considers the specific example of hydrogen adsorption on the surface of an adsorbent [40,41]. Note that the mechanisms explained hereafter are applicable to any adsorbate/adsorbent system (see for instance Fig. 2.12 for the case of nitrogen).

2.3.3.1 Molecular physisorption

As the H_2 molecule approaches the surface as a result of weak attractive forces, the potential energy of the system moves toward a shallow minimum (H_2 physisorbed) at a relatively large distance ($Z_{physisorbed}$) from the surface, typically >0.3 nm (Fig. 2.11). The molecule enters the physisorption well without any energy barrier. In other words, the process is considered to be *nonactivated* and the kinetics of adsorption is consistently *fast*. When the molecule moves further toward the surface, strong repulsive forces resulting from the overlap of electron densities cause a rapid increase in potential energy.

2.3.3.2 Dissociative and molecular chemisorption

In another scenario, and at a very large distance from the surface, the hydrogen molecule can dissociate into two hydrogen atoms. However, a considerable amount of energy (c. 435 kJ mol^{-1}) is required to break the H—H bond. This energy is called the bond

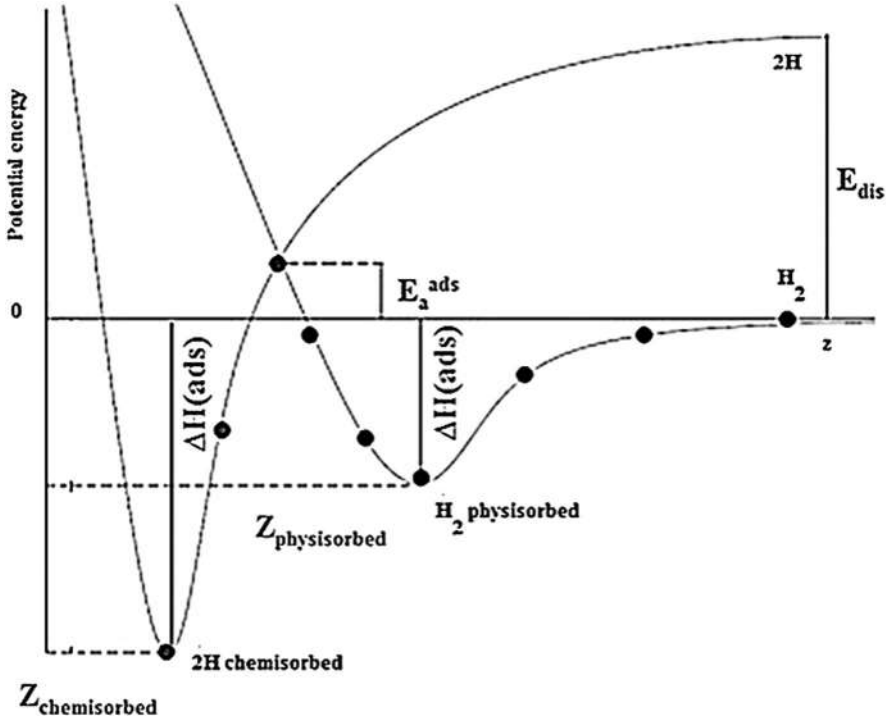

Figure 2.11

Chemisorption and physisorption of hydrogen on a surface. *z*: distance from the surface, $Z_{physisorbed}$: distance between the surface and a physisorbed hydrogen molecule (physisorbed H_2), $Z_{chemisorbed}$: distance between the surface and a chemisorbed hydrogen atom (two H atoms chemisorbed), E_{dis}: bond dissociation energy, E_a^{ads}: activation energy for chemisorption, and $\Delta H(ads)$: enthalpy of adsorption. Source: *Reproduced from [40].*

dissociation energy, E_{dis}. As the two H atoms approach the surface, they form strong chemical bonds with the adsorbent surface. As a result, the potential energy of the system moves toward a deep minimum (2H chemisorbed) with a distance ($Z_{chemisorbed}$) from the surface corresponding to the equilibrium bond distance between the H atom and the surface. Hydrogen can also chemisorb on a surface as a molecule. Here, the same path as dissociative chemisorption is followed. However, instead of starting at a potential energy of E_{dis}, the path begins at the zero potential energy level, which is the one characterizing a gaseous molecule H_2.

The adsorption energy, $\Delta E(ads)$, may be associated with the enthalpy of adsorption, $\Delta H(ads)$. According to the condensation approximation, the heat of adsorption, Q, on a heterogeneous surface, corresponds to the adsorption energy, $\Delta E(ads)$, on the homogenous

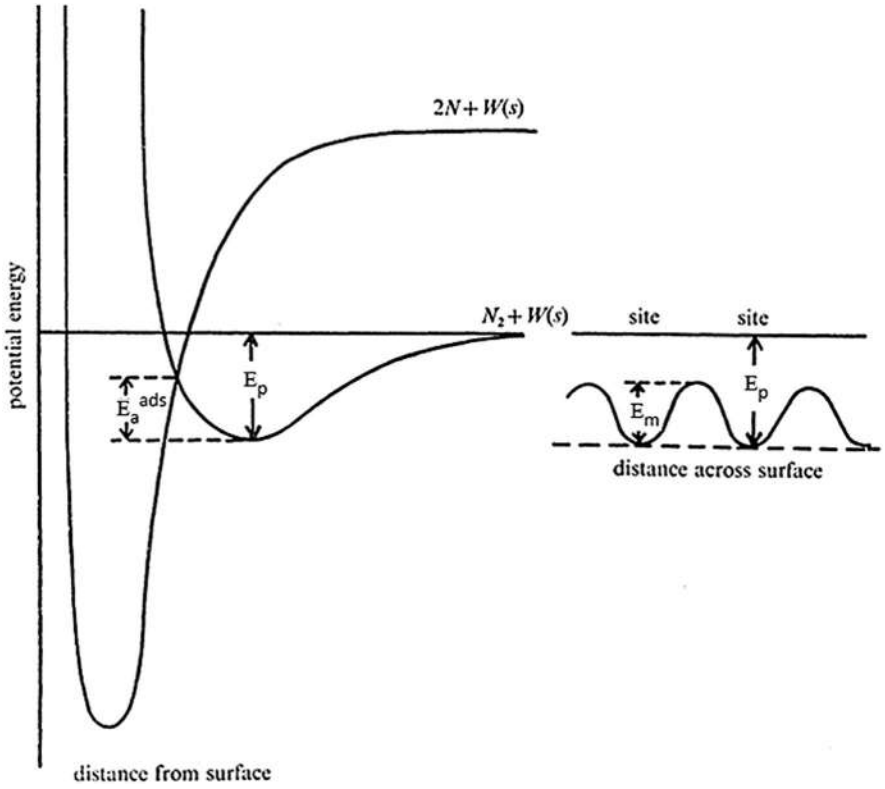

Figure 2.12
Potential energy diagram for physisorbed and chemisorbed nitrogen as a function of both the distance from the adsorbent's surface (left) and the distance across the adsorbent's surface in the case of physisorption (right). E_a^{ads}: activation energy of chemisorption; E_p measures the strength of physisorption and is a direct representation of the adsorption energy, $\Delta E(ads)$; E_m: activation barrier for surface migration. Source: *Reproduced from [42].*

surface where condensation takes place. In other words, the approximation states that the heat of adsorption does not depend on the heterogeneity of the surface [43]. Note that the heat of adsorption, Q, is a positive quantity equal in magnitude to the enthalpy of adsorption, $\Delta H(ads)$, that is, $Q = -\Delta H(ads)$ *for exothermic adsorptions* (Fig. 2.11).

If it possesses enough potential energy, a *physisorbed or chemisorbed adsorbate can migrate from one site to another* neighboring one: as shown in Fig. 2.12 the migration for a physisorbed state occurs if $E > E_m$. The mean−square displacement, R^2, can be expressed as:

$$\langle R^2 \rangle = Dt \tag{2.23}$$

where D is the diffusion coefficient in $cm^2\ s^{-1}$ and t is the time. The diffusion coefficient is temperature-dependent and is defined as:

$$D = D_0 exp\left(\frac{-E_m}{RT}\right) \tag{2.24}$$

The diffusion coefficient is typically determined experimentally through one of many well-established methods. Eq. (2.24) can then be used to evaluate the activation barrier for surface migration, E_m. In chemisorption, E_m generally lies between 10% and 20% of the magnitude of the bond energy holding the chemisorbed species to the surface [2]. The frequency with which an adsorbed species moves along a catalytic surface may be described by analogy with Eq. (2.13):

$$\tau' = \tau_0' exp\left(\frac{E_m}{RT}\right) \tag{2.25}$$

If $E_m << RT$, then the adsorbed species migrates freely over the surface and it behaves as a two-dimensional gas. This is the case in many catalytic reactions, especially those operating at high temperature. As a final note, the migration activation energy E_m for physisorbed states is typically smaller than the one for chemisorbed states, as can be easily understood.

2.3.3.3 "Precursor-mediated" dissociative chemisorption

The mechanism of dissociative hydrogen chemisorption, which starts from two H atoms in the gas phase (Fig. 2.11), is not practical due to the large amount of energy required to break a hydrogen molecule in the gas phase [3]. Instead, a more realistic approach would be for the H_2 molecule to initially follow the physisorption curve as indicated by the green path in Fig. 2.13. Then, the molecule undergoes a *transient physisorption process*, where it can either desorb back as a molecule into the gas phase or dissociatively chemisorb on the surface. In the latter case, the mechanism is defined as a "precursor-mediated" chemisorption process and is schematically illustrated by the green path in Fig. 2.13A. Alternatively, if the hydrogen molecule approaches the surface with sufficient energy, it may dissociate and pass directly into the chemisorption well in a process known as *"direct" chemisorption* (green path in Fig. 2.13B). Here the molecule does not undergo a physisorption process or pass into a physisorption well.

In "precursor-mediated" chemisorption, the position of the crossing point of the molecular physisorption curve with the dissociative chemisorption curve is of great significance. If the crossing point lies below the zero energy line, as is the case in Fig. 2.12, then there is no activation barrier to dissociative adsorption and the process is considered to be nonactivated [41]. In other words, there is no activation energy for adsorption ($E_a^{ads} = 0$). However, if the point lies above the zero energy line as shown in Fig. 2.11, then there is a significant barrier to chemisorption (E_a^{ads}) and the process is said to be activated [40].

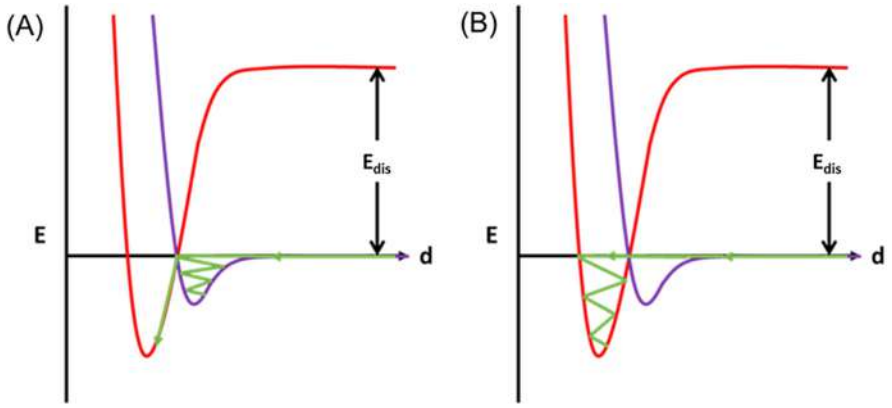

Figure 2.13
Potential energy diagrams where the green line represents (A) a transient physisorption process and (B) a direct chemisorption process. The red line represents a dissociative chemisorption process while the purple line represents a molecular physisorption process. *E* represents the potential energy, *d* represents the distance from the surface, and E_{dis} represents the bond dissociation energy.

Contrary to adsorption, the *reversible desorption process is always activated*. The activation energy of desorption, E_a^{des}, is the summation of $-\Delta E(ads)$ and the activation energy of adsorption, E_a^{ads}:

$$E_a^{des} = -\Delta E(ads) + E_a^{ads} \tag{2.26}$$

Since $E_a^{ads} << E_a^{des}$ and $\Delta E(ads) \sim \Delta H(ads)$, Eq. (2.26) may be rewritten as:

$$E_a^{des} \sim -\Delta H(ads) \tag{2.27}$$

As previously discussed in Section 2.2, the majority of adsorption processes are exothermic while only a few are endothermic [44]. In the potential energy diagram of an exothermic adsorption process, the energy of the adsorbed atoms is below that of the gaseous adsorbate molecule. Conversely, in the potential energy diagram of an endothermic adsorption process, the energy of the adsorbed atoms is above that of the gaseous adsorbate molecule. Both cases are illustrated in the potential energy curve diagram of Fig. 2.14A. The adsorption of hydrogen on a transition metal is usually exothermic [45,46]. However, *there are some cases where endothermicity is claimed to be dominant such as for the chemisorption on glass, silver, gold, or zinc surface* [18]. Fig. 2.14B shows the potential energy diagram of the endothermic adsorption H_2 on Zn(0001), where the energy in the adsorbed state, that is, Zn—H, is higher than that of molecular hydrogen [45].

Potential energy diagrams can also be represented in two dimensions with the energy varying as a function of both the distance from the surface and the interatomic distance within a diatomic

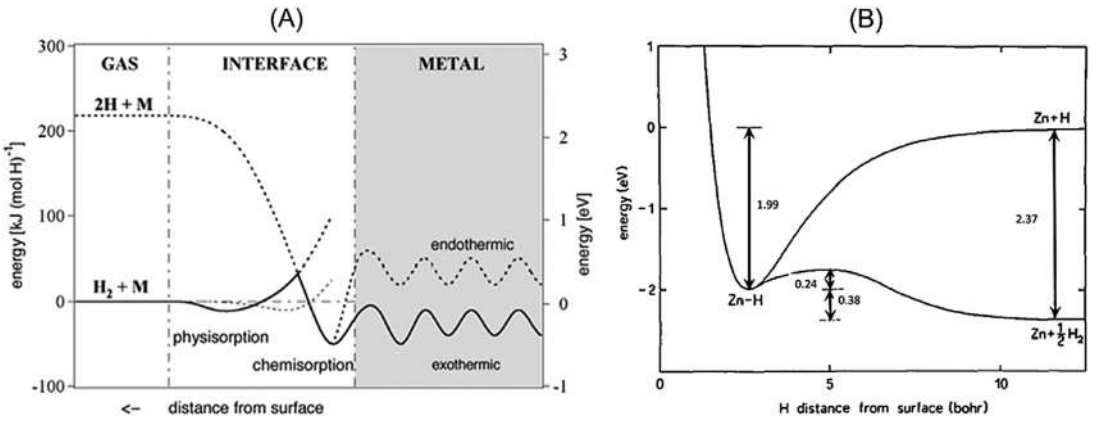

Figure 2.14

(A) Potential energy curve of a hydrogen molecule as it approaches a metal surface.(B) Energy diagram of the endothermic adsorption of H_2 on Zn(0001). Source: *(A) Reproduced from [47]. (B) Reproduced from [45].*

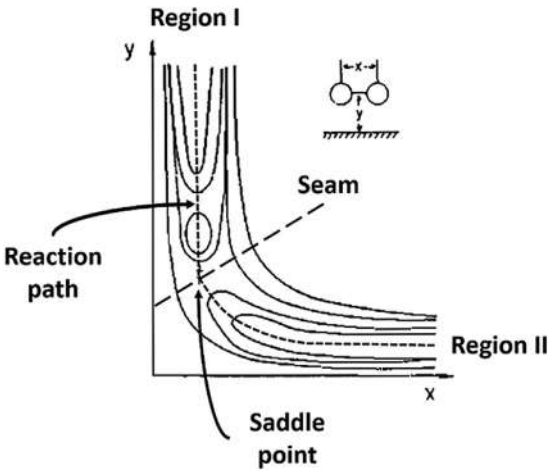

Figure 2.15

Two-dimensional potential energy diagram of a diatomic molecule approaching a surface. Source: *Reproduced from [2].*

molecule (Fig. 2.15). The potential energy along each equipotential line, however, is constant, just as the altitude along each contour line on a map is the same. Following the reaction path as indicated in Figs. 2.15 and 2.16, the molecule first moves toward the surface and enters the *weakly bound physisorption state* (Region I). As the distance between the molecule and the surface decreases, the interatomic distance remains almost unchanged (corresponding to the bond

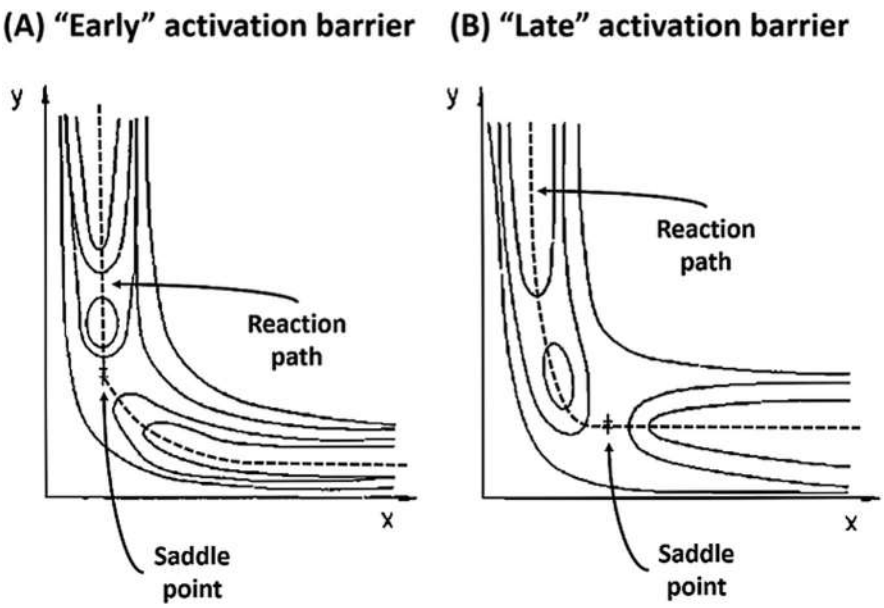

Figure 2.16
Two-dimensional potential energy diagrams of a diatomic molecule approaching a surface with a barrier (A) at the entrance channel of adsorption and (B) at the exit channel of adsorption
Source: *Reproduced from [2].*

length). However, after a certain molecule-surface distance has been reached, the antibonding electronic levels begin to fill. This weakens the interatomic bond and consequently increases the interatomic distance. Eventually, the molecule dissociates and enters the *strongly bound chemisorption state* (Region II). The two-dimensional potential energy diagram in Fig. 2.15 consists of two main regions: the *molecular potential region (region I and II) and the atomic potential region (seam)*. Unlike the molecular potential region, the atomic potential region corresponds to an energy maximum that cannot be overcome. The crossover between the molecular potential and the atomic potential is defined by the saddle point in the potential energy surface diagram [48]. The location of the saddle point is of extreme importance as it determines the type of activation barrier for dissociative adsorption. A saddle point located at the entrance channel of adsorption (Fig. 2.16A) signifies an *"early" activation barrier*, while one located at the exit channel (Fig. 2.16B) signifies a *"late" barrier* [48]. An early activation barrier can be overcome by kinetic energy, while a late activation barrier can only be overcome by excitation through an appropriate molecular vibration [2]. In some cases, the two-dimensional potential energy diagram might show the presence of only one region and, thus, no saddle point exists [49]. If the diagram shows only Region I, then the molecule either is repelled or weakly binds to the surface through physisorption and no dissociative chemisorption takes place (Fig. 2.17A and B, respectively). On the other hand, if the diagram shows only Region II, then the molecule

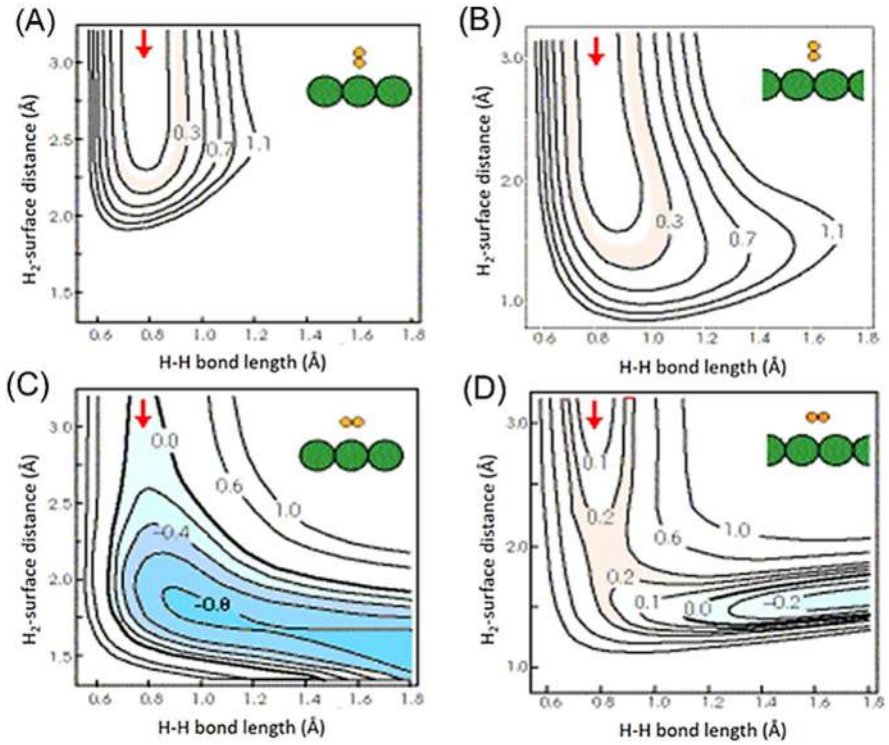

Figure 2.17

Higher dimensionality potential energy diagrams of H_2 approaching a surface in two different orientations at two different sites. The red arrow represents the reaction path, the green circles represent atoms of the adsorbent surface, and the orange circles represent atoms of the hydrogen molecule. (A) The molecule is strongly repelled from the surface, (B) the molecule is weakly repelled from the surface, (C) the molecule dissociates without any barrier, and (D) the molecule dissociates with a barrier. The reported contour values represent the potential energies in eV. Source: *Reproduced from [49].*

dissociates without any barrier and adsorbs to the surface through dissociative chemisorption (Fig. 2.17C). Fig. 2.17D represents the case where both regions are present (i.e., a saddle point "or an activation barrier" exits).

2.3.4 The Elovich equation in chemisorption kinetics

To describe the *chemisorption kinetics of gases*, Zeldovich and others proposed an equation of the form [50]:

$$\frac{dq}{dt} = aexp(-\alpha q) \tag{2.28}$$

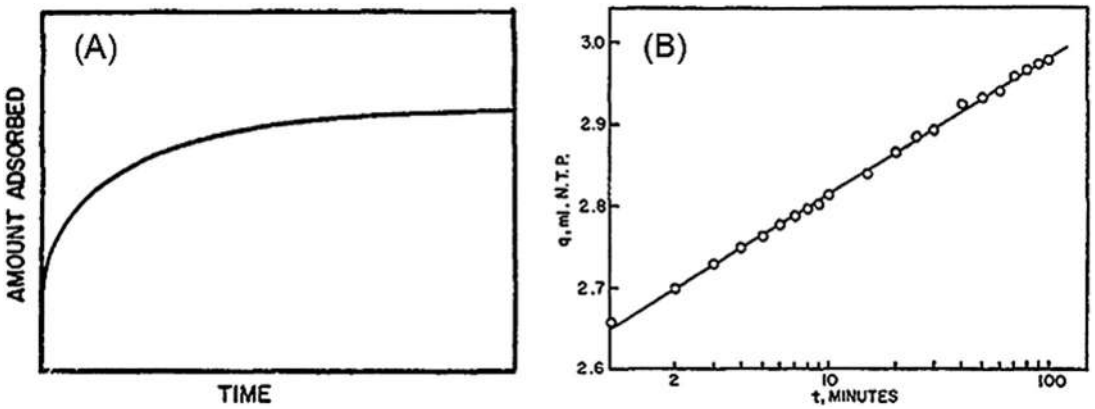

Figure 2.18

(A) Typical time profile of a slow chemisorption process. (B) The amount of hydrogen adsorbed on ruthenium, q, as a function of time, t. White circles represent experimental data points while the solid line represents data obtained by application of the Elovich equation (integrated form). Source: *Reproduced from [50].*

where q is the amount adsorbed at a time t, and a and α are pressure- and temperature-dependent constants. Eq. (2.28) is better known as the *Elovich equation*. The Elovich equation, which agrees well with experimental results, is often used to describe slow chemisorption processes typical to a wide range of gas–catalyst interactions [2]. The general kinetic characteristics of slow chemisorption are presented in Fig. 2.18A. The adsorption starts out rapidly but later decelerates gradually until it becomes excessively slow or stops completely. The adsorption of hydrogen and carbon monoxide on iron and nickel films, for instance, was shown to perfectly fit the Elovich kinetic model. However, when the chemisorption process becomes extremely slow, which is usually the case at the end of a reaction, the Elovich model fails. Nonetheless, the Elovich equation has seen widespread application in a variety of different fields, where it demonstrated high precision in reproducing kinetic data [50].

Assuming that $q = 0$ at $t = 0$, the integrated form of the Elovich equation may be expressed as [50]:

$$q = \frac{2.3}{\alpha} log(t + t_0) - \frac{2.3}{\alpha} log(t_0) \tag{2.29}$$

where $t_0 = 1/a\alpha$. If a volume of gas, q_0, adsorbs instantaneously, then Eq. (2.29) becomes:

$$q = \frac{2.3}{\alpha} log(t + k) - \frac{2.3}{\alpha} log(t_0) \tag{2.30}$$

where $k = t_0 exp(\alpha q_0)$. A plot of q versus $log(t + k)$, the Elovich plot, is linear with a slope equivalent to $2.3/\alpha$. Fig. 2.18B shows the Elovich plot for hydrogen adsorption on ruthenium.

Focus 2.7: Numerical example on the estimation of the constant α of the Elovich equation

Consider the data in the following table for the chemisorption of hydrogen on zinc oxide at 413K. Discuss the variation of the constant α (of the Elovich equation) with pressure.

Pressure (mmHg)	Time (min)	Amount adsorbed STP (cc)	Pressure (mmHg)	Time (min)	Amount adsorbed STP (cc)
15	2	1.733	72	2	2.746
	10	2.209		10	4.083
	20	2.521		20	4.503
	100	3.042		100	5.515
	200	3.302		200	6.014

Solution

Using Eq. (2.29), plot $log(t + t_0)$ against q with t_0 adjusted to give a best-fit linear curve. The plot is shown as follows and the value of α is determined from the slope (slope = $2.3/\alpha$).

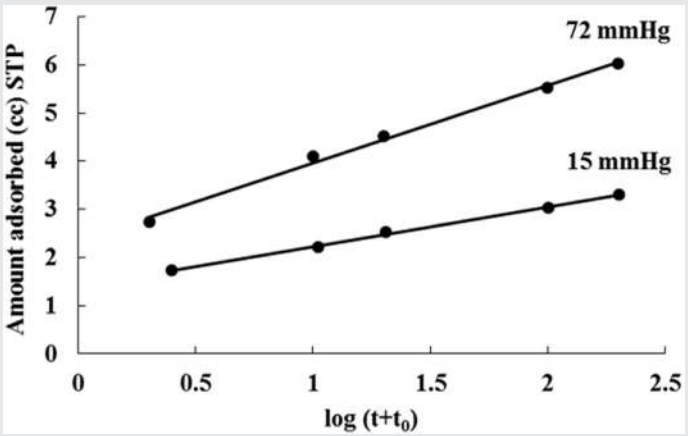

At 15 mmHg, the slope of the line is 0.8255 cc, hence α is 2.786 cc^{-1}. Similarly, at 72 mmHg, the slope of the line is 1.6008 cc and α is 1.437 cc^{-1}. Results indicate that the slope of the Elovich plot increases with pressure and that the constant α decreases with pressure. This variation in α with pressure is attributed to the different sets of sites being occupied upon changing the pressure. Additionally, the contribution of desorption in the adsorption rate measurements is altered when the pressure is changed. Note that the same variation in α is also observed with temperature and for analogous reasons [51].

2.3.5 Desorption rate

The rate of desorption, r_d, is commonly expressed with the *Polanyi–Wigner equation*:

$$r_d = \frac{-dN_a}{dt} = vN_a^m exp\left(\frac{-E_a^{des}}{RT}\right) \tag{2.31}$$

where N_a is the number of binding sites of the admolecules, ν is a frequency factor, m is the kinetic order of the desorption process, and E_a^{des} is the activation energy of desorption. These four important kinetic parameters (N_a, ν, m, and E_a^{des}) provide mechanistic insights on the desorption process [2]. The Polanyi–Wigner equation may also be expressed as:

$$r_d = \frac{-d\theta}{dt} = \nu' \theta^m exp\left(\frac{-E_a^{\text{des}}}{RT}\right) \tag{2.32}$$

where ν' is different from ν only by a numerical factor.

Zero-order kinetics with respect to the coverage θ is an indication of desorption from a multilayer. *First-order kinetics* indicates the presence of a single surface species. *Second-order kinetics* may be indicative of the recombination of adsorbate atoms to form a diatomic molecule [2] (note that if adsorption is nonactivated, then the activation energy of desorption is equal to the heat of adsorption, as described in Section 2.3.3).

The thermal desorption from a GaAs surface exposed to different doses of hydrogen sulfide is shown in Fig. 2.19. Hydrogen sulfide binds to the surface in three distinct states: α, β_1, and β_2. The α state represents weakly bound molecular hydrogen sulfide, while the β states

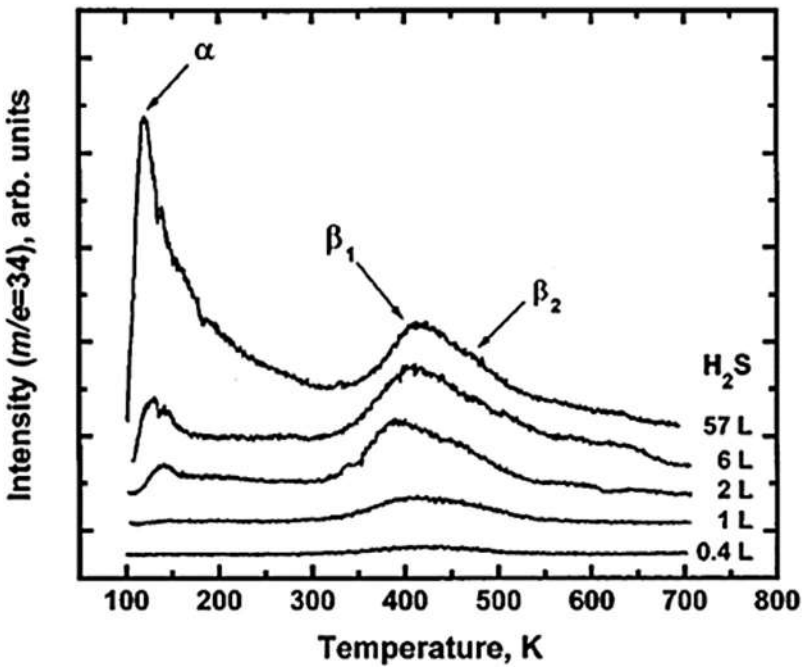

Figure 2.19
Thermal desorption spectra recorded after hydrogen sulfide exposure to GaAs. Heating rate = 1 K s^{-1}. α, β_1, and β_2 represent the three distinct states by which hydrogen sulfide adsorbs onto GaAs. Source: *Reproduced from [52].*

represent dissociatively chemisorbed hydrogen sulfide [52]. The low temperature peak (α state) occurs at a temperature that is independent of hydrogen sulfide coverage, indicating first-order desorption kinetics. The high temperature peak (β states) occurs at a temperature that changes with coverage revealing second-order desorption kinetics.

Focus 2.8: Numerical example on the estimation of activation energy of desorption from thermal desorption spectra

Consider the thermal desorption of Ag from Ru (001) [53]. The thermal desorption spectra (TDS) at different coverages are shown in figure A. Calculate the activation energy of desorption (figure reproduced from [54]).

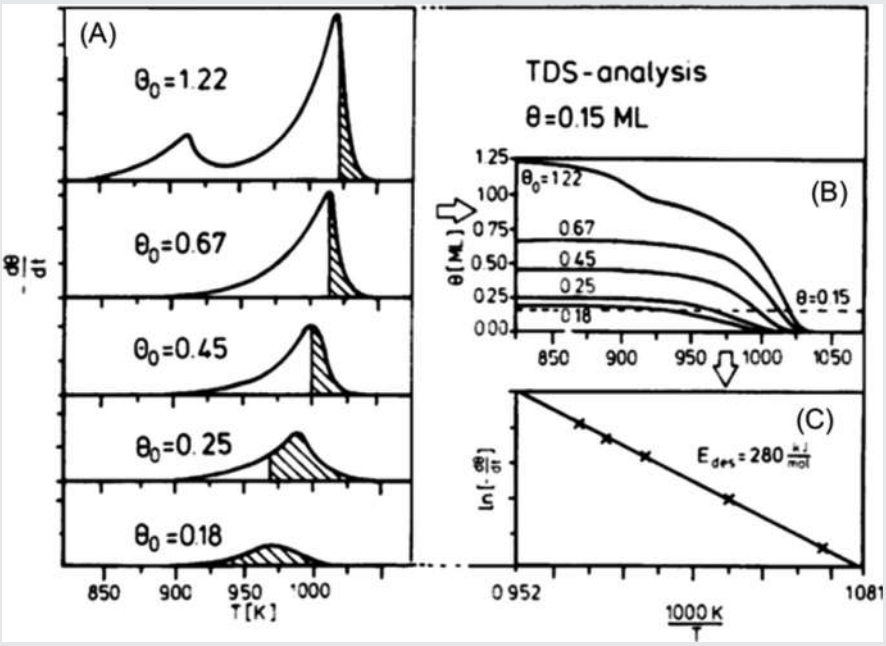

Solution

First, the TDS are integrated, yielding the figure B. Then, a coverage that can be reached at different temperatures is chosen (e.g., 0.15). From the original TDS (i.e., figure A), the rate of desorption values at different temperatures that correspond to a coverage of 0.15 is obtained. Finally, using Eq. (2.32), ln (r_d) versus $1/T$ is plotted to get figure C. The activation energy of desorption can then be calculated from the slope of the resulting line.

2.4 Questions and problems

1. A spontaneous chemisorption process has been found to have a positive enthalpy. Provide two possible interpretations of such behavior, considering that the adsorption is spontaneous.
2. Based on simulation studies, it was hypothesized that the desorption of nitrogen from a silicon surface follows zero-order kinetics. Analyze possible experimental tests which can corroborate this hypothesis and provide a physical interpretation of this desorption rate order.
3. Describe the chemisorption of a free atom on the surface of a transition metal by using the molecular orbital approach. If you use two different metals, and you notice that the antibonding orbital is empty in one case and partially filled in another case, what can you conclude?
4. When can we approximate the activation energy of desorption with the heat of adsorption? Why is this helpful in the study of an adsorption process?
5. Explain how (i) an increased kinetic energy or (ii) a molecular vibration of an adsorbate can help to overcome energy barriers and result in a stable chemisorption state.
6. The enthalpy of chemisorption is usually variable with the surface coverage. Why? What can you conclude in instances in which it does not change with coverage?
7. Under which circumstances can adsorbates migrate from a surface site to the adjacent ones?
8. If a desorption rate is linear with θ, what can you say about the process?
9. The following table reports data extracted from thermal desorption spectra recorded after atomic hydrogen exposure to a rhodium catalyst. What can you conclude about the reaction order and the desorption kinetics? What is the activation energy of desorption? The desorption rate is given as peak intensity in arbitrary units and the corresponding coverage and temperature are reported.

Thermal desorption peak intensity (au)	Coverage	Temperature (K)
0.675	1.00	564
0.821	0.96	569
1.395	0.86	583
1.955	0.73	596
2.668	0.49	619
1.645	0.23	642
0.436	0.09	655

10. Consider the dissociative chemisorption of oxygen gas on the surface of a nickel catalyst. Construct, and then explain, a qualitative potential energy diagram that represents the exothermic adsorption of the free oxygen atoms. How is the enthalpy of chemisorption related to the activation energy of desorption?

11. Consider the nondissociative adsorption of nitric oxide onto the surface of a rhodium catalyst taking place at 8.6 Torr and 820K. The rate of desorption, r_d, was found to follow the following kinetics:

$$r_d = \nu n_0 \theta exp\left(\frac{-E_a^{\text{des}}}{RT}\right)$$

where n_0 is the concentration of available sites on the surface (10^{14} cm^{-2}), ν is the frequency factor (10^{15} s^{-1}), and E_a^{des} is the activation energy of desorption (equal to the heat of adsorption, 210 kJ mol^{-1}).
    a. What is the activation energy of adsorption?
    b. Calculate the rate of adsorption assuming that the surface coverage is zero. Note that the condensation coefficient for this system is equal to 0.36.
    c. Calculate the coverage assuming that the rate of desorption is equal to 7.125×10^{10} molecules m^{-2} s^{-1}.
12. The desorption of O_2 from the surface of a W catalyst was found to follow first-order kinetics. The volume of O_2 desorbed in 36 min at 747K is the same as that desorbed in 3 min at 889K. What is the activation energy of desorption? Calculate the time required for the same amount of O_2 to desorb at 689K.
13. Calculate the time during which a hydrogen atom remains adsorbed on the sites of a flat surface of a zinc catalyst at 30°C, given that the enthalpy of adsorption is 26 kcal mol^{-1} and that the adsorption process is nonactivated.

References

[1] H.S. Fogler, Elements of Chemical Reaction Engineering, Prentice Hall PTR, 2006.
[2] J.M. Thomas, W.J. Thomas, Principles and Practice of Heterogeneous Catalysis, John Wiley & Sons, 2014.
[3] R.M. Nix, An Introduction to Surface Chemistry, School of Biological & Chemical Sciences Queen Mary, University of London, 2003.
[4] C. Erkey, Supercritical Fluids and Organometallic Compounds: From Recovery of Trace Metals to Synthesis of Nanostructured Materials, Elsevier, 2011.
[5] F. Rosei, Nanostructured surfaces: challenges and frontiers in nanotechnology, J. Phys.: Condens. Matter 16 (2004) S1373.
[6] A. Patrykiejew, S. Sokołowski, K. Binder, Phase transitions in adsorbed layers formed on crystals of square and rectangular surface lattice, Surf. Sci. Rep. 37 (2000) 207–344.
[7] H. Over, Crystallographic study of interaction between adspecies on metal surfaces, Prog. Surf. Sci. 58 (1998) 249–376.
[8] W. Nichtl-Pecher, J. Gossmann, W. Stammler, G. Besold, L. Hammer, K. Heinz, et al., Hydrogen on Rh (110): a walk through the phase diagram, Surf. Sci. 249 (1991) 61–74.
[9] D. Woodruff, Surface crystallography and its relationship to catalysis, Crystallography Rev. 11 (2005) 35–47.
[10] Z. Quan, Y. Wang, J. Fang, High-index faceted noble metal nanocrystals, Acc. Chem. Res. 46 (2013) 191–202.
[11] B. Hammer, Special sites at noble and late transition metal catalysts, Top. Catal. 37 (2006) 3–16.

[12] N. Tian, Z.-Y. Zhou, S.-G. Sun, Y. Ding, Z.L. Wang, Synthesis of tetrahexahedral platinum nanocrystals with high-index facets and high electro-oxidation activity, Science 316 (2007) 732–735.
[13] T. Ming, W. Feng, Q. Tang, F. Wang, L. Sun, J. Wang, et al., Growth of tetrahexahedral gold nanocrystals with high-index facets, J. Am. Chem. Soc. 131 (2009) 16350–16351.
[14] C. Xie, D. Yan, H. Li, S. Du, W. Chen, Y. Wang, et al., Defect chemistry in heterogeneous catalysis: recognition, understanding, and utilization, ACS Catal. 10 (2020) 11082–11098.
[15] I. Chorkendorff, J.W. Niemantsverdriet, Concepts of Modern Catalysis and Kinetics, John Wiley & Sons, 2017.
[16] J.W. Niemantsverdriet, Appendix: Metal surfaces and chemisorption, in: J.W. Niemantsverdriet (Ed.), Spectroscopy in Catalysis: An Introduction, third ed., John Wiley & Sons, 2007, pp. 297–320.
[17] D.C. Koningsberger, D.E. Ramaker, J.T. Miller, J. de Graaf, B.L. Mojet, The direct influence of the support on the electronic structure of the active sites in supported metal catalysts: evidence from Pt–H anti-bonding shape resonance and Pt–CO FTIR data, Top. Catal. 15 (2001) 35–42.
[18] J.M. Thomas, The existence of endothermic adsorption, J. Chem. Educ. 38 (1961) 138.
[19] M. Roberts, Chemisorption and reactions at metal surfaces, Surf. Sci. 299 (1994) 769–784.
[20] K.-I. Tanaka, K. Tamaru, A general rule in chemisorption of gases on metals, J. Catal. 2 (1963) 366–370.
[21] G. Sethia, R.S. Somani, H.C. Bajaj, Adsorption of carbon monoxide, methane and nitrogen on alkaline earth metal ion exchanged zeolite-X: structure, cation position and adsorption relationship, RSC Adv. 5 (2015) 12773–12781.
[22] S. Eyer, N.P. Stadie, A. Borgschulte, L. Emmenegger, J. Mohn, Methane preconcentration by adsorption: a methodology for materials and conditions selection, Adsorption 20 (2014) 657–666.
[23] W. Ding, Simulation-Assisted Design of Polycrystalline Zeolite Catalysts, KIT Scientific Publishing, 2016.
[24] D.A. Kennedy, M. Mujcin, E. Trudeau, F.H. Tezel, Pure and binary adsorption equilibria of methane and nitrogen on activated carbons, desiccants, and zeolites at different pressures, J. Chem. Eng. Data 61 (2016) 3163–3176.
[25] K.V. Kumar, M.M. de Castro, M. Martinez-Escandell, M. Molina-Sabio, F. Rodriguez-Reinoso, A site energy distribution function from Toth isotherm for adsorption of gases on heterogeneous surfaces, Phys. Chem. Chem. Phys. 13 (2011) 5753–5759.
[26] A. Aşkın, C. Bilgiç, Thermodynamics of adsorption of hydrocarbons on molecular sieves NaY and CaY by inverse gas chromatography, Chem. Eng. J. 112 (2005) 159–165.
[27] D.R. Lide, CRC Handbook of Chemistry and Physics, 85, CRC Press, 2004.
[28] D. Nicholson, K.E. Gubbins, Separation of carbon dioxide–methane mixtures by adsorption: effects of geometry and energetics on selectivity, J. Chem. Phys. 104 (1996) 8126–8134.
[29] D.D. Eley, P. Norton, Heats of adsorption on metal wires-I. Hydrogen on polycrystalline tungsten, Proc. R. Soc. London A Math. Phys. Sci. 314 (1970) 301–318.
[30] D.D. Eley, P. Norton, Heats of adsorption on metal wires-II. The heat of adsorption of hydrogen on nickel, Proc. R. Soc. London A Math. Phys. Sci. 314 (1970) 319–328.
[31] D. Eley, A calculation of heats of chemisorption, Discuss. Faraday Soc. 8 (1950) 34–38.
[32] D. Eley, Molecular hydrogen and metallic surfaces, J. Phys. Chem. 55 (1951) 1017–1036.
[33] S. Trasatti, Electronegativity, work function, and heat of adsorption of hydrogen on metals, J. Chem. Soc. Faraday Trans. 1: Phys. Chem. Condens. Phases 68 (1972) 229–236.
[34] G. Schirripa Spagnolo, F. Leccese, M. Leccisi, LED as transmitter and receiver of light: a simple tool to demonstration photoelectric effect, Crystals 9 (2019) 531.
[35] T. Engel, G. Ertl, Elementary steps in the catalytic oxidation of carbon monoxide on platinum metals, Adv. Catal. 28 (1979) 1–78. Elsevier.
[36] J. Frenkel, Theorie der Adsorption und verwandter Erscheinungen, Z. Phys. 26 (1924) 117–138.
[37] K. Oura, M. Katayama, A. Zotov, V. Lifshits, A. Saranin, Elementary processes at surfaces i. adsorption and desorption, Surf. Sci. (2003) 295–323. Springer.

[38] P. Kisliuk, The sticking probabilities of gases chemisorbed on the surfaces of solids, J. Phys. Chem. Solids 3 (1957) 95–101.
[39] Y.Y. Yeo, L. Vattuone, D.A. King, Calorimetric heats for CO and oxygen adsorption and for the catalytic CO oxidation reaction on Pt{111}, J. Chem. Phys. 106 (1997) 392–401.
[40] A.N. Pour, Z. Keyvanloo, M. Izadyar, S.M. Modaresi, Dissociative hydrogen adsorption on the cubic cobalt surfaces: a DFT study, Int. J. Hydrog. Energy 40 (2015) 7064–7071.
[41] M. Hirscher, B. Panella, Nanostructures with high surface area for hydrogen storage, J. Alloy. Compd. 404 (2005) 399–401.
[42] D.A. King, M. Wells, Reaction mechanism in chemisorption kinetics: nitrogen on the {100} plane of tungsten, Proc. R. Soc. London A Math. Phys. Sci. 339 (1974) 245–269.
[43] L.B. Harris, Adsorption on a patchwise heterogeneous surface: II. Heats of adsorption from the condensation approximation, Surf. Sci. 13 (1969) 377–392.
[44] M. Dornheim, Thermodynamics of metal hydrides: tailoring reaction enthalpies of hydrogen storage materials, Thermodynamics-Interaction Studies-Solids, Liquids and Gases, IntechOpen, 2011.
[45] P. Cremaschi, G. Tantardini, J. Muilu, T. Pakkanen, Adsorption of hydrogen on zinc—calculation of potential energy surface and dynamics, Vacuum 41 (1990) 260–264.
[46] J. Lipkowski, P.N. Ross, Electrocatalysis, Wiley, 1998.
[47] A. Züttel, Materials for hydrogen storage, Mater. Today 6 (2003) 24–33.
[48] A. Winkler, Reaction studies on nanostructured surfaces, in: Oxford Handbook of Nanoscience and Technology: Volume 1: Basic Aspects, Oxford University Press Inc, New York, 2010, p. 355.
[49] Pennsylvania State University, Adsorption at surfaces. Available: https://www.coursehero.com/file/24846864/Adsorption-at-surfacespdf/, 2009.
[50] M. Low, Kinetics of chemisorption of gases on solids, Chem. Rev. 60 (1960) 267–312.
[51] Y. Kubokawa, An interpretation of the Elovich equation for the rate of chemisorption on the basis of surface heterogeneity, Bull. Chem. Soc. Jpn. 33 (1960) 734–738.
[52] C.-H. Chung, S.I. Yi, W.H. Weinberg, Adsorption state of hydrogen sulfide on the GaAs (001)-(4 × 2) surface, J. Vac. Sci. Technol. A: Vacuum, Surfaces, Films 15 (1997) 1163–1167.
[53] J. Niemantsverdriet, P. Dolle, K. Markert, K. Wandelt, Thermal desorption of strained monoatomic Ag and Au layers from Ru (001), J. Vac. Sci. Technol. A: Vacuum, Surfaces, Films 5 (1987) 875–878.
[54] W. Ranke, Modern methods in heterogeneous catalysis research: theory and experiment. Thermal analysis-TDS, modern methods in heterogeneous catalysis research: theory and experiment, Fritz Haber Institute of the Max Planck Society in Berlin, Germany (2002).

CHAPTER 3

Adsorption models, surface reaction, and catalyst architectures

The equilibrium distribution of adsorbate molecules between the surface of an adsorbent and the gas phase is a function of namely five parameters: (1) pressure, (2) temperature, (3) surface area of the adsorbent, (4) nature of the adsorbent, and (5) nature of the adsorbate. An *adsorption isotherm* describes the amount of gas adsorbed on the surface of an adsorbent at a constant temperature as a function of its relative pressure [1,2]. An *adsorption isobar* is a plot that describes the amount of gas adsorbed on the surface of an adsorbent at a constant pressure as a function of temperature [2]. An *adsorption isostere* is a plot that describes the relationship between pressure and temperature for a constant amount of adsorbed gas [2]. Following adsorption, *surface reaction* takes place through different mechanisms, which will be discussed and both the adsorption and reactions steps are strongly dependent on the architecture of catalysts, which can be aided by *cocatalysts* and *supports*.

3.1 Adsorption isotherms and their classification

Adsorption isotherms are recorded typically in *two branches*, an *adsorption* and a *desorption* one, by varying the partial pressure of the adsorbate from 0 to 1 and back from 1 to 0. The fact that the two branches sometimes do not overlap will be explained in Chapter 4, Surface Area and Porosity. To allow for comparison of different materials, the amount adsorbed is almost always reported by normalizing by the mass of the adsorbent [3]. Adsorption isotherms are the most common tool to assess the adsorption of a species on a solid catalyst. Depending on physicochemical conditions, solid porous texture, interaction between adsorbate and adsorbent and more features, adsorption isotherms curves can have different shapes. Based on the convention established by the *International Union of Pure and Applied Chemistry* (IUPAC), the isotherms are classified into *six different types* as illustrated in Fig. 3.1 [4–7]. Most catalytic materials, however, will usually only display an adsorption isotherm that is either Type I, Type II, Type IV, or Type VI [6]. Adsorption isotherms may be empirically described by theoretically derived isotherm equations. The most commonly applied models in catalysis include Langmuir, Henry, Freundlich, Temkin, Brunauer-Emmett-Teller (BET), and Polanyi [2].

Heterogeneous Catalysis.
DOI: https://doi.org/10.1016/B978-0-323-89845-4.00005-9

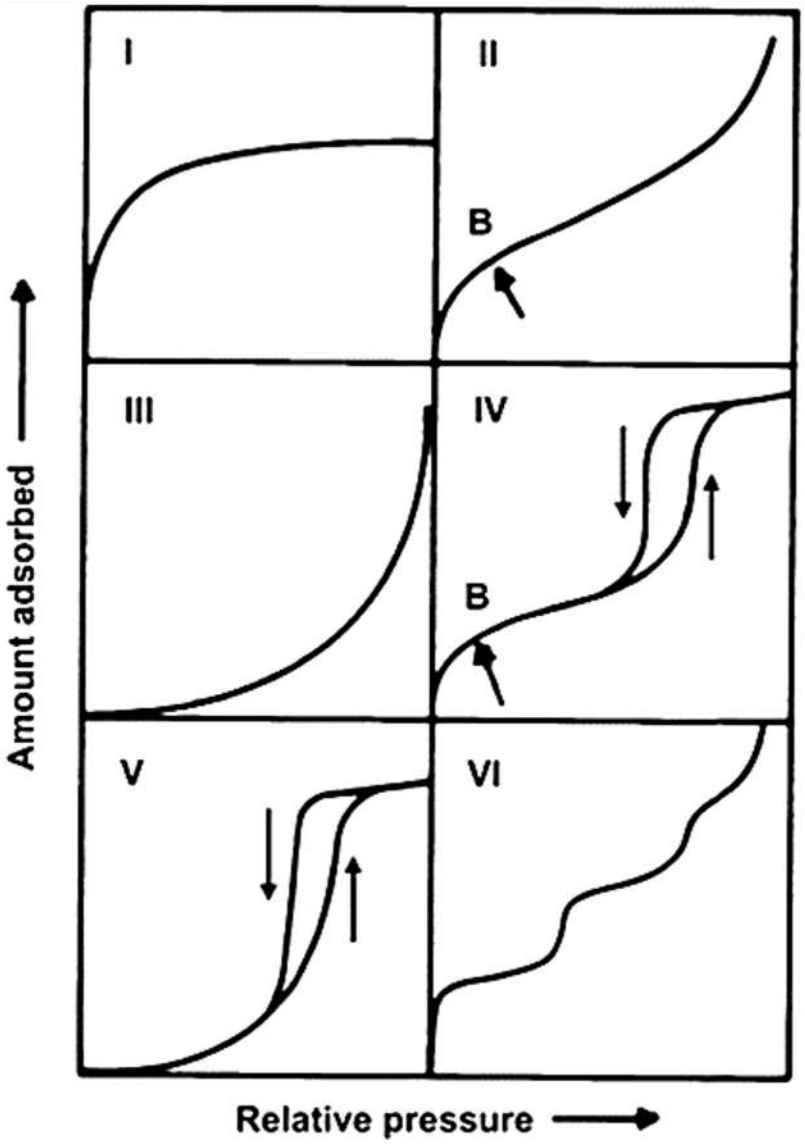

Figure 3.1
IUPAC classification of adsorption isotherms (Type I–VI). Point B represents the completion of the first adsorbed monolayer and the start of multilayer adsorption. The upward and downward arrows represent the adsorption and desorption paths, respectively. Source: *Reproduced from [4].*

Note that, depending on their size, the pores of a solid are commonly categorized as *micropores (<2 nm), mesopores (2–50 nm), or macropores (>50 nm)* [4–6].

Adsorbents exhibiting a *Type I* isotherm are typically microporous with gas molecules adsorbing through chemisorption as a monolayer [4,6–8]. Due to the strong

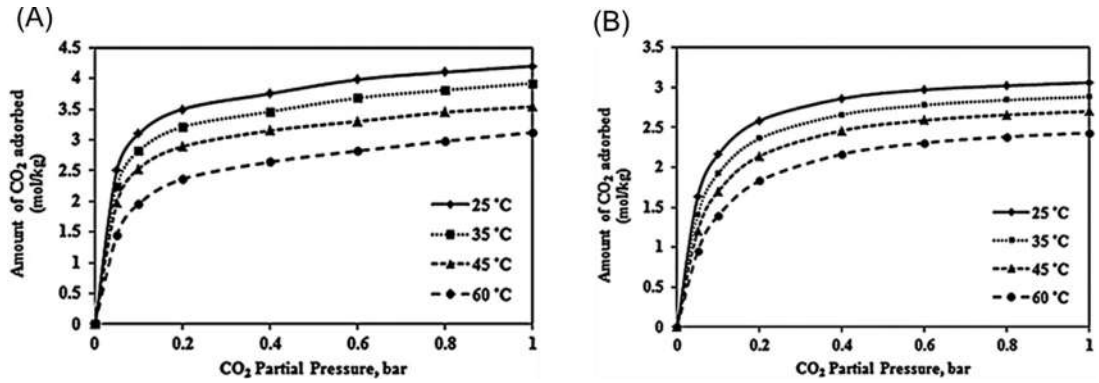

Figure 3.2
Type I adsorption isotherms: CO_2 adsorption on (A) Zeolite 13X and (B) Zeolite 4A at different temperatures. Source: *Reproduced from [9].*

adsorbate–adsorbent interactions, adsorption begins rapidly at very low relative pressures where the surface is still full of free binding sites. As the relative pressure increases, the amount of free sites decreases and, consequently, the probability of adsorption also drops. Once the micropores are filled, adsorption continues on the external surface. However, little, if any, external surface will be available for further adsorption since, in this case, the exposed surface is almost entirely present within the micropores of the solid. Eventually, after all binding sites have been occupied, the isotherm saturates (plateau) and any further increase in relative pressure will not affect the amount adsorbed. Activated carbon, zeolite, and zeolite-like crystals are all microporous materials that have been shown to follow a Type I isotherm behavior [1]. Fig. 3.2 shows the specific example of carbon dioxide adsorption on two different zeolites under varying isothermal conditions.

Adsorbents exhibiting a *Type II* isotherm are typically nonporous or macroporous with gas molecules adsorbing through physisorption as multilayers [4,6–8]. Adsorption begins with the formation of the first adsorbed monolayer at low relative pressures. The completion of monolayer adsorption and the start of multilayer adsorption is represented by the inflection point, B. As the relative pressure increases, multilayer adsorption continues and, consequently, the thickness of the adsorbate layer also increases until the condensation pressure is reached. The pressure at which point B appears depends on the strength of the adsorbate–adsorbent interactions. If the interaction is strong, then point B will appear at a lower pressure than in the case of a weak interaction [1]. The adsorption of nitrogen on volcanic ash and argon on sodalite nanozeolite, for example, has been shown to follow a Type II isotherm behavior (Fig. 3.3).

Adsorbents exhibiting a *Type III* isotherm typically involve a heat of adsorption that is less than the adsorbate's heat of liquefaction. In other words, the interaction of the adsorbate

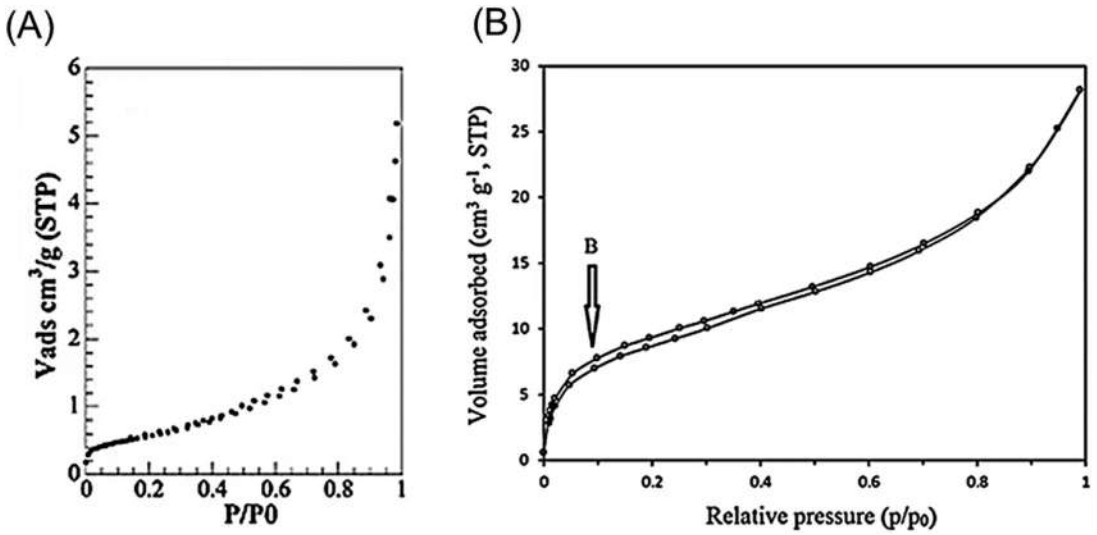

Figure 3.3
Type II adsorption isotherms: (A) N_2 adsorption on volcanic ash at 77K. (B) Argon adsorption on sodalite nanozeolite at 77K. Point B represents the completion of the first adsorbed monolayer and the start of multilayer adsorption. Source: *(A) Reproduced from [10]. (B) Reproduced from [11].*

with an adsorbed layer is greater than its interaction with the adsorbent surface. Hence, the adsorbate–adsorbent interaction is considered weak with respect to the interaction among adsorbate molecules. A general example would be the adsorption of polar molecules on nonpolar adsorbents [4,7]. Due to the low adsorption capacity, adsorption proceeds with a very slow uptake at low relative pressures. As the relative pressure increases to higher values, the number of adlayers of adsorbate molecules grows and, consequently, the adsorption uptake will also increase. Although gas molecules adsorb as multilayers, the point at which monolayer adsorption is complete cannot be determined from the curve of a Type III isotherm [1]. The adsorption of nitrogen on a 1,3,5-benzenetricarboxylate-based metal organic framework, for example, has been shown to follow a Type III isotherm behavior (Fig. 3.4A).

Adsorbents exhibiting a *Type IV* isotherm are typically mesoporous with gas molecules adsorbing through physisorption as multilayers [4,6,7]. Adsorption begins with the formation of the first adsorbed monolayer at low relative pressures. The completion of monolayer adsorption and the start of multilayer adsorption is represented by the inflection point, B. As the relative pressure increases, multilayer adsorption continues and, once condensation pressure is surpassed, capillary condensation begins with a steep increase in the amount adsorbed. Capillary condensation is commonly associated with a hysteresis loop, whereby adsorption and desorption follow different paths. Section 4.3 will provide a

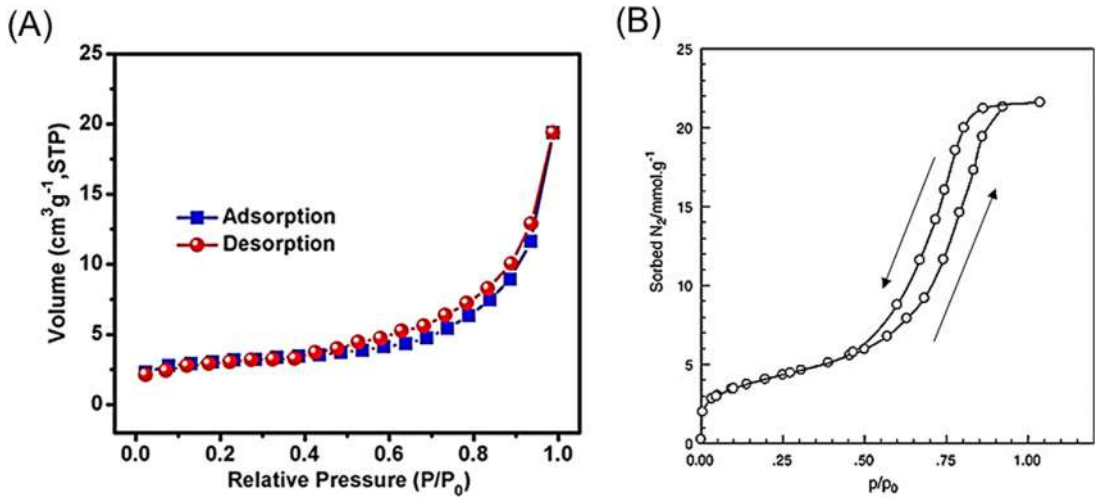

Figure 3.4

(A) Type III adsorption isotherm: N_2 adsorption on a 1,3,5-benzenetricarboxylate-based metal organic framework at 77K. (B) Type IV adsorption isotherm: N_2 adsorption on silica gel at 77K. The upward and downward arrows represent the adsorption and desorption paths, respectively. Source: *(A) Reproduced from [12]. (B) Reproduced from [13].*

more detailed description of this phenomenon and on how it leads to the formation of a hysteresis. Once the mesopores are filled, adsorption continues on the external surface. After all the binding sites have been occupied, the isotherm saturates and any further increase in relative pressure will not affect the amount adsorbed. The majority of catalytic materials have been shown to follow a Type IV isotherm trend [1]. Fig. 3.4B shows the specific example of nitrogen adsorption on silica gel at 77K.

Adsorbents exhibiting a *Type V* isotherm are typically mesoporous with gas molecules adsorbing through physisorption as multilayers. However, similar to Type III, the heat of adsorption is, in this case, less than the adsorbate's heat of liquefaction. Hence, the adsorbate–adsorbent interaction is considered weak [4,7]. Due to the low adsorption capacity, adsorption proceeds with a very slow uptake at low relative pressures. The completion of monolayer adsorption and the start of multilayer adsorption cannot be determined through an inflection of the isotherm curve. As the relative pressure increases, multilayer adsorption continues and capillary condensation begins. Once the mesopores are filled, adsorption continues on the external surface. After all the binding sites have been occupied, the isotherm saturates [1]. The adsorption of water vapor on activated carbon is an example of Type V isotherm (Fig. 3.5A).

Type VI isotherm is quite uncommon and it has been justified by considering the presence of different types of adsorption sites in the adsorbent, on which gases build up at different

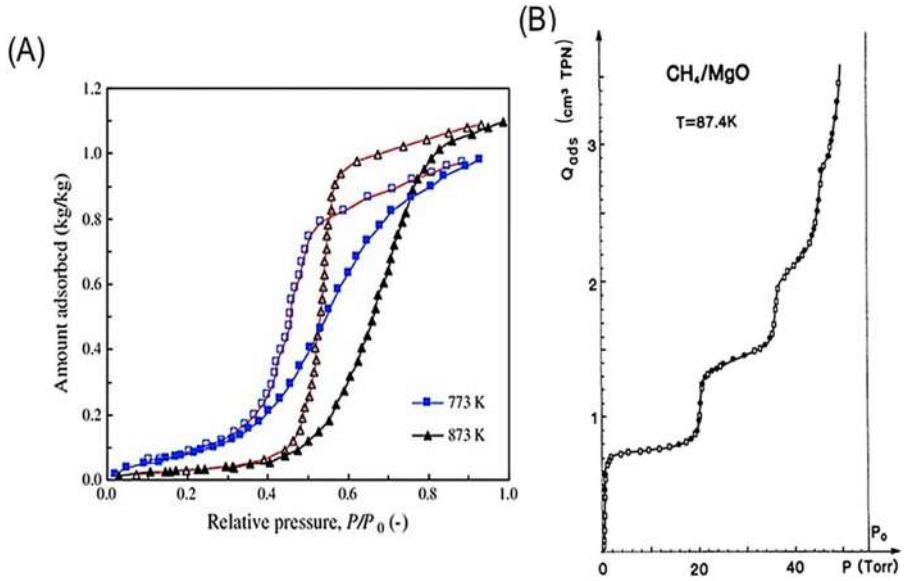

Figure 3.5

(A) Type V adsorption isotherm: H_2O adsorption on polycarbonate-derived activated carbon at 298K. 773K and 873K represent the pyrolysis temperature used in synthesizing the activated carbon. Close and open symbols represent the adsorption and desorption paths, respectively. (B) Type VI adsorption isotherm: CH_4 adsorption on magnesium oxide at 87K. Close and open symbols represent the adsorption and desorption paths, respectively. Source: *(A) Reproduced from [14]. (B) Reproduced from [15].*

partial pressures, step-wise, and through multilayers including clusters with a varied number of molecules [4,6,7]. The height of each step corresponds to the amount of gas adsorbed in that respective layer and the adsorbents exhibiting such isotherm have been found to have a low porosity with a rather uniform surface. Well-crystalized zeolites and silicate are some materials that have been shown to follow a Type VI isotherm behavior [1,6]. Fig. 3.5B shows the specific example of methane adsorption on magnesium oxide with each step corresponding to the condensation of a single layer.

3.1.1 Langmuir isotherm

Let's recall from Chapter 2, Fundamentals of the Adsorption Process, that the rate of adsorption, r, and the rate of desorption, r_d, are expressed as:

$$r = \frac{s'f(\theta)P}{(2\pi mkT)^{\frac{1}{2}}} exp\left(\frac{-E_a^{ads}}{RT}\right) \tag{3.1}$$

$$r_d = vN_a^m exp\left(\frac{-E_a^{des}}{RT}\right) \tag{3.2}$$

Equating the above two equations yields the equation of an adsorption isotherm [2]:

$$vN_a^m exp\left(\frac{-E_a^{des}}{RT}\right) = \frac{s'f(\theta)P}{(2\pi mkT)^{\frac{1}{2}}} exp\left(\frac{-E_a^{ads}}{RT}\right) \tag{3.3}$$

In nondissociative adsorption, $f(\theta) = (1-\theta)$ and $N_a{}^m = \theta$. Substitution and rearrangement gives:

$$P = \frac{(2\pi mkT)^{\frac{1}{2}}v}{s'}\left(\frac{\theta}{1-\theta}\right)exp\left(\frac{\Delta H}{RT}\right) = \frac{\theta}{b(1-\theta)} \tag{3.4}$$

where $\Delta H = E_a{}^{ads} - E_a{}^{des}$. It is of extreme significance to note that, in this model, *the heat of adsorption is assumed to remain constant with coverage*, which is not true for the majority of heterogeneous catalytic reactions. Rearranging, the Langmuir isotherm equation is obtained:

$$\theta = \frac{bP}{1+bP} \tag{3.5}$$

where b is a function of temperature only. This *Langmuir theory of adsorption is restricted only to the formation of a monolayer* on a solid surface and disregards any possibility of multilayer formation. Moreover, it assumes that *all adsorbent sites are equal* to each other and the *interactions among the molecules of adsorbate are negligible*.

In dissociative adsorption, $f(\theta) = (1-\theta)^n$ and $N_a{}^m = \theta^n$ where n represents the number of parts the molecule disassociates into. As such, the Langmuir isotherm becomes:

$$\theta = \frac{(bP)^{1/n}}{1+(bP)^{1/n}} \tag{3.6}$$

As per the above derived equations and as can be seen in Fig. 3.6, *dissociative adsorption is favored at low pressures* while *nondissociative adsorption is favored at high pressures* [2].

For two gases, A and B, adsorbing simultaneously and nondissociatively, the Langmuir isotherm for each gas is given as:

$$\theta_A = \frac{b_A P_A}{1+b_A P_A + b_B P_B} \tag{3.7}$$

$$\theta_B = \frac{b_B P_B}{1+b_A P_A + b_B P_B} \tag{3.8}$$

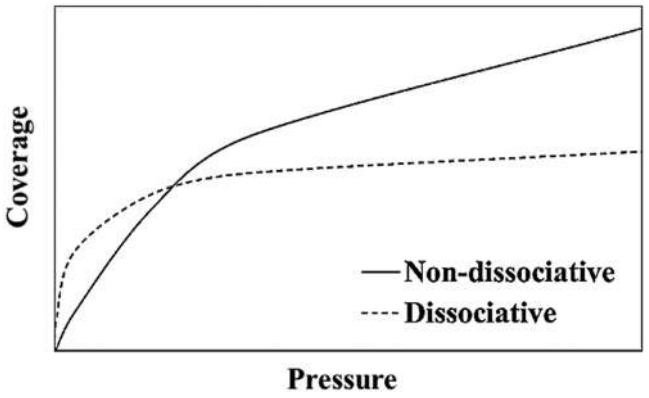

Figure 3.6
Langmuir adsorption isotherm for nondissociative and dissociative adsorption processes.

Focus 3.1: Numerical application of the Langmuir adsorption isotherm

The nondissociative adsorption of methane gas on a catalyst sample at 300K may be described by the Langmuir adsorption isotherm. Calculate the pressure required to attain a coverage of 60%, given that, at 300K, $b = 0.8\ \text{kPa}^{-1}$. What if a coverage of 90% is desired?

Solution
Using Eq. (3.4), and for a coverage of 60%:

$$P = \frac{\theta}{b(1-\theta)} = \frac{0.6}{0.8(1-0.6)} = 1.875\ \text{kPa}$$

Similarly, for a coverage of 90%:

$$P = \frac{\theta}{b(1-\theta)} = \frac{0.9}{0.8(1-0.9)} = 11.25\ \text{kPa}$$

3.1.2 Henry's isotherm

At *low pressures*, $bP \ll 1$. Therefore, the Langmuir adsorption isotherm reduces to give Henry's adsorption isotherm:

$$\theta = bP \tag{3.9}$$

which is simply Henry's law applied to a two-dimensional "solution" [2]. Similar to Henry's law, the Henry's isotherm applies to systems in which the adsorbate is diluted enough, that is, its partial pressure is low.

3.1.3 Freundlich isotherm

Contrary to the Langmuir adsorption isotherm, which assumes that all adsorption sites are energetically identical and that adlayers do not interact with one another, the Freundlich isotherm is developed on the basis that *sites are of different types* and are distributed exponentially with respect to the heat of adsorption and it tries to account for interactions among molecules of adsorbate [2]. The Freundlich adsorption isotherm equation, which is valid only at *low pressures*, is commonly written as:

$$\theta = kP^{1/n} \tag{3.10}$$

where $n > 1$.

Focus 3.2: Numerical example on the determination of the constants of Freundlich isotherm equation

The following table shows data from an adsorption study performed in an experimental laboratory. Assuming that the adsorption may be described by the Freundlich isotherm equation, determine the value of the constants k and n.

Coverage (mL g^{-1})	0.070	0.082	0.093	0.107	0.138	0.166
Pressure (Pa)	4.8	7.1	9.4	17	33	63

Solution

From Eq. (3.10), a plot of log θ versus log P will yield a straight line with a slope equal to $1/n$ and an intercept equal to log k. The plot is shown as follows, where the slope of the straight line is found to be equal to 0.3308 and the intercept equal to −1.397.

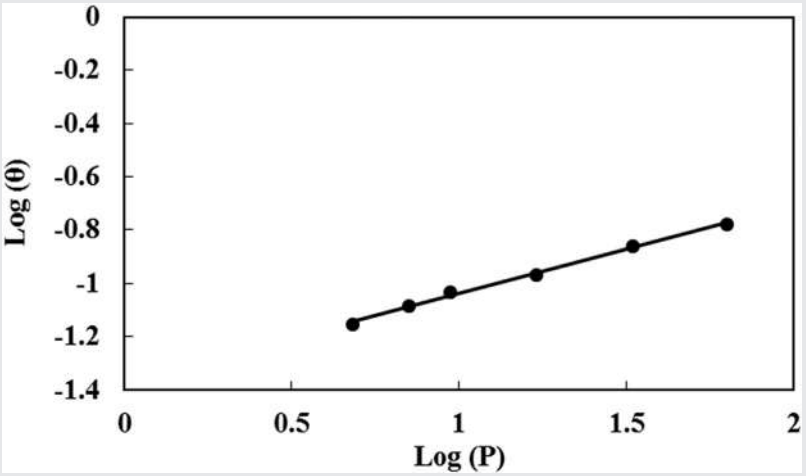

Hence, the values of n and k are calculated to be 3.02 and 0.043, respectively.

3.1.4 Temkin isotherm

The Temkin isotherm, which assumes that *the heat of adsorption is not constant* but instead decreases linearly with coverage, is represented according to the following relation [2]:

$$\theta = A \ln (BP) \tag{3.11}$$

where A is a temperature-dependent constant and B is a term that represents the heat of adsorption.

3.1.5 BET isotherm

In 1938 Brunauer, Emmett, and Teller used the basis of the Langmuir theory to derive an expression which explains *multilayer adsorption* (physisorption) [2]. This model, popularly known as BET, assumes that the solid surface consists of uniform localized sites where the adsorption on one site is not affected by the adsorption on nearby sites. It also assumes that the first layer of adsorbate is taken up with a certain heat of adsorption, while the second and subsequent layers adsorb with a heat of adsorption equal to that of the heat of liquefaction. Consider the adsorption of a gaseous species A on a vacant active site S [16]:

$$A + S \leftrightarrow \mathrm{A \cdot S} \tag{3.12}$$

where $A \cdot S$ refers to species A adsorbed on site S. The adsorption equilibrium constant of the first layer, K_1, is defined as:

$$K_1 = \frac{C_{A \cdot S}}{P_A C_v} \tag{3.13}$$

where $C_{A \cdot S}$ is the surface concentration of sites occupied by A, P_A is the partial pressure of A in the gas phase, and C_v is the molar concentration of vacant sites. In terms of coverage:

$$K_1 = \frac{\theta_1}{P_A \theta_v} \tag{3.14}$$

where θ_1 is the fraction of sites occupied by A and θ_v is the fraction of vacant sites. Similarly, for the second, third, and n^{th} successive layers (Fig. 3.7):

$$A + A \cdot \mathrm{S} \leftrightarrow \mathrm{A_2 \cdot S} \tag{3.15}$$

$$K_2 = \frac{\theta_2}{P_A \theta_1} \tag{3.16}$$

$$A + A_2 \cdot \mathrm{S} \leftrightarrow \mathrm{A_3 \cdot S} \tag{3.17}$$

$$K_3 = \frac{\theta_3}{P_A \theta_2} \tag{3.18}$$

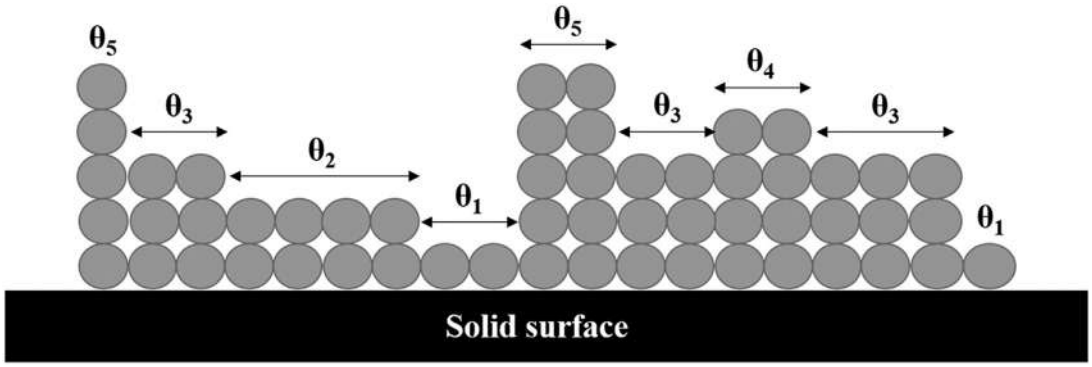

Figure 3.7
Schematic illustration of the multilayer BET adsorption model with θ_i representing the fraction of sites occupied by *i* layers.

$$A + A_{n-1} \cdot \mathrm{S} \leftrightarrow \mathrm{A}_n \cdot \mathrm{S} \tag{3.19}$$

$$K_n = \frac{\theta_n}{P_A \theta_{n-1}} \tag{3.20}$$

Since *the heats of adsorption of the second, third, and n^{th} layers are all similar and almost equal to the heat of liquefaction*, then the adsorption equilibrium constants of the second, third, and n^{th} layers are all approximately equivalent [2]:

$$K_2 \cong K_3 \cong \cdots \cong K_n = K \tag{3.21}$$

where K is the equilibrium constant for the liquefaction reaction, defined as:

$$K = \frac{1}{P_{0,A}} \tag{3.22}$$

where $P_{0,A}$ is the equilibrium vapor pressure of liquid A.

Substitution into Eqs. (3.16), (3.18), and (3.20) and rearranging in terms of coverage yields:

$$\theta_2 = K P_A \theta_1 \tag{3.23}$$

$$\theta_3 = K P_A \theta_2 \tag{3.24}$$

$$\theta_n = K P_A \theta_{n-1} \tag{3.25}$$

Then, replacing Eq. (3.23) into Eq. (3.24):

$$\theta_3 = (K P_A)^2 \theta_1 \tag{3.26}$$

For n layers, the general expression for coverage will therefore be:

$$\theta_n = (KP_A)^{n-1}\theta_1 \tag{3.27}$$

By definition, the summation of the fraction of vacant sites and the fraction of all occupied sites should be equal to 1:

$$\theta_v + \sum_{n=1} \theta_n = \theta_v + \sum_{n=1} (KP_A)^{n-1}\theta_1 = 1 \tag{3.28}$$

Expanding the summation term:

$$\theta_v + \theta_1(1 + KP_A + (KP_A)^2 + (KP_A)^3 + \cdots + (KP_A)^{n-1}) = 1 \tag{3.29}$$

Assuming that n approaches infinity:

$$\theta_v + \frac{\theta_1}{1 - KP_A} = 1 \tag{3.30}$$

Rearranging Eq. (3.14) for θ_v and substitution into Eq. (3.30):

$$\frac{\theta_1}{K_1 P_A} + \frac{\theta_1}{1 - KP_A} = 1 \tag{3.31}$$

Rearranging and introducing the constant C as K_1/K:

$$\theta_1 \left(\frac{1}{CKP_A} + \frac{1}{1 - KP_A} \right) = 1 \tag{3.32}$$

In terms of monolayer coverage:

$$\theta_1 = \frac{CKP_A(1 - KP_A)}{1 + KP_A(C - 1)} \tag{3.33}$$

The total number of molecules adsorbed per unit mass adsorbent, N, may be expressed as:

$$N = C_t(\theta_1 + 2\theta_2 + 3\theta_3 + \cdots + n\theta_n) = C_t \sum_{n=1} n\theta_n \tag{3.34}$$

where C_t is the total number of active sites per unit mass. Substituting Eq. (3.27) into Eq. (3.34):

$$N = C_t\theta_1 \sum_{n=1} n(KP_A)^{n-1} \tag{3.35}$$

Expanding the summation term:

$$N = C_t\theta_1(1 + 2KP_A + 3(KP_A)^2 + 4(KP_A)^3 + \cdots + n(KP_A)^{n-1}) \tag{3.36}$$

Note that the summation term is in fact a Taylor series expansion of $1/(1 - KP_A)^2$. Hence:

$$N = \frac{C_t\theta_1}{(1 - KP_A)^2} \tag{3.37}$$

Assuming that the entire surface of the adsorbent is covered by a monolayer:

$$N = \frac{N_m \theta_1}{(1 - KP_A)^2} \tag{3.38}$$

where N_m is the total number of molecules adsorbed as a monolayer per unit mass adsorbent. Substitution of Eq. (3.33) into Eq. (3.38) yields:

$$N = \frac{N_m CKP_A}{(1 - KP_A)[1 + KP_A(C - 1)]} \tag{3.39}$$

At standard temperature and pressure, the number of molecules is directly proportional to the volume, thus:

$$V = \frac{V_m CKP_A}{(1 - KP_A)[1 + KP_A(C - 1)]} \tag{3.40}$$

Substitution of Eq. (3.22) into Eq. (3.40) yields:

$$V = \frac{\frac{V_m CP_A}{P_{0,A}}}{\left(1 - \frac{P_A}{P_{0,A}}\right)\left[1 + \frac{P_A}{P_{0,A}}(C - 1)\right]} = \frac{V_m CP_A}{\left(P_{0,A} - P_A\right)\left[1 + \frac{P_A}{P_{0,A}}(C - 1)\right]} \tag{3.41}$$

As can be deduced from the above expression, the total volume of adsorbed molecules, V, approaches infinity when $P_A = P_{0,A}$. Rearranging yields the *BET adsorption isotherm equation* [2]:

$$\frac{P_A}{V\left(P_{0,A} - P_A\right)} = \frac{1}{V_m C} + \frac{(C - 1)}{V_m C}\left(\frac{P_A}{P_{0,A}}\right) \tag{3.42}$$

A plot of $P_A/[V(P_{0,A}-P_A)]$ versus $P_A/P_{0,A}$ is linear with a slope of $(C-1)/V_mC$ and an intercept of $1/V_mC$. This *linear* relationship, however, is applicable *only when* $P < 1/3P_0$ [2]. The coefficient C *is correlated to the heat of adsorption* and the higher it is, the stronger the adsorption. The BET equation applied to low partial pressures data is the most popular tool to estimate the surface area from adsorption isotherms, as detailed in Chapter 4, Surface Area and Porosity.

3.1.6 Potential theory of Polanyi

Polanyi's adsorption potential theory, which is valid mainly for microporous solids, states that the adsorption space in the vicinity of a solid surface is characterized by a series of

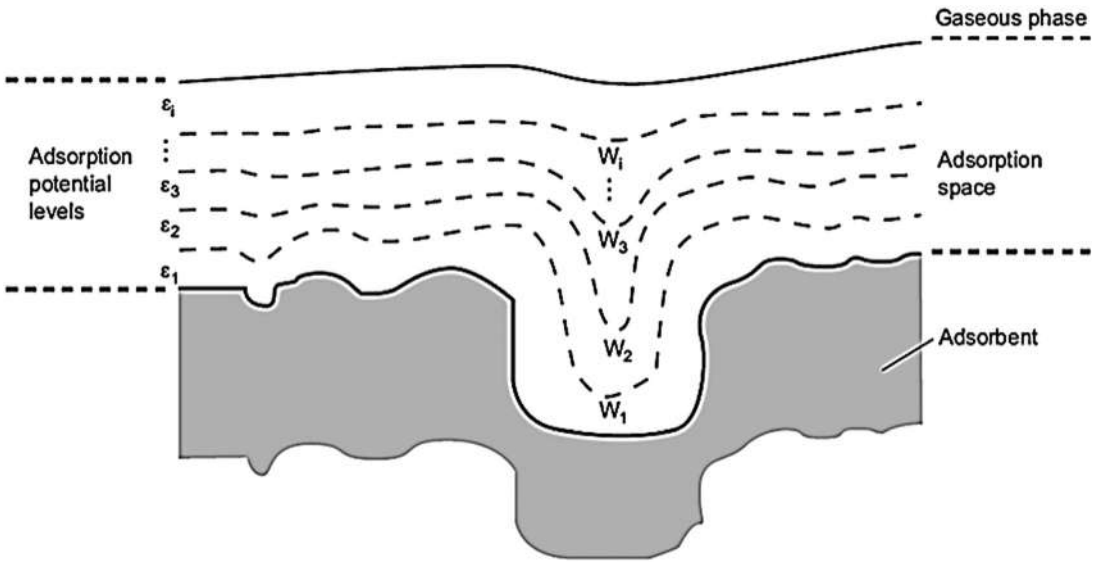

Figure 3.8
Schematic diagram of the adsorption space in the vicinity of an adsorbent. ε_i represents different potential levels and W_i represents the adsorbate volume. Source: *Reproduced from [17].*

equipotential surfaces as represented in Fig. 3.8 [2]. When the space of volume W is filled with adsorbate, the adsorption potential ε is defined as:

$$\varepsilon = RT \ln\left(\frac{P_0}{P}\right) \tag{3.43}$$

The adsorption potential, which is independent of temperature, results from dispersion and polar forces between the adsorbent and the adsorbate. Accordingly, the adsorption potential will depend on the nature of the adsorbent/adsorbate or, more specifically, the adsorbate's polarizability α. The adsorption potential of two different adsorbates with the same value of W will therefore retain a constant ratio to one another [2]:

$$\frac{\varepsilon_1}{\varepsilon_2} = \frac{\alpha_1}{\alpha_2} = \beta \tag{3.44}$$

where β is the affinity coefficient. Taking another adsorbate as an arbitrary standard (defined with a zero suffix):

$$\frac{\varepsilon}{\varepsilon_0} = \frac{\alpha}{\alpha_0} = \beta \tag{3.45}$$

On the basis of Polanyi's work, a new adsorption isotherm was derived by *Dubinin* and *Radushkevich* whereby they propose that the volume of the space where adsorption takes

place can be defined in terms of a Gaussian function [2]:

$$W = W_0\, exp\left(-A\varepsilon_0{}^2\right) \tag{3.46}$$

where W_0 is the total volume of the micropores and A is a constant that is dependent on the pore size distribution. Substitution of Eq. (3.45) into Eq. (3.46) gives:

$$W = W_0\, exp\left(-A\left(\frac{\varepsilon}{\beta}\right)^2\right) \tag{3.47}$$

Using Eq. (3.43) and noting that the volume, W, is equal to the mass adsorbed, x, divided by the liquid density, ρ:

$$W = W_0\, exp\left(-\frac{A}{\beta^2}\left(RT\, ln\left(\frac{P_0}{P}\right)\right)^2\right) = \frac{x}{\rho} \tag{3.48}$$

Rearranging:

$$lnx = ln\, W_0\rho - D\left(ln\left(\frac{P_0}{P}\right)\right)^2 \tag{3.49}$$

where $D = A(RT/\beta)^2$. A plot of $ln\ x$ versus $ln\ (P_{0,A}/P_A)^2$ is linear with a slope of D and an intercept of $ln\ (W_0\ \rho)$.

A modified expression of Eq. (3.49) was later introduced by *Kaganer* to account for the monolayer region [2]:

$$ln\, x = ln\, x_m - B\left(ln\left(\frac{P_0}{P}\right)\right)^2 \tag{3.50}$$

where x_m is the mass of adsorbed monolayer and $B = A(RT)^2$. Eq. (3.50) is known as the *Dubinin-Kaganer-Radushkevich* adsorption isotherm equation.

3.1.7 Recent approaches to model adsorption isotherms

The adsorption isotherm models by Langmuir, Henry, and Freundlich perform well but only in the low pressure range. On the other hand, the adsorption isotherm equation derived by Dubinin and Radushkevich is consistent at near saturation pressures but fails at low pressures [18]. To overcome the limitations of the conventional isotherm models, recently several approaches have been suggested. The Langmuir adsorption isotherm equation, for

instance, has been reformulated to describe the energetic and structural heterogeneity of the adsorbent using the Fermi–Dirac distribution function [19]. The simple form of this proposed isotherm equation may be expressed as:

$$\theta = \frac{\beta\left(\frac{P}{\varphi}\right)}{\left[1+(\beta^m-\alpha)\left(\frac{P}{\varphi}\right)^m\right]^{1/m}} \tag{3.51}$$

where φ is a factor dependent on the heat of adsorption, β is the load correction factor, and m is the surface structure heterogeneity factor. $\alpha = [1/exp(z)]^m$, where z is the compressibility factor. Eq. (3.51) showed great success in predicting the behavior of Type I, Type II, Type III, and Type V adsorption isotherms. However, it revealed to be inconsistent for Type IV and Type VI.

Another recent approach utilized the grand canonical ensemble in statistical physics to establish a modified BET expression for each adsorption isotherm type [20]. The developed equations were shown to work well for Type I to Type V adsorption isotherms.

In another strategy, the Langmuir model was revised through the introduction of the Homotattic Patch Approximation (HPA) and the fractional probability factor [18]. The HPA subdivides the heterogeneous surface of an adsorbent into a number of finite homogenous patches, n, each being a distinct adsorption energy site. The fractional parameter, α_i, represents the probability factor for the distribution of energy site sets. In simple terms, the obtained adsorption isotherm model is given as:

$$\theta = \sum_{i=1}^{n} \alpha_i \left\{ \frac{\left(\frac{P}{P_s} exp\left(\frac{\varepsilon_{0i}}{RT}\right)\right)^{RT/m_i}}{1+\left(\frac{P}{P_s} exp\left(\frac{\varepsilon_{0i}}{RT}\right)\right)^{RT/m_i}} \right\}_i \tag{3.52}$$

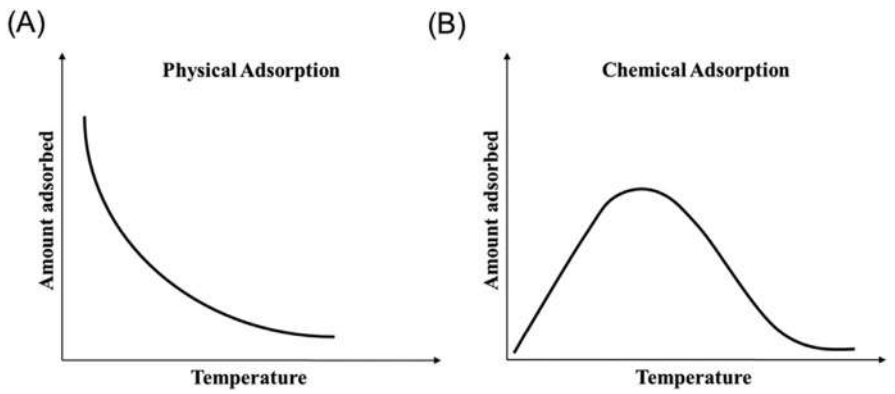

Figure 3.9
Schematic illustration of adsorption isobars for (A) physisorption and (B) chemisorption processes.

where α_i is the probability factor, P_s is the saturation pressure, ε_{0i} is the adsorption energy site with maximum frequency, and m_i is a factor that represents the standard deviation of the energy distribution curve from its mean value ε_{0i}. A larger value of m signifies a more heterogeneous surface.

3.2 Adsorption isobars and isosteres

An *adsorption isobar* is a plot that describes the amount of gas adsorbed on the surface of an adsorbent at a constant pressure as a function of temperature [2]. *For physisorption*, which usually occurs at temperatures lower than 300K, an increase in temperature results in a decrease in the amount adsorbed as illustrated in Fig. 3.9A. In particular, *an increase in temperature leads to weaker adsorbate–adsorbent interactions*. This is attributed to the higher kinetic energy of adsorbate molecules, which lowers the sticking probability after collision. Consequently, a decrease in the amount adsorbed is anticipated. Moreover, adsorption is an exothermic process and, as such, it is thermodynamically hindered by higher temperatures.

However, *for chemisorption*, which usually occurs at temperatures higher than 300K, *an increase in temperature results in an initial increase in the amount adsorbed* as demonstrated in Fig. 3.9B.

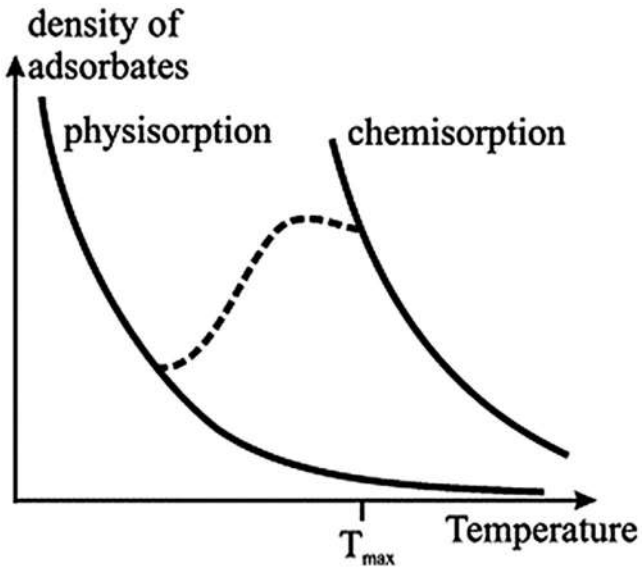

Figure 3.10
A typical adsorption isobar demonstrating the shift from physisorption to chemisorption after overcoming the chemisorption energy barrier. Solid lines represent equilibrium isobars while the dashed line represents irreversible chemisorption. T_{max} represents the temperature at which the maximum chemisorption coverage may be achieved. Source: *Reproduced from [21].*

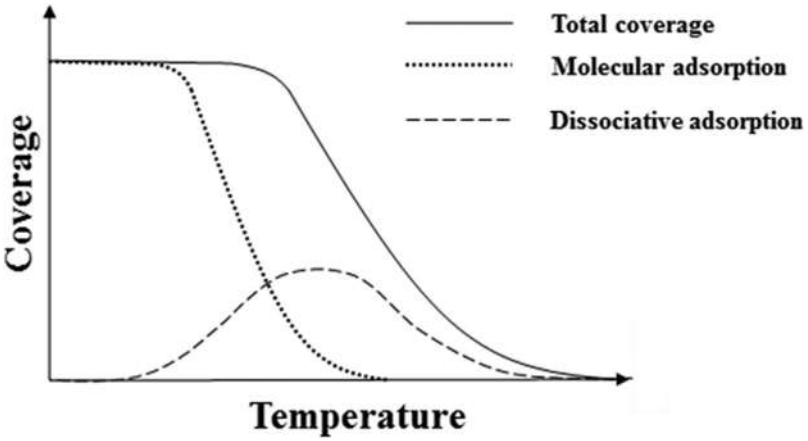

Figure 3.11
Adsorption isobars for dissociative and molecular adsorption.

This is because low temperatures come with kinetic limitations and the impossibility to overcome the activation energy implied by chemisorption, which is an activated process involving the breakage and formation of new bonds, that is, a chemical reaction. Nonetheless, and after the activation barrier is overcome, a further increase in temperature leads to the expected decrease in the adsorbed amount. The isobar reported in Fig. 3.10 shows the adsorption shift from physisorption to chemisorption after overcoming the chemisorption energy barrier.

Consider a molecule adsorbing dissociatively on a surface by breaking into two parts. In this case, and at low temperatures, the surface will adsorb twice as many molecular species as dissociated ones. Hence, the energy of the system is minimized and molecular adsorption is favored. Nonetheless, *as temperature increases*, entropy effects become significant and nonnegligible. At temperatures higher than 300K, entropy effects are large enough to overcome the energy difference between molecular adsorption and dissociative adsorption. Driven by this change in entropy, *the adsorption process converts from molecular to dissociative* as illustrated in Fig. 3.11 [2].

An *adsorption isostere* is a plot that describes the relationship between pressure and temperature for a constant amount of adsorbed gas [2]. After adsorption/desorption equilibrium has been established, the heat of adsorption, $-\Delta H$, for a coverage θ may be obtained from adsorption isotherms measured at different temperatures [2]. Then, using the *Clausius−Clapeyron equation*:

$$\frac{d(\ln P)}{d(1/T)} = \frac{-\Delta H}{R} \tag{3.53}$$

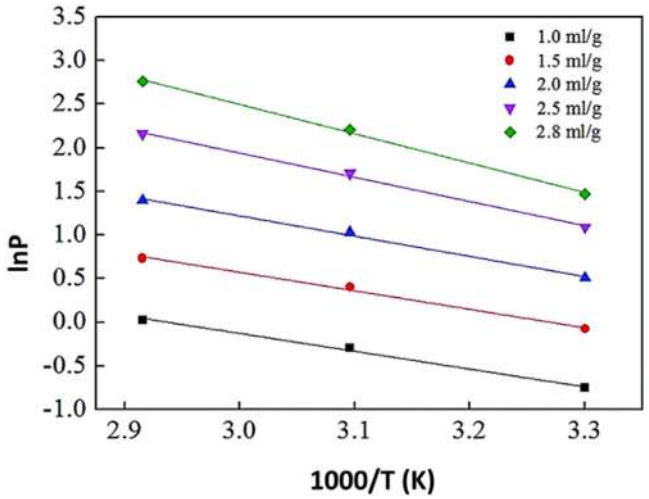

Figure 3.12
Adsorption isosteres of CH_4 on shale samples at different coverages (1.0–2.8 mL g^{-1}).
Source: *Reproduced from [22].*

a plot of *ln P* versus 1/*T* may be constructed with a slope that yields the isosteric heat of adsorption at a constant coverage (Fig. 3.12). Information on the nature of the adsorbate–adsorbent link may be drawn from the magnitude of the heat of adsorption. For instance, a heat of adsorption that is greater than the heat of liquefaction signifies that the adsorbate is chemisorbed to the adsorbent surface [2].

3.3 Models for surface reactions

In the surface-catalyzed transformation of gaseous reactants A and B into a product AB (Fig. 3.13), either one of two distinct mechanistic reaction models is typically followed: *Langmuir–Hinshelwood (LH) or Eley–Rideal (ER)* [2]. In the LH mechanism, both reactants A and B adsorb on two separate active sites, S_S, prior to conversion into a product AB. In the ER mechanism, one of the reactants adsorbs to the surface while the other reacts with it from the gas phase. Both models are based on the following assumptions: (1) at equilibrium, the number of adsorption sites is fixed; (2) only a single species may adsorb at each active site; (3) the enthalpy of adsorption is independent of surface coverage and is identical for every site; (4) there is no interaction among adjacent adsorbates; (5) the adsorption rate is greater than the surface reaction rate; and (6) the equilibrium desorption process is fast (in other words, active sites are not irreversibly blocked by the adsorbed products) [24].

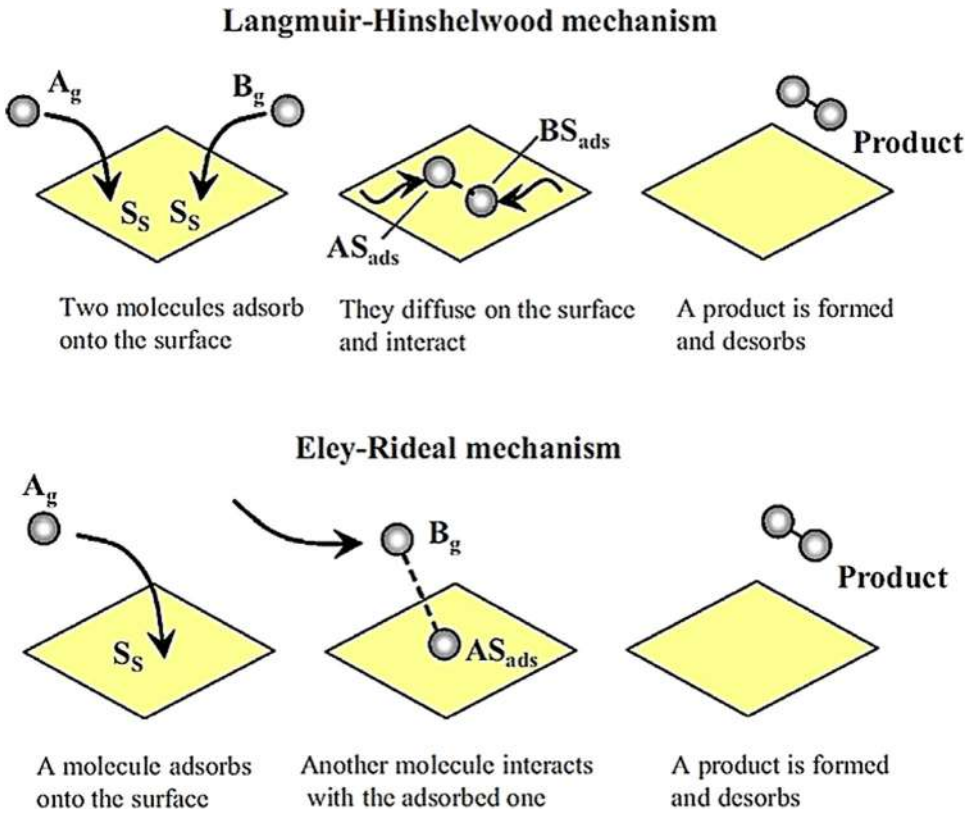

Figure 3.13
A graphical representation of the two possible mechanisms through which heterogeneous catalysis may proceed on a solid surface: Langmuir–Hinshelwood and Eley–Rideal. Source: *Reproduced from [23].*

The *rate of a reaction following the LH mechanism* may be written as:

$$r_{LH} = k\theta_A\theta_B \tag{3.54}$$

Applying the Langmuir adsorption model by substitution of Eqs. (3.7) and (3.8) into Eq. (3.54):

$$r_{LH} = \frac{kb_A P_A b_B P_B}{(1 + b_A P_A + b_B P_B)^2} \tag{3.55}$$

Similarly, the *rate of a reaction following the ER mechanism* may be written as:

$$r_{ER} = k\theta_A P_B \tag{3.56}$$

Applying the Langmuir adsorption model by substitution of Eq. (3.5) into Eq. (3.56):

$$r_{ER} = \frac{kb_A P_A P_B}{1 + b_A P_A} \tag{3.57}$$

For a reaction where $A_{ads} \rightarrow B + C$, the rate is expressed as:

$$r = \frac{kb_A P_A}{1 + b_A P_A} \tag{3.58}$$

The kinetics of this reaction are considered to be first order with respect to P_A if $b_A P_A \ll 1$ and zero order if $b_A P_A \gg 1$. Note that b is typically large for strongly adsorbed species.

Focus 3.3: Fitting the Langmuir–Hinshelwood and Eley–Rideal kinetic models to experimental data: furfural hydrogenation over supported copper catalysts

A major concern in heterogeneous catalysis is the identification of the mechanism governing the kinetics of the surface reaction. As an example, consider the hydrogenation reaction of furfural on the surface of three different supported copper catalysts (Cat#1 to Cat#3). The following Langmuir–Hinshelwood (LH) and Eley–Rideal (ER) mechanisms were suggested [25] to express its rate of disappearance:

Solution

1. ER – adsorption of furfural (A) onto the surface while hydrogen (B) reacts in the gas phase (i.e., it does not adsorb). The rate of a reaction following the ER mechanism by applying the nondissociative Langmuir adsorption model for furfural may be written as:

$$r_{ER} = k\theta_A P_B = k\left(\frac{b_A P_A}{1 + b_A P_A}\right) P_B = \frac{k' P_A P_B}{1 + b_A P_A}$$

2. LH1 – the dissociative sequential addition of hydrogen atoms to furfural on the same adsorption site:
   In dissociative adsorption, the Langmuir isotherm becomes:

$$\theta = \frac{(bP)^{1/n}}{1 + (bP)^{1/n}}$$

   where n represents the number of parts the molecule disassociates into. Hence, the rate of a reaction following the LH mechanism by applying the dissociative Langmuir adsorption model for hydrogen may be written as:

(*Continued*)

Focus 3.3: Fitting the Langmuir–Hinshelwood and Eley–Rideal kinetic models to experimental data: furfural hydrogenation over supported copper catalysts (Continued)

$$r_{LH1} = k\theta_A\theta_B{}^n = k\left(\frac{b_AP_A}{1 + b_AP_A + b_B{}^{0.5}P_B{}^{0.5}}\right)\left(\frac{b_B{}^{0.5}P_B{}^{0.5}}{1+b_AP_A+b_B{}^{0.5}P_B{}^{0.5}}\right)^2$$
$$= \frac{k'P_AP_B}{\left(1+b_AP_A+b_B{}^{0.5}P_B{}^{0.5}\right)^3}$$

3. LH2 – the noncompetitive dissociative adsorption of hydrogen molecule on two different types of sites:
   For two gases, A and B, adsorbing nondissociatively on two different types of sites, the Langmuir isotherm for each gas becomes:

$$\theta_A = \frac{b_AP_A}{1 + b_AP_A}$$

$$\theta_B = \frac{b_BP_B}{1 + b_BP_B}$$

   Hence, the rate of a reaction following the LH mechanism for the noncompetitive dissociative adsorption of hydrogen molecule on two different types of sites may be written as:

$$r_{LH2} = k\theta_A\theta_B{}^n = \left(\frac{b_AP_A}{1 + b_AP_A}\right)\left(\frac{b_B{}^{0.5}P_B{}^{0.5}}{1+b_B{}^{0.5}P_B{}^{0.5}}\right)^2 = \frac{k'P_AP_B}{(1+b_AP_A)\left(1+b_B{}^{0.5}P_B{}^{0.5}\right)^2}$$

4. LH3 – adsorption of hydrogen molecule:

   For two gases, A and B, adsorbing simultaneously and nondissociatively on the same type of sites, the Langmuir isotherm for each gas becomes:

$$\theta_A = \frac{b_AP_A}{1 + b_AP_A + b_BP_B}$$

$$\theta_B = \frac{b_BP_B}{1 + b_AP_A + b_BP_B}$$

   Hence, the rate of a reaction following the LH mechanism for the nondissociative adsorption of hydrogen molecule may be written as:

$$r_{LH3} = k\theta_A\theta_B = k\left(\frac{b_AP_A}{1 + b_AP_A + b_BP_B}\right)\left(\frac{b_BP_B}{1 + b_AP_A + b_BP_B}\right) = \frac{k'P_AP_B}{(1+b_AP_A+b_BP_B)^2}$$

   For each model, the equation was fitted to experimental data and the model constants were determined. Results are presented in the following table as well as in Fig. 3.14:

(Continued)

Focus 3.3: Fitting the Langmuir–Hinshelwood and Eley–Rideal kinetic models to experimental data: furfural hydrogenation over supported copper catalysts (Continued)

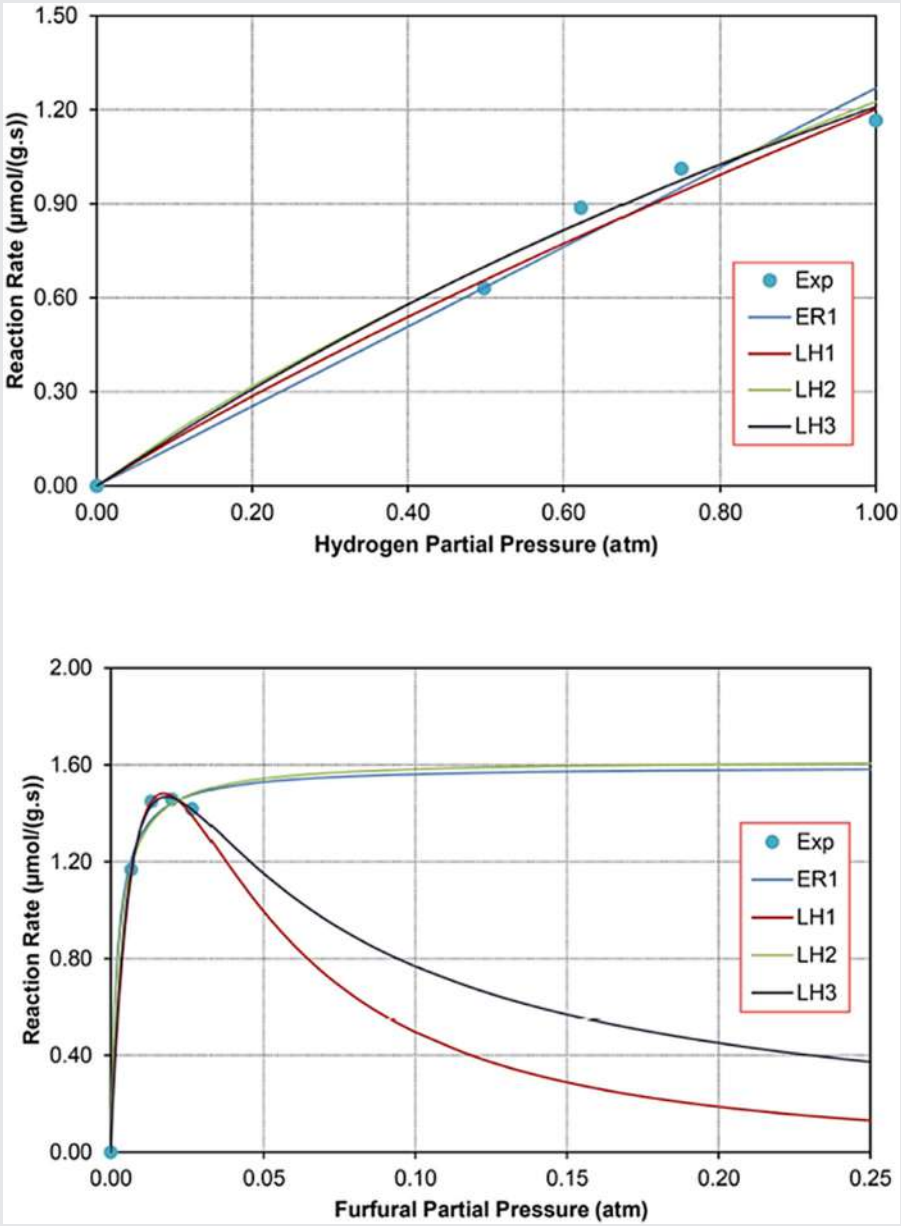

Figure 3.14
Rate of furfural conversion on Cat#2 versus partial pressure of hydrogen (top) and furfural (bottom). Source: *Reproduced from [25].*

(*Continued*)

Focus 3.3: Fitting the Langmuir–Hinshelwood and Eley–Rideal kinetic models to experimental data: furfural hydrogenation over supported copper catalysts (Continued)

Mechanism	k or k'	b_A	b_B	R^2
Cat#1				
ER1	0.437	3066	–	99.2
LH1	174	41	0.025	99.4
LH2	1160	1820	0.042	99.3
LH3	186	86	0.197	99.6
Cat#2				
ER1	1.661	461	–	98.7
LH1	438	32	0.019	99.3
LH2	1073	390	0.079	99.1
LH3	186	67	0.244	99.6
Cat#3				
ER1	1.967	910	–	97.6
LH1	909	40	0.106	97.8
LH2	3572	568	0.605	99.7
LH3	1236	97	0.678	99.0

Although it is widely assumed that most catalytic reactions, including furfural hydrogenation on copper catalysts, are better described by the LH kinetic model, results here show that the ER model is equally applicable. However, it is important to note that a good fit to any rate expression should not be taken as proof of the assumed mechanism unless the opponent cases are excluded by complimentary experimental evidence [25].

3.4 Catalysts, cocatalysts, and supports

Currently, the most common types of catalysts in use are *metals, oxides, and sulfides*. Each one of these materials may, by itself, act independently as an active catalyst. Alternatively, these materials may be combined with one another and/or used in conjunction with other components, either as cocatalysts or as supports (Fig. 3.15). Almost all metals may be used as catalysts; however, due to their higher reactivity, which results from their empty d-band orbitals, transition metals are more frequently utilized (see Section 2.1). In order for metal catalysts to be thermodynamically stable, they must be used under reducing conditions in which neither oxygen nor sulfur is present in the reaction mixture. If the reaction necessitates the presence of oxygen or sulfur, then a metal that is not susceptible to oxidation or sulfidation must be carefully selected [28].

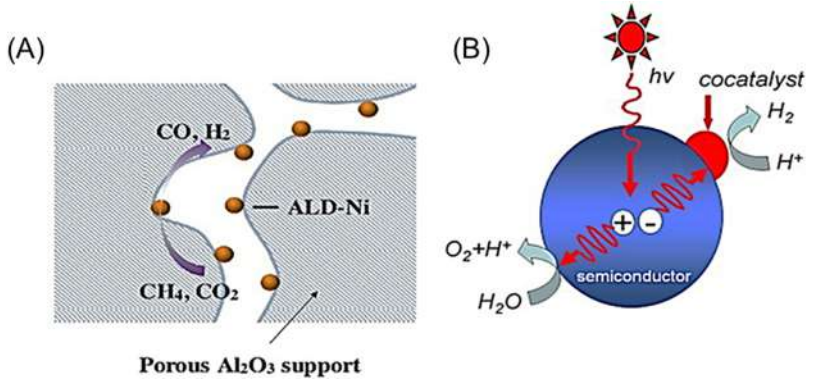

Figure 3.15
(A) Dry reforming of methane over atomic layer deposited (ALD)-nickel nanoparticles supported on highly active and stable alumina. (B) Photocatalytic water splitting over a semiconductor loaded with a cocatalyst. The negative and positive circles represent photogenerated electrons and holes, respectively. Source: *(A) Reproduced from [26]. (B) Reproduced from [27].*

3.4.1 Catalyst supports

Although pure metals can be employed to carry out a number of catalytic processes, the use of oxides or other materials as supports presents significant advantages. These *supports may be inert*; but, in most cases, they have been reported to *contribute to the overall activity and selectivity* of the catalyst. Since the majority of heterogeneous catalytic reactions take place at relatively high temperatures, pure, or unsupported, metal catalysts are typically vulnerable to sintering, resulting in permanent agglomeration of metal particles and the consequent reduction of surface available for adsorption and reaction. The addition of a support helps in anchoring the metal atoms on a surface, consequently preventing the particles from coalescing, at the same time *maximizing the exposed surface area* [28].

The surface area of a catalyst is considered to be one of its most important characteristics, specifically for processes that are limited by surface reaction and not by mass transfer, which represent the majority of cases. Hence, a metal catalyst with a high and accessible surface area is extremely desirable. The metal catalyst must also be stable enough to withstand the conditions of the reaction. Metallic powders, for instance, retain a high surface area but are very unstable under most reaction conditions so they deactivate easily (see Section 5.6 for a detailed discussion on deactivation). As such, *metal catalysts are preferentially accompanied by supports*, to increase their useful life with important economic implications, given that metals are usually much more expensive than the materials used as supports [28].

Single oxides, such as alumina and silica, complex oxides, such as zeolites, and activated carbon *are some of the most frequently used supports*. The metal atoms are generally located within the pores of the support, which are large enough to allow for the diffusion of reactants and products to and from the metal surface. At temperatures that are circa half the temperature of the metal oxide's melting point, the metal atoms constituting the oxide become mobile. Therefore metal oxides with high melting points ($>1500°C$) are usually chosen as supports since they can maintain their stability even under severe reaction conditions. Other than stability, high reaction temperatures can also affect the metal oxide's crystal phase. As temperature rises, the metal oxide might transition to another phase that is either more reactive or that possesses a much lower surface area [28].

The oxygen atoms of a metal oxide support usually play a significant role in the mechanism of many catalytic reactions. Consider, for example, the dry reforming of methane on a Pt/ZrO_2 catalyst. Methane adsorbs on the surface of the Pt catalyst and dissociates into carbon and hydrogen atoms. The liberated carbon atoms diffuse to the metal-support interface where they react with oxygen from the support, forming CO. The CO_2 present in the reaction mixture will then reoxidize the ZrO_2 support. Although the majority of the Pt surface will be covered with carbon, sites at the metal-support interface will remain largely free of adsorbed carbon and the catalytic activity will consequently be maintained [28]. This feature is of great importance since it slows down the deactivation of the catalyst as a result of carbon poisoning (i.e., coking), which forces to regenerate the catalyst with a temporary shutdown of production plants.

Due to its low cost and ease of preparation, *alumina, Al_2O_3*, has been widely used as a catalytic support. Alumina has a high surface area (several hundred $m^2\ g^{-1}$) and a readily accessible pore structure. More importantly, it retains a significant number of hydroxyl groups on its surface. The Al—OH surface species give rise to protons and, therefore, contribute to the activity of the final catalyst. The surface hydroxyl groups not only provide this acidic character to the support, but they may also act as adsorption sites for the reacting species [28].

The *acidic/alkaline* nature of the supports plays an important role in tuning catalytic activity. In the dry reforming of methane, for instance, basic sites help improve the activation (or chemisorption) of acidic CO_2 while also limiting the deposition of coke, which is favorable at acidic sites [29]. On the other hand, acidic sites are equally important since they promote methane cracking via dissociative adsorption. Therefore, the supports used for dry methane reforming catalyst are typically consisting of a combination of both acidic and basic sites as shown in Fig. 3.16. It is important however to create a perfect balance between the number of acidic sites versus the number of basic ones. Too many acidic sites will favor the reverse reaction (the reverse water—gas shift reaction) and coke formation, while too many basic sites can cause metal oxidation and subsequent catalyst

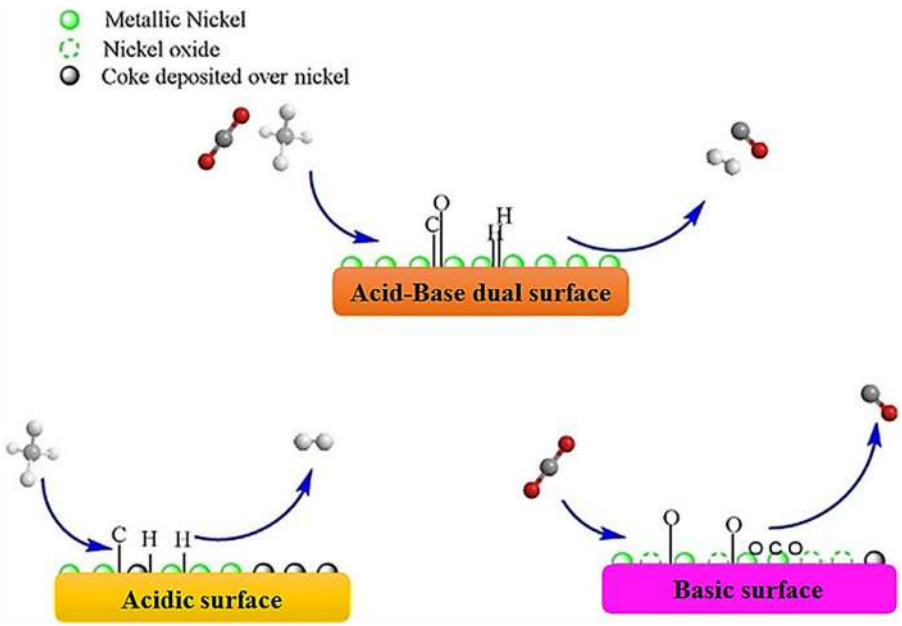

Figure 3.16
Synergy between acidic and basic sites of supported nickel nanoparticles for the dry reforming of methane. Red circles represent oxygen atoms, dark gray circles represent carbon atoms, and light gray circles represent hydrogen atoms. Source: *Reproduced from [30].*

deactivation [30]. In general, unsaturated metal sites provide an acidic character, while surface oxygen sites provide a basic one [29].

Acidic supports, such as *zeolites, silica, and mixed oxides*, are more frequently used in catalytic reactions when compared to basic supports, such as *ZnO and* ZrO_2. This is attributable to the strong thermal pretreatment required for basic supports to ensure the complete elimination of any surface adsorbed acidic species such as hydroxyl groups from atmospheric water vapor and carbonyl groups from atmospheric CO_2 [31].

The most widely used methods for the preparation of supported metal catalysts include *impregnation* (ion adsorption and ion exchange) and *precipitation* (coprecipitation and deposition–precipitation) techniques (Fig. 3.17) [33,34]. Regardless of the method used, the synthesis of supported catalysts will always begin with a metal precursor, usually in the form of an inorganic salt. In the impregnation method, the support material is first contacted with a metal precursor solution. Then, the active metal is deposited onto the support either through ion adsorption whereby the precursor molecules adsorb onto the surface group of the support or through the exchange of ions between the precursor and the support. If low metal loading is desired, then excess precursor must be removed by

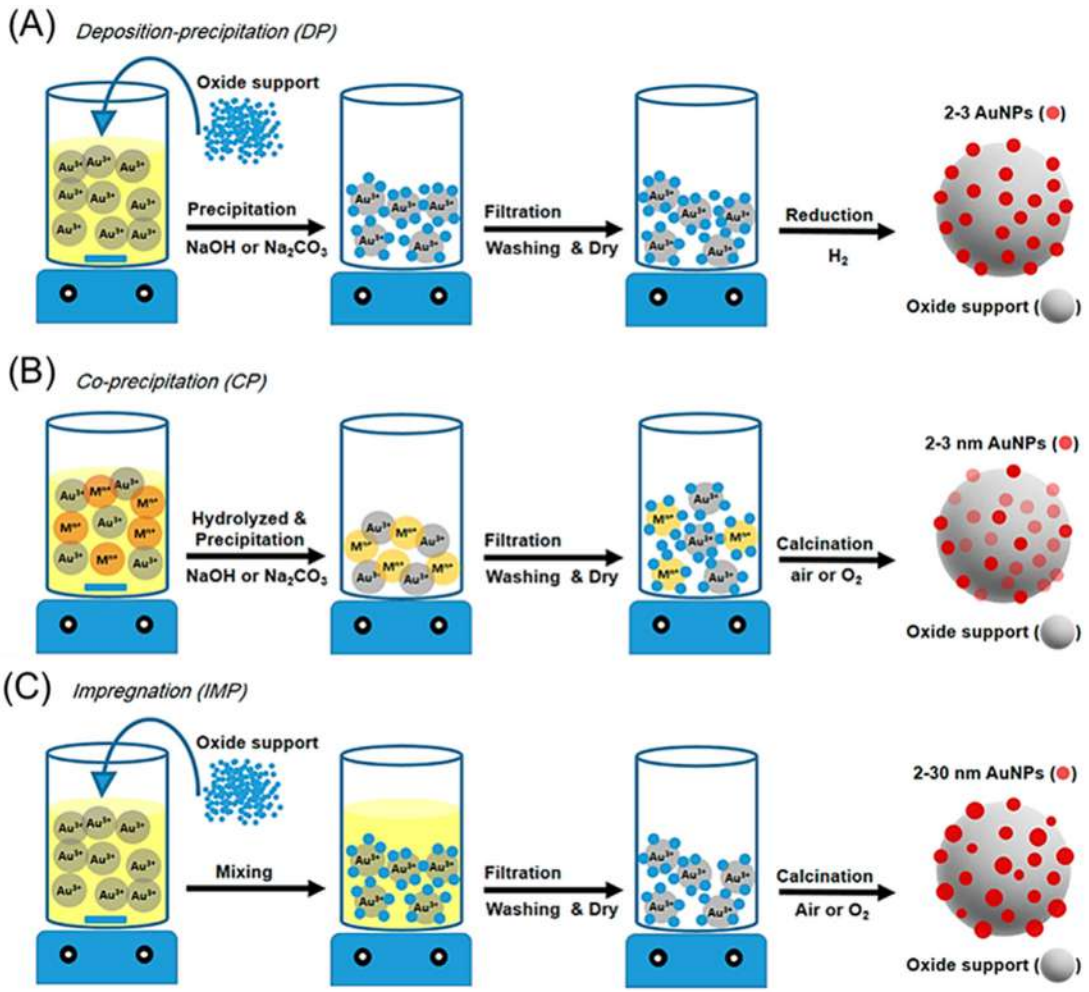

Figure 3.17
Schematic representation of the different methods used for the preparation of gold catalysts supported on metal oxides: (A) deposition–precipitation, (B) coprecipitation, and (C) impregnation techniques. Source: *Reproduced from [32].*

washing the support following the deposition process. If, on the other hand, a high metal loading is required, then no washing is carried out and the support is instantly dried. This ensures that all the precursor used ends up on the support. The impregnation method that was just described earlier is more commonly known as the "wet" impregnation method. Conversely, in the "dry" impregnation method, only the pores of the support are filled with the precursor solution. This may be achieved by using a precursor solution with a volume that is equal or slightly less than the pore volume of the support. In the precipitation method, the supported metal catalyst develops as a result of metal particle nucleation and

growth, induced by the supersaturation of the precursor solution. If the growth of the metal particle takes place in conjunction with the formation of the support, then the process is called *coprecipitation*. Alternatively, if it takes place on an existing support, then the process is called *deposition–precipitation*.

Recently, new preparation techniques have emerged as a substitute to the aforementioned traditional methods. These include melt infiltration, colloidal deposition, and vapor deposition [34]. *Melt infiltration*, also sometimes referred to as melt intrusion, capillary infiltration, or the solvent-free method, originates from the field of ceramic nanomaterials and is based on the infiltration of porous matrices with the melted active phase or precursor [35]. In particular, a low melting point precursor solution is heated and directly contacted with a support. Upon melting, the precursor gets sucked up by the support as a result of capillary forces. The melting behavior of the infiltrate and its interaction with the support are some challenges of this preparation technique. Nonetheless, *it is applicable to an extensive array of materials, including metals, polymers, ceramics, metal hydrides, and metal oxides*. Furthermore, and in a number of situations, it enables an extended control over the nanostructure of the materials. For instance, melt infiltration is usually used instead of solution impregnation to synthesize supported nanomaterials since it provides a higher degree of pore filling in a single infiltration step with the exclusion of solvents. Melt infiltration can also be applied to prepare nanostructured materials that are not accessible by other synthesis techniques due to reactivity of the active phase with solvents or lack of solubility. Finally, the solvent removal step (and large capillary forces associated with it) in melt infiltration typically leads to the rearrangement of the active phase or its precursors, causing a different distribution of the active phase compared to solution impregnation [34,35].

In *colloidal deposition*, colloidal metal nanoparticles are first created and then later deposited on a support material [36]. More specifically, *this method decouples particle formation from the supporting process*. Hence, many factors, which are difficult to control in coprecipitation or deposition–precipitation methods, where the particle formation on the support is a heterogeneous nucleation process (i.e., the metal particles are either formed with the support or on the support), are eliminated. For example, in heterogeneous nucleation, the nature of the substrate on which the forming particle nucleates governs the properties of the particle [36]. Therefore different supports will result in different particle types. This may be avoided via the method of colloidal deposition, where particle formation in solution is controlled by stabilizing agents or ligands [34,36].

Finally, in the *vapor deposition method*, metal atoms (or clusters) in the gas phase selectively react with the surface groups of the support. Vapor deposition techniques are classified into physical (PVD) and chemical (CVD) vapor deposition methods, depending on the origin of the gas phase atoms [37]. In *PVD*, the gas phase atoms originate from the

vaporization of a solid material. Specific examples of PVD processes include vacuum evaporation, ion implantation, and magnetron sputtering. In vacuum evaporation, the PVD process occurs under vacuum conditions. This prevents the vapor molecules from reacting with other species that may be present in the atmosphere. In ion implantation, metallic ions bombard the surface of the support leading to their subsequent implantation. Finally, in magnetron sputtering, reactive gas molecules are used to strike the material of interest (i.e., the material to be deposited), causing the atoms of this material to travel toward the support. The most significant advantage of magnetron sputtering is that materials with high melting points can be sputtered onto support substrates at low temperatures. Additionally, nanocomposite supports can be easily obtained by the cosputtering of various materials [37]. Conversely, in *CVD*, the gas phase atoms originate from volatile by-products of a chemical reaction. This technique necessitates operation under high temperatures for the reaction to proceed. Hence, it has been recently modified to allow for operation at low reaction temperatures. These modified CVD techniques include plasma-enhanced CVD and photo-CVD [37].

3.4.2 Cocatalysts

In heterogeneous catalysis, and particularly in photocatalysis and photoelectrocatalysis (see Sections 6.2 and 6.3), *cocatalysts greatly contribute to the overall activity of the reaction*. Out of the many catalytic applications, cocatalysts have been found to be essential in photocatalytic water splitting reactions for boosting the evolution of hydrogen. Cocatalysts provide additional active reaction sites for oxidation and reduction, lower the overpotential of the reaction, and improve the adsorption of reactants [38]. More importantly, they enhance the separation of photogenerated charges by acting as traps for electrons and holes [39]. Cocatalysts are also known to improve the (photo)stability of the catalyst in addition to increasing its light-harvesting ability. The latter is specifically true when plasmon metals, such as gold and copper, are used as cocatalysts. This is attributed to their localized surface plasmon resonance (LSPR) effect [40].

The noble metals *platinum, palladium, silver,* and *gold* are the most commonly used cocatalysts, with platinum showing the best performance in the majority of reactions. This is because platinum has the highest work function (5.65 eV) among all noble metals and, as a result, it has the best ability of working as an electron sink (Fig. 3.18) [40]. Besides noble metals, nonnoble transition metals have also been employed as effective cocatalysts. Unlike noble metals, nonnoble metals are readily available and comparatively cheaper. Moreover, some nonnoble metals, such as nickel and cobalt, possess work functions that are as high as those of noble metals. Hence, they may be used for efficient electron trapping and transfer. Other well-known and broadly studied metal-based cocatalysts include *metal phosphides* (CoP, Ni_2P, FeP, etc.), *metal oxides* (TiO_2, CuO, and NiO), and *metal sulfides* (MoS_2, NiS, Cu_xS, etc.) [40]. Besides the mostly common

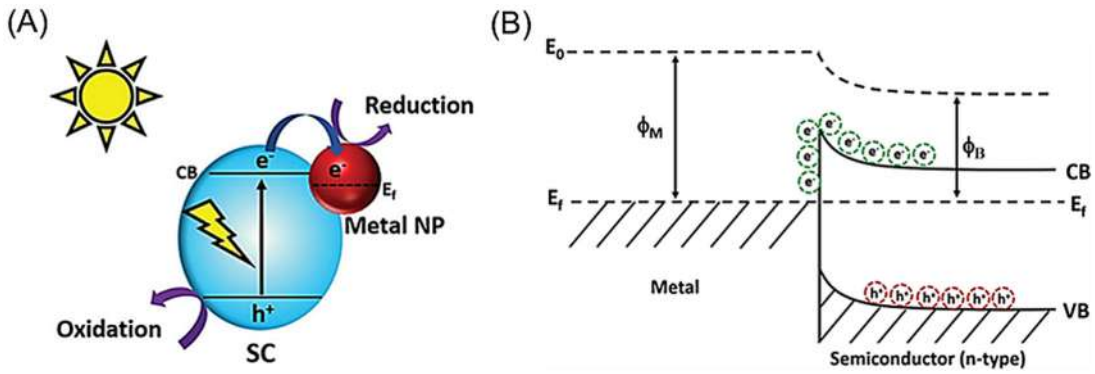

Figure 3.18

(A) Combination of a semiconductor photocatalyst (SC) with a metal nanoparticle cocatalyst (metal NP). (B) Band structure of the hybrid material composed of the metal cocatalyst and the semiconductor photocatalyst in contact under equilibrium. ϕ_B, Semiconductor work function; ϕ_M, metal work function; *CB*, conduction band; e^-, electrons; E_0, vacuum level; E_f, Fermi level; h^+, holes; *VB*, valence band. Source: *Reproduced from [41].*

metal-based cocatalysts, metal-free carbon-based cocatalysts can also be employed to enhance the catalytic activity. Carbon-based materials, such as carbon quantum dots, graphene, and carbon nanotubes, are characterized by a large work function, excellent electron reception, large surface area, and varied morphologies, which can play a critical role in the reactivity. Moreover, they are cheap, stable, abundant, and nontoxic [40].

Cocatalysts may be simple systems made of single metals or complex systems made of bimetallic alloys. As a result of the synergistic effect from coupling two metals, *bimetallic cocatalysts*, such as PtPd, PtCo, AuPd, AgCu, among others, show higher catalytic activity in comparison to monometallic cocatalysts. An even better performance may be achieved when plasmonic metals are used as bimetallic cocatalysts, that is, AuCu and AuPd [40].

Introducing a cocatalyst into *Z-scheme heterojunction systems* has been shown to efficiently improve the photocatalytic activity [42,43]. For example, reduced graphene oxide (rGO) was used as a cocatalyst for a Z-scheme photocatalyst during the process of CO_2 reduction [44]. The addition of rGO as a cocatalyst (1) facilitated the charge−carrier migration in Z-scheme mode, (2) promoted CO_2 adsorption, and (3) enhanced electron capture. This is attributed to the unique $\pi-\pi$ conjugation interaction and the abundant active sites that were made available by rGO.

One approach that has stimulated recent interest is the rational design of spatially separated oxidative and reductive cocatalysts. The carefully orientated distribution of such dual cocatalysts on the surface of a photocatalyst can further promote the separation of photogenerated charges by providing a structured flow for electrons and holes as illustrated in Fig. 3.19 [40]. Reductive

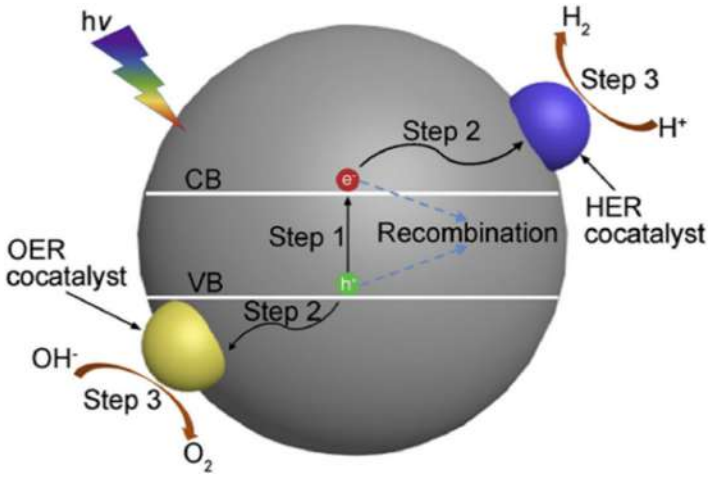

Figure 3.19
Schematic representation of the photocatalytic water splitting process. *CB*, Conduction band; *HER*, hydrogen evolution reaction; *OER*, oxygen evolution reaction; *VB*, valence band.
Source: *Reproduced from [45].*

cocatalysts are excellent electron traps and are hence typically employed for hydrogen evolution reactions and CO_2 reduction reactions. The majority of cocatalysts, ranging from noble and nonnoble metals to metal phosphides, oxides, and sulfides, can serve as reductive cocatalysts. Alternatively, oxidative cocatalysts, such as some transition metal oxides (MnO_x, CoO_x, Fe_2O_3) and some transition metal phosphates (such as cobalt phosphate) are excellent hole traps and are thus used for oxygen evolution and organic degradation reactions [38].

The *morphology* (size/shape), *crystallinity*, and *composition* of the cocatalyst play a crucial role in determining its activity [45]. Smaller cocatalysts retain a larger specific surface area and a shorter charge transfer path. Thus they are generally more favorable in catalytic reactions. Cocatalysts of different shapes will have different exposed facets with distinct active sites and different adsorption energies. As a result, they will display diverse catalytic activities. Highly crystalline cocatalysts with their almost defect-free structure usually demonstrate good catalytic performance. Recently, amorphous cocatalysts have also been shown to perform well in many catalytic applications. This has been attributed to a number of reasons including (1) presence of more active surface reaction sites, (2) lower catalytic overpotential, and (3) faster kinetics in charge transfer.

Other important aspects include the cocatalyst's *location*, the cocatalyst's *built-in electric field*, and the *interfacial contact* between the cocatalyst and the host catalyst [45]. To better facilitate charge transfer and separation, oxidative and reductive cocatalysts must be deposited on different surface points of the host catalyst. The formation of a built-in electric field, which typically results from the construction of a p–n junction between the cocatalyst

and the host catalyst, and the creation of a direct contact between the cocatalyst and the host catalyst can also expedite the transfer and separation of electrons and holes. Consequently, the overall catalytic activity may be enhanced. Recently, cocatalyst/catalyst systems with indirect contact and collision contact have also led to improved catalytic performances. Indirect contact indicates the existence of a mediator as a bridge to connect cocatalyst and host photocatalyst; while collision contact means that the cocatalyst is organized in free-standing clusters (in contrary to being anchored on the photocatalyst). Both systems result in the spatial separation of photoexcited electrons and holes, significantly enhancing the photocatalytic activity.

The techniques typically used for the deposition of cocatalysts onto the surface of a host catalyst include impregnation, deposition−precipitation, electrodeposition, and photodeposition methods [46]. The impregnation and deposition−precipitation methods have been previously discussed in Section 3.4.1 for the preparation of supported metal catalysts. Here, the same principles apply; however, instead of contacting the metal precursor solution with a support material, the cocatalyst precursor solution is contacted with the host catalyst. In electrodeposition, the cocatalyst deposition is achieved by applying a potential to the catalyst, which is present in the form of electrode. The deposition process is controlled by adjusting the applied potential, the current density, and the concentration of cocatalyst in the precursor solution. In photodeposition, the cocatalyst deposition takes place as a result of the action of photogenerated charge carriers that form from the irradiation of a semiconducting photocatalyst.

3.5 Questions and problems

1. In a chemisorption process, you have to investigate under which conditions the adsorption is taking place with a chemical dissociation of the adsorbate. Describe the experiments you would carry out and their assessment.
2. The adsorption enthalpy may vary depending on the catalytic site. Which adsorption models take this into account? And how?
3. If an adsorption isotherm does not reach a plateau at high pressure, what can you say about the adsorption process?
4. Analyze the analytical expression of the coefficient C in the BET model and explain its physical significance.
5. Why can an adsorption isobar exhibit a peak at intermediate temperatures?
6. How can a catalyst support affect the activity and selectivity of a process? Report few examples taken from literature and comment on them.
7. The use of cocatalyst is very common. Report few cases where noble metals such as Au and Pt are applied and comment on them.

8. At −83°C, a CO partial pressure of 64 mbar was required to achieve 10% surface coverage on a palladium catalyst. The same surface coverage was also attained at a temperature of −23°C and a pressure of 427 mbar. Based on the information provided, calculate the molar enthalpy of adsorption. What is the nature of the adsorption process (physisorption or chemisorption)? List some additional measurements that may be performed to confirm your answer.
9. Using the data in the following table for CO_2 adsorption on a zeolite sample, plot the adsorption isostere curves at different coverages (0.1, 0.2, and 0.3 mL g^{-1}). Then, calculate the isosteric heat of adsorption for each coverage.

Coverage (mL g^{-1})	Temperature (°C)	Pressure (Pa)
0.1	8	28
	24	60
	40	164
0.2	8	67
	24	174
	40	467
0.3	8	236
	24	478
	40	834

10. Using the data in the following table, where the adsorbed amount expressed in mmol of adsorbate per gram of adsorbent is reported as a function of pressure, plot the adsorption isotherm curve for each data set (1, 2, and 3). What information can you glean from the different plots?

1	X (mmol g^{-1})	0.809	0.864	0.916	0.980	1.100	1.314	1.587	1.641		
	Pressure (Torr)	11.8	24.3	31.9	36.8	39.4	50.5	105.5	135.8		
2	X (mmol g^{-1})	0.853	0.875	0.886	0.8955	0.918	0.942	1.048	1.233	1.389	1.513
	Pressure (Torr)	4.70	11.3	16.4	18.3	20.8	23.3	25.4	26.0	26.0	26.3
3	X (mmol g^{-1})	0.416	0.472	0.522	0.539	0.556	0.577	0.595	0.646	0.707	
	Pressure (Torr)	2.75	4.40	10.5	17.8	24.2	33.9	40.9	46.1	50.5	

11. Using the data in the following table for the nondissociative adsorption of hydrogen on silica at 77K, determine if the adsorption isotherm may be empirically described by the Langmuir isotherm equation. If so, calculate the temperature-dependent constant b. What volume of gas corresponds to complete coverage of the solid surface?

V (cm^3)	14	23	31	37	43	47
Pressure (mbar)	200	333	467	600	734	850

12. Using the BET method, the volume of nitrogen adsorbed on 0.413 g of activated carbon at 77K was measured. Then, the amount adsorbed in mmol was calculated

using the ideal gas law and the results were tabulated as follows. Determine the value of the coefficient C. Note that the saturation vapor pressure of nitrogen at 77K is 101.3 kPa.

n (mmol)	1.00	1.25	1.65
Pressure (Torr)	150	250	350

13. The gas-phase hydrogenation of acetic acid to ethanol is taking place over a Pt-Sn/CNT solid catalyst at 623K, with a conversion >97% and a selectivity >92%. Two mechanisms were suggested: Langmuir−Hinshelwood and Eley−Rideal. In both cases, the hydrogen dissociatively adsorbs onto the catalytic active sites. Derive the rate expression of acetic acid for each model.

References

[1] S. Yurdakal, C. Garlisi, L. Özcan, M. Bellardita, G. Palmisano, (Photo) catalyst characterization techniques: adsorption isotherms and BET, SEM, FTIR, UV−Vis, photoluminescence, and electrochemical characterizations, Heterogeneous Photocatalysis, Elsevier, 2019, pp. 87−152.

[2] J.M. Thomas, W.J. Thomas, Principles and Practice of Heterogeneous Catalysis, John Wiley & Sons, 2014.

[3] V. Augugliaro, S. Yurdakal, V. Loddo, G. Palmisano, L. Palmisano, Determination of photoadsorption capacity of polychrystalline TiO_2 catalyst in irradiated slurry, Adv. Chem. Eng. 36 (2009) 1−35.

[4] K.S. Sing, Reporting physisorption data for gas/solid systems with special reference to the determination of surface area and porosity (Recommendations 1984), Pure Appl. Chem. 57 (1985) 603−619.

[5] H.-J. Butt, K. Graf, M. Kappl, Physics and Chemistry of Interfaces, John Wiley & Sons, 2013.

[6] G. Leofanti, M. Padovan, G. Tozzola, B. Venturelli, Surface area and pore texture of catalysts, Catal. Today 41 (1998) 207−219.

[7] S.J. Gregg, K.S. W. Sing, H. Salzberg, Adsorption surface area and porosity, J. Electrochem. Soc. 114 (1967) 279C.

[8] I. Levine, Physical Chemistry, McGraw-Hill Education, 2009.

[9] L. Hauchhum, P. Mahanta, Carbon dioxide adsorption on zeolites and activated carbon by pressure swing adsorption in a fixed bed, Int. J. Energy Environ. Eng. 5 (2014) 349−356.

[10] P. Delmelle, F. Villiéras, M. Pelletier, Surface area, porosity and water adsorption properties of fine volcanic ash particles, Bull. Volcanol. 67 (2005) 160−169.

[11] M. Rahimnejad, S.K. Hassaninejad-Darzi, S.M. Pourali, Preparation of template-free sodalite nanozeolite−chitosan-modified carbon paste electrode for electrocatalytic oxidation of ethanol, J. Iran. Chem. Soc. 12 (2015) 413−425.

[12] S. Maiti, A. Pramanik, U. Manju, S. Mahanty, Reversible lithium storage in manganese 1, 3, 5-benzenetricarboxylate metal−organic framework with high capacity and rate performance, ACS Appl. Mater. Interfaces 7 (2015) 16357−16363.

[13] L. Zhou, X. Liu, J. Li, Y. Sun, Y. Zhou, Sorption/desorption equilibrium of methane in silica gel with pre-adsorption of water, Colloids Surf. A: Physicochem. Eng. Asp. 273 (2006) 117−120.

[14] Z. Li, K. Wang, J. Song, Q. Xu, N. Kobayashi, Preparation of activated carbons from polycarbonate with chemical activation using response surface methodology, J. Mater. Cycles Waste Manag. 16 (2014) 359−366.

[15] J. Gay, J. Suzanne, J. Coulomb, Wetting, surface melting, and freezing of thin films of methane adsorbed on MgO (100), Phys. Rev. B 41 (1990) 11346.

[16] H.S. Fogler, Elements of Chemical Reaction Engineering, Prentice Hall PTR, 2006.
[17] M. Ponce, L. Munguía, M. Esparza, I. Kornhauser, F. Rojas, On scrutinizing the classical Polanyi adsorption potential theory for vapour uptake occurring in the mesopores of curved shapes, Adsorption Sci. Technol. 29 (2011) 585–594.
[18] K.C. Ng, M. Burhan, M.W. Shahzad, A.B. Ismail, A universal isotherm model to capture adsorption uptake and energy distribution of porous heterogeneous surface, Sci. Rep. 7 (2017) 1–11.
[19] A. Chakraborty, B. Sun, An adsorption isotherm equation for multi-types adsorption with thermodynamic correctness, Appl. Therm. Eng. 72 (2014) 190–199.
[20] M. Khalfaoui, S. Knani, M. Hachicha, A.B. Lamine, New theoretical expressions for the five adsorption type isotherms classified by BET based on statistical physics treatment, J. Colloid Interface Sci. 263 (2003) 350–356.
[21] M. Batzill, U. Diebold, The surface and materials science of tin oxide, Prog. Surf. Sci. 79 (2005) 47–154.
[22] Y. Changtao, L. Shuyuan, W. Hailong, Y. Fei, Pore structure characteristics and methane adsorption and desorption properties of marine shale in Sichuan Province, China, RSC Adv. 8 (2018) 6436–6443.
[23] V. Loddo, M. Bellardita, G. Camera-Roda, F. Parrino, L. Palmisano, Heterogeneous photocatalysis: A promising advanced oxidation process, Current Trends and Future Developments on (Bio-) Membranes, Elsevier, 2018, pp. 1–43.
[24] G. Hancock, R. Compton, Applications of Kinetic Modelling, Elsevier, 1999.
[25] S. Shirvani, M. Ghashghaee, Mechanism discrimination for bimolecular reactions: revisited with a practical hydrogenation case study, Phys. Chem. Res. 5 (2017) 727–736.
[26] Z. Shang, S. Li, L. Li, G. Liu, X. Liang, Highly active and stable alumina supported nickel nanoparticle catalysts for dry reforming of methane, Appl. Catal. B: Environ. 201 (2017) 302–309.
[27] H.-L. Chou, B.-J. Hwang, C.-L. Sun, New and future developments in catalysis: Chapter 9, Catalysis in Fuel Cells and Hydrogen Production, Elsevier Inc., 2013.
[28] J.R. Ross, Heterogeneous Catalysis: Fundamentals and Applications, Elsevier, 2011.
[29] M. Aziz, A. Jalil, S. Wongsakulphasatch, D.-V.N. Vo, Understanding the role of surface basic sites of catalysts in CO_2 activation in dry reforming of methane: a short review, Catal. Sci. Technol. 10 (2020) 35–45.
[30] S. Das, M. Sengupta, J. Patel, A. Bordoloi, A study of the synergy between support surface properties and catalyst deactivation for CO_2 reforming over supported Ni nanoparticles, Appl. Catal. A: Gen. 545 (2017) 113–126.
[31] J.C. Vedrine, Acid–base characterization of heterogeneous catalysts: an up-to-date overview, Res. Chem. Intermed. 41 (2015) 9387–9423.
[32] A.S. Alshammari, Heterogeneous gold catalysis: from discovery to applications, Catalysts 9 (2019) 402.
[33] F. Pinna, Supported metal catalysts preparation, Catal. Today 41 (1998) 129–137.
[34] P. Munnik, P.E. de Jongh, K.P. de Jong, Recent developments in the synthesis of supported catalysts, Chem. Rev. 115 (2015) 6687–6718.
[35] P.E. de Jongh, T.M. Eggenhuisen, Melt infiltration: an emerging technique for the preparation of novel functional nanostructured materials, Adv. Mater. 25 (2013) 6672–6690.
[36] F. Schüth, Colloidal deposition as method to study the influence of the support on the activity of gold catalysts in CO-oxidation, Phys. Status Solidi (b) 250 (2013) 1142–1151.
[37] M. Montazer, T. Harifi, 7 - Nanocoating and lamination, in: M. Montazer, T. Harifi (Eds.), Nanofinishing of Textile Materials, Woodhead Publishing, 2018, pp. 95–107.
[38] A. Meng, L. Zhang, B. Cheng, J. Yu, Dual cocatalysts in TiO_2 photocatalysis, Adv. Mater. 31 (2019) 1807660.
[39] J. Yang, D. Wang, H. Han, C. Li, Roles of cocatalysts in photocatalysis and photoelectrocatalysis, Acc. Chem. Res. 46 (2013) 1900–1909.
[40] N. Xiao, S. Li, X. Li, L. Ge, Y. Gao, N. Li, The roles and mechanism of cocatalysts in photocatalytic water splitting to produce hydrogen, Chin. J. Catal. 41 (2020) 642–671.

[41] I.F. Teixeira, J. Quiroz, M.S. Homsi, P.H. Camargo, An overview of the photocatalytic H_2 evolution by semiconductor-based materials for nonspecialists, J. Braz. Chem. Soc. 31 (2020) 211−229.
[42] R. Li, H. Chen, J. Xiong, X. Xu, J. Cheng, X. Liu, et al., A mini review on bismuth-based Z-scheme photocatalysts, Materials 13 (2020) 5057.
[43] X. Li, C. Garlisi, Q. Guan, S. Anwer, K. Al-Ali, G. Palmisano, et al., A review of material aspects in developing direct Z-scheme photocatalysts, Mater. Today (2021). Available from: https://doi.org/10.1016/j.mattod.2021.02.017.
[44] W.-K. Jo, S. Kumar, S. Eslava, S. Tonda, Construction of Bi2WO6/RGO/g-C3N4 2D/2D/2D hybrid Z-scheme heterojunctions with large interfacial contact area for efficient charge separation and high-performance photoreduction of CO_2 and H_2O into solar fuels, Appl. Catal. B: Environ. 239 (2018) 586−598.
[45] Y. Chen, X. Feng, X. Guo, W. Zheng, "Toward a fundamental understanding of factors affecting the function of cocatalysts in photocatalytic water splitting,", Curr. Opin. Green Sustain. Chem. 17 (2019) 21−28.
[46] K. Takanabe, K. Domen, Preparation of inorganic photocatalytic materials for overall water splitting, ChemCatChem 4 (2012) 1485−1497.

CHAPTER 4

Surface area and porosity

Given that heterogeneous catalytic reactions take place on the *surface of porous materials*, the formation rate of the product will therefore be heavily dependent on the surface area available for adsorption and subsequent reaction, along with the morphology and extent of pores. The ensemble of these characteristics is referred to as textural properties of a catalyst.

It is intuitive that an increase in surface area will boost the catalytic conversion rate for a fixed weight of the catalyst. The amount of *surface area accessible to reactants* depends on the synthesis method that is followed in the preparation of the catalysts. Depositing metal catalysts on porous supports, for instance, is one way that helps to maximize the surface area of a solid material [1].

The catalytic conversion rate increases proportionally with the specific surface area if the surface is homogenous and the pores are large enough to prevent restrictions of the flow of reactants or products. Conversely, the conversion rate will be limited by diffusion if the pores of the catalyst are too narrow [1].

A decrease in a catalyst's surface area upon continuous use may be an indication of *deactivation*. The catalyst may have been thermally deactivated if the decrease in surface area is associated with a decline in the catalytic reaction rate. On the other hand, the catalyst may have been fouled with a poisoning species if the reaction rate decays faster than the decrease in surface area. Commercial catalysts typically retain large surface areas to support their long-term use without any rapid loss in activity that may result from surface poisoning [1].

It is important to note that out of the total surface area in a porous catalytic material, only a certain fraction is *chemically active*.

4.1 Estimation of the surface area

For applications based on porous materials, the specific surface area is a vital characteristic to describe a material. The surface area of a catalyst can be determined experimentally through various methods, including gravimetric, dynamic, and volumetric [Langmuir, point "B", Brunauer–Emmett–Teller (BET), *t*-plot] methods.

Heterogeneous Catalysis.
DOI: https://doi.org/10.1016/B978-0-323-89845-4.00003-5

4.1.1 Gravimetric and dynamic methods

In the *gravimetric method*, changes in the weight of an adsorbent during the process of adsorption are recorded and used to measure the surface area (the weight increases due to the adsorption of a gas on its surface). The most common types of *balances* used for this purpose are the spring and the beam balance. The spring balance is cheaper and provides direct measurements of the adsorbed amount; however, it is difficult to assemble, challenging to operate, and is limited to physical adsorption measurements. The beam balance is more sensitive and precise; however, it is more sophisticated and necessitates the installation and use of optical and electromagnetic detectors. Temperature gradients and buoyancy forces must be accounted for since they are considered to be two very common sources of error in gravimetric measurements [1]. In the dynamic method a continuous flow of an adsorbate through an adsorbent bed is employed for the determination of the surface area. Changes in the concentration of the adsorbing gas are monitored with a thermal conductivity detector. Prior to the start of the experiment, the adsorbate must be thoroughly dried and the adsorbent outgassed in order to ensure accurate measurements [1].

Focus 4.1: Intelligent gravimetric analyzer

The intelligent gravimetric analyzer (IGA) is an *electronic beam balance widely used for measuring gas and vapor sorption* in the presence of a variety of different materials, including solid adsorbents and ionic liquids [2]. At first, the IGA microbalance was developed specifically for the chemisorption measurements of H_2 adsorption in metals and metal alloys. Since then, applications of the IGA microbalance have expanded to several research areas including, for instance, CO_2 capture through solid adsorbents. The IGA microbalance measures changes in the sample mass as a function of temperature, pressure, and gas composition. Furthermore, it allows for the simultaneous determination of kinetic parameters and the prediction of sorption equilibrium in real time. The IGA instrument can handle multiple gas inlets (which is significant for studies involving competitive adsorption with mixed gases) and it can also be coupled to a mass spectrometer. On this basis, it has gained great interest in the past few years.

The IGA microbalance is commonly used to study the solubility and diffusivity of gases. However, it can also be used to measure the sorption properties of aqueous and organic vapors. During vapor sorption analysis, the IGA instrument is operated either in the "static mode" or in the "dynamic mode" [2]. In the static mode the vapor is generated by tuning the partial pressure of a liquid using a vacuum system. Alternatively, in the dynamic mode, an inert gas first contacts the liquid and then a saturated vapor stream with a specified partial pressure is generated by controlling the temperature of the vapor in a cell.

The IGA microbalance (shown in Fig. 4.1) consists of a balance beam connected to a sample cup and counterweight by a series of hang-down wires and hooks [2]. The IGA instrument, which can be operated at pressures ranging from vacuum (10^{-10} MPa) to 2 MPa and

(*Continued*)

Focus 4.1: Intelligent gravimetric analyzer (Continued)

temperatures between 77 and 1273K, utilizes a force balance method to determine the sample mass in pressure and temperature-controlled environment. More specifically, it detects incremental changes in the position of the balance beam which moves in response to buoyancy and gravity forces acting on the components within the system. The mass resolution of the IGA microbalance can reach up to 0.1 μg.

Since the IGA microbalance is fully automated, the pressure and temperature can be controlled with high precision [2]. A number of vacuum pumps are typically used to achieve a pressure as low as 10^{-10} MPa. The vacuum pumps are especially useful for in situ sample pretreatment, where volatile impurities including moisture can be removed from the sample before analysis. The temperature of the IGA instrument can be controlled in three different zones: the balance, the counterweight, and the sample chamber. The temperature in the balance is typically maintained at 318K by a band heater. The temperature in the sample chamber is regulated according to the required conditions. For example, if operating in a temperature range between 278 and 358K, then a jacketed water bath may be utilized. If, on the other hand, the temperature in the sample chamber is to be set at higher values ($>$358K), then a furnace would be the most appropriate tool. Finally, for applications that require subambient temperatures ($<$278K), a cryo-furnace must be used.

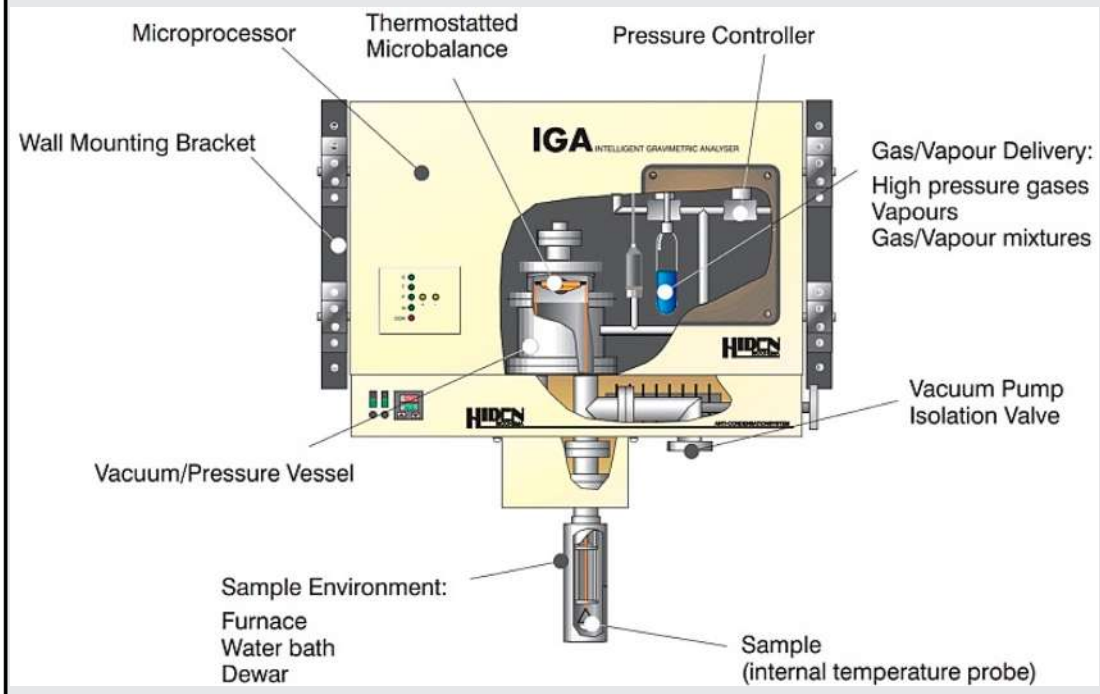

Figure 4.1
Schematic representation of the Intelligent Gravimetric Analyzer (*IGA*) instrument.
Source: *Reproduced from [3].*

4.1.2 Volumetric methods

In the *volumetric method* the adsorption volume of an inert gas is used to assess the surface area of a solid. This method, however, is applicable only to adsorbate–adsorbent systems that follow a Type I, Type II, or Type IV adsorption isotherm. That is because the *volume of the first adsorbed monolayer*, V_m, can be univocally determined only from these isotherm types [1].

4.1.2.1 Langmuir method

Consider an adsorption isotherm of Type I. Here, the adsorption behavior may be satisfactorily described with the Langmuir isotherm equation (Section 3.1.1):

$$\frac{V}{V_m} = \frac{bP}{1 + bP} \tag{4.1}$$

Rearranging gives:

$$\frac{P}{V} = \frac{P}{V_m} + \frac{1}{bV_m} \tag{4.2}$$

A plot of *P/V versus P is linear* with a slope of $1/V_m$ and an intercept of $1/(bV_m)$. Hence, the volume of the monolayer, V_m, is identified [1].

4.1.2.2 Point "B" and BET methods

Now, consider an adsorption isotherm of Type II or IV. Here, the volume of the monolayer can be determined either directly from the isotherm plot of V versus P or by linearizing the BET isotherm equation. The first method, known as the "point B" method, defines the volume of the monolayer, V_m, as the ordinate value of V where the isotherm sharply bends over with a change in the sign of the second derivative. To obtain reliable results, this sharp change in the isotherm's curvature must be clearly visible and recognizable. The second method, which gives a more definitive estimate of the monolayer volume, uses the BET isotherm equation (Section 3.1.5) to describe the adsorption process:

$$\frac{P}{V(P_0 - P)} = \frac{1}{V_m C} + \frac{(C-1)}{V_m C}\left(\frac{P}{P_0}\right) \tag{4.3}$$

A plot of *$P/[V(P_0 - P)]$ versus P/P_0 is linear* with a slope of $(C-1)/(V_m C)$ and an intercept of $1/(V_m C)$. This is applied in regions where P/P_0 is low enough (typically $<1/3$) to minimize the chance to get into nonlinear regions generated by the condensation in mesopores. Hence, the volume of the monolayer, V_m, is identified and the adsorbent's specific surface area, S_g, in $m^2\ g^{-1}$, can then be calculated [1]:

$$S_g = \frac{V_m}{0.0224} \times \left(6.023 \times 10^{23}\right) \times A \tag{4.4}$$

where 6.023×10^{23} is Avogadro's number and A is the area occupied by each adsorbate molecule. For *nitrogen*, which is the most common adsorbate used in the determination of the specific surface area, the area occupied by a single molecule is 16.2×10^{-20} m^2. As long as the adsorbent retains a specific surface area that is greater than 0.2 m^2, nitrogen-based measurements will yield acceptable results. However, if the sample possesses a specific surface area that is less than 0.2 m^2, then it is preferable to use an adsorbate with a saturated vapor pressure that is less than that of nitrogen. A fitting example would be *krypton* [1].

Focus 4.2: BET surface analyzer

Measurements required for the BET method are typically performed in a surface analyzer equipment (Fig. 4.2). Before the actual analysis begins, *catalyst samples*—in the form of dry powder or monolith—*must first be degassed* to ensure the complete removal of any surface adsorbed water molecules or any other contaminant. This will yield the most accurate measurements of the surface area since the entire catalytic surface will be available for adsorption. The degassing process takes place under vacuum (or alternatively under a continuous flow of an inert gas) and at high temperatures. However, it is important to consider that at extremely high temperatures and at prolonged times, the surface of catalytic solids is highly susceptible to alteration. Hence, it is suggested to perform the degassing at the highest possible temperature that will not cause a change in the morphology of the sample. Not only will this protect the integrity of the sample's structure, but it will also shorten the degassing time, which under room temperature conditions is usually set for at least 16 h [as per IUPAC (International Union of Pure and Applied Chemistry) recommendations]. It is also suggested that, in order to obtain successful measurements, a minimum sample weight of 0.01 g per m^2 of expected sample surface area is analyzed.

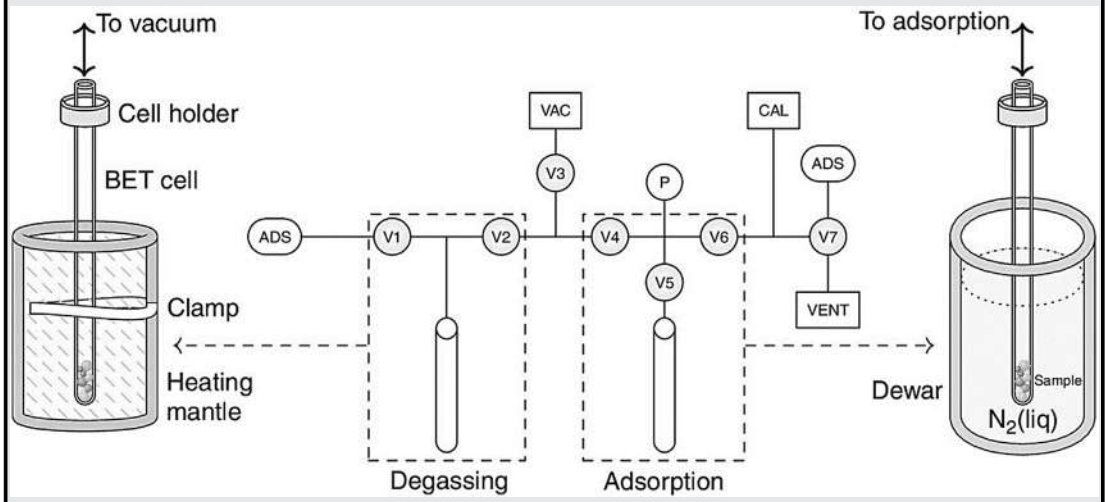

Figure 4.2
Schematic representation of a Brunauer–Emmett–Teller (*BET*) surface analyzer. Source: *Reproduced from [4].*

(*Continued*)

Focus 4.2: BET surface analyzer (Continued)

When operating a BET surface analyzer equipment, appropriate quantities of catalyst samples are first weighed and then placed in designated glass cells, which come in various shapes and sizes. Then, these glass cells are placed into heating mantles and connected to the outgas port of the surface analyzer equipment for the degassing process. After the samples have been degassed, the heating mantle is removed, allowing the glass cells to cool down and then the connection to the analysis port is opened. Once connected, the cells are submerged in a liquid nitrogen dewar in order to maintain the low temperature required for the adsorbate condensation on the surface of the solid, measuring adsorption/desorption at different partial pressures of the adsorbate in order to build a full isotherm curve.

During surface area analysis, the dead volume of the sample cell must be accounted for. Thus, a blank run with helium gas is typically performed by the equipment before and after each measurement. Helium does not adsorb onto the catalyst surface and, as such, is ideal for calibrating the dead volume. The effect of dead volume, which is particularly relevant at large ratios between the volume of the sample cell and the volume occupied by the sample or for low-porous samples, can be minimized—whenever needed—by placing a large nonporous rod inside the sample cell.

Focus 4.3: Numerical example on calculating the specific surface area using the BET isotherm equation

Using the data in the table below for the adsorption of nitrogen on alumina at 77K, calculate the specific surface area in $m^2\ g^{-1}$. Note that the saturation pressure of nitrogen at 77K is 734 mmHg and the weight of the alumina sample is 1 g.

Pressure (mmHg)	**46.76**	**83.30**	**123.63**	**151.10**	**194.42**
Volume (cm^3) STP	32.23	37.20	42.20	45.44	50.58

Solution

Using Eq. (4.3), plot $P/[V(P_0 - P)]$ versus P/P_0 to get a straight line with a slope of $(C - 1)/(V_m C)$ and an intercept of $1/(V_m C)$. Note that the vertical axis is multiplied by 10^3 for presentation purposes. The resulting plot is shown in the figure below, where the slope is found to be equal to 0.0248 cm^{-3} and the intercept equal to 0.5802×10^{-3} cm^{-3}. Hence, the volume of the monolayer is calculated to be equal to 39.40 cm^3 and the value of C equal to 43.76.

(*Continued*)

Focus 4.3: Numerical example on calculating the specific surface area using the BET isotherm equation (Continued)

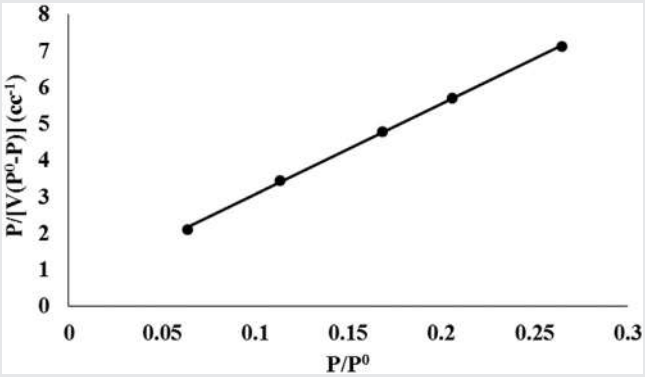

The specific surface area in $m^2\ g^{-1}$ can then be calculated using Eq. (4.4):

$$S_g = \frac{V_m}{0.0224} \times \left(6.023 \times 10^{23}\right) \times A = \frac{39.40 \times 10^{-6}}{0.0224} \times \left(6.023 \times 10^{23}\right) \times 16.2 \times 10^{-20} = 171.62\ m^2 g^{-1}$$

4.1.2.3 t-Plot method

In the *t-method* of Lippens and De Boer [5], the specific surface area is determined from the *t*-curve. Instead of using the fraction of monolayer capacity (V/V_m) as the dependent variable, the *t*-curve uses the *statistical thickness of the adsorbed film (t)*, which can be determined as per the following expression [6]:

$$t = \sigma \frac{V}{V_m} \tag{4.5}$$

where σ is the thickness of a single adsorbed layer (σ = 3.54 Å for nitrogen [7]) and V/V_m identifies the number of molecular layers adsorbed on the solid's surface. A *plot of V versus t, a t-plot, is linear* with a slope of V_m/σ and it passes through the origin. Hence, the volume of the monolayer, V_m, is identified and the adsorbent's specific surface area, S_g, can then be calculated from Eq. (4.4).

In most real-life applications, the *t*-plot will deviate from its idealistic linear behavior (Fig. 4.3). These deviations, however, can be interpreted to provide insights into the nature of the pores and the micropore volume [6]. A strong upward deviation from linearity suggests a rapid increase in the gas uptake at certain relative pressures. This observation is indicative of capillary condensation in mesopores. On the other hand, a downward deviation typically results when multilayer adsorption takes place in narrow micropores where the surface becomes unavailable for adsorption. The presence of slit-shaped pores, for instance, can lead to this observed behavior.

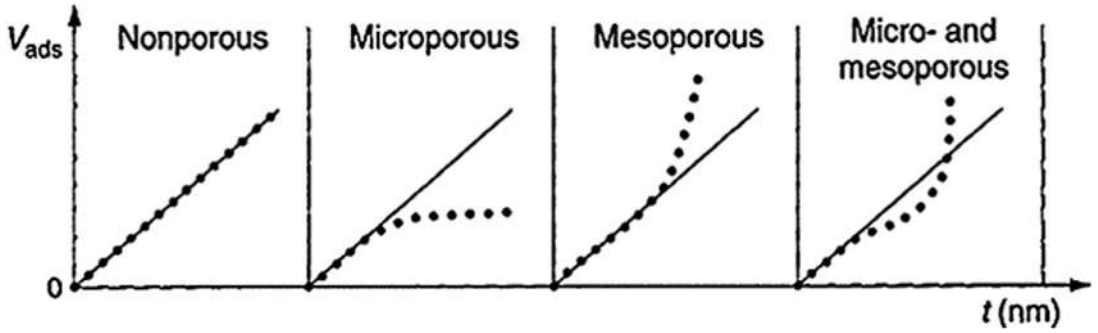

Figure 4.3
Determination of micropore and mesopore volumes based on *t*-plots. Source: *Reproduced from [8].*

The linear *t*-plot might also depict a positive intercept, implying that large quantities of gas are being adsorbed at very low partial pressures. This behavior is usually attributed to strong adsorption in micropores. In this case, the extent of micropore volume of the adsorbent can be estimated from the intercept value.

An extension of the *t*-method was proposed by Mikhail, Brunauer, and Bodor [9]. The method is known as the *micropore analysis method*, abbreviated as MP. In this method the downward deviation from the *t*-plot is used for the determination of the micropore volume. Consider the *t*-plot in Fig. 4.4, where each downward deviation line from 1 to 9 signifies a group of narrow pores with the same specific surface area, *S*, that has become filled. The total pore volume, V_p, can then be calculated using the following expression:

$$V_p = \sum_{i=1}^{9} 10^4 (S_i - S_{i+1}) \left(\frac{t_{i+1} + t_i}{2} \right) \tag{4.6}$$

In a modified form of the *t*-method, known as the α_S-*method* by Sing [10], the monolayer capacity is replaced by the amount adsorbed at some arbitrarily chosen relative pressure. Hence, the knowledge of the statistical thickness (*t*), which depends on the monolayer capacity, is not needed. In this method a standard isotherm plot of α_S versus P/P_0 is obtained, where α_S is defined as the amount adsorbed on a material normalized by the amount adsorbed at some arbitrarily chosen relative pressure. The reference material is a nonporous (or pore-free) sample with chemical properties and chemical composition similar to that of the sample being analyzed. The α_S-curve is then constructed by plotting the adsorbed liquid volume against α_S [11]. Extrapolation of the α_S curve to $\alpha_S = 0$ gives the micropore volume, while the slope of the linear portion yields information on the nature of the pores.

4.2 Estimation of porosity and pore size

The *mean pore diameter* and the *pore size distribution* of a catalyst can be determined experimentally through various methods (Table 4.1). For catalysts with pore sizes *below 20 Å*, gas adsorption methods including Dubinin–Radushkevich (DR), Dubinin–Astakhov

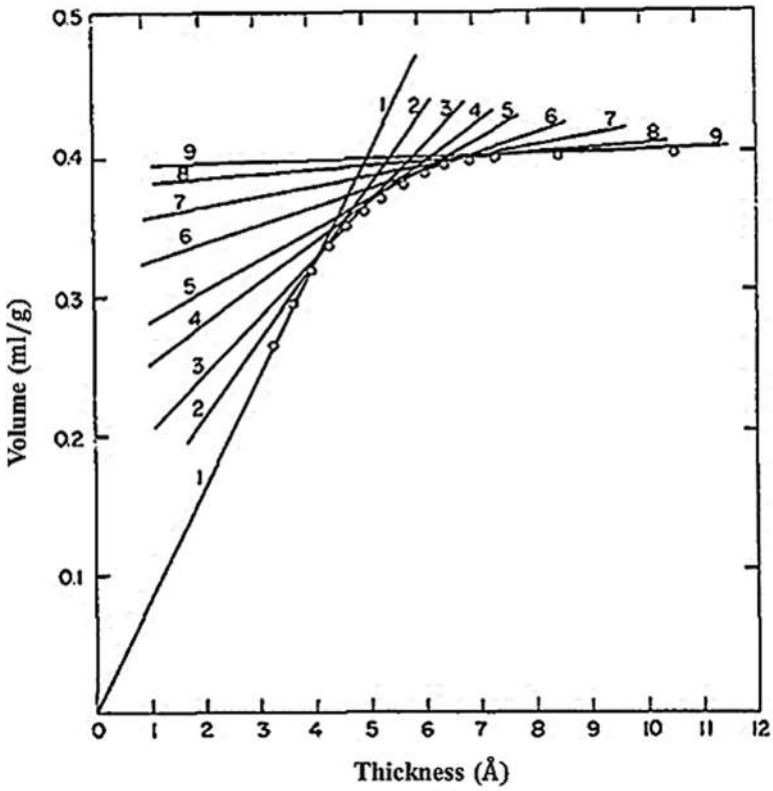

Figure 4.4
Determination of the micropore volume from a *t*-plot using the micropore (*MP*) analysis method. Source*: Reproduced from [9].*

Table 4.1: Summary of the most popular models used to estimate the textural properties of porous catalysts.

Measured property	Model
Surface area	BET, Langmuir, Temkin, Freundlich
Total pore volume	BET, BJH, Wheeler, Kelvin
Mesopore volume, area, and distribution	BJH, DH, DFT
Micropore volume, area, and distribution	DR–DA, HK, SF
Pore size modeling	DFT
Surface energy	DFT

BET, Brunauer–Emmett–Teller; *BJH*, Barrett–Joyner–Halenda; *DA*, Dubinin–Astakhov; *DFT*, density functional theory; *DH*, Dollimore–Heal; *DR*, Dubinin–Radushkevich; *HK*, Horvath–Kawazoe; *SF*, Saito–Foley.

(DA), Horvath–Kawazoe (HK), and Saito–Foley (SF) methods, are recommended. On the other hand, for catalysts with pore sizes *in the range of 15–200 Å*, gas adsorption methods, including Barrett–Joyner–Halenda (BJH), Dollimore–Heal (DH), density functional theory

(DFT), and nonlocal DFT (NLDFT) methods, are typically applied. For catalysts with pore sizes *in the range of 100–105 Å*, mercury porosimetry is more appropriate [1,4].

4.2.1 Dubinin–Radushkevich and Dubinin–Astakhov methods

Dubinin and *Radushkevich* developed the following empirical equation to describe the amount of gas adsorbed, W, in micropores [12]:

$$W = W_0 e^{\left[-\left(\frac{\varepsilon}{\beta E_0}\right)^2\right]} \tag{4.7}$$

where W_0 is the limiting (or maximum allowable) micropore volume, ε is the adsorption potential derived by Polanyi, β is an affinity coefficient, and E_0 is the characteristic energy of adsorption. The *adsorption potential* ε has been earlier defined in Eq. (3.43).

Substituting ε into Eq. (4.7) gives:

$$\ln W = \ln W_0 - \left(\frac{RT}{\beta E_0}\right)^2 \left(\ln \frac{P_0}{P}\right)^2 \tag{4.8}$$

A plot of *ln W versus* $[\ln(P_0/P)]^2$ *is linear* with a slope of $-(RT/\beta E_0)^2$ and an intercept of $\ln W_0$. It should be noted that in some cases the plot will deviate substantially from a straight line. Interpretations of this behavior are still under investigation.

Later, *Dubinin* and *Astakhov* further developed the DR equation to obtain a more general approach for the description of the amount of gas adsorbed, W, in micropores [13]:

$$W = W_0 e^{\left[-\left(\frac{\varepsilon}{\beta E_0}\right)^n\right]} \tag{4.9}$$

where n is a coefficient—in the range between 1 and 3—that is selected to give the best linear fit.

4.2.2 Horvath–Kawazoe method

During the development of the *HK* model, several assumptions were made, including the following [6,14,15]:

- The adsorbent consists entirely of noninterconnecting, chemically homogeneous slit-shaped micropores.
- The relative pressure required to fill the micropores is directly related to the adsorbate–adsorbent interaction energy. This indicates that the micropores are gradually filled as the adsorbate pressure increases. Hence, only pores that are smaller than a specific size will be filled at a certain relative pressure.

- Interactions with the pore walls result only because of dispersion forces.
- The local adsorbate density in the slit-shaped micropore is uniform everywhere in the accessible volume of the pore.
- The gas adsorbed in the micropores behaves like a 2D gas.
- Horvath and Kawazoe proposed that the change in entropy upon adsorption is much smaller than the change in enthalpy. Thus, the *adsorption free energy change (ΔG)* can be described as [6]:

$$\Delta G^{\text{ads}} = RT\ln\left(\frac{P}{P_0}\right) = U_0 + P_a \tag{4.10}$$

where U_0 represents the adsorbate−adsorbent interaction and P_a the adsorbate−adsorbate−adsorbent interaction.

The potential energy of interaction, E, between an adsorbate molecule and the surface of an adsorbent is expressed by the HK method as [6]:

$$E(z) = K\varepsilon_0\left[-\left(\frac{\sigma}{z}\right)^4 + \left(\frac{\sigma}{z}\right)^{10} - \left(\frac{\sigma}{L-z}\right)^4 + \left(\frac{\sigma}{L-z}\right)^{10}\right] \tag{4.11}$$

where z is the distance between the adsorbate atom and a surface atom in the adsorbent's slit walls, K is a constant, ε_0 is the potential energy minimum, σ is the distance between the adsorbate atom and a surface atom at zero interaction energy, and L is the distance separating two infinite lattice planes of adsorbent.

The average interaction energy, which may be obtained by taking the volumetric average of the potential energy of interaction (E), is related to the adsorption free energy change by the following expression [6]:

$$\Delta G^{\text{ads}} = RT\ln\left(\frac{P}{P_0}\right) = N_a\left(\frac{N_{AS}A_{AS} + N_{AA}A_{AA}}{\sigma^4(L-2d)}\right)\left[\frac{\sigma^4}{3(L-d)^3} - \frac{\sigma^{10}}{9(L-d)^9} - \frac{\sigma^4}{3d^3} + \frac{\sigma^4}{3d^9}\right] \tag{4.12}$$

where N_a is Avogadro's constant, N_{AS} is the number of atoms per unit area of solid surface, N_{AA} is the number of molecules adsorbed per unit area of solid surface, A_{AS} and A_{AA} are constants in the Lennard−Jones potential for adsorbate−adsorbent and adsorbate−adsorbate interactions, and d is the distance between the adsorbed molecule and the adsorbent. In a simpler form [6]:

$$RT\ln\left(\frac{P}{P_0}\right) = U_0 + P_a = N_a\xi(L) \tag{4.13}$$

where $Na\xi(L)$ is a function of the specific pore width L.
Eq. (4.13) can then be used to estimate the pore size in microporous solids.

As for the determination of the pore size distribution, Eq. (4.12) is first used to calculate the relative pressure at a specific pore width (L). Then, using the experimental adsorption isotherm, the amount of gas adsorbed at that particular relative pressure is estimated. Finally, the pore size distribution in the microporous range is determined by differentiating the amount adsorbed with respect to the pore width.

4.2.3 Saito–Foley method

The *SF* method is very similar to the HK method. However, instead of assuming a slit-shaped geometry for the micropores, the SF method assumes that the *micropores* have a *cylindrical* morphology. The below assumptions were made during the development of the SF model [16]:

- The pore is a perfect cylinder of infinite length and finite radius.
- The cylindrical wall is composed of a single layer of atoms, taken as a continuum of potential interaction. Interaction with the pore wall results only because of dispersion forces (similarly to the assumption made by the HK model).
- Adsorption takes place only on the interior walls of cylindrical micropores.
- Adsorption results only from interactions between the adsorbate and the adsorbent.

The *potential energy of interaction, E*, between an adsorbate molecule and the surface of an adsorbent is expressed through the SF model as [16]:

$$E(r) = \frac{5}{2}\pi\varepsilon_0\left[\frac{21}{32}\left(\frac{d}{r_p}\right)^{10}\sum_{k=0}^{\infty}\alpha_k\left(\frac{r}{r_p}\right)^{2k} - \left(\frac{d}{r_p}\right)^{4}\sum_{k=0}^{\infty}\beta_k\left(\frac{r}{r_p}\right)^{2k}\right] \tag{4.14}$$

where r_p is the pore radius, r is the distance from the central axis of a cylindrical pore, ε_0 is the potential energy minimum, and d is the distance between the adsorbed molecule and the adsorbent. The constants α_k and β_k are defined as [16]:

$$\alpha_k^{0.5} = \frac{\Gamma(-4.5)}{\Gamma(-4.5-k)\Gamma(k+1)} \tag{4.15}$$

$$\beta_k^{0.5} = \frac{\Gamma(-1.5)}{\Gamma(-1.5-k)\Gamma(k+1)} \tag{4.16}$$

The average interaction energy, which may be obtained by taking the area average of the potential energy of interaction (E), is related to the free energy change of adsorption by the following expression [16]:

$$\ln\left(\frac{P}{P_0}\right) = \frac{3\pi N_a}{4RT}\left(\frac{N_{AS}A_{AS}+N_{AA}A_{AA}}{d^4}\right)\sum_{k=0}^{\infty}\left[\frac{1}{k+1}\left(1-\frac{d}{r_p}\right)^{2k}\left\{\frac{21}{32}\alpha_k\left(\frac{d}{r_p}\right)^{10} - \beta_k\left(\frac{d}{r_p}\right)^{4}\right\}\right] \tag{4.17}$$

4.2.4 Barrett–Joyner–Halenda method

The *BJH method*, which is applicable only to *cylindrical pores*, accounts for both the physical adsorption on pore walls and the capillary condensation in mesopores. Hence, the pore radius, r_p, estimated through this method is the summation of the thickness of the adsorbed multilayers, t, and the radius of the meniscus, r (kindly refer to Section 4.3 for an in-depth explanation on the phenomenon of capillary condensation and the concept of meniscus formation). The multilayers thickness may be calculated from the BET equation (Section 3.1.5), while the meniscus radius may be obtained from the below reported *Kelvin equation* (applied to the desorption branch):

$$\ln\frac{P}{P_0} = \frac{2\gamma V_M}{rRT} \tag{4.18}$$

where γ is the surface tension of the liquid adsorbate and V_M is its molar volume [6]. The change in film thickness is calculated from the decrease in relative pressure of the desorption path. As the relative pressure decreases, capillary condensate is evacuated from the largest pores and, at the same time, the thickness of the adsorbate layer is reduced [4].

The Kelvin equation (Eq. 4.18) may be derived by equating the work done in enlarging the surface area of a spherical drop of liquid to the work done in adding the molecules to the drop's interior [1]:

$$8\pi r\Delta r\gamma = (\mu - \mu_0)\Delta n \tag{4.19}$$

where μ_0 is the chemical potential of the vapor over a plane liquid surface, μ is the chemical potential over a curved surface, and Δn is the change in the number of moles of the liquid. The change in the drop's volume is given as:

$$V_M\Delta n = 4\pi r^2\Delta r \tag{4.20}$$

Solving for Δn and substitution in Eq. (4.19) yield:

$$(\mu - \mu_0) = \frac{2\gamma V_M}{r} \tag{4.21}$$

From the thermodynamic definition of chemical potential:

$$\mu_0 = \mu^* + RT\ln P_0 \tag{4.22}$$

$$\mu = \mu^* + RT\ln P \tag{4.23}$$

where μ^* is the standard chemical potential at unit pressure. Substitution into Eq. (4.21) gives Kelvin equation (Eq. 4.18).

Due to different physical properties, such as tensile strength and pore network effects, the BJH method fails to correctly estimate the diameter of micropores and narrow mesopores

by as much as several tens of Å less than the actual. The classical Kelvin equation (Eq. 4.18) disregards the existence of an attractive adsorption potential within the catalyst pores. This, in turn, results in a pore size estimation that is smaller than the real one. Therefore the Kelvin equation has been improved by Broekhoff and de Boer (BdB) to include the adsorption potential interactions, which define the stability of the fluid inside a cylindrical pore against capillary forces. The modified Kelvin−BdB expression is [17]:

$$RT\ln\frac{P}{P_0} = \frac{\gamma V_M}{r-t} + F(t) \tag{4.24}$$

where $F(t)$ accounts for the adsorption potential field between the adsorbent and the adsorbate. Harkins and Jura developed a simple expression for the determination of $F(t)$:

$$F(t) = RT\exp\left(\frac{13.99}{t^2} - 0.034\right) \tag{4.25}$$

Capillary condensation begins when $RT\ln(P/P_0)$ reaches a maximum value. In other words, the derivative of the right-hand side of Eq. (4.24) has to cancel at the critical thickness, t_c:

$$\frac{dF(t)}{dt}|_{t_c} - \frac{\gamma V_M}{(r-t_c)^2} = 0 \tag{4.26}$$

Solving Eqs. (4.24) and (4.26) for a given relative vapor pressure gives the critical thickness, t_c.

4.2.5 Dollimore−Heal method

The *method proposed by DH* for calculating the pore size distribution from adsorption isotherms is based on Wheeler's general equation for desorption. In particular, *Wheeler* described the total capillary adsorbate volume (V_c), the geometric area (S), and the pore length (L) according to the below equations [18]:

$$V_c\left[r_p < r_{pn}\right] = \int_0^{r_{pn}} \pi r_p^2 L\left(r_p\right) dr_p \quad \text{for pores in future desorption steps} \tag{4.27}$$

$$S\left[r_p > r_{pn}\right] = \int_{r_{pn}}^{\infty} 2\pi r_p L\left(r_p\right) dr_p \quad \text{for pores in previous desorption steps} \tag{4.28}$$

$$L\left[r_p > r_{pn}\right] = \int_{r_{pn}}^{\infty} L\left(r_p\right) dr_p \quad \text{for pores in previous desorption steps} \tag{4.29}$$

where n is the number of completed desorption steps. Note that the length of the pores is a continuous function of r_p, namely $L(r_p)$, which is the required length distribution and not a length itself.

The total volume of multilayer adsorbate on the walls of all pores with $r_p > r_{pn}$ is given as [18]:

$$V_m = \int_{r_{pn}}^{\infty} \pi\left(2r_p t_n - t_n^2\right) L\left(r_p\right) dr_p = t_n \int_{r_{pn}}^{\infty} 2\pi r_p L\left(r_p\right) dr_p - \pi t_n^2 \int_{r_{pn}}^{\infty} L\left(r_p\right) dr_p \tag{4.30}$$

Or, in simpler terms:

$$V_m = t_n S\left[r_p > r_{pn}\right] - \pi t_n^2 L\left[r_p > r_{pn}\right] \tag{4.31}$$

Differentiating, changing finite steps to delta terms, and changing area and length functions to finite terms yields:

$$\Delta V_m = \Delta t_n \sum S_p - 2\pi t_n \Delta t_n \sum L_p \tag{4.32}$$

The value of ΔV_p may then be calculated for a particular step using the following expression [18]:

$$\Delta V_p = R_n(\Delta V_n - \Delta V_m) = R_n\left(\Delta V_n - \Delta t_n \sum S_p + 2\pi t_n \Delta t_n \sum L_p\right) \tag{4.33}$$

where R_n is a function of the pore radius (r_p), the meniscus radius (r), and the adsorbate thickness (t), and V_n is the total volume of adsorbate (capillary adsorbate and multilayer adsorbate) at step n.

The DH method is very similar to the BJH method and, in most cases, both methods will yield comparable results. In addition, both models assume *cylindrical pore geometries* and are therefore applicable only to cylindrical pores. However, unlike the BJH method, the DH method does not require any approximation for multilayer desorption. This provides an easier and a less tedious approach for the estimation of the pore size distribution [18].

4.2.6 Density functional theory

The *DFT/NLDFT methods*, which are recommended for a more precise calculation and a more realistic approach, describe the experimental adsorption isotherm with the following theoretical equation:

$$N_e\left(\frac{P}{P_0}\right) = \int_{D_m}^{D_M} N_t\left(\frac{P}{P_0}, D\right) f(D) dD \tag{4.34}$$

where $N_e(P/P_0)$ represents the experimental isotherm, $N_t(P/P_0,D)$ represents the individual theoretical isotherms for pores of diameter D, $f(D)$ is an unknown pore diameter distribution function, D_M is the maximum pore size, and D_m is the minimum pore size [4,17]. Using statistical thermodynamic principles, DFT/NLDFT utilizes molecular models based on the *grand canonical ensemble* to connect macroscopic observables (i.e., adsorption isotherms)

with microscopic (i.e., pore size/geometry and energy interaction parameters) properties. The DFT/NLDFT method provides a more accurate representation of the adsorption/desorption process in porous solids because it accounts for the equilibrium density profile of the heterogeneous fluid at the surface and within the pores as a function of pore radius [6]. Unlike the classical methods, the DFT/NLDFT approach may be applied *not only to cylindrical pores but also to slit-shaped pores*. Furthermore, compared to experimental methods, the DFT/NLDFT method has been shown to yield more agreeable results whether applied to the adsorption path or the desorption path, with the latter being slightly more exact [17], as opposed to the BJH method which shows that pore sizes estimated from the adsorption path are inconsistent with those obtained from the desorption path (especially when the classical Kelvin equation is used). In any case, and regardless of the method employed, it is always preferential to apply the pore size estimation to the desorption branch of an adsorption/desorption isotherm. This is because, in pores of finite length (which is always the case in real adsorbents), pore condensation is associated with nonequilibrium metastable states of the fluid [19]. The metastable adsorption branch terminates when the limit of stability for the metastable states is achieved and the fluid spontaneously condenses into a liquid-like state. On the other hand, metastability is not expected to occur during desorption since vaporization can occur via a receding meniscus. This indicates that the desorption branch of a hysteresis loop reflects the equilibrium phase transition and, hence, must be used for a precise calculation of the pore size, especially when methods that are based on the determination of the gas−liquid phase transition (such as BJH) are applied for the analysis. Conversely, if a method is developed to account for metastability and if it provides a correlation between the relative pressure at which condensation occurs and the pore size, then the pore size analysis can be performed on the adsorption branch.

4.2.7 Mercury porosimetry

The *mercury porosimeter* method estimates the size of pores by measuring the liquid volume forced into the capillaries as a result of pressure [6]. The pore radius, r_p, is calculated by equating the force that is impeding the entry of the liquid into the narrow cylindrical pores to the force that is driving mercury into the pores:

$$r_p = -\frac{2\gamma cos\alpha}{P} \tag{4.35}$$

where α is the contact angle between the liquid and the solid and P is the pressure imparted to the liquid mercury. It is important to note that *pores of radius less than 100 Å cannot be detected* with this method. That is because a pressure greater than 1.15×10^{15} N m^{-2} (which is impractical) is required to fill these smaller pores [1].

The pore-volume distribution function, $V(r)$, may be expressed as follows [1]:

$$V(r) = \frac{dV}{dr} = \frac{dV}{dP} \times \frac{dP}{dr} = -\frac{sP}{r} \tag{4.36}$$

where s is the slope to a plot of the volume of liquid adsorbed V as a function of the applied pressure P at a particular P.

4.3 Hysteresis and capillary condensation

The adsorption/desorption *isotherm* of a mesoporous material is often characterized by a *hysteresis*, in which the desorption process follows a path that is different from the one followed during adsorption. This comes as a direct result of the *pore network topology* [20]. For instance, consider the filling and emptying of a *cylindrical pore*, as illustrated in Fig. 4.5. The process of adsorption begins at low pressure, where a thin monolayer of vapor adsorbs (i.e., condenses) onto the pore walls. As pressure increases, the thickness of the adsorbed layer increases until it reaches a critical value. At this point, *capillary condensation* occurs at a certain, virtually constant pressure, and the entire pore is instantaneously filled with liquid. This explains the steep increase of the amount adsorbed in the adsorption isotherm. Alternatively, the process of desorption begins at high pressure, where the liquid desorbs (i.e., evaporates) starting at the vapor−liquid interface and forming a meniscus (V to IV in Fig. 4.5) [6,21]. As the pressure decreases, the thickness of the liquid layer in between the two meniscuses decreases until it reaches a critical value. At this point, capillary evaporation occurs and the adsorbed amount decreases significantly. The thickness of the adsorbed layer continues to decrease with decreasing pressure until all the adsorbed liquid has evaporated. When compared to *capillary condensation*, the critical thickness that is needed to initiate *capillary evaporation* is smaller and, therefore, a lower pressure must be reached [20]. As a result, a hysteresis is observed in the adsorption/desorption isotherm. This may be explained via the Kelvin equation as discussed below.

For open-ended cylindrical capillaries, a relationship between the pressure at which capillary condensation (P_a) and the pressure at which capillary evaporation (P_d) takes place may be deduced by the Kelvin equation. During adsorption, an annular liquid ring forms in the capillary. A meniscus, however, is not formed until the pore is full. The change in the surface area on formation of an annular ring is twice the one for an analogous spherical drop of the same radius. Hence, from the Kelvin equation, P_a and P_d are expressed as:

$$P_a = P_0 \exp\left(\frac{-\gamma V}{rRT}\right) \tag{4.37}$$

$$P_d = P_0 \exp\left(\frac{-2\gamma V}{rRT}\right) \tag{4.38}$$

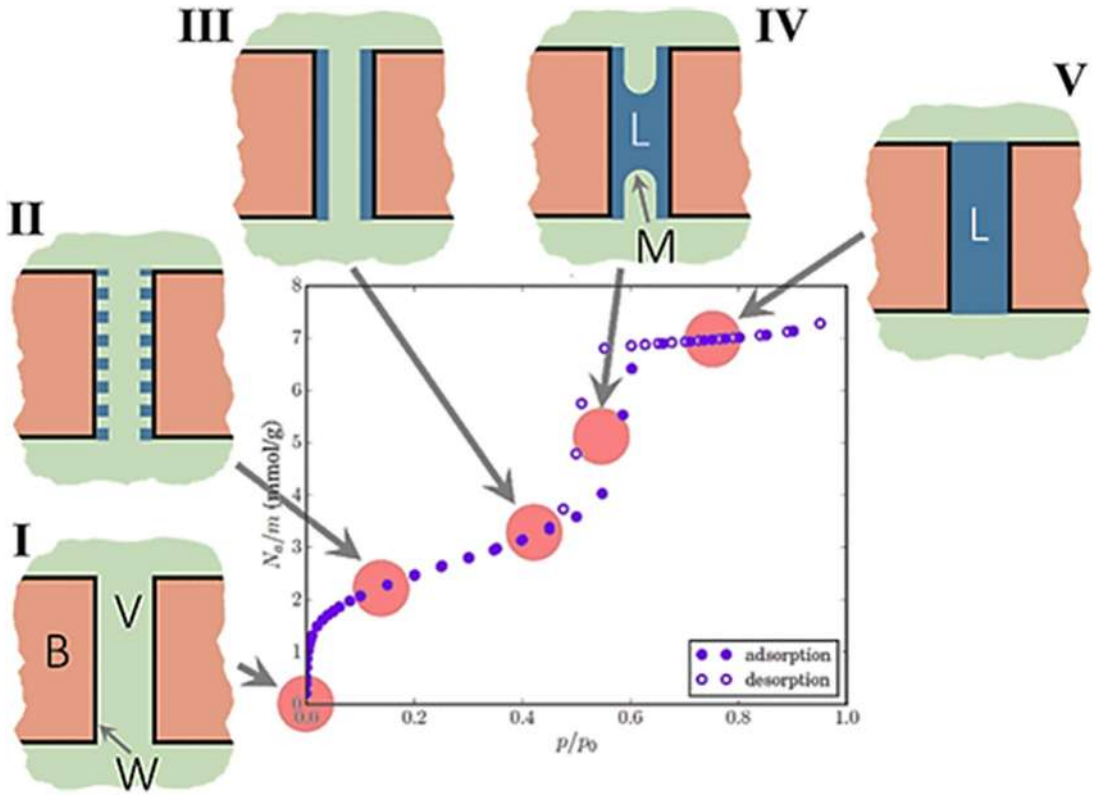

Figure 4.5
Schematic illustration of condensation and evaporation in a cylindrical capillary pore along with its corresponding adsorption/desorption isotherm. The letters represent the following: *B*, bulk; *W*, wall; *V*, vapor; *L*, liquid; and *M*, meniscus. The numbers represent the following: *I*, clean surface; *II*, partial monolayer adsorption; *III*, complete monolayer adsorption; *IV*, capillary condensation/evaporation; and *V*, saturation. Source: *Reproduced from [21].*

Combining both equations yields:

$$\left(\frac{P_a}{P_0}\right)^2 = \frac{P_d}{P_0} \tag{4.39}$$

This indicates that *the radius corresponding to* P_a *is twice that corresponding to* P_d (i.e., $P_a > P_d$) [1].

The relative pressure at which evaporation takes place is dependent on the pore size, the network connectivity, and the neighboring pores. If a pore is surrounded by other liquid-filled pores, then evaporation will not take place. Instead, it will begin first in pores that have access to the vapor phase. This phenomenon, in which a liquid is preserved below its condensation pressure until evaporation takes place in a neighboring pore, is known as the pore-blocking

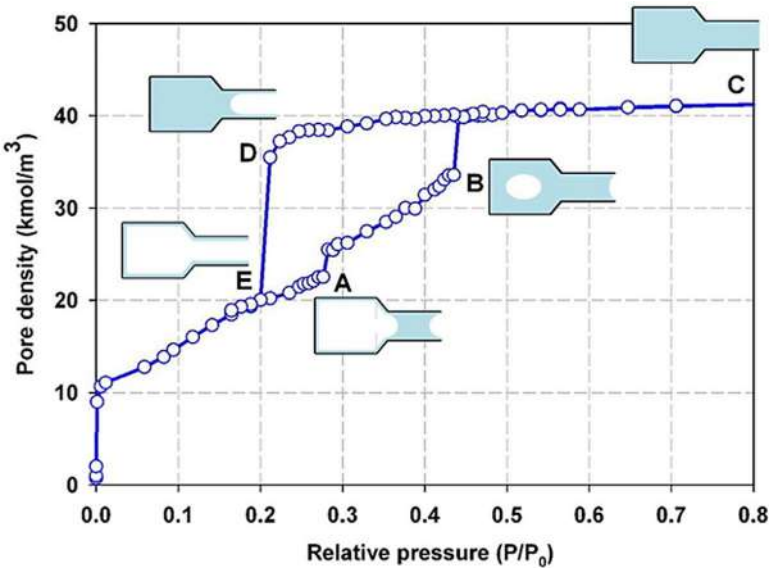

Figure 4.6

Schematic illustration of condensation and evaporation in an ink-bottle pore along with its corresponding adsorption/desorption isotherm. The letters represent the following: *A*, neck condensation; *B*, cavity condensation; *C*, saturation; *D*, neck evaporation; and *E*, cavity evaporation. The colors inside the pore represent the following: *White*, vapor; *Cyan*, liquid. Source*: Reproduced from [22].*

effect [20]. As an example, consider the filling and emptying of the *ink-bottle pore* as demonstrated in Fig. 4.6. Adsorption begins at low pressure, where a thin vapor layer adsorbs onto the walls of both the pore neck and the pore cavity. As pressure increases, the thickness of the adsorbed layer increases. Since the radius of the neck (r_n) is less than that of the cavity (r_c), the *critical condensation thickness in the neck is attained first*. Consequently, at this point, condensation occurs instantly at the pore neck (A in Fig. 4.6). Then, as pressure increases, vapor inside the pore cavity condenses (A to B in Fig. 4.6) [22]. The process of adsorption is, therefore, seen to be limited by the radius of the large inner cavity [20]. On the other hand, during desorption, the liquid evaporates starting at the vapor−liquid interface of the pore neck, with a meniscus receding from the pore mouth (C to D in Fig. 4.6). As the pressure decreases and the meniscus reaches the junction between the neck and the cavity (i.e., the liquid in the neck has evaporated), the liquid in the cavity evaporates instantly since the radius of the neck is constant and a sharp drop in the amount adsorbed is observed (D to E in Fig. 4.6) [22]. This demonstrates how the *desorption process is limited by the radius of the small pore neck* [20].

During adsorption in ink-bottle pores, the neck fills at relatively low pressure, but the cavity fills only when the pressure (from the Kelvin equation) is

$$P_a = P_0 \exp\left(\frac{-2\gamma V}{r_c RT}\right) \tag{4.40}$$

Similarly, and during desorption, the pore will not empty until the pressure is reduced to the point where the liquid in the neck is unstable or, in other words, when the pressure is

$$P_d = P_0 \exp\left(\frac{-2\gamma V}{r_n RT}\right) \tag{4.41}$$

Since the radius of the neck (r_n) is less than that of the cavity (r_c), then *a given volume will desorb at a pressure lower than that at which it was adsorbed* ($P_a > P_d$) [1].

Depending on the capillary shape of the adsorbent, and as classified by *IUPAC* in 1984 [23], one of four typical types of *hysteresis loops* may be observed in adsorption isotherms (Fig. 4.7). H1 and H2 hysteresis loops usually appear in Type IV isotherms, H3 in Type II, and H4 in Type I (adsorption isotherm types have been previously discussed in Section 3.1) [1]. In the H1 hysteresis loop the adsorption and desorption branches are almost vertical and nearly parallel. On the other hand, in the H4 hysteresis loop, the two branches are nearly horizontal and parallel.

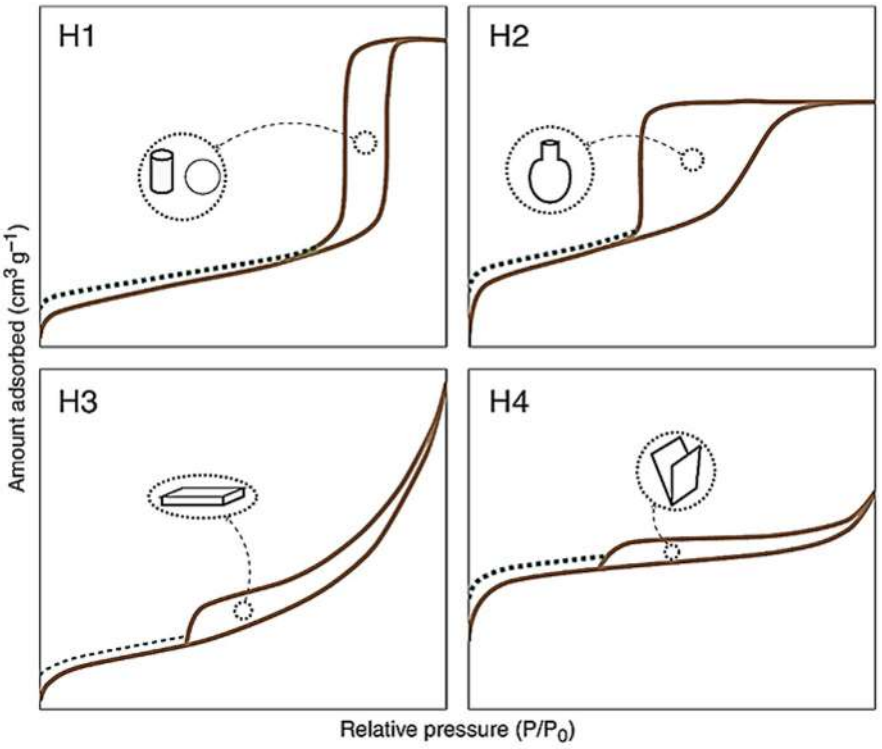

Figure 4.7
Types of hysteresis loops according to the International Union of Pure and Applied Chemistry (*IUPAC*). Source: *Reproduced from [4].*

Hysteresis loops of type H2 and H3 are considered to be intermediate cases between the two extremes, H1 and H4 [23]. Note how the steepness of the isotherm decreases from H1 to H4.

Porous adsorbents with well-defined cylindrical pores or agglomerates of identical spheres will usually exhibit the *H1 hysteresis loop*. Adsorbents with ink-bottle pores or disordered pores with ill-defined pore size distribution will probably give rise to the *H2 hysteresis loop*. The *H3 hysteresis loop* is common for adsorbents with slit-shaped pores that form as a result of the nonrigid agglomeration of plate-like particles. As can be inferred from Fig. 4.7, these adsorbents do not demonstrate any limiting adsorption at high relative pressure. Finally, the *H4 hysteresis loop* is generally seen in the case of adsorbents with narrow, slit-like pores [1,4]. More details on hysteresis loops will follow in Section 4.4.

The dashed lines in Fig. 4.7 show desorption paths above the adsorption path at low relative pressure. This type of behavior may be observed in some microporous materials if the nonrigid micropores of the adsorbent swell during adsorption, or if the adsorbate is irreversibly attached to the adsorbent, or, more in general, if the adsorbate chemically interacts with the adsorbent [4]. These dashed lines may also be observed as the result of certain experimental issues such as insufficient equilibration time for the desorption branch and insufficient extent of surface area measured.

Prior to the introduction of the IUPAC classification system, in the late 1950s, hysteresis loops had been categorized by the *de Boer system* [24] into the five groups reported in Fig. 4.8: Type A (presently H1), Type B (presently H3), Type C, Type D, or Type E (presently H2). However, given the limited topologies in porous structures known at that time, IUPAC has omitted some of these loop types when it developed the current official classification system. Nonetheless, and due to the recent advancements in the synthesis of porous solids with complex pore networks, lately many hysteresis loops depicted in the de Boer classification have been experimentally observed [25].

In *Type A* hysteresis loops, the adsorption and desorption paths are steep at intermediate relative pressures. In *Type B*, the isotherm shows a steep adsorption branch at a high relative pressure (c. 1) and a sloping desorption branch at intermediate relative pressures,

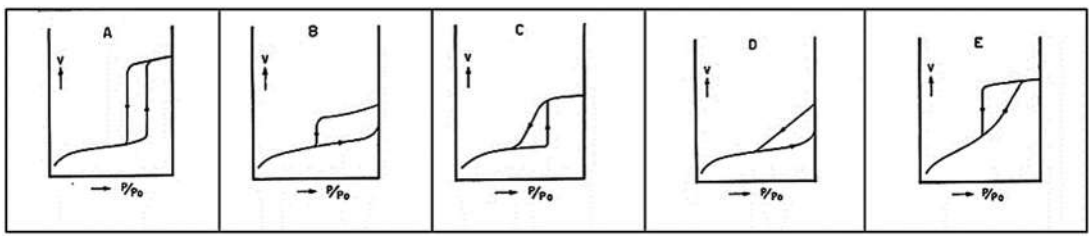

Figure 4.8
Five typical types of hysteresis loops according to de Boer. Source: *Reproduced from [24].*

while, in *Type C*, the adsorption path is steep and the desorption path is sloping, both at intermediate relative pressures. Isotherms with a *Type D* hysteresis loop, which are extremely rare, exhibit the same steep adsorption branch and the same sloping desorption branch as that of Type C, yet occurring at high relative pressures rather than intermediate ones. Finally, and in contrast to Type C, *Type E*, which is very common, has a sloping adsorption path and a steep desorption path, both at intermediate relative pressures [1].

When the dimensions of the cross sections of the different parts of the pores are all equal in size and are mainly of one shape, then *a steep and vertical adsorption/desorption branch* is observed in the hysteresis loop since the pressure at which adsorption/desorption takes place is the same for all the adsorbate volumes. On the other hand, when the cross sections are of various sizes and/or of different shapes, then a sloping adsorption/desorption branch is seen [1]. Since the process of adsorption in ink-bottle pores is limited by the radius of the large cavity, then the slope of the adsorption branch will depend on the dimension and uniformity of the cavity part of the pore. Similarly, the process of desorption in ink-bottle pores is limited by the radius of the small neck. Therefore the slope of the desorption branch will depend on the dimensions and uniformity of the neck.

Adsorbents consisting of tubular-shaped capillaries, with circular or noncircular cross sections that are open at both ends, typically exhibit a Type A hysteresis loop. This type of hysteresis loop is also characteristic of ink-bottle capillaries, but only those that possess a cavity radius that is less than twice the neck radius ($r_c < 2r_n$) [1]. Here, the entire pore will fill at a pressure corresponding to r_c and empty at a pressure corresponding to r_n. Eqs. (4.39) and (4.40) are applied and Eq. (4.39) is obeyed. On the other hand, if $r_c > 2r_n$, then the pore neck will fill at a pressure corresponding to $2r_n$ while the whole pore will fill at a pressure corresponding to r_c, resulting in the hysteresis loop shown in Fig. 4.6.

Adsorbents with slit-shaped pores will display a Type B hysteresis loop, while those composed of spherical pores with various-sized entrances generally result in a hysteresis loop of Type C. The Type C hysteresis loop is also representative of materials with ink-bottle pores that possess a heterogeneous distribution of neck radii. The hysteresis loop of Type D is common for heterogeneous capillaries with large bodies and narrow necks of various sizes. Finally, capillaries with cavities of various sizes but the same neck dimensions will yield an isotherm with a Type E hysteresis loop. Ink-bottle pores that possess a large cavity radius (more than twice the neck radius) have also shown this type of hysteresis loop [1].

In certain situations, there will be no delay in the formation of a meniscus upon adsorption and, hence, no hysteresis is observed for mesoporous adsorbents. In these cases, the adsorbent is usually composed of tubular-shaped capillaries that are closed at one end or of open-ended capillaries that are extremely narrow [1].

4.4 Pore models—morphology

Pore models can provide a qualitative geometric description of porous adsorbents, providing insights into the ease or difficulty with which chemical species diffuse through porous catalysts. In addition to that, pore models can also provide a quantitative mathematical description, which is useful for the prediction of whether or not the rate of the chemical reaction taking place within catalyst pores is influenced by diffusion effects [1].

The *average pore radius,* r_{avg}, for most geometric configurations of pore assemblies can be modeled as [1]:

$$r_{\text{avg}} = \frac{1}{F}\left(\frac{2V}{S}\right) \tag{4.42}$$

where V is the volume contained by pores and S is the surface area created by these same pores. The proportionality factor, F, is characteristic of a particular pore geometry. Hence, if the average pore radius of a material was to be measured experimentally (through the use of an electron microscope, for example), then F can be evaluated and the pore geometry deduced [1].

In 1951, *Wheeler* developed a *semiempirical pore model* for the average pores radius, r_{avg}, and pore length, L, of cylindrically shaped pores in terms of experimentally determinable parameters [26]. The model was able to successfully predict rates of industrial catalytic reactions. More specifically, Wheeler described the volume of pores, V, according to the following equation [1]:

$$V = nS_x\pi r_{\text{avg}}^2 L \tag{4.43}$$

where n is the number of pores per unit surface area, and S_x is the external surface area. Equating this pore volume to the experimental pore volume gives:

$$V_p\rho_g V_g = nS_x\pi r_{\text{avg}}^2 L \tag{4.44}$$

where V_p is the total volume of the catalyst particle, ρ_g is the density of the catalyst particle, and V_g is the specific pore volume. Wheeler also described the surface area of pores, S, in a similar manner, accounting for both the roughness and intersection of pores:

$$S = nS_x 2\pi r_{\text{avg}} L\tau(1-\psi) \tag{4.45}$$

where τ is a dimensionless factor indicative of the roughness of pore walls and $(1-\psi)$ represents the fraction of pore walls interrupted by intersections. Note that ψ, which is the porosity of the catalyst particle, is equivalent to the fraction of walls that are not intersecting. Equating Wheeler's pore surface area to the experimental pore surface area gives:

$$V_p\rho_g S_g = nS_x 2\pi r_{\text{avg}} L\tau(1-\psi) \tag{4.46}$$

where S_g is the BET specific surface area. Dividing Eq. (4.44) by Eq. (4.46) yields Wheeler's average pores radius, r_{avg}:

$$r_{avg} = \left(\frac{2V_g}{S_g}\right)\tau(1-\psi) \tag{4.47}$$

In a different pore model the porous adsorbent is presumed to behave like a number of fixed particles impeding the transport of diffusing molecules. This theory is well-known as the *dusty gas model* and it is one of the most basic models used to represent porous materials [1]. If the mean free path of the diffusing molecule is greater than the dimension of the free space, then transport in the narrow capillaries can be described by the *effective Knudsen diffusion coefficient, D_{eK}*:

$$D_{eK} = K_0 D_K \tag{4.48}$$

where K_0 is a parameter that represents the pore structure geometry and D_K is the Knudsen diffusion coefficient in a straight capillary. Further details on the specifics of the diffusion mechanism and the definition of the different diffusion parameters will be given in Section 4.5.

Conversely, if the mean free path of the diffusing molecule is less than the dimension of the free space, then transport in the intraparticle free space can be described by the *effective Maxwell diffusion coefficient, D_{eM}*:

$$D_{eM} = K_1 D_M \tag{4.49}$$

where K_1 is a parameter that represents the pore structure geometry and D_M is the Maxwell diffusion coefficient in a bulk gaseous mixture.

The dusty gas model, however, only accounts for small intraparticle pores and neglects large pores formed due to the voids among compressed particles. Accordingly, the *random pore model* was developed to describe materials consisting of both micropores and macropores, which is the case in many industrial pellet catalysts [1]. Here, the *effective diffusivity, D_e*, is given as:

$$D_e = \varepsilon_m{}^2 D_{avg,m} + \frac{\varepsilon_\mu(1+3\varepsilon_\mu)}{1-\varepsilon_\mu} D_{avg,\mu} \tag{4.50}$$

where ε is the voidage and D_{avg} is the average diffusion coefficient. The subscripts m and μ represent macro- and micropores, respectively. The average diffusion coefficients may be calculated from the following equations:

$$\frac{1}{D_{avg,m}} = \frac{1}{D_{M,m}} + \frac{1}{D_{K,m}} \tag{4.51}$$

$$\frac{1}{D_{\text{avg},\mu}} = \frac{1}{D_{M,\mu}} + \frac{1}{D_{K,\mu}} \tag{4.52}$$

All the above-mentioned idealistic pore models are used to describe *well-defined and uniform cylindrical and slit-shaped pores with both ends open* to the surrounding [25]. However, more complex geometric pore structures, such as capillaries with nonuniform cross sections, cannot be appropriately described by such simple models. Factors including the energetic variation along the pore axis, the connectivity between adjacent pores, and the presence of functional groups must be considered. In fact, the aforementioned factors are currently being accounted for in many of the newly developed pore models [25]. These newer models are being increasingly applied in molecular simulations, such as the Grand Canonical Monte Carlo (GCMC) for the characterization of complex pore geometries. Recent studies based on GCMC simulations of novel pore models have been able to highlight the effect of different pore configurations on the shape of adsorption/desorption isotherms [25,27].

One case study investigated the condensation and evaporation in adsorbents with connected pores of *different cross-sectional pore sizes* (Fig. 4.9). The isotherm of isolated and uniform pores would each represent an H1 hysteresis loop (Type A in the de Boer classification). However, as can be seen in Fig. 4.9, the shape of the hysteresis loop for the connected and nonuniform pores (Type C in de Boer classification) is characterized by a sharp adsorption step and a sloping desorption step [25].

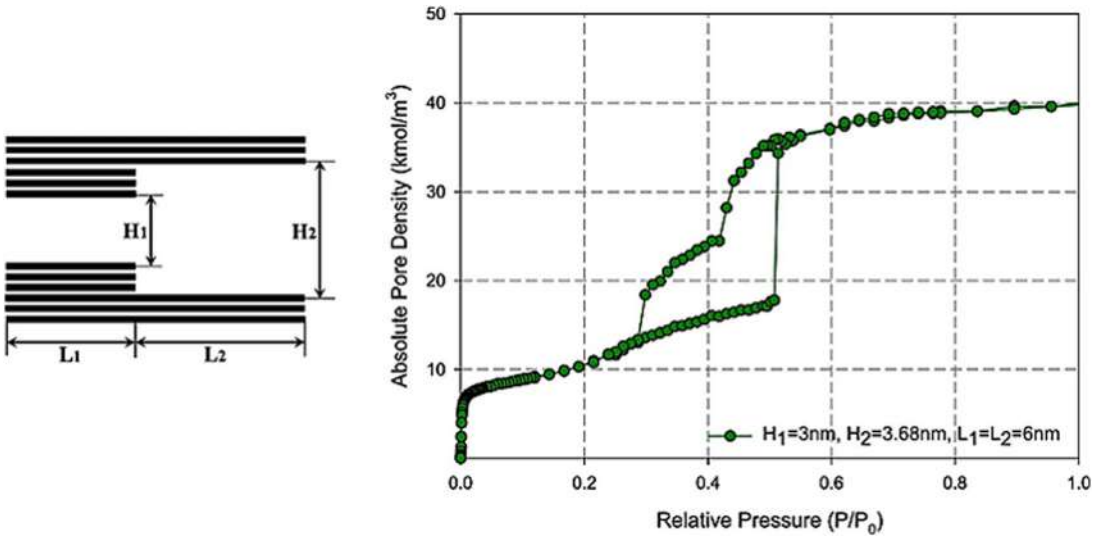

Figure 4.9
Adsorption isotherm of a solid adsorbent with cylindrical pores of nonuniform cross section. *H1* and *H2* represent the pore width, while *L1* and *L2* represent the pore length. Source: *Reproduced from [25].*

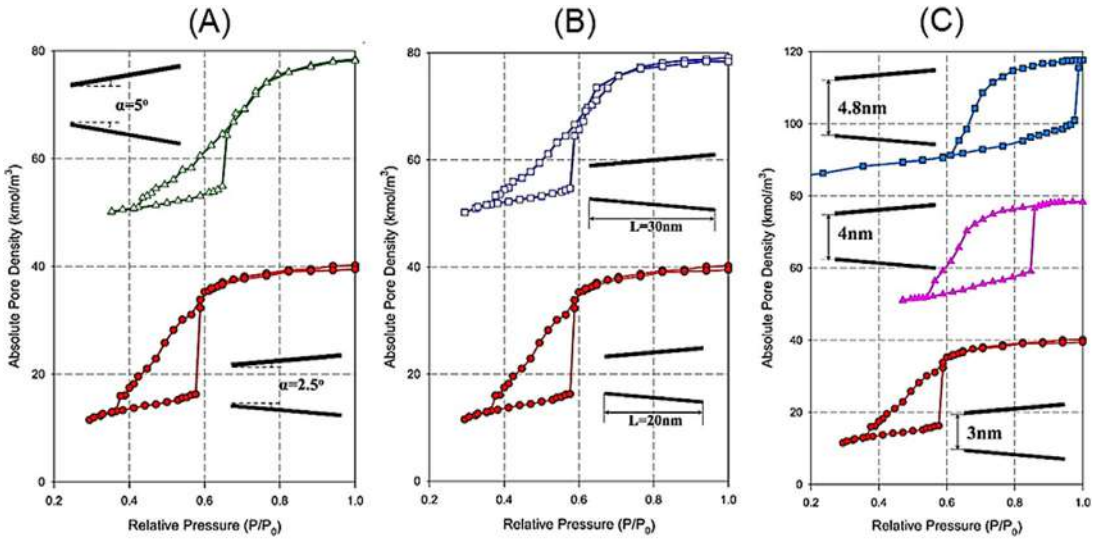

Figure 4.10
Adsorption isotherms of a solid adsorbent with wedge pores: effect of (A) wedge angle, α, (B) pore length, *L*, and (C) narrow-end width on the shape of the hysteresis loop. Source: *Reproduced from [25].*

In addition to nonuniform connected pores, the study also examined adsorbents with *wedge pores*, that is, pores with planar surfaces that are not parallel (Fig. 4.10). The isotherm of these materials also exhibited a Type C hysteresis loop. As shown in Fig. 4.10, the hysteresis shape varied depending on the wedge angle, the pore length, and the width of the narrow end [25,27]. When the wedge angle increases, the fraction of adsorption capacity associated with capillary condensation is reduced (the sharp adsorption step is smaller). This is because the fraction of pore space filled with adsorbate immediately after capillary condensation is smaller. As the pore width increases, solid−fluid interactions become progressively weaker. Moreover, the curvature of the meniscus formed after capillary condensation also decreases, leading to weaker fluid−fluid interactions at the interface. As a result of the aforementioned, the adsorbate fills a smaller fraction of the pore space. The same observation with similar reasoning is applied when the pore length is increased. For changes in the width of the narrow end from 3 to 4 nm, a shift from a Type C hysteresis loop to a mixture of Type C and H1 is demonstrated. At narrow-end widths equal to or greater than 4.8 nm, capillary condensation takes place only when saturation pressure is achieved, hence displaying a hysteresis loop of Type D. The condensation and evaporation pressure depend only on the width at the narrow end of the pore because that is where both processes are initiated.

Another pore model that was recently examined is that of pores formed from *convex and concave curved surfaces* (Fig. 4.11). As can be deduced from Fig. 4.11, pores with convex walls give rise to the Type C (De Boer) hysteresis loop, while those with concave walls yield a H1 hysteresis loop [27]. For pores with convex walls (Fig. 4.11 bottom right), an early onset of adsorption to

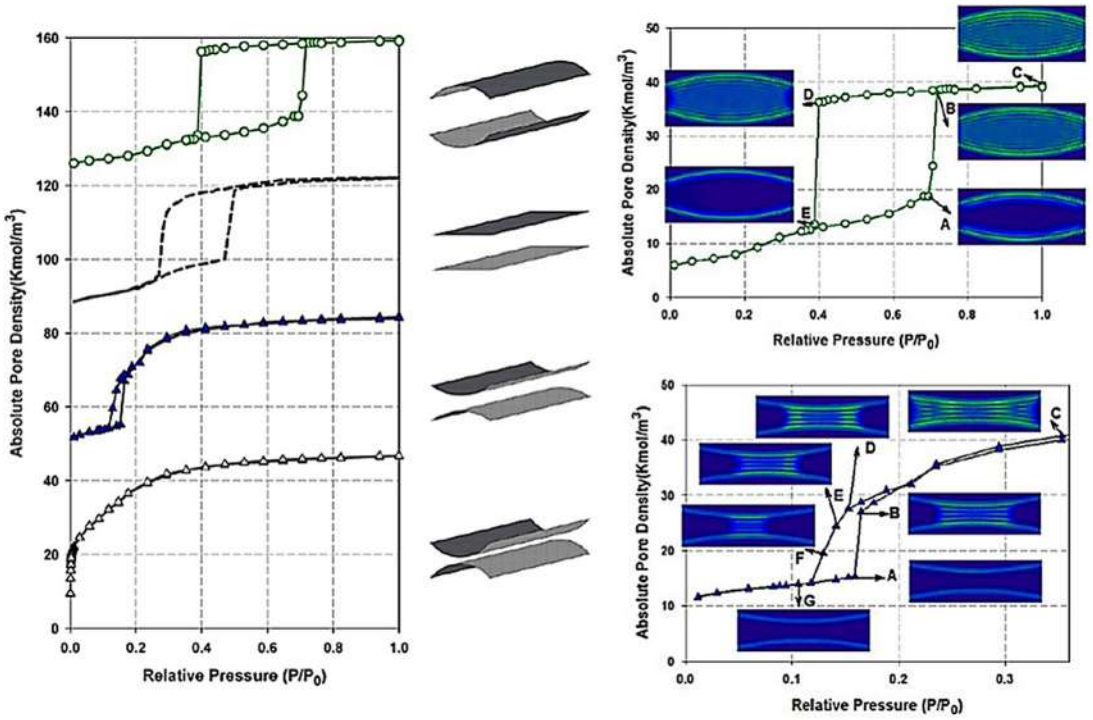

Figure 4.11

(Left) Adsorption isotherms of a solid adsorbent with curved pore walls. (Right) 2D density profiles of condensation and evaporation in a solid adsorbent with convex and concave curved pore walls. Source: *Reproduced from [25].*

form a liquid "bridge" where the walls are most closely separated (i.e., at the center) is triggered by the potential overlap of adsorbate from opposite walls of the adsorbent. The convexity of the walls will determine the thickness of the liquid bridge. In particular, pores with flatter walls will give rise to a thicker liquid bridge. The adsorption/desorption process is manifested in the 2D density plot of the convex wall on the right-hand side of Fig. 4.11. After the formation of a liquid bridge (A to B), adsorption proceeds via the advancement of the two menisci toward the pore mouth (B to C). On the other hand, desorption takes place by the withdrawal of the menisci from the pore mouth toward the pore center (C to F). Once the thickness of the liquid bridge reaches the critical value, capillary evaporation occurs (F to G). For concave walls (Fig. 4.11 top right), capillary condensation is induced by the formation of a thin liquid bridge at the two open ends of the pore at a pressure equal to that of the saturated vapor pressure. Once the liquid bridge forms, the pore will immediately be completely filled with adsorbate at this saturation pressure (A to B in the 2D density plot of the concave wall on the right-hand side of Fig. 4.11). During desorption, menisci are first formed at the pore ends and then they begin to withdraw toward the pore center as the relative pressure is reduced. When the menisci have reached deep enough into the pore, capillary evaporation takes place (D to E).

Note that all pore models considered in this section were open at both ends. The shape of the adsorption isotherm and the formation of the hysteresis loop will be different for models with pores closed at one end.

4.5 Mechanisms of diffusion within catalyst pores

In heterogeneous reactions limited by internal diffusion, the reaction rate per unit mass of catalyst will be highly dependent on the particle size and the average pore diameter. The *Knudsen diffusion* mechanism and the *Maxwell (molecular) diffusion* mechanism are two of the most common diffusion mechanisms used to describe the transport of gaseous molecules through the narrow channels of porous catalysts [1]. As has been stated in Section 4.4, if the *mean free path* of the diffusing molecule is greater than the *pore diameter*, then collisions of molecules with pore walls will be more frequent than collisions between gas molecules. In this case, transport in the narrow capillaries is described as Knudsen diffusion. Conversely, if the mean free path of the diffusing molecule is less than the pore diameter, then collisions between gas molecules will be more frequent than collisions of molecules with pore walls. In this case, transport in the intraparticle free space is described as Maxwell diffusion. *Surface diffusion* is another mechanism that can be used to describe transport within catalyst pores. Here, adsorbed gas molecules move across the catalyst surface in the direction of decreasing surface concentration. As a result of the reaction stoichiometry, the total number of moles in a solid catalyst can increase or decrease. This creates a difference in pressure between the exterior and the interior of the porous catalyst, forcing molecules to flow from areas where the concentration (or pressure) is high to areas where the concentration (or pressure) is low. This mechanism of forced transport within catalyst pores is known as *Poiseuille flow* and prevails only when the mean free path is small compared to the pore diameter. The Poiseuille diffusion coefficient, D_P, is defined as [1]:

$$D_P = \frac{r^2 \Delta P}{8\mu} \tag{4.53}$$

where r is the pore radius, ΔP is the total pressure difference, and μ is the viscosity. This mechanism, however, is highly unlikely in heterogeneous catalysis, especially at elevated reaction temperatures [1]. The different mechanisms of gas diffusion in porous media are schematically described in Fig. 4.12.

To account for pore geometry factors, specifically porosity and tortuosity, the term *effective diffusivity, D_e*, is introduced and is defined as [1]:

$$D_e = \frac{\psi}{\tau} D \tag{4.54}$$

where D is the diffusion coefficient (Maxwell or Knudsen), ψ is the *porosity* and τ is the *tortuosity*. Hence, the flux is now considered to be flowing through a homogenous medium

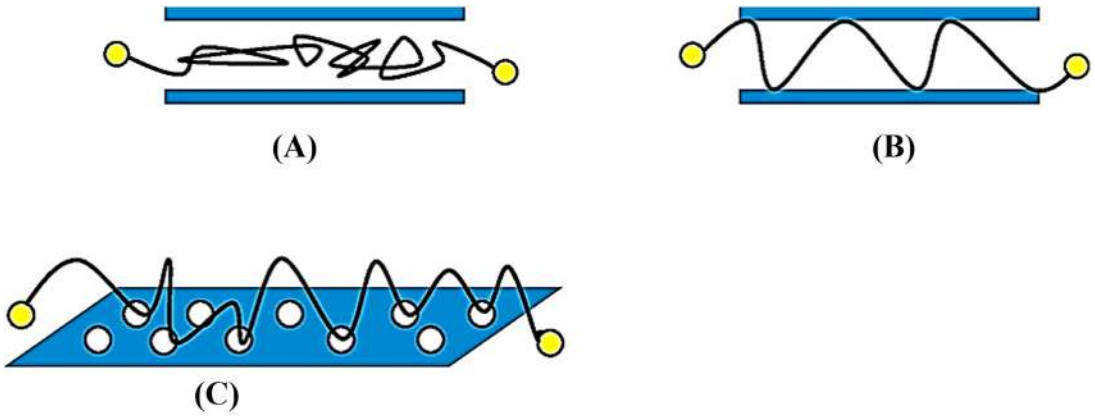

Figure 4.12
Schematic illustration of the different diffusion mechanisms in porous catalysts: (A) free molecular diffusion; (B) knudsen diffusion; (C) surface diffusion. Source: *Reproduced from [28].*

equivalent to the actual heterogeneous medium after correcting for the geometric factor. The effective diffusivity of a catalyst can be estimated experimentally using various techniques, some of which include permeability methods, diffusion methods, time-lag methods, sorption rate methods, and gas chromatography [29]. The porosity of the catalyst may be calculated using the following equation [1]:

$$\psi = 1 - \frac{\rho_{\text{apparent}}}{\rho_{\text{true}}} \tag{4.55}$$

where ρ_{true} is the true solid density (excluding voids), ρ_{apparent} is the apparent density (including voids), and the ratio $\rho_{\text{apparent}}/\rho_{\text{true}}$ is the fraction of solid present in the particles. The tortuosity is the ratio of the path length traveled by the diffusing particles between two points to the direct linear separation between those two points.

The *Maxwell diffusion coefficient,* D_M, is derived from a modified form of the kinetic theory of gases, where it takes into account attraction and repulsion forces between particles. The *Knudsen diffusion coefficient,* D_K, is also based on the kinetic theory of gases and may be defined as [1]:

$$D_K = \frac{2}{3} r \sqrt{\frac{8RT}{\pi M}} \tag{4.56}$$

where r is the radius of a circular capillary pore and M is the molecular mass of the diffusing gas. Eq. (4.56), however, is only applicable to porous solids with straight cylindrical capillaries. To account for different pore geometry configurations, the radius in Eq. (4.56) must be calculated using Eq. (4.42) or Eq. (4.47).

The Knudsen diffusion coefficient, D_K, may also be represented as [1]:

$$D_K = \frac{16}{3}\frac{\psi}{\rho_p S_g}\sqrt{\frac{RT}{\pi M}} \tag{4.57}$$

where ρ_p is the particle density (including voids) and S_g is the specific surface area.

Focus 4.4: Tortuosity of mesoporous alumina catalyst supports: influence of the pore network organization

The porosity of a solid catalyst may be easily evaluated using classical porosimetry techniques. The determination of the tortuosity, however, is not as simple. Here, the effective diffusivity must first be measured experimentally, and then the tortuosity is calculated using Eq. (4.54). The *diffusion coefficient* may be estimated from the kinetic theory of gases (see Eqs. 4.56 and 4.57 for instance) or from any of the other widely available diffusion coefficient correlations.

Typically, the experimental tortuosity values very much agree with any of the widely available theoretical correlations. In the case of mesoporous alumina supports, however, the experimental values were higher and varied much more with porosity [30]. This was attributed to the hierarchized organization present inside the alumina support. Alumina supports are usually obtained by the precipitation of aluminum salts in an aqueous solution (see Section 3.4.1 for more details on the preparation of catalyst supports). As can be seen in Fig. 4.13A, alumina nanocrystals are first stacked into aggregates (interaggregate porosity) that are then later gathered together to form the final alumina support (interaggregate porosity). The particle size, the average pore diameter, the total pore volume, and the surface area of the final support increase with temperature. Thus catalyst supports are often subjected to a thermal treatment at elevated temperatures (525°C–975°C) with the aim of optimizing these properties.

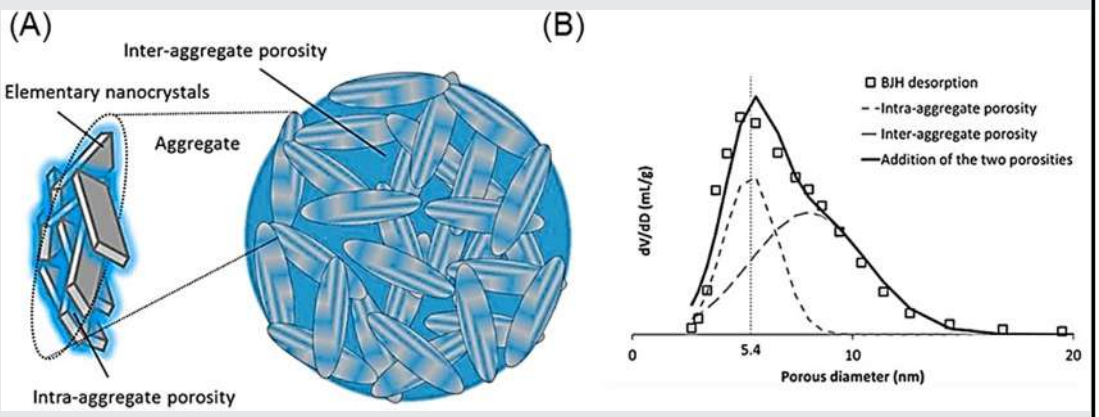

Figure 4.13
(A) Schematic representation of the two porosity levels: intra-aggregate porosity and interaggregate porosity. (B) Deconvolution of the Barrett–Joyner–Halenda (*BJH*) pore size distribution. Source: *Reproduced from [30].*

(*Continued*)

Focus 4.4: Tortuosity of mesoporous alumina catalyst supports: influence of the pore network organization (Continued)

It is important to note that the mass transfer across such porous networks is only limited by the fraction of pores that are interaggregated. To determine the porous volume associated with the interaggregate porosity (V_{inter}), the BJH pore size distribution is deconvoluted as illustrated in Fig. 4.13B. Then, using the following equation, the interaggregate tortuosity τ_{inter} is calculated:

$$\tau_{inter} = V_{inter}\tau$$

On the basis of the aforementioned, one can conclude that in order to maximize mass transfer in alumina supports, the *volume between the aggregates must be maximized*. To achieve that, synthesis conditions must be adapted to minimize nanocrystal aggregation. One very popular example is the use of organic surfactants during wet-preparation techniques. The presence of these organic moieties in the reaction mixture ensures minimal nanocrystal aggregation and allows for control over catalyst porosity [31]. The addition of polymeric stabilizers has also been shown to efficiently prevent the aggregation of nanoparticles [32]. In a more simplified approach, it has been suggested that highly dispersible nanocrystals can be obtained by wet-preparation techniques without the use of surfactants or stabilizers by simply carrying out the synthesis at elevated temperatures and without any mechanical mixing/stirring [33].

Focus 4.5: Numerical example on calculating the effective diffusivity within catalyst pores

Oxygen gas diffuses through the pores of a catalyst at 0.1 atm and 20°C. The average pore diameter of the catalyst is 0.1 μm, the porosity is 35%, and the tortuosity is 3.4. Estimate the effectivity diffusivity of oxygen, given that the diffusion inside the pores occurs mainly via the Knudsen diffusion mechanism.

Solution

First, the Knudsen diffusivity is calculated by application of Eq. (4.56):

$$D_K = \frac{2}{3} r \sqrt{\frac{8RT}{\pi M}} = \frac{2}{3} \times 5 \times 10^{-8} \times \sqrt{\frac{8 \times 8314 \times 293}{\pi \times 32}} = 1.5 \times 10^{-5}\ \mathrm{m^2 s^{-1}}$$

Then, using Eq. (4.54), the effective diffusivity is estimated:

$$D_e = \frac{\psi}{\tau} D = \frac{0.35}{3.4} \times 1.5 \times 10^{-5} = 1.5 \times 10^{-6}\ \mathrm{m^2 s^{-1}}$$

Although the *Knudsen formulation* (Eq. 4.56) has been widely used for years to describe the transport of fluids in microporous materials, it *does not account for the effect of fluid–solid intermolecular interactions*. This might not be a problem in catalysts with wide pores; however, it has been shown to overestimate the low-density diffusivity (i.e., the diffusivity of low-density fluids) in pores with sizes of a few nanometers. As a result, Bhatia et al. [34] developed the oscillator model as an alternative for the *prediction of diffusivity in the*

low-density limit. The oscillator model is based on statistical–mechanical principles and it accounts for adsorption forces from pore walls. Calculation of the low-density diffusivity through the oscillator model is extremely tedious and, therefore, is not as widespread as the Knudsen formulation. To overcome this challenge, Bonilla and Bhatia [35] developed a simple correlation whereby the low-density diffusivity of Lennard–Jones fluids is expressed as a function of only two parameters: a size-related parameter and an energy-related parameter. It has been proven that, as long as the fluid–fluid interactions are negligible (low-density limit), the motion of particles is oscillatory in the fluid–solid potential coordinate. The *low-density diffusivity,* D_0, may therefore be expressed as:

$$D_0 = \frac{k_B T}{m}\tau \tag{4.58}$$

where k_B is the Boltzmann constant, T is the temperature, m is the particle mass, and τ is the mean oscillation period. The mean oscillation period can be determined by solving the Newtonian equations of motion for a single particle moving in the adsorbent potential field and averaging over the canonical distribution. Dispersion forces tend to lower the oscillation period and, consequently, the axial molecular motion slows down. If such adsorption effects are to be ignored, then the low-density diffusivity will be overpredicted. Hence, the Knudsen formulation (Eq. 4.56) may only be applied to sufficiently large pores where adsorption effects are negligible.

If the diffusion mechanism cannot be shown to be predominantly described by either the Maxwell or the Knudsen mechanisms, then the *effective diffusivity,* D_e, may be expressed as [1]:

$$D_e = \frac{1}{\frac{1}{D_{eM}} + \frac{1}{D_{eK}} - \frac{x_A\left(1+\frac{N_B}{N_A}\right)}{D_{eM}}} \tag{4.59}$$

where D_{eM} and D_{eK} are the effective Maxwell and Knudsen diffusivities, respectively, N_A and N_B are the molar fluxes of the fluid components A and B, and x_A is the mole fraction of A. Eq. (4.59) describes the flow of a binary mixture but can be extended to include multicomponent mixtures.

More recently, detailed modeling methodologies that are based on the actual structure of the porous material (particle and pore size distributions) are being used for the prediction of effective diffusivity [36]. The effective diffusivity previously described in Eqs. (4.54) and (4.59) is calculated from random pore model correlations, which sometimes assume uniform thickness and transport properties across the porous catalyst. This leads to inaccurate predictions of the effective diffusivity and, consequently, to misleading estimates of diffusion limitations. A modeling approach suggested by Novák and coworkers [36–40] utilizes a *3D digital reconstruction of the porous catalyst* based on information extracted from cross-sectional SEM images and particle size distribution data. The effective diffusivity through the reconstructed porous medium is then calculated from the mass fluxes

acquired by the simulation of the system with an imposed concentration gradient. The boundary concentrations of the diffusing gas component i at z_0 and z_1 are set as follows:

$$Y_i \Big|_{z=z_0} = Y_i^{\text{bnd},z_0} \tag{4.60}$$

$$Y_i \Big|_{z=z_1} = Y_i^{\text{bnd},z_1} \tag{4.61}$$

where Y_i^{bnd} is the boundary molar fraction of i. The difference between $Y_i^{\text{bnd},z1}$ and $Y_i^{\text{bnd},z0}$ is the driving force for diffusion in the z direction. The effective diffusivity, D_e, of component i is calculated as per the following equation:

$$D_e = \frac{-J_i(z_1 - z_0)}{A_z c\left(Y_i^{\text{bnd},z_1} - Y_i^{\text{bnd},z_0}\right)} \tag{4.62}$$

where c is the gas concentration and J_i is the overall molar flux through the medium. J_i may be obtained by integrating the fluxes across the cross-sectional area, A_z, perpendicular to the z direction:

$$J_i = \int -D_i \frac{\partial c_i}{\partial z} dxdy \tag{4.63}$$

The diffusion coefficient D may be described by the below fundamental equations:

$$\frac{1}{D} = \frac{1}{\varphi}\left(\frac{1}{\frac{1}{D_M} + \frac{1}{D_K}}\right) \tag{4.64}$$

where

$$\varphi = 1 \quad \text{in the macropore space} \tag{4.65}$$

$$\varphi = \frac{\psi}{\tau} \quad \text{in the mesopore space} \tag{4.66}$$

$$D_M = \frac{1.449 \times 10^{-2} T^{1.75}/P}{\sqrt{2/\left(\frac{10^{-3}}{M_i} + \frac{10^{-3}}{M_{\text{ref}}}\right)}\left(\sigma_i^{1/3} + \sigma_{\text{ref}}^{1/3}\right)^2} \tag{4.67}$$

$$D_K = \frac{d}{3}\sqrt{\frac{8RT}{\pi M_i}} \tag{4.68}$$

where σ_i is the diffusion volume of component i, σ_{ref} is the diffusion volume of a reference gas (typically nitrogen) and d is the mean micropore or mesopore diameter (evaluated from porosimetry). Using the above-mentioned model, the effective diffusivity is obtained directly from the simulations depending only on the known morphology of the porous structure without the use of any adjustable parameters.

Focus 4.6: Diffusion-enhanced hierarchically structured macro-mesoporous catalysts

Fig. 4.14 below illustrates the spontaneous *self-assembly formation of hierarchically structured macro/mesoporous catalysts* [41]. A droplet of aluminum alkoxide precursor, such as threo-beta-benzyloxyaspartate, is first introduced into an aqueous solution (Fig. 4.14A), where a thin and semipermeable shell is simultaneously formed at the droplet's outer surface (Fig. 4.14B). Hydrolysis and condensation reactions then result in the micro-phase separated regions, generating macroporous channels (Fig. 4.14C). If no surfactant is added, the self-assembly and aggregation of aluminum oxide particles produce the mesopores (Fig. 4.14D). If, on the other hand, a surfactant, such as cetrimonium bromide, is added, then the surfactant molecules will adsorb onto the surface of the aluminum oxide particles, forming a bilayer structure (Fig. 4.14E). This, in turn, will widen the size distribution of the mesopores in the synthesized catalyst.

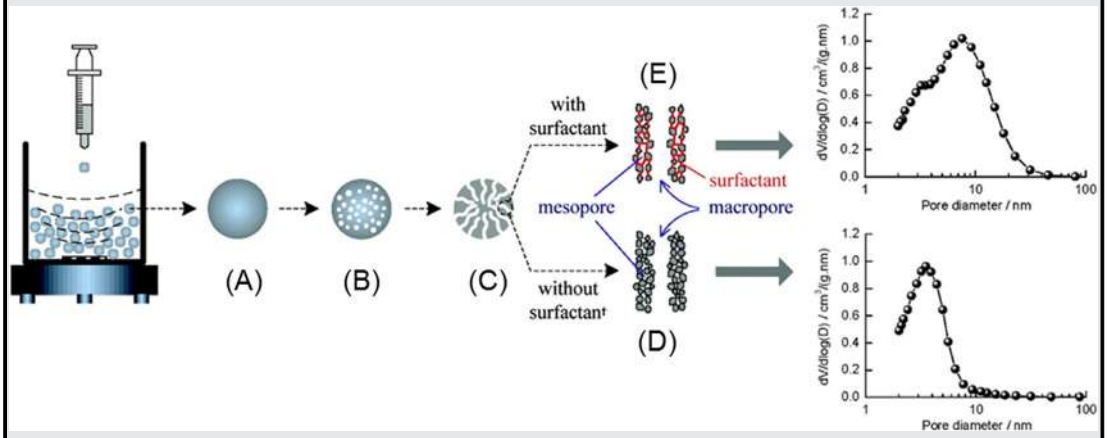

Figure 4.14
Schematic representation of the synthesis mechanism for the preparation of hierarchically macro/mesoporous aluminum oxide catalyst. Source: *Reproduced from [41].*

Hierarchically structured macro-mesoporous catalysts have been shown to lower the internal diffusion limitations of reacting species [42]. The diffusion-enhanced effect of the hierarchically structured macro-mesoporous catalyst has been attributed to two main aspects:

1. Due to the macroporous channels, the diffusion resistance of reactants from the outer catalyst surface to the inner surface has been significantly lowered. This is because, in catalysts with macroporous structures, intraparticle transport can greatly enhance the effective diffusivity.
2. The narrow walls separating the macropores reduce the diffusion path of reactants to the active sites. This, in turn, lowers the concentration gradient of the species, leading to an increase in the reaction rate.

This phenomenon is of great significance in industrial catalytic processes where unstable reacting species can form poisonous intermediate products, that is, species that can adsorb onto active sites and lead to catalyst deactivation. Both the macroporous channels

(*Continued*)

Focus 4.6: Diffusion-enhanced hierarchically structured macro-mesoporous catalysts (Continued)

and the narrow walls of hierarchically structured macro-mesoporous catalysts reduce the residence time of the intermediate products inside the catalyst. Hence, the overall catalytic performance is considerably improved.

4.6 Questions and problems

1. Explain why in some cases the adsorption and desorption branches of an isotherm do not overlap at intermediate partial pressures of the adsorbate.
2. What conclusions can you drive if the adsorption and desorption branches of an isotherm do not overlap at partial pressures of c. 0 and/or 1?
3. Comment on the below isotherms and pore size distributions. (a) refers to pure Al_2O_3, whereas (b)–(d) refer to magnetic Fe_2O_3–Al_2O_3 prepared in different atmospheres. Explain how you think that the materials differ in terms of porosity, pore size distribution, and surface area (image reproduced from [43]).

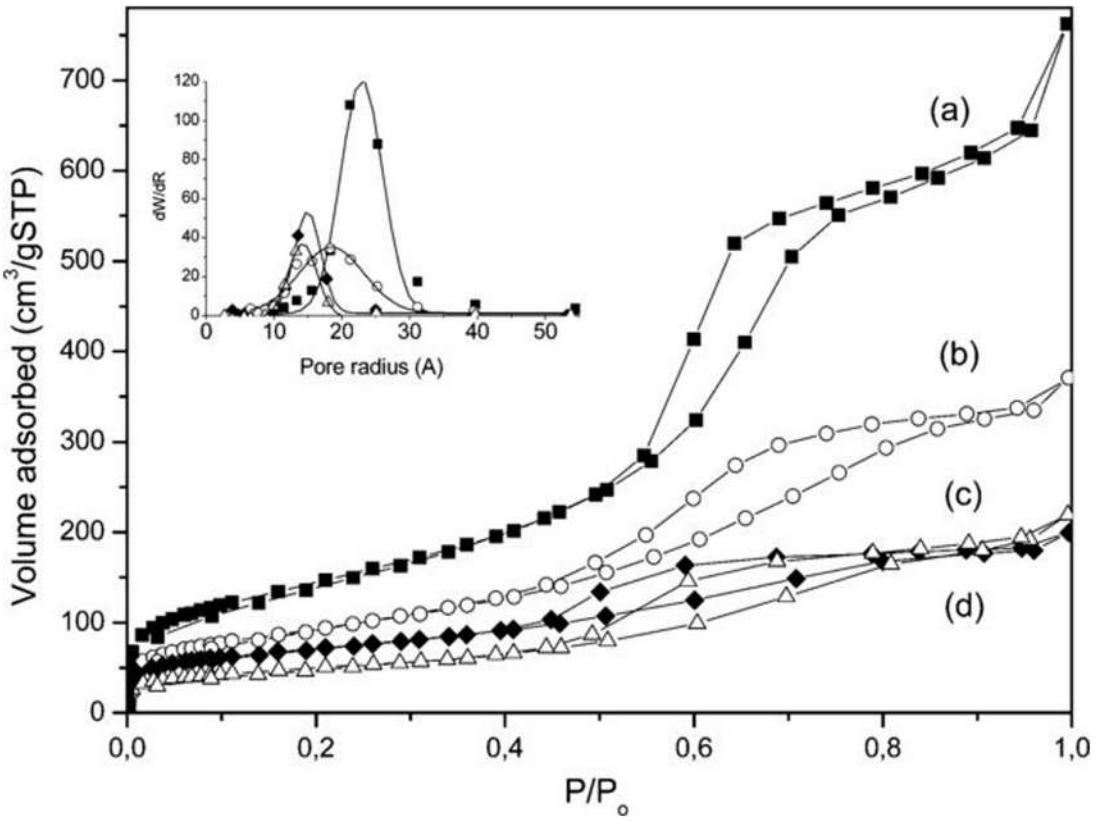

4. Comment on the adsorption−desorption isotherms presented below. How do the hysteresis type, the pore shape, and the pore size differ for each of the three porous samples S#1, S#2, and S#3? (images reproduced from [44]).

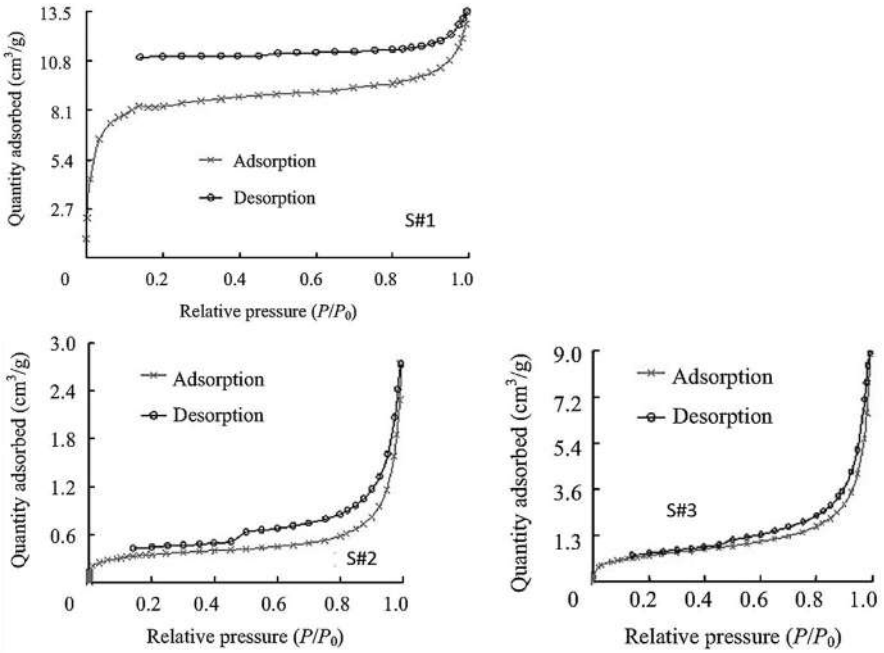

5. The specific surface area of a titanium dioxide catalyst sample (85 mg) was determined using nitrogen adsorption experiments performed at 77K ($P_0 = 779$ mmHg). From the data in the table below, calculate the specific surface area of titanium dioxide by using: (1) the point "B" method, (2) the Langmuir method, and (3) the BET method. Is there a difference between the values obtained? If yes, comment on the reasons. Among the results obtained from the three different methods, which specific surface area value would you consider to be the most accurate? Why?

Pressure (mmHg)	Volume @ STP (cm^3)	Pressure (mmHg)	Volume @ STP (cm^3)
11.0293	0.0680	191.3136	0.1142
30.0138	0.0761	206.2590	0.1183
50.4251	0.0820	227.1905	0.1231
76.6030	0.0883	251.5452	0.1281
97.1647	0.0930	272.0687	0.1330
120.7677	0.0984	280.6843	0.1352
142.1284	0.1032	295.8703	0.1385
163.0655	0.1080	326.4044	0.1463
182.6341	0.1126	339.2787	0.1489

6. Carry out a literature review to find two examples of catalysts exhibiting an H3 hysteresis and describe the reported isotherms by correlating their trend to the morphology of the material.
7. The pore size distribution of a porous activated carbon catalyst was investigated via mercury porosimetry. Using the raw data presented in the table below, plot a cumulative pore-volume curve as a function of pore radius. Then, plot a differential pore size distribution curve. Finally, estimate the mean pore radius. Assume a contact angle of 120 degrees and a surface tension of 0.485 N m^{-1}.

Pressure (bar)	Volume (cm^3 g^{-1})	Pressure (bar)	Volume (cm^3 g^{-1})
21.91	0.022	262.46	0.343
34.09	0.038	337.05	0.582
46.56	0.057	465.87	0.851
59.13	0.080	604.36	0.895
77.39	0.115	756.19	0.904
102.06	0.160	946.42	0.908
127.77	0.202	1241.51	0.911
159.68	0.246	1758.36	0.913
206.46	0.295	3061.58	0.921
245.38	0.329		

8. For the adsorption−desorption isotherm presented below, comment on the hysteresis type and the possible pore geometry. The data for the porous catalyst sample were obtained using argon gas at −195°C.

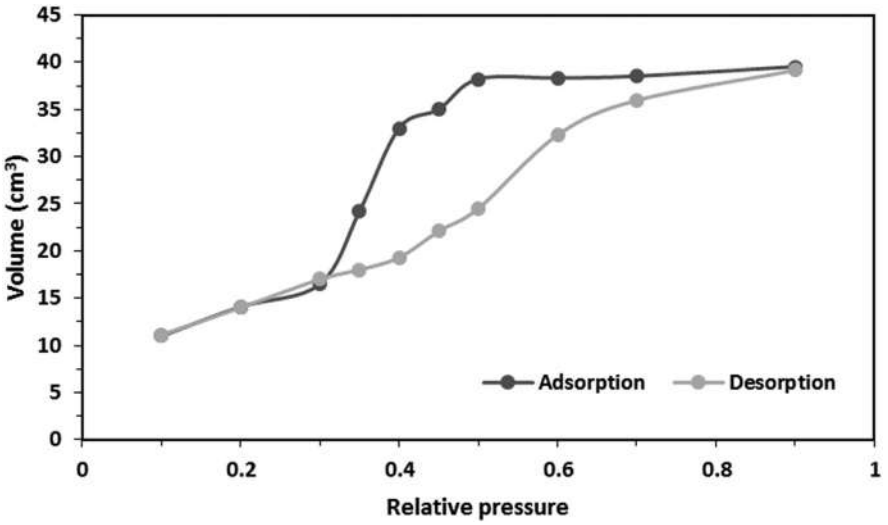

9. Classify the methods to estimate pore size distribution and porosity (Section 4.2) into three categories. Discuss the different types of the used approaches and their potential benefits and drawbacks.
10. What is the difference between Maxwell and Knudsen diffusivities? How are they correlated to the effective diffusivity? And which are the approaches to estimate the three of them?
11. How can the pore's tortuosity affect the diffusivity coefficients? Report the methods to correlate diffusivity to tortuosity and discuss the relevant equations.
12. Consider a porous silica-alumina catalyst with a BET surface area of 130 $m^2\ g^{-1}$, a pellet density of 1.70 g cm^{-3}, and a solid density of 2.16 g cm^{-3}. At room temperature (20°C) and atmospheric pressure, what would the effective Knudsen diffusivity of hydrogen across the catalyst be? What is the pore radius of the catalyst? Assume a tortuosity factor of 2.
13. Using mercury porosimetry, the particle density of two different catalysts, X and Y, were determined to be 1.217 and 1.053 g cm^{-3}, respectively. For both catalysts, the true density of the solid material is 2.46 g cm^{-3}. The surface area of catalyst X is 476 $m^2\ g^{-1}$ and that of catalyst Y is 381 $m^2\ g^{-1}$. Which catalyst has a larger mean pore radius?
14. Given the information below, calculate the specific pore volume, the porosity, and the mean pore radius of activated alumina.
    True solid density: 3.766 g cm^{-3}
    Particle density: 1.638 g cm^{-3}
    Surface area: 184 $m^2\ g^{-1}$
15. For the determination of the surface area, 40 g of Al_2O_3 underwent nitrogen adsorption experiments at 77K. The resulting data are presented in the table below. The Al_2O_3 catalyst has a particle density of 1.34 g cm^{-3} and a solid density of 3.16 g cm^{-3}. Calculate the surface area, the mean pore radius, and the porosity of the catalyst. Note that the saturation pressure of nitrogen at 77K is 734 mmHg.

Pressure (atm)	0.1	0.2	0.3	0.4	0.45
Volume (cm^3) STP	63	87	104	125	138

References

[1] J.M. Thomas, W.J. Thomas, Principles and Practice of Heterogeneous Catalysis, John Wiley & Sons, 2014.
[2] D.L. Minnick, T. Turnaoglu, M.A. Rocha, M.B. Shiflett, Gas and vapor sorption measurements using electronic beam balances, J. Vac. Sci. Technol. A: Vacuum, Surfaces, Films 36 (2018) 050801.
[3] M. Kudasik, N. Skoczylas, A. Pajdak, The repeatability of sorption processes occurring in the coal-methane system during multiple measurement series, Energies 10 (2017) 661.
[4] R. Bardestani, G.S. Patience, S. Kaliaguine, Experimental methods in chemical engineering: specific surface area and pore size distribution measurements—BET, BJH, and DFT, Can. J. Chem. Eng. 97 (2019) 2781–2791.

[5] B.C. Lippens, J. De Boer, Studies on pore systems in catalysts: V. The t method, J. Catal. 4 (1965) 319–323.
[6] E. Pidko, E. Hensen, Adsorption methods for characterization of porous materials, Catalysis: From Principles to Applications, Wiley-VCH Verlag, 2012, pp. 514–535.
[7] B. Lippens, B. Linsen, J. De Boer, Studies on pore systems in catalysts I. The adsorption of nitrogen; apparatus and calculation, J. Catal. 3 (1964) 32–37.
[8] S. Mintova, J. Čejka, Chapter 9—Micro/mesoporous composites, Introductionto Zeolite Molecular Sieves. In: J. Čejka, H. van Bekkum, A. Corma, F. Schüth (Eds.), Stud. Surf. Sci. Catal., 168, Elsevier, 2007, pp. 301–326.
[9] R.S. Mikhail, S. Brunauer, E. Bodor, Investigations of a complete pore structure analysis: I. Analysis of micropores, J. Colloid Interface Sci. 26 (1968) 45–53.
[10] K. Sing, Empirical method for analysis of adsorption isotherms, Chem. Ind. 44 (1968) 1520–1521.
[11] J. Villarroel-Rocha, D. Barrera, A.A. G. Blanco, M.E. R. Jalil, K. Sapag, Importance of the αs-plot method in the characterization of nanoporous materials, Adsorpt. Sci. Technol. 31 (2013) 165–183.
[12] M. Dubinin, L. Radushkevich, Three-dimensional filling of micropores, Proc. Acad. Sci. USSR Phys. Chem. Sect 55 (1947) 331–340.
[13] M.M. Dubinin, V.A. Astakhov, Description of adsorption equilibria of vapors on zeolites over wide ranges of temperature and pressure, ed, Molecular Sieve Zeolites-II, 102, American Chemical Society, 1971, pp. 69–85.
[14] G. Horváth, K. Kawazoe, Method for the calculation of effective pore size distribution in molecular sieve carbon, J. Chem. Eng. Jpn. 16 (1983) 470–475.
[15] R.J. Dombrowski, C.M. Lastoskie, D.R. Hyduke, The Horvath–Kawazoe method revisited, Colloids Surf. A: Physicochem. Eng. Asp. 187 (2001) 23–39.
[16] A. Saito, H. Foley, Curvature and parametric sensitivity in models for adsorption in micropores, AIChE J. 37 (1991) 429–436.
[17] M.L. Ojeda, J.M. Esparza, A. Campero, S. Cordero, I. Kornhauser, F. Rojas, On comparing BJH and NLDFT pore-size distributions determined from N2 sorption on SBA-15 substrata, Phys. Chem. Chem. Phys. 5 (2003) 1859–1866.
[18] D. Dollimore, G. Heal, An improved method for the calculation of pore size distribution from adsorption data, J. Appl. Chem. 14 (1964) 109–114.
[19] S. Lowell, J.E. Shields, M.A. Thomas, M. Thommes, Mesopore analysis, Characterization of Porous Solids and Powders: Surface Area, Pore Size and Density, ed, Springer, 2004, pp. 101–128.
[20] H.-J. Butt, K. Graf, M. Kappl, Physics and Chemistry of Interfaces, John Wiley & Sons, 2013.
[21] G.Y. Gor, P. Huber, J. Weissmüller, Elastocapillarity in nanopores: sorption strain from the actions of surface tension and surface stress, Phys. Rev. Mater. 2 (2018) 086002.
[22] P.T. Nguyen, C. Fan, D. Do, D. Nicholson, On the cavitation-like pore blocking in ink-bottle pore: evolution of hysteresis loop with neck size, J. Phys. Chem. C. 117 (2013) 5475–5484.
[23] K.S. Sing, Reporting physisorption data for gas/solid systems with special reference to the determination of surface area and porosity (Recommendations 1984), Pure Appl. Chem. 57 (1985) 603–619.
[24] J. De Boer, The Structure and Properties of Porous Materials, 389, *Butterworths*, *London*, 1958, pp. 68–94.
[25] C. Fan, V. Nguyen, Y. Zeng, P. Phadungbut, T. Horikawa, D. Do, et al., Novel approach to the characterization of the pore structure and surface chemistry of porous carbon with Ar, N_2, H_2O and CH_3OH adsorption, Microporous Mesoporous Mater. 209 (2015) 79–89.
[26] A. Wheeler, Reaction rates and selectivity in catalyst pores, ed, Advances in Catalysis, 3, Elsevier, 1951, pp. 249–327.
[27] C. Fan, D. Do, D. Nicholson, Condensation and evaporation in capillaries with nonuniform cross sections, Ind. Eng. Chem. Res. 52 (2013) 14304–14314.
[28] M. Chen, Y. Kang, T. Zhang, L. You, X. Li, Z. Chen, et al., Methane diffusion in shales with multiple pore sizes at supercritical conditions, Chem. Eng. J. 334 (2018) 1455–1465.

[29] H.W. Haynes Jr, The experimental evaluation of catalyst effective diffusivity, Catal. Rev. Sci. Eng. 30 (1988) 563–627.
[30] S. Kolitcheff, E. Jolimaitre, A. Hugon, J. Verstraete, P.-L. Carrette, M. Tayakout-Fayolle, Tortuosity of mesoporous alumina catalyst supports: Influence of the pore network organization, Microporous Mesoporous Mater. 248 (2017) 91–98.
[31] Y. Yin, A.P. Alivisatos, Colloidal nanocrystal synthesis and the organic–inorganic interface, Nature 437 (2005) 664–670.
[32] I. Lázár, H.J. Szabó, Prevention of the aggregation of nanoparticles during the synthesis of nanogold-containing silica aerogels, Gels (Basel, Switz.) 4 (2018) 55.
[33] D. Li, R.B. Kaner, Shape and aggregation control of nanoparticles: not shaken, not stirred, J. Am. Chem. Soc. 128 (2006) 968–975.
[34] S.K. Bhatia, O. Jepps, D. Nicholson, Tractable molecular theory of transport of Lennard-Jones fluids in nanopores, J. Chem. Phys. 120 (2004) 4472–4485.
[35] M.R. Bonilla, S.K. Bhatia, The low-density diffusion coefficient of soft-sphere fluids in nanopores: accurate correlations from exact theory and criteria for applicability of the Knudsen model, J. Membr. Sci. 382 (2011) 339–349.
[36] M. Dudák, V. Novák, P. Kočí, M. Marek, P. Blanco-García, G. Jones, Prediction of diffusivity and conversion of n-decane and CO in coated Pt/γ-Al_2O_3 catalyst depending on porous layer morphology, Appl. Catal. B: Environ. 150 (2014) 446–458.
[37] V. Novák, P. Kočí, M. Marek, F. Štěpánek, P. Blanco-García, G. Jones, Multi-scale modelling and measurements of diffusion through porous catalytic coatings: an application to exhaust gas oxidation, Catal. Today 188 (2012) 62–69.
[38] P. Kočí, M. Isoz, M. Plachá, A. Arvajová, M. Václavík, M. Svoboda, et al., 3D reconstruction and pore-scale modeling of coated catalytic filters for automotive exhaust gas aftertreatment, Catal. Today 320 (2019) 165–174.
[39] J. Pereira, J. Navalho, A. Amador, J. Pereira, Multi-scale modeling of diffusion and reaction–diffusion phenomena in catalytic porous layers: comparison with the 1D approach, Chem. Eng. Sci. 117 (2014) 364–375.
[40] M. Dudák, V. Novák, P. Kočí, M. Marek, P. Blanco-García, D. Thompsett, Impact of zeolite and γ-alumina intra-particle diffusion on the performance of a dual layer catalyst, Chem. Eng. J. 301 (2016) 178–187.
[41] Z. Zhou, T. Zeng, Z. Cheng, W. Yuan, Preparation of a catalyst for selective hydrogenation of pyrolysis gasoline, Ind. Eng. Chem. Res. 49 (2010) 11112–11118.
[42] Z. Zhou, T. Zeng, Z. Cheng, W. Yuan, Diffusion-enhanced hierarchically macro-mesoporous catalyst for selective hydrogenation of pyrolysis gasoline, AIChE J. 57 (2011) 2198–2206.
[43] M.A. Karakassides, D. Gournis, A.B. Bourlinos, P.N. Trikalitis, T. Bakas, Magnetic Fe_2O_3–Al_2O_3 composites prepared by a modified wet impregnation method, J. Mater. Chem. 13 (2003) 871–876.
[44] L. Qi, X. Tang, Z. Wang, X. Peng, Pore characterization of different types of coal from coal and gas outburst disaster sites using low temperature nitrogen adsorption approach, Int. J. Min. Sci. Technol. 27 (2017) 371–377.

CHAPTER 5

Catalytic reaction engineering

In chemical reaction engineering, one of the main tasks is the designing of chemical reactors. To achieve that, a rate law must be developed based on the analysis of rate data. Formulating rate laws from rate data is somewhat challenging in heterogeneous catalysis, mainly because these rate laws do not usually follow standard power-law models. Viewing trends in rate data and subsequently deducing an appropriate rate law become easier when knowing the different forms a catalytic rate equation can take [1]. After developing the rate law, the rate law parameters may be evaluated and a reaction mechanism that is consistent with the rate data may be postulated. Reaction mechanisms in heterogeneous catalysis generally consist of an *adsorption* step, a *surface reaction* step, and a *desorption* step, one of which is usually *rate-limiting* [1]. Finally, a catalytic reactor may be designed using the formulated rate law.

It is important to note that, since catalysts are made of porous networks, *the rate law will vary throughout the porous catalyst*. That is because reactants must first diffuse inside the catalyst pores in order to react. Consequently, the concentration in the internal surface of the catalyst will be less than that of the external surface and, as a result, the rate of the reaction will differ [1].

Estimating rate law parameters and hypothesizing a reaction mechanism become more complicated when considering *catalyst deactivation*. As the reaction takes place on the surface of the catalyst, the total concentration of active sites decreases, leading to a loss in catalytic activity. Hence, the design of the catalytic reactor must be adjusted to account for catalyst decay [1].

5.1 Catalytic reaction steps

Fig. 5.1 shows the *sequence of individual steps* by which any heterogeneous catalytic reaction proceeds. The subsequent subsections will discuss each of these steps in great detail. However, for now, the steps can be described in general as follows [1]:

1. *Diffusion* (mass transfer) of species A (the reactant) from the bulk of the fluid to the external surface of the catalyst (pore entrance);
2. *Diffusion* of species A from the pore entrance, through the pore, and to the internal surface of the catalyst (active site inside catalyst pore);
3. *Adsorption* of species A onto the surface of the active catalytic site;

Heterogeneous Catalysis.
DOI: https://doi.org/10.1016/B978-0-323-89845-4.00006-0

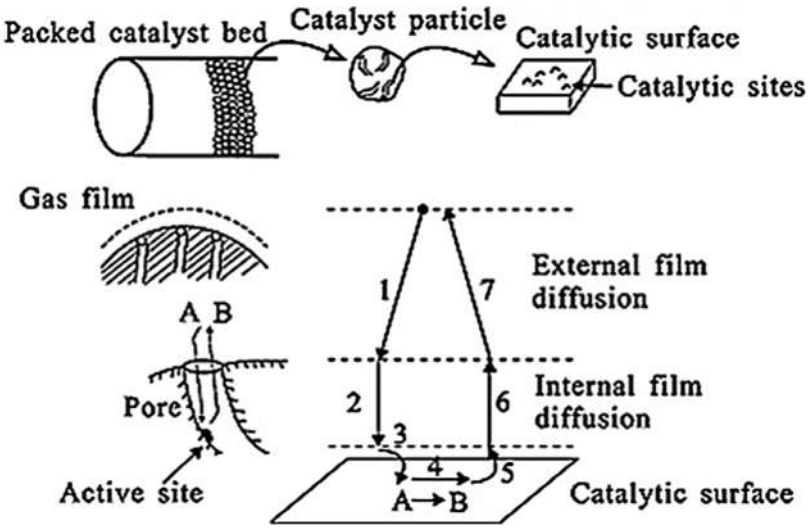

Figure 5.1
Schematic illustration of the reaction steps (1–7) in a heterogeneous catalytic packed-bed reactor. (A) represents the reactant species while (B) represents the product species
Source: *Reproduced from [2].*

4. *Reaction* on the catalytic surface (A→B);
5. *Desorption* of species B (the product) from the surface of the catalytic site;
6. *Diffusion* of species B from the internal surface of the catalyst (active site inside catalyst pore), through the pore, and to the external surface of the catalyst (pore entrance); and
7. *Diffusion* of species B from the pore entrance to the bulk of the fluid.

The rate of the slowest step typically determines the rate of the overall reaction mechanism [1]. If steps 1, 2, 6, and 7 (the diffusion steps) are comparatively faster than steps 3, 4, and 5 (i.e., the reaction steps), then the overall reaction rate is not affected by diffusion and the surface concentration is indistinguishable from that of the bulk. If, on the other hand, the diffusion steps are much slower than the reaction steps, then the overall reaction rate is affected by either external or internal diffusion.

5.1.1 External diffusion

If the *slowest step* in the sequence of heterogeneous catalytic reaction steps is *external diffusion*, then the overall reaction rate, $-r_A$, may be expressed as [1]:

$$-r_A = k_C(C_{Ab} - C_{As}) \tag{5.1}$$

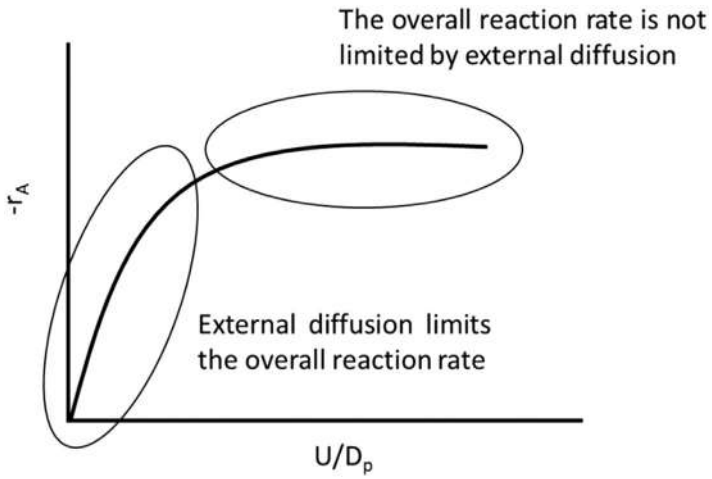

Figure 5.2
Effect of fluid velocity, U, and particle diameter, D_p, on the overall reaction rate, $-r_A$.

where k_C is the mass transfer coefficient, C_{Ab} is the concentration of the reactant A in the bulk of the fluid, and C_{As} is the concentration of reactant A on the external surface of the catalyst. Reactant A will travel from the bulk of the fluid, where its concentration is C_{Ab}, through a thickness of δ, reaching the external surface of the catalyst, where the concentration drops to C_{As} (note that $C_{As} \ll C_{Ab}$). The mass transfer coefficient, k_C, is directly proportional to the diffusion coefficient, D_{AB}, and inversely proportional to the boundary layer thickness, δ:

$$k_C = \frac{D_{AB}}{\delta} \tag{5.2}$$

Moreover, the mass transfer coefficient, k_C, is dependent on both the fluid velocity, U, and the particle diameter, D_p [1]. At low fluid velocities the thickness through which A diffuses across, to get from the bulk to the surface, is large. As a result, the travel time will be long and, consequently, the mass transfer coefficient will be small. The slower mass transfer will then subsequently limit the overall reaction rate as per Eq. (5.1). As the fluid velocity increases, however, the thickness of the boundary layer decreases, and the mass transfer increases. At very high fluid velocities, the thickness is too small to offer any resistance to diffusion. Therefore, the overall reaction rate is not anymore limited by mass transfer. Resistance to external diffusion also decreases with decreasing particle size. Fig. 5.2 demonstrates how the mass transfer coefficient (or the overall rate) increases with increasing fluid velocity and/or decreasing particle size. This continues until a plateau is reached where $C_{Ab} \approx C_{As}$. The plateau indicates that external diffusion is not the slowest step in the sequence anymore and that the overall rate is limited by some other step.

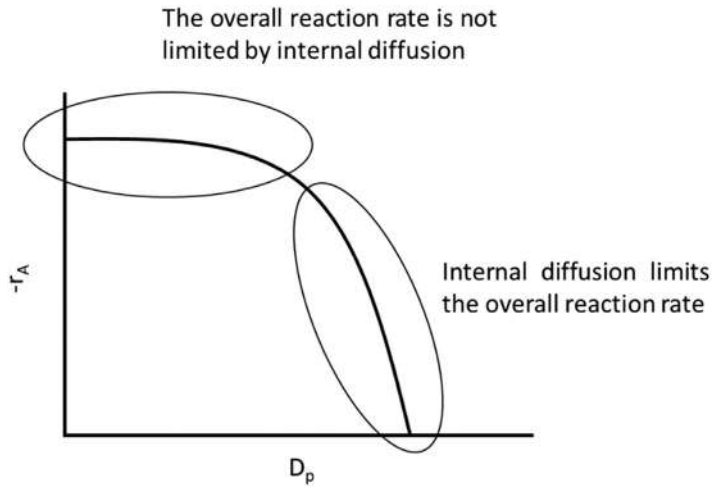

Figure 5.3
Effect of particle diameter, D_p, on the overall reaction rate, $-r_A$.

5.1.2 Internal diffusion

If the *slowest step* in the sequence of heterogeneous catalytic reaction steps is *internal diffusion*, then the overall reaction rate, $-r_A$, may be expressed as [1]:

$$-r_A = k_r C_{As} \tag{5.3}$$

where k_r is the overall rate constant. Reactant A will diffuse from the external surface of the catalyst, where its concentration is C_{As}, to the internal surface, where its concentration is now C_A (note that $C_{As} \gg C_A$). The overall rate constant, k_r, is dependent on the particle diameter, D_p [1]. For large particle diameters the time it takes for reactant A to travel through the catalyst pore is greater than the time it takes for the reaction to occur. As a result, the reaction rate will be limited by internal diffusion. For small particle diameters the travel time is very short and, therefore, the rate will no longer be limited by internal diffusion. Instead, it will be limited by some other steps (surface reaction, for instance). Fig. 5.3 demonstrates how the overall rate constant (or the overall rate) decreases with increasing particle size.

5.1.3 Adsorption

The *adsorption of species A*, which can be an atom or a molecule, *on a vacant active site S* may be represented by [1]:

$$\mathrm{A} + \mathrm{S} \rightleftarrows \mathrm{A \cdot S} \tag{5.4}$$

where A · S refers to species A adsorbed on site S. As previously discussed in Chapter 2, Fundamentals of the Adsorption Process, a molecule can adsorb on the surface nondissociatively or dissociatively.

First, consider the *nondissociative molecular adsorption of AB*:

$$AB + S \rightleftarrows AB \cdot S \tag{5.5}$$

The adsorption rate of AB is directly proportional to the rate of collisions between the AB molecule and the active site S. The collision rate is, in turn, proportional to the partial pressure of AB in the gas phase, P_{AB}. The adsorption rate is also directly proportional to the molar concentration of vacant sites, C_v, that is, the number of vacant sites per unit mass of catalyst divided by Avogadro's number (i.e., moles of sites per gram of catalyst). According to the aforementioned, the adsorption rate of AB, r_{ads}, is expressed as:

$$r_{\text{ads}} = k_A P_{AB} C_v \tag{5.6}$$

where k_A is the adsorption rate constant. The desorption rate of AB, r_{des}, is directly proportional to the surface concentration of sites occupied by AB, $C_{AB \cdot S}$, that is:

$$r_{\text{des}} = k_{-A} C_{AB \cdot S} \tag{5.7}$$

where k_{-A} is the desorption rate constant. The net rate of adsorption, r_{AD}, is equal to the adsorption rate minus the desorption rate [1]:

$$r_{\text{AD}} = r_{\text{ads}} - r_{\text{des}} \tag{5.8}$$

Substitution gives:

$$r_{\text{AD}} = k_A P_{AB} C_v - k_{-A} C_{AB \cdot S} \tag{5.9}$$

Eq. (5.9) may be rearranged to give:

$$r_{\text{AD}} = k_A \left(P_{AB} C_v - \frac{C_{AB \cdot S}}{K_A} \right) \tag{5.10}$$

where the adsorption equilibrium constant, K_A, is defined as the ratio of k_A over k_{-A} (with a clear analogy to homogeneous reversible reactions). For molecular adsorption the equilibrium adsorption constant, K_A, decreases exponentially by increasing the temperature, the adsorption rate constant, k_A, increases slightly by increasing the temperature (it is almost independent of temperature), and the desorption rate constant, k_{-A}, grows exponentially with temperature [1].

At equilibrium, the adsorption rate is equal to the desorption rate and, consequently, the net rate of adsorption, r_{AD}, equals zero. Solving Eq. (5.10) for $C_{AB\cdot S}$ with r_{AD} equal to zero:

$$C_{AB\cdot S} = K_A P_{AB} C_v \tag{5.11}$$

The total molar concentration of active sites, C_t, that is, the total number of active sites per unit mass of catalyst divided by Avogadro's number, is given as:

$$C_t = C_v + C_{AB\cdot S} \tag{5.12}$$

Solving for C_v and substitution into Eq. (5.11) give:

$$C_{AB\cdot S} = K_A P_{AB}(C_t - C_{AB\cdot S}) \tag{5.13}$$

Eq. (5.13) may be rearranged to give the concentration of adsorbed AB as a function of its partial pressure:

$$C_{AB\cdot S} = \frac{K_A P_{AB} C_t}{1 + K_A P_{AB}} \tag{5.14}$$

This specific equation represents a Langmuir isotherm, which has been extensively discussed in Chapter 3, Adsorption Models, Surface Reaction, and Catalyst Architectures.

Next, consider the *dissociative adsorption of AB*:

$$\mathrm{AB} + 2\mathrm{S} \rightleftarrows \mathrm{A}\cdot\mathrm{S} + \mathrm{B}\cdot\mathrm{S} \tag{5.15}$$

where the adsorption rate of AB is directly proportional to the partial pressure of AB, P_{AB}, and to the square of the concentration of vacant sites, C_v^2. This is because two adjacent vacant active sites are required for AB to dissociate onto as it adsorbs. Since the probability of having two neighboring unoccupied sites is proportional to C_v^2 [1], the adsorption rate of AB, r_{ads}, may be expressed as:

$$r_{ads} = k_A P_{AB} C_v^2 \tag{5.16}$$

The desorption rate of AB is proportional to the product of the concentration of sites occupied by A, $C_{A\cdot S}$, and those occupied by B, $C_{B\cdot S}$. This is because two adjacent occupied sites are required for desorption [1]. Hence, the desorption rate of AB, r_{des}, may be expressed as:

$$r_{des} = k_{-A} C_{A\cdot S} C_{B\cdot S} \tag{5.17}$$

The net rate of adsorption, r_{AD}, is then:

$$r_{AD} = k_A P_{AB} C_v^2 - k_{-A} C_{A\cdot S} C_{B\cdot S} \tag{5.18}$$

which may be rearranged to give:

$$r_{AD} = k_A \left(P_{AB} C_v^2 - \frac{C_{A\cdot S} C_{B\cdot S}}{K_A} \right) \tag{5.19}$$

For *dissociative exothermic adsorption,* the equilibrium adsorption constant, K_A, decreases with increasing temperature, while both the adsorption rate constant, k_A, and the desorption rate constant, k_{-A}, grow exponentially by increasing the temperature [1].

At equilibrium, the net rate of adsorption, r_{AD}, equals zero. Solving Eq. (5.19) for $C_{B\cdot S}$ with r_{AD} equal to zero and $C_{A\cdot S}$ equal to $C_{B\cdot S}$:

$$C_{B\cdot S} = (K_A P_{AB})^{1/2} C_v \tag{5.20}$$

The total molar concentration of active sites, C_t, is given as:

$$C_t = C_v + C_{A\cdot S} + C_{B\cdot S} = C_v + 2\left((K_A P_{AB})^{\frac{1}{2}} C_v\right) = C_v\left(1 + 2\left((K_A P_{AB})^{\frac{1}{2}}\right)\right) \tag{5.21}$$

Solving for C_v and substitution into Eq. (5.20) yield the concentration of adsorbed B as a function of the partial pressure of AB:

$$C_{B\cdot S} = \frac{(K_A P_{AB})^{1/2} C_t}{1 + 2(K_A P_{AB})^{1/2}} \tag{5.22}$$

This equation, just as Eq. (5.14), also represents a Langmuir isotherm.

In the presence of more than one species, the same principles and derivations are followed [1]. Consider, for instance, the molecular adsorption of species A on a vacant active site S in the presence of species B:

$$\mathrm{A} + \mathrm{B} + 2\mathrm{S} \rightleftarrows \mathrm{A}\cdot\mathrm{S} + \mathrm{B}\cdot\mathrm{S} \tag{5.23}$$

The concentration of adsorbed A as a function of the partial pressures of A and B will then be given by:

$$C_{A\cdot S} = \frac{K_A P_A C_t}{1 + K_A P_A + K_B P_B} \tag{5.24}$$

Several assumptions were made throughout this section in the derivation of the Langmuir adsorption models. The most important one states that the surface of the catalyst is uniform [1], that is, all active sites interact with a molecule of adsorbate always in the same way.

5.1.4 Surface reaction

A *surface adsorbed species may react* in many different ways to form a product. The most common mechanisms, which were previously discussed in Section 3.3, include *Langmuir–Hinshelwood (single-site and dual-site)* and *Eley–Rideal* [1].

1. *If only the site on which the reactant is adsorbed* is involved, then the surface reaction represents a single-site Langmuir–Hinshelwood mechanism:

$$A \cdot S \rightleftarrows B \cdot S \tag{5.25}$$

The rate of the surface reaction, r_S, is:

$$r_S = k_S\left(C_{A\cdot S} - \frac{C_{B\cdot S}}{K_S}\right) \tag{5.26}$$

where the surface reaction equilibrium constant, K_S, is defined as the ratio of k_S over k_{-S}. An example of single-site mechanism is the isomerization of n-pentane to i-pentane on Al_2O_3.

2. *If the adsorbed reactant interacts with another site*, then the surface reaction represents a dual-site Langmuir–Hinshelwood mechanism:

$$A \cdot S + S \rightleftarrows S + B \cdot S \tag{5.27}$$

The rate of the surface reaction, r_S, is:

$$r_S = k_S\left(C_{A\cdot S}C_v - \frac{C_{B\cdot S}C_v}{K_S}\right) \tag{5.28}$$

3. *If the reaction takes place between two adsorbed species*, such as the oxidation reaction between CO and O on Pt, then the surface reaction also represents a dual-site Langmuir–Hinshelwood mechanism:

$$A \cdot S + B \cdot S \rightleftarrows C \cdot S + D \cdot S \tag{5.29}$$

The rate of the surface reaction, r_S, is:

$$r_S = k_S\left(C_{A\cdot S}C_{B\cdot S} - \frac{C_{C\cdot S}C_{D\cdot S}}{K_S}\right) \tag{5.30}$$

4. *If the reaction takes place between two species adsorbed on different types of sites* (S and S′), then the surface reaction also represents another kind of dual-site Langmuir–Hinshelwood mechanism:

$$A \cdot S + B \cdot S' \rightleftarrows C \cdot S' + D \cdot S \tag{5.31}$$

The rate of the surface reaction, r_S, is:

$$r_S = k_S\left(C_{A\cdot S}C_{B\cdot S'} - \frac{C_{C\cdot S'}C_{D\cdot S}}{K_S}\right) \tag{5.32}$$

An example of this dual-site mechanism is the oxidation reaction between CO and O on a Pt/Fe composite catalyst.

5. *If the reaction takes place between an adsorbed molecule and a molecule in the gas phase*, then the surface reaction represents an Eley–Rideal mechanism:

$$A \cdot S + B_{(g)} \rightleftarrows C \cdot S \tag{5.33}$$

The rate of the surface reaction, r_S, is:

$$r_S = k_S\left(C_{A\cdot S}P_B - \frac{C_{C\cdot S}}{K_S}\right) \tag{5.34}$$

One example of the Eley–Rideal mechanism is the reaction between a benzene molecule adsorbed on a Pt catalyst and a gaseous propene molecule.

5.1.5 Desorption

The *desorption of a product*, for example, species C, into the gas phase may be represented by [1]:

$$C \cdot S \rightleftarrows C + S \tag{5.35}$$

The net rate of desorption, r_{DE}, is:

$$r_{DE} = k_D\left(C_{C\cdot S} - \frac{P_C C_v}{K_D}\right) \tag{5.36}$$

where the desorption equilibrium constant, K_D, is defined as the ratio of k_D over k_{-D}. The net rate of desorption for a particular species, r_{DE}, is equal in magnitude to the net rate of adsorption of that same species, r_{AD}, but is opposite in sign:

$$r_{DE} = -r_{AD} \tag{5.37}$$

Also, the desorption equilibrium constant, K_D, is the reciprocal of the adsorption equilibrium constant, K_A:

$$K_D = \frac{1}{K_A} \tag{5.38}$$

Substitution into Eq. (5.36) gives:

$$r_{DE} = k_D(C_{C\cdot S} - K_A P_C C_v) \tag{5.39}$$

5.2 Reaction mechanism and the rate-limiting step

Based on Langmuir's adsorption principles, Hinshelwood proposed an approach for determining the mechanism of a heterogeneous catalytic reaction [3]. The *Langmuir–Hinshelwood approach*, which gained further reputation after the work by Hougen and Watson [4], is followed by going through the steps below:

1. Write a sequence of reaction steps by assuming mechanisms for adsorption and reaction.

2. Write rate laws for each reaction step, that is, adsorption, surface reaction, and desorption.
3. Assume a rate-limiting step. The rate-limiting step, sometimes also referred to as the rate-determining step, is the slowest step in a reaction sequence and it determines the overall rate of the reaction. The rate-limiting step in the water–gas-shift reaction, for example, is the dissociative adsorption of hydrogen. In other cases, such as the isomerization of n-pentene to i-pentene over Al_2O_3, the rate-limiting step is the surface reaction.

It is important to note that the Langmuir–Hinshelwood approach assumes that the *surface of the catalyst is uniform*, with identical catalytic sites of equal energy. Moreover, the surface activity toward adsorption, surface reaction, and desorption does not depend on the degree of coverage [1]. Section 3.3 provides a full description of the Langmuir–Hinshelwood model.

For the application of the Langmuir–Hinshelwood approach, consider the following example where molecule A decomposes to form molecules B and C [1]. The first step is to hypothesize a sequence of reaction steps:

$$\mathrm{A} + \mathrm{S} \rightleftarrows \mathrm{A} \cdot \mathrm{S} \tag{5.40}$$

$$\mathrm{A} \cdot \mathrm{S} \rightleftarrows \mathrm{B} \cdot \mathrm{S} + \mathrm{C} \tag{5.41}$$

$$\mathrm{B} \cdot \mathrm{S} \rightleftarrows \mathrm{B} + \mathrm{S} \tag{5.42}$$

Next, rate laws for each step are formulated. For the nondissociative molecular adsorption of A (Eq. 5.40), the net rate of adsorption, r_{AD}, is:

$$r_{\mathrm{AD}} = k_A \left(P_A C_v - \frac{C_{A \cdot S}}{K_A} \right) \tag{5.43}$$

For the single-site surface reaction of A (Eq. 5.41), the rate of the surface reaction, r_S, is:

$$r_S = k_S \left(C_{A \cdot S} - \frac{C_{B \cdot S} P_C}{K_S} \right) \tag{5.44}$$

For the desorption of B (Eq. 5.42), the net rate of desorption, r_{DE}, is:

$$r_{\mathrm{DE}} = k_D \left(C_{B \cdot S} - \frac{P_B C_v}{K_{D,B}} \right) \tag{5.45}$$

As previously discussed in Section 5.1.5, the desorption equilibrium constant of B, $K_{D,B}$, is the reciprocal of the adsorption equilibrium constant of B, $K_{A,B}$. Accordingly, Eq. (5.45) can be written as:

$$r_{\mathrm{DE}} = k_D \left(C_{B \cdot S} - K_{A,B} P_B C_v \right) \tag{5.46}$$

Finally, the rate-limiting step must be determined. First, assume that the rate-limiting step is adsorption. Therefore the overall reaction rate, $-r_A$, is:

$$-r_A = r_{AD} = k_A\left(P_A C_v - \frac{C_{A\cdot S}}{K_A}\right) \tag{5.47}$$

The unmeasurable quantities in Eq. (5.47), C_v and $C_{A\cdot S}$, must be replaced with more practical ones. Since the reaction is assumed to be adsorption-limited (i.e., adsorption is slower than the surface reaction and the desorption steps), then k_S and k_D are large. As such, r_S/k_S and r_{DE}/k_D are approximately zero [1]. Using this relation to solve Eq. (5.44) for $C_{A\cdot S}$:

$$C_{A\cdot S} = \frac{C_{B\cdot S} P_C}{K_S} \tag{5.48}$$

Similarly, solving Eq. (5.46) for $C_{B\cdot S}$ with $r_{DE}/k_D \approx 0$:

$$C_{B\cdot S} = K_{A,B} P_B C_v \tag{5.49}$$

Substitution in Eq. (5.48) gives:

$$C_{A\cdot S} = \frac{K_{A,B} P_B P_C C_v}{K_S} \tag{5.50}$$

Replacing into Eq. (5.47) results in:

$$-r_A = r_{AD} = k_A C_v\left(P_A - \frac{K_{A,B} P_B P_C}{K_S K_A}\right) \tag{5.51}$$

The total molar concentration of active sites, C_t, is given as:

$$C_t = C_v + C_{A\cdot S} + C_{B\cdot S} = C_v + \frac{K_{A,B} P_B P_C C_v}{K_S} + K_{A,B} P_B C_v \tag{5.52}$$

Solving for C_v and substitution into Eq. (5.51) give the *rate law for the adsorption-limited catalytic decomposition of A*:

$$-r_A = r_{AD} = \frac{k_A C_t\left(P_A - \frac{K_{A,B} P_B P_C}{K_S K_A}\right)}{1 + \frac{K_{A,B} P_B P_C}{K_S} + K_{A,B} P_B} \tag{5.53}$$

If the decomposition of A is limited by adsorption (Fig. 5.4A), then the initial overall reaction rate, $-r_{A0}$, increases linearly with the initial partial pressure of A, P_{A0}, according to the following expression:

$$-r_{A0} = k_A C_t P_{A0} \tag{5.54}$$

Note that initially no products are present, that is, P_{B0} and P_{C0} are equal to zero.

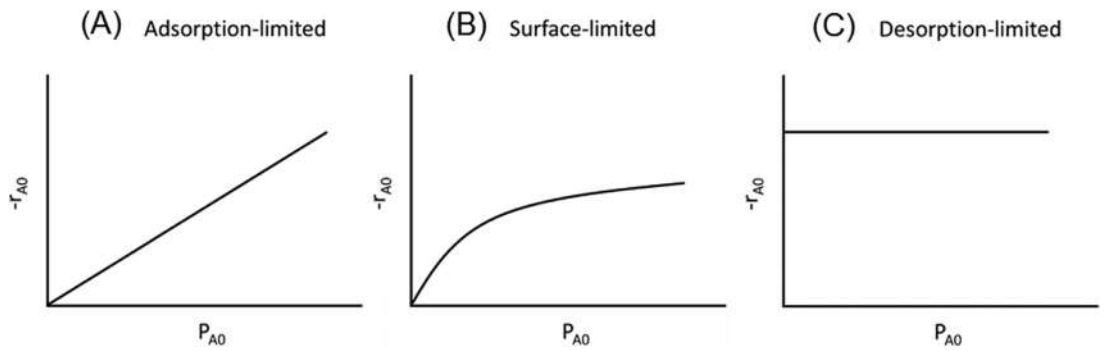

Figure 5.4

(A) Adsorption-limited, (B) surface reaction-limited, and (C) desorption-limited reactions. $-r_{A0}$ represents the initial overall reaction rate and P_{A0} represents the initial partial pressure of reactant A.

Next, assume that the surface reaction step is the rate-limiting step. Therefore the overall reaction rate, $-r_A$, is:

$$-r_A = r_S = k_S\left(C_{A\cdot S} - \frac{C_{B\cdot S}P_C}{K_S}\right) \tag{5.55}$$

The unmeasurable quantities in Eq. (5.55), $C_{A\cdot S}$ and $C_{B\cdot S}$, must be replaced with more meaningful ones. Since the whole process is assumed to be reaction-limited, then k_A and k_D are large. As such, r_{AD}/k_A and r_{DE}/k_D are approximately zero [1]. Using this relation to solve Eq. (5.43) for $C_{A\cdot S}$:

$$C_{A\cdot S} = K_A P_A C_v \tag{5.56}$$

Similarly, solving Eq. (5.46) for $C_{B\cdot S}$ with $r_{\mathrm{DE}}/k_D \approx 0$:

$$C_{B\cdot S} = K_{A,B} P_B C_v \tag{5.57}$$

Replacing into Eq. (5.55) results in:

$$-r_A = r_S = k_S C_v\left(K_A P_A - \frac{K_{A,B}P_B P_C}{K_S}\right) \tag{5.58}$$

The total molar concentration of active sites, C_t, is given as:

$$C_t = C_v + C_{A\cdot S} + C_{B\cdot S} = C_v + K_A P_A C_v + K_{A,B} P_B C_v \tag{5.59}$$

Solving for C_v and substitution into Eq. (5.58) give the *rate law for the reaction-limited catalytic decomposition of A*:

$$-r_A = r_S = \frac{k_S C_t\left(K_A P_A - \frac{K_{A,B}P_B P_C}{K_S}\right)}{1 + K_A P_A + K_{A,B} P_B} \tag{5.60}$$

If the decomposition of A is limited by the surface reaction (Fig. 5.4B), then, at low P_{A0} ($1 \gg K_A P_{A0}$), the initial overall reaction rate, $-r_{A0}$, will increase linearly with P_{A0} according to the following expression:

$$-r_{A0} = k_S K_A C_t P_{A0} \tag{5.61}$$

However, at high P_{A0} ($1 \ll K_A P_{A0}$), the initial overall reaction rate, $-r_{A0}$, will be independent of P_{A0} according to the following expression:

$$-r_{A0} = \frac{k_S C_t (K_A P_{A0})}{K_A P_{A0}} = k_S C_t \tag{5.62}$$

Finally, *assume that the desorption step is the rate-limiting step*. Therefore, the overall reaction rate, $-r_A$, is:

$$-r_A = r_{DE} = k_D \left(C_{B \cdot S} - K_{A,B} P_B C_v \right) \tag{5.63}$$

The unmeasurable quantities in Eq. (5.63), $C_{B \cdot S}$ and C_v, must be replaced with more meaningful ones. Since the reaction is assumed to be desorption-limited, then k_A and k_S are large. As such, r_{AD}/k_A and r_S/k_S are approximately zero [1]. Using this relation to solve Eq. (5.44) for $C_{B \cdot S}$:

$$C_{B \cdot S} = \frac{K_S C_{A \cdot S}}{P_C} \tag{5.64}$$

Similarly, solving Eq. (5.43) for $C_{A \cdot S}$ with $r_A/k_A \approx 0$:

$$C_{A \cdot S} = K_A P_A C_v \tag{5.65}$$

Substitution in Eq. (5.64) gives:

$$C_{B \cdot S} = \frac{K_S K_A P_A C_v}{P_C} \tag{5.66}$$

Replacing into Eq. (5.63) results in:

$$-r_A = r_{DE} = k_D C_v \left(\frac{K_S K_A P_A}{P_C} - K_{A,B} P_B \right) \tag{5.67}$$

The total molar concentration of active sites, C_t, is given as:

$$C_t = C_v + C_{A \cdot S} + C_{B \cdot S} = C_v + K_A P_A C_v + \frac{K_S K_A P_A C_v}{P_C} \tag{5.68}$$

Solving for C_v, substitution into Eq. (5.67), and multiplying the numerator and denominator by P_C give the *rate law for the desorption-limited catalytic conversion of A*:

$$-r_A = r_{DE} = \frac{k_D C_t \left(K_S K_A P_A - K_{A,B} P_B P_C \right)}{P_C + K_A P_A P_C + K_S K_A P_A} \tag{5.69}$$

If the decomposition of A is limited by desorption (Fig. 5.4C), then the initial overall reaction rate, $-r_{A0}$, will be independent of P_{A0} according to the following expression:

$$-r_{A0} = \frac{k_D C_t (K_S K_A P_{A0})}{K_S K_A P_{A0}} = k_D C_t \tag{5.70}$$

Although it would not participate in the reaction, an adsorbing inert in the feed, I, will still occupy sites on the catalytic surface:

$$\mathrm{I} + \mathrm{S} \rightleftarrows \mathrm{A} \cdot \mathrm{S} \tag{5.71}$$

Hence, the total concentration of active sites, C_t, will be given as:

$$C_t = C_v + C_{A \cdot S} + C_{B \cdot S} + C_{I \cdot S} \tag{5.72}$$

where $C_{I \cdot S}$ is the concentration of sites where the inert is adsorbed and it is defined as:

$$C_{I \cdot S} = K_I P_I C_v \tag{5.73}$$

An alternative way to derive catalytic rate laws is to use the *pseudo-steady-state hypothesis (PSSH)*, which states that the net formation rate of reactive intermediates is zero, by assuming that each surface adsorbed species is a reactive intermediate [1]. For instance, consider the isomerization reaction of molecule A to molecule B:

$$\mathrm{A} + \mathrm{S} \rightleftarrows \mathrm{A} \cdot \mathrm{S} \tag{5.74}$$

$$\mathrm{A} \cdot \mathrm{S} \rightarrow \mathrm{B} \cdot \mathrm{S} \tag{5.75}$$

$$\mathrm{B} \cdot \mathrm{S} \rightleftarrows \mathrm{B} + \mathrm{S} \tag{5.76}$$

For the irreversible surface reaction (Eq. 5.75), the overall reaction rate, $-r_A$, is:

$$-r_A = r_S = k_S C_{A \cdot S} \tag{5.77}$$

The net formation rates of the reactive intermediates A · S and B · S are, respectively:

$$-r^*_{A \cdot S} = k_A P_A C_v - k_{-A} C_{A \cdot S} - k_S C_{A \cdot S} = 0 \tag{5.78}$$

$$-r^*_{B \cdot S} = k_S C_{A \cdot S} - k_D C_{B \cdot S} + k_{-D} P_B C_v = 0 \tag{5.79}$$

Solving for $C_{A \cdot S}$ and $C_{B \cdot S}$:

$$C_{A \cdot S} = \frac{k_A P_A C_v}{k_{-A} + k_S} \tag{5.80}$$

$$C_{B \cdot S} = \frac{k_S C_{A \cdot S} + k_{-D} P_B C_v}{k_D} = \frac{k_S k_A P_A C_v}{k_D (k_{-A} + k_S)} + \frac{k_{-D} P_B C_v}{k_D} \tag{5.81}$$

Replacing $C_{A\cdot S}$ into Eq. (5.77) results in:

$$-r_A = r_S = \frac{k_S k_A P_A C_v}{k_{-A} + k_S} \tag{5.82}$$

The total molar concentration of active sites, C_t, is given as:

$$C_t = C_v + C_{A\cdot S} + C_{B\cdot S} = C_v + \frac{k_A P_A C_v}{k_{-A} + k_S} + \frac{k_S k_A P_A C_v}{k_D(k_{-A} + k_S)} + \frac{k_{-D} P_B C_v}{k_D} \tag{5.83}$$

Solving for C_v and substitution into Eq. (5.82) give the rate law for the catalytic isomerization of A:

$$-r_A = r_S = \frac{k_S k_A P_A C_t}{k_{-A} + k_S}\left(\frac{1}{1 + \frac{k_A P_A}{k_{-A} + k_S} + \frac{k_S k_A P_A}{k_D(k_{-A} + k_S)} + \frac{k_{-D} P_B}{k_D}}\right) \tag{5.84}$$

If the surface reaction is assumed to be rate-limiting, then $k_S \ll k_{-A}$ and Eq. (5.84) becomes:

$$-r_A = r_S = \frac{k_S K_A P_A C_t}{1 + K_A P_A + K_{A,B} P_B} \tag{5.85}$$

At high temperatures, and due to the exothermic nature of the adsorption process, the adsorption equilibrium constants (K_A and $K_{A,B}$) are small, that is, $1 \gg (K_A P_A + K_{A,B} P_B)$. Eq. (5.85) may then be approximated as:

$$-r_A = r_S = k_S K_A P_A C_t \tag{5.86}$$

The PSSH approach is preferred if (1) two or more reaction steps are rate-limiting, (2) some of the reaction steps are irreversible, and (3) none of the reaction steps are rate-limiting [1].

5.3 Catalytic reactor design

In designing catalytic reactors, a sequential algorithm is typically followed [1]. First, a *rate law* is deduced from experimental data. Second, a *mechanism* consistent with experimental observations is hypothesized. Third, *rate law parameters* are evaluated. Lastly, a *catalytic reactor* is designed. For example, consider the following catalytic reaction with its corresponding experimental data presented in Table 5.1 [1]:

$$\mathrm{A} + \mathrm{B} \rightarrow \mathrm{C} + \mathrm{D} \tag{5.87}$$

In runs 1 and 2, the *partial pressure of C is varied* while all other partial pressures remain constant. This will show how the overall reaction rate is affected by the partial pressure of C. Similarly, in runs 3 and 4, runs 5−8, and runs 9−11, the partial pressure of a single species is varied while all other partial pressures are kept constant. The reaction rate law can be deduced from a careful analysis of this experimental data.

Table 5.1: Experimental data for a catalytic reaction where A and B react to yield C and D.

Run	Overall reaction rate, $-r_A$	Partial pressure of A, P_A	Partial pressure of B, P_B	Partial pressure of C, P_C	Partial pressure of D, P_D
1	47	1	1	1	0
2	47	1	1	4	0
3	28	1	1	0	1
4	13	1	1	0	4
5	47	1	1	0	0
6	75	4	1	0	0
7	81	10	1	0	0
8	83	20	1	0	0
9	47	1	1	0	0
10	188	1	4	0	0
11	752	1	16	0	0

Runs 1 and 2 show that the overall reaction rate did not change much by increasing the partial pressure of C. This indicates that the reaction rate law will not include a term that accounts for P_C. When changes in the concentration of a product do not affect the reaction rate, then it is assumed that the product either desorbs immediately into the gas phase or adsorbs very weakly onto the catalytic surface ($1 \gg K_{A,C}P_C$) [1].

In runs 3 and 4, the overall reaction rate decreased with an *increase in* P_D. This suggests that product D remains adsorbed on the surface of the catalyst once formed [1]. To reflect this type of dependent relation in the reaction rate law, the P_D term must appear in the denominator of the expression:

$$-r_A \sim \frac{1}{1 + K_{A,D}P_D + \cdots} \tag{5.88}$$

Runs 5 and 6 show that when the *partial pressure of A increases*, the overall reaction rate also increases. However, at high P_A (runs 7 and 8), the rate seems to be unaffected by the increase in P_A. This observed behavior indicates that reactant A adsorbs to the surface and that the rate law may be expressed as [1]:

$$-r_A \sim \frac{P_A}{1 + K_A P_A + \cdots} \tag{5.89}$$

In runs 9, 10, and 11, the *increase in the partial pressure of B* produced a linear growth of the overall rate of the reaction. A rate law that describes this type of behavior may be of the form:

$$-r_A \sim P_B \tag{5.90}$$

In this case, reactant B most probably reacts in the gas phase without adsorbing to the surface, that is, it follows the Eley–Rideal model. Another possible explanation is that reactant B adsorbs on the surface very weakly ($1 \gg K_{A,B}P_B$) [1].

To find the expression for the overall reaction rate, Eqs. (5.88), (5.89), and (5.90) are combined:

$$-r_A = \frac{kP_AP_B}{1 + K_AP_A + K_{A,D}P_D} \tag{5.91}$$

with k being a constant value that lumps up all other relevant constants of the rate law.

Next, a mechanism is proposed based on the interpretations made earlier while deducing the rate law. Accordingly, it is assumed that reactant A adsorbs and reacts with species B in the gas phase. This yields C in the gas phase and adsorbed D as product. Species D then later desorbs from the catalytic surface. Furthermore, the surface reaction step is assumed to be the rate-limiting step since c. 75% of all heterogeneous reactions are limited by the surface reaction [1]. The mechanism is then hypothesized to be:

$$\mathrm{A_{(g)} + S \rightleftarrows A \cdot S} \tag{5.92}$$

$$\mathrm{A \cdot S + B_{(g)} \rightleftarrows C_{(g)} + D \cdot S} \tag{5.93}$$

$$\mathrm{D \cdot S \rightleftarrows D_{(g)} + S} \tag{5.94}$$

Next, the rate laws for each step are formulated. For the adsorption of A (Eq. 5.92), the net rate of adsorption, r_{AD}, is:

$$r_{\mathrm{AD}} = k_A\left(P_AC_v - \frac{C_{A\cdot S}}{K_A}\right) \tag{5.95}$$

For the reaction of adsorbed A with gaseous B (Eq. 5.93), the rate of the surface reaction, r_S, is:

$$r_S = k_S\left(C_{A\cdot S}P_B - \frac{P_CC_{D\cdot S}}{K_S}\right) \tag{5.96}$$

For the desorption of D (Eq. 5.94), the net rate of desorption, r_{DE}, is:

$$r_{\mathrm{DE}} = k_D\left(C_{D\cdot S} - \frac{P_DC_v}{K_{D,D}}\right) \tag{5.97}$$

As previously discussed in Section 5.1.5, the desorption equilibrium constant of D, $K_{D,D}$, is the reciprocal of the adsorption equilibrium constant of D, $K_{A,D}$. Accordingly, Eq. (5.97) can be written as:

$$r_{\mathrm{DE}} = k_D\left(C_{D\cdot S} - K_{A,D}P_DC_v\right) \tag{5.98}$$

Since the surface reaction step is assumed to be rate-limiting, then the overall reaction rate, $-r_A$, is:

$$-r_A = r_S = k_S\left(C_{A\cdot S}P_B - \frac{P_CC_{D\cdot S}}{K_S}\right) \tag{5.99}$$

The unmeasurable quantities in Eq. (5.99), $C_{A\cdot S}$ and $C_{D\cdot S}$, must be replaced with more meaningful ones. Since the surface reaction is the limiting step, then k_A and k_D are large. As such, r_{AD}/k_A and r_{DE}/k_D are approximately zero [1]. Using this relation to solve Eq. (5.95) for $C_{A\cdot S}$:

$$C_{A\cdot S} = K_A P_A C_v \tag{5.100}$$

Similarly, solving Eq. (5.98) for $C_{B\cdot S}$ with $r_{DE}/k_D \approx 0$:

$$C_{D\cdot S} = K_{A,D} P_D C_v \tag{5.101}$$

Replacing into Eq. (5.99) results in:

$$-r_A = r_S = k_S C_v \left(K_A P_A P_B - \frac{K_{A,D} P_D P_C}{K_S} \right) \tag{5.102}$$

The total molar concentration of active sites, C_t, is given as:

$$C_t = C_v + C_{A\cdot S} + C_{D\cdot S} = C_v + K_A P_A C_v + K_{A,D} P_D C_v \tag{5.103}$$

Solving for C_v and substitution into Eq. (5.102) give the rate law:

$$-r_A = r_S = \frac{k_S C_t \left(K_A P_A P_B - \frac{K_{A,D} P_D P_C}{K_S} \right)}{1 + K_A P_A + K_{A,D} P_D} \tag{5.104}$$

Neglecting the reverse reaction, that is, assuming the reaction is irreversible:

$$-r_A = r_S = \frac{k_S C_t K_A P_A P_B}{1 + K_A P_A + K_{A,D} P_D} = \frac{k P_A P_B}{1 + K_A P_A + K_{A,D} P_D} \tag{5.105}$$

with k being a constant value that lumps up all other relevant constants of the rate law.

Next, the rate law parameters (k, K_A, and $K_{A,D}$) are estimated. For that, the rate law is linearized (dividing both sides of Eq. 5.105 by $P_A P_B$ and inverting) to give an expression:

$$\frac{P_A P_B}{-r_A} = \frac{1}{k} + \frac{K_A P_A}{k} + \frac{K_{A,D} P_D}{k} \tag{5.106}$$

in the form:

$$Y_j = a_0 + a_1 X_{1j} + a_2 X_{2j} \tag{5.107}$$

Eq. (5.106) may then be solved to evaluate the rate law parameters using one of the many well-known regression techniques.

After that, the final step in designing a catalytic reactor is to express P_A, P_B, and P_D in terms of conversion X. Then, substitution of the expressions of the partial pressures in the rate law equation yields a *rate law in terms of X*. The design equation can then be solved to determine

important catalytic reactor design parameters such as catalyst weight and reactor volume. For a *packed-bed reactor (PBR)*, for instance, the *design equation* to be solved is [1]:

$$\frac{dX}{dW} = \frac{-r_A}{F_{A0}} \tag{5.108}$$

where W is the catalyst weight and F_{A0} is the inlet flow rate of A. This design equation can be derived by first writing out the general mole balance equation of a PBR:

$$\frac{dF_A}{dW} = r_A \tag{5.109}$$

Defining the flow rate of A, F_A, in terms of conversion, X:

$$F_A = F_{A0} - F_{A0}X \tag{5.110}$$

Differentiating and then substitution into Eq. (5.109) yield the design equation for a PBR.

A *fluidized, continuously-stirred tank reactor (CSTR)* may also be used to carry out catalytic reactions. The mole balance for a fluidized CSTR may be expressed as:

$$W = \frac{F_{A0} - F_A}{-r_A} \tag{5.111}$$

Substituting Eq. (5.110) into Eq. (5.111) yields the design equation for a fluidized CSTR:

$$W = \frac{F_{A0}X}{-r_A} \tag{5.112}$$

The two reactors mentioned above along with some other ones commonly employed in the industry are discussed in Focus 5.1.

Focus 5.1: Types of catalytic reactors

Catalytic reactors are typically classified into two different categories, according to whether the catalyst bed is fixed or mobile [5]. *Fixed-bed catalytic reactors include packed-bed, trickle-bed, and structured reactors*. On the other hand, *mobile-bed catalytic reactors include fluidized-bed, moving-bed, and slurry reactors*. Fig. 5.5 shows a schematic representation of some of these catalytic reactor types.

PBRs are widely used in the chemical industry. Two of the most popular examples include the synthesis of ammonia and the reforming of natural gas [5]. In PBRs, the solid catalyst particles are randomly packed in an enclosed volume to form a catalytic bed. The reactive mixture consists of a single-phase fluid (a gas) that flows through the bed in irregular and random paths. As a result, different elements of the reactive mixture can pass through the bed at different rates, leading to a wide distribution of

(*Continued*)

Focus 5.1: Types of catalytic reactors (Continued)

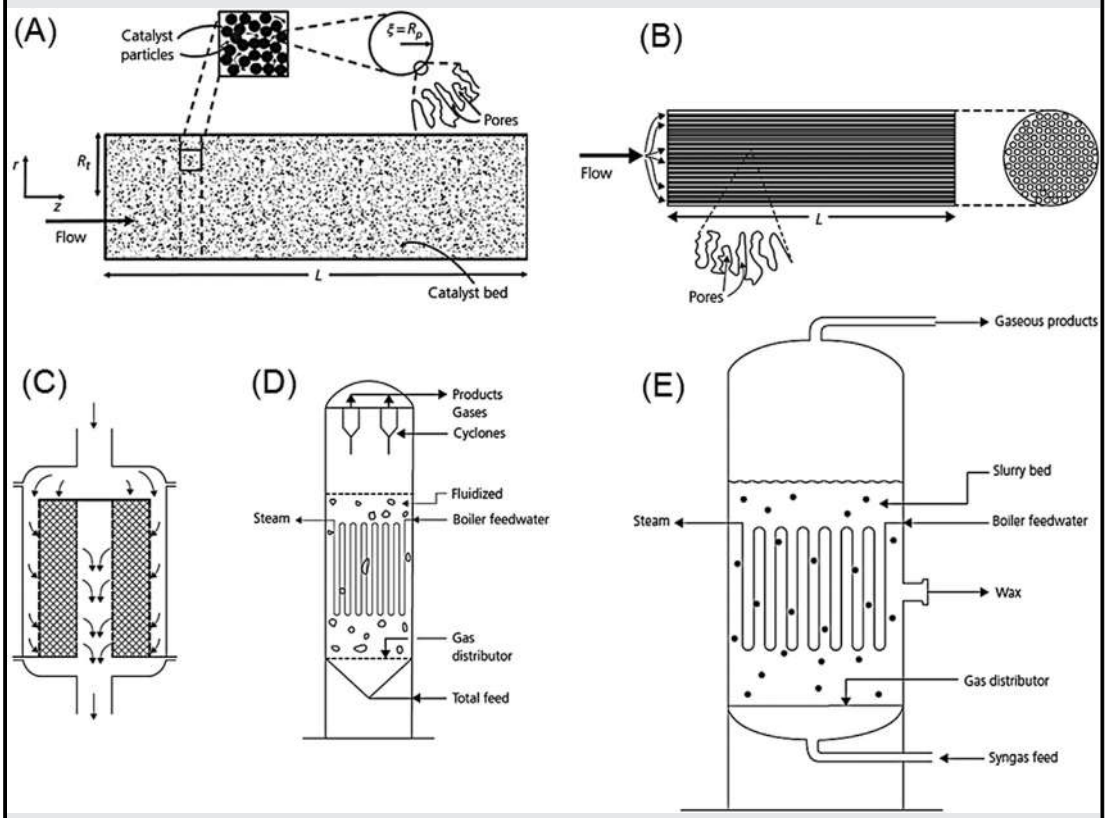

Figure 5.5
Schematic representation of the different types of catalytic reactors: (A) packed-bed reactor, (B) monolith reactor, (C) radial flow reactor, (D) fluidized-bed reactor, (E) slurry reactor.
Source: *Reproduced from* [5].

residence times. In order to ensure uniform distribution of the gaseous feed, the headspace above the catalyst bed is usually filled with inert ceramic balls. If gas and liquid phases coexist in the reactive mixture, then the PBR will be categorized as a trickle-bed reactor. Here, a more sophisticated distributor, such as a bubble cap tray, is required to mix the two phases and then distribute them uniformly across the catalyst bed. *Trickle-bed reactors*, which may contain up to six successive catalytic beds, are extremely common in petroleum refining applications including hydrocracking, hydrodesulfurization, and hydroisomerization [5].

If the fixed-bed catalytic reactor offers a structured and well-defined path for the flow of the reacting mixture, then it may be categorized as a *structured reactor* [5]. The existence of a structured flow pattern leads to a predictable residence time and a narrow residence

(*Continued*)

Focus 5.1: Types of catalytic reactors (Continued)

time distribution. This is of extreme relevance in industrial reactions where an intermediate species is the desired product and has to be removed from the reactor before it is converted into an undesired species. Examples of *structured reactors include monolith reactors and microchannel reactors*. Monolith reactors are composed of a large number of small diameter, parallel channels, all of which contain catalyst coated on their inner walls. One notable advantage of monolith reactors is the significant reduction in pressure drop compared to other types of reactors. Monolith reactors are used as catalytic converters in vehicles to regulate emission levels and for NO_x removal from flue gas in power stations. Pressure drop in fixed-bed catalytic reactors can also be diminished by using radial flow reactors. Instead of flowing in the axial direction, the reacting mixture in radial flow reactors moves in the direction perpendicular to the catalyst bed. Microchannel reactors are very similar to monolith reactors, except that they consist of channels with much smaller diameters (i.e., in the submillimeter range). Hence, microchannel reactors possess higher heat and mass transfer coefficients as well as higher surface area-to-volume ratios. Since the throughput of microchannel reactors is typically small, they are better suited for low production capacity industries such as pharmaceutical and fine chemical production [5].

If the volumetric flow rate of the gaseous reacting feed exceeds the minimum fluidization flow rate, then the catalytic bed is no longer fixed and, instead, becomes fluidized [5]. Such types of catalytic reactors are known as *fluidized-bed reactors (FBRs)*. FBRs offer enhanced mixing between the gas and solid phases, consequently leading to a more uniform distribution of temperature across the reactor. This minimizes the chance of hot spot formation in exothermic reactions. FBRs also allow constant catalytic activity either by online addition of fresh catalyst or by its continuous regeneration in a separate zone. The flow of the reacting mixture in FBRs, however, is irregular and random and thus the residence time distribution is wide. FBRs have very limited industrial applications and are usually only used for specific processes such as high-temperature Fischer–Tropsch synthesis and fluidized catalytic cracking [5]. If the catalytic process necessitates the continuous regeneration of the catalyst bed, then moving-bed reactors are usually preferred. Here, the spent catalyst leaves the reactor at the bottom and is continuously replaced with fresh catalyst that is fed from the top. *Moving-bed reactors* are commonly used in the catalytic hydrotreating of heavy oils [5].

The reactive mixture in FBRs and moving-bed reactors consists of a single-phase fluid (a gas). If gas and liquid phases coexist in the reactive mixture, then the reactor will be categorized as a *slurry reactor* [5]. Slurry reactors involve intense mixing of the gas, liquid, and solid phases and therefore provide excellent heat transfer properties and great temperature control. In this regard, they are considered to be promising for a variety of different industrial processes, most popularly is the low-temperature Fischer–Tropsch synthesis reaction. Other applications include the oxidation and hydroformylation of olefins, methanation and polymerization reactions, and the ethynylation of aldehydes [5].

5.4 Diffusion and reaction in heterogeneous catalysis

5.4.1 Mass transfer-limited and reaction rate-limited reactions

Two limiting cases of diffusion and reaction in heterogeneous catalysis will be discussed in this section [1]. In the first case, the overall reaction is said to be mass transfer limited because the rate of the surface reaction is so rapid compared to the rate of reactant diffusion to the surface. In the second case, the overall reaction is limited by the rate of the surface reaction, because the latter is relatively much slower than the diffusion rate. Consider the isomerization reaction of A to B by which the surface reaction is well fitted by a Langmuir–Hinshelwood single-site mechanism with the following rate law:

$$-r_A = r_S = \frac{k_S K_A C_{As} C_t}{1 + K_A C_{As} + K_{A,B} C_{Bs}} = \frac{k_r C_{As}}{1 + K_A C_{As} + K_{A,B} C_{Bs}} \tag{5.113}$$

where k_r is the specific reaction rate constant. At high temperatures, the adsorption equilibrium constants (K_A and $K_{A,B}$) are small, that is, $1 \gg (K_A C_{As} + K_{A,B} C_{Bs})$. Eq. (5.113) may then be approximated as:

$$-r_A = r_S = k_r C_{As} \tag{5.114}$$

The surface concentration, C_{As}, must be eliminated from the reaction rate since it cannot be determined easily. At steady state, all the reactants diffusing into the pellet are converted. In other words, the rate of consumption of A on the surface is equal to the molar flux of A to the surface, W_A [1]:

$$-r_A = W_A = k_C (C_{Ab} - C_{As}) \tag{5.115}$$

where k_C is the mass transfer coefficient. Equating Eq. (5.114) with Eq. (5.115):

$$k_r C_{As} = k_C (C_{Ab} - C_{As}) \tag{5.116}$$

and solving Eq. (5.116) for C_{As}:

$$C_{As} = \frac{k_C C_{Ab}}{k_r + k_C} \tag{5.117}$$

gives the reaction rate as:

$$-r_A = \frac{k_r k_C C_{Ab}}{k_r + k_C} = k_{\text{eff}} C_{Ab} \tag{5.118}$$

where k_{eff} is the effective transport coefficient.

If the reaction is rapid (mass transfer limited), the specific reaction rate constant is much larger than the mass transfer coefficient ($k_r \gg k_c$). Consequently, Eq. (5.118) becomes:

$$-r_A = k_C C_{Ab} \tag{5.119}$$

In the case where the reaction is slow (reaction rate-limited), the mass transfer coefficient is much larger than the kinetic constant ($k_c \gg k_r$). Consequently, Eq. (5.118) becomes:

$$-r_A = k_r C_{Ab} \tag{5.120}$$

Rate-limited reactions have been extensively discussed in Sections 5.2 and 5.3. In this section, a detailed analysis of mass transfer-limited reactions will be presented. Hence, consider the following mass transfer-limited reaction taking place in a PBR as shown in Fig. 5.6:

$$\mathrm{A} + \mathrm{B} \rightarrow \mathrm{C} + \mathrm{D} \tag{5.121}$$

A steady-state mole balance on reactant A gives:

$$F_A|_z - F_A|_{z+\Delta z} + r_A a_c A_c \Delta z = 0 \tag{5.122}$$

where F_A is the molar flow rate of A, r_A is the generation rate of A per unit surface area, a_c is the external surface area of the catalyst per unit volume, and A_c is the cross-sectional area. Dividing by $A_c \Delta z$ and taking the limit as Δz approaches zero:

$$-\frac{1}{A_c}\left(\frac{dF_A}{dz}\right) + r_A a_c = 0 \tag{5.123}$$

The molar flow rate of A is defined as:

$$F_A = W_A A_c = (J_A + B_A) A_c \tag{5.124}$$

with the molar flux W_A accounting for both diffusive transport, J_A, and convective transport, B_A. In PBRs, however, $J_A \ll B_A$ [1]. Consequently:

$$F_A = B_A A_c = U C_{Ab} A_c \tag{5.125}$$

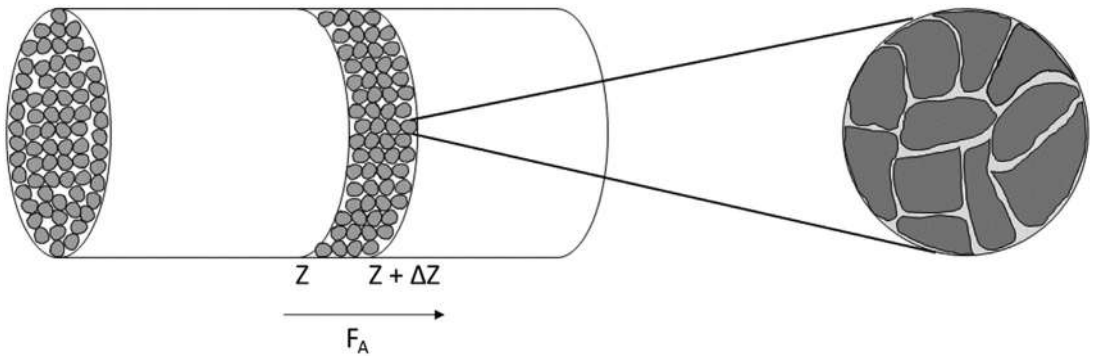

Figure 5.6
Schematic illustration of a packed-bed reactor with F_A representing the molar flow rate of A in the direction of the arrow. Source: *Reproduced from [6].*

where U is the average molar velocity. Substitution in Eq. (5.123) (and assuming constant U) gives the equation describing flow and reaction in a PBR:

$$-U\left(\frac{dC_{Ab}}{dz}\right) + r_A a_c = 0 \tag{5.126}$$

Substituting Eq. (5.119) into Eq. (5.126):

$$-U\left(\frac{dC_{Ab}}{dz}\right) = k_C C_{Ab} a_c \tag{5.127}$$

Integrating with $C_{Ab} = C_{Ab0}$ at $z = 0$:

$$\frac{C_{Ab}}{C_{Ab0}} = \exp\left(\frac{-k_C a_c z}{U}\right) \tag{5.128}$$

In terms of conversion X and at $z = L$, where L is the rector length:

$$ln\frac{1}{1-X} = \frac{k_C a_c L}{U} \tag{5.129}$$

In 1958, Thoenes and Kramers developed a correlation for flow through PBRs that shows the effect of different operating conditions and equipment parameters on the mass transfer coefficient [7]:

$$\left[\frac{k_C d_p}{D_{AB}}\left(\frac{\Phi}{1-\Phi}\right)\frac{1}{\gamma}\right] = \left[\frac{U d_p \rho}{\mu(1-\Phi)\gamma}\right]^{1/2}\left(\frac{\mu}{\rho D_{AB}}\right)^{1/3} \tag{5.130}$$

where Φ is the porosity, γ is the shape factor, ρ is the fluid density, and μ is the viscosity. At constant fluid properties and particle diameter, $k_C \alpha U^{1/2}$.

5.4.2 Diffusion with reaction in a catalyst pellet

Neglecting external resistance to mass transfer, consider a reactant species, A, diffusing and then reacting inside the spherical catalyst pellet described in Fig. 5.7. A steady-state mole balance on A gives [8]:

$$W_A 4\pi r^2|_r - W_A 4\pi r^2|_{r+\Delta r} + r_A S_A \rho_c 4\pi r^2 \Delta r = 0 \tag{5.131}$$

where W_A is the molar flux of A, r is the radius, r_A is the generation rate of A per unit surface area, S_A is the surface area of the catalyst per unit mass, and ρ_c is the density of the catalyst. Dividing by $-4\pi\Delta r$ and taking the limit as Δr approaches zero:

$$\frac{d(W_A r^2)}{dr} - r_A S_A \rho_c r^2 = 0 \tag{5.132}$$

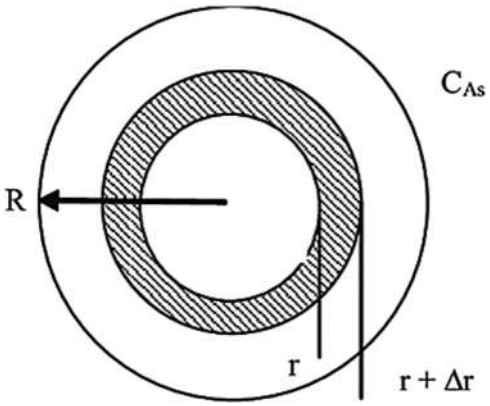

Figure 5.7
Shell balance on a spherical catalyst pellet. C_{As} represents the surface concentration of reactant species A and R represents the radius of the porous catalyst particle. Source: *Reproduced from [8].*

The molar flux W_A is:

$$W_A = -D_{\text{eff}}\left(\frac{dC_A}{dr}\right) \tag{5.133}$$

where D_{eff} is the effective diffusivity which accounts for pore tortuosity, porosity, and other internal diffusion-constraining factors [1]. Substituting into Eq. (5.132) yields:

$$\frac{d}{dr}\left(-D_{\text{eff}}\left(\frac{dC_A}{dr}\right)r^2\right) - r_A S_A \rho_c r^2 = 0 \tag{5.134}$$

At high temperatures, the rate law of the n^{th}-order reaction may be approximated as:

$$-r_A = k_n C_A^n \tag{5.135}$$

Substituting into Eq. (5.134):

$$\frac{d}{dr}\left(-D_{\text{eff}}\left(\frac{dC_A}{dr}\right)r^2\right) + k_n C_A^n S_A \rho_c r^2 = 0 \tag{5.136}$$

Differentiating and dividing by $-r^2 D_{\text{eff}}$ gives the differential equation describing diffusion with reaction in a catalyst pellet:

$$\frac{d^2C_A}{dr^2} + \frac{2}{r}\left(\frac{dC_A}{dr}\right) - \frac{k_n C_A^n}{D_{\text{eff}}} = 0 \tag{5.137}$$

Focus 5.2: Three-dimensional modeling of reaction and transport in porous catalysts

Nowadays, and in contrast to the conventional one-dimensional models, reaction and transport within a porous catalyst are typically studied on the nano- and micro-scale using three-dimensional spatial models [9]. Prior to the application of mathematical modeling, the porous catalyst is first digitally reconstructed based on morphological characteristics obtained from transmission electron microscopy and scanning electron microscopy images. One three-dimensional model describing reaction and diffusion in a reconstructed catalyst was recently developed by Kočí et al. [9] based on the following assumptions: (1) the reactants and products are present in low concentration, (2) the pressure remains constant, and (3) the number of molecules in the system is sufficient enough to satisfy continuity requirements. In this three-dimensional model, the following balance of gas components ($k = 1, \ldots, K$) is considered:

$$\varepsilon^{\mu}\frac{\partial c y_k(X,Y,Z,t)}{\partial t} = D_{\text{eff},k}c\left(\frac{\partial^2 y_k}{\partial X^2}+\frac{\partial^2 y_k}{\partial Y^2}+\frac{\partial^2 y_k}{\partial Z^2}\right)+\sum_{j-1}^{J}\nu_{k,j}\bullet R_j$$

where ε^{μ} is the porosity of the meso-/micro-pores, c is the gas concentration, y is the mole fraction, D_{eff} is the effective diffusivity, v is the linear velocity, R is the reaction rate, and j is the reaction index.

Depending on the local pore size (i.e., mesopore or macropore), the effective diffusivity is calculated as follows:

$$D_{\text{eff},k} = \frac{\varepsilon^{\mu}}{\gamma^{\mu}}\frac{d^{\mu}}{3}\sqrt{\frac{8R^{g}T}{10^{3}W_k\pi}} \quad \text{for mesopores}$$

$$D_{\text{eff},k} = \frac{144.9T^{1.75}/P}{\sqrt{\frac{2}{\left(\frac{10^{-3}}{W_k}+\frac{10^{-3}}{W_{\text{ref}}}\right)}\left(\sigma_k^{\frac{1}{3}}+\sigma_{\text{ref}}^{\frac{1}{3}}\right)^2}} \quad \text{for macropores}$$

where γ is the tortuosity, d is the diameter, R^g is the universal gas constant, W is the molar weight, and σ is the volume diffusion coefficient.

Two boundary conditions are used with this model: constant components concentrations on the boundaries with the source of the reactants and zero flux on the other boundaries.

Results from the nano- and micro-levels may be quantitatively utilized in the macro-scale model to optimize the catalytic reactor design.

Focus 5.3: Structuring and processing of porous catalytic powders into pellets

In industrial applications of catalysis, the microporous catalytic powder must be structured into a macroscopic shape for effective utilization [10]. The macroscopic catalytic structure must possess some key features including the tendency to promote high flow rate and rapid

(*Continued*)

Focus 5.3: Structuring and processing of porous catalytic powders into pellets (Continued)

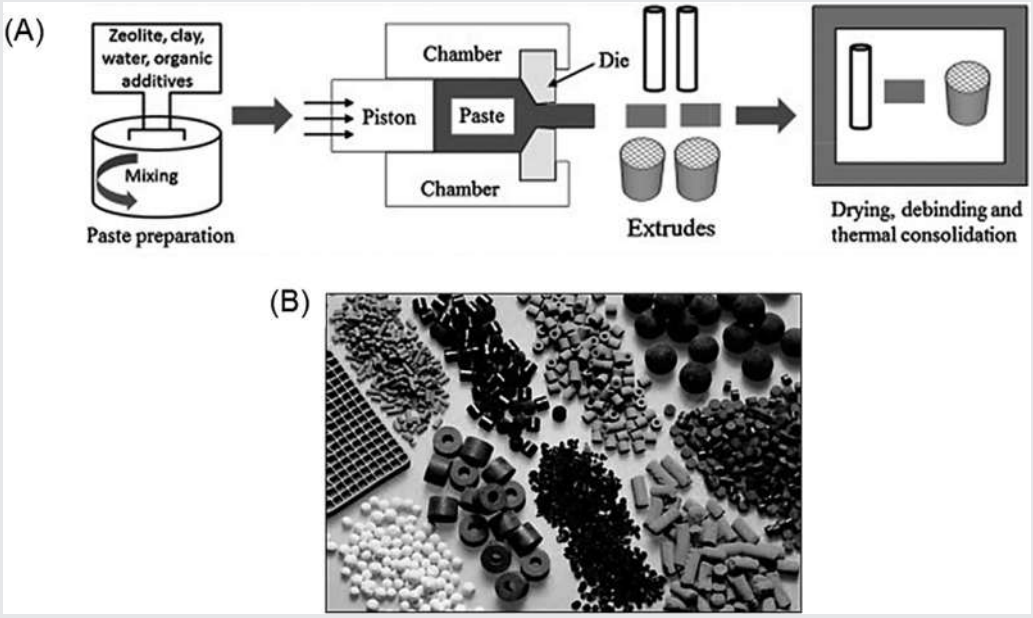

Figure 5.8

(A) Schematic representation of the extrusion process which is commonly used for the preparation of catalyst pellets. (B) Different geometries, shapes, and dimensions of solid catalyst pellets. Source: *(A) Reproduced from [10]. (B) Reproduced from [11].*

mass transport, as well as the ability to strongly resist mechanical and chemical wear. The main processing steps involved in the production of structured macroscopic catalysts include [10]:

1. mixing the porous powder with inorganic/organic additives,
2. shaping the powder into the desired preengineered shape, and
3. removing the additives and thermally treating the final catalyst to produce a mechanically strong structure.

The processing of porous catalytic powders into pellets may be achieved via a variety of different techniques including extrusion, slip and tape casting, foaming, gel casting, coating, spray drying, and dry pressing [10]. Among these, the most popular method used to structure and shape porous powders for catalytic applications is extrusion. Many of today's industrial catalysts are, in fact, being commercially produced via the process of extrusion, which is schematically presented in Fig. 5.8A. The different processing steps followed in extrusion include (1) preparation of the paste, (2) extrusion of the paste through a die, and finally (3) drying and thermal treatment of the extrudes. The molding paste is usually prepared by mixing the porous catalytic powder with inorganic/organic additives and a solvent (typically water). Inorganic binders, such as clays, alumina, and silica, are

(*Continued*)

Focus 5.3: Structuring and processing of porous catalytic powders into pellets (Continued)

added for two main reasons: to make the paste moldable and to increase the mechanical strength of the final product. On the other hand, organic binders, such as water-soluble cellulose products, polyethylene glycol, polyvinyl alcohol, and glycerine, are added to enhance the plasticity of the paste and to increase the strength of the extruded bodies [10].

Catalyst pellets prepared with smaller dimensions will help increase the degree of fluid mixing in PBRs. As a result, the heat transfer rates in the axial and the radial directions will also increase. Moreover, smaller pellets will increase the catalyst surface area per unit bed volume, consequently increasing the catalytic reaction rate. Despite the aforementioned, pellets with smaller dimensions will, unfortunately, also increase the pressure drop in the reactor [11]. Hence, a balance between heat transfer requirements and pressure drop limitations must be carefully considered when engineering the catalyst pellet geometry. As can be seen in Fig. 5.8B, a variety of different pellet shapes and dimensions with different heat transfer properties are widely available. This enables possible operation under conditions where heat transfer is maximized with a pressure drop value that is still within the acceptable range [11].

5.4.3 Thiele modulus

The differential equation, Eq. (5.137), derived in Section 5.4.2 to describe diffusion with reaction in a spherical catalyst pellet, can be rewritten in dimensionless form. First, the following two dimensionless variables are introduced, namely, a concentration and a radius [1]:

$$\psi = \frac{C_A}{C_{As}} \tag{5.138}$$

$$\lambda = \frac{r}{R} \tag{5.139}$$

Using the chain rule:

$$\frac{dC_A}{dr} = \frac{dC_A}{d\lambda}\frac{d\lambda}{dr} = \frac{d\psi}{d\lambda}\frac{dC_A}{d\psi}\frac{d\lambda}{dr} \tag{5.140}$$

Differentiating Eqs. (5.138) and (5.139) accordingly and substitution into Eq. (5.140) yield:

$$\frac{dC_A}{dr} = \frac{d\psi}{d\lambda}\frac{C_{As}}{R} \tag{5.141}$$

The molar flux W_A can now be written with dimensionless variables:

$$W_A = -D_{\text{eff}}\left(\frac{dC_A}{dr}\right) = \frac{-D_{\text{eff}}C_{As}}{R}\left(\frac{d\psi}{d\lambda}\right) \tag{5.142}$$

At steady state, the rate of consumption of A on the surface is equal to the molar flow rate of A to the surface [1]:

$$-r_A = W_A 4\pi R^2 = -4\pi R D_{\text{eff}} C_{As}\left(\frac{d\psi}{d\lambda}\right) \tag{5.143}$$

Using Eqs. (5.139) and (5.141):

$$\frac{d^2C_A}{dr^2} = \frac{d}{dr}\frac{dC_A}{dr} = \frac{d}{d\lambda}\left(\frac{d\psi}{d\lambda}\frac{C_{As}}{R}\right)\frac{d\lambda}{dr} = \frac{d^2\psi}{d\lambda^2}\frac{C_{As}}{R^2} \tag{5.144}$$

Substitution into Eq. (5.137) and dividing by C_{As}/R^2 give the dimensionless form of the differential equation that describes diffusion with reaction in a catalyst pellet:

$$\frac{d^2\psi}{d\lambda^2} + \frac{2}{\lambda}\left(\frac{d\psi}{d\lambda}\right) - \frac{k_n R^2 C_{As}^{n-1}\psi^n}{D_{\text{eff}}} = \frac{d^2\psi}{d\lambda^2} + \frac{2}{\lambda}\left(\frac{d\psi}{d\lambda}\right) - \Phi_{Th}^2\psi^n = 0 \tag{5.145}$$

where Φ_{Th} *is the Thiele modulus.* ${\Phi_{Th}}^2$ is a measure of the ratio of surface reaction rate to diffusion rate:

$$\Phi_{Th}^2 = \frac{k_n R^2 C_{As}^{n-1}}{D_{\text{eff}}} \tag{5.146}$$

The overall reaction rate is limited by internal diffusion at high Thiele moduli (i.e., when the particle diameter is very large). Conversely, the rate is limited by the surface reaction when the Thiele modulus is small (i.e., when the particle diameter is very small). Accordingly, at large Thiele modulus values, metal catalysts should be deposited on the external surface rather than within the interior of the porous pellet. This is because, when the reaction rate is limited by internal diffusion, the surface reaction is very rapid and the reactant is consumed mostly at the external pellet surface instead of in the interior [1].

For a first-order reaction, Eq. (5.145) can be solved by setting $y = \psi\lambda$ [1]:

$$\frac{d\psi}{d\lambda} = \frac{1}{\lambda}\left(\frac{dy}{d\lambda}\right) - \frac{y}{\lambda^2} \tag{5.147}$$

$$\frac{d^2\psi}{d\lambda^2} = \frac{1}{\lambda}\left(\frac{d^2y}{d\lambda^2}\right) - \frac{2}{\lambda^2}\left(\frac{dy}{d\lambda}\right) + \frac{2y}{\lambda^3} \tag{5.148}$$

Substitution into Eq. (5.145) yields:

$$\frac{d^2y}{d\lambda^2} - \Phi_{Th}^2 y = 0 \tag{5.149}$$

Differentiating:

$$y = A\cosh\Phi_{Th}\lambda + B\sinh\Phi_{Th}\lambda \tag{5.150}$$

Therefore:

$$\psi = \frac{A}{\lambda} cosh\Phi_{Th}\lambda + \frac{B}{\lambda} sinh\Phi_{Th}\lambda \tag{5.151}$$

At $\lambda = 0$ (i.e., $r = 0$), ψ is finite (i.e., C_A is finite and less than C_{AS}) and at $\lambda = 1$ (i.e., $r = R$), $\psi = 1$ (i.e., $C_A = C_{As}$) [1]. The constants A and B are evaluated using the aforementioned boundary conditions to give the dimensionless concentration profile:

$$\psi = \frac{C_A}{C_{As}} = \frac{1}{\lambda}\left(\frac{sinh\Phi_{Th}\lambda}{sinh\Phi_{Th}}\right) \tag{5.152}$$

5.4.4 Internal and overall effectiveness factors

The relative importance of diffusion and reaction limitations is indicated by the magnitude of the effectiveness factor—internal and overall. The *internal effectiveness factor,* η, measures how far a reactant can diffuse into a catalyst pellet before reacting. It is defined as the ratio of the actual overall reaction rate to the reaction rate that would result if the entire interior surface of the pellet was exposed to the external surface conditions (i.e., C_{As} and T_s) [1]:

$$\eta = \frac{-r_A}{-r_{As}} \tag{5.153}$$

As has been discussed previously in Section 5.4.3 (Eq. 5.143), the actual overall reaction rate is:

$$r_A = 4\pi R D_{\text{eff}} C_{As}\left(\frac{d\psi}{d\lambda}\right) \tag{5.154}$$

Differentiating Eq. (5.152) at $\lambda = 1$ (i.e., $r = R$) yields:

$$\frac{d\psi}{d\lambda} = \Phi_{Th} coth\Phi_{Th} - 1 \tag{5.155}$$

Substitution into Eq. (5.154) gives:

$$r_A = 4\pi R D_{\text{eff}} C_{As}(\Phi_{Th} coth\Phi_{Th} - 1) \tag{5.156}$$

The internal effectiveness factor can now be expressed as:

$$\eta = \frac{-r_A}{-r_{As}} = \frac{4\pi R D_{\text{eff}} C_{As}(\Phi_{Th} coth\Phi_{Th} - 1)}{\frac{4}{3}\pi R^3 k C_{As}} \tag{5.157}$$

Simplifying gives the internal effectiveness factor in the case of a first-order reaction for a spherical catalyst particle:

$$\eta = \frac{3(\Phi_{Th} coth\Phi_{Th} - 1)}{\Phi_{Th}^2} \tag{5.158}$$

The overall reaction rate is limited by internal diffusion when the internal effectiveness factor is small (i.e., when the Thiele modulus is large). Conversely, the rate is limited by the surface reaction when the internal effectiveness factor is large (i.e., when the Thiele modulus is small) [12–14]. For large values of the Thiele modulus, Eq. (5.158) can be written as:

$$\eta \cong \frac{3}{\Phi_{Th}} = \frac{3}{R}\sqrt{\frac{D_{\text{eff}}}{k}} \tag{5.159}$$

Using Eq. (5.153), the overall reaction rate can be expressed as:

$$-r_A = \eta k C_{As} = \frac{3C_{As}}{R}\sqrt{kD_{\text{eff}}} = \frac{3C_{As}}{R}\sqrt{k_1 S_A \rho_c D_{\text{eff}}} \tag{5.160}$$

From this expression, which applies to a first-order reaction, it can be deduced that the rate for a process limited by internal diffusion can be increased by (1) decreasing the pellet radius R, (2) increasing the reaction temperature, (3) increasing the concentration C_{As}, and (4) increasing the internal surface area S_A [1].

Similarly, the internal effectiveness factor for n^{th}-order reactions can be expressed as:

$$\eta = \frac{-r_A}{-r_{As}} = \frac{4\pi R D_{\text{eff}} C_{As}(\Phi_{Th} coth\Phi_{Th} - 1)}{\frac{4}{3}\pi R^3 k C_{As}^n} \tag{5.161}$$

In simpler terms, it may also be written as:

$$\eta = \left(\frac{2}{n+1}\right)^{1/2} \frac{3(\Phi_{Th} coth\Phi_{Th} - 1)}{\Phi_{Th}^2} \tag{5.162}$$

For large values of the Thiele modulus:

$$\eta \cong \left(\frac{2}{n+1}\right)^{1/2} \frac{3}{\Phi_{Th}} = \left(\frac{2}{n+1}\right)^{\frac{1}{2}} \left(\frac{3C_{As}^{\left(\frac{1-n}{2}\right)}}{R}\right)\sqrt{\frac{D_{\text{eff}}}{k}} \tag{5.163}$$

From this expression, it can be deduced that the effectiveness factor for $n > 1$ can be raised by decreasing the concentration C_{As}. Using Eq. (5.153), *the overall reaction rate can be expressed as*:

$$-r_A = \eta k C_{As}^n = \left(\frac{2}{n+1}\right)^{\frac{1}{2}} \frac{3kC_{As}^n}{\Phi_{Th}} = \left(\frac{2}{n+1}\right)^{\frac{1}{2}} \frac{3kC_{As}^n}{R}\sqrt{\frac{D_{\text{eff}} C_{As}^{(1-n)}}{k}} = \frac{3k^{\frac{1}{2}} C_{As}^{\left(\frac{n+1}{2}\right)}}{R}\sqrt{\frac{2D_{\text{eff}}}{n+1}} \tag{5.164}$$

Eq. (5.164) represents the true reaction rate with the true reaction order, n, and the true specific reaction rate constant, k. However, the measured reaction rate with the apparent reaction order, n', and the apparent rate constant, k', is [1]:

$$-r_A = k' C_{As}^{n'} \tag{5.165}$$

Equating the true reaction rate to the measured reaction rate gives:

$$-r_A = \frac{3k^{\frac{1}{2}}C_{As}^{\left(\frac{n+1}{2}\right)}}{R}\sqrt{\frac{2D_{\text{eff}}}{n+1}} = k'C_{As}^{n'} \tag{5.166}$$

The overall exponent of the concentration C_{As} must be the same for the true and the measured reaction rates [1]. As such:

$$n' = \frac{n+1}{2} \tag{5.167}$$

Rewriting the specific reaction rate constants of Eq. (5.166) in terms of activation energies gives:

$$-r_A = \frac{3\left(A_T\exp\left(\frac{-E_T}{RT}\right)\right)^{\frac{1}{2}}C_{As}^{\left(\frac{n+1}{2}\right)}}{R}\sqrt{\frac{2D_{\text{eff}}}{n+1}} = \left(A_{\text{App}}\exp\left(\frac{-E_{\text{App}}}{RT}\right)\right)C_{As}^{n'} \tag{5.168}$$

Taking the natural log of both sides:

$$ln\left[\frac{3(A_T)^{\frac{1}{2}}C_{As}^{\left(\frac{n+1}{2}\right)}}{R}\sqrt{\frac{2D_{\text{eff}}}{n+1}}\right] - \left(\frac{E_T}{2RT}\right) = \ln\left[\left(A_{\text{App}}\right)C_{As}^{n'}\right] - \left(\frac{E_{\text{App}}}{RT}\right) \tag{5.169}$$

Equating the temperature-dependent terms on the right-hand side and the left-hand side:

$$E_T = 2E_{\text{App}} \tag{5.170}$$

Differences between the true and the measured reaction rates typically arise in reactions limited by internal diffusion [1].

Effectiveness factor values greater than 1 are typically observed only in exothermic reactions taking place in nonisothermal reactors. Under such conditions, the temperature of the external pellet surface is lower than the one inside the pellet where an exothermic reaction is occurring. Thus the reaction rate inside the pellet is greater than the one at the surface and, as per its definition, the internal effectiveness factor will exceed 1. This however depends on two parameters: γ, which is the Arrhenius number, and β, which is the maximum difference in temperature that could exist in the pellet relative to the surface temperature [15]:

$$\gamma = \frac{E}{RT_s} \tag{5.171}$$

$$\beta = \frac{\Delta T_{\max}}{T_s} = \frac{T_{\max} - T_s}{T_s} \tag{5.172}$$

Fig. 5.9 shows how the internal effectiveness factor, η, and the Thiele modulus, Φ_{Th}, depend on γ and β for a nonisothermal reaction. When the internal effectiveness factor is greater than 1, multiple steady states can exist. In 1968, Dan Luss developed the

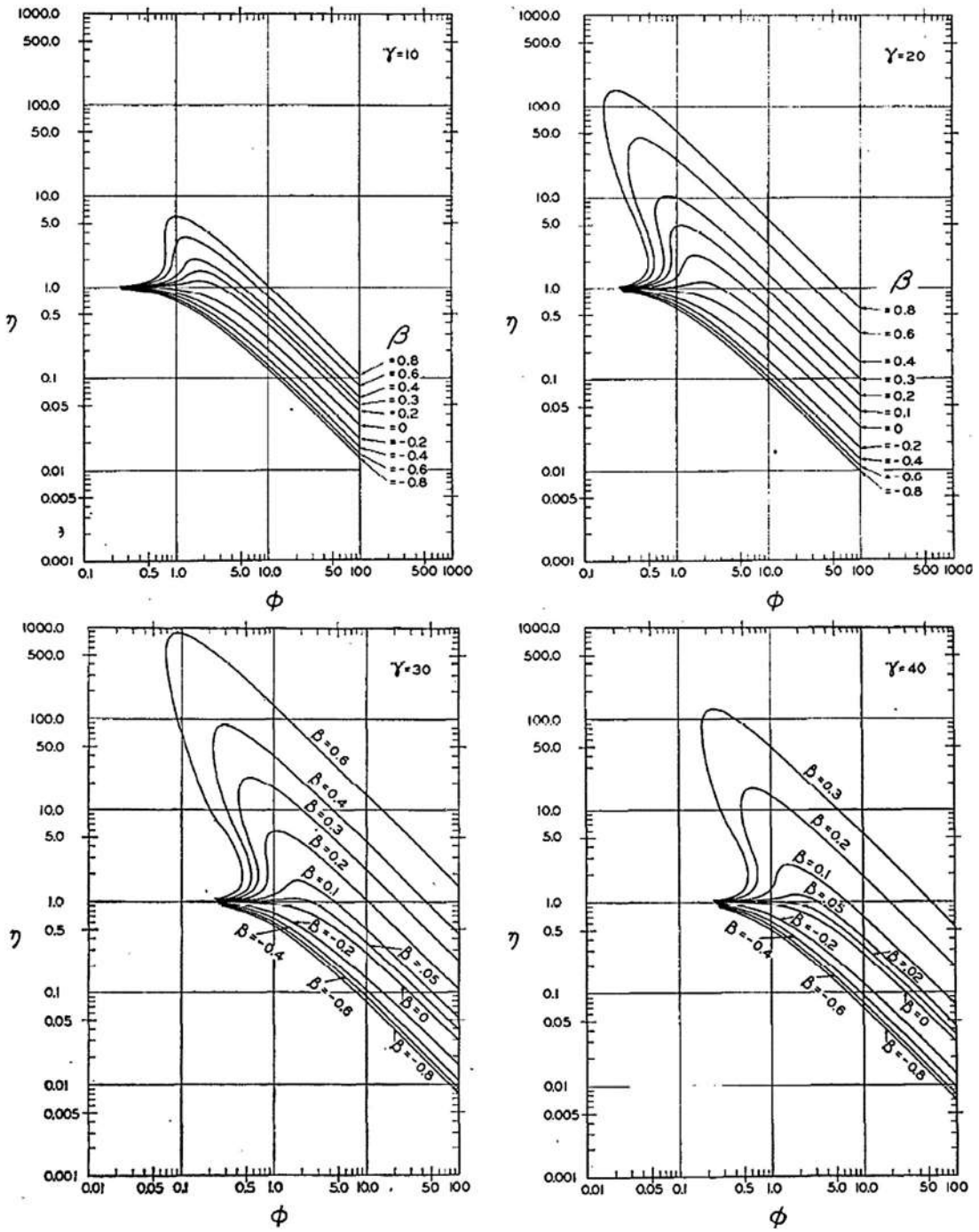

Figure 5.9

Dependency of the internal effectiveness factor, η, and the Thiele modulus, Φ, on γ and β for a nonisothermal reaction. γ represents the Arrhenius number and β is the highest ΔT that could exist in the pellet with respect to the surface temperature. Source: *Reproduced from [15].*

following criterion that must be fulfilled in order to ensure that multiple steady states do not exist in the pellet [16]:

$$4(1+\beta) > \beta\gamma \tag{5.173}$$

In Section 5.4.2, the external resistance to mass transfer was neglected when considering a reactant species, A, diffusing and then reacting inside a spherical catalyst pellet. Now, consider diffusion with reaction in a catalyst pellet where both internal and external diffusion cannot be neglected. At steady state, the rate of mass transfer from the bulk to the external pellet surface is equal to the rate of reaction on and within the pellet [1]:

$$W_A a_c \Delta V = -r_A(a_c \Delta V + S_A \rho_b \Delta V) \tag{5.174}$$

where ρ_b is the bulk density of the catalyst. Simplifying:

$$W_A a_c = -r_A(a_c + S_A \rho_b) \tag{5.175}$$

However, the internal surface area of most catalysts is much larger than the external one [1]. Hence:

$$W_A a_c = -r_A S_A \rho_b \tag{5.176}$$

Using Eq. (5.153), the reaction rate can be rewritten in terms of internal effectiveness factor and surface concentration:

$$W_A a_c = \eta k C_{As} S_A \rho_b \tag{5.177}$$

Moreover, the molar flux of A from the bulk to the external pellet surface is defined as:

$$W_A = k_C(C_{Ab} - C_{As}) \tag{5.178}$$

Substitution into Eq. (5.177) gives:

$$k_C a_c (C_{Ab} - C_{As}) = \eta k C_{As} S_A \rho_b \tag{5.179}$$

Solving to give the surface concentration as a function of the bulk concentration:

$$C_{As} = \frac{k_C a_c C_{Ab}}{k_C a_c + \eta k S_A \rho_b} \tag{5.180}$$

Using Eqs. (5.153) and (5.180), the overall reaction rate can be expressed as:

$$-r_A = \eta k C_{As}^n = \frac{\eta k k_C a_c C_{Ab}}{k_C a_c + \eta k S_A \rho_b} \tag{5.181}$$

Dividing the numerator and the denominator by $k_C a_c$ yields:

$$-r_A = \frac{\eta k C_{Ab}}{1 + \frac{\eta k S_A \rho_b}{k_C a_c}} = \Omega k C_{Ab} \tag{5.182}$$

where Ω *is the overall effectiveness factor*. It is defined as the ratio of the actual overall reaction rate to the reaction rate that would result if the entire surface of the pellet was exposed to the bulk conditions (i.e., C_{Ab} and T_b) [1]:

$$\Omega = \frac{-r_A}{-r_{Ab}} \tag{5.183}$$

5.4.5 Weisz–Prater and the Mears criteria

To determine if internal diffusion is limiting the overall reaction rate, the Weisz–Prater criteria is used [1]. Previously, the internal effectiveness factor for a first-order reaction in a spherical catalyst pellet was shown to be:

$$\eta = \frac{3(\Phi_{Th} coth \Phi_{Th} - 1)}{\Phi_{Th}^2} \tag{5.184}$$

Rearranging gives:

$$\eta \Phi_{Th}^2 = 3(\Phi_{Th} coth \Phi_{Th} - 1) \tag{5.185}$$

The left-hand side defines the Weisz–Prater parameter, C_{WP}:

$$C_{\mathrm{WP}} = \eta \Phi_{Th}^2 \tag{5.186}$$

Substituting Eq. (5.146) and Eq. (5.153) into Eq. (5.186) gives:

$$C_{\mathrm{WP}} = \frac{-r_A}{-r_{As}}\left(\frac{kR^2}{D_{\mathrm{eff}}}\right) = \frac{-r_A}{-r_{As}}\left(\frac{k_1 S_A \rho_c R^2}{D_{\mathrm{eff}}}\right) = \frac{-r_A}{-r_{As}}\left(\frac{-r_{As}\rho_c R^2}{C_{As} D_{\mathrm{eff}}}\right) = \frac{-r_A \rho_c R^2}{C_{As} D_{\mathrm{eff}}} \tag{5.187}$$

Internal diffusion will severely limit the reaction if the Weisz–Prater parameter is greater than 1. Conversely, internal diffusion will not limit the reaction (i.e., no concentration gradient will exist within the pellet) if the Weisz–Prater parameter is less than 1 [1].

To determine if external diffusion is limiting the overall reaction rate, the *Mears' criteria* is used. In 1971, Mears proposed that external diffusion is limiting if [17]:

$$\frac{-r_A \rho_b R n}{k_C C_{Ab}} > 0.15 \tag{5.188}$$

Focus 5.4: Numerical example on the identification of internal/external diffusion as overall reaction rate limitation

The first-order gas-phase catalytic decomposition of ozone (A) to oxygen is carried out over a spherical MnO_2 catalyst with a diameter of 3.342 mm. Ozone is to first diffuse from the bulk to the surface of the catalyst and then into the catalyst pores. Given that the mass transfer

(*Continued*)

Focus 5.4: Numerical example on the identification of internal/external diffusion as overall reaction rate limitation (Continued)

coefficient is 420 $m^3\ h^{-1}$ per m^2.cat and that the concentration of ozone at the catalyst surface is 31.02 mol m^{-3}, determine if the overall reaction rate is limited by external or internal diffusion. The experimental reaction rate ($-r_A$) was observed to be 3×10^4 mol h^{-1} per m^3.cat. The effective diffusivity of ozone inside the catalyst particle is $6.5 \times 10^{-5}\ m^3\ h^{-1}$ per m.cat.

Solution

To check if external diffusion is limiting the overall reaction rate, we need to compare the observed rate with the external diffusion-limited rate. If the two rates are of the same order of magnitude, then we may say that the external diffusion is limiting the rate. On the other hand, if the observed rate is much smaller, then we may ignore the resistance to mass transport across the bulk. Given the diameter, the volume (V_p) and the external surface area (a) of the spherical catalyst may be calculated to be $1.95 \times 10^{-8}\ m^3$ and $3.51 \times 10^{-5}\ m^2$, respectively. Then,

$$\frac{\text{observed rate}}{\text{external diffusion limited rate}} = \frac{kV_p}{k_C a} = \frac{\frac{-r_A}{C_{As}}V_p}{k_C a} = \frac{\frac{3\times10^4}{31.02}\left(1.95\times10^{-8}\right)}{420\left(3.51\times10^{-5}\right)} = 0.00128$$

The external diffusion-limited rate is much higher than the observed rate. Hence, it may be concluded that the overall reaction rate is NOT limited (or controlled) by external diffusion. As a matter of fact, and in almost all heterogeneous catalytic reactions, external diffusion is unlikely to influence the reaction rate of the porous catalyst [18].

To determine if internal diffusion is limiting the overall reaction rate, the Weisz–Prater criteria is used. From Eq. (5.187),

$$C_{WP} = \frac{-r_A R^2}{C_{As} D_{\text{eff}}} = \frac{3\times10^4 \times \left(1.671\times10^{-3}\right)^2}{31.02\times6.5\times10^{-5}} = 45$$

Internal diffusion severely limits the overall reaction rate since the Weisz–Prater parameter is greater than 1.

5.5 Multiple steady states and thermal hysteresis

Highly exothermic heterogeneous catalytic reactions, such as the oxidation of ammonia, usually *display more than one single steady state*. If the heat generation rate, Q_g, in a catalyst pellet of volume V_p is equal to the heat loss rate, Q_l, from an external surface area a, then a steady state of thermal equilibrium is achieved under which the reactor can operate continuously. For a first-order reaction, and neglecting diffusion effects, the heat generation rate is [19]:

$$Q_g = V_p(-\Delta H)kc_i \tag{5.189}$$

where k is a temperature-dependent rate constant, $-\Delta H$ is the heat of the reaction, and c_i is the concentration at the interface. At steady state, the reaction rate is equal to the mass flux,

and therefore:

$$V_p k c_i = h_D a (c_g - c_i) \tag{5.190}$$

where h_D is the mass transfer coefficient and c_g is the concentration of the gas in the bulk.

The heat loss rate is [19]:

$$Q_l = ha(T_i - T_g) \tag{5.191}$$

where h is the heat transfer coefficient and T_i is the temperature at the interface.

As shown in Fig. 5.10, a steady state is attained at every point where the heat generation rate is equal to the heat loss rate. Points A and C represent stable steady-state conditions, while point B is considered to be a metastable state. This is because, for points A and C, an upward perturbation in temperature would result in a heat generation that is less than the heat lost. On the other hand, a downward perturbation in temperature would result in a heat generation that is greater than the heat lost. Hence, *the system, if operating at point A or C, is said to be self-compensating*. For point B, however, an upward perturbation in temperature would result in a heat generation that is more than the heat lost. Consequently, the temperature of the reactor system will continue to rise until the stable steady state at point C is reached. Alternatively, a downward perturbation in temperature would result in a heat generation that is less than the heat lost. Accordingly, the reaction will reach the stable point A with a minimal conversion of the reactant(s) [19].

Depending on the direction of perturbation, the catalytically reacting system can move from one steady state to another. The path followed by the system as it adjusts to thermal

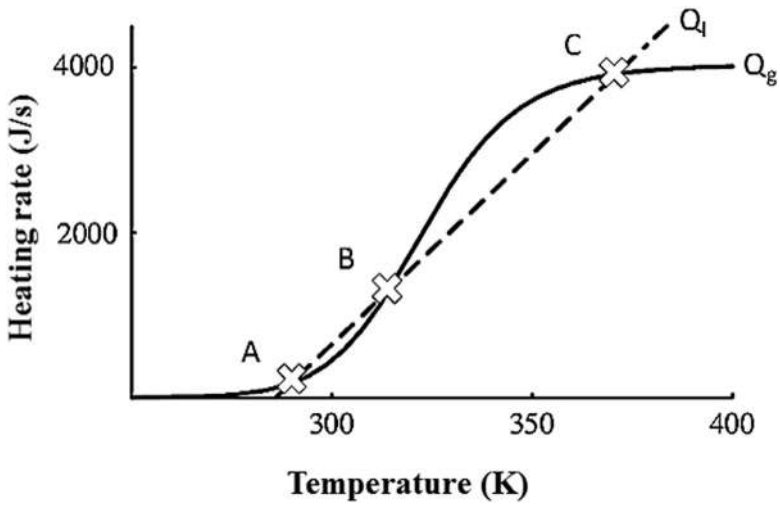

Figure 5.10

Heat generation rate, Q_g, and heat loss rate, Q_l, as a function of reactor temperature. Points A, B, and C represent all possible steady-state conditions. Source: *Reproduced from [20].*

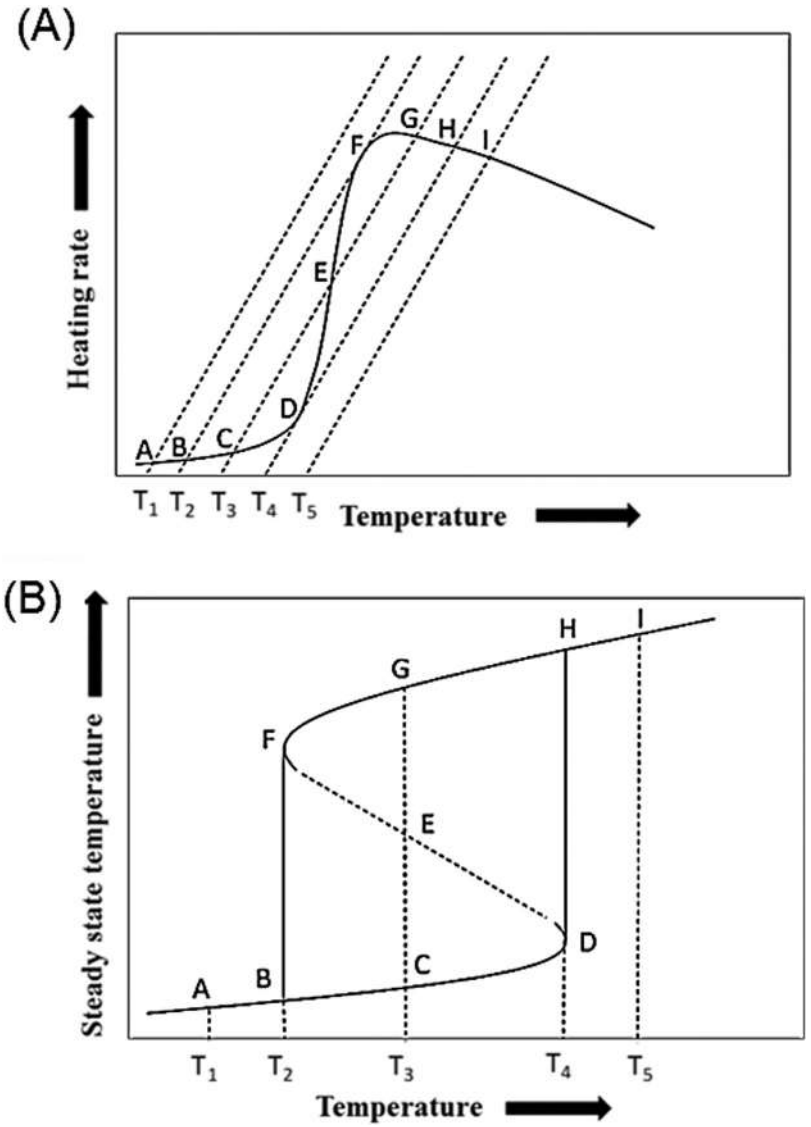

Figure 5.11

(A) Heat generation rate and heat loss rates as a function of reactor temperature. Each heat loss curve represents the heat loss rate for a given gas-phase temperature (T_1 to T_5). Points A to I represent all possible steady-state conditions. (B) Diagram illustrating a thermal hysteresis.

changes leads to the phenomena of hysteresis. For instance, consider Fig. 5.11A shows a number of heat loss curves, each representing the heat loss rate for a given gas-phase temperature. If the gas-phase temperature is increased from T_1 to T_5, the system will proceed through the following sequence of stable steady-state points: A, B, F, G, H, and I. Conversely, if the gas-phase temperature is decreased from T_5 to T_1, then the system will

follow the path I, H, D, C, B, and A, sequentially. A plot of the steady-state temperature at the interface as a function of gas-phase temperature (Fig. 5.11B) clearly shows that the path followed as the temperature increases is different than the one followed as temperature decreases, that is, a thermal hysteresis takes place [19].

Focus 5.5: Numerical example on the calculation of ΔT between the surface of the catalyst and the surrounding bulk

For the reaction described in Focus 5.4, calculate the variation in temperature between the surface of the catalyst and the surrounding bulk. Note that the heat of the reaction is −260 kJ mol^{-1} and that the heat transfer coefficient is 260 kJ h^{-1} K^{-1}per m^2.cat.

Solution

Equating the rate of heat removal across the bulk (Eq. 5.191) with the rate of heat generation by reaction within the catalyst (Eq. 5.189) and solving for $(T_i - T_g)$,

$$(T_i - T_g) = \frac{V_p(-\Delta H)kc_{AS}}{ha} = \frac{V_p(-\Delta H)(-r_A)}{ha} = \frac{1.95 \times 10^{-8} \times 260 \times 3 \times 10^4}{260 \times 3.51 \times 10^{-5}} = 16.67\text{K}$$

The results indicate that the catalyst surface is hotter than the surrounding fluid by c. 17K.

5.6 Catalyst deactivation and regeneration

In most industrial catalytic reactions, the total *concentration of catalytic sites available for the reaction changes with time* [1]. As the reaction proceeds on the surface of a catalyst, a loss in the catalytic activity is commonly observed [21,22]. Rate laws derived earlier in this chapter must therefore be adjusted to account for catalyst deactivation. As such, a term representing the activity of the catalyst at time t, $a(t)$, is introduced and is defined as the *ratio of the reaction rate of a used catalyst at time t to the reaction rate of a fresh catalyst at* $t = 0$ [1]:

$$a(t) = \frac{-r_A(t)}{-r_A(t=0)} \tag{5.192}$$

The rate of disappearance of reactant A, $-r_A$, expressed according to a reaction rate law which considers the decay of the activity is given as:

$$-r_A = a(t)k(T)f(C_A, C_B, \ldots) \tag{5.193}$$

The rate of decay, r_d, is also introduced and is defined as:

$$r_d = -\frac{da}{dt} = p[a(t)]k_d(T)h(C_A, C_B, \ldots) \tag{5.194}$$

where $p[a(t)]$ *is a function of the activity*, k_d *is the specific decay constant*, and $h(C_i)$ is a function of the concentrations of the reacting species. For first-order decay, $p(a) = a$.

Similarly, for second-order decay, $p(a) = a^2$. The function h can be independent ($h = 1$) or linearly dependent ($h = C_i$) with respect to concentration.

Deactivation of a catalyst can derive from one or more of the following three phenomena: sintering (aging) [23], fouling (coking) [24], and poisoning [25]. In sintering, prolonged exposure to high temperatures leads to a loss of active surface area and, consequently, a loss in catalytic activity. At high temperatures, crystals may agglomerate, deposited metals may grow, and pores may shrink [1]. As a result, a certain fraction of active surface area is lost. Fig. 5.12A shows how small metal atoms deposited on a surface can migrate and agglomerate into larger clusters with less surface area. Nonetheless, sintering can be avoided if the reaction is operated at temperatures that are at least 30%–40% below the melting temperature of the catalyst [27].

A second-order decay is most commonly observed in deactivations caused by sintering [1]. Hence, the sintering decay rate law is:

$$r_d = -\frac{da}{dt} = k_d a^2 \tag{5.195}$$

Integrating with $a(t = 0) = 1$:

$$a(t) = \frac{1}{1 + k_d t} \tag{5.196}$$

The sintering decay constant, k_d, is defined according to the Arrhenius equation as:

$$k_d = k_d(T_0)\exp\left[\frac{E_d}{R}\left(\frac{1}{T_0} - \frac{1}{T}\right)\right] \tag{5.197}$$

where E_d is the decay activation constant.

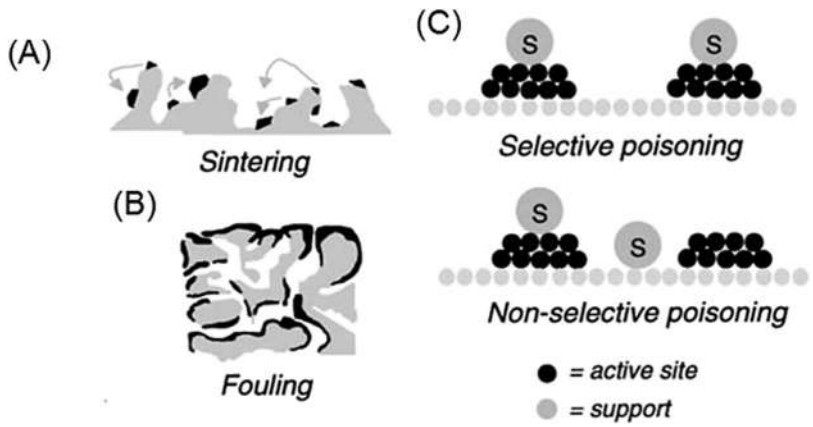

Figure 5.12
The three major categories of deactivation in heterogeneous catalysis: (A) sintering (aging), (B) fouling (coking), and (C) poisoning. Source: *Reproduced from [26].*

The decrease in active surface area, S_a, represents the extent of deactivation by sintering and can be measured as follows:

$$s_a = \frac{S_{a0}}{1 + k_d t} \tag{5.198}$$

In *fouling* (Fig. 5.12B), the active surface area is lost due to the deposition of coke (a carbonaceous material) on the catalyst surface [1]. Consequently, the catalyst decays and the catalytic activity diminishes. Catalytic reactions involving hydrocarbons, such as the cracking of cumene to yield benzene and propylene [28], are typically deactivated by fouling. To minimize fouling, the reaction can be run at elevated pressures and/or with hydrogen-rich streams [29–31]. More importantly, catalysts deactivated as a result of coke formation can be regenerated, usually by burning off the carbon [1].

In 1945, Voorhies developed an empirical relationship to express the concentration of carbon deposited on a surface, C_C, at time t [32]:

$$C_C = At^n \tag{5.199}$$

where A and n are some fouling parameters. For the fouling decay rate law, many different models have been investigated and they include [1]:

$$a = \frac{1}{1 + k_{Ck} C_c^p} \tag{5.200}$$

$$a = \exp(-\alpha_1 C_C) \tag{5.201}$$

$$a = \frac{1}{1 + \alpha_2 C_C} \tag{5.202}$$

In *poisoning*, a loss in the surface area occurs when a molecule, S, irreversibly chemisorbs onto the active sites of a catalyst as demonstrated in Fig. 5.12C. Impurities in the feed stream, like the ones commonly present in petroleum feedstock, can cause deactivation by poisoning. Alternatively, in other situations, reactants and/or products of the catalytic reaction carried out may, themselves, act as poisoning species. In the Sabatier reaction where methane is formed over a ruthenium catalyst, the main reactants, carbon monoxide and hydrogen, have been shown to poison the active catalytic surface [1,33].

For the case where poison P is an impurity in the feed, the poisoning decay rate law is given as [1]:

$$r_d = -\frac{da}{dt} = k'_d C_P^m a^q \tag{5.203}$$

where k'_d is the decay rate constant, C_P is the concentration of poison P and a is the activity of the catalyst. The poison removal rate, $r_{P \cdot S}$, from the gas stream toward the catalyst

surface is proportional to the concentration of un-poisoned sites and also to the concentration of poison in the gas phase, C_P:

$$r_{P\cdot S} = k_d C_P (C_{t0} - C_{P\cdot S}) \tag{5.204}$$

where C_{t0} is the initial total concentration of available sites and $C_{P\cdot S}$ represents the concentration of poisoned sites. The poison adsorption rate, $r_{P\cdot S}$, is also equal to the deactivation rate of the total active sites, C_t:

$$-\frac{dC_t}{dt} = \frac{dC_{P\cdot S}}{dt} = r_{P\cdot S} = k_d C_P (C_{t0} - C_{P\cdot S}) \tag{5.205}$$

Dividing by C_{t0}:

$$\frac{df}{dt} = k_d C_P (1 - f) \tag{5.206}$$

where λ represents the fraction of poisoned sites and $(1 - f)$ represents the fraction of available sites. Since the fraction of available sites is basically the activity, $a(t)$, then Eq. (5.206) becomes:

$$-\frac{da}{dt} = k_d C_P a(t) \tag{5.207}$$

For the case where reactant A is the poison, the poisoning decay rate law is given as [1]:

$$r_d = -\frac{da}{dt} = k'_d C_A^m a^q = k'_d C_A a(t) \tag{5.208}$$

Depending on the speed of catalytic activity loss, three different types of reactors have been developed to handle systems with decaying catalysts [1]. In systems where the decay rate is relatively slow, constant conversion is maintained by gradually increasing the temperature of the feed as illustrated in Fig. 5.13A. In turn, the reaction rate increases and the conversion continues [34]. Large-scale hydrotreating reactors and reactions deactivated by poisoning exhibit this type of slow catalytic decay behavior. In 1979, Krishnaswamy and Kittrell developed the temperature-time trajectory expression showing that the temperature of a catalytic reactor, T, has to be increased over time, t, to maintain a constant conversion [37]:

$$t = \frac{1 - \exp\left[\frac{E_A - nE_A + E_d}{R}\left(\frac{1}{T} - \frac{1}{T_0}\right)\right]}{k_{d0}\left(1 - n + \frac{E_d}{E_A}\right)} \tag{5.209}$$

where E_A is the activation energy of the reaction, E_d *is the activation energy of the catalyst decay*, k_{d0} *is the decay constant at* T_0 *and* n *is the decay order.*

In systems where the decay rate is somewhat moderate, production is maintained through the utilization of a *moving-bed reactor* [1]. Catalytic cracking reactors and reactions deactivated by

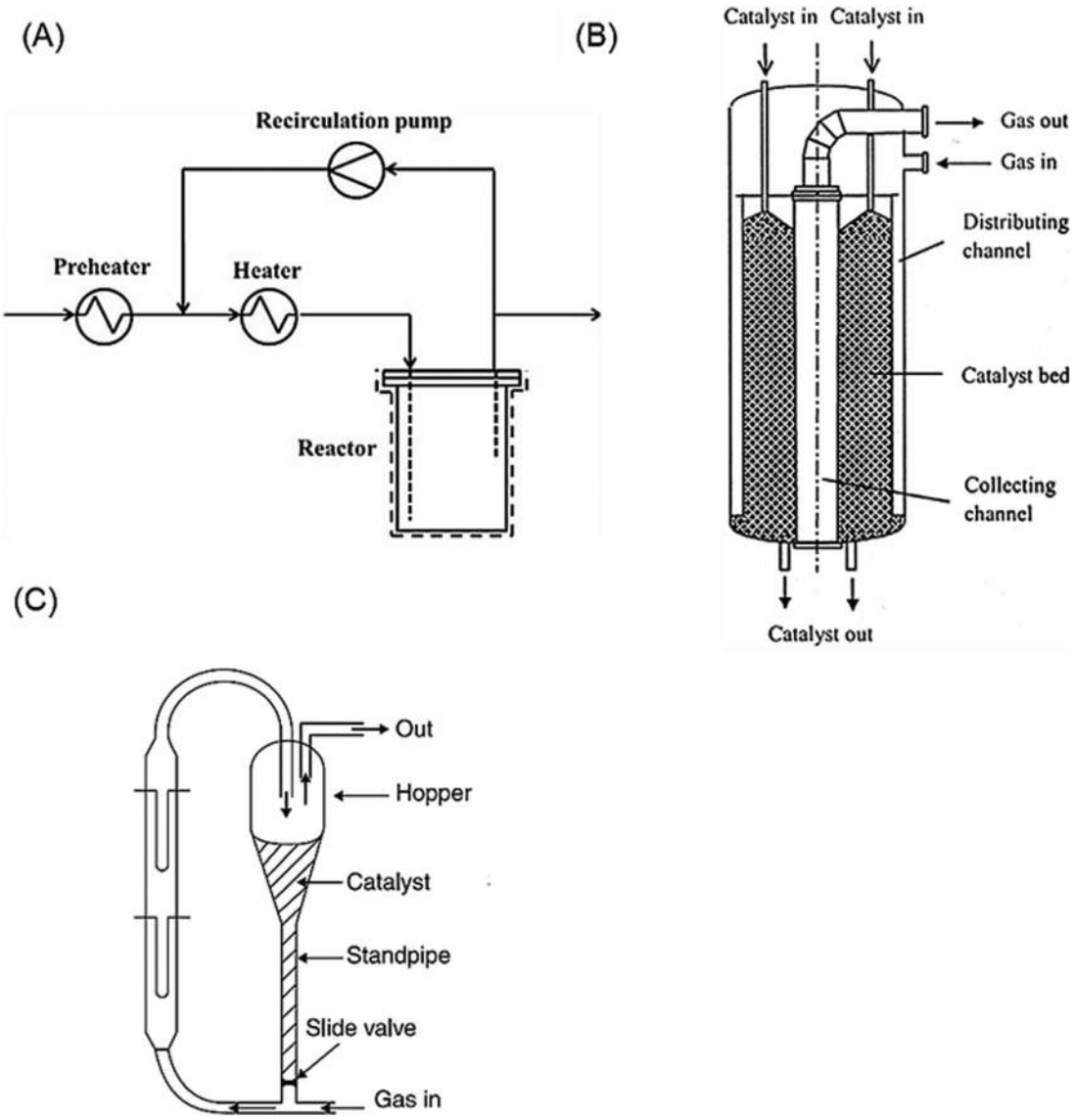

Figure 5.13

(A) Reactor with a preheater to increase the temperature of the feed. (B) Moving-bed reactor. (C) Straight-through transport reactor. Source: *Reproduced from [34–36].*

fouling typically exhibit this type of moderate catalytic decay behavior. As schematically shown in Fig. 5.13B, fresh catalyst enters the reactor from the top and moves downward through the reactor as a compact packed bed. As it moves downward, the catalyst is steadily deactivated by coking until it exits the reactor at the bottom. Subsequently, the catalyst is regenerated by burning off the carbon and is then recycled back to the top of the reactor. The reacting gas also enters the

reactor from the top and flows through the reactor with a relatively faster flow rate than that of the moving catalyst [35]. For moving-bed reactors where U_s is the flow rate of the catalyst, the decay rate law is expressed as [1]:

$$-\frac{d_a}{d_W} = \frac{k_d}{U_s} a^n \tag{5.210}$$

where W is the catalyst weight.

In systems where the decay rate is very fast, a *straight-through transport reactor* (Fig. 5.13C) is used to offset the loss in catalytic activity [1]. This type of rapid catalyst decay occurs in catalytic cracking reactors and when catalysts are deactivated by fouling. Here, the catalyst and the feed gas enter the reactor together and move through the reactor at a very high flow rate [36]. The coking decay rate law in straight-through transport reactors, more recently known as circulating FBRs, is described as [1]:

$$a = \frac{1}{1 + At^n} = \frac{1}{1 + A\left(\frac{z}{U}\right)^n} \tag{5.211}$$

with t being the time a catalyst, traveling at a velocity of U, has spent inside the reactor when it reached a height of z.

One of the most common examples of catalyst regeneration processes is the reactivation of a fouled catalyst pellet through the burning off of carbon [30,38]. As shown in Fig. 5.14A, the removal of carbon first begins from the outer surface of the spherical catalyst and then, with time, moves inward toward the center core depicting a shrinking-shell behavior [39]. In order for the regeneration reaction to keep on progressing, oxygen must continually diffuse farther into the porous catalyst pellet to reach the unreacted carbon core. Increasing the concentration of oxygen and the temperature of the reaction can help in reducing the time required to burn off all of the carbon from the catalyst [1].

Consider the following carbon removal reaction taking place at the surface of a catalyst particle:

$$C + O_2 \rightarrow CO_2 \tag{5.212}$$

The unreacted carbon core is represented in Fig. 5.14B *with a radius of* r_c. The intermediate layer between R and r_c represents carbon that has been removed from the porous matrix. Oxygen diffuses from the outer radius R to the core radius r_c, where it reacts with carbon to form carbon dioxide, which then diffuses out of the pellet matrix [39]. The diffusion rate of oxygen to the surface is very slow in comparison to the reaction rate of carbon removal and, as such, the overall reaction is said to be mass transfer limited. The concentration profile of carbon in the intermediate layer at any time instant is assumed to be steady state [1].

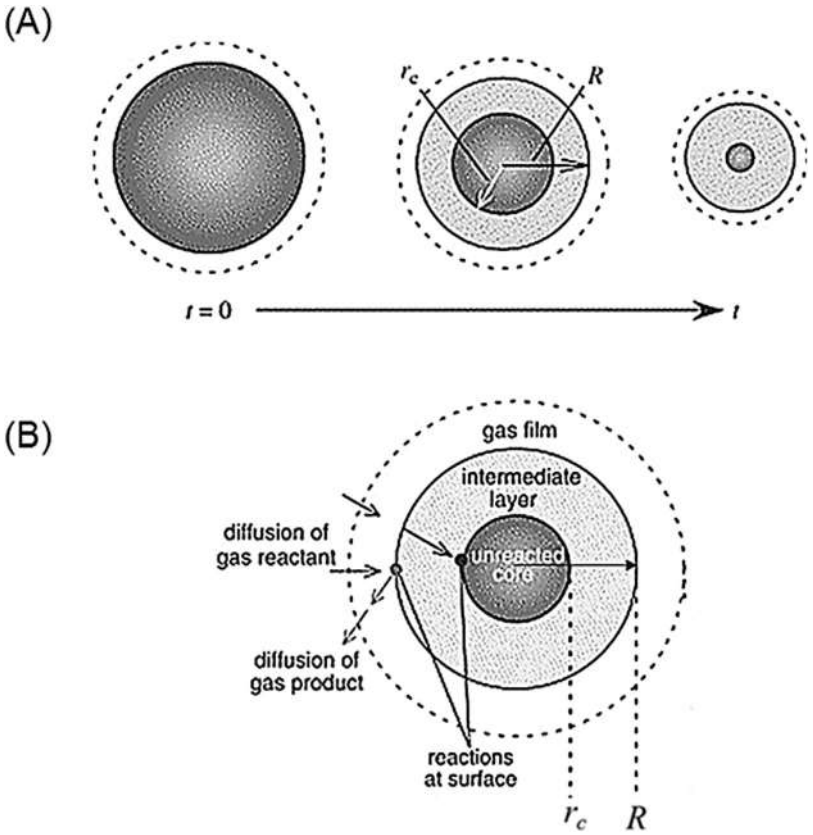

Figure 5.14
(A) Schematic diagram illustrating the progressive regeneration of a fouled catalyst pellet. (B) Schematic diagram illustrating the reaction model used to describe carbon removal. Source: *Reproduced from [39].*

To describe the kinetics of catalyst regeneration, the shrinking core model is applied [1]. A differential oxygen mole balance over an increment Δr located in the intermediate layer gives:

$$F_A|_r - F_A|_{r+\Delta r} = 0 \tag{5.213}$$

where F_A is the molar flow rate of oxygen and is defined as the product of the molar flux W_A and the cross-sectional area A_c:

$$F_A = W_A A_c = W_A(4\pi r^2) \tag{5.214}$$

Substitution into Eq. (5.213) yields:

$$W_A 4\pi r^2|_r - W_A 4\pi r^2|_{r+\Delta r} = 0 \tag{5.215}$$

Dividing by $-4\pi\Delta r$ and taking the limit as Δr approaches zero gives the mole balance on oxygen:

$$\frac{d(W_A r^2)}{dr} = 0 \tag{5.216}$$

The molar flux W_A is:

$$W_A = -D_{\text{eff}}\left(\frac{dC_A}{dr}\right) \tag{5.217}$$

where D_{eff} is the effective diffusivity. Substituting into Eq. (5.216) yields:

$$\frac{d}{dr}\left(-D_{\text{eff}}\left(\frac{dC_A}{dr}\right)r^2\right) = 0 \tag{5.218}$$

Dividing by $-D_{\text{eff}}$:

$$\frac{d}{dr}\left(\left(\frac{dC_A}{dr}\right)r^2\right) = 0 \tag{5.219}$$

Integration yields:

$$C_A = \frac{-K_1}{r} + K_2 \tag{5.220}$$

Since $C_A = C_{A0}$ at $r = R$ and $C_A = 0$ at $r = r_c$, K_1 and K_2 may be replaced to give the concentration profile of oxygen as a function of radius, r:

$$\frac{C_A}{C_{A0}} = \frac{\frac{1}{rc} - \frac{1}{r}}{\frac{1}{rc} - \frac{1}{R}} \tag{5.221}$$

Solving for C_A, substituting in Eq. (5.217), and integrating:

$$W_A = -D_{\text{eff}}\left(\frac{dC_A}{dr}\right) = \frac{-D_{\text{eff}}C_{A0}}{\left(\frac{1}{rc} - \frac{1}{R}\right)r^2} \tag{5.222}$$

An overall mole balance on the shrinking carbon core gives:

$$r_B 4\pi r_c^2 = \frac{d\left(\frac{4}{3}\pi r_c^3 \rho_C \Phi_C\right)}{dt} \tag{5.223}$$

where ρ_C is the molar density of carbon and Φ_C is the volume fraction of carbon. Simplifying yields:

$$\frac{dr_c}{dt} = \frac{r_B}{\rho_C \Phi_C} \tag{5.224}$$

Setting the rate of carbon disappearance, $-r_B$, equal to the rate of oxygen flux, W_A, at $r = r_c$:

$$-r_B = -W_A = \frac{D_{\text{eff}} C_{A0}}{\left(r_c - \frac{r_c^2}{R}\right)} \tag{5.225}$$

Substitution in Eq. (5.224) yields:

$$-\frac{dr_c}{dt} = \frac{D_{\text{eff}} C_{A0}}{\rho_C \Phi_C} \left(\frac{1}{\left(r_c - \frac{r_c^2}{R}\right)} \right) \tag{5.226}$$

Integrating with $r_c = R$ at $t = 0$ gives the time required for the carbon core to reduce to a radius of r_c:

$$t = \frac{\rho_C \Phi_C R^2}{6 D_{\text{eff}} C_{A0}} \left(1 - 3\left(\frac{r_c}{R}\right)^2 + 2\left(\frac{r_c}{R}\right)^3 \right) \tag{5.227}$$

The time needed to complete a full catalyst regeneration, or to remove all carbon in the pellet, is:

$$t = \frac{\rho_C \Phi_C R^2}{6 D_{\text{eff}} C_{A0}} \tag{5.228}$$

5.7 Questions and problems

1. A ceramic monolith catalyst has a honeycomb structure and is used with gaseous reactants-products.
   a. Explain under which conditions you have: bulk diffusion; Knudsen diffusion; transitional region and forced flow in pores.
   b. How would you prevent diffusion-controlled regimes in favor of reaction control?
2. Explain the relationship among a catalyst particle size, the Thiele modulus, the effectiveness factor, and the catalyst amount. How can you use this information to design a packed-bed reactor? If you decide to use a large catalyst particle, do you expect to be operating under reaction-limited or diffusion-limited regimes? Why? Assume that the catalyst pellets are spherical and that the reaction is first order.
3. Precious metal catalysts are noble metals widely used in the chemical industry due to their ability to speed up chemical processes. Gold, palladium, platinum, rhodium, and silver are some examples of precious metals. However, these metal catalysts are extremely expensive. Let's assume that you are to deposit platinum on a porous inert catalyst support to be used for some chemical reaction. The reaction was found to have a large Thiele modulus value. What does this large value tell you about the reaction? How would you deposit the platinum given this large Thiele modulus?

4. Derive the internal effectiveness factor for a cylindrical catalyst pellet where the reactants are diffusing inward in the radial direction. Assume that the reaction is first order and neglect any variations in the axial direction.
5. Consider three different catalytic reactions. The dependence of the reaction rate on temperature for each of the three reactions is shown in the figure below. From the temperature dependence behavior, identify if the reaction is limited by internal diffusion, external diffusion, or surface reaction.

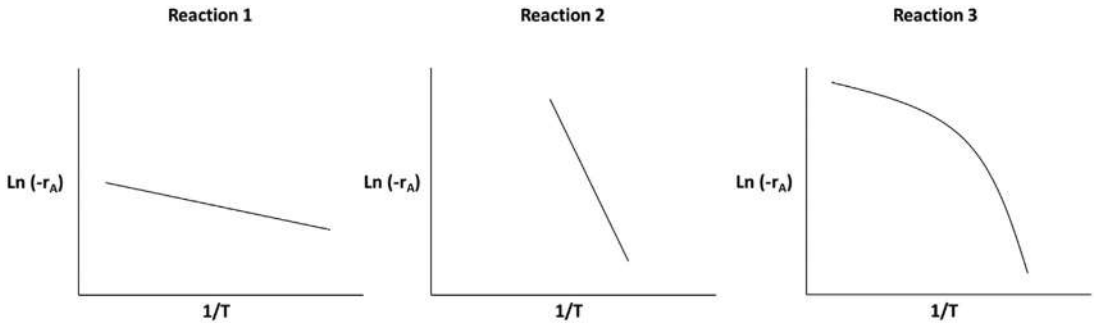

6. List and describe a few strategies that may be used to mitigate catalyst deactivation. These strategies can stem either from modifications performed on the catalyst itself or from changes made in the process.
7. The rate law of a gas-phase reaction $A \rightarrow B$ taking place over a solid catalyst may be expressed as:

$$-r_A = \frac{kP_A}{1 + K_A P_A}$$

   a. Suggest a mechanism that is consistent with the above rate law. What is the rate-limiting step?
   b. A series of experimental reaction runs were performed at different concentrations of A and the results are presented in the table below. Calculate the values of k and K_A.

Run	Overall reaction rate (mol min^{-1} per kg.cat)	Partial pressure of A (atm)
1	0.38	0.7
2	0.52	2.5
3	0.60	7.5
4	0.63	15

8. The mechanism for the gas-phase reaction $A + B \rightleftarrows C$ is postulated as follows:

$$A_{(g)} + S \rightleftarrows A \cdot S$$

$$B_{(g)} + S \rightleftarrows B \cdot S$$

$$A \cdot S + B \cdot S \rightleftarrows C \cdot S + S$$

$$C \cdot S \rightleftarrows C_{(g)} + S$$

a. Derive an expression for the rate law assuming that the rate is limited by the surface reaction.
b. If the reaction is postulated to follow the Eley–Rideal kinetics instead, how would the reaction mechanism differ?

9. Ethene (A) reacts with hydrogen (B) over a nickel catalyst at a temperature of 150°C to produce ethane (C). The rate law of this catalytic hydrogenation reaction may be expressed as:

$$-r_A = \frac{k\left(P_A P_B - \frac{P_C}{K_P}\right)}{\left[1 + K_A P_A + (K_B P_B)^{1/2} + K_C P_C\right]^3}$$

Suggest a mechanism that is consistent with the above rate law. What is the rate-limiting step?

10. The gas-phase reaction $A + B \rightarrow C$ is taking place over a solid catalyst. Suggest a mechanism that is consistent with the data in the table below. What is the rate-limiting step? Derive an expression for the rate law and calculate all rate law parameters.

Run	Overall reaction rate (mol s^{-1} per g.cat)	Partial pressure of A (atm)	Partial pressure of B (atm)	Partial pressure of C (atm)
1	0.50	2	2	2
2	0.75	2000	2	2
3	2.25	2	9	2
4	2.25	0.002	2006	0
5	2.25	0.004	1006	0
6	2.25	2	1008	2000
7	2.25	2	8	0
8	2.40	8	8	8

11. Neglecting external resistance to mass transfer, consider species A diffusing and then reacting inside a spherical catalyst pellet with a diameter of 1 cm. The first-order reaction has a reaction rate constant per unit volume of $5 \times 10^{-4}\ s^{-1}$. If the concentration of A at the surface of the catalyst pellet is 0.5 mol m^{-3}, what will the concentration be at $r = 0.4$ cm? Note that the effective diffusivity of A is $10^{-8}\ m^2\ s^{-1}$ and that the boundary conditions are:

$$\text{At } r = 0.5 \text{ cm}, \quad C_A = 0.5 \text{ mol m}^{-3}$$

$$\text{At } r = 0, \quad C_A = 5 \text{ mol m}^{-3}$$

12. The gas-phase decomposition of methanol to carbon monoxide and hydrogen is taking place in a packed-bed reactor. The second-order reaction has a reaction rate constant of 61.5 $m^4\ mol^{-1}s^{-1}$ and is limited by internal diffusion. Given the data below, calculate the internal and overall effectiveness factors. The initial concentration of methanol in the feed is 0.206 mol L^{-1}.

Pellet diameter: 0.005 m

Pellet density: 37×10^5 g m^{-3}

Pellet surface area: 519 $m^2\ g^{-1}$

Effective diffusivity: 357×10^{-10} $m^2\ s^{-1}$

13. The irreversible gas-phase conversion of A to B is taking place over a spherical catalyst pellet with a diameter of 8 mm. The first-order reaction has a reaction rate constant per unit volume of 5.04 s^{-1}. Given the data below, calculate the Thiele modulus and the internal effectiveness factor. The concentration of A in the bulk is 0.017 mol L^{-1}.

Pellet porosity: 0.6

Pellet tortuosity: 3.0

Molecular diffusivity: 0.21 $cm^2\ s^{-1}$

Knudsen diffusivity: 0.018 $cm^2\ s^{-1}$

14. The catalytic isomerization of n-butane into isobutane is taking place in a packed-bed reactor. With time, the catalyst activity decreases as a result of sintering. The second-order decay rate law is expressed as:

$$r_d = -\frac{da}{dt} = 0.423a^2$$

a. What is the conversion of n-butane on the first day of operation (i.e., $t = 0$)? What is the conversion after 10 days of operation? And after 100 days? The conversion in terms of activity is given as:

$$X = \frac{20a}{1 + 20a}$$

b. After how many days of operation should the catalyst be regenerated? The regeneration of the catalyst is to take place when the conversion of n-butane drops below 25%.

15. The following gas-phase reaction takes place in a catalytic packed-bed reactor (PBR):

$$A + B \rightarrow C + D; -r_A = k_A C_A C_B$$

The inlet pressure is 25 atm, the temperature is 127 °C and k_A is 100 L^2 mol^{-1} g^{-1} min^{-1}. If the feed, which is a stoichiometric mixture of A and B, enters the reactor at 40 mol min^{-1}, how much catalyst is required to achieve 68% conversion of A? (Assume ideal gas and no pressure drop).

References

[1] H.S. Fogler, Elements of Chemical Reaction Engineering, Prentice Hall PTR, 2006.
[2] Y.-C. Lin, G.W. Huber, The critical role of heterogeneous catalysis in lignocellulosic biomass conversion, Energy Environ. Sci. 2 (2009) 68–80.
[3] C.N. Hinshelwood, The Kinetics of Chemical Change, Oxford Clarendon Press, 1940.
[4] O.A. Hougen, K.M. Watson, Solid catalysts and reaction rates, Ind. Eng. Chem. 35 (1943) 529–541.
[5] Z.I. Önsan, A.K. Avci, Catalytic reactor types and their industrial significance, Multiphase Catalytic Reactors: Theory, Design, Manufacturing and Applications, Wiley-Blackwell, 2016, pp. 1–16.
[6] R. Sadegh-Vaziri, M.U. Babler, Removal of hydrogen sulfide with metal oxides in packed bed reactors—a review from a modeling perspective with practical implications, Appl. Sci. 9 (2019) 5316.
[7] D. Thoenes Jr, H. Kramers, Mass transfer from spheres in various regular packings to a flowing fluid, Chem. Eng. Sci. 8 (1958) 271–283.
[8] V. Manokaran, P. Saiprasad, S. Srinath, Studies on heat and mass transfer limitations in oxidative dehydrogenation of ethane over Cr_2O_3/Al_2O_3 catalyst, Procedia Eng. 127 (2015) 1338–1345.
[9] P. Kočí, V. Novák, F. Štěpánek, M. Marek, M. Kubíček, Multi-scale modelling of reaction and transport in porous catalysts, Chem. Eng. Sci. 65 (2010) 412–419.
[10] F. Akhtar, L. Andersson, S. Ogunwumi, N. Hedin, L. Bergström, Structuring adsorbents and catalysts by processing of porous powders, J. Eur. Ceram. Soc. 34 (2014) 1643–1666.
[11] A.K. Avci, Z.I. Önsan, 2.16 Catalysts, in: I. Dincer (Ed.), Comprehensive Energy Systems, Elsevier, Oxford, 2018, pp. 475–523.
[12] C.N. Satterfield, Mass Transfer in Heterogeneous Catalysis, MIT Press, 1970.
[13] R. Aris, Introduction to the Analysis of Chemical Reactors, Prentice-Hall, Englewood Cliffs, N.J, 1965.
[14] V.W. Weekman Jr, R.L. Gorring, Influence of volume change on gas-phase reactions in porous catalysts, J. Catal. 4 (1965) 260–270.
[15] P. Weisz, J. Hicks, The behaviour of porous catalyst particles in view of internal mass and heat diffusion effects, Chem. Eng. Sci. 17 (1962) 265–275.
[16] D. Luss, Sufficient conditions for uniqueness of the steady state solutions in distributed parameter systems, Chem. Eng. Sci. 23 (1968) 1249–1255.
[17] D.E. Mears, Tests for transport limitations in experimental catalytic reactors, Ind. Eng. Chem. Process. Des. Dev. 10 (1971) 541–547.
[18] O. Levenspiel, Chemical Reaction Engineering, John Wiley & Sons, 1999.
[19] J.M. Thomas, W.J. Thomas, Principles and Practice of Heterogeneous Catalysis, John Wiley & Sons, 2014.
[20] B. Gray, R. Ball, Thermal stabilization of chemical reactors. I. The mathematical description of the Endex reactor, Proc. R. Soc. London, Ser. A: Math. Phys. Eng. Sci. 455 (1999) 163–182.
[21] J. Butt, E. Petersen, Activation, Deactivation and Poisoning of Catalysts, Academic Press, New York, 1988.
[22] S. Szépe, O. Levenspiel, Optimal temperature policies for reactors subject to catalyst deactivation—I. Batch reactor, Chem. Eng. Sci. 23 (1968) 881–894.
[23] G. Kuczynski, Sintering and Catalysis, 10, Springer Science & Business Media, 2012.
[24] J. Rostrup-Nielsen, Fouling of catalysts. Industrial examples, Fouling Science and Technology, Springer, 1988, pp. 351–367.
[25] E. Maxted, The poisoning of metallic catalysts, ed, Adv. Catal., 3, Elsevier, 1951, pp. 129–178.

[26] J.A. Moulijn, A. Van Diepen, F. Kapteijn, Catalyst deactivation: is it predictable?: What to do? Appl. Catal. A: Gen. 212 (2001) 3–16.
[27] R. Hughes, Deactivation of Catalysts, Academic Press, San Diego, CA, 1984.
[28] C.D. Prater, R.M. Lago, The kinetics of the cracking of cumene by silica-alumina catalysts, ed, Adv. Catal., 8, Elsevier, 1956, pp. 293–339.
[29] C.H. Bartholomew, Mechanisms of catalyst deactivation, Appl. Catal. A: Gen. 212 (2001) 17–60.
[30] M.D. Argyle, C.H. Bartholomew, Heterogeneous catalyst deactivation and regeneration: a review, Catalysts 5 (2015) 145–269.
[31] C. Bartholomew, Catalyst deactivation and regeneration, Kirk-Othmer Encycl. Chem. Technol. (2000).
[32] A. Voorhies Jr, Carbon formation in catalytic cracking, Ind. Eng. Chem. 37 (1945) 318–322.
[33] C.H. Bartholomew, R.J. Farrauto, Fundamentals of Industrial Catalytic Processes, John Wiley & Sons, 2011.
[34] T.D.H. Nguyen, M. Maschietti, L.-E. Åmand, L. Vamling, L. Olausson, S.-I. Andersson, et al., The effect of temperature on the catalytic conversion of kraft lignin using near-critical water, Bioresour. Technol. 170 (2014) 196–203.
[35] Z. Mu, J. Wang, T. Wang, Y. Jin, Optimum design of radial flow moving-bed reactors based on a mathematical hydrodynamic model, Chem. Eng. Process.: Process. Intensif. 42 (2003) 409–417.
[36] A. Lappas, E. Heracleous, in: Handbook of Biofuels Production, Production of biofuels via Fischer–Tropsch synthesis: biomass-to-liquids, A. Steynberg, M. Dry, (Eds.), Elsevier, 2004, pp. 64–195
[37] S. Krishnaswamy, J. Kittrell, Analysis of temperature-time data for deactivating catalysts, Ind. Eng. Chem. Process. Des. Dev. 18 (1979) 399–403.
[38] J.T. Richardson, Experimental determination of catalyst fouling parameters. Carbon profiles, Ind. Eng. Chem. Process. Des. Dev. 11 (1972) 8–11.
[39] S. Homma, S. Ogata, J. Koga, S. Matsumoto, Gas–solid reaction model for a shrinking spherical particle with unreacted shrinking core, Chem. Eng. Sci. 60 (2005) 4971–4980.

CHAPTER 6

Green heterogeneous catalysis

The development of *green and sustainable processes* is a central focus of modern heterogeneous catalysis and its applications in a multitude of fields such as the generation of biofuels, water and air remediation, synthesis of commodity chemicals, hydrogen generation, and carbon dioxide reduction. This chapter focuses on the fundamentals and applications of three emerging branches of heterogeneous catalysis: catalytic conversion of biomass to biofuels, electrocatalysis, and photocatalysis.

The use of *biomass* is widely contemplated as a potential route for the sustainable production of fine chemicals, commodity materials, and fuels. This research line is particularly relevant in the transportation fuel sector that is strongly dependent on petroleum. In this area the depletion of worldwide reserves, uncertainty in crude oil prices, and concern over emission problems have compelled the scientific community to widen the search for alternative fuels complying with the stringent sustainability criteria. A great advantage of biomass fuel over the other renewable energy options for transportation, such as hydrogen fuel cells, is the possibility to produce liquid biofuels such as bioethanol and biodiesel. These do not entail extensive variations of the traditional transport infrastructure and the internal combustion engine. Catalytic processes are increasingly applied to the production of biofuels, playing a crucial role in improving product quality and achieving mild operational conditions compared to uncatalyzed reactions.

Electrocatalysis is a subclass of heterogeneous catalysis involving redox reactions through the direct transfer of electrons between an electrode (i.e., the catalyst) and electrolyte. Electrocatalysis is a key discipline for the development of a multitude of electrochemical processes including energy storage, fuel cells, organic electrosynthesis, and hydrogen generation. Depending on the electrochemical device involved, the catalytic reaction can convert chemical energy into electrical energy or vice versa. The first kind of reaction occurs in fuel cells and batteries, while the second one aims to convert the oxidized product back to its reusable form through an electricity input. This chapter will cover the fundamentals of two important electrocatalytic processes: electrochemical splitting of water into O_2 and H_2, and reduction of CO_2 into value-added fuels.

Photocatalysis relies on the unique properties of semiconductor catalysts to harvest incident light and generate electron−hole pairs. Electrons and holes that reach the catalyst surface trigger the reduction and oxidation reaction, respectively. Photocatalysis is a rapidly expanding technology with a high potential for a wide range of industrial applications

Heterogeneous Catalysis.
DOI: https://doi.org/10.1016/B978-0-323-89845-4.00007-2

which include mineralization of organic pollutants, remediation of water and air, production of renewable fuels and organic synthesis. From the point of view of pollutant degradation, photocatalysis is a viable alternative to energy- and cost-intensive traditional methods such as adsorption, reverse osmosis, and ultrafiltration among others. One of its key advantages lies in the possibility to mineralize organic pollutants completely to form harmless products using only atmospheric oxygen and light under mild reaction conditions. After covering the fundamentals of photocatalysis, this chapter will focus on two important applications: wastewater treatment and organic synthesis.

6.1 Conversion of biomass to biofuels

6.1.1 Biomass feedstock

Biomass can be obtained from a wide range of sources that span from crops, wood agricultural and forest residues to municipal and industrial solid waste. The feedstocks derived from biomass that are suitable for the generation of renewable fuels can be classified according to three main categories: (1) sugar and starches, (2) triglycerides, and (3) lignocellulosic biomass. Fig. 6.1A shows the chemical structures and the main sources of starch, triglycerides, and cellulose, the last being the dominant component of lignocellulosic biomass.

Starch serves as a sugar store in many plants. It is a long-chain polymer made up of a mixture of two polysaccharides, that is, amylose and amylopectin, which can be easily hydrolyzed to the constituent sugar monomers and processed to produce the so-called first-generation biofuels, mainly ethanol (Fig. 6.1B). *Triglyceride* feedstocks, comprising fatty acids and glycerol derived from both plants and animals, are intended to the production of first-generation biodiesel. The technologies involved in the production of first-generation biofuels are well consolidated so the main challenge for research lies not so much in the development of novel technologies but in the optimization of the existing processes to reduce costs and make the renewable fuels competitive with the ones obtained from petroleum [1]. First-generation biofuels derived from edible biomass pose ethical issues due to the shortage of agricultural land and competition with the food market [2].

Second-generation biofuels are derived from nonfood sources such as *lignocellulosic biomass* which is the most abundant type of biomass. It consists of three different fractions, namely, lignin, hemicellulose (carbohydrate polymers), and cellulose aromatic polymer [3]. The different fractions are isolated through pretreatment followed by hydrolysis.

Lignocellulose is always present in plants and contributes to their structural integrity. Its conversion to biofuel involves obtaining upgradeable intermediates, such as bio-oil, furfural, hydroxymethylfurfural, levulinic acid, which are processed to obtain renewable biofuels (Fig. 6.1B). The development of efficient processes for the conversion of

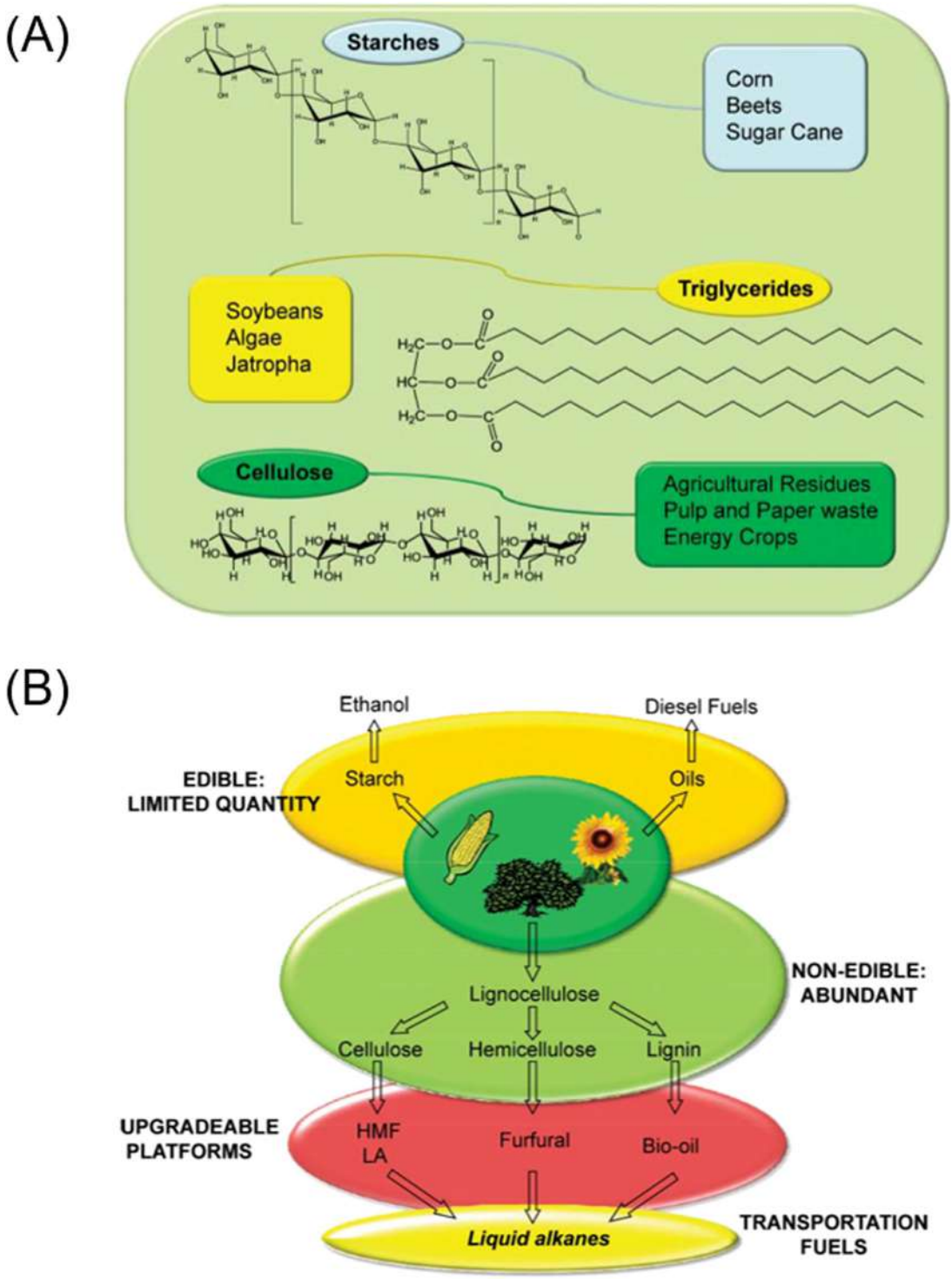

Figure 6.1

(A) Chemical structure and sources of biomass feedstocks; (B) biomass feedstocks and platforms for conversion to biofuels. *Source*: *Reproduced from [1]*.

lignocellulosic materials is a hot research topic because of the possibility to generate valuable bioproducts from a great variety of abundant nonedible sources that include agriculture, forestry, pruning residues, and agroindustrial waste.

However, there are some challenges in the utilization of lignocellulosic biomass related to its growth on land in competition with food production and to the expensive and energy-demanding processes required for its processing into value-added chemicals. The main purpose of these processes is to separate the different fractions of lignocellulosic biomass and make these more accessible to enzymes or chemicals used in the following steps. *Pretreatment* methods can be divided into three main categories: physical, chemical, and physicochemical (Fig. 6.2). Physical methods, which are divided into mechanical,

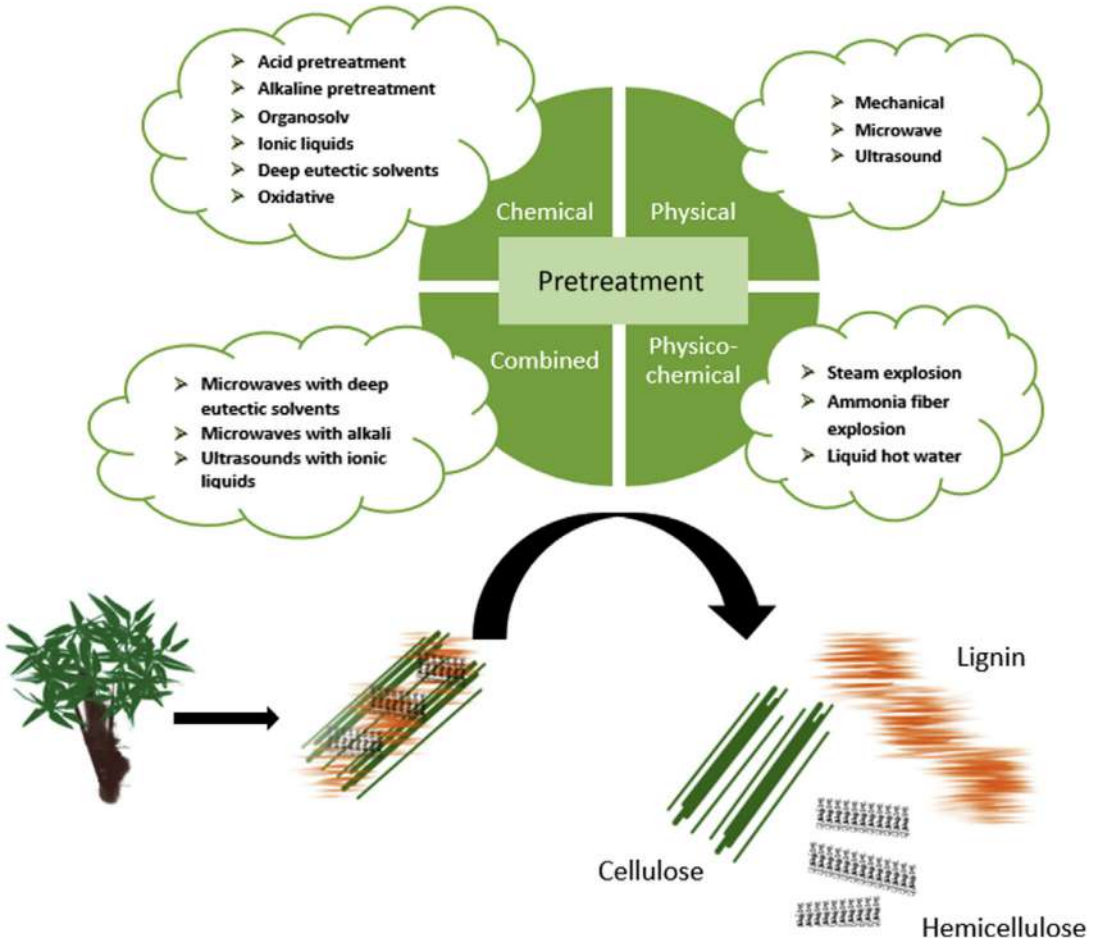

Figure 6.2
Pretreatment methods for lignocellulosic biomass. *Source*: *Reproduced from [4]*.

microwave, and ultrasound pretreatments, aim to reduce biomass recalcitrance through an alteration in its structure caused by an increase in pressure or temperature. Chemical methods make use of those organic or inorganic molecules (i.e., acids, alkalines, and ionic liquids) that are able to disrupt the structure of the biomass through the interaction with its intrapolymer or interpolymer bonds. Physicochemical treatments imply both chemical and physical changes of the biomass such as in the steam explosion methods where the biomass undergoes a treatment with high-pressure saturated steam followed by an explosive decompression to atmospheric pressure [4]. Physical and chemical pretreatment can also be combined to improve the digestibility of biomass and the yield of desired products.

Recently, *algae* grown from aquaculture in fresh, seawater, and wastewater have emerged as an appealing feedstock for future biofuels [5]. Algae-derived fuels, usually referred to as third-generation biofuels, present undoubted advantages over traditional biomass feedstock, primarily because (1) their production does not compete with food and land; (2) algae grow much faster than other feedstocks; and (3) CO_2 is exploited as a food source, releasing oxygen into the atmosphere. As a consequence, it can be tied directly to carbon-emitting sources such as power plants and manufacturing facilities, with the possibility of directly converting emissions into biofuels. On the other hand, the technologies making use of algae as feedstock are still at an early stage of development and more research is needed for process optimization and to overcome the challenges entailed in its availability and production [6].

6.1.2 Traditional thermochemical processes for catalytic conversion of biomass

Biomass can be converted to biofuels or useful bioproducts through physicochemical, biochemical, and thermochemical routes. *Physicochemical conversion* is the simplest route for the production of biofuels and it involves the processing of organic matter containing oils and/or fats (e.g., sunflower seeds and oil palm fruits) to produce liquid fuel. The oil is separated from the seeds by extraction and cleaned. The product can thus be used in its straight form or undergo chemical treatment. For example, it can be converted to fatty acid methyl ester through transesterification or hydrogenated, isomerized, and finally distilled to hydrotreated esters and fatty acids or, also, processed in oil refineries along with crude oil. The *biochemical processes* produce biofuels via fermentation or anaerobic respiration. In anaerobic fermentation the biomass is processed to obtain biogas, mainly CH_4 and CO_2. In aerobic fermentation the target product is bioethanol produced from sugars, starch, and cellulose [7]. There are some challenges and technical issues that make biochemical conversion uncompetitive such as the high cost of enzymes, and low fermentability of some substrates. The research is also focusing on new ways to eliminate fermentation inhibitors, identifying inexpensive high-quality feedstock and engineering more effective microbial strains able to simultaneously ferment various carbon sugars [8].

When compared to biochemical conversion, *thermochemical technologies* are more implementable on a large scale, being characterized by a lower number of processing steps, shorter processing time, and thus fewer technological challenges [9]. Thermochemical conversion involves the controlled heating and/or oxidation of biomass. The main thermochemical conversion technologies, on which we will focus in the following, are pyrolysis, torrefaction, hydrothermal liquefaction, and gasification. The operating conditions of these processes are summarized in Fig. 6.3.

Pyrolysis involves the heating of biomass in the absence of oxygen to produce biochar, bio-oil, and syngas. Slow pyrolysis is employed to maximize the solid product yield (i.e., biochar) through low heating rates and long reaction times. The vapor residence time inside the pyrolysis reactor should be kept at a minimum, in order to prevent secondary reactions between the steam and the formed porous char. Slow pyrolysis is a well-consolidated technology able to process large biomass particle sizes without any need for energy-intensive preprocessing procedures [11].

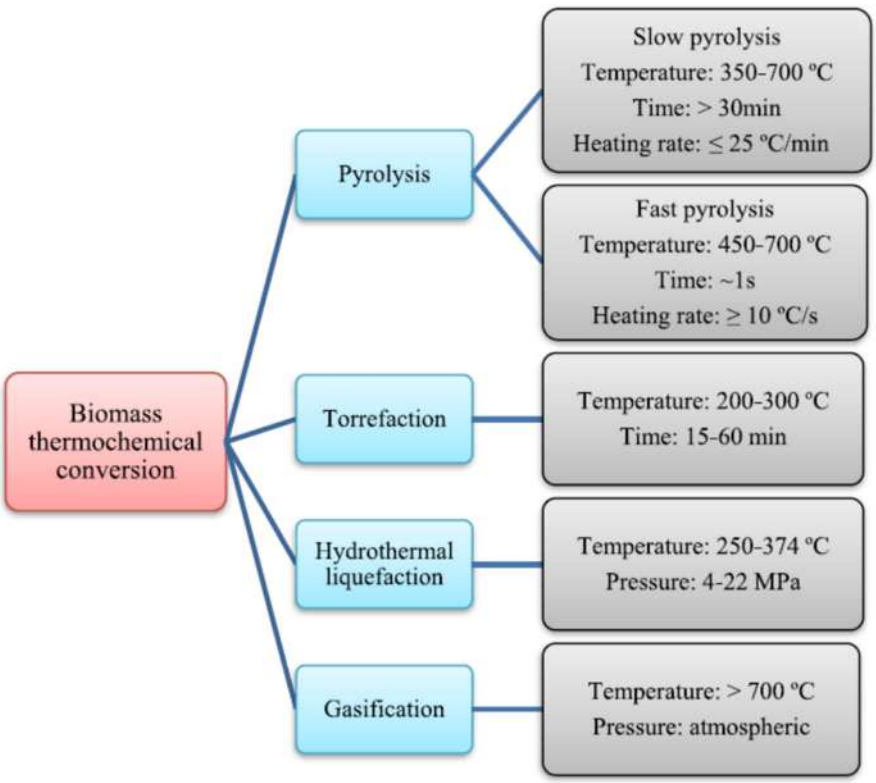

Figure 6.3
Processes for thermochemical conversion of biomass to biofuel and related operating conditions.
Source: Reproduced from [10].

Fast pyrolysis is employed to maximize yield in the liquid products (bio-oil). It is achieved by rapid heating and immediate quenching of the liquid product to prevent reactions forming gases [12]. Unlike slow pyrolysis, the high rate of heat transfer requires finely ground particles of biomass feed to ensure that the process occurs quickly. Depending on the nature of the feedstock, the typical distribution of fast pyrolysis products consists of 60%–75% of bio-oil, 15%–25% of biochar, and 10%–20% of syngas. The bio-oil can be used as fuel for diesel engines and gas turbines intended for electricity and heat generation.

A variant of the fast pyrolysis is the flash pyrolysis that is carried out at higher temperatures (up to 1300°C). This process ensures higher yields of bio-oil with shorter residence times (less than 0.5 s) than those in fast pyrolysis (0.5–10 s) [13,14]. The main drawback of flash pyrolysis is the generation of pyrolytic water that has a detrimental impact on the energy properties of the bio-oil [15].

Torrefaction is similar to slow pyrolysis but the thermal degradation reaction takes place at milder temperatures with the aim of upgrading the physical and chemical properties of the fuel. In this way, the biomass can be cocombusted with coal or employed as independent fuel by being pelletized and stored without any microbial degradation [11]. This enables for a long-term preservation of the products that otherwise would suffer from degradation when stored in an environment exposed to the weather.

Hydrothermal liquefaction is essentially pyrolysis in hot liquid water [16]. Biomass is processed in a hot pressurized water environment for less than 60 min to be converted into bio-oil (target product), biochar, and gases. This technology is particularly suitable to convert high-moisture biomass such as algae feedstock and no drying is required. Three main steps are applied sequentially: depolymerization, decomposition, and polymerization [10,17]. Upstream of the thermochemical conversion process, the biomass feedstock, that is, algae or lignocellulosic biomass, is depolymerized and decomposed into small monomers. These highly reactive and unstable monomers then evolve to bio-oil and solid products through polymerization. The role of the catalyst in this process is to enhance the bio-oil yield while suppressing tar and char formation.

The *gasification* process aims to produce syngas that can be subsequently upgraded to liquid fuels such as gasoline and diesel through the Fischer–Tropsch synthesis [1]. Other gases such as CH_4 and N_2 are also produced during gasification. This process is carried out in the temperature range 800°C–900°C and can be divided into four main stages: drying, pyrolysis, oxidation, and reduction. After a quick drying process, the feedstock undergoes fast pyrolysis to produce char and gas products. The oxidation step involves the cracking of pyrolysis products and the generation of light gases upon reaction at high temperature with oxidants such as O_2, CO_2, steam, or a mixture of these components. The reduction step is the process of stripping the oxygen off combustion products of hydrocarbon molecules so that the latter can be

reconverted to forms that can burn again. The main reactions taking place during gasification are the following [18,19]:

Pyrolysis:

$$\text{Feedstock} \rightleftharpoons \text{Char} + \text{Tar} + \text{volatiles}(C_xH_{2x} + C_xH_x + H_2O + H_2S + H_2 + CO_2) \quad (6.1)$$

Oxidation reactions:

$$C + \frac{1}{2}O_2 \rightleftharpoons CO \quad (6.2)$$

$$CO + \frac{1}{2}O_2 \rightleftharpoons CO_2 \quad (6.3)$$

$$H_2 + \frac{1}{2}O_2 \rightleftharpoons H_2O \quad (6.4)$$

Boudouard reaction:

$$C + CO_2 \rightleftharpoons 2CO \quad (6.5)$$

Water–gas reaction:

$$C + H_2O \rightleftharpoons CO + H_2 \quad (6.6)$$

Water–gas shift (WGS) reaction:

$$CO + H_2O \rightleftharpoons CO_2 + H_2 \quad (6.7)$$

Methanation reactions:

$$C + 2H_2 \rightleftharpoons CH_4 \quad (6.8)$$

$$CO + 3H_2 \rightleftharpoons CH_4 + H_2O \quad (6.9)$$

$$CO_2 + 4H_2 \rightleftharpoons CH_4 + 2H_2O \quad (6.10)$$

The benefits derived from the use of *catalysts in thermochemical conversion of biomass* are multiple. Table 6.1 summarizes the main effect of the most commonly employed heterogeneous catalysts on thermochemical processes [10]. Zeolites, transition metals, and alkaline earth metals (AAEMs) are widely used for this purpose. AAEMs, such as sodium, potassium, calcium, and manganese and their relative oxides, have been reported to reduce liquid yield in slow pyrolysis in favor of a higher biochar yield and gas generation; they also ensure an end product with improved energy density and thermal degradation properties in torrefaction [20–22]. Zeolites allow obtaining high gas yield and high-quality bio-oil in pyrolysis [23]. Transition metals such as nickel, platinum, ruthenium, cobalt, and iron have high activity for upgrading bio-oil in hydrothermal

Table 6.1: Catalyst effects on thermochemical conversion processes.

Thermochemical process	Catalyst	Catalyst effect on the process and end-products
Pyrolysis	Zeolites	• High gas yield • Upgraded quality of bio-oil • Possibility of obtaining different compositions of bio-oil depending on the catalyst structure • High aromatic hydrocarbons in bio-oil • Hydrogenation and hydrodeoxygenation of bio-oil in fast pyrolysis
	AAEMs[a]	• Slow pyrolysis: promote the formation of lighter hydrocarbons, char, gas yield, thereby suppressing the liquid yield • Fast pyrolysis: promote the generation of bio-oil with high content of aromatics
Torrefaction	AAEMs[a]	• Increase in energy density and short thermal degradation time
Hydrothermal liquefaction	Transition metals, zeolites	• Increase in bio-oil yield • Zeolites allow the removal of oxygen from oxygenated compounds • Synthetic zeolites promote the formation of hydrocarbon compounds with low acids • Transition metals allow the generation of a bio-oil with low viscosity and high hydrocarbons content • Platinum promotes the formation of H_2, CO_2, and CH_4
Gasification	AAEMs[a], transition metals	• Reduced tar formation • High reaction rate

[a]Alkaline earth metals.

liquefaction; they can reduce tar generation and increase hydrogen formation in gasification [24].

It is clear that there are numerous advantages associated with a future large-scale implementation of heterogeneous catalysis in the production of biofuels via thermochemical conversion processes. However, there are still different challenges that need to be addressed in future research. These are not only related to the optimization of the operating conditions of the current thermochemical catalytic processes and the development of increasingly efficient catalysts but also to particular intrinsic features of the biomass feedstock. Some of the main challenges are the following [10,25]:

1. As aforementioned, biomass feedstock often requires pretreatments. These may be more stringent, laborious, and expensive when dealing with catalytic processes in order to facilitate the contact between biomass and catalyst. For instance, high water content, in many cases with nonneutral pH, can have a detrimental impact on the catalyst performance.
2. Generation of carbonaceous deposits via nondesired transformations, which may facilitate catalyst poisoning and deactivation. The generation of such deposits is

ascribed to the complexity of the biomass matrix, highly reactive due to the presence of a multitude of components with varied functional groups.
3. Presence of a high amount of heteroatoms such as oxygen, phosphorous, and nitrogen that need to be removed to enhance the energy density of the feedstock and provide the target products.
4. Tailoring of the catalyst properties for biomass valorization, particularly in terms of improved accessibility, tight control of the acidic and basic features, surface polarity, metal support interactions, and hydrothermal stability.
5. Scale-up of the current technologies and need for pilot-scale studies.

6.1.3 Aqueous-phase reforming for hydrogen and alkanes production

Aqueous-phase reforming (APR) of biomass-derived sources is a valuable route for the production of hydrogen and alkanes. The main advantages of this process are related to (1) compatibility with wet or water-soluble feedstocks; (2) facilitated WGS reaction (Eq. 6.7) and suppressed generation of CO; (3) mild operating conditions with much lower temperatures (c. 225°C) compared to traditional alkane steam reforming process (c. 620°C) [26].

Oxygenated feedstocks including ethylene glycol, sorbitol, glycerol, and methanol can be efficiently reformed into renewable hydrogen, which can be used directly in fuel cells or for biomass upgrading processes (e.g., hydrodeoxygenation and aldol condensation). The catalytic conversion involves the transformation of the oxygenated feedstock to adsorbed intermediates upon a hydrogenation step, followed by the cleavage of C—C or C—O bonds. For the purpose of hydrogen generation, the optimal catalytic pathway is the scission of the C—C bond followed by WGS reaction. On the other hand, the C—O cleavage preferentially gives rise to organic acids that are hard to be reformed and can deactivate the catalyst and corrode the equipment [27,28].

Fig. 6.4 displays a representative catalytic pathway in APR of ethylene glycol over a metal catalyst. Before the cleavage of C—C or C—O bonds, ethylene glycol is first dehydrogenated to adsorbed intermediates which bind to the catalyst (M) by M—C bonds and/or M—O bonds. On metals like Pt, the Pt—C bonds are usually more stable than Pt—O bonds [29]. The dehydrogenation pathway (I in Fig. 6.4) is the most desirable reaction pathway that proceeds with the scission of C—C, followed by the conversion of CO with water to CO_2 and H_2 by WGS reaction. On metals such as Ni, Rh, and Ru, subsequent reactions can give rise to alkanes and Fischer–Tropsch and methanation reactions. Pathway II involves the C—O cleavage and generation of an alcohol followed by hydrogenation. The alcohol can thus form CO_2 and H_2 upon C—C cleavage or alkanes upon C—O cleavage. Pathway III proceeds with desorption and subsequent rearrangement to produce an acid that decomposes to alkanes, CO_2, CO, H_2, and H_2O. Pathway IV proceeds through the dehydration reaction which often takes place on the acidic sites to form alkenes [30].

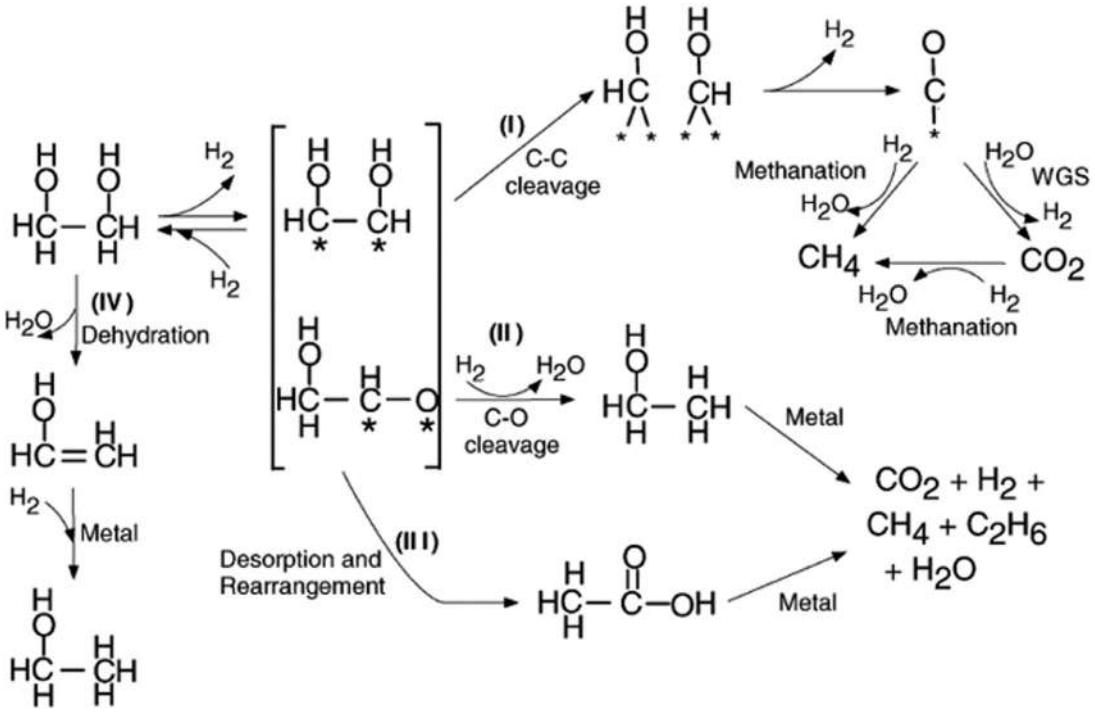

Figure 6.4
Reaction pathways for the production of H_2 on metal catalyst from ethylene glycol through APR (*represents a surface metal site) [27]. *APR*, Aqueous-phase reforming.

Fig. 6.5 illustrates the impact of various factors on the *selectivities of hydrogen and alkanes* in the APR process [27]. Metals such as Pd, Pt, and Ni—Sn favor the formation of H_2, while Ru and Rh are more active in alkane generation (Fig. 6.5A). The support also plays a crucial role: acidic supports such as silica—alumina result in high selectivities for alkanes formation, more basic/neutral supports such as alumina benefit hydrogen production (Fig. 6.5B). The acidity of the aqueous solution depends not only on the nature of the formed byproducts and intermediates but also on the CO_2 dissolved in the solution which, at high pressure, leads to slightly acidic pH (4–5). Acidic solutions facilitate alkane formation owing to acid-catalyzed dehydration reactions, which take place in solution (followed by hydrogenation on the metal). On the other hand, neutral and basic pHs are beneficial for high H_2 selectivities (Fig. 6.5C). The feedstock has also a significant effect on the reaction selectivity: polyols, such as sorbitol, give rise to higher H_2 selectivities than sugars, such as glucose, which, on the other hand, are preferential feeds for alkane formation (Fig. 6.5D). An increase in the feed concentration of sugars typically yields a higher alkane formation and the H_2 selectivity decreases accordingly due to homogeneous decomposition reactions typical of sugars.

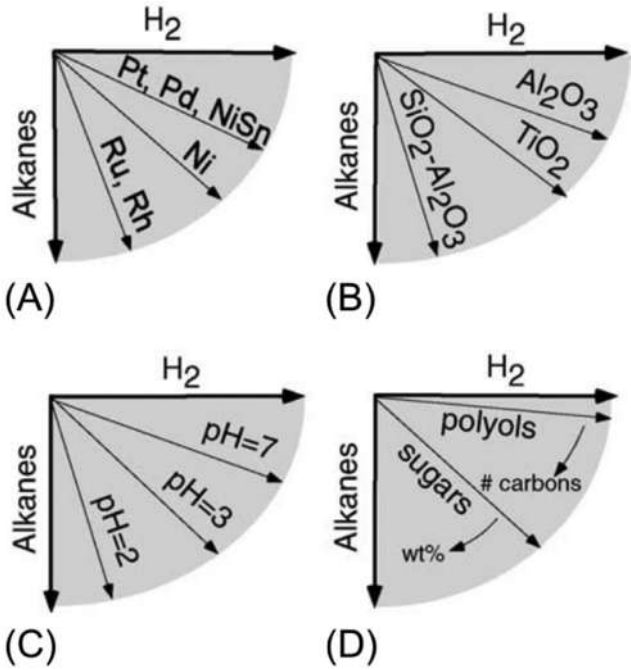

Figure 6.5
Influence of various factors on the selectivity of APR process: (A) metal, (B) support, (C) solution, and (D) feed. *Source*: *Reproduced from [27]*. *APR*, Aqueous-phase reforming.

Focus 6.1: Nano-magnetic catalyst for biodiesel production

One of the main challenges faced by heterogeneous catalysis is the separation of the solid catalyst from the reaction medium. Nano-magnetic catalysts are *easily separated from the product stream* by the application of a magnetic field, preventing significant loss of the catalyst and increasing the chances for its reusability. With this aim, Hu et al. [31] prepared magnetic KF/CaO−Fe_3O_4 catalysts by an impregnation method and evaluated their catalytic activity for the production of biodiesel by transesterification of stillingia oil.

The preparation of the nano-magnetic catalysts consisted of three steps: (1) mixing of Fe_3O_4 with different metal oxides, namely, MgO, CaO, or SrO; (2) dipping the mixture in aqueous solutions with varying KF concentrations to obtain different loading levels; (3) drying and calcination in a temperature range of 300°C−800°C. As shown in Fig. 6.6, the catalyst KF/CaO−Fe_3O_4 led to a higher biodiesel yield compared to KF/MgO−Fe_3O_4 and KF/SrO−Fe_3O_4. The increase in KF loading fostered the emergence of active catalyst sites with a consequent improvement in the reactivity (Fig. 6.6A). However, when the KF loading exceeded a certain threshold (25 wt.% for KF/CaO−Fe_3O_4), the yield decreased due to the blockage of the active sites. The biodiesel yield exhibited a similar trend versus the annealing temperature as shown in Fig. 6.6B. After reaching a maximum (600°C for KF/CaO−Fe_3O_4), the reactivity decreased due to surface sintering and consequent reduction of specific surface area.

(*Continued*)

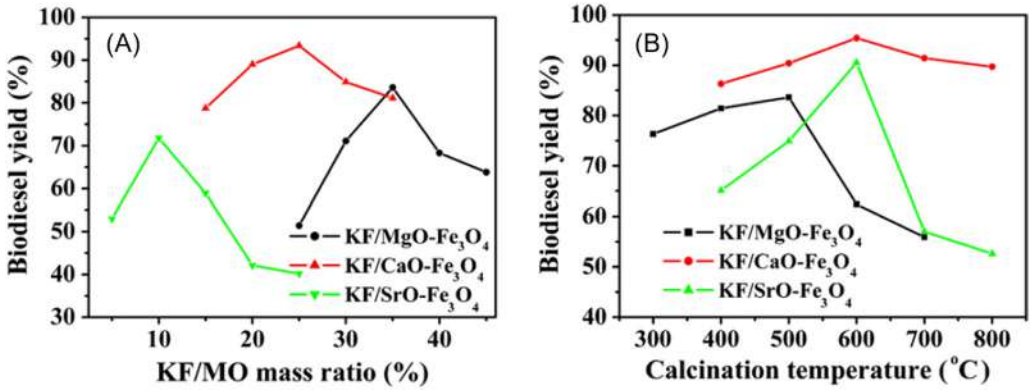

Figure 6.6
Effects of (A) KF loading and (B) calcination temperature on the activity of nano-magnetic catalysts for biodiesel production. *Source: Reproduced from [31].*

Focus 6.1: Nano-magnetic catalyst for biodiesel production (Continued)

The KF/CaO−Fe_3O_4 catalyst presented a porous structure with an average particle diameter of c. 50 nm and was reused up to 14 times without much loss in activity.

6.2 Electrocatalysis

6.2.1 Fundamentals of electrocatalytic processes

6.2.1.1 Types of electrochemical cells

Electrochemical cells can be broadly categorized into galvanic and electrolytic. *Galvanic cells*, such as batteries and fuel cells, are driven by spontaneous redox reactions ($\Delta G < 0$), while electrolytic cells rely on electric current to bring about nonspontaneous reactions ($\Delta G > 0$). The main components of an electrochemical cell are the electrolyte, made up of a solution of ions that can conduct electricity, and the two electrodes called anode and cathode. The oxidation reaction takes place at the anode, while the reduction reaction occurs at the cathode. The standard cell potential is defined as the standard potential difference between the two electrodes:

$$\Delta E^0_{\text{cell}} = E^0_{\text{cathode}} - E^0_{\text{anode}} \tag{6.11}$$

The change in Gibbs free energy for an electrochemical cell is related to cell potential through the following equation:

$$\Delta G^0 = -mF\Delta E^0_{\text{cell}} \tag{6.12}$$

where ΔG^0 is the Gibbs free energy of the system under standard conditions, m the moles of electrons transferred, F the Faraday's constant, 96,485 C mol^{-1}.

$\Delta E^0_{cell} > 0$ implies $\Delta G^0 < 0$ and thus spontaneous reactions, which is the case of galvanic cells. Here, the polarity of the anode is negative and the one of the cathode is positive. In this case, the species getting oxidized provide the electrons which travel to the cathode through the external circuit. Conversely, in *electrolytic cells*, the electrodes have opposite polarity and chemical reactions are enforced since $\Delta E^0_{cell} < 0$ and $\Delta G^0 > 0$. In this case, an external source of electrical energy is used to supply electrons that enter through the cathode and come out through the anode. The working principle of both electrochemical cells is displayed in Fig. 6.7 [32].

The difference between the electrode potential E needed to drive a certain current and the equilibrium potential E_{eq} is defined as *overpotential* η:

$$\eta = E - E_{eq} \tag{6.13}$$

The *total cell voltage* decreases by increasing the current in galvanic cells, while it increases with the latter in electrolytic cells (Fig. 6.7) according to the following equations:

$$V_{galv} = \Delta E^0_{cell} - \Sigma|\eta| - RI \tag{6.14}$$

$$V_{elec} = \Delta E^0_{cell} + \Sigma|\eta| + RI \tag{6.15}$$

where V_{galv} and V_{elec} are the total cell voltage of the galvanic and electrolytic cells, respectively, $\Sigma|\eta|$ refers to the sum of anodic and cathodic overpotentials (η_a and η_c) and RI accounts for the ohmic losses in the electrolyte and external connections.

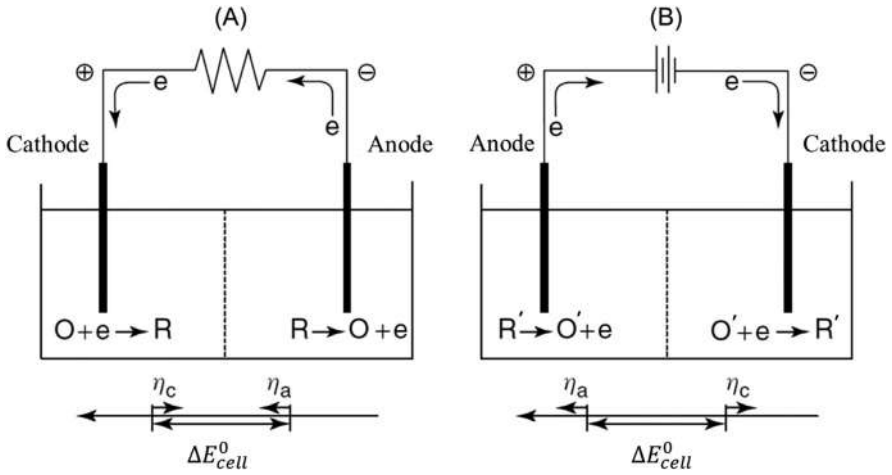

Figure 6.7

(A) Galvanic cell and (B) electrolytic cell. η_a: anodic overpotential, η_c: cathodic overpotential, e: electron, ΔE^0_{cell}: standard cell potential, R and R': species undergoing oxidation reaction, O and O': species undergoing oxidation reaction. *Source*: *Readapted from [32].*

6.2.1.2 Electrochemical kinetics

The fundamental relationship between the electrical current through an electrode and the electrode potential is described by the *Butler–Volmer equation*:

$$i = i_a + i_c = i_0 \left\{ \exp\left[\frac{\alpha_a n F \eta}{RT}\right] - \exp\left[-\frac{\alpha_c n F \eta}{RT}\right] \right\} \tag{6.16}$$

where i is the total current density, $i_a = i_0\left[\exp\alpha\left(\frac{\alpha_a n F \eta}{RT}\right)\right]$ the anodic current density, $i_c = i_0\left[-\exp\alpha\left(\frac{\alpha_c n F \eta}{RT}\right)\right]$ the cathodic current density, i_0 the exchange current density, n the number of exchanged electrons, α_a the anodic transfer coefficient, α_c the cathodic transfer coefficient, F the Faraday's constant (96,485 C mol^{-1}), η the overpotential defined as above, R the gas constant, and T the temperature. The catalytic performance of an electrode material mainly depends on i_0 and α.

The exchange current density is the current density that flows through the electrode equally in both directions (i.e., oxidation and reduction) at equilibrium. In this condition the net current intensity is zero, since the two electrode reactions proceed at the same rate. As shown in Fig. 6.8A, the larger i_0 for a given α, the larger is the shift of the current density–overpotential curve toward lower η at the same i. An increase in i_0 is the desired effect when using an electrocatalyst [33].

The charge transfer coefficient denotes the fraction of the interfacial potential at the electrode–electrolyte interface that contributes to lowering the free energy barrier for the electrochemical process. For instance, an increase in α_a enhances the magnitude of the anodic current density, at a fixed η, while decreasing the magnitude of the cathodic current density.

In the high overpotential region, Butler–Volmer equation simplifies to *Tafel equation*. When working at high anodic overpotentials, i_c can be neglected compared to i_a, which implies that $i = i_a$. Similarly, i_a can be excluded at high cathodic overpotential and $i = i_c$. The electrochemical kinetics at high anodic or cathodic η can be described by Eqs. (6.17) and (6.18), respectively:

$$i_a = i_0\left[\exp\left(\frac{\eta}{b}\right)\right] \tag{6.17}$$

$$i_c = i_0\left[-\exp\left(-\frac{\eta}{b}\right)\right] \tag{6.18}$$

where b is the Tafel slope. Thus a plot of *log i versus η yields a straight line*:

$$\eta = a + b\log i \tag{6.19}$$

where a is the intercept of the Tafel plot. The Tafel constants depend on the nature of electrode materials since they are correlated to i_0 and α [35]:

$$|a| = \frac{2.3RT}{\alpha n F}\log i_o \tag{6.20}$$

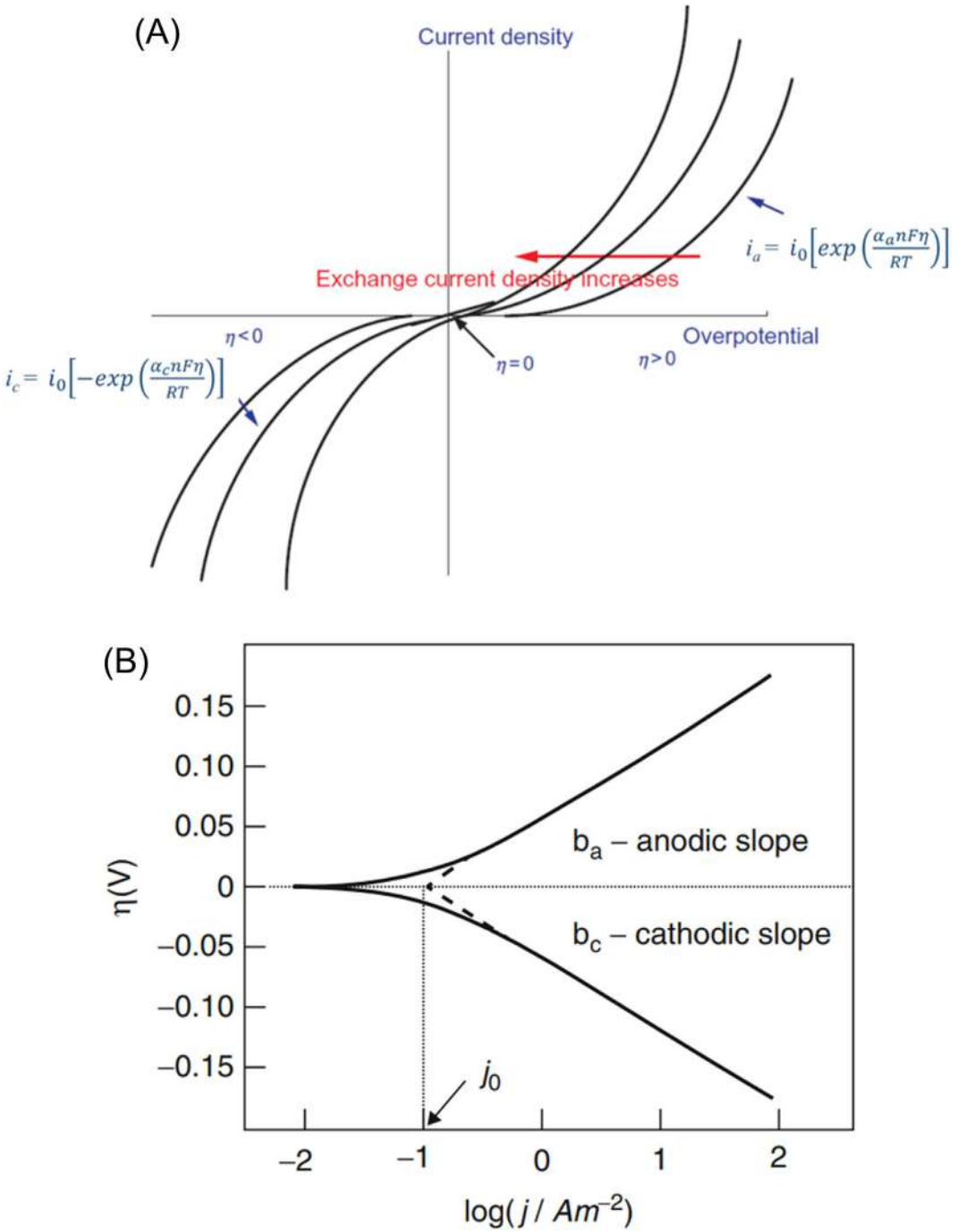

Figure 6.8
(A) Influence of exchange current density and transfer coefficient on reaction kinetics. (B) Example of Tafel plot. *Source: (A) Readapted from [33]. (B) Reproduced from [34].*

$$|b| = \frac{2.3RT}{\alpha nF} \tag{6.21}$$

The constant a can be used to extract i_0 (Fig. 6.8B). The Tafel slope b is used to gain an insight into the reaction mechanism and allows the calculation of the transfer coefficient. It also indicates the number of electrons exchanged in the electrochemical process. For instance, in a reaction in which only one electron is exchanged and $\alpha = 1$, the theoretical value of b at 25°C should be 118 mV per decade. The linear dependence predicted by the Tafel equation occurs usually at $\eta = 50-100$ mV [34].

6.2.2 Water electrolysis

Water splitting involves the dissociation of water into H_2 and O_2. It is an *endothermic* reaction and hence requires energy that can be provided by the flow of an electric current through a suitable electrochemical cell. In an ideal combined energy system, similar to that shown in Fig. 6.9A, renewable energy is converted into chemical energy stored in H_2 through water electrolysis; afterward, hydrogen, which serves as an energy carrier, is converted back to H_2O through fuel cells to release the stored energy. In such a system, heterogeneous catalysis can play a primary role in the development of electrocatalysts for efficient integration of the two electrochemical technologies. Electrocatalysts are indeed used to drive the four electrochemical reactions in the two devices: hydrogen evolution reaction (HER) and oxygen evolution reaction (OER) in the electrolytic cell; and hydrogen oxidation reaction (HOR) and oxygen reduction reaction (ORR) in the fuel cell. The key goal for electrocatalysis is to effectively catalyze these four reactions in order to achieve the lowest overpotential and highest current density for optimum efficiency [36].

The following part will cover only *electrolytic cells*. Yet, from the point of view of the catalyst development, most of the considerations made for the two half-reactions in one device can be similarly applied to the opposite reactions in the parent cell.

There are two main low-temperature commercial technologies for electrochemical water splitting: *alkaline and proton exchange membrane* (PEM) electrolysis. The working principle of the two types of cells is depicted in Fig. 6.9B. Alkaline cells rely on a diaphragm to separate the two electrodes and keep the generated gases apart from each other. The diaphragm is also permeable to the hydroxide ions and water molecules. The typical electrolyte is the caustic potash solution at a level of 20%–30% KOH. On the other hand, a PEM electrolyzer makes use of a polymeric membrane such as Nafion to provide high proton conductivity and avoid gas crossover. This type of cell can operate at much higher current densities compared to the alkaline one, but the highly corrosive environment (due to the acidic environment, pH ~ 2) requires the use of expensive constructive materials and catalysts [37].

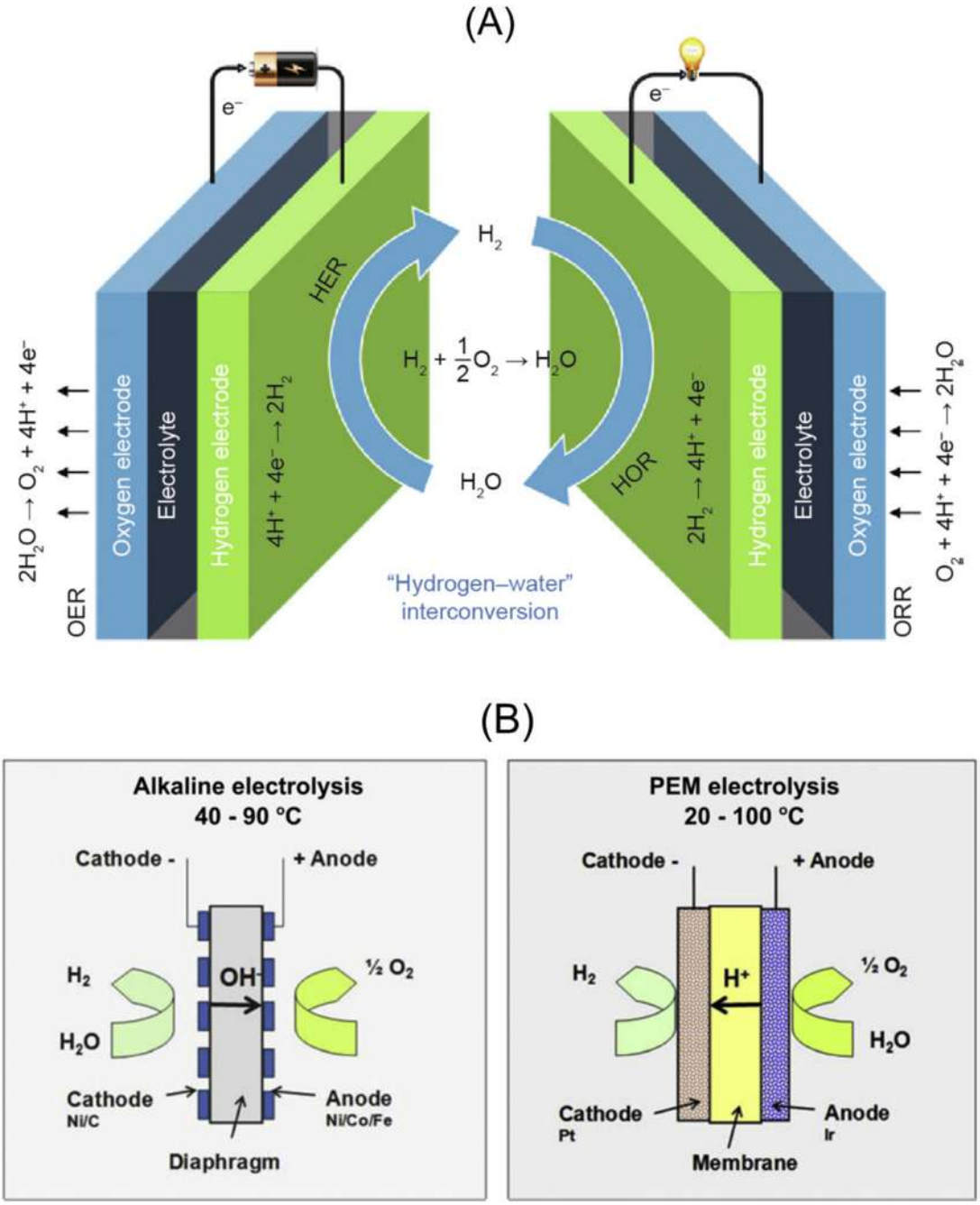

Figure 6.9

(A) Schematic of water electrolysis and fuel cell reactions in an electrochemical conversion system which relies on the combination of the two technologies. (B) Schematic of the working principle of alkaline and PEM electrolysers. *PEM*, Proton exchange membrane. *Source: (A) Reproduced from [36]. (B) Reproduced from [37].*

6.2.2.1 Hydrogen evolution reaction

The cathodic reactions in alkaline and PEM cells with the corresponding standard reduction potentials are the following [38]:

$$2H_2O + 2e^- \rightarrow H_2 + 2OH^- \qquad E^0 = -0.83\ V \tag{6.22a}$$

$$2H^+ + 2e^- \rightarrow H_2 \qquad E^0 = 0.00\ V \tag{6.22b}$$

The first step involved in HER is the binding of atomic hydrogen to the cathode at an adsorption site (Volmer step) resulting from either water or protons:

$$S + H_2O + e^- \rightarrow H{\cdot}S + OH^- \tag{6.23a}$$

$$S + H^+ + e^- \rightarrow H{\cdot}S \tag{6.23b}$$

where S denotes catalytically active sites, while $\cdot S$ refers to adsorbed species.

The process is completed with a desorption step that takes place either through the Tafel reaction (i.e., chemical desorption):

$$2H{\cdot}S \rightarrow 2S + H_2 \tag{6.24}$$

or through the Heyrovsky reaction (i.e., electrochemical desorption):

$$H_2O + H{\cdot}S + e^- \rightarrow S + H_2 + OH^- \tag{6.25a}$$

$$H{\cdot}S + H^+ + e^- \rightarrow S + H_2 \tag{6.25b}$$

As discussed in Chapter 1, Introduction, the exchange current density as a function of the hydrogen adsorption free energy ($\Delta G_{H\cdot S}$) describes a "volcano curve" with a maximum corresponding to Pt having $\Delta G_{H\cdot S} \approx 0$ (Fig. 1.7B). The hydrogen adsorption free energy is usually computed by DFT calculations and it is widely used as an activity descriptor of not only many traditional metals, metals alloys, but also nonmetallic materials. The rate-determining step (RDS) for *HER depends on the adsorption strength of hydrogen* on the catalyst. Too weak adsorption energy (right part of the volcano plot) inhibits the hydrogen adsorption on the catalyst surface and hence the Volmer step will determine the overall reaction rate. On the other hand, too strong adsorption (left part of the volcano plot) leads to a difficult breaking of the catalyst–hydrogen bond that will cause Heyrovsky/Tafel step to be the RDS [36].

Fig. 6.10 is a compilation of the *HER Tafel plots* for various catalysts operating in a strongly acidic medium. Pt is confirmed to be the most active catalyst by keeping in mind that (1) the lower the overpotential at a fixed current or (2) the higher the current density at a fixed overpotential, the higher is the efficiency of the catalyst for HER [39].

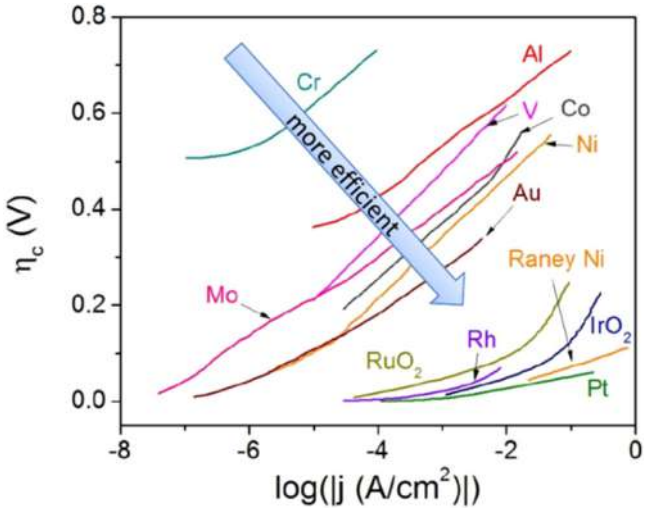

Figure 6.10
Compilation of the HER Tafel plots for various catalysts. *HER*, Hydrogen evolution reaction.
Source: *Reproduced from [39].*

The morphological properties of the electrode can be optimized to increase the rate of electrolysis. If the Volmer step is the RDS, an electrode with cavities and edges on its surface, which supports an easy electron transfer, will usually produce more electrolysis centers for hydrogen adsorption. On the other hand, if Heyrovsky and Tafel steps are the RDS, physical properties such as surface roughness will typically enhance the electron transfer by increasing reaction area and avoid the bubbles to grow, eventually boosting the rate of electrolysis [40].

A change in the applied overpotential can also lead to a mechanism modification. At low overpotentials, hydrogen adsorption is the RDS, while hydrogen adsorption rate is usually greater than the desorption rate at high overpotentials which implies that, in this case, the hydrogen desorption is the RDS [40].

The Tafel slope is widely used to discern the reaction mechanism. Kinetic models, obtained under certain conditions and assumptions, have shown that a rate-determining Volmer step often translates into a Tafel slope of $\sim$120 mV per decade, whereas a rate-determining Heyrovsky/Tafel step results in slopes of $\sim$40 or $\sim$30 mV per decade [39].

6.2.2.2 Oxygen evolution reaction

In alkaline and acidic electrolytes, respectively, the anodic reactions with the corresponding standard reduction potentials are [38]:

$$2OH^- \rightarrow \frac{1}{2}O_2 + H_2O + 2e^- \quad E^0 = 0.40\ \text{V} \tag{6.26a}$$

$$H_2O \rightarrow \frac{1}{2}O_2 + 2e^- + 2H^+ \quad E^0 = 1.23\ V \tag{6.26b}$$

The OER mechanism is more complex compared to the pathways suggested for HER evolution because it involves the formation of different intermediates (O·S, HO·S, HOO·S) that makes the elucidation of OER kinetics a difficult task.

In alkaline medium, one most credited mechanism is the following [41,42]:

$$OH^- + S \rightarrow HO{\cdot}S + e^- \tag{6.27}$$

$$HO{\cdot}S + OH^- \rightarrow O{\cdot}S + H_2O + e^- \tag{6.28}$$

$$2O{\cdot}S \rightarrow 2S + O_2 \tag{6.29}$$

$$O{\cdot}S + OH^- \rightarrow HOO{\cdot}S + e^- \tag{6.30}$$

$$HOO{\cdot}S + OH^- \rightarrow S + O_2 + H_2O + e^- \tag{6.31}$$

In acidic medium:

$$S + H_2O \rightarrow HO{\cdot}S + H^+ + e^- \tag{6.32}$$

$$HO{\cdot}S + OH^- \rightarrow O{\cdot}S + H_2O + e^- \tag{6.33}$$

$$2O{\cdot}S \rightarrow 2S + O_2 \tag{6.34}$$

$$O{\cdot}S + H_2O \rightarrow HOO{\cdot}S + H^+ + e^- \tag{6.35}$$

$$HOO{\cdot}S + 2H_2O \rightarrow S + 2O_2 + 5H^+ + 5e^- \tag{6.36}$$

It should be noted that Reaction (6.36) may not occur due to the kinetic hindrance arising from the transfer of five electrons in a single step and the reaction between three different entities. Similarly to HER, volcano plots can be used for OER (Fig. 6.11) [43]. Metal oxides that are difficult or easy to oxidize are not good catalysts for OER. A difficult oxidation implies a weak adsorption of the intermediates and, in this case, water dissociation is usually the RDS. Conversely, an easy oxidation leads to a strong adsorption of the intermediates (i.e., O·S, HO·S, and HOO·S) and the desorption of these is the RDS. The difference between the calculated free energy of reaction ΔG^0 of two subsequent intermediates such as O·S and HO·S, namely, $\Delta G^0_{O\cdot S} - \Delta G^0_{HO\cdot S}$, is a common descriptor of the OER activity [44].

There is a wide range of catalysts tested for oxygen evolution including simple metal oxides, perovskite, spinel, rock salt, and bixbyite oxides. IrO_2 and RuO_2 are traditionally considered benchmark catalysts due to their high activity in both acidic and alkaline solution. RuO_2 has typically a higher reactivity, but lower stability compared to IrO_2 [45].

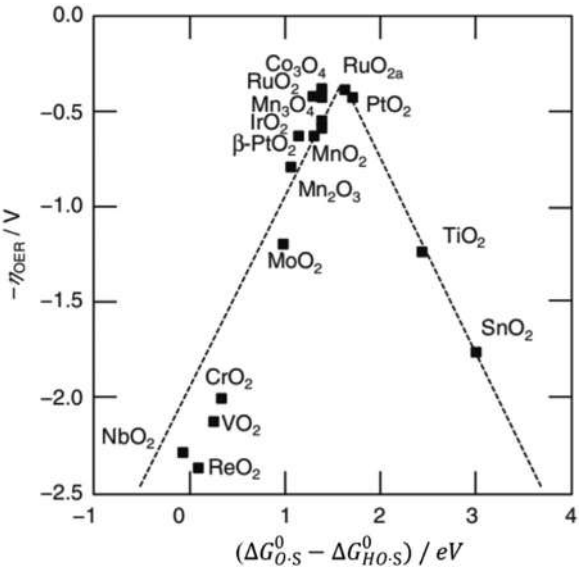

Figure 6.11
Volcano plot for OER. *OER*, Oxygen evolution reaction. *Source*: *Reproduced from [43].*

6.2.3 Electrochemical CO_2 reduction

The reduction of CO_2 (CO_2R) to various hydrocarbons via the electrochemical route is one of the most attractive CO_2 utilization strategies for several reasons: (1) *the process can be easily controlled* by electrode potentials and reaction temperature; (2) the possibility to tune the process toward the *target product*; (3) the overall chemicals consumption is reduced and limited to the supporting electrolyte, which can be fully recycled; and (4) a modular and compact reaction system that lends itself well to scale-up applications [46]. Moreover, compared to hydrogen, CO_2-derived fuels present higher volumetric energy density and easier integration in the existing infrastructure.

Fig. 6.12A shows a typical CO_2 electrolyzer composed of a cathode where CO_2 is converted to CO and various hydrocarbons; an anode where water is oxidized via OER (Eqs. 6.26a and 6.26b); an aqueous alkaline or acid electrolyte ($KHCO_3$, KCl, and K_2SO_4) that conducts ions, dissolves and transports CO_2 to the cathode active sites; and an ion exchange membrane or porous diaphragm to separate the electrodes [47].

The one-electron reduction of CO_2 *to* $CO_2^{\bullet-}$ *is highly energy demanding* given its thermodynamic potential of -1.90 versus SHE [48]. Conversely, proton-assisted electron transfer half-reactions are more thermodynamically favorable. They proceed through two-, four-, six-, and eight-electron reduction pathways to form C_1 and C_{2+}.

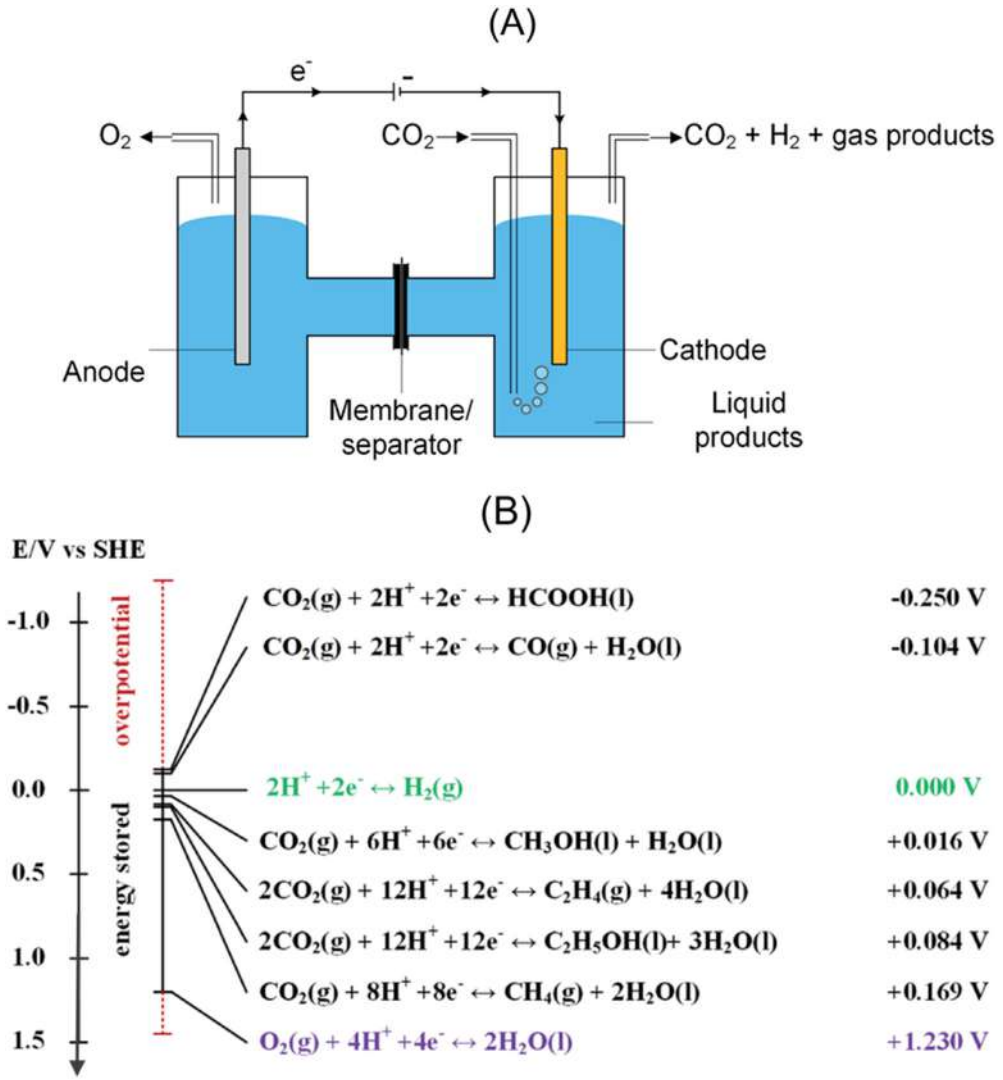

Figure 6.12

(A) Schematic of an electrolyzer for CO_2 reduction. (B) Standard equilibrium potentials for HER, OER, and several half-cell reactions to reduce CO_2 into various products at 1 atm and 25°C in aqueous electrolyte. *HER*, Hydrogen evolution reaction; *OER*, oxygen evolution reaction. *Source*: *Reproduced from [47].*

The commonly reported electrochemical half-reactions of CO_2 reduction and their associated standard electrode potentials are listed in Fig. 6.12B.

The main steps involved in CO_2R are as follows: (1) mass transfer of CO_2 from gas phase to the bulk electrolyte; (2) transport of the dissolved CO_2 to the electrode/electrolyte

interface; (3) adsorption of CO_2 on the cathode catalyst; (4) dissociation of adsorbed CO_2 into reaction intermediates such as CO·S, COOH·S, and CHO·S; (5) electron transfer from the electrocatalyst to the intermediates; (6) desorption of the products from the cathode; and (7) their migration from the cathode/electrolyte interface to the bulk liquid or gas phases [47].

The *proton-assisted reactions* involving CO_2 reduction can thus potentially lead to a wide range of chemicals. Yet, tuning the selectivity to the target products in these reactions is extremely challenging due to their similar potentials. The same consideration is applicable to the HER, the reduction potential of which makes it an important side reaction competing with CO_2R at the cathode. This implies that the product of the electrochemical process is not a single species but a mixture of several chemical compounds.

Another great challenge of this electrolytic process is the *poor kinetics of CO_2R* because of the complexity of the reaction involved, the rates of which are very slow even when working at high overpotentials. The process thus requires a significant energy input, not least because the OER occurring at the anode also suffers from kinetics limitations and the number of electrons needed for the reduction is generally significant as shown in Fig. 6.12B.

The electrocatalysts for CO_2R can be grouped into three main categories: metallic, nonmetallic, and molecular catalysts (Fig. 6.13A). *Polycrystalline monometallic* are the traditional ones and they are easy to handle, structurally simple, and, thus, more suitable for fundamental studies [49]. This class of catalyst can, in turn, be divided into different subgroups: Sn, In, Hg, and Pb produce primarily formate ($HCOO^-$); Au, Ag, and Zn produce mainly CO; Fe, Ni, and Pt are hydrogen-selective metals with very little activity for CO_2R; *Cu is the most active catalyst* able to produce a wide range of hydrocarbons, aldehydes, and alcohols [48]. It is the only monometallic electrocatalyst that can reduce CO_2 to products requiring more than two electron transfers with reasonable faradaic efficiencies. The remarkable performance of Cu may be ascribed to the fact that it is the only metal with negative adsorption energy for CO·S and positive adsorption energy for H·S, as displayed in Fig. 6.13B [50,51]. An example of the reaction mechanism for CO_2R over this metal catalyst is shown in Fig. 6.13C, displaying the free energy diagram with the elementary steps involved in the conversion of CO_2 to CH_4 on Cu(211). The CO·S hydrogenation to CHO·S is the RDS due to its highest energy barrier. This step is followed by a series of proton-electron transfers to form CHOH·S, CH·S, CH_2·S, CH_3·S, and CH_4 [52].

Other catalysts such as ion-modified metallic, bimetallic, nanostructured, nonmetallic, and molecular catalysts have been proven to have good potentials, but more research is still needed to make these materials suitable candidates for CO_2R.

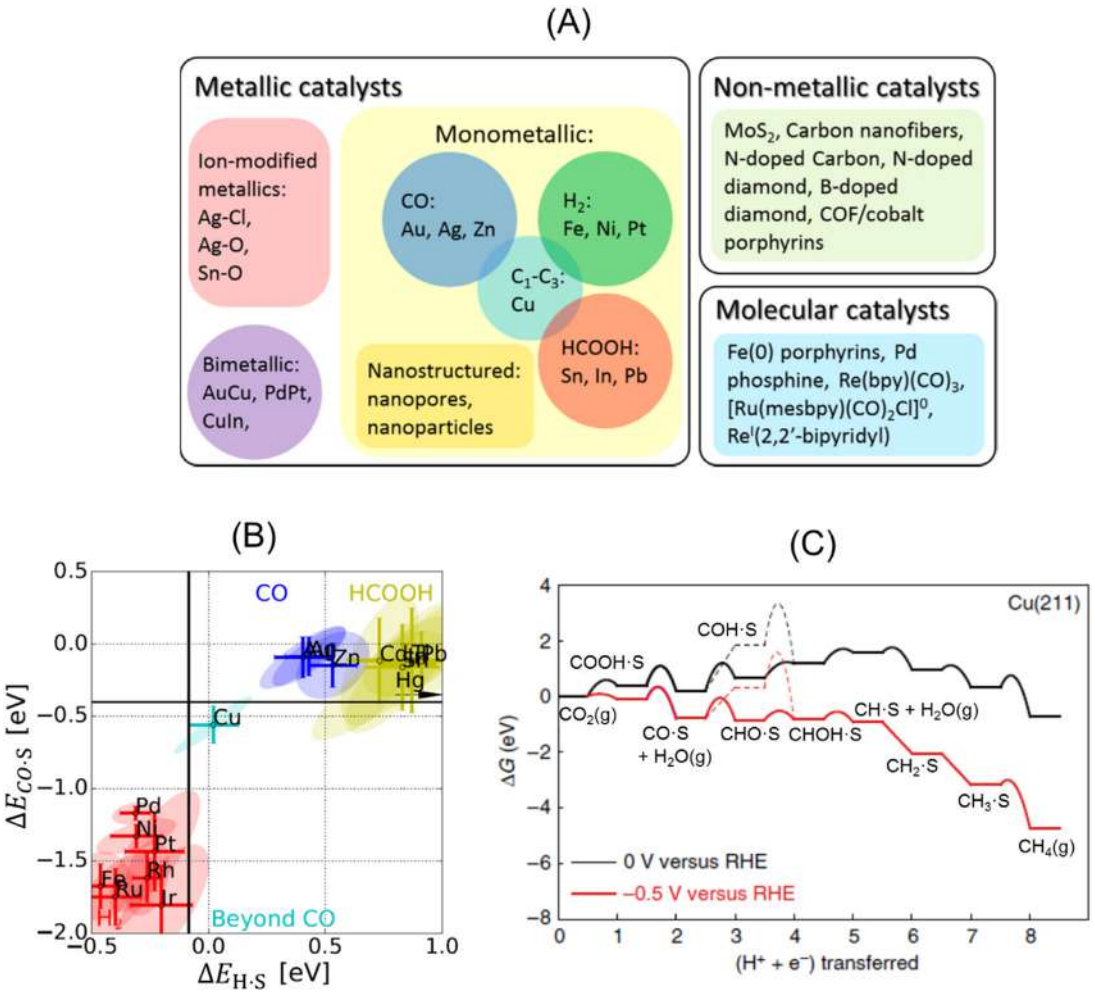

Figure 6.13

(A) An outline of three main categories of electrocatalysts for CO_2R. (B) Metal classification for CO_2R. $\Delta E_{CO\cdot S}$ and $\Delta E_{H\cdot S}$ are the adsorption energies of and $CO\cdot S$ and $H\cdot S$, respectively. (C) Free energy diagram for the reduction of CO_2 to CH_4 on Cu (211) at 0 and -0.5 V versus RHE. *RHE*, Reversible hydrogen electrode. *Source: (A) Reproduced from [48]. (B) Readapted from [51]. (C) Readapted from [52].*

Focus 6.2: Silver/carbon nanotubes catalysts for selective reduction of CO_2 to CO

Carbon nanotubes are attractive support materials for CO_2 electrocatalysis due to their *hydrophobicity and porosity* which facilitate gas transport. Moreover, they hinder nanoparticle (NP) agglomeration providing an excellent conductive network that allows to minimize the noble metal loading and boost catalytic activity. In this area, Ma et al. [53] combined multiwalled carbon nanotubes (MWCNT) with Ag NPs using air-brush method to form a gas diffusion electrode for

(*Continued*)

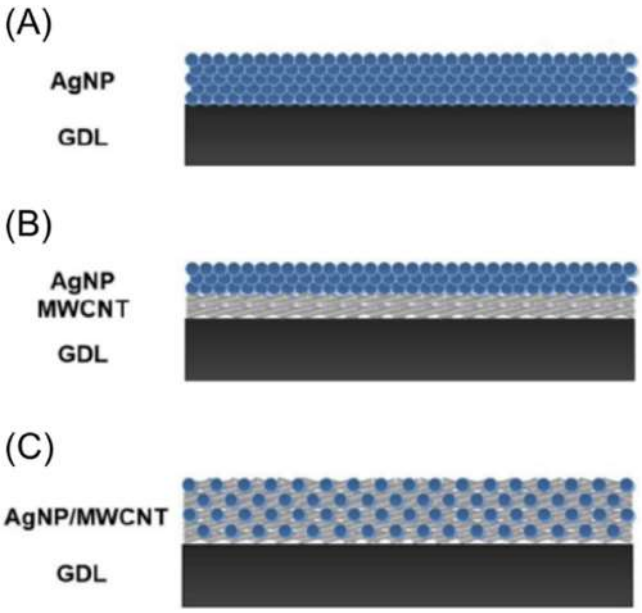

Figure 6.14
GDE configurations tested for selective CO_2R to CO: (A) ES1, (B) ES2, and (C) ES3. *Source*: *Reproduced from [53]*. *ES*, Electrode structure; *GDE*, gas diffusion electrode.

Focus 6.2: Silver/carbon nanotubes catalysts for selective reduction of CO_2 to CO (Continued)

selective CO_2R to CO. They investigated three different configurations: (1) in the electrode structure 1 (ES1), a layer of Ag NPs is deposited on a gas diffusion layer (GDL) (Fig. 6.14A); (2) in the electrode structure 2 (ES2), a layer of Ag NPs is deposited on the top MWCNT layer which is in turn deposited on a GDL (Fig. 6.14B); (3) in the electrode structure 3 (ES3), a composite layer of a uniform mixture of Ag NPs and MWCNTs is deposited on a GDL (Fig. 6.14C).

ES1 and ES2 were formed by the agglomeration of Ag NPs into bigger chunks. Conversely, aggregation of Ag NPs is prevented on the surface of ES3. The electrode ES3 presented a current density of 350 mA cm^{-2}, significantly higher than those achieved by ES2 (280 mA cm^{-2}) and ES1 (230 mA cm^{-2}). The decrease in the charge transfer resistance within the catalyst layer following the incorporation of MWCNTs was the main reason behind the superior performance of ES3.

6.3 Photocatalysis

6.3.1 Fundamentals of photocatalytic processes

Photocatalysis is a process in which a change in the rate of a chemical reaction or its initiation under the action of ultraviolet, visible, or infrared radiation takes place in the

presence of a substance—the photocatalyst—that absorbs light and is involved in the chemical transformation of the reaction partners [54]. As any other catalytic processes, a photocatalytic reaction can be divided into the five steps summarized at the beginning of Chapter 2, Fundamentals of the Adsorption Process. Yet, a photocatalytic reaction presents some differences compared to conventional catalytic processes: (1) the reactants are weakly adsorbed usually at *environment or low temperature and pressure*; (2) the catalyst, and thus the surface reaction, is activated by exciting a semiconductor with a suitable *light source*, whereas the driving force for the activation of a classical thermal catalytic process is an increase in temperature [55].

The photocatalytic activity of a semiconductor depends on several factors such as the position of the *band edges*, the mobility and mean *lifetime of the electrons and holes* generated upon irradiation, the *light absorption* coefficient, etc. Many semiconductor materials have been utilized as photocatalysts such as TiO_2, WO_3, CdSe, $BiVO_4$, ZnO, WO_3, CdS, and C_3N_4.

In semiconductors or insulators, the valence band (VB) is usually defined as the highest energy level filled by electrons at absolute zero temperature, while the conduction band (CB) is the lowest energy level of allowed states, which can be reached by electrons upon excitation from their ground state. The term *bandgap* (E_g) refers to the energy difference between the top of the VB and the bottom of the CB and it is a forbidden region. Each semiconductor possesses a different E_g and band edges position as displayed in Fig. 6.15. When a semiconductor is irradiated with photon energy $h\upsilon \geq E_g$, an electron is excited to the CB of the semiconductor (e^-_{CB}) leaving behind a positive hole in the valance band of the semiconductor (h^+_{VB}). The energy of the valance band (E_V) corresponds to the potential of the photogenerated holes, while the energy of the CB (E_C) corresponds to the energy of the electrons. If E_C lies at a more negative potential than that of the redox couple in the solution (e.g., H^+/H_2), the photogenerated electrons that reach the interface solid/fluid can reduce the oxidized form of the couple (e.g., H^+). On the other hand, if E_V is more positive than the potential of the redox couple (e.g., O_2/H_2O), the photogenerated holes can oxidize their reduced form (e.g., H_2O). The thermodynamics of a photocatalytic process, and thereby the occurrence of the reduction and/or oxidation, thus depends on the relative *position of the band edges with respect to* the energetic levels of the *redox couples* [56]. The more negative the E_{CB}, the more efficient is the semiconductor for the reduction reaction, while the more positive the E_{VB}, the more effective is the semiconductor for the oxidation reaction. However, the wider is the gap between E_{CB} and E_{VB}, the higher is the energy of the light source needed to excite the photocatalyst.

In a *photoelectrochemical cell* an oxidation or reduction reaction takes place on the semiconductor electrode. Fig. 6.16A shows a typical electrochemical cell equipped with an n-type semiconductor anode (e.g., TiO_2) and a metal cathode (e.g., Pt). Most of the

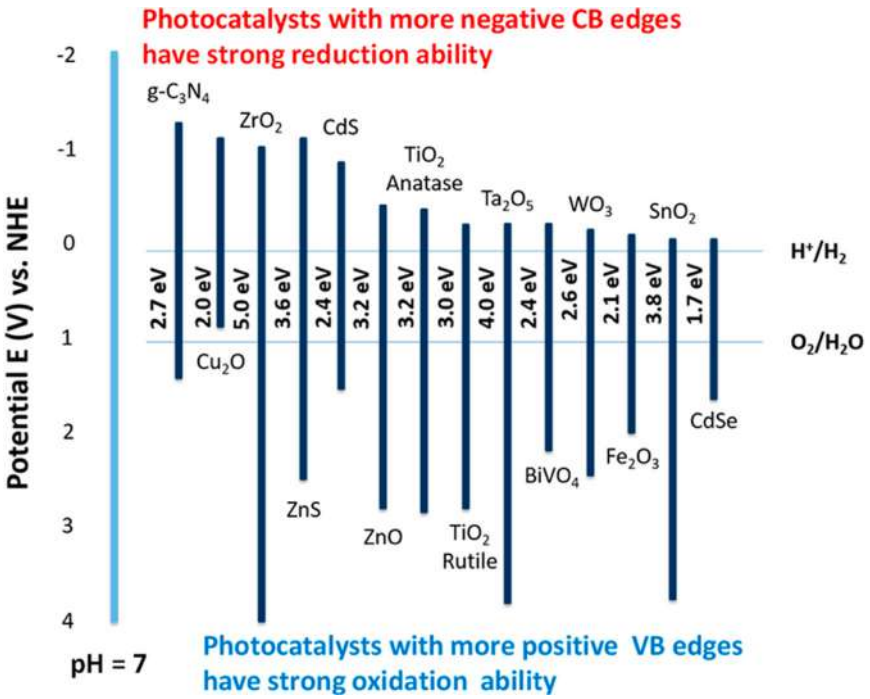

Figure 6.15
Band edges positions for various semiconductors at pH 7 in aqueous solutions. *Source: Reproduced from [57].*

concepts regarding electrolytic cells discussed in Section 6.2 can be similarly applied to this type of photoelectrochemical devices. However, the main advantage of such cells is that the energy input is provided by light energy that is converted into chemical energy. The light harvesting is made possible by the use of suitable semiconductor materials: the OER can be carried out on n-type semiconductors (Fig. 6.16A), while HER or CO_2R on p-type semiconductors.

As shown in Fig. 6.16B, a semiconductor particle immersed in an electrolyte solution behaves like a small photoelectrochemical cell, where oxidation and reduction reactions occur simultaneously by h^+_{VB} transfer from E_V and by e^-_{CB} transfer from the E_C, respectively. The photogenerated holes/electrons migrate toward the catalyst surface and trigger a series of chemical reactions giving rise to very reactive oxygen species (ROS) which can degrade a large variety of organic pollutants. Specifically, electrons can reduce O_2 to superoxide radical anion ($O_2^{\bullet -}$) which may evolve to further ROS, while the holes react with surface adsorbed H_2O or OH^-, producing hydroxyl radicals ($OH^{\bullet}$), hydrogen peroxide (H_2O_2), and hydroperoxyl radicals ($HO_2^{\bullet}$). When TiO_2 is

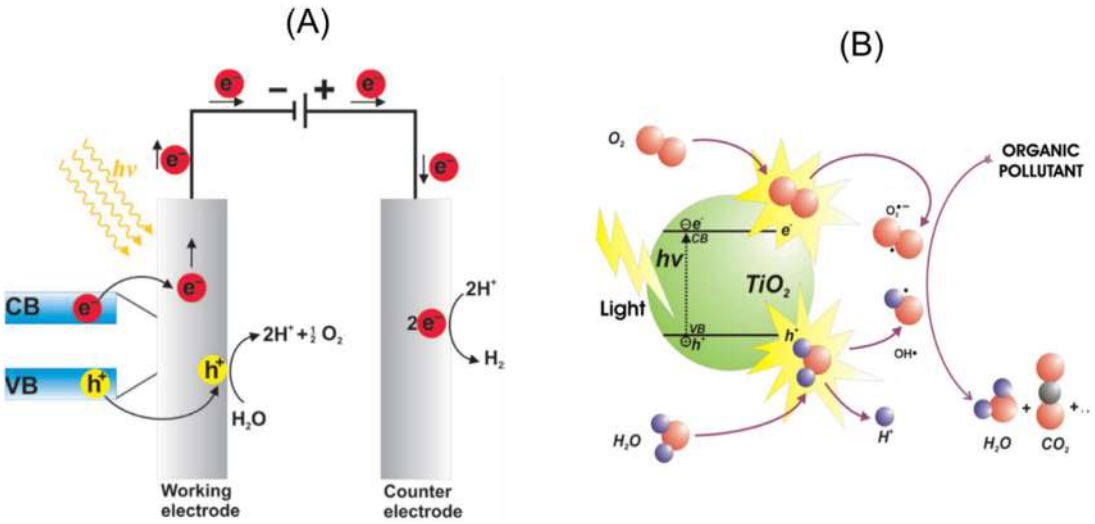

Figure 6.16
(A) Schematic of a photoelectrochemical cell for H_2 generation. (B) Schematic of semiconductor particle excitation and subsequent generation of ROS. *ROS*, Reactive oxygen species. *Source*: *(A) Reproduced from [59]. (B) Reproduced from [60].*

used as a photocatalyst, some of the reactions involving the generation of ROS are the following [56]:

$$TiO_2 + h\upsilon \rightarrow TiO_2\left(e^-_{CB} + h^+_{VB}\right) \tag{6.37}$$

$$OH^- + h^+_{VB} \rightarrow OH^\bullet \tag{6.38}$$

$$O_2 + e^-_{CB} \rightarrow O_2^{\bullet -} \tag{6.39}$$

$$O_2^{\bullet -} + H^+ \rightarrow HO_2^\bullet \tag{6.40}$$

$$2HO_2^\bullet \rightarrow O_2 + H_2O_2 \tag{6.41}$$

$$H_2O_2 + O_2^{\bullet -} \rightarrow OH^- + OH^\bullet + O_2 \tag{6.42}$$

The ROS can subsequently oxidize the organic pollutants with the formation of various intermediates and their eventual mineralization producing mineral salts, H_2O, and CO_2 [58]:

$$OH^\bullet + \text{organic pollutant} \rightarrow \rightarrow \rightarrow H_2O + CO_2 \tag{6.43}$$

$$O_2^{\bullet -} + \text{organic pollutant} \rightarrow \rightarrow \rightarrow H_2O + CO_2 \tag{6.44}$$

$$HO_2^\bullet + \text{organic pollutant} \rightarrow \rightarrow \rightarrow H_2O + CO_2 \tag{6.45}$$

Many inorganic pollutants in water such as metals can be also removed by reducing them to their elemental form on the catalyst surface:

$$M_{aq}^{n+} + ne_{CB}^{-} \rightarrow M_{surf} \tag{6.46}$$

The photocatalytic reaction occurring on the catalyst surface can be assessed by either *Langmuir–Hinshelwood (LH) or Eley–Rideal model* (Section 3.3). Especially the LH model is widely applied to describe the degradation of organic species both in liquid and gas phases in a batch reactor in the presence of oxygen [61–63]. The assumptions of this model are: (1) the adsorption/desorption takes place through equilibrium steps at all times and the adsorption or desorption rate is higher than that of reaction, (2) the RDS is thus the surface reaction that implies that the coverage of the reacting adsorbed species on the catalyst surface is always at equilibrium with the concentration of the species in the fluid phase [56]. The adsorption features related to a certain catalyst can be determined from a suitable isotherm (Chapter 3: Adsorption Models, Surface Reaction, and Catalyst Architectures). Under these assumptions and considering that both the organic substrate to be degraded and oxygen must be present on the catalyst surface, the total disappearance rate of the substrate per unit of area, r_{Sub}, follows a second-order kinetics:

$$r_{Sub} = \frac{1}{S}\frac{dn_{Sub}}{dt} = -k''\theta_{Sub}\theta_{Ox} \tag{6.47}$$

where t is the time, k'' the second-order rate constant, n_{Sub} the substrate moles in the fluid phase, S the catalyst surface area, while θ_{Sub} and θ_{Ox} are the substrate and oxygen fractional coverages, respectively.

By assuming that oxygen is continuously bubbled in the stirred batch reactor, θ_{Ox} does not change during the photocatalytic process. Hence, θ_{Ox} does not depend on time and the term $k''\theta_{Ox}$ in Eq. (6.47) can be substituted by k. Eq. (6.47) thus becomes a *pseudo-first-order rate equation*:

$$r_{Sub} = \frac{1}{S}\frac{dn_{Sub}}{dt} = -k\theta_{Sub} \tag{6.48}$$

where k is a pseudo-first-order rate constant. The following expression for the substrate coverage can be used by assuming that (1) the mineralization is negligible for the time frame under investigation and (2) the intermediates compete with the starting substrate for adsorption:

$$\theta_{Sub} = \frac{K_{Sub}C_{Sub}}{1 + K_{Sub}C_{Sub} + \sum K_i C_i} \tag{6.49}$$

where C_{Sub} and C_i are the concentrations of the substrate and the various intermediates, respectively, and K_{Sub} and K_i are the corresponding equilibrium adsorption constants. Eq. (6.49) can be rearranged by assuming that (1) the concentration of the intermediates is low due to the low conversion of the substrate and the limited mineralization rate during the first stages of the reaction; (2) K_{Sub} and K_i can be considered similar if the chemical nature

of the intermediates is similar to the one of the starting substrates [64]:

$$\theta_{Sub} = \frac{K_{Sub} C_{Sub}}{1 + K_{Sub} C_{Sub,0}} \tag{6.50}$$

where $C_{Sub,0}$ is the initial concentration of the substrate. After introducing the liquid volume V and under the previous assumptions, Eq. (6.48) may be rewritten as:

$$-\frac{dC_{Sub}}{dt} = \frac{S}{V} \frac{kK_{Sub}}{1 + K_{Sub} C_{Sub,0}} C_{Sub} = k_{obs} C_{Sub} \tag{6.51}$$

The last equation can be integrated with the boundary condition $C_{Sub} = C_{Sub,0}$ at $t = 0$ by obtaining:

$$C_{Sub} = C_{Sub,0} \exp(-k_{obs} t) \tag{6.52}$$

By applying a best-fitting procedure to the C_{Sub} versus t data, the values of k_{obs} may be determined for experiments carried out at different initial concentrations of the substrate [65].

Among the various semiconductors, TiO_2 is the most effective photocatalyst due to its superior photoactivity, long-term stability, low cost, and toxicity [66]. Another advantage of TiO_2 over other semiconductors is the photoinduced hydrophilicity that makes it an elective material for those applications requiring thin-film coatings with enhanced wettability. For instance, in self-cleaning glass, this peculiar ability of TiO_2 allows to wash off dirt and grime deposited on the glass surface. Under prolonged UV irradiation, TiO_2 indeed becomes superhydrophilic making the water form sheets on the glass surface rather than droplets, while reverting back to its original state when the light is switched off. The physicochemical mechanism behind the photoinduced hydrophilicity is displayed in Fig. 6.17. The first step

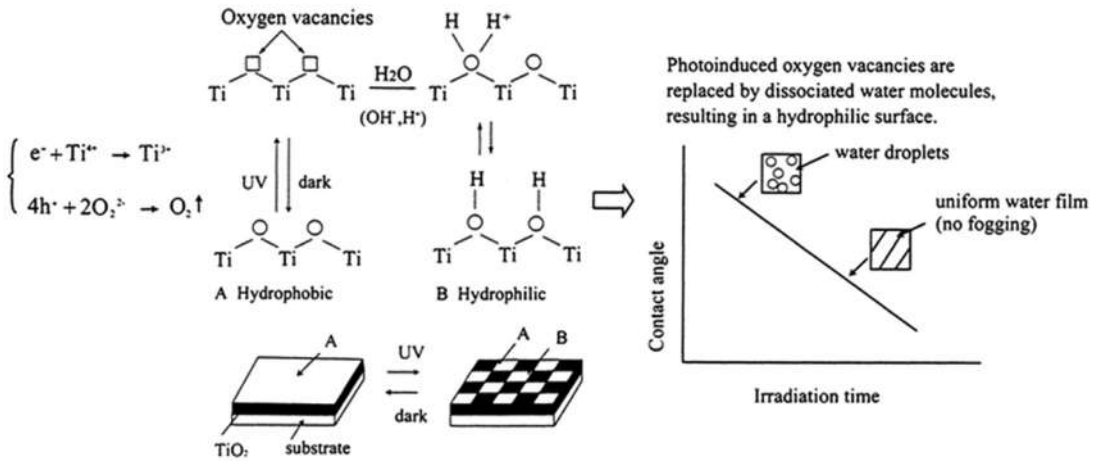

Figure 6.17

Mechanism of photoinduced hydrophilicity on TiO_2. The plot on the right shows the effect of the radiation on the decrease in the contact angle which is the angle that the water droplet creates with respect to the solid surface. *Source*: *Reproduced from [67].*

involves the reduction of Ti^{4+} to Ti^{3+} by the photogenerated electrons and oxidation of O^{2-} anions by the trapped holes. Then, the water molecules occupy oxygen vacancies left behind by the ejected oxygen atoms. The presence of a high density of adsorbed −OH groups boosts the surface hydrophilicity, enabling water molecules to form a uniform film on the surface. After stopping the radiation, TiO_2 gradually loses its hydrophilicity owing to the replacement of the adsorbed −OH groups by oxygen coming from the air [67].

The two typical light-activated TiO_2 mechanisms, that is, *photoinduced hydrophilicity and photocatalytic effect*, may take place simultaneously on the irradiated surface but, depending on the properties of the latter, one of them can occur preferentially at the expense of the other [68].

Despite its undoubted advantages, TiO_2 has some limitations. The most important drawback of this photocatalyst is related to its wide bandgap energy (E_g = 3.2 eV in anatase phase) which makes it active only in the UV region ($\lambda \leq 387$ nm). Several modification strategies are used to extend the spectral response to the visible region as well as to improve the separation of electrons and holes. Doping with metal (e.g., Fe and Cu) or nonmetal (e.g., N and S) impurities can result in subbandgap states in the semiconductor bandgap and in the shift of the absorption edge toward the visible region. Loading TiO_2 with noble metals such as Pt, Au, and Ag typically creates a Schottky barrier in the composite structure due to the higher work function of the metals, thus enabling efficient trapping of the photogenerated electrons and enhanced charge separation. Finally, coupling TiO_2 with low-bandgap semiconductors (e.g., CdS and WO_3) or carbon-based nanostructures (e.g., graphene and carbon nanotubes) favors the formation of heterostructures that boost both visible-light absorption and charge separation. The reader is referred to Refs. [69–71] for further details on these strategies.

In addition to the methods involving TiO_2 chemical alteration by incorporation of additional components, morphological modification is another consolidated approach to boost TiO_2 photoactivity. Zero-dimensional (0D) morphologies (e.g., nanodots), having all dimensions at the nanoscale, are characterized by an enhanced surface area. The advantages of 1D morphologies (e.g., nanotubes, nanowires, and nanobelts), having two dimensions at the nanoscale and one at the micro/macroscale, are derived from their controlled porosity, tailored morphology, and low recombination at grain boundaries [58]. On the other hand, 2D morphologies (e.g., thin films), having one dimension at the nanoscale and two at the micro/macroscale, are more suitable for large-scale applications since they do not present issues related to separation from the reaction medium, which are a great limitation of those nanostructures with lower dimensionality.

6.3.2 Water and wastewater purification

Advanced oxidation processes (AOPs) are deemed to be promising methods for the *removal of a wide range of contaminants* of emerging concern from wastewater effluents. Among the various AOPs, photocatalysis is extensively applied to wastewater treatment. TiO_2 is a

photocatalyst with a strong photoinduced oxidation power to destroy pollutants and it is widely used alone or in combination with other semiconductors.

Photocatalysis has been used for the transformation of organic compounds such as dyes, pesticides, and pharmaceutical compounds into harmless products including CO_2, H_2O, and light mineral salts. Moreover, photocatalysis has been applied to the treatment of seawater in case of oil spills, mostly for the removal of the water-soluble fraction of crude oil [72].

The photodegradation of water pollutants is mainly driven by the oxidizing power of holes and hydroxyl radicals that are known as indiscriminate oxidizing species. In particular, $HO^{\bullet}$ radicals can degrade most of the organic pollutants due to their standard oxidizing potential of $\sim$2.80 V, being exceeded only by fluorine [73]. Four possible different mechanisms over TiO_2 under near-UV illumination were proposed based on the attack of $OH^{\bullet}$ [74,75]:

1. Reaction takes place while both species are adsorbed.
2. An unbound radical reacts with the adsorbed organic substrate.
3. An adsorbed radical reacts with a free organic molecule impinging upon the catalyst surface.
4. Reaction occurs between two free species in the fluid phase in the nearby of the catalyst surface.

The photocatalytic degradation starts with the adsorption of the involved species on the catalyst surface:

$$O_L^{2-} + Ti^{IV} + H_2O \rightleftharpoons O_LH^- + Ti^{IV} - OH^- \tag{6.53a}$$

$$Ti^{IV} + H_2O \rightleftharpoons Ti^{IV} - H_2O \tag{6.53b}$$

$$S + R_1 \rightleftharpoons R_1 \cdot S \tag{6.54}$$

where O_L^{2-} is the lattice oxygen, R_1 an organic molecule, and R_{1ads} an adsorbed organic molecule. After Reaction (6.37), electron–hole recombination can take place, generating thermal energy:

$$e_{CB}^- + h_{VB}^+ \rightarrow \text{heat} \tag{6.55}$$

Trapping of holes and electrons can also occur:

$$Ti^{IV} - OH^- + h_{VB}^+ \rightleftharpoons Ti^{IV} - OH^{\bullet} \tag{6.56a}$$

$$Ti^{IV} - H_2O + h_{VB}^+ \rightleftharpoons Ti^{IV} - OH^{\bullet} + H^+ \tag{6.56b}$$

$$R_1 \cdot S + h_{VB}^+ \rightleftharpoons R_1 \cdot S^+ \tag{6.57}$$

$$Ti^{IV} + e_{CB}^- \rightleftharpoons Ti^{III} \tag{6.58a}$$

$$Ti^{III} + O_2 \rightleftharpoons Ti^{IV} - O_2^{\bullet -} \tag{6.58b}$$

For Reactions (6.56a) and (6.56b) to occur, the oxidation potential should lie above (i.e., be more negative than) E_V. In anatase TiO_2, E_V lies around 2.6 V (vs NHE) at neutral pH and varies by −0.059 V/pH unit. The oxidation potentials for (6.56a) and (6.56b) remain above E_V at any pH so the oxidation of surface-bound OH^- and H_2O by the h^+_{VB} of TiO_2 to form $OH^\bullet$ is always thermodynamically possible. Reaction (6.56a) is favored at high pH, while Reaction (6.56b) is favored at low pH [74].

Attack of $OH^\bullet$ (adsorbed or free) under different conditions (adsorbed or free organic species) can thus occur according to the four aforementioned mechanisms:

Case 1

$$Ti^{IV} - OH^\bullet + R_1 \cdot S \rightarrow Ti^{IV} + R_2 \cdot S \tag{6.59}$$

Case 2

$$OH^\bullet + R_1 \cdot S \rightarrow R_2 \cdot S \tag{6.60}$$

Case 3

$$Ti^{IV} - OH^\bullet + R_1 \rightarrow Ti^{IV} + R_2 \tag{6.61}$$

Case 4

$$OH^\bullet + R_1 \rightarrow R_2 \tag{6.62}$$

Further possible reactions are:

$$e^-_{CB} + Ti^{IV} - O_2^{\bullet -} + 2H^+ \rightleftharpoons Ti^{IV}(H_2O_2) \tag{6.63}$$

$$Ti^{IV} - O_2^{\bullet -} + H^+ \rightleftharpoons Ti^{IV}\left(HO_2^\bullet\right) \tag{6.64}$$

$$H_2O_2 + OH^\bullet \rightleftharpoons HO_2^\bullet + H_2O \tag{6.65}$$

Reactions (6.40) and (6.41) can also occur.

Fig. 6.18 shows the influence of five important physical parameters governing the photocatalytic activity expressed in terms of the reaction rate r. Whatever the design of the photoreactor or the regime used (static or dynamic, slurry or fixed bed, UV or visible radiation), r will be linearly proportional to the *mass m of the catalyst* before reaching a plateau caused by the full adsorption of photons by the photocatalyst (Fig. 6.18A). The optimum catalyst loading (m_{opt}) needs to be determined to ensure the total absorption of photons and avoid the excessive use of photocatalyst. The latter may create a light-screening effect that reduces the active surface area of the catalyst being irradiated at the expense of photocatalytic efficiency [59].

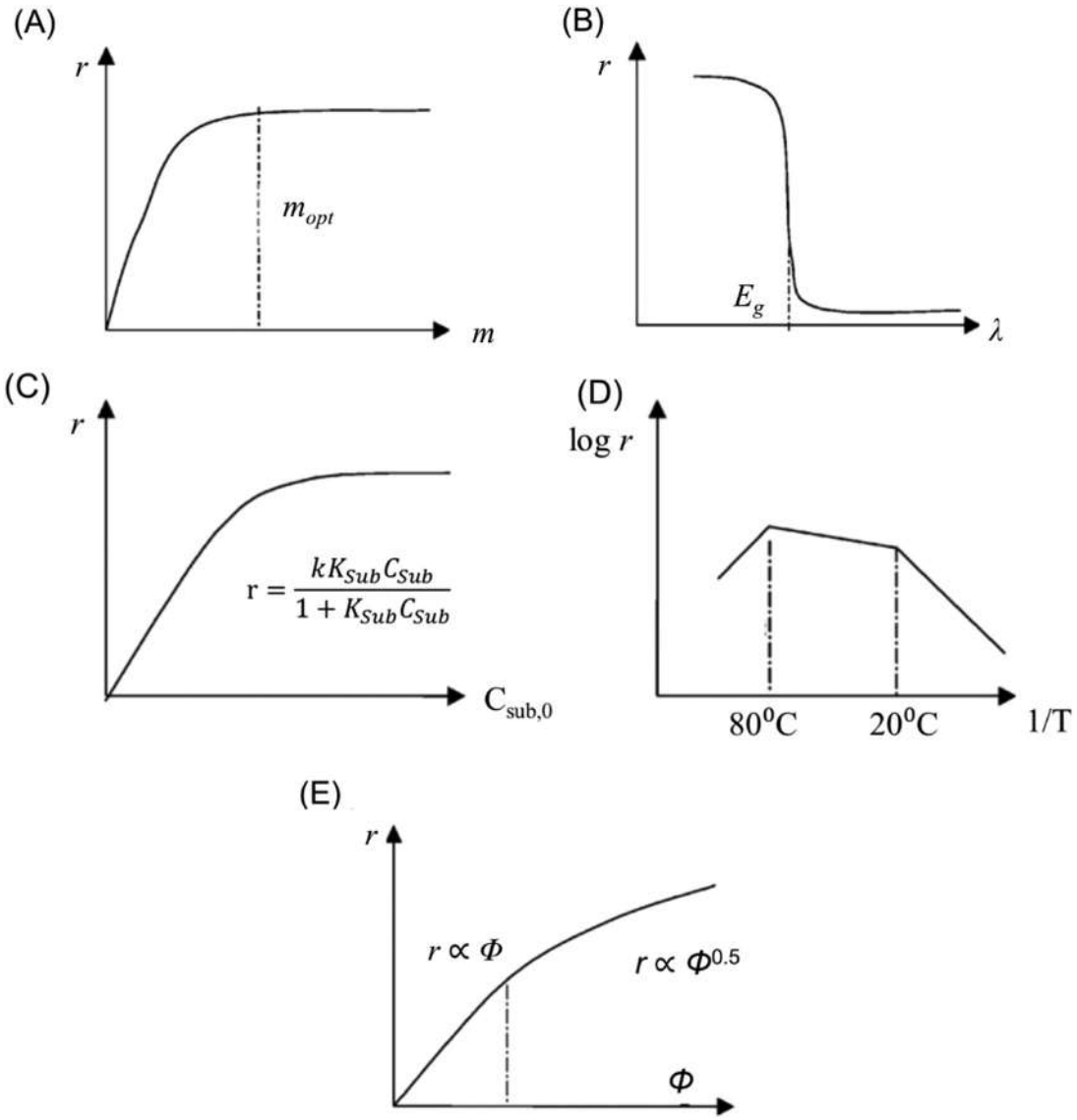

Figure 6.18

Influence of different physical parameters on the reaction rate r of a photocatalytic degradation process: (A) mass of photocatalyst m; (B) wavelength λ; (C) temperature T; (D) initial concentration of substrate $C_{sub,0}$; (E) radiant flux Φ. *Source: Readapted from [76].*

The reaction rate as a function of the *irradiation wavelength* follows the same trend as the adsorption spectrum of the catalyst with a sharp rise in correspondence of E_g (Fig. 6.18B).

The *initial concentration* of the substrate also has a strong impact on the photocatalytic activity (Fig. 6.18C). The catalyst surface can be saturated at high concentrations in some

cases leading to the catalyst deactivation. The initial reaction rate r typically fits LH kinetic scheme when dealing with organic pollutants.

The photocatalytic activity increases with *reaction temperature* (Fig. 6.18D). However, at temperatures above 80°C, the rate of recombination of the photocarriers increases and the adsorption is increasingly inhibited given its prevailing exothermic nature. On the other hand, the activation energy may become too high at low temperature (below 20°C). Therefore the optimal range of the reaction temperature in a photocatalytic process is usually 20°C−80°C.

Generally, photocatalytic reactions take place in two regimes depending on the *photon flux* of the light: first-order regime and half-order regime. In the first case the photogenerated carriers are consumed more rapidly by chemical reactions than by recombination reaction; whereas, in the half-order regime, the recombination rate is dominant [77]. Therefore, at low radiant fluxes (Φ) of the light sources (0−20 mW cm^{-2}), r is linearly proportional to Φ, while r declines from proportionality to follow a root variation at moderate and high radiant fluxes (Fig. 6.18E).

Toxic metals can be removed from wastewater through photoreduction (Eq. 6.46). In particular, photocatalysis has been proven to be effective not only for the removal of heavy metals such as lead, cadmium, mercury, and arsenic but also for the recovery of expensive metals such as silver, gold, and platinum [60].

Photocatalytic treatment of wastewater also allows its disinfection, namely, the inactivation of a wide range of pathogenic microorganisms that can be recalcitrant to other methods of disinfection. $OH^{\bullet}$ radicals have been indicated as the primary actors for the inactivation of microorganisms, and also H_2O_2, $O_2^{\bullet -}$ and $HO_2^{\bullet}$ have been suggested to greatly contribute to the biocidal reactions [78]. Importantly, ROS attack is not specific to one site or an individual pathway that implies that the development of bacterial resistance to photocatalytic treatment is almost impossible. On the other hand, other methods including antibiotics treatment usually are extremely selective as they target a specific biological process within the lifecycle of bacterial organisms [79].

The mechanism of photocatalytic inactivation of microorganisms via ROS attack usually leads to the damage of their cell wall and subsequent impairment of the cytoplasmic membrane and intracellular components. These steps are schematized in Fig. 6.19 for the photokilling of the bacterium *Escherichia coli* by TiO_2 photocatalyst [80]. The initial step involves the partial decomposition of the outer membrane by ROS through photocatalysis (Fig. 6.19B). This change in the permeability of the outer membrane enables ROS to easily reach the cytoplasmic membrane through a monolayer of peptidoglycan (Fig. 6.19C). The cytoplasmic membrane is finally attacked by ROS, resulting in the peroxidation of membrane lipid, with consequent loss of cell viability and cell death.

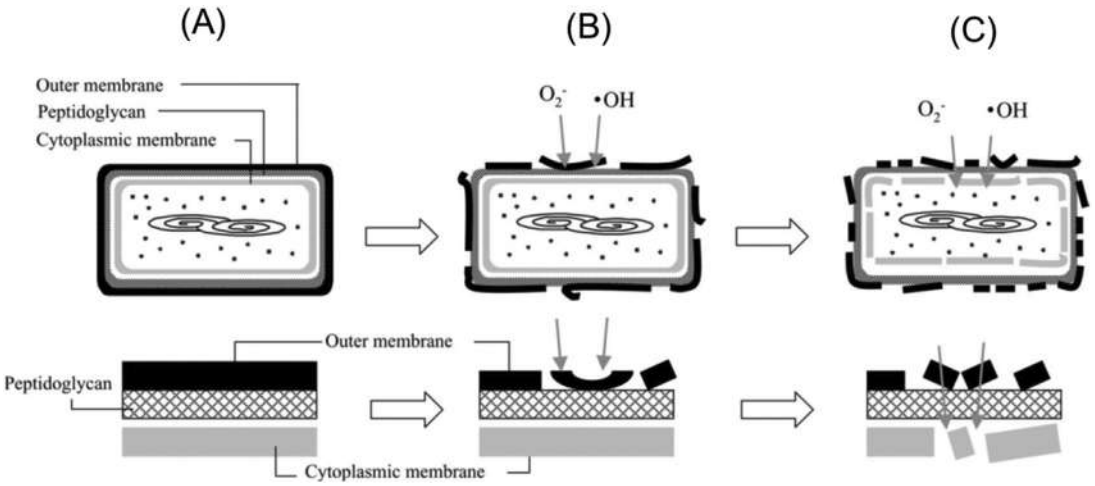

Figure 6.19

Schematic illustration of the process of *Escherichia coli* inhibition by TiO_2 photocatalyst. (A) Constituent parts of the bacterium, (B) ROS attack and decomposition of the outer menbrane, (C) ROS reach the cytoplasmic membrane. In the lower row, the cell envelope is magnified. *Source*: *Reproduced from [80].*

Focus 6.3: Tailoring of the crystalline structure of g-C_3N_4 structure for photocatalytic production of H_2

Graphitic carbon nitride (g-C_3N_4) is considered the most promising *metal-free and visible-light active* photocatalyst due to its favorable electronic structure, "earth-abundant" nature, high physicochemical stability, and facile synthesis [81]. The material synthesized by traditional thermally induced pyrolysis of nitrogen- and carbon-rich molecules such as melamine and urea above 525°C is a polymeric carbon nitride with a zigzag structure known as Liebig's melon [82]. The incomplete condensation of the melon and the presence of some incompletely reacted N-rich intermediates (e.g., amino and cyanogroups) lead to hydrogen bonds between the layers of g-C_3N_4 with adverse effects on the photocatalytic activity. Huang et al. [83] recently proposed a novel synthesis strategy able to ensure a high-quality layer plane carbon nitride by suppressing incomplete reaction pathways in the condensation process. The authors demonstrated that the thermal-induced condensation of melem in pure O_2 atmosphere can lead to a layer plane ordered porous carbon nitride (LOP-CN). As shown in Fig. 6.20A, the synthesis process involves two steps: (1) production of melem from melamine in Ar atmosphere; (2) polycondensation of melamine to LOP-CN in O_2 atmosphere at three different temperatures to obtain 500 LOP-CN, 530 LOP-CN, and 560 LOP-CN. Pure bulk g-C_3N_4 (G-CN) was also synthesized by conventional thermal polycondensation, that is, heating melamine at 550°C in air.

The X-ray diffraction (XRD) revealed two main peaks at 13 and 27.7 degrees assigned to (1 0 0) and (0 0 2) planes (Fig. 6.20B). The first peak is derived from the in-plane structural packing motif, while the second one from the van der Waals forces controlled layer stacking along the *c*-axis in LOP-CN. With the heating temperature increasing from 500°C to 530°C, the intensity of the first peak increases and then decreases at 560°C. The enhanced intensity of this peak denotes

(*Continued*)

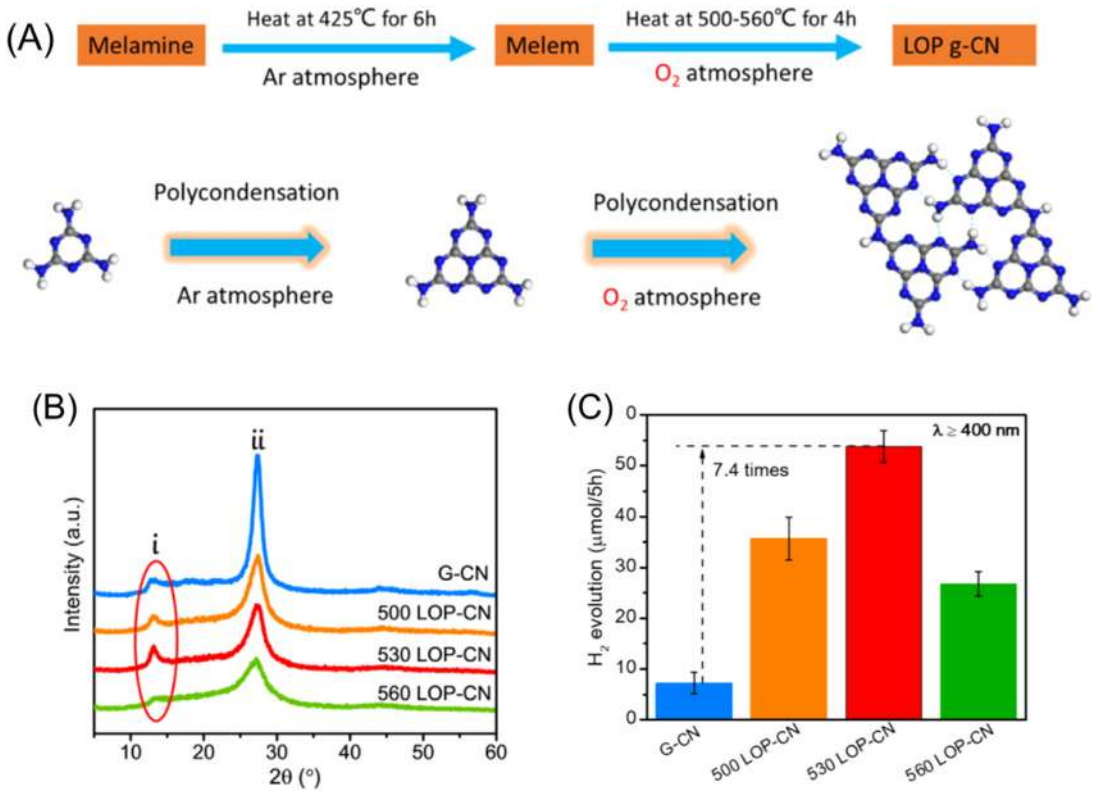

Figure 6.20

(A) Schematic illustration of the synthesis steps of LOP-CN samples, (B) XRD patterns, and (C) photocatalytic production of H_2. *LOP-CN*, Layer plane ordered porous carbon nitride; *XRD*, X-ray diffraction. *Source*: *(C) Reproduced from [83].*

Focus 6.3: Tailoring of the crystalline structure of g-C_3N_4 structure for photocatalytic production of H_2 (Continued)

long-range atomic order intralayer structure. On the other hand, the broadening of the peak at 27.7 degrees with increasing temperature can be ascribed to a disturbance of the interlayer stacking.

The sample 530 LOP-CN showed the highest production of H_2 under visible-light irradiation, being 7.4 times higher than that over G-CN (Fig. 6.20C). The enhanced photocatalytic activity is mainly due to the efficient charge separation and the extended visible-light absorption. On the other hand, the reduction in the photocatalytic activity above 530°C probably arises from the disturbance of the plane atomic arrangements and collapse of the porous structure as observed in the XRD patterns.

6.3.3 Organic synthesis

Traditional industrial routes for the production of several key organic chemicals rely on harmful solvents, heavy metals as catalysts, and oxidant/reducing agents of environmental

concern, ending up with the production of large quantities of harmful waste. Moreover, they mostly require severe operating conditions such as high pressure and temperature. In this context, photocatalysis is a viable route to carry out a multitude of chemical transformations of great interest in synthesis and, at the same time, to ensure a *sustainable chemistry with a minimal environmental impact*. Compared to the case of photocatalysts for organic degradation mainly targeting the complete mineralization of the organic substrate, the photocatalysts for organic synthesis should be highly customized on a case-by-case basis, as the main goal here is to tailor the selectivity of the photocatalytic process and direct the reaction to yield the desired product.

Most of the photocatalytic reactions for organic synthesis involve oxidation or reduction reactions. The substrates used for oxidation reactions are alkanes, aromatics, alkenes, alcohols, and polyaromatics, while CO_2 and nitrogen-containing compounds are typical substrates for photocatalytic reductions. Polymerization reactions and coupling reactions (carbon−nitrogen or carbon−carbon bond forming) are also extensively studied. This section provides significant examples of oxidation and reduction reactions. The reader is referred to Refs. [84−88] for the study of polymerization and coupling reactions and further examples of oxidation/reduction reactions.

The *hydroxylation of aromatics* is an example of photocatalytic synthesis used to produce industrially important chemicals such as phenol, catechol, and hydroquinone, which are precursors of resins and pharmaceuticals. In particular, the photocatalytic synthesis of phenol from direct hydroxylation of benzenes involves the electrophilic addition of an $OH^{\bullet}$ radical to benzene [88,89]. The formed phenol is usually decomposed upon further reaction with $OH^{\bullet}$ radicals so that phenol selectivity is usually very low, unless a membrane reactor is used [90]. A significant research effort has been devoted to developing more efficient catalysts able to ensure high phenol selectivity. Some of the most effective approaches include using zeolite as support of TiO_2 [91] or fabricating mesoporous TiO_2 particles, the mesopores of which play a crucial role for the selective phenol production [92].

As displayed in Fig. 6.21, hydroxylation of mono-substituted benzene derivatives by photoexcited TiO_2 depends on the electron-withdrawing properties of the substituents [93,94]. In particular, benzene derivatives with an electron-donating group, such as aniline and phenol, enable $OH^{\bullet}$ radical attack according to the selectivity rules for electrophilic substitution, leading to the formation of ortho- and para-hydroxylated isomers. Conversely, benzene derivatives with an electron-withdrawing group such as nitrobenzene and benzoic acid are subjected to unselective $OH^{\bullet}$ radical attack with the consequent formation of all three possible isomers (ortho, para, and meta). Such $OH^{\bullet}$ radical substitution rules are of great importance for the development of selective hydroxylation processes for benzene derivatives.

The *partial oxidation of alcohols* to corresponding carbonyl compounds (i.e., aldehydes ketones, acids) is another challenging chemical transformation for the production of fine and specialty chemicals. The “overoxidation” of these compounds to the corresponding

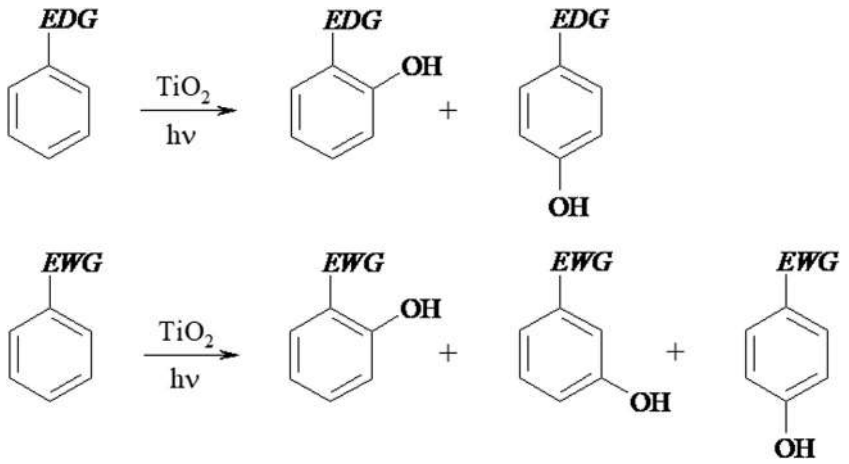

Figure 6.21
Main hydroxylated products obtained during the photocatalytic oxidation of benzene derivatives containing either an EDG or an EWG. *EDG*, Electron donor group; *EWG*, electron-withdrawing group. *Source*: *Reproduced from [93]*.

carboxylic acids and CO_2 may be a drawback of such reactions. The selectivity typically depends on several parameters such as structure of alcohols, presence of oxygen, and used solvent. The photocatalytic oxidation has been reported to start with the adsorption of the alcohol as an alkoxide intermediate and proceed with two dominant pathways: oxidation of the formed intermediate by direct electron transfer to the positive holes or by mediation from $OH^{\bullet}$ radicals formed following Reaction (6.38) [95–97]. Subsequent coupling reactions lead to partial oxidation products.

The *conversion of alkanes to oxygenated compounds* such as alcohols, ketones, aldehydes, and carboxylic acids is another noteworthy example of selective photocatalytic oxidation. The photocatalytic route enables selective oxygenation of C–H bonds by O_2 under mild temperature and pressure [87]. In this area the liquid-phase oxygenation of cyclohexane to cyclohexanol and cyclohexanone is extensively studied because these products are key intermediates of ε-caprolactam used to produce nylon polymers. The type of solvent affects significantly the selectivity to cyclohexanol and cyclohexanone by TiO_2 catalyst. Nonpolar solvents cause cyclohexanol to preferentially adsorb on TiO_2 with complete mineralization to CO_2 and extremely low selectivity. Conversely, in polar solvents such as dichloromethane, the selectivity is higher because cyclohexanol is poorly adsorbed on the catalyst surface due to the competition with the polar solvent (Fig. 6.22A) [98].

Photocatalytic reduction is generally safer than the conventional reduction methods employing aggressive and/or hazardous reducing agents such as sodium borohydride, hydrogen, and carbon monoxide among others. The reduction of nitrobenzenes to the

corresponding anilines is one of the most investigated photocatalytic reactions (Fig. 6.22B). It is driven by the CB electrons generated in the photoexcited semiconductor and is typically carried out in the presence of alcohols such as methanol and 2-propanol that serve as electron donors to scavenge h^{+}_{VB} [99,100]. This inhibits electron–hole recombination and avoids undesirable side reactions. In addition, the removal of O_2 boosts the reduction efficiency and selectivity because O_2 acts as a competitive scavenger of e^{-}_{CB} being converted to highly reactive $O_2^{\bullet -}$ (Reaction 6.39).

Photocatalytic CO_2 reduction to CO and organic species is carried out both in gas and liquid phases. Even here, the use of alcohols as hole scavengers is quite usual [101,102]. Inorganic hole scavengers such as sodium sulfite are also employed [103]. Fig. 6.23 shows

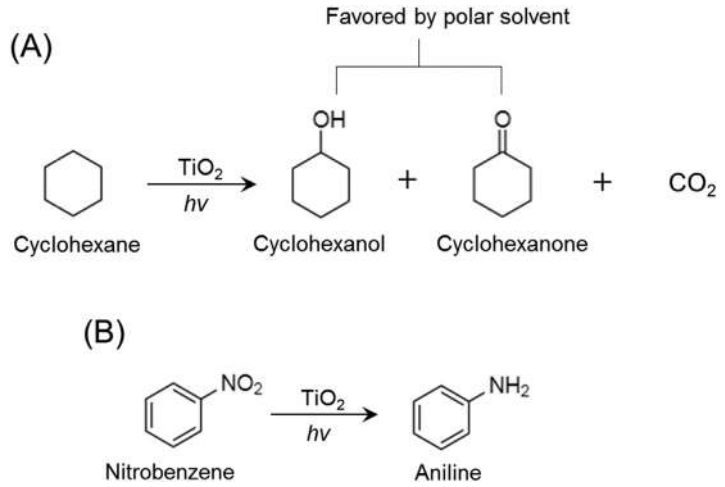

Figure 6.22
(A) Photooxidation of cyclohexane to cyclohexanol, cyclohexanone, and CO_2 by TiO_2 photocatalyst. (B) Photoreduction of nitrobenzene to aniline by TiO_2 photocatalyst.

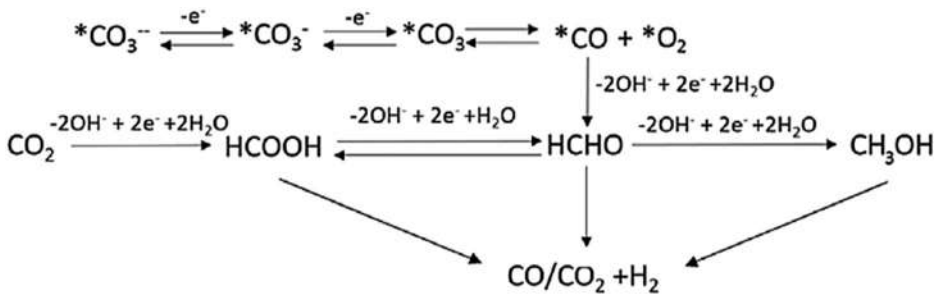

Figure 6.23
Photocatalytic reduction of CO_2 by TiO_2 at basic pH. *Source*: *Reproduced from [103].*

some of the typical reduction reactions that can occur over TiO_2 at an alkaline pH, thus in the presence of dissolved CO_2 and carbonate anions [103]. The scheme reports two reaction pathways taking place in parallel. The first involves CO_2 photoreduction to formic acid (HCOOH), which may give rise to gas-phase products or methanol (CH_3OH) after being reduced to formaldehyde (HCHO). Formaldehyde can also be generated through the second reaction pathway in which the carbonates are gradually reduced.

6.4 Questions and problems

1. Describe the main advantages and drawbacks of the physicochemical, biochemical, and thermochemical methods to convert biomass.
2. Carry out a literature review on the recent progress of the implementation of bio-oil for diesel engines and gas turbines. How does it compare to traditional types of fuel?
3. Assess the thermodynamics of the steps of the gasification process (Eqs. 6.1–6.10) and comment on the benefits brought about by catalysts.
4. Analyze the recent literature on the use of ethylene glycol as a source of hydrogen. Elaborate on the efficiency of alternative biomass-derived sources undergoing aqueous-phase reforming.
5. Catalytic upgrading of biorefinery oil from algal biofuel is a promising route for renewable energy generation which, however, is at an earlier stage compared to that using other biomass-derived feedstocks. Explain the reasons behind that. Suggested references: [104–106].
6. Identify the thermodynamic and kinetic constraints of the electrocatalytic splitting of water. Carry out a literature review to check how these have been addressed and describe the use of some efficient catalysts and reactors recently implemented.
7. Coupling inorganic materials with nanocarbon structures is an elective strategy to design increasingly efficient electrocatalysts. By referring to the various types of carbon/inorganic nanomaterial hybrids shown in the image below, discuss the advantages of nanocarbon catalysts compared with traditional carbon materials such as activated carbon.

   The image (reproduced from Ref. [107]) shows inorganic/nanocarbon hybrids with different nanostructures: (A) 0D carbon quantum dots, (B) 1D carbon nanotubes, (C) 2D graphene, and (D) 3D graphene framework, which can be, in turn, classified into micro-, meso-, and macroscale hybrids depending on the structure of graphene substrates.

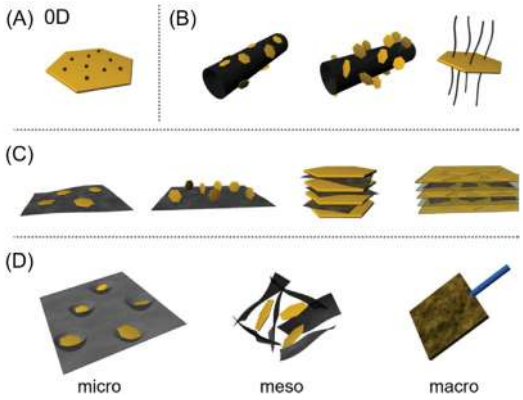

8. Nitrogen-containing polymers (N-polymers) are an emerging class of materials in CO_2R. These materials contain nitrogen functionalities that complex metal cations or anchor metal nanoparticles either within the polymer backbone or pendant group. Two main categories of N-polymers have been tested for CO_2R: electroactive and ion-exchanging polymers. By referring to some of the polymers shown in the image below, discuss the working principle of the two categories.

   The image (reproduced from Ref. [108]) shows (A) electroactive and (B) ion-exchanging N-polymers and their complexes with metals used in CO_2R.

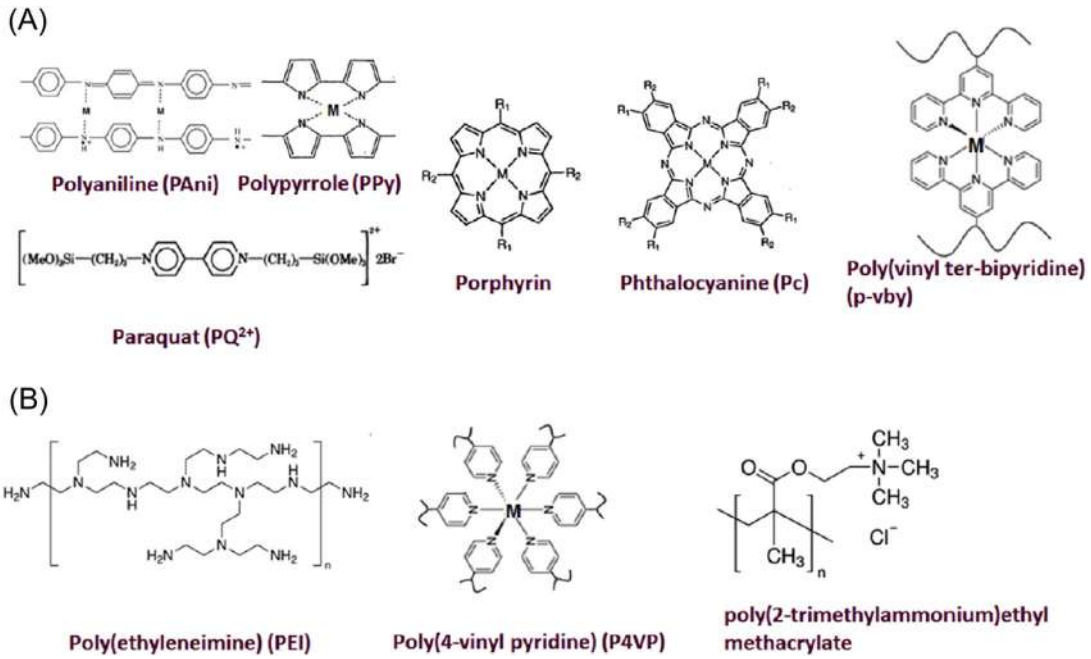

9. How do the photocatalytic and electrocatalytic approaches compare for the splitting of water? Identify recent studies in literature and proceed with a critical assessment of merits and demerits.
10. The reduction of CO_2 to organic molecules is a multielectron process that is thermodynamically and kinetically hindered. Coupling photocatalysis and electrocatalysis is an approach that can provide better efficiencies. What is the mechanism of such photoelectrocatalytic process and how can the two technologies work synergically? (Suggested reading: Refs. [109,110]).
11. How does the photon flux affect a photocatalytic process? Why does the dependence of rate on photon flux change depending on the reaction conditions?
12. If you had to choose three key properties for a photocatalyst, what would they be and why?
13. How can the thermodynamic compatibility between two semireactions (red/ox) and a photocatalyst be verified? Provide an example with a schematic showing a semiconductor and two semireactions of your choice.
14. Heterostructured photocatalysts allow to extend the range of light absorption and suppress electron–hole recombination compared to conventional photocatalysts. Z-scheme photocatalysts mimic the natural photosynthesis system by making use of one oxidation photocatalyst and one reduction photocatalyst. As shown in the image below, the charge transfer between the two components is ensured by (1) a shuttle redox ion mediator (i.e., $Fe^{3+/}Fe^{2+}$), (2) an electron conductor (i.e., Ag, Au NPs, and graphene), or (3) direct contact between the two semiconductors. Provide examples of good reduction and oxidation photocatalysts used in Z-scheme systems and highlight the benefits and weaknesses of the three mentioned configurations.

    The image (reproduced from Ref. [111]) reports the schematic of charge carrier transfer in Z-scheme photocatalysts with (A) a redox ion mediator, (B) an electron conductor, (C) direct transfer between the two semiconductors. PCI and PCII stand for photocatalysts I and II; A and D for electron acceptor and donor; and E for electric field.

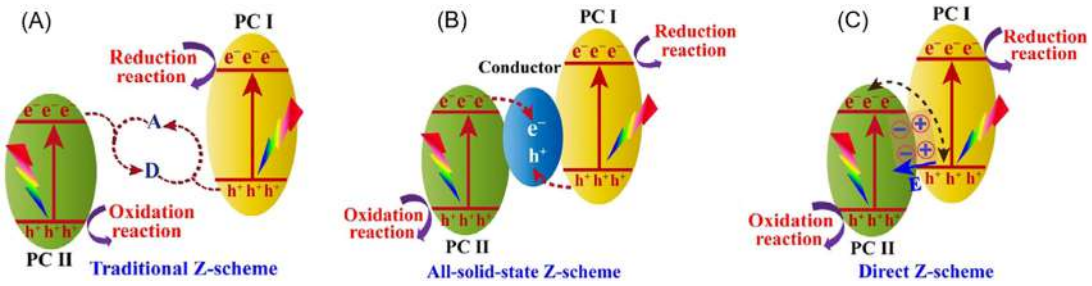

References

[1] D.M. Alonso, J.Q. Bond, J.A. Dumesic, Catalytic conversion of biomass to biofuels, Green Chem. 12 (2010) 1493–1513.

[2] S. Nonhebel, Renewable energy and food supply: will there be enough land? Renew. Sustain. Energy Rev. 9 (2005) 191–201.

[3] J. Baruah, B.K. Nath, R. Sharma, S. Kumar, R.C. Deka, D.C. Baruah, et al., Recent trends in the pretreatment of lignocellulosic biomass for value-added products, Front. Energy Res. 6 (2018) 141.

[4] M. Jédrzejczyk, E. Soszka, M. Czapnik, A.M. Ruppert, J. Grams, Physical and chemical pretreatment of lignocellulosic biomass, Second and Third Generation of Feedstocks: The Evolution of Biofuels, Elsevier, 2019, pp. 143–196.

[5] A. Raheem, P. Prinsen, A.K. Vuppaladadiyam, M. Zhao, R. Luque, A review on sustainable microalgae based biofuel and bioenergy production: recent developments, J. Cleaner Prod. 181 (2018) 42–59.

[6] L. Brennan, P. Owende, Biofuels from microalgae—a review of technologies for production, processing, and extractions of biofuels and co-products, Renew. Sustain. Energy Rev. 14 (2010) 557–577.

[7] M. Kaltschmitt, Biomass biomass as renewable source of energy biomass as renewable source of energy: Possible conversion routes, Energy from Organic Materials (Biomass), Springer, New York, 2019, pp. 353–389.

[8] G. Stephanopoulos, Challenges in engineering microbes for biofuels production, Science (80–) 315 (2007) 801–804.

[9] E.L. Kunkes, D.A. Simonetti, R.M. West, J.C. Serrano-Ruiz, C.A. Gärtner, J.A. Dumesic, Catalytic conversion of biomass to monofunctional hydrocarbons and targeted liquid-fuel classes, Science (80–) 322 (2008) 417–421.

[10] H.C. Ong, W.H. Chen, A. Farooq, Y.Y. Gan, K.T. Lee, V. Ashokkumar, Catalytic thermochemical conversion of biomass for biofuel production: a comprehensive review, Renew. Sustain. Energy Rev. 113 (2019) 109266.

[11] S. Gent, M. Twedt, C. Gerometta, E. Almberg, Introduction to thermochemical conversion processes, Theoretical and Applied Aspects of Biomass Torrefaction: For Biofuels and Value-Added Products, Elsevier, 2017, pp. 1–16.

[12] S. Al Arni, Comparison of slow and fast pyrolysis for converting biomass into fuel, Renew. Energy 124 (2018) 197–201.

[13] J. Fermoso, J.M. Coronado, D.P. Serrano, P. Pizarro, Pyrolysis of microalgae for fuel production, Microalgae-Based Biofuels and Bioproducts: From Feedstock Cultivation to End-Products, Elsevier Inc, 2017, pp. 259–281.

[14] L. Li, J.S. Rowbotham, H. Christopher Greenwell, P.W. Dyer, An introduction to pyrolysis and catalytic pyrolysis: versatile techniques for biomass conversion, New and Future Developments in Catalysis: Catalytic Biomass Conversion, Elsevier B.V, 2013, pp. 173–208.

[15] M. Balat, M. Balat, E. Kirtay, H. Balat, Main routes for the thermo-conversion of biomass into fuels and chemicals. Part 1: Pyrolysis systems, Energy Convers. Manag. 50 (2009) 3147–3157.

[16] D.C. Elliott, P. Biller, A.B. Ross, A.J. Schmidt, S.B. Jones, Hydrothermal liquefaction of biomass: developments from batch to continuous process, Bioresour. Technol. 178 (2015) 147–156.

[17] A.R.K. Gollakota, N. Kishore, S. Gu, A review on hydrothermal liquefaction of biomass, Renew. Sustain. Energy Rev. 81 (2018) 1378–1392.

[18] A. Molino, S. Chianese, D. Musmarra, Biomass gasification technology: the state of the art overview, J. Energy Chem. 25 (2016) 10–25.

[19] R.G. dos Santos, A.C. Alencar, Biomass-derived syngas production via gasification process and its catalytic conversion into fuels by Fischer Tropsch synthesis: a review, Int. J. Hydrogen Energy 45 (2020) 18114–18132.

[20] A. Saddawi, J.M. Jones, A. Williams, C. Le Coeur, Commodity fuels from biomass through pretreatment and torrefaction: effects of mineral content on torrefied fuel characteristics and quality, Energy Fuels 26 (2012) 6466–6474.
[21] E. Pütün, Catalytic pyrolysis of biomass: effects of pyrolysis temperature, sweeping gas flow rate and MgO catalyst, Energy 35 (2010) 2761–2766.
[22] S.B. Saleh, B.B. Hansen, P.A. Jensen, K. Dam-Johansen, Influence of biomass chemical properties on torrefaction characteristics, Energy Fuels 27 (2013) 7541–7548.
[23] Z. Sebestyén, E. Barta-Rajnai, J. Bozi, M. Blazsó, E. Jakab, N. Miskolczi, et al., Thermo-catalytic pyrolysis of biomass and plastic mixtures using HZSM-5, Appl. Energy 207 (2017) 114–122.
[24] K. Zubek, G. Czerski, S. Porada, Determination of optimal temperature and amount of catalysts based on alkali and alkaline earth metals for steam gasification process of bituminous coal, Thermochim. Acta 665 (2018) 60–69.
[25] G. Morales, J. Iglesias, J.A. Melero, Sustainable catalytic conversion of biomass for the production of biofuels and bioproducts, Catalysts 10 (2020) 581.
[26] G.-Y. Chen, W.-q Li, H. Chen, B.-b Yan, Progress in the aqueous-phase reforming of different biomass-derived alcohols for hydrogen production, J. Zhejiang Univ. Sci. A 16 (2015) 491–506.
[27] R.R. Davda, J.W. Shabaker, G.W. Huber, R.D. Cortright, J.A. Dumesic, A review of catalytic issues and process conditions for renewable hydrogen and alkanes by aqueous-phase reforming of oxygenated hydrocarbons over supported metal catalysts, Appl. Catal. B: Environ. 56 (2005) 171–186.
[28] B. Meryemoglu, A. Hesenov, S. Irmak, O.M. Atanur, O. Erbatur, Aqueous-phase reforming of biomass using various types of supported precious metal and raney-nickel catalysts for hydrogen production, Int. J. Hydrogen Energy 35 (2010) 12580–12587.
[29] R. Alcalá, M. Mavrikakis, J.A. Dumesic, DFT studies for cleavage of C–C and C–O bonds in surface species derived from ethanol on Pt(111), J. Catal. 218 (2003) 178–190.
[30] L. He, J. Yang, D. Chen, Hydrogen from biomass: advances in thermochemical processes, Renewable Hydrogen Technologies. Production, Purification, Storage, Applications and Safety, Elsevier B.V, 2013, pp. 111–133.
[31] S. Hu, Y. Guan, Y. Wang, H. Han, Nano-magnetic catalyst KF/CaO-Fe_3O_4 for biodiesel production, Appl. Energy 88 (2011) 2685–2690.
[32] K. Krischer, E.R. Savinova, Fundamentals of electrocatalysis, Handbook of Heterogeneous Catalysis, Wiley-VCH Verlag GmbH & Co. KGaA, Weinheim, 2008, pp. 1873–1905.
[33] K. Scott, Electrochemical principles and characterization of bioelectrochemical systems, Microbial Electrochemical and Fuel Cells. Fundamentals and Applications, Elsevier Inc, 2016, pp. 29–66.
[34] S.B. Strbac, R.R. Adzic, Electrocatalysis, fundamentals – electron transfer process; current-potential relationship; volcano plots, Encyclopedia of Applied Electrochemistry, Springer, New York, 2014, pp. 417–423.
[35] L. Gorker, V. Dimitrov, Modified Tafel equation for electroless metal deposition, Prog. React. Kinet. Mech. 34 (2009) 127–140.
[36] L. Peng, Z. Wei, Catalyst engineering for electrochemical energy conversion from water to water: water electrolysis and the hydrogen fuel cell, Engineering 6 (2020) 653–679.
[37] M. Carmo, D.L. Fritz, J. Mergel, D. Stolten, A comprehensive review on PEM water electrolysis, Int. J. Hydrogen Energy 38 (2013) 4901–4934.
[38] S. Marini, P. Salvi, P. Nelli, R. Pesenti, M. Villa, M. Berrettoni, et al., Advanced alkaline water electrolysis, Electrochim. Acta 82 (2012) 384–391.
[39] Z. Chen, D. Cummins, B.N. Reinecke, E. Clark, M.K. Sunkara, T.F. Jaramillo, Core-shell MoO_3-MoS_2 nanowires for hydrogen evolution: a functional design for electrocatalytic materials, Nano Lett. 11 (2011) 4168–4175.
[40] K. Zeng, D. Zhang, Recent progress in alkaline water electrolysis for hydrogen production and applications, Prog. Energy Combust. Sci. 36 (2010) 307–326.

[41] N.T. Suen, S.F. Hung, Q. Quan, N. Zhang, Y.J. Xu, H.M. Chen, Electrocatalysis for the oxygen evolution reaction: recent development and future perspectives, Chem. Soc. Rev. 46 (2017) 337–365.
[42] H. Narayanan, B. Viswanathan, K.R. Krishnamurthy, H. Nair, Hydrogen from photo-electrocatalytic water splitting, Solar Hydrogen Production: Processes, Systems and Technologies, Elsevier, 2019, pp. 419–486.
[43] R.L. Doyle, M.E.G. Lyons, The oxygen evolution reaction: mechanistic concepts and catalyst design, Photoelectrochemical Solar Fuel Production: From Basic Principles to Advanced Devices, Springer International Publishing, 2016, pp. 41–104.
[44] I.C. Man, H.Y. Su, F. Calle-Vallejo, H.A. Hansen, J.I. Martínez, N.G. Inoglu, et al., Universality in oxygen evolution electrocatalysis on oxide surfaces, ChemCatChem 3 (2011) 1159–1165.
[45] N.T. Suen, S.F. Hung, Q. Quan, N. Zhang, Y.J. Xu, H.M. Chen, Electrocatalysis for the oxygen evolution reaction: recent development and future perspectives, Chem. Soc. Rev. 46 (2017) 337–365.
[46] J. Qiao, Y. Liu, F. Hong, J. Zhang, A review of catalysts for the electroreduction of carbon dioxide to produce low-carbon fuels, Chem. Soc. Rev. 43 (2014) 631–675.
[47] S. Garg, M. Li, A.Z. Weber, L. Ge, L. Li, V. Rudolph, et al., Advances and challenges in electrochemical CO_2 reduction processes: an engineering and design perspective looking beyond new catalyst materials, J. Mater. Chem. A 8 (2020) 1511–1544.
[48] Q. Lu, F. Jiao, Electrochemical CO_2 reduction: electrocatalyst, reaction mechanism, and process engineering, Nano Energy 29 (2016) 439–456.
[49] Y. Hori, Electrochemical CO_2 reduction on metal electrodes, Modern Aspects of Electrochemistry, Springer, New York, 2008, pp. 89–189.
[50] S. Nitopi, E. Bertheussen, S.B. Scott, X. Liu, A.K. Engstfeld, S. Horch, et al., Progress and perspectives of electrochemical CO_2 reduction on copper in aqueous electrolyte, Chem. Rev. 119 (2019) 7610–7672.
[51] A. Bagger, W. Ju, A.S. Varela, P. Strasser, J. Rossmeisl, Electrochemical CO_2 reduction: a classification problem, ChemPhysChem 18 (2017) 3266–3273.
[52] X. Liu, J. Xiao, H. Peng, X. Hong, K. Chan, J.K. Nørskov, Understanding trends in electrochemical carbon dioxide reduction rates, Nat. Commun. 8 (2017) 1–7.
[53] S. Ma, R. Luo, J.I. Gold, A.Z. Yu, B. Kim, P.J.A. Kenis, Carbon nanotube containing Ag catalyst layers for efficient and selective reduction of carbon dioxide, J. Mater. Chem. A 4 (2016) 8573–8578.
[54] IUPAC, IUPAC Compendium of Chemical Terminology, 2009.
[55] G. Marcì, L. Palmisano, Preface, Heterogeneous Photocatalysis: Relationships with Heterogeneous Catalysis and Perspectives, Elsevier, 2019, pp. ix–xi.
[56] V. Augugliaro, V. Loddo, M. Pagliaro, G. Palmisano, L. Palmisano, Clean by Light Irradiation, Royal Society of Chemistry, 2010.
[57] F. Parrino, M. Bellardita, E.I. García-López, G. Marcì, V. Loddo, L. Palmisano, Heterogeneous photocatalysis for selective formation of high-value-added molecules: some chemical and engineering aspects, ACS Catal. 8 (2018) 11191–11225.
[58] M. Pelaez, N.T. Nolan, S.C. Pillai, M.K. Seery, P. Falaras, A.G. Kontos, et al., A review on the visible light active titanium dioxide photocatalysts for environmental applications, Appl. Catal. B: Environ. 125 (2012) 331–349.
[59] B. Bajorowicz, M.P. Kobylański, A. Malankowska, et al., Application of metal oxide-based photocatalysis, Metal Oxide-Based Photocatalysis: Fundamentals and Prospects for Application, Elsevier, 2018, pp. 211–340.
[60] A. Ibhadon, P. Fitzpatrick, Heterogeneous photocatalysis: recent advances and applications, Catalysts 3 (2013) 189–218.
[61] C.S. Turchi, D.F. Ollis, Mixed reactant photocatalysis: intermediates and mutual rate inhibition, J. Catal. 119 (1989) 483–496.
[62] H. Ibrahim, H. de Lasa, Kinetic modeling of the photocatalytic degradation of air-borne pollutants, AIChE J. 50 (2004) 1017–1027.
[63] A.V. Vorontsov, E.N. Kurkin, E.N. Savinov, Study of TiO_2 deactivation during gaseous acetone photocatalytic oxidation, J. Catal. 186 (1999) 318–324.

[64] G. Palmisano, V. Loddo, V. Augugliaro, Two-dimensional modeling of an externally irradiated slurry photoreactor, Int. J. Chem. React. Eng. 11 (2013) 675–685.
[65] G. Palmisano, V. Loddo, V. Augugliaro, M. Bellardita, G. Camera Roda, F. Parrino, Validation of a two-dimensional modeling of an externally irradiated slurry photoreactor, Chem. Eng. J. 262 (2015) 490–498.
[66] S.N. Ahmed, W. Haider, Heterogeneous photocatalysis and its potential applications in water and wastewater treatment: a review, Nanotechnology 29 (2018).
[67] A. Fujishima, T.N. Rao, D.A. Tryk, Titanium dioxide photocatalysis, J. Photochem. Photobiol. C. Photochem. Rev. 1 (2000) 1–21.
[68] C. Garlisi, E. Trepci, X. Li, R. Al Sakkaf, K. Al-Ali, R.P. Nogueira, et al., Multilayer thin film structures for multifunctional glass: self-cleaning, antireflective and energy-saving properties, Appl. Energy 264 (2020) 114697.
[69] J. Moma, J. Baloyi, Modified titanium dioxide for photocatalytic applications, Photocatalysts - Applications and Attributes, IntechOpen, 2019.
[70] S.G. Kumar, L.G. Devi, Review on modified TiO_2 photocatalysis under UV/visible light: selected results and related mechanisms on interfacial charge carrier transfer dynamics, J. Phys. Chem. A 115 (2011) 13211–13241.
[71] S. Al Jitan, G. Palmisano, C. Garlisi, Synthesis and surface modification of TiO_2-based photocatalysts for the conversion of CO_2, Catalysts 10 (2020) 227.
[72] S.N. Ahmed, W. Haider, Heterogeneous photocatalysis and its potential applications in water and wastewater treatment: a review, Nanotechnology 29 (2018).
[73] Y. Lan, Y. Lu, Z. Ren, Mini review on photocatalysis of titanium dioxide nanoparticles and their solar applications, Nano Energy 2 (2013) 1031–1045.
[74] C.S. Turchi, D.F. Ollis, Photocatalytic degradation of organic water contaminants: mechanisms involving hydroxyl radical attack, J. Catal. 122 (1990) 178–192.
[75] K. Kabra, R. Chaudhary, R.L. Sawhney, Treatment of hazardous organic and inorganic compounds through aqueous-phase photocatalysis: a review, Ind. Eng. Chem. Res. 43 (2004) 7683–7696.
[76] J.M. Herrmann, Photocatalysis fundamentals revisited to avoid several misconceptions, Appl. Catal. B: Environ. 99 (2010) 461–468.
[77] S.B. Kim, S.C. Hong, Kinetic study for photocatalytic degradation of volatile organic compounds in air using thin film TiO_2 photocatalyst, Appl. Catal. B: Environ. 35 (2002) 305–315.
[78] M. Cho, H. Chung, W. Choi, J. Yoon, Linear correlation between inactivation of *E. coli* and OH radical concentration in TiO_2 photocatalytic disinfection, Water Res. 38 (2004) 1069–1077.
[79] J.A. Byrne, P.S.M. Dunlop, J.W.J. Hamilton, P. Fernández-Ibáñez, I. Polo-López, P.K. Sharma, et al., A review of heterogeneous photocatalysis for water and surface disinfection, Molecules 20 (2015) 5574–5615.
[80] K. Sunada, T. Watanabe, K. Hashimoto, Studies on photokilling of bacteria on TiO_2 thin film, J. Photochem. Photobiol. A Chem. 156 (2003) 227–233.
[81] L. Wang, K. Wang, T. He, Y. Zhao, H. Song, H. Wang, Graphitic carbon nitride-based photocatalytic materials: preparation strategy and application, ACS Sustain. Chem. Eng. 8 (2020) 16048–16085.
[82] F.K. Kessler, Y. Zheng, D. Schwarz, C. Merschjann, W. Schnick, X. Wang, et al., Functional carbon nitride materials-design strategies for electrochemical devices, Nat. Rev. Mater. 2 (2017) 1–17.
[83] S. Huang, Y. Xu, F. Ge, D. Tian, X. Zhu, M. Xie, et al., Tailoring of crystalline structure of carbon nitride for superior photocatalytic hydrogen evolution, J. Colloid Interface Sci. 556 (2019) 324–334.
[84] Q. Gu, Q. Jia, J. Long, Z. Gao, Heterogeneous photocatalyzed C–C cross-coupling reactions under visible-light and near-infrared light irradiation, ChemCatChem 11 (2019) 669–683.
[85] S. Gisbertz, B. Pieber, Heterogeneous photocatalysis in organic synthesis, ChemPhotoChem 4 (2020) 456–475.
[86] D. Friedmann, A. Hakki, H. Kim, W. Choi, D. Bahnemann, Heterogeneous photocatalytic organic synthesis: state-of-the-art and future perspectives, Green Chem. 18 (2016) 5391–5411.

[87] A. Maldotti, A. Molinari, Design of heterogeneous photocatalysts based on metal oxides to control the selectivity of chemical reactions, Top. Curr. Chem. 303 (2011) 185–216.
[88] Y. Shiraishi, T. Hirai, Selective organic transformations on titanium oxide-based photocatalysts, J. Photochem. Photobiol. C. Photochem. Rev. 9 (2008) 157–170.
[89] M. Fujihira, Y. Satoh, T. Osa, Heterogeneous photocatalytic reactions on semiconductor materials. Part II. Photoelectrochemistry at semiconductor TiO_2/insulating aromatic hydrocarbon liquid interface, J. Electroanal. Chem. 126 (1981) 277–281.
[90] R. Molinari, T. Poerio, Remarks on studies for direct production of phenol in conventional and membrane reactors, Asia-Pacific J. Chem. Eng. 5 (2010) 191–206.
[91] J. Chen, L. Eberlein, C.H. Langford, Pathways of phenol and benzene photooxidation using TiO_2 supported on a zeolite, J. Photochem. Photobiol. A Chem. 148 (2002) 183–189.
[92] Y. Shiraishi, N. Saito, T. Hirai, Adsorption-driven photocatalytic activity of mesoporous titanium dioxide, J. Am. Chem. Soc. 127 (2005) 12820–12822.
[93] G. Palmisano, M. Addamo, V. Augugliaro, T. Caronna, E. García-López, V. Loddo, et al., Influence of the substituent on selective photocatalytic oxidation of aromatic compounds in aqueous TiO_2 suspensions, Chem. Commun. (2006) 1012–1014.
[94] G. Palmisano, M. Addamo, V. Augugliaro, T. Caronna, A. Di Paola, E.G. López, et al., Selectivity of hydroxyl radical in the partial oxidation of aromatic compounds in heterogeneous photocatalysis, Catal. Today 122 (2007) 118–127.
[95] A. Molinari, M. Montoncello, H. Rezala, A. Maldotti, Partial oxidation of allylic and primary alcohols with O_2 by photoexcited TiO_2, Photochem. Photobiol. Sci. 8 (2009) 613–619.
[96] O.S. Mohamed, A.E.A.M. Gaber, A.A. Abdel-Wahab, Photocatalytic oxidation of selected aryl alcohols in acetonitrile, J. Photochem. Photobiol. A Chem. 148 (2002) 205–210.
[97] J. Chen, D.F. Ollis, W.H. Rulkens, H. Bruning, Photocatalyzed oxidation of alcohols and organochlorides in the presence of native TiO_2 and metallized TiO_2 suspensions. Part (II): Photocatalytic mechanisms, Water Res. 33 (1999) 669–676.
[98] C.B. Almquist, P. Biswas, The photo-oxidation of cyclohexane on titanium dioxide: an investigation of competitive adsorption and its effects on product formation and selectivity, Appl. Catal. A Gen. 214 (2001) 259–271.
[99] V. Brezová, A. Blažková, I. Šurina, B. Havlínová, Solvent effect on the photocatalytic reduction of 4-nitrophenol in titanium dioxide suspensions, J. Photochem. Photobiol. A Chem. 107 (1997) 233–237.
[100] J.L. Ferry, W.H. Glaze, Photocatalytic reduction of nitro organics over illuminated titanium dioxide: role of the TiO_2 surface, Langmuir 14 (1998) 3551–3555.
[101] S. Kaneco, Y. Shimizu, K. Ohta, T. Mizuno, Photocatalytic reduction of high pressure carbon dioxide using TiO_2 powders with a positive hole scavenger, J. Photochem. Photobiol. A Chem. 115 (1998) 223–226.
[102] K. Li, X. An, K.H. Park, M. Khraisheh, J. Tang, A critical review of CO_2 photoconversion: catalysts and reactors, Catal. Today 224 (2014) 3–12.
[103] F. Galli, M. Compagnoni, D. Vitali, C. Pirola, C.L. Bianchi, A. Villa, et al., CO_2 photoreduction at high pressure to both gas and liquid products over titanium dioxide, Appl. Catal. B: Environ. 200 (2017) 386–391.
[104] N.H. Tran, J.R. Bartlett, G.S.K. Kannangara, A.S. Milev, H. Volk, M.A. Wilson, Catalytic upgrading of biorefinery oil from micro-algae, Fuel 89 (2010) 265–274.
[105] D. Castello, M.S. Haider, L.A. Rosendahl, Catalytic upgrading of hydrothermal liquefaction biocrudes: different challenges for different feedstocks, Renew. Energy 141 (2019) 420–430.
[106] S.V. Vassilev, C.G. Vassileva, Composition, properties and challenges of algae biomass for biofuel application: an overview, Fuel 181 (2016) 1–33.
[107] C. Tang, M.M. Titirici, Q. Zhang, A review of nanocarbons in energy electrocatalysis: multifunctional substrates and highly active sites, J. Energy Chem. 26 (2017) 1077–1093.
[108] S. Ponnurangam, I.V. Chernyshova, P. Somasundaran, Nitrogen-containing polymers as a platform for CO_2 electroreduction, Adv. Colloid Interface Sci. 244 (2017) 184–198.

[109] D. Ješić, D. Lašič Jurković, A. Pohar, L. Suhadolnik, B. Likozar, Engineering photocatalytic and photoelectrocatalytic CO_2 reduction reactions: mechanisms, intrinsic kinetics, mass transfer resistances, reactors and multi-scale modelling simulations, Chem. Eng. J. 407 (2021) 126799.
[110] F.O. Ochedi, D. Liu, J. Yu, A. Hussain, Y. Liu, Photocatalytic, electrocatalytic and photoelectrocatalytic conversion of carbon dioxide: a review, Environ. Chem. Lett. (2020) 1–27.
[111] Q. Xu, L. Zhang, J. Yu, S. Wageh, A.A. Al-Ghamdi, M. Jaroniec, Direct Z-scheme photocatalysts: principles, synthesis, and applications, Mater. Today 21 (2018) 1042–1063.

CHAPTER 7

Characterization techniques

Material characterization plays a crucial role in heterogeneous catalysis as it allows to shed light on the catalyst performance and correlate its activity to *physicochemical, morphological, structural*, and *optical properties*. The need of gaining better control on the catalyst properties derives from the requirements for further optimization of a catalytic system already in operation and/or for the development of new systems. Because of the huge variety of available methods, it is impossible to cover all of them in the following. For this reason, this chapter focuses on the most common techniques, which have been selected based on their popularity, applicability to a wide variety of catalytic systems, and capacity to deliver manifold information (i.e., multipurpose techniques). These techniques with the corresponding type of delivered information are summarized in Table 7.1.

Considering that the state of a catalyst ultimately depends on the conditions under which it operates, examples of in situ experiments performed under reaction conditions are reported for the different techniques, whenever applicable. Advancement in technical capabilities of the characterization equipment has helped to make *in situ investigation* a powerful strategy to probe the catalytic systems over a wide range of chemical environment, pressure, and temperature, with the inherent advantage of ensuring a growing grasp of the catalytic mechanisms.

7.1 X-ray diffraction

X-ray diffraction (XRD) is the main technique for the study of catalyst bulk structure. In a laboratory, X-rays are generated from the bombardment of a target material (i.e., anode) by electrons produced from the heating of a filament. The resulting monochromatic X-ray beam is projected into the sample where it is elastically scattered by the atoms in the lattices. At specific angles of incidence, the diffracted parallel X-rays are in phase and produce constructive interference, yielding peaks with a measurable intensity. This process, illustrated in Fig. 7.1, is described by *Bragg's law*, which states that *constructive interference* only occurs when the following condition is satisfied:

$$n\lambda = 2d \sin\theta \tag{7.1}$$

where n is an integer referred to as the order of reflection, λ is the wavelength of the X-ray, d is the characteristic spacing between the crystal planes of the given material, and θ is the

Heterogeneous Catalysis.
DOI: https://doi.org/10.1016/B978-0-323-89845-4.00008-4

Table 7.1: Main techniques used for the characterization of catalysts.

Technique	Type of information
XRD	Bulk crystal structure.
XPS	Surface elemental analysis and oxidation states.
XAS	Elemental analysis, oxidation states. Possibility to investigate local geometric and/or electronic structure.
SEM	Surface structure and morphology.
TEM	Morphology and crystal structure.
IR spectroscopy	Molecular structure.
Raman spectroscopy	Molecular and crystalline structure.
Temperature-programed chemisorption	Surface coverage, kinetic parameters of the desorption process, strength of acidic/alkaline sites, reduction/oxidation activity.
Voltammetry	Redox activity and reversibility of the redox process.
EIS	Charge and mass transfer in redox reactions.
UV/Vis spectroscopy	Optical properties, surface plasmon resonance.
Photoluminescence	Charge recombination in semiconductors, acidity/basicity of catalytic sites, identification of traces of adsorbed intermediates.
Nuclear magnetic resonance	Molecular structure, acidity of catalytic sites.
Electron magnetic resonance	Paramagnetic states.
Density functional theory, molecular dynamics simulations	Modeling of catalytic structure, elementary steps of catalytic reactions, atoms location.

EIS, Electrochemical impedance spectroscopy; *IR*, infrared; *SEM*, scanning electron microscopy; *TEM*, transmission electron microscopy; *UV/Vis*, UV/visible; *XAS*, X-ray absorption spectroscopy; *XPS*, X-ray photoelectron spectroscopy; *XRD*, X-ray diffraction.

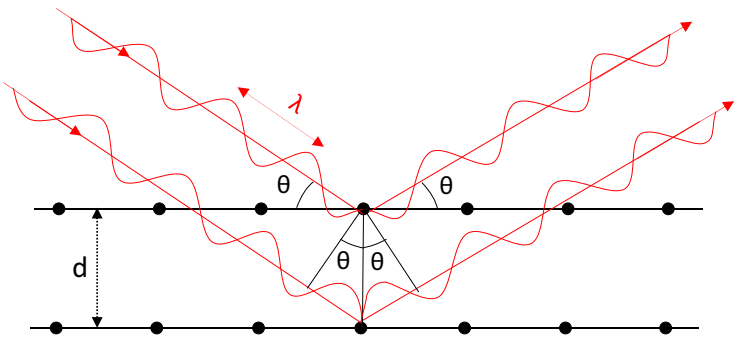

Figure 7.1
Schematic of the constructive interference of X-rays produced upon elastic scattering by the atoms in the lattice.

angle between the incident X-ray and the scatter plane [1]. The result of the measurement is a plot of the X-ray intensity measured by the detector versus the angle 2θ, which can be seen as a *fingerprint of the periodic atomic arrangements in the sample*. As λ is known (wavelength of the used X-rays) and θ is continuously varied in a controlled way during the experiment, Bragg's law allows to compute d. The wide availability of libraries (ASTM,

JCPDS, etc.), reporting the characteristic lattice spacings for a variety of materials, usually enables a quick phase identification of crystal phases.

A *crystalline material* usually contains many sets of planes, the orientation and interplanar spacings of which are defined by the three integer numbers h, k, and l, called Miller indices. These are determined by the points at which a certain crystal plane intersects the three axes in a Cartesian coordinate system (i.e., x, y, z). To account for all the possible planes which satisfy Bragg's Law, the latter is usually expressed (in a case of a cubic system) as follows:

$$\frac{1}{d_{hkl}^2} = \frac{h^2 + k^2 + l^2}{a^2} \tag{7.2}$$

where a is the lattice spacing of the cubic crystal which can be calculated once d_{hkl}, which is the interplanar spacing with Miller indices (hkl), is known from the XRD measurement [2]. Likewise, similar correlations apply to noncubic crystalline cells.

In catalysis, *XRD is used to identify crystalline phases*, determine the degree of crystallinity of catalysts, their crystal lattice parameters such as d-spacings and unit cell dimensions of the relevant crystal structure, and the average crystal size and facet parameters. In situ experiments can be conducted for instance to study the impact of the reactant gas mixture on the structural properties of the catalysts or the transitions from one crystal phase to another one by acquiring diffractograms at increasing temperature and/or pressure. Moreover, qualitative and quantitative analysis of multicomponent catalytic materials can also be performed to assess the relative contribution of the individual components and phases. Fig. 7.2A shows the XRD patterns of catalytic systems used for the synthesis of linear α-olefins from CO_2. Such catalysts are made of a mixture of iron carbide (Fe_5C_2), magnetite (Fe_3O_4), metallic iron (Fe^0), and further constituents (SiO_2 and KCl) [3]. By using the existing libraries as a reference, the different components can be identified and correlated to the catalytic performance. For example, the authors found that more Fe_5C_2 is beneficial for the enhancement of C−C coupling and inhibition of methane formation.

The broadening of the XRD peaks is related to the degree of structural order in the solid, as shown in Fig. 7.2B. Single-crystal materials and large crystalline particles give rise to sharp narrow lines in the XRD due to their perfect long-range order. On the other hand, amorphous materials with their short-range order exhibit no or very broad diffraction peaks as a result of the lack of planes that produce Bragg diffraction. Catalysts are usually characterized by structural domains of medium-range order typical, for example, of nanoparticles (NPs). In nanoscale crystallites, the *crystallite size* can be correlated through the *Debye−Scherrer's equation* to the broadening of the diffraction peak in the XRD pattern:

$$\tau = \frac{K\lambda}{B\cos\theta} \tag{7.3}$$

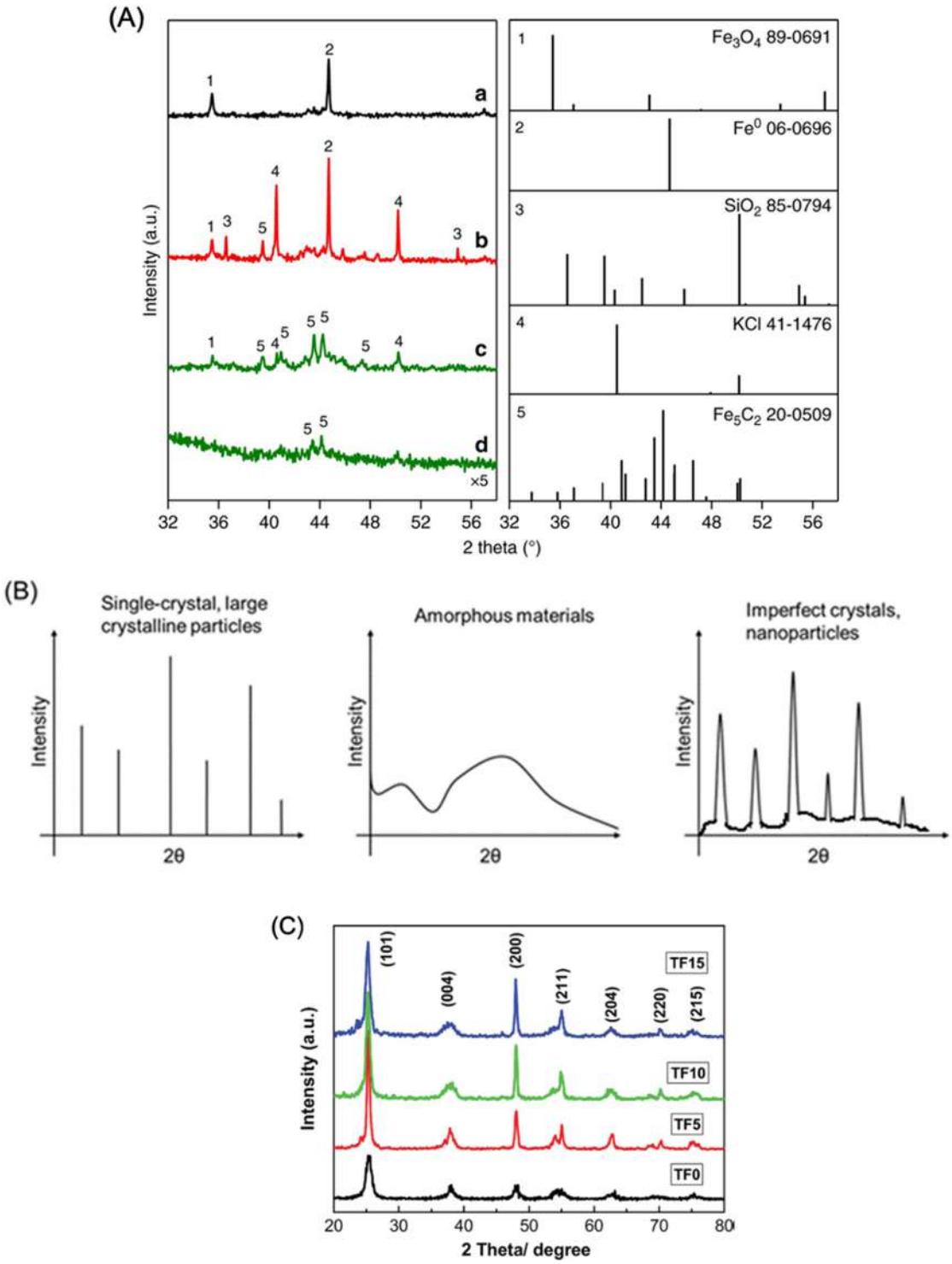

(*Continued*)

where τ is the crystallite size perpendicular to the reflecting plane under consideration, K is a shape factor with a value close to unity, λ is the X-ray wavelength, B is the full width at half maximum (FWHM) of the diffraction peak, and θ is the diffraction angle. It is worth noting that the Scherrer's method gives a rough value of the crystallite size because the peak broadening depends on further factors which may introduce inaccuracy. In addition to the size of crystallites, the peak broadening indeed may be affected by distortions of the lattice owing to dislocations, twinning internal stresses, surface and boundaries of crystallites, etc. [5]. The crystallite size often differs from particle size, since particles are usually made up of several crystallites. A more accurate determination of the particle size can be performed by transmission electron microscopy (TEM) and *small-angle X-ray scattering (SAXS)*. The latter technique makes use of the same type of X-ray sources as diffractometers but, unlike them, it measures the scattering in a very low range of angles, typically 0.1−5 degrees (see Focus 7.1). Unlike TEM, SAXS *yields information about particle sizes* from a macroscopic amount of sample. According to Bragg's law, larger structural features can be probed at smaller scattering angles with an extremely accurate picture of the *"nano" region*, spanning from few nanometers to a few hundred nanometers. Unlike XRD, SAXS generates a particle size distribution instead of average crystallite sizes.

The *noncrystalline content* of a sample (amorphous phase) can be indirectly determined by XRD analysis if all the crystal phases present in the samples are known. The quantification is performed by admixing an internal standard in stated quantities. A good internal standard should be chemically inert so as not to react with the sample, highly crystalline (ideally 100%) with few intense diffraction peaks, in the form of a very fine powder to avoid texturing (i.e., preferred orientation of crystal planes with respect to the beam), and it should have a low (ideally zero) stoichiometric variability. Some of the most common internal standards are Si (NIST SRM 640e), corundum (NIST SRM 676a), and mica (NIST SRM 675).

XRD technique is also used to investigate the abundance of *exposed facets of crystalline samples*, which often affects the interaction between the adsorbate and the catalyst surface, and, in turn, the catalytic activity. In particular, crystal facet engineering of semiconductors plays an important role in tuning and optimizing both the physicochemical properties and reactivity of photocatalysts. In TiO_2, for example, it has been found that redox reactions preferentially occur on {1 0 1} and {0 0 1} facets, respectively [6]. Fig. 7.2C displays the XRD pattern of anatase TiO_2 obtained with

Figure 7.2

(A) XRD of different catalytic systems for the production of linear α-olefins from CO_2 [3]. (B) Qualitative representation of XRD patterns of materials with different degrees of structural order; (C) XRD pattern of TiO_2-based catalysts prepared with different volumes of hydrofluoric acid (TFO is pure TiO_2, while TF5, TF10, and TF15 are obtained with an increasing amount of HF) [4]. *HF*, Hydrofluoric acid; *XRD*, X-ray diffraction. *Source: (A) Reproduced from [3]. (C) Source: Reproduced from [4].*

different volumes of hydrofluoric acid (HF) during the preparation of the catalysts [4]. The reduction in the intensity of the (0 0 4) peak and the broadening of its FWHM with doping indicate that the thickness of TiO_2 particles along the [0 0 1] direction decreases. Moreover, the increase in the intensity of (2 0 0) peak and the narrowing of its FWHM with doping amount testify the increasing side length of the NPs along the [1 0 0] direction. Both phenomena can be ascribed to the boosting of {0 0 1} facets at the expense of the {1 0 1} ones with increasing doping amounts.

In situ XRD can be employed to study the changes in the crystalline structure during gas reactions in a controlled environment with a temperature up to 2000°C and pressure up to 100 bar. Both laboratory and synchrotron-based X-ray sources can be used for in situ XRD. Such experiments are aimed at inducing phase transitions in the catalyst to study in detail their effect on the kinetics of the target reaction. Moreover, thermal treatment of the catalyst can be carried out in situ to find the optimal annealing parameters that induce alterations in the crystalline structures favorable for the target reaction performed ex situ.

Fig. 7.3 shows an example of in situ time-resolved XRD experiment on the reduction of copper oxide (CuO) powders to metallic copper with carbon monoxide [7]. The XRD patterns at different reaction times reveal how the diffraction peaks of CuO disappear as the reaction proceeds, giving the way to those typical of the intermediate, that is, Cu_2O, and the target product, that is, Cu (Fig. 7.3A). The XRD data are processed to construct the weight fraction profiles of the three copper species, confirming that the reaction starts after an induction period of c. 35 min and that Cu_2O is not fully converted to Cu at the end of the reaction (Fig. 7.3B).

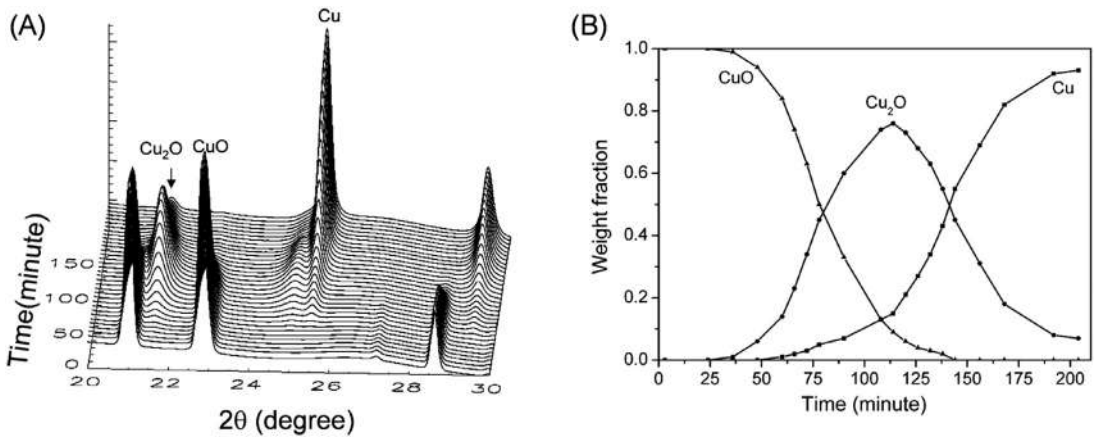

Figure 7.3

(A) Time-resolved XRD patterns for the reduction of CuO to Cu at 224°C, 5% CO−95% He gas, flow rate of c. 1 mL/min; (B) weight fraction profiles of the three copper species during the reaction. *Source: (B) Reproduced from [7].*

Focus 7.1: In situ SAXS to probe the synthesis of nanoparticles

SAXS allows structural investigation in the size range between 1 nm and a few hundred nanometers, which is the relevant range for catalysts. This technique has been successfully applied to the study of NP nucleation and growth during colloidal synthesis, providing an in-depth mechanistic understanding of reaction kinetics. In this area, Wu et al. [8] employed SAXS to monitor the formation of palladium NPs by thermal decomposition of Pd—TOP (TOP: trioctylphosphine) in 1-octadecene. The synthesis of the NPs involved the mixing of palladium(II) acetylacetonate and 1-octadecene under argon flow and subsequent injection of the ligand, that is, TOP, to form the Pd—TOP complex. The complex solution was finally heated from 60°C to 280°C and kept at 280°C for 30 min. The SAXS patterns acquired during the synthesis reaction after subtracting the background signal are displayed in Fig. 7.4A. A typical SAXS pattern shows the scattering intensity versus the scattering vector $q = \frac{4\pi}{\lambda}\sin\theta$ where θ denotes the half scattering angle and λ the wavelength of the incident X-ray.

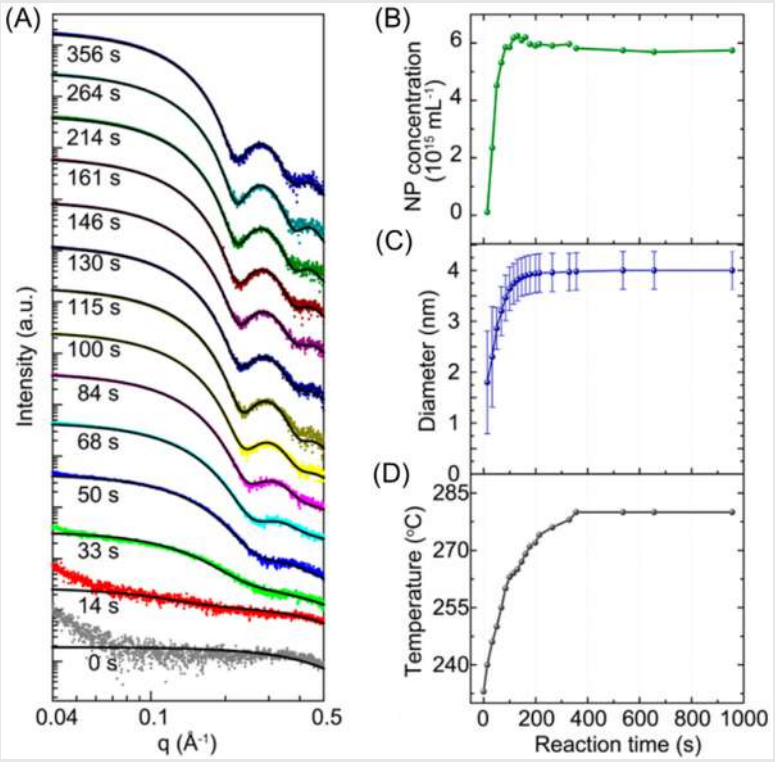

Figure 7.4

(A) SAXS patterns (dotted lines) and corresponding fits (solid lines) of Pd NPs at different reaction times. (B) Concentration, (C) size (dots) and size distribution (bars) of Pd NPs at different reaction times. (D) Reaction temperature during NPs synthesis *NP*, Nanoparticle; *SAXS*, small-angle X-ray scattering. *Source: (D) Reproduced from [8].*

(*Continued*)

Focus 7.1: In situ SAXS to probe the synthesis of nanoparticles (Continued)

The scattering deriving from nuclei with diameter >1 nm appears when the reaction temperature exceeded 230°C (nucleation temperature, taken as $t = 0$ s). As the reaction proceeds, the particle becomes bigger as confirmed by the increasing scattering intensity at low q. The emergence of oscillation peaks is indicative of the narrowing of the NP size distribution. A spherical NP model was used to fit the data and obtain quantitative information about the mean diameter, polydispersity, and concentration of the NPs with increasing reaction time (Fig. 7.4B–D). The nucleation takes place in the first 50 s of reaction, with NPs increasing their concentration with a constant nucleation rate of 1.22×10^{14} mL^{-1} s^{-1} (Fig. 7.4B). In parallel, the polydispersity of the formed nuclei drops to 14% (Fig. 7.4C).

7.2 X-ray photoelectron spectroscopy

X-ray photoelectron spectroscopy (XPS) is a surface-sensitive technique that is widely used to study the *composition* and *electronic structure* of solid surfaces. XPS, the sampling volume of which extends from the surface to a depth of 5–10 nm, relies on the *photoelectric effect* resulting from the emission of electrons from a sample following its irradiation by a beam of X-rays in ultra-high vacuum conditions ($<10^{-8}$ mbar). A conventional XPS instrument consists of (1) X-ray tube, where the X-ray beam is generated by bombarding magnesium or aluminum to produce $K\alpha_{1,2}$ radiation; (2) an electron detector consisting of an electron velocity analyzer called spectrometer; and (3) a pumping system for the vacuum.

A schematic of the photoelectric effect is provided in Fig. 7.5A. The balance between the *energy of the X-ray photons ($h\nu$)* and the *kinetic energy of the ejected electron (E_k)* is expressed through the *Einstein's law*:

$$E_k = h\nu - E_b - \phi \tag{7.4}$$

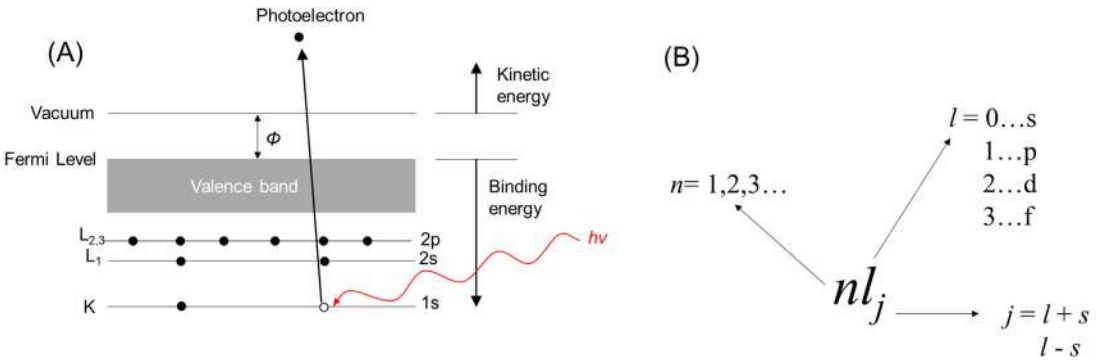

Figure 7.5
(A) Schematic of the photoemission process involved in XPS; (B) nomenclature for XPS peaks.
XPS, X-ray photoelectron spectroscopy.

where E_b is the binding energy of the electron to the nucleus against the Fermi level and ϕ is the work function, which is dependent on both the sample and the spectrometer [9]. The specific element can be identified in terms of E_b, which can be easily computed from the measured E_k and known quantities, namely, $h\nu$ and ϕ.

Electrons at various energy levels can be excited depending on the energy of the incident photon. The resulting spectrum shows all the energy levels as a plot of the photoelectron intensity versus the corresponding E_k of the ejected electrons. As shown in Fig. 7.5B, the labeling of the different peaks in the spectrum is carried out according to the level (namely, the principal quantum number n) from which the photoelectron is excited, the corresponding orbital quantum number l, and the spin momentum number s (i.e., 1/2 or $-1/2$). The electron has a total momentum number j which can be calculated as:

$$j = l + s \tag{7.5}$$

All orbital levels but s ($l = 0$) yield doublet in the spectrum with the two possible states characterized by different binding energies. *The peaks in the doublet* have specific area ratios based on the degeneracy of each spin state (Table 7.2).

Additional signals may appear in the XPS spectrum such as *satellites* (shake-off and shake-up) and *Auger peaks*. Satellites peaks are caused by a sudden change in Coulombic potential as the photoexcited electron passes through the valence band (VB) of the materials. For instance, shake-up peaks, which originate at binding energies higher than the main line, are the result of the emission of photoelectrons with reduced kinetic energy. These photoelectrons are emitted from the atom left in an excited energy state a few eV above the ground state after the previous photoelectron ejection. Such peaks play an important role in the determination of the oxidation state. On the other hand, The Auger peak originates when an outer shell electron fills the vacancy in the core level created by the previous emission of a photoelectron. The energy released during this transition can yield the ejection of a further electron, named after Auger. The Auger peaks are identified through a notation that takes into account all the levels involved in the process. For instance, a peak KL_2L_3 derives from the ionization of an electron in $1s$ (i.e., K) orbital, leaving behind a vacancy filled by an electron from the level $2p_{1/2}$ (i.e., L_2), resulting in the emission of an electron from the level $2p_{3/2}$ (i.e., L_3) [10].

Table 7.2: *j* Values and area ratio of the peaks in the doublet for the different subshells.

Subshell	*j* Values	Area ratio
s	1/2	n/a
p	1/2 3/2	1:2
d	3/2 5/2	2:3
f	5/2 7/2	3:4

In the field of heterogeneous catalysis, XPS is used to gain a better understanding of the relationship between catalytic surfaces and their performance. It enables to quantify the *elemental composition* of the surface of a catalyst as well as identify the *oxidation state* of the elements and its possible variation, which manifests as a certain shift in the binding energy. This technique can also provide valuable information on the physicochemical alterations of the catalyst upon exposure to the reaction environment and thermal annealing. A complete picture of the surface features of the catalyst allows to go into the details of the precursor stages of the studied catalytic process and, hence, into the underlying reaction mechanism.

It is a common practice to run a survey analysis to obtain a snapshot of the elements present in the sample and then record narrow scan spectra with higher resolution to accurately analyze the single elements. Fig. 7.6 shows the XPS results obtained on CuO/TiO_2 catalyst for the electrochemical reduction of CO_2 to ethanol [11]. The survey in

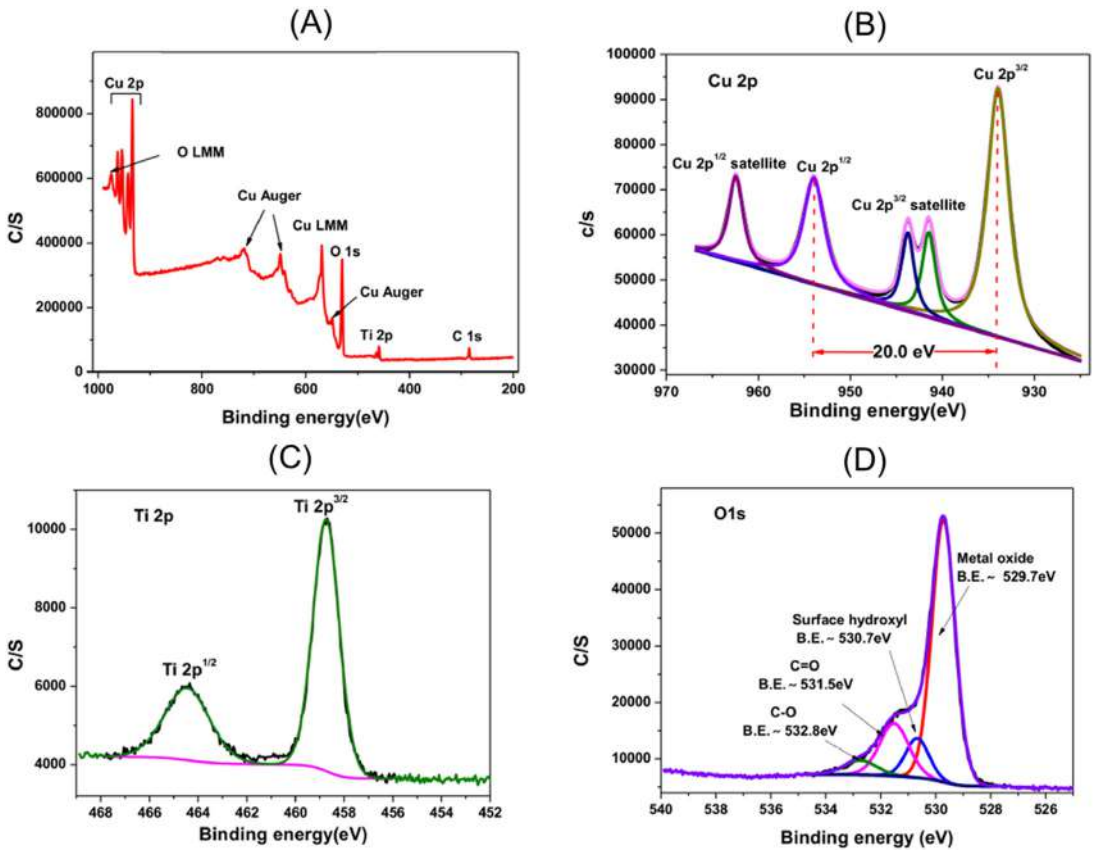

Figure 7.6

(A) XPS survey of a CuO/TiO_2 catalyst and corresponding high-resolution spectra of (B) Cu 2*p*, (C) Ti 2*p*, (D) O 1*s*. *XPS*, X-ray photoelectron spectroscopy. *Source: (D) Reproduced from [11].*

Fig. 7.6A confirms the presence of the expected elements, namely, Ti, Cu, and O. The high-resolution spectrum of Cu 2p in Fig. 7.6B reveals the characteristic doublet with Cu $2p_{3/2}$ and Cu $2p_{1/2}$ separated by a distance of 20 eV typical of CuO. Moreover, the two satellite peaks at higher binding energy further confirm the presence of CuO. Regarding the spectrum of Ti 2*p* (Fig. 7.6C), the Ti $2p_{3/2}$ and Ti $2p_{1/2}$ peaks with a separation of 5.7 eV indicate that TiO_2 exists in the catalyst. Finally, the O 1*s* spectrum in Fig. 7.6D shows the main peak at 529.7 eV arising from O^{2-} in the two metal oxides. The less intense peaks derive from surface hydroxyls, C = O and CO groups on the catalyst surface.

XPS can be used to assess the *uniformity of elemental composition* as a function of depth in thin-film samples. Depth-profiling is carried out by alternating ion gun etching and XPS measurements on newly formed surfaces. An ion gun etches the sample's surface for a certain time, before being turned off while XPS spectra are recorded. Fig. 7.7A shows the depth profile of a photocatalytic TiO_2—Cu thin film deposited on polyester for antibacterial purposes [12]. The atomic concentrations of the three elements in the films, that is, Ti, O, and Cu, decrease with the etching of the coating, especially upon reaching a penetration depth of 50 Å. On the other hand, the rise in the C-content is due to the polyester, the signal of which increases as the etching proceeds.

The ultra-high vacuum conditions needed in conventional spectrometers represent a limitation for the in situ characterization of catalytic materials, which are in this case tested

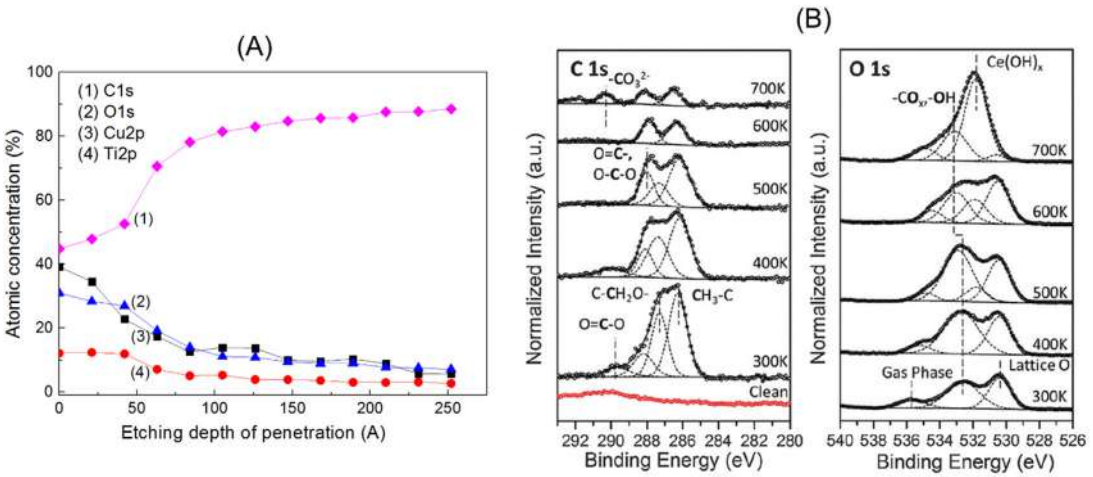

Figure 7.7

(A) XPS depth profile of a TiO_2—Cu thin film deposited on polyester. (B) In situ XPS results obtained on a Ni—CeO_2(1 1 1) catalyst heated under ethanol steam reforming conditions (40 mTorr ethanol + 200 mTorr H_2O). *XPS*, X-ray photoelectron spectroscopy. *Source: (A) Reproduced from [12]. (B) Reproduced from [13].*

only before and after the reaction. However, the recent development of XPS instruments able to operate in the mbar pressure range enables the monitoring of the catalyst surface under reaction conditions closer to those of most catalytic processes. Fig. 7.7B displays the C 1*s* and O 1*s* spectra of a Ni−CeO_2(1 1 1) catalyst heated under ethanol steam reforming conditions [13]. The C 1*s* spectra reveal the presence of dioxyethylene and ethoxy species and the formation of carbonate groups at the maximum temperature (i.e., 700K). On the other hand, the peaks of the lattice O of ceria and that of the water/ethanol gas phase mixture appear in the O 1*s* spectra. Further peaks originate from the overlap of signals characteristic of surface hydroxyls and hydrocarbon oxygenated species.

7.3 X-ray absorption spectroscopy

X-ray absorption spectroscopy (XAS) is a *core-level spectroscopy technique* relying on an intense and tunable X-ray beam to irradiate the sample and produce a characteristic continuous energy spectrum that delivers information on the atomic local structure of the material as well as on its electronic states. The need to tune the energy of photons often requires the use of *synchrotron facilities* for a satisfactory signal-to-noise ratio. Here, X-rays of all wavelengths (whitebeam) are produced by high-energy electrons traveling around the storage ring, where they pass through various types of magnets. The X-ray beam enters a monochromator to select the desired band of wavelengths and then passes through an ionization chamber to measure the incoming intensity. After interacting with the sample, the outgoing beam is sent to the final ionization chamber to measure the intensity after absorption (see Focus 7.2). In the last decades the popularity of this technique has increased dramatically due to the steady growth of synchrotron radiation laboratories all over the world.

A qualitative absorption spectrum obtained from XAS measurements is shown in Fig. 7.8A. *Three regions* can be usually identified. In the first one, located *before the edge*, there is no significant absorption because the energy of the incident X-ray is lower than the binding energy of the electron in the element's orbital (e.g., *s* orbital). Preedge features may appear due to low-energy transitions such as those from 1*s* to 3*d* in transition metals. The second region, known as *X-ray absorption near-edge structure (XANES)*, is characterized by the excitation of the core electrons to unoccupied states (Fig. 7.8B), which results in a characteristic edge jump. The corresponding sharp peak in the spectrum is called "*white line*." This region is used to assign the oxidation states of the elements in the catalyst since the energy of the edge position shifts depending on the electron density. A further increase in the X-ray energy produces an oscillating signal in the spectrum, named *extended X-ray absorption fine structure (EXAFS)* region, which usually extends from 50 eV above the edge [14,15]. The oscillations are generated by the wave interference between the ejected photoelectrons and electrons

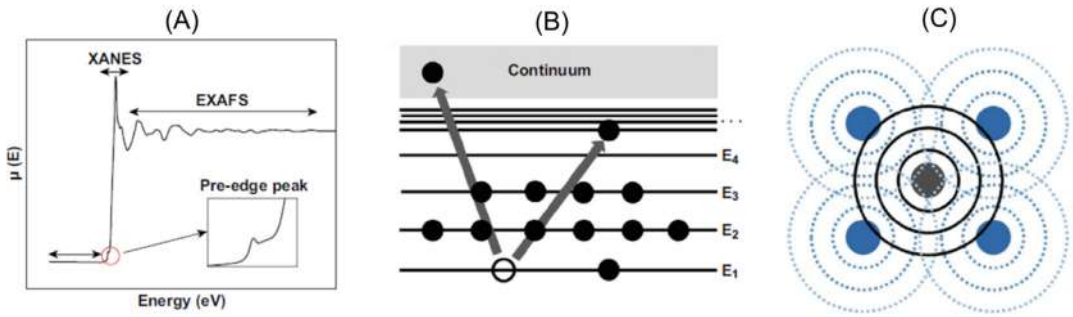

Figure 7.8
(A) Schematic of XAS with the three different regions; (B) schematic of the X-ray photon absorption and electron excitation; (C) schematic of the interference pattern between the absorbing atom (gray) and its nearest atoms (blue), generated from the outgoing (solid black line) and reflected (dashed blue lines) electron waves. *Source: (C) Reproduced from [16].*

surrounding the absorbing atoms (Fig. 7.8C). This region reveals information on the atoms' local environment and, therefore, can be used to probe bond distance and coordination number in the catalyst.

One of the main advantages of XAS is the possibility to study the local structural information of those samples (such as amorphous catalysts) which are unresponsive to other characterization techniques such as XRD. It can characterize both homogeneous and heterogeneous catalysts and is better suited for in situ studies than conventional XPS which requires ultra-high vacuum conditions. Moreover, unlike the latter, which is surface sensitive, *XAS can be utilized for simultaneous surface and bulk sensitive measurements*.

Fig. 7.9A shows the XANES analyses of a cobalt-based catalyst for Fischer–Tropsch synthesis [17], giving evidence on how XAS is a very powerful and sensitive technique for the determination of the oxidation state. Fig. 7.9A displays the spectra recorded on cobalt reference compounds, namely CoO, Co_3O_4, $CoAl_2O_4$, and cobalt foil (Co^0). The oxidized species present a preedge feature deriving from the $1s-3d$ absorption transition. Moreover, the sharp white line is peculiar of spectral features arising from the presence of Co atoms in various Co–O environments and oxidation states. By comparing the XANES spectra of a series of spent Co/Pt/Al_2O_3 catalyst samples (Fig. 7.9B) with those of the reference compounds, one can note a gradual reduction of these catalysts during the Fischer–Tropsch synthesis. Indeed, after an 8-day period, the XANES spectrum was very similar to that of the Co foil.

In situ XAS is used to investigate the oxidation state and local structure under reaction conditions as well as during annealing treatments at different temperatures. In this respect, Fig. 7.10 shows the XAS results obtained on TiO_{2-x}-modified Ni nanocatalyst

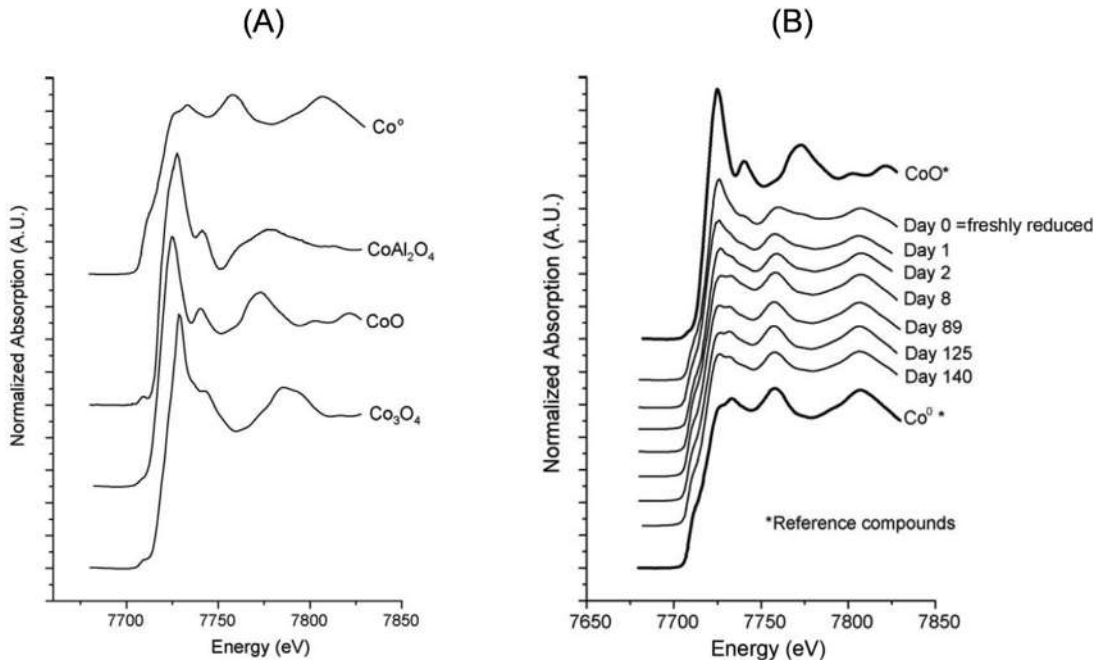

Figure 7.9

(A) XANES spectra of different cobalt reference compounds; (B) XANES analysis of a set of spent Co/Pt/Al_2O_3 catalysts extracted by a slurry bubble column reactor during Fischer–Tropsch synthesis (220°C; 20 bar; [H_2 + CO] conversion between 50% and 70%; feed gas composition of about 50 vol.% H_2 and 25 vol.% CO; $P_{H_2O}/P_{H_2} = 1-1.5$; $P_{H_2O} = 4-6$ bar). *Source: (B) Reproduced from[17]. XANES,* X-ray absorption near-edge structure.

for the water–gas shift reaction [18]. The structure of the catalyst was monitored while undergoing a reduction treatment at different temperatures (400°C–600°C range). The normalized Ni K-edge XANES in Fig. 7.10A reveals the simultaneous presence of metallic and NiO phase in the sample treated at 400°C, while metallic Ni is predominant in the other three samples. All the samples exhibit a shift of the absorption edge toward lower energy compared to Ni foil attributed to the enrichment of electrons on the Ni atom (referred to as $Ni^{\delta-}$). It is a common practice to obtain the Fourier transform from the EXAFS region of the spectrum. This allows obtaining a radial distribution function with the peaks corresponding to the most likely distances of the nearest neighboring atoms. The Fourier-transform EXAFS spectra at Ni K-edge of the catalysts show a gradual decrease of the metallic Ni–Ni distance with the increment of the reduction temperature, which testifies the enhancement of bonding interaction between metallic Ni and TiO_{2-x} (Fig. 7.10B).

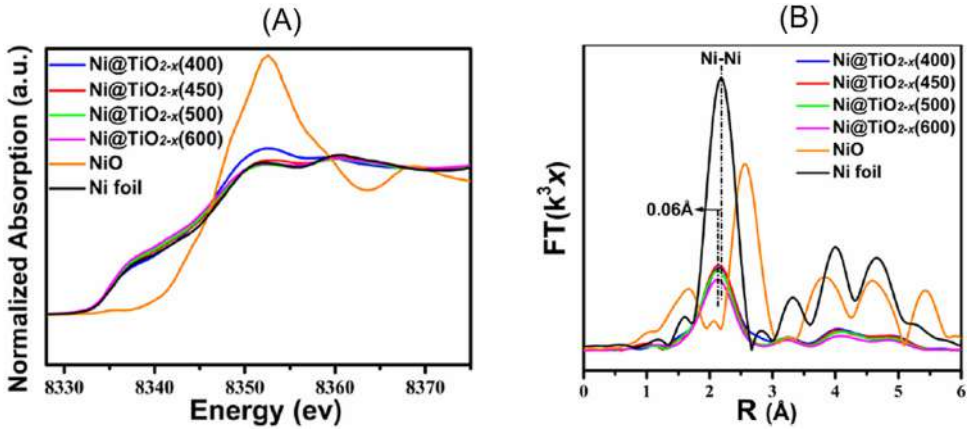

Figure 7.10

(A) Normalized XANES spectra at Ni K-edge for a TiO_{2-x}-modified Ni nanocatalyst treated at different temperatures in an H_2/N_2 (2:3, v/v) stream; (B) Fourier-transform EXAFS spectra at Ni K-edge of the same samples. *Source: (B) Reproduced from [18]. XANES,* X-ray absorption near-edge structure.

Focus 7.2: Layout of a synchrotron radiation facility

Synchrotron radiation is one of the most powerful tools to study the properties of matter in many fields. The peculiar features of this type of radiation have resulted in a variety of new opportunities in diffraction, small-angle scattering, and tomographical studies of catalytic materials. Furthermore, synchrotron radiation has covered a primary role in the successful growth of in situ investigation of catalytic processes under realistic operating conditions [19].

The schematic of a typical synchrotron radiation facility is shown in Fig. 7.11. It consists of three main hutches (Fig. 7.11A). *The storage ring is where the X-ray beam is produced by radial acceleration of electrons*. The emission, collected by a beamline, reaches the optic hutch usually equipped with a collimating mirror that intercepts the X-ray photons and removes higher harmonics. The beam, thus, reaches a double-crystal monochromator that selects the desired X-ray energy and, finally, a second focusing mirror that focuses the monochromatic beam and sends it to the sample. The experimental hutch includes detectors, samples, and tools to control its environment [20].

The storage ring is an evacuated pipe passing through a ring of magnets where the magnetic field can be held constant (Fig. 7.11B). An injection system generates and accelerates the electrons that are conveyed to the ring where they circulate at a speed close to that of light. The electrons are kept in a closed trajectory by a system of bending magnets that exert a Lorentz force perpendicular to the velocity of electrons. This force does not result in any work but only in a centripetal acceleration that modifies the direction of the velocity. The energy lost by the electrons, which emit electromagnetic waves when accelerated, is compensated by a radiofrequency cavity. This accelerates the electrons in the longitudinal direction by applying an electric field in phase with the passage of

(*Continued*)

Focus 7.2: Layout of a synchrotron radiation facility (Continued)

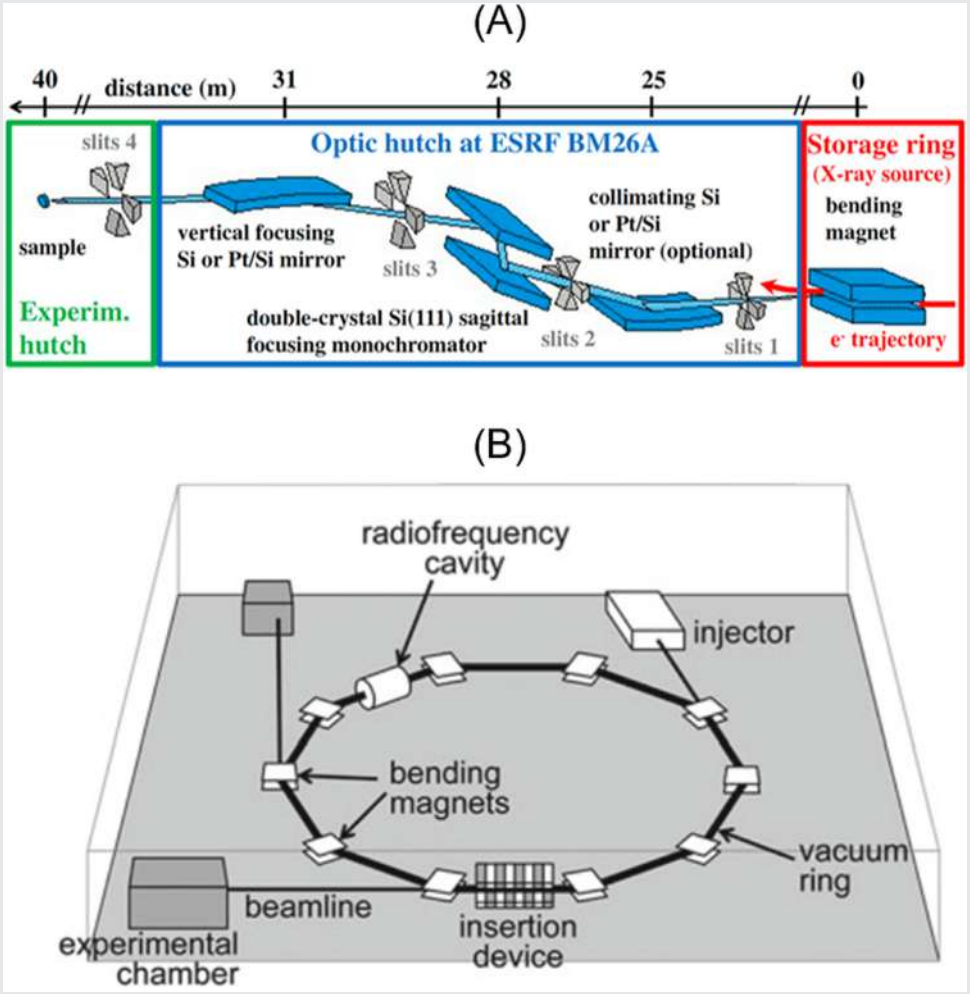

Figure 7.11

(A) Schematic of the three main hutches in a typical synchrotron radiation facility (ESRF BM26A beamline). (B) Schematic of the storage ring and its main components. *Source: (A) Reproduced from [20]. (B) Reproduced from [21].*

the particles, allowing to preserve a stable trajectory around the ring [21]. An insertion device may be also present, especially in the modern facilities. Such a device consists of a periodic series of magnets that force the electrons to follow an oscillation pattern. The insertion device allows producing synchrotron radiation with high brightness (photons s^{-1} mm^{-2} $mrad^{-2}$) over a wide energy range and a tunable polarization.

7.4 Electron microscopy

Electron microscopy uses electrons to generate an image of the sample. This technique includes a wide range of methods that process the signals arising from the *interaction of the electron beam with the sample* to provide information on the structure, surface topography, and composition. Due to their much shorter wavelength compared to visible photons, electrons allow to reach a higher resolving power with respect to optical instruments [22]. The resolution of a typical SEM instrument is about 10 nm, while that of TEM can reach 0.1 nm. Electron microscopy allows for the analysis of catalyst structure at various length scales, from micro- to nanoscale, even within an imaging session. Typical pressures inside the sample chamber are in the range $0.1-10^{-4}$ Pa for SEM and $10^{-4}-10^{-7}$ Pa for TEM.

The modus operandi of SEM and TEM is outlined in Fig. 7.12A and B. Both microscopes are equipped with a set of *lenses that focuses the electron beam* on the sample surface. In SEM, the beam is rastered across the surface of a specimen by means of scanning coils and the resulting signal is collected by a detector. The outgoing signal from the detector is synchronized with the known location of the beam on the sample, and finally, the signal intensity is processed to modulate the image pixel (Fig. 7.12A). *Scanning electron microscopy can be combined with focused ion beam (SEM-FIB)* in a dual-beam system, where a beam of gallium ions is directed on the surface, causing local etching and removing material in a controlled way, while the electron beam is used to image the specimen. SEM-FIB technique is particularly useful for the analysis of thin films or membranes as it allows to access, through FIB etching, the inner regions of the catalyst which are inaccessible by the single-beam SEM due to the intrinsic surface sensitivity of scanning electron microscopy.

In TEM, the beam is projected onto a certain area of a very thin sample (ideally <100 nm). Electrons transmitted through the sample are focused by lenses and collected by a parallel detector to deliver the image (Fig. 7.12B). *TEM can also be operated in scanning mode* (*scanning transmission electron micrscopy*, *STEM*) as shown in Fig. 7.12C.

The interaction between the primary electron beam and the specimen leads to a series of signals, which provide a wide range of information (Fig. 7.12D). SEM imaging makes use of *secondary electrons (SEs) and backscattered electrons (BSEs)*. SEs originate from the atoms in the specimen as a result of inelastic scattering phenomena and give detailed surface and topographic information. BSEs are those electrons of the primary beam reflected back after elastic interactions and are sensitive to the composition of the sample [24]. X-rays are also generated by the ejection of electrons from atom shells and subsequent filling of the vacancies by electrons from higher states. X-rays provide information on chemical composition of the sample through *energy-dispersive X-ray spectroscopy (EDS)*.

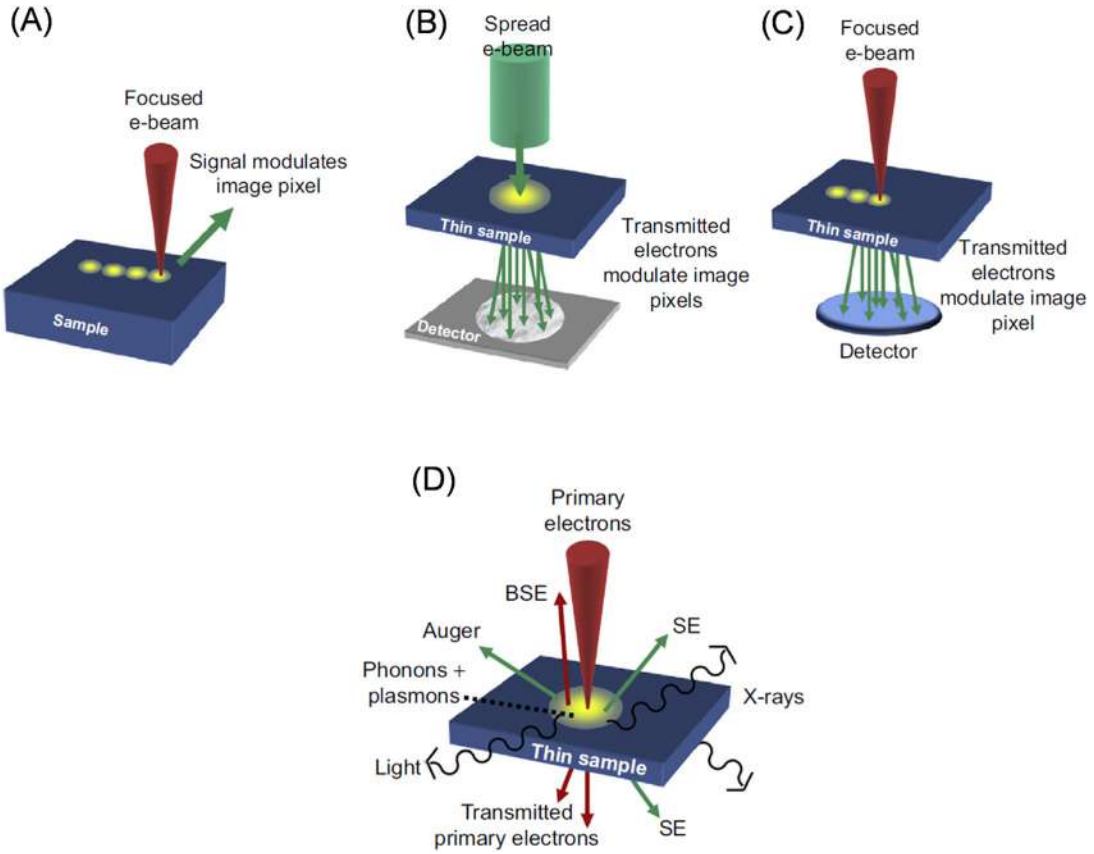

Figure 7.12

Schematic of (A) SEM, (B) TEM, (C) STEM working principle. (D) Signals produced by electron-sample interaction in a thin sample. *Source: Reproduced from [23]. SEM,* Scanning electron microscopy; *TEM,* transmission electron microscopy: *STEM* scanning transmission electron microscpopy.

SEM is a routine characterization for the analysis of catalysts and their *micro- and nanostructural characteristics* including dimensionality, particle agglomeration, size, porosity, and aspect ratio [24]. These features depend on the used technique of synthesis and, more specifically, on the experimental conditions, and they have a major impact on the catalytic performance. Fig. 7.13A-D show SEM micrographs of CeO_2 catalysts with four types of morphology: (A) rods with $\sim$20 nm in diameter and 100−300 nm in length; (B) cubes with size 30−50 nm; (C) spheres with average diameter of $\sim$300 nm, (D) random nanoparticles with size 10−50 nm [25]. The catalysts were prepared by hydrothermal method and tested for H_2S selective oxidation.

When dealing with catalytic membranes, SEM investigation can provide information on pore size, asymmetry, swelling, rugosity, shape and catalyst dispersion and stability over

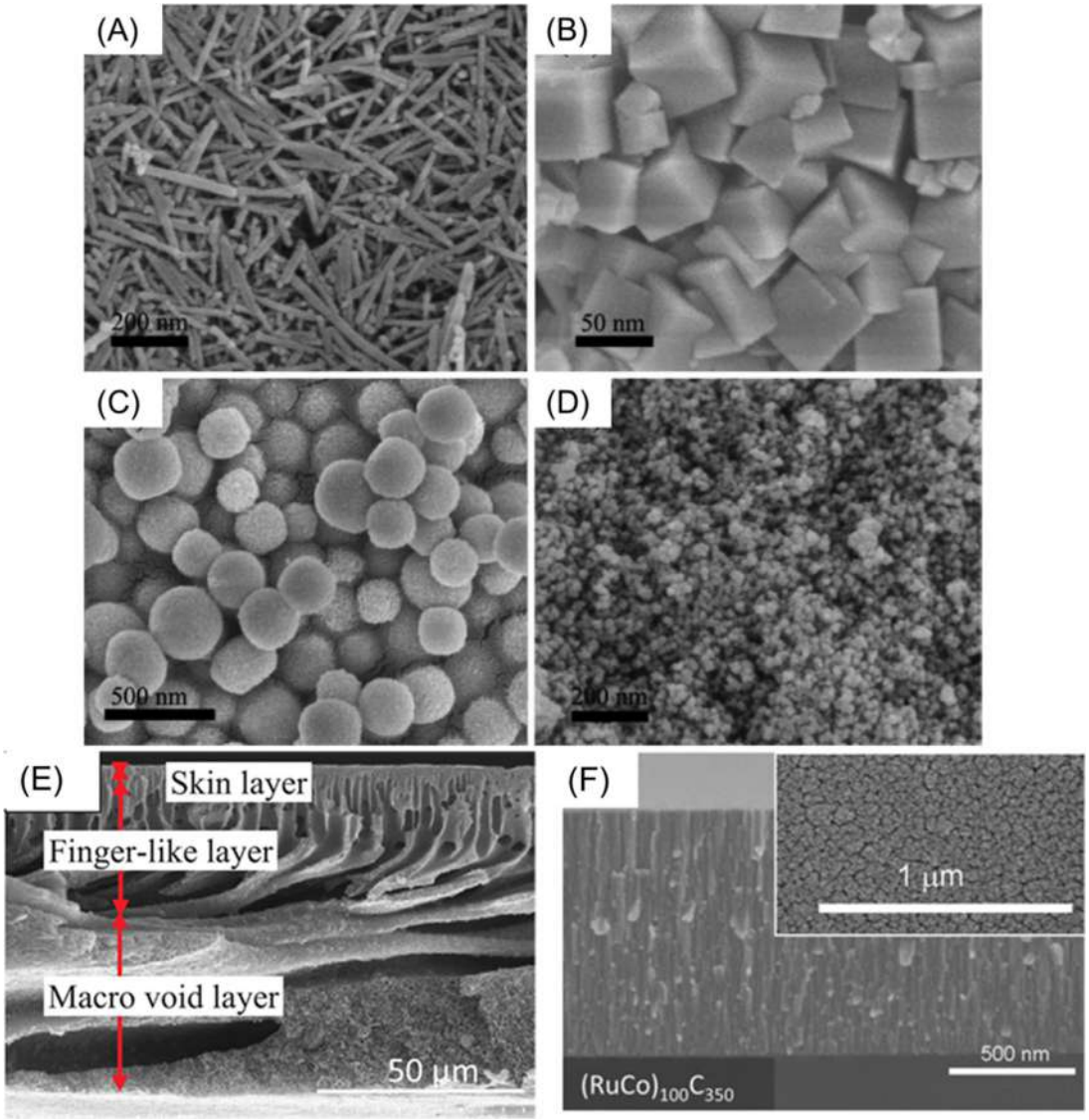

Figure 7.13

(A-D) SEM micrographs of CeO_2 catalysts with different morphologies; (E) SEM image of polymeric membrane for photocatalytic applications; (F) SEM image of a thin film sample made up of a cobalt-ruthenium alloy. *Source: (A-D) Reproduced from [25]. (E) Reproduced from [26]. (F) Reproduced from [27].*

the membrane. Fig. 7.13E displays the SEM image of a photocatalytic membrane for phenol removal [26]. Three distinct layers clearly stand out in the membrane: (1) a dense skin layer being the active part for the membrane performance; (2) a porous layer consisting of finger-like structures; and (3) a macrovoid layer.

SEM technique is also used for assessing the thickness, porosity, and uniformity of thin-film structures. Fig. 7.13F shows the cross-sectional image of a nickel foam-supported cobalt–ruthenium thin film intended to be used for the hydrolysis of sodium borohydride [27]. The catalytic thin film presents a nanocolumnar feature and a compact dense top-surface displayed in the inset of the same figure.

TEM is the elective technique for the investigation of the *structure and properties of catalysts at the nano and atomic scale*. It can be utilized for the determination of (1) shape and size distribution of NPs; (2) spatial distribution of phases, atom ordering, and measurements of lattice parameters; and (3) local elemental composition and electronic structure which is usually carried out in STEM mode and *analysis run with EDS or EELS (electron energy loss spectroscopy)* detectors. EDS has a resolution limited to few nanometers and it is more sensitive to heavier elements. EELS has a spatial resolution of 0.1 nm, is more sensitive for light elements, and reveals information on the electronic structure of the atoms such as their oxidation states. One of the main limitations of the TEM technique is the laborious sample preparation required by certain nanostructures (i.e., thin films). The sample has indeed to be thin enough to ensure electron transparency. Moreover, TEM has a relatively small field of view with the risk that the analyzed area may not be representative of the whole sample.

Fig. 7.14 shows the TEM analysis of iron nitride NPs (Fe_3N) supported on nitrogen-doped carbon for the electrocatalytic reduction of oxygen [28]. Fe_3N particles appear as dark spots (Fig. 7.14A) with an average size of 23.7 nm (Fig. 7.14B). The characteristic *d*-spacing of (1 1 1) plane in Fe_3N can be measured at high resolution (Fig. 7.14C). Selected area electron diffraction (SAED) can also be obtained by TEM analysis. The outcome of SAED analysis is a diffraction pattern generated by the electron beam elastically scattered by the lattice according to Bragg's law (Eq. 7.1). The resulting diffraction spots in single-crystal or ring in polycrystalline catalysts are indexed and used for the identification of the crystal phases, similarly to XRD, with a significant difference: SAED is representative of a small fraction of the sample and it is surface sensitive since electrons are not energetic enough to travel through a solid, whereas X-ray diffractograms are representative of the whole mass of the analyzed sample. The SAED is the diffraction pattern obtained in the reciprocal space of the lattice planes, so the scale bars in the SAED image have 1/nm units. The obtained pattern can be indexed by keeping in mind that the inverse of the radii of the rings should match the interplanar distances d_{hkl} characteristic of the crystal phases in the sample (Eq. 7.2). The SAED pattern of Fe_3N NPs supported on nitrogen-doped carbon (Fig. 7.14D) can be assigned to (111) planes in Fe_3N, almost overlapping to (0 0 2) planes in carbon.

In the last decades a great effort has been devoted to the development of instrumental solutions that allow in situ studies through the introduction of liquid and gas in the SEM/TEM chamber without any threat to the vacuum system. Especially in situ TEM

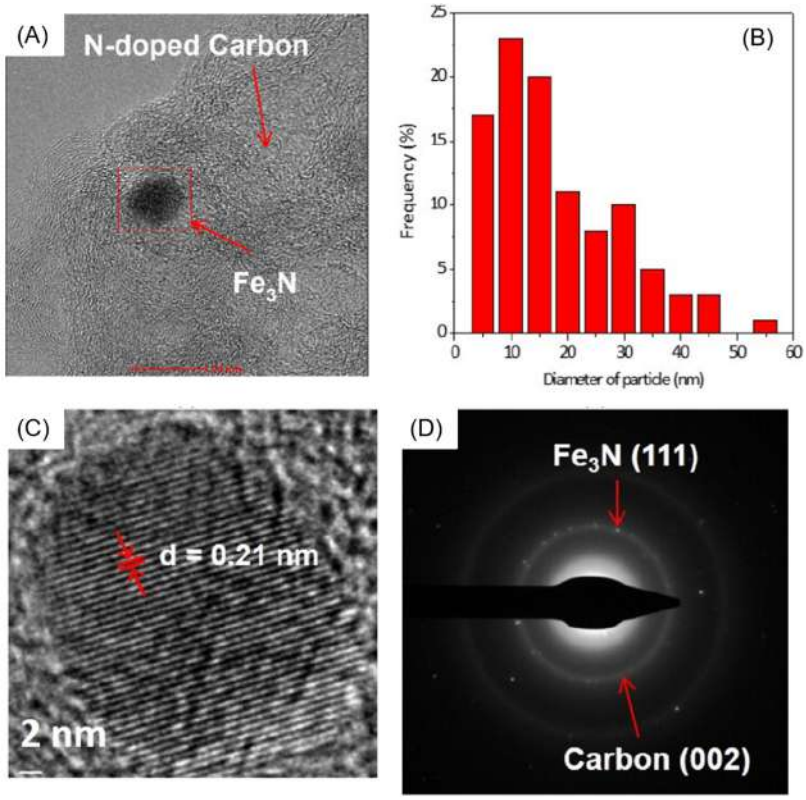

Figure 7.14
(A) TEM micrograph; (B) particle size distribution; (C) high-resolution TEM micrograph (scale bar is 10 nm); (D) SAED pattern of Fe_3N nanoparticle supported on nitrogen-doped carbon. *Source: (D) Reproduced from [28]. SAED,* Selected area electron diffraction*; TEM,* transmission electron microscopy.

analysis can shed light on the morphological, structural, and compositional evolutions of heterogeneous catalysts during the reaction, enabling the imaging of the active sites involved in the reaction and gaining a better understanding of the local dynamics [29].

Fig. 7.15A displays the *STEM-EDS images and maps* of a nanoporous NiCo catalyst tested for dry reforming of methane [30]. This catalyst was prepared by dealloying alloy ribbons containing Ni, Co, and Mn, all present in EDS maps. Fig. 7.15B–G shows an in situ TEM analysis on the same catalyst obtained by controlling the temperature and introducing the reacting gas mixture (i.e., $CH_4 + CO_2$). The increase in temperature up to 600°C (Fig. 7.15B) leads to significant pore/ligament coarsening. In the presence of the gas mixture the grains in the ligaments become finer (Fig. 7.15C and D). The grains tend to merge each other to form larger agglomerates upon evacuation of the gas mixture

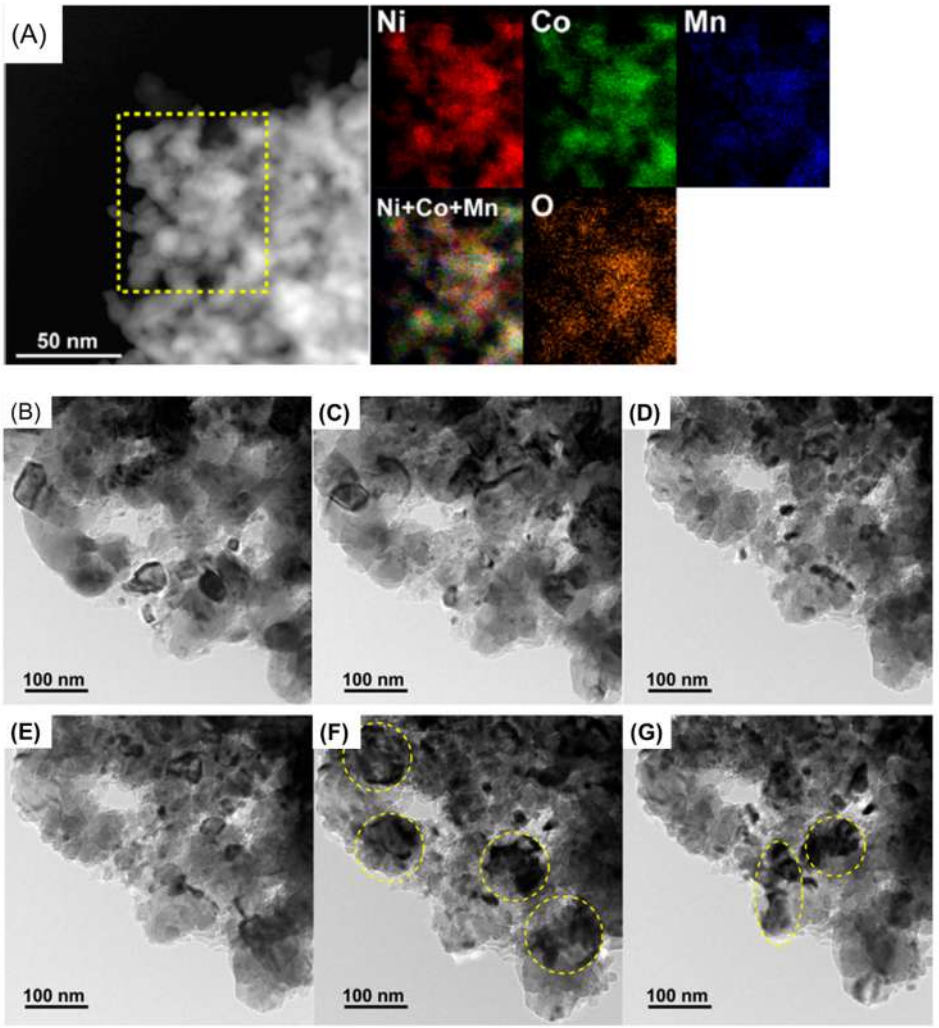

Figure 7.15
(A) STEM-EDS analysis of a nanoporous NiCo catalyst; (B–F) in situ TEM images taken on the same catalyst: (B) after reaching 600°C; (C and D) after 5 and 10 min of exposure to the gas mixture; (E) after evacuation of the gas mixture; (F, G) during cooling to room temperature. *Source: (F, G) Reproduced from [30]. EDS,* Energy-dispersive X-ray spectroscopy*; TEM,* transmission electron microscopy.

(Fig. 7.15E) and, more markedly, during cooling at room temperature (Fig. 7.15F and G). The authors concluded that the dry reforming reaction of methane induces chemical demixing of Ni and Co that is accompanied by finer grains of Co and Ni acting as additional active sites at high temperatures.

Focus 7.3: Scanning tunneling microscopy: atomic-scale investigation of catalyst surface

Over the last decades, scanning tunneling microscopy (STM) has emerged as a new characterization tool for resolving the *atomic-scale electronic structure of surfaces* as well as the *configuration, dynamics, dissociation, and adsorption/desorption* of surface adsorbates [31]. The working principle of an STM microscope is illustrated in Fig. 7.16A. This tool relies on an

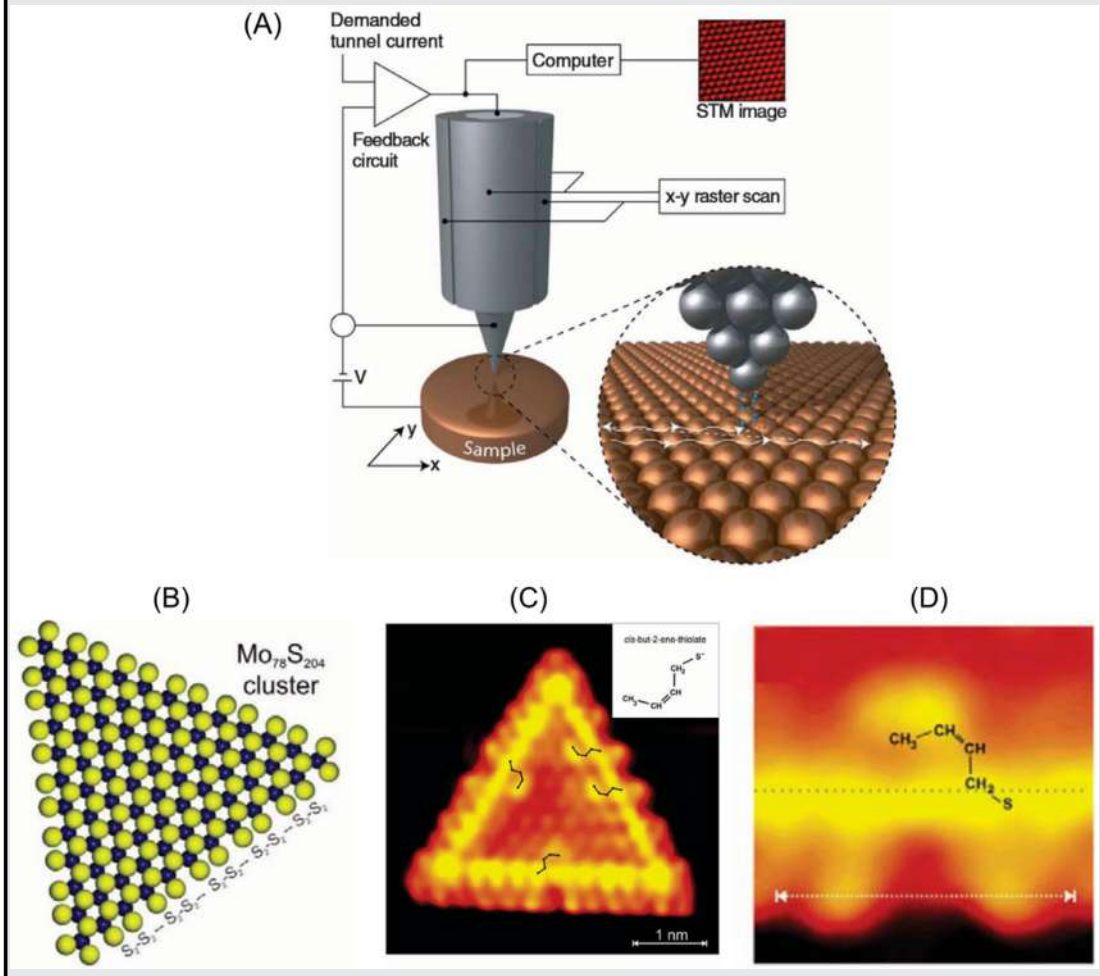

Figure 7.16

(A) Schematic of the working principle and main components of an STM microscope; (B) structural model of a MoS_2 nanocluster; (C) atom-resolved STM image of a single-layer MoS2 nanocluster and adsorbed reaction intermediate (cis-but-2-ene-thiolate); (D) zoom on the reaction intermediate. *Source: (D) Reproduced from [33].* STM, *Scanning tunneling microscopy.*

(*Continued*)

Focus 7.3: Scanning tunneling microscopy: atomic-scale investigation of catalyst surface (Continued)

extremely sharp conducting tip that is held sufficiently close to a surface (0.4–0.7 nm). A voltage difference enables electrons to tunnel through the gap in between, and the resulting tunneling current is a function of the tip position, applied voltage, and local density of states on the sample surface [32]. A topographical map of the surface (*x-y* raster scan) with atomic resolution can be obtained in two ways: the changes in the tunneling current are mapped at constant height *z* (constant height mode) or the deflection of the tip is measured at a constant current (constant current mode) to generate a graded height map of the sample.

Fig. 7.16B shows the structural model of a MoS_2 nanocluster catalyst for hydrodesulfurization [33]. High-resolution STM was used to image the triangular morphology of the nanocluster synthesized on an Au substrate and the characteristic pronounced bright brim of high electron state density all the way around the cluster edge. STM is also able to resolve the adsorbed intermediate, cis-but-2-ene-thiolates, which is coordinated through the terminal S atom to the metallic brim (Fig. 7.16C and D).

7.5 Infrared and Raman spectroscopy

Vibrational spectroscopy includes several techniques, among which infrared (IR) and Raman spectroscopy are the most used in catalyst characterization. These two types of spectroscopy are complementary for the fingerprinting of molecules [34]. Although some vibrational modes may be active in both Raman and IR, they rely on different probing mechanisms. Fig. 7.17A displays an energy-level diagram with the transitions involved in IR and Raman spectroscopy. *IR absorption induces a transition from a ground vibrational state to an excited vibrational state via one-photon event*. The energy of the IR photon is transferred to the molecule leading to a change in its dipole moment. This interaction is associated with a direct resonance between the vibrational frequency of a particular normal mode of vibration and the frequency of the IR radiation. Vibrations fall into the two main categories of *stretching* and *bending* (Fig. 7.17B) [35]. The former arises from the change in the interatomic distance along the bond axis, while the latter one is due to an alteration in the angle between two bonds [24].

An IR spectrum is a plot of the percentage of absorbance (or transmittance) of the IR radiation through the molecule versus the wavenumber of radiation.

In a similar way as in IR spectroscopy, the energetic events involved in Raman are transitions between vibrational states. Yet, while IR spectroscopy uses a broadband IR source and depends on a change in the dipole moment of a molecule, *Raman spectroscopy*

relies on a change in polarizability during vibration that is generated by the *inelastic scattering* of narrow-band, monochromatic radiation on the sample. Conversely to the *dominant elastic scattering* (*Rayleigh scattering*) that leads the molecule to return to its original states, inelastic scattering causes the molecule to relax in a different energy state (Fig. 7.17A). *Raman scattering is thereby a two-photon process* and it is precisely the difference in the energy of these two photons that determines the energy of the vibrational transition. When the released energy is lower than the absorbed energy, the resulting Raman dispersion is called *Stokes*, while it is called *anti-Stokes* in the opposite case (Fig. 7.17A and C). [36]. A Raman spectrum is a plot of the peaks arising from Raman scattered radiation displaced to higher and lower frequencies with respect to Rayleigh peak. This displacement is known as Raman shift.

Raman spectroscopy involves the use of lasers emitting a monochromatic light at visible, near UV, or near IR wavelengths, as excitation light sources. In the traditional instruments the beam emitted by the laser hits the samples and the outgoing signal is filtered to remove the contribution of the Rayleigh scattering. The rest is collected by a charge coupled device and the Raman spectrum is finally shown.

An important landmark in IR spectroscopy was the introduction of Fourier-transform IR (FTIR) spectrometers in the 1940s, which gradually replaced the dispersive instruments. FTIR spectrometers simultaneously collect high-spectral resolution data over a wide range of wavelengths, offering enhanced sensitivity and optical throughput over dispersive spectrometers, where wavelengths were measured one at a time, with the slit controlling the spectral bandwidth. An FTIR spectrometer makes use of an interferometer to identify the sample by generating an optical signal with all the IR frequencies encoded into it (i.e., interferogram). After digitizing the signal, a Fourier transform is performed to obtain the full spectrum as a function of wavenumber.

A wide range of setups can be used depending on the nature of the catalyst under investigation. The most common setups are summarized in Fig. 7.18 [37]. FTIR spectrometer can be operated in *transmission mode (transmission infrared spectroscopy, TIR)*, where a self-sustaining form of the catalyst is inserted inside the cell and the IR beam is analyzed after passing through it. This setup is quite simple but it requires thin, sturdy, and self-sustaining materials, features that are not always present in catalysts (usually the sample is prepared in the form of a thin pellet made of KBr, which is transparent to IR, and a small fraction of the catalyst powder). In *diffuse reflectance mode (DRIFTS)*, the IR radiation reflected by the roughened surface of the sample is collected by a parabolic mirror and analyzed. This mode of operation allows to achieve a higher surface sensitivity compared to TIR mode and it is particularly suitable for probing highly absorbing catalysts characterized by a weak signal in transmission. In *attenuated total reflection (ATR)* mode, the IR beam is sent to a high-refractive index crystal and the

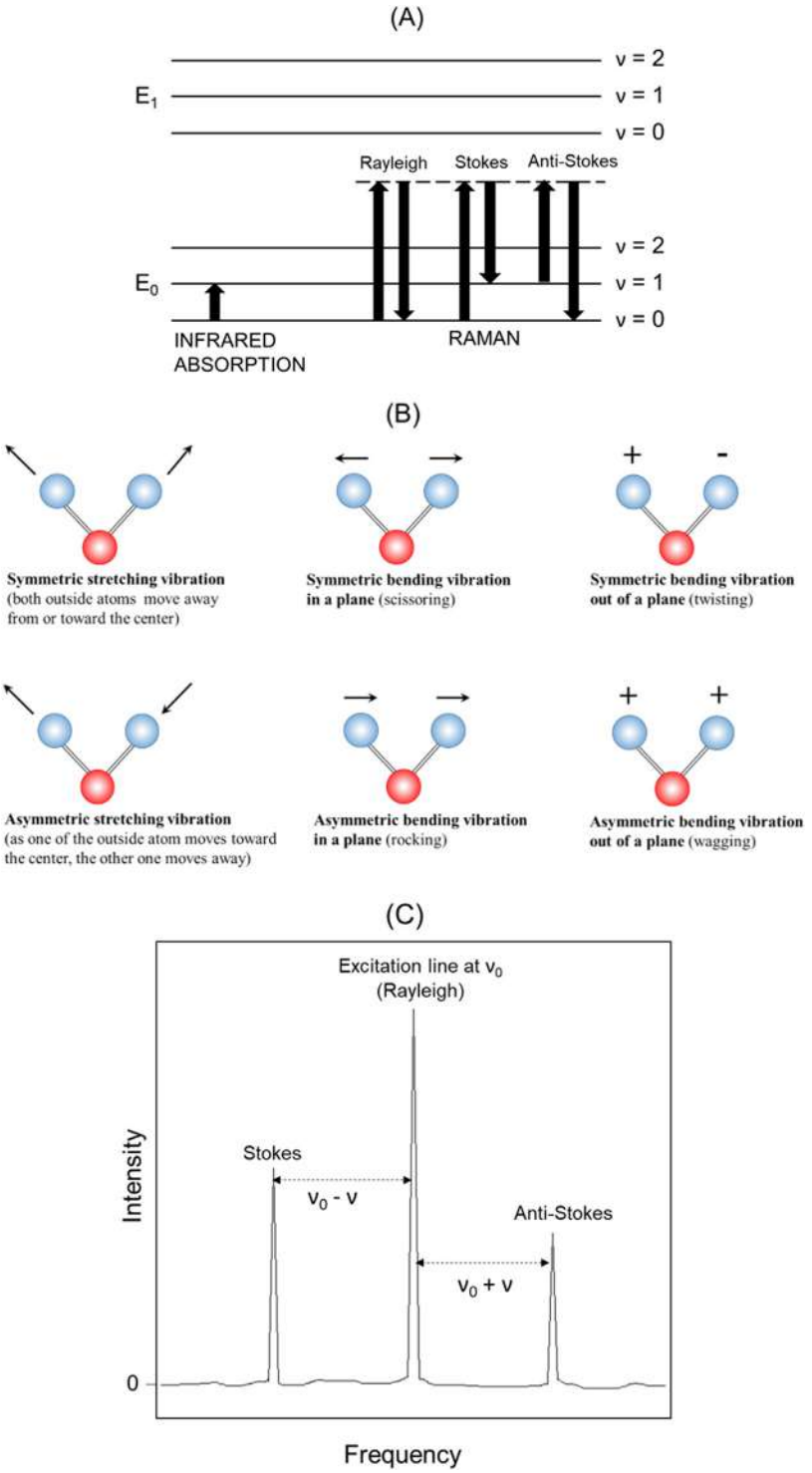

Figure 7.17

(A) Schematic of energy transitions in IR absorption and Raman scattering. ν and E denote vibrational level and electronic level, respectively; (B) types of vibrational modes; (C) typical Raman spectrum. *IR*, Infrared.

resultant evanescent wave is projected orthogonally into the sample which is in close contact with the crystal. The wave is both absorbed and reflected by the sample. The reflected waves thus reach the detector and the signal is processed to obtain the IR spectrum. The big advantage of ATR mode is the easy sample preparation since the catalyst can be analyzed in its natural state, not requiring any process of heating, grinding, and pressing into pellets. In reflection-absorption infrared spectrocopy (RAIRS), the IR beam with a low incident angle is absorbed and reflected by the surface of reflective or polished samples. Metals are usually used as substrates to support reflection and results are delivered in terms of the change in the reflectance spectrum of the substrate. This technique is ideal for probing low surface-area systems and adsorption processes at either solid/liquid or solid/gas interfaces.

IR spectroscopy is one of the most powerful spectroscopic techniques for catalyst characterization able to provide a huge amount of information, for example, about the surface hydroxyl chemistry, poisoning of catalytic sites, occurrence of surface Lewis and Brønsted acid sites. In situ studies can shed light on the active sites where adsorption and reaction take place, nature and geometry of the adsorbed species on the surface, as well as provide kinetic data describing the surface reactions through time-resolved spectra. The energies typical of molecular vibrations in catalysts are in the mid-IR ($400-4000\ cm^{-1}$).

Some vibration modes may be active in both Raman and IR, but Raman is generally more sensitive to homo-nuclear and nonpolar bonds while hetero-nuclear functional group vibrations and polar bonds are more easily detectable by IR spectroscopy. Raman allows to easily access the region below $400\ cm^{-1}$, which can be hard to probe with traditional FTIR instruments. Moreover, Raman can deliver information on the crystal phases in the catalyst and it is very sensitive to amorphous phases which are not detectable by XRD. However, Raman spectroscopy presents two major limitations: (1) heating of the sample by the laser and thus possible alteration of the catalyst structure; (2) fluorescence phenomena deriving from fluorescent impurities in the catalyst can produce very intense peaks that overwhelm the Raman signal [36].

Fig. 7.19 shows two significant examples of how these two types of spectroscopy can provide complementary information. Fig. 7.19A and B displays the Raman and FTIR spectra of nickel phosphate-based catalysts (named NiPO-a, NiPO-b, NiPO-c, NiPO-d in the figure) applied to urea electrooxidation and prepared with different reagents and methods [38]. Similarly to commercial NiO, all the samples exhibit a peak at $\sim 520\ cm^{-1}$ characteristic of Ni−O stretching mode (Fig. 7.19A). The FTIR spectra of the prepared catalysts present weak bands at ~ 456 and $\sim 588\ cm^{-1}$, assigned to symmetrical bending vibration and asymmetric bending vibration of PO_4^{3-}, respectively. The strong peak at $\sim 1050\ cm^{-1}$ can be assigned to antisymmetrical stretching vibration of the phosphate,

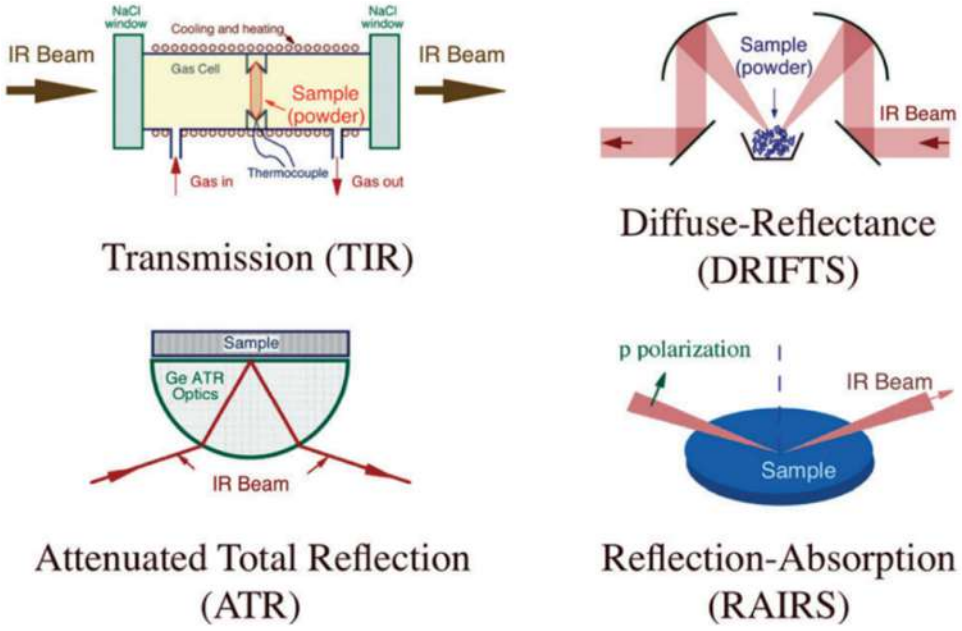

Figure 7.18
Different setups for the characterization of catalytic materials by IR spectroscopy. *Source: Reproduced from [24]. IR, Infrared.*

while that at $\sim 1627\ cm^{-1}$ to crystal water incorporated in the catalyst. The band at $3000-3600\ cm^{-1}$ is due to the stretching vibration of OH groups. This band is more intense in NiPO-a, indicating a higher surface hydroxylation compared to the other catalysts.

Raman spectroscopy is one of the most sensitive techniques for the characterization of the *disorder in sp2 carbon materials* such as graphene. This is done by computing the ratio of the D band to G band integrated intensity (I_D/I_G). The G band at $\sim 1584\ cm^{-1}$ originates from the scattering on Brillouin zone center phonons, while D band at $\sim 1350\ cm^{-1}$ is associated with defect-induced resonant scattering [40]. Fig. 7.19C shows the Raman spectra of Fe- and N-doped carbon catalysts with graphene structure for oxygen reduction reaction [39]. The catalyst C-PANI was prepared from pure polyaniline, while melamine was added to the precursor to obtain PANI/C-Mela; the sample Fe-PANI/C-Mela was Fe-doped. The sample Fe-PANI/C-Mela exhibits the lowest I_D/I_G ratio (~ 1.22) and thus a reduced defect concentration compared to the other two catalysts. The FTIR spectra of the same samples in Fig. 7.19D present the bands of the coordination-bonded, pyridine-type C−N bond and of the stretching mode of C−N bonds. These bands are more intense in PANI/C-Mela and Fe-PANI/C-Mela, confirming that the catalyst with melanine includes a higher extent of C−N bonds.

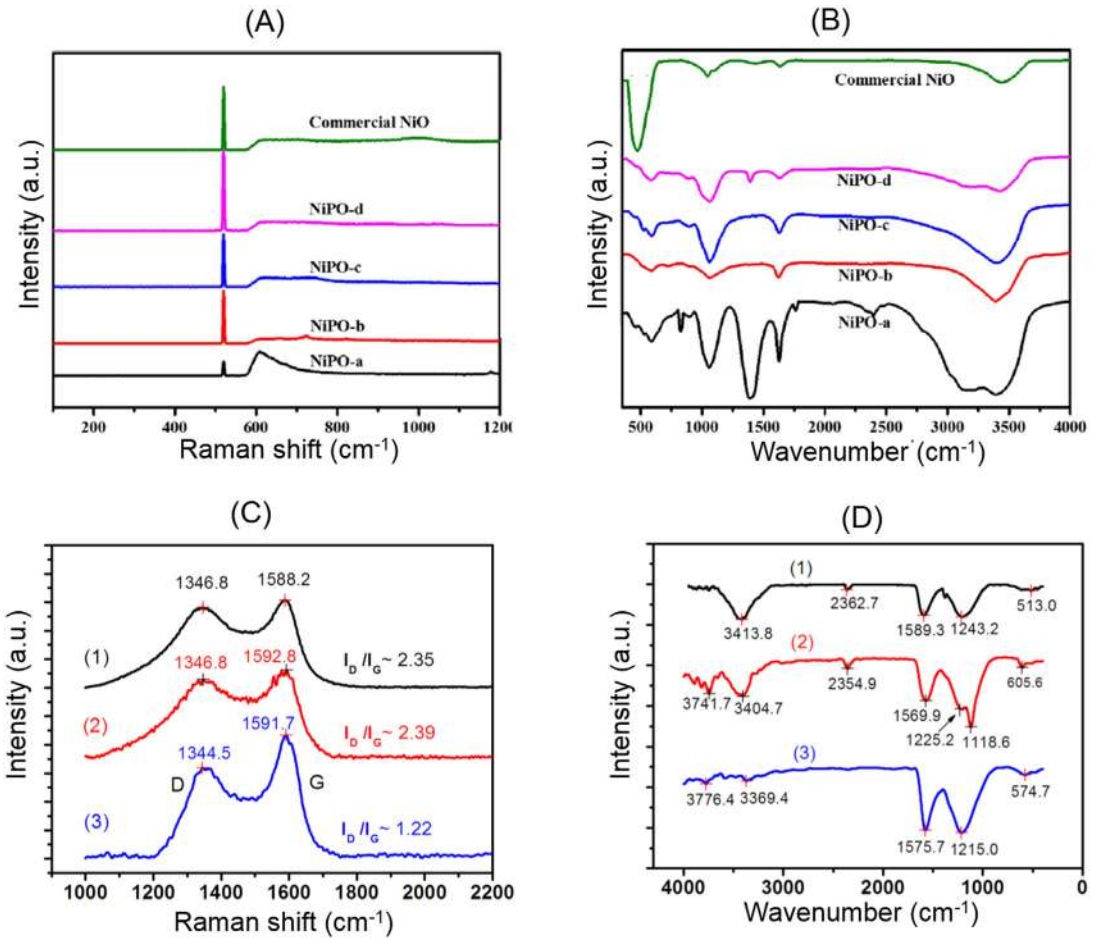

Figure 7.19

(A) Raman and (B) FTIR spectra of nickel phosphate-based catalysts (C) Raman and (D) FTIR spectra of C-PANI (1), PANI/C-Mela (2), and Fe-PANI/C-Mela (3) *FTIR*, Fourier-transform infrared. *Source: (B) Reproduced from [38]. (D) Reproduced from [39].*

In situ Raman and IR spectroscopies have been increasingly applied under *in situ conditions*. Fig. 7.20 shows an in situ study on a platinum catalyst supported on CeO_2 under H_2 reducing conditions [41]. The Raman analysis in Fig. 7.20A reveals that the reduction of the PtO_x phase starts at 150°C−200°C with the decrease in intensity of the relevant peaks. The IR spectra on the same catalyst show that surface hydroxylation is affected by the reducing conditions (Fig. 7.20B). The IR band at 3695 cm^{-1} is assigned to type I hydroxyl groups, that is, OH(I), arising from isolated −OH groups on the CeO_2, while that at 3655 cm^{-1} is due to type II hydroxyl groups, that is, OH(II), deriving from bridging surface hydroxyl groups. Both types of −OH groups are present in the temperature range

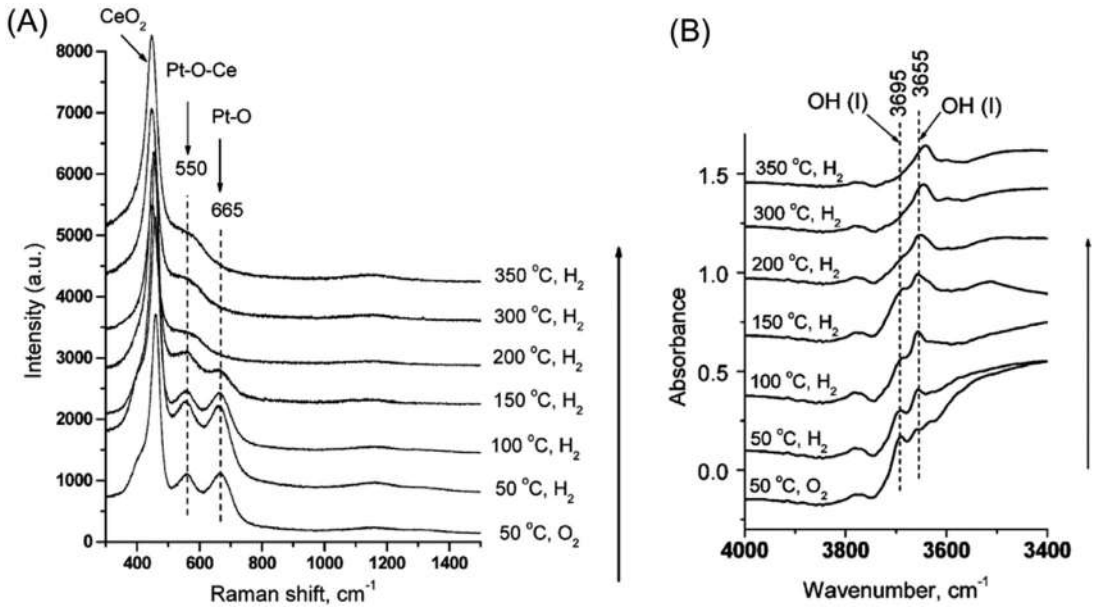

Figure 7.20

(A) In situ Raman and (B) in situ IR analysis of Pt catalyst supported on CeO_2 under H_2/Ar flow (3% balanced by Ar, total flow 30 cm^3/min). *Source: (B) Reproduced from [41]. IR, Infrared.*

50°C–200°C. Above 300°C, OH(I) band disappears while the surface OH(II) band shifts to smaller wavenumbers.

7.6 Temperature-programed methods

Temperature-programed (TP) methods are extremely useful in characterizing the activation and the reactivity of catalysts. During TP analysis, the catalyst undergoes an increase in temperature with a constant rate and the concentration of the reacting/desorbing species (such as oxygen and hydrogen) is recorded and plotted as a function of temperature. These measurements can provide fundamental insights about surface changes and bulk reactivity by varying the catalyst composition and synthesis method as well as pretreatment for catalyst activation. The types of thermal analysis commonly used in catalyst characterization can be divided into two main categories: (1) *TP desorption (TPD)*, which involves surface processes; (2) *TP oxidation (TPO) and reduction (TPR)*, which involve both surface and bulk reactions.

TP techniques have been widely employed in the development of industrial catalysts, particularly because they can reproduce operating conditions (i.e., temperature and gas flow) similar to those encountered in industrial catalytic processes. Moreover, the transient

nature of TP measurements, where temperature, reaction kinetics, and surface coverage all change with time, has the great advantage of delivering information not available from most of the characterization techniques which mainly operate at steady-state conditions [42].

Fig. 7.21 shows a schematic of typical instrumentation for TP analysis, which can be utilized for TPD, TPO, and TPR. Pretreatment gases (reducing/oxidizing mixtures) are fed to the reactor before the TP analysis to remove undesired adsorbed contaminants which may affect the analysis. The adsorbate—CO, CO_2, NO, NH_3, etc. in TPD—and reacting gases—H_2 in TPR and O_2 in TPO—are contained in a carrier gas such as helium, nitrogen, or argon and can be delivered to the reactor through separate lines. The exit of the heated reactor is usually connected to analytical systems (gas chromatograph, mass spectrometer, etc.) which analyze the gases evolved from the reactor.

During TPD characterization, the rate of desorption initially increases exponentially with temperature due to the gradual depletion of the adsorbed gas on the catalyst surface. After reaching a maximum, the desorption rate drops back to zero indicating the complete desorption of the adsorbate. The acquired spectrum depends on the nature of the catalyst, surface coverage, and heating rate and it may contain several peaks if the desorption process involves more than one mechanism or if different binding sites coexist for a given species. The information that can be inferred from the spectrum includes the following: (1) surface coverage; (2) presence of homogeneous/heterogeneous binding sites for the probed adsorbate; (3) kinetic parameters of

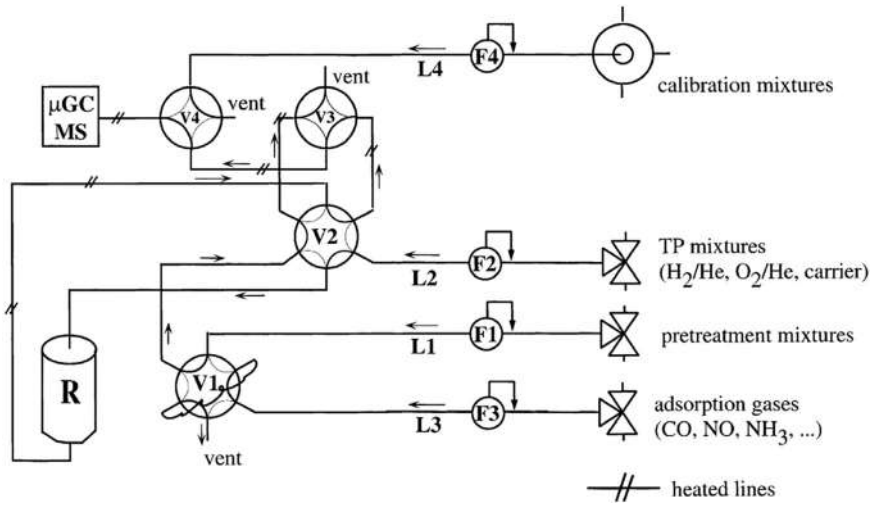

Figure 7.21
Schematic of a typical instrument for TPD, TPO, and TPR measurements (L1—L4 lines, F1—F4 mass-flow controllers, V1—V2 six-way two-position valves, V3—V4 four-way two-position valves, R reactor). *Source: Reproduced from [42]. TPD,* Temperature-programed desorption*; TPO,* temperature-programed oxidation*; TPR,* temperature-programed reduction.

the desorption process including reaction order, activation energy, and preexponential factor; and (4) strength of acidic/basic sites in the catalyst.

In TPR/O, a reductive/oxidant gas, usually H_2/O_2, is consumed by the sample while the temperature is increased with a constant heating rate. The H_2/O_2 concentration is monitored over the time by analytical systems (Fig. 7.21). The TPR/O profiles provide information on (1) the difference in reduction/oxidation temperature among different catalysts which can be estimated from the different positions of the peaks; (2) presence of one or more species which can be reduced/oxidized; and (3) total H_2/O_2 consumption extracted from the peak area that can be used to compute the exact amounts of those species which are reduced/oxidized at the surface [43]. TPR experiments are sometimes combined with TPO experiments in order to assess the reversibility of reduction/reoxidation cycles [44].

Fig. 7.22 displays the TPD, TPR, and TPO profiles of various Ca−Mn oxides (i.e., $Ca_xMn_yO_z$) used as supports for Pd NPs in the aerobic oxidation of 5-hydroxymethyl-2-furfural [45]. The peak at the lower temperature in the TPD spectra can be attributed to the desorption of chemically adsorbed oxygen species (i.e., O_2^- and O_2^{2-}), while that at the higher temperature arises from the desorption of surface lattice oxygen (Fig. 7.22A). The oxide $CaMn_2O_4$ exhibits the lowest desorption temperatures in both regions, suggesting an easier desorption of the oxygen species and surface lattice oxygen from the surface compared to the other $Ca_xMn_yO_z$ oxides. The same sample also reveals the highest relative amount of desorbed O_2 species calculated from the area of the first TPD peak and thus a superior oxygen adsorption capacity. The TPR profiles in Fig. 7.22B reveal two groups of peaks for H_2 consumption due to the removal of oxygen from redox sites with different chemical environments. The sample $CaMn_2O_4$ shows the lowest reduction temperature as well as the lowest initial reduction temperature, indicative of the highest reducibility of the redox sites. Similarly, $CaMn_2O_4$ presents the best oxidizability compared to the other samples as confirmed by the appearance at lower temperatures of the TPO peaks related to the oxidation processes of the reduced redox sites (Fig. 7.22C). It can be thus concluded that $CaMn_2O_4$ is characterized by the best adsorption capacity and redox properties among $Ca_xMn_yO_z$ oxides.

Fig. 7.23 shows an example of how TPD measurements can be used to estimate the energy of desorption from the profiles recorded at different heating rates [46]. The desorption activation energy can be obtained from the *Kissinger (Redhead) equation*:

$$\ln\left(\frac{T_{\max}^2}{\beta}\right) = \left(-\frac{E_a}{R}\right)\frac{1}{T_{\max}} + K \tag{7.6}$$

where β is the heating rate (K min^{-1}), T_{max} is the maximum peak temperature (K), E_a is the activation energy for desorption (J mol^{-1}), K is a constant and R is the universal gas constant (8.314 J mol^{-1} K^{-1}). The activation energy can be computed from the slope of a curve $\ln\left(\frac{T_{\max}^2}{\beta}\right)$ versus $\frac{1}{T_{\max}}$. The TPD profiles and the corresponding plots for the determination of E_a

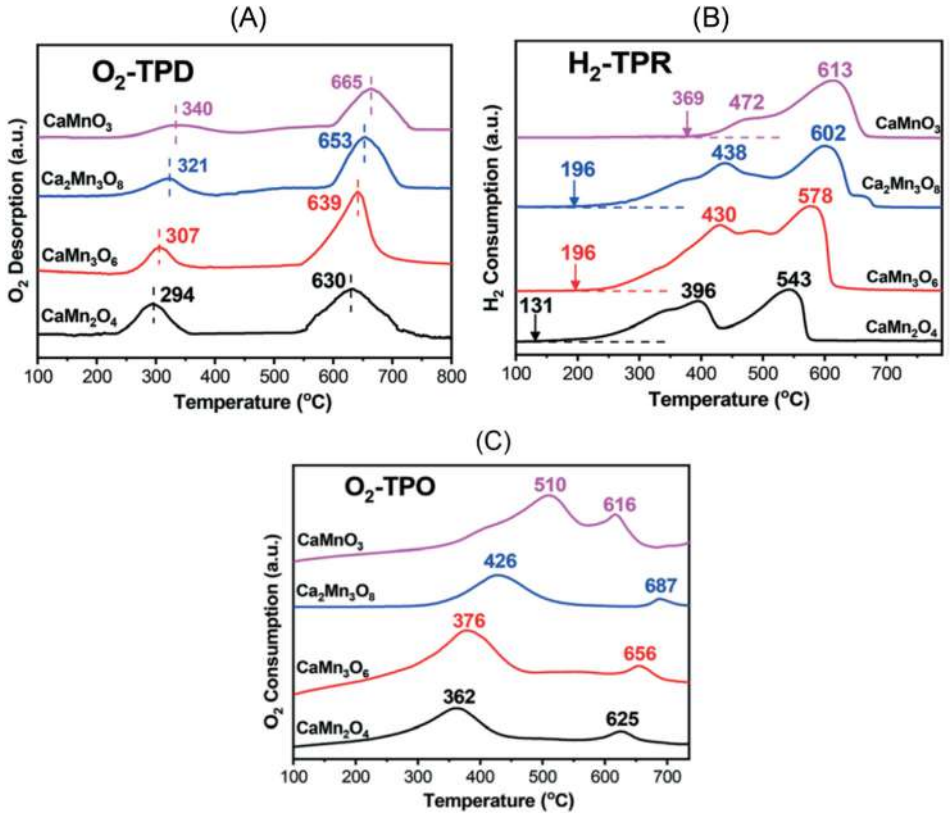

Figure 7.22

(A) TPD, (B) TPR and (C) TPO profiles of various Ca—Mn oxides. *Source: (C) Reproduced from [45].* *TPD,* Temperature-programed desorption; *TPO,* temperature-programed oxidation; *TPR,* temperature-programed reduction.

in Fig. 7.23 are obtained on Pd NPs stabilized with a thin mesoporous SiO_2 shell. The catalysts are labeled according to their morphology: rhombic dodecahedra, that is, $RD_S@SiO_2$ (TPD data in Fig. 7.23A and C) and branched NPs, that is, $BNP_S@SiO_2$ (TPD data in Fig. 7.23B and D). The sample $RD_S@SiO_2$ shows only one peak and the corresponding activation energy for H_2 desorption was higher compared to $BNP_S@SiO_2$, which exhibits heterogeneous binding sites confirmed by a secondary peak at a lower temperature.

TPD is a valuable tool for estimating the strength of acidic/basic sites in the catalyst. Fig. 7.24 displays the NH_3-TPD profiles of a Cu-zeolite catalyst, Cu/SSZ-13, intended for the selective reduction of NOx [47]. The results are shown for the catalyst undergoing progressive mild hydrothermal aging at 600°C. The TPD profiles reveal the presence of two peaks, the intensity of which changes in opposite directions in response to aging. The low-temperature peak at c. 275°C can be ascribed to NH_3 adsorbed on Cu ions being

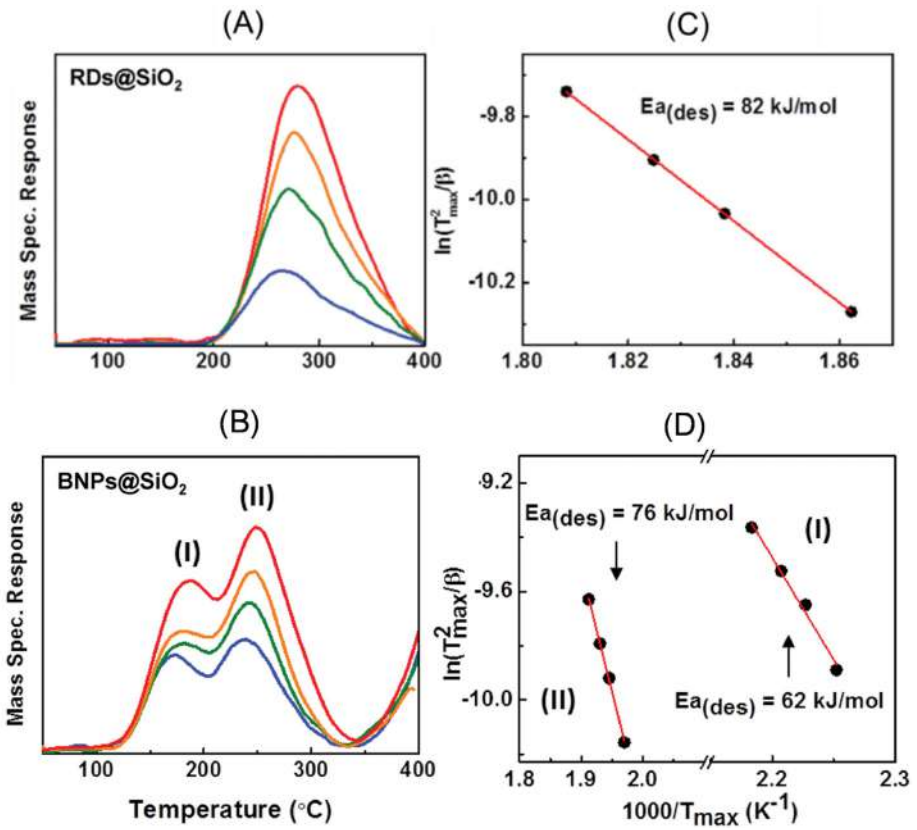

Figure 7.23
TPD spectra of (A) $RD_S@SiO_2$ and (B) $BNP_S@SiO_2$. Plots of $\ln\left(\frac{T_{max}^2}{\beta}\right)$ versus $\frac{1}{T_{max}}$ for the determination of H_2 desorption energy for (C) $RD_S@SiO_2$ and (D) $BNP_S@SiO_2$. *Source: (D) Reproduced from [46].* *TPD,* Temperature-programed desorption.

predominant Lewis acid sites in Cu/SSZ-13. Other Lewis acid sites such as extra-lattice Al sites are too weak at this temperature and thus less prone to adsorb NH_3.

On the other hand, the high-temperature peak at c. 425°C is ascribed to zeolite Brønsted acid sites. The decrease in the intensity of this desorption peak during the aging is indicative of a reduction in the number of Brønsted acid sites attributed to the transformation of Cu sites. Indeed, the latter are converted from ZCuOH (Cu^{2+} singly coordinated with the zeolite) to Z2Cu (Cu^{2+} doubly coordinated with the zeolite) at the expense of Brønsted protons. On the other hand, the increased NH_3-storage at lower temperatures, confirmed by the increase in intensity of the relevant peak, is due to the fact that each Z2Cu can adsorb $\sim$2 NH_3 molecules while each ZCuOH can only adsorb $\sim$1 NH_3 molecule.

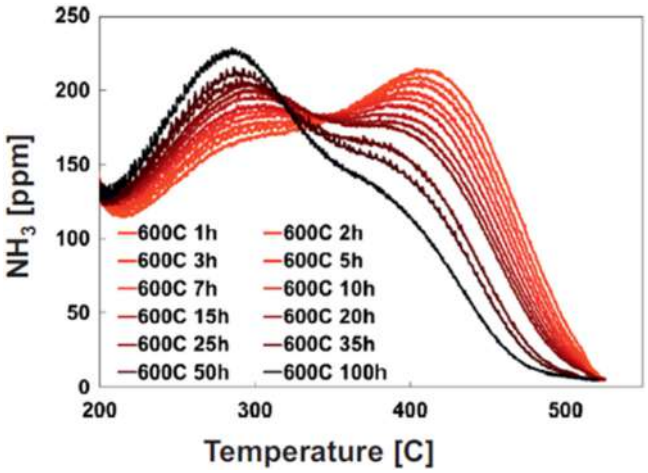

Figure 7.24
NH_3-TPD profiles of Cu/SSZ-13 during gradual aging at 600°C. *Source: Reproduced from [47]. TPD,* Temperature-programed desorption.

Thermogravimetric analysis (TGA) and differential scanning calorimetry (DSC) are further techniques used to investigate how the catalyst reacts to a temperature change. In TGA, the weight change of a sample is measured over time through a microbalance in a controlled heat treatment taking place inside a furnace. TGA is mainly used to probe the thermal stability behavior in different atmospheres (e.g., inert or oxidizing), providing important information on decomposition temperature, moisture content, degradation mechanisms, solid−gas reactions, and phase transitions. It can also be used to quantify the humidity of a catalyst and its content of hydroxyl groups or other moieties which desorb or degrade at certain temperatures, producing a drop in weight. DSC analysis aims to measure the heat flow into or out of a sample as a function of temperature or time under a controlled temperature program. Whether more or less heat is required by the sample depends on whether the process is exothermic or endothermic. TGA and DSC analysis can be coupled to simultaneously monitor changes in crystal phases and thermal decomposition reactions of the catalysts. The reader is referred to specialized reviews and textbooks [48−51] for further information on these two thermal analysis techniques.

7.7 Electrochemical techniques

Electrochemical techniques are deemed to play a primary role in the catalyst characterization when assessing the various types of elementary charge-transfer processes between adsorbates and catalyst surface. These techniques allow to shed the light on (1) the

electroactivity in different reactions (oxygen reduction, hydrogen evolution, etc.); (2) determination of *electrochemically active surface area* (i.e., area of the electrode material that is accessible to the electrolyte which can be used for charge transfer and/or storage); (3) *reversibility of the target redox reaction*; and (4) *stability of the catalysts* involved in redox processes.

The characterization is performed in the conventional three-electrode setup shown in Fig. 7.25, where the catalyst forms the *working electrode*, the potential or current of which is controlled by a potentiostat [52,53]. Unless the catalyst is self-sustaining and conductive, it is usually immobilized on a conductive support such as gold, platinum, glassy carbon, fluorine-doped thin oxide-coated glass slide, among others. The current flows between the working electrode and the *counter electrode*; an electrolyte is needed in order to provide electrical conductivity between the two electrodes. The counter electrode must not affect

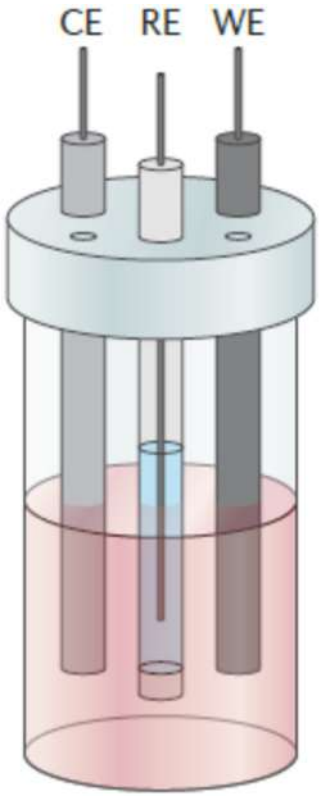

Figure 7.25
Three-electrode setup for electrochemical characterization. The cell consists of WE, RE, and CE, all immersed in an electrolyte. *Source: Reproduced from [52]. CE,* Counter electrode*; RE,* reference electrode*; WE,* working electrode.

the measurements and, therefore, it should be made of an inert material such as carbon or platinum so as not to contaminate the solution. It should also have a relatively low polarization resistance so that the potential drop between the counter electrode and the electrolyte does not limit the polarization that can be applied.

The potential of the working electrode is measured with respect to the *reference electrode*. Ideally, the latter is nonpolarizable and its high impedance ensures that the current flowing between the working and reference electrode is negligible [54]. The most popular reference electrodes are $Hg/Hg_2Cl_2/Cl^-$ (calomel electrode), $Pt/H_2/H^+$ (standard or normal or dynamic hydrogen electrode), $Ag/AgCl/Cl^-$ (silver/silver chloride electrode).

The typical electrochemical techniques employed for catalyst characterization are *voltammetry* and *electrochemical impedance spectroscopy (EIS)*.

In voltammetry, a varying potential is applied to a working electrode and the corresponding current is measured. There are different types of voltammetry such as potential step, linear sweep, square wave, cyclic, cathodic/anodic stripping, adsorptive stripping, alternating current (AC), normal/differential pulse, and chronoamperometry. In addition to EIS, we discuss here three voltammetric methods, namely, linear sweep voltammetry (LSV), cyclic voltammetry (CV), and chronoamperometry, which are the most popular techniques for electrochemical characterization of catalysts. The reader is referred to Refs. [55,56] for the study of the other methods.

7.7.1 Voltammetry

In LSV, the potential of the working electrode is varied linearly with time at rates generally between 1 and 1000 mV s^{-1} and the results are plotted as current density (J) versus the applied potential (V). The resulting plot is referred to as *linear sweep voltammogram*. Any species adsorbed on the catalyst that is reduced/oxidized in the scanned potential range results in a characteristic peak in the voltammogram.

In *chronoamperometry* a potential step is applied to the working electrode and the measured current density is plotted versus time. Changes in the current result from the rise or decrease in the diffuse layers of the analyte at the surface of the working electrode.

CV is carried out by cycling the potential of the working electrode, which can be reversed between two values multiple times during the same experiment (Fig. 7.26A), and measuring the resulting current. The potential is changed linearly and the sweeping rate is typically between 1 and 1000 mV s^{-1} [56]. The current density is plotted versus the applied potential in the so-called cyclic voltammogram, where the current peaks arise from the oxidation/reduction of the species in the electrolyte (Fig. 7.26B). The same redox species that are oxidized/reduced (depending on the initial scan direction) during the forward scan are

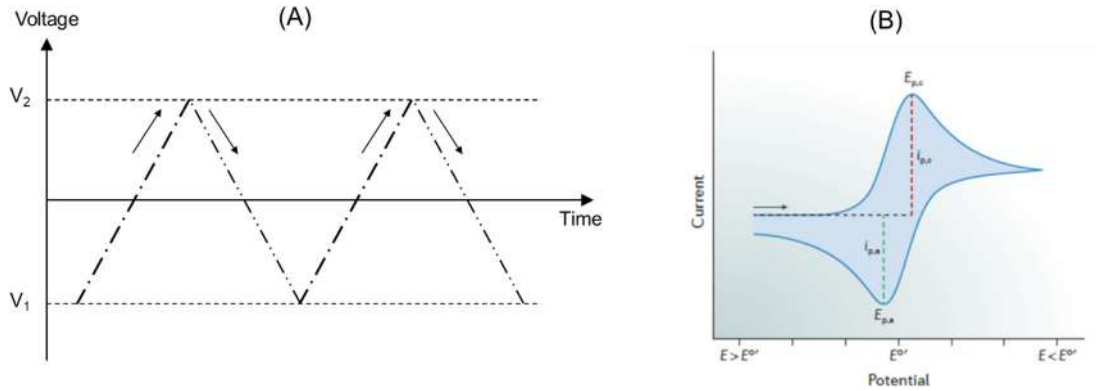

Figure 7.26
(A) Cycled potential sweep in cyclic voltammetry. (B) current density versus potential response for cyclic voltammetry. *Source: (B) Reproduced from [52].*

reduced/oxidized during the reverse scan, at least in the case of reversible reactions. Let us consider the reversible redox reaction of a solution-phase species A to produce B with n electrons transferred:

$$A + ne^- \rightleftharpoons B \tag{7.7}$$

In a thermodynamically reversible reaction the process is fast enough to ensure the equilibrium between A and B at the electrode surface and the equilibrium ratio can be determined by the Nernst equation:

$$E = E^0 + \frac{RT}{nF} + \ln\frac{C_A}{C_B} \tag{7.8}$$

where E^0 is the standard potential, R is the universal gas constant (8.314 J mol^{-1} K^{-1}), T is the temperature (in Kelvin), F is the Faraday constant ($96.5 \cdot 10^3$ J mol^{-1}), C_A and C_B are the concentrations of A and B at the electrode surface. C_A and C_B are equal at $E = E^0$ and the cathodic peak occurs at the same potential as the anodic peaks for ideal reversible redox processes. The resulting current can be obtained from the *Fick's Law* for mass transfer diffusion taking into account that diffusion of the involved redox species is limited to the narrow Nernst diffusion region adjacent to the electrode surface. The following equation can be used ($T = 25°$C) [57]:

$$i_p = \left(2.69 \cdot 10^5\right) n^{3/2} A D^{1/2} \nu^{1/2} C \tag{7.9}$$

where i_p is the peak current (Amperes), A is the electrode area (cm^2), ν is the potential sweeping rate (V s^{-1}), D is the diffusion coefficient (cm^{2}s^{-1}), and C is the bulk concentration of the reactant (mol cm^{-3}, $C_A = C_B = C$). If the reaction is not completely

reversible, the cathodic peak current ($i_{p,c}$) differs from the anodic one ($i_{p,a}$) and the two respective peaks move apart, with the anodic one ($E_{p,a}$) appearing at a more positive potential and the cathodic one ($E_{p,c}$) at a more negative potential with respect to E^0 (Fig. 7.26B). The irreversibility is due to two main factors: (1) slow electron transfer kinetics not allowing to maintain the surface concentrations of the redox species at the values required by the Nernst equation; (2) further chemical reactions involving the redox species under study.

Fig. 7.27 shows some case studies of heterogeneous catalysts characterized by the three voltammetric techniques. Fig. 7.27A displays the LSV of pure nitrogen (N)- and copper (Cu)-doped TiO_2 thin-film semiconductors [58]. A negligible current flows in dark conditions, while under UV/Vis (UV/visible) irradiation, a photocurrent appears due to the generation of the photocarriers and oxidation of water triggered by holes. The onset potential, namely, the potential at which the current starts to increase, was similar in all the catalysts but the photocurrent densities were significantly different with increasing anodic bias. The sample N-TiO_2 exhibits a higher photocurrent compared to the other two samples. The trend is confirmed by the chronoamperograms in Fig. 7.27B, which are obtained by applying a constant potential of 0.9 V versus normal hydrogen electrode to the working electrode and recording the response to intermittent on/off illumination cycles. All the samples show an anodic stationary photocurrent with the presence of spikes of the same sign. N-TiO_2 is confirmed as the sample with the highest photocurrent and, thus, the best photoelectrochemical properties due to an enhanced separation of the photogenerated electron−hole pairs and a minor concentration of trap states compared to the other two semiconductors.

Fig. 7.27C shows a typical cyclic voltammogram of a Pt catalyst in acid solution with three characteristic regions [59]. At intermediate potentials the current density is low and almost constant in both cathodic and anodic scans. This is the capacitive region where the charge accumulates in the "double layer," leading to a non-Faradic current (i_{NF}, not attributable to any redox processes occurring at an electrode surface). This current is proportional to the double-layer capacitance C_{dl} and scan rate ν:

$$i_{NF} = C_{dl}\nu \tag{7.10}$$

The second region called *"oxygen region"* occurs at more anodic potentials, where a monolayer of hydrated platinum oxide forms on the electrode surface. On the other hand, the third region, called *"hydrogen region,"* occurs at cathodic potential and is characterized by the formation of a monolayer of adsorbed hydrogen on the electrode as this is polarized more cathodically:

$$H^+(\text{aq}) + e^- + \text{site} \rightleftharpoons H_{ads} - \text{site} \tag{7.11}$$

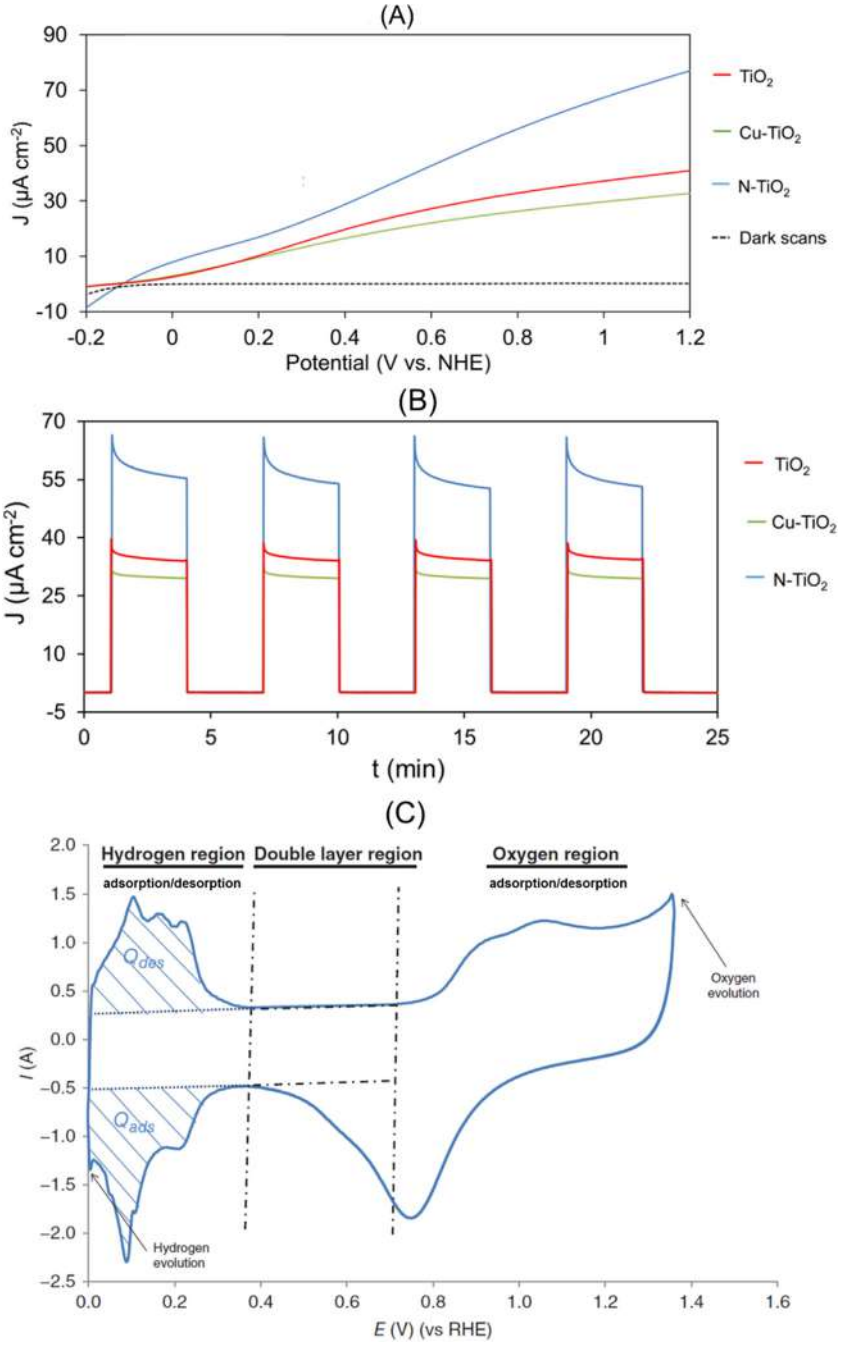

Figure 7.27

(A) Linear sweep voltammetry and (B) chronoamperometry of TiO_2 -based thin films in a Na_2SO_4 electrolyte. (C) Typical cyclic voltammetry of a Pt electrode in acidic electrolyte. *Source: (B) Reproduced from [58]. (C) Reproduced from [59].*

Bubbles form and a marked rise in current occurs due to hydrogen evolution reaction (HER). When the scan direction is reversed, hydrogen desorbs and goes back into solution as H^+.

7.7.2 Electrochemical impedance spectroscopy

EIS is a powerful method to investigate the charge and mass transfer occurring at the interface between the catalyst and the electrolyte. In this technique, *low amplitude AC voltages are applied to the working electrode at different frequencies* and the electrical current is measured. The resultant impedance Z can be calculated as:

$$Z = \frac{V}{i} \tag{7.12}$$

where V is AC voltage applied at a certain frequency ($f = \frac{\omega}{2\pi}$, where ω is the angular frequency) and i is the recorded current. In general, the impedance can be expressed as:

$$Z = Z_{\mathrm{Re}} + jZ_{\mathrm{Im}} \tag{7.13}$$

where Z_{Re} and Z_{Im} are the real and imaginary part of the impedance, while $j = \sqrt{-1}$ is the imaginary unit.

Since AC current can be produced at various frequencies, EIS allows probing processes with different time constants, the individual contribution of which cannot be separated in DC measurements as they are combined and convoluted.

The results are usually reported in *Nyquist plots*, representing the opposite of the imaginary versus the real part of the impedance at different frequencies (Fig. 7.28A). Low-frequency data appear on the right-hand side of the plot, while higher frequency data on the left. The impedance measurements can be also reported in the *Bode plots* in which the impedance magnitude and phase angle θ are plotted against frequency (Fig. 7.28B and C).

EIS data are analyzed in terms of equivalent circuit elements, including resistances, capacitances, inductances, and Warburg elements. Fig. 7.28D displays the typical Nyquist plot of an electrochemical reaction with charge transfer at the electrode–electrolyte interface. A basic equivalent circuit to describe such a process is shown in the inset of the same figure. R_s represents the *ohmic resistance* of the electrolyte between the working and the reference electrode, R_{ct} is the *resistance associated with the charge-transfer* process at the electrode–electrolyte interface and is called charge-transfer resistance, C_{dl} is the *double-layer capacitance* resulting from the accumulation of two layers of charge with opposite polarity at the electrode–electrolyte interface (one at the surface of the electrode and the other one in the electrolyte). Double-layer regions in EIS experiments usually

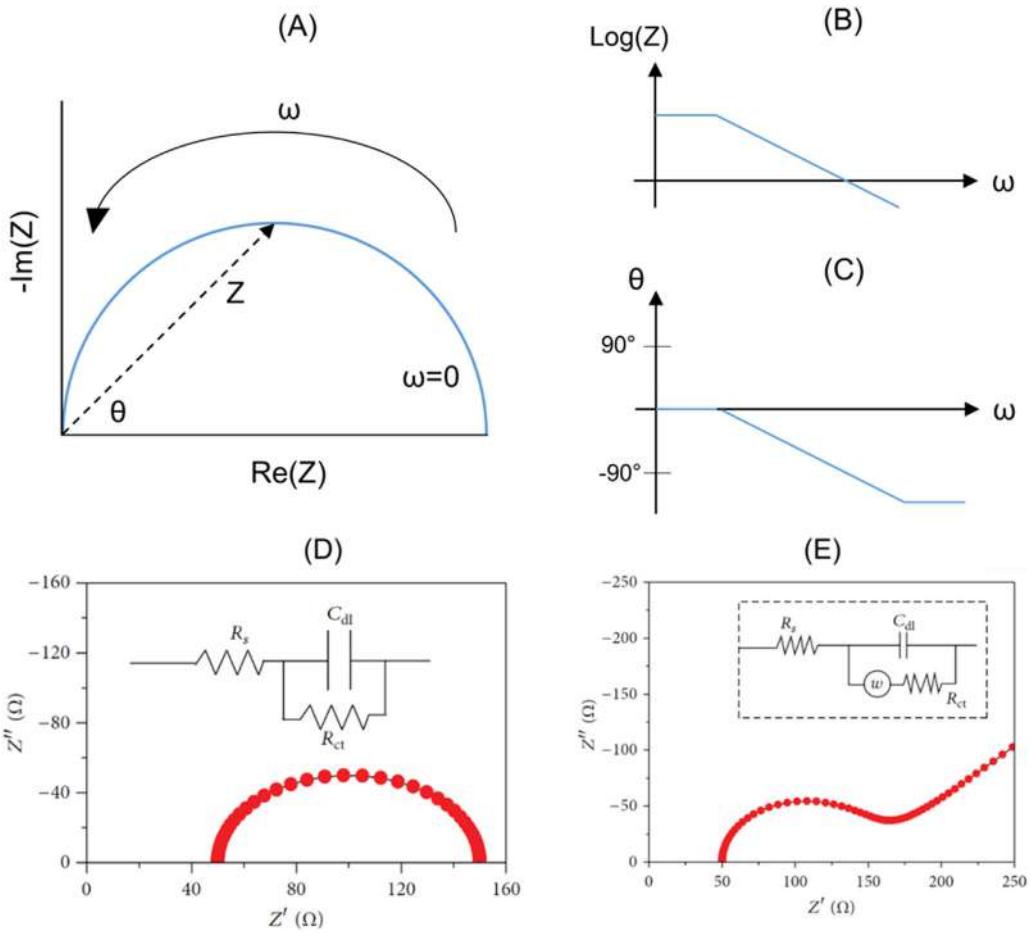

Figure 7.28

Representation of EIS measurements in Nyquist plot (A), Bode plots for impedance magnitude (B) and phase (C). Nyquist plots and equivalent circuit for an electrochemical reaction without (D) and with (E) dominant transport of reactant at the electrode–electrolyte interface. *Source: (E) Reproduced from [60]. EIS,* Electrochemical impedance spectroscopy.

behave as imperfect capacitors so the pure capacitor is replaced by the so-called constant phase element, which results in slightly flattened arcs in Nyquist plots [60].

A redox reaction can be strongly affected by diffusion of the species toward the electrode surface. When the diffusion effects become dominant, the equivalent circuit is modified by introducing Warburg impedance (W) in parallel to R_{ct} as shown in the inset of Fig. 7.28E. This element describes the resistance arising from the mass transport process, which leads to the appearance of a straight line with a slope of c. 45 degrees on the Nyquist plot [60].

Mott–Schottky analysis can be performed through EIS in order to obtain information on the flat band potential (E_{FB}) and doping densities of the semiconductor. Doping is the process of introducing impurities into an intrinsic semiconductor for the purpose of modulating its electrical, optical, and structural properties. In the field of catalysis, doping is often used to improve thermal durability, enhance the surface area, boost electron/hole separation, and extend the spectral response of wide bandgap semiconductors to the visible regions [61,62].

In the Mott–Schottky experiment, the *impedance of the working-electrode interface is measured as a function of voltage at a fixed frequency* to obtain the capacitance of the space charge layer (C_{sc}). When a semiconductor comes into contact with an electrolyte, the thermodynamic equilibrium is established on both sides of the interface, leading to the equalization of the Fermi levels of the electrode and the redox species in the solution. This equilibration takes place through the transfer of electrons across the interface, which leads to the creation of a *space charge layer* in proximity of the interface. This electron transfer causes the formation of an electric field at the interface (i.e., built-in electric field) which, in the case of an n-type semiconductor, for instance, is triggered by the excess of positive charge in the semiconductor (ionized donors) counterbalanced by an excess of negative charge in the electrolyte [63]. In the space charge region, due to this built-in electric field, the energy band edges of the semiconductor are also shifted continuously, being this phenomenon called band bending [64]. The *flat band potential* E_{FB} is that potential that needs to be applied in order to bring back the band edges to their flat band position (i.e., no charge accumulation and space charge layer). According to the Mott–Schottky equation, C_{sc} is obtained from the following equation:

$$\frac{1}{{C_{sc}}^2} = \frac{2}{\varepsilon_0 \varepsilon e N}\left(E - E_{FB} - \frac{kT}{e}\right) \tag{7.14}$$

where N is doping density (electron donor concentration for an n-type semiconductor or hole acceptor concentration for a p-type semiconductor), E is the applied potential, T is the temperature, k is the Boltzmann constant, ε_0 is the vacuum permittivity, ε is the dielectric constant and e is the electron charge. In a plot of $1/{C_{sc}}^2$ versus E, the flat band potential E_{FB} and the doping density N can be obtained as the intercept with the x-axis and from the slope of the linear part, respectively.

Fig. 7.29 illustrates the Mott–Schottky plots of pure and doped TiO_2-based thin films, the voltammetric measurements of which have been presented in Fig. 7.27A and B [58]. Doped films exhibited an anodic shift of E_{FB} indicative of a reduction in the bending of the band edges caused by the doping. Moreover, the donor density increased with the doping as confirmed by the decreasing slope of the linear part from TiO_2 to N-TiO_2. The increase in N in TiO_2 is usually associated with the rise in oxygen vacancies due to the reduction of Ti^{4+} to Ti^{3+}, which tends to form donor states below the conduction band (CB) of TiO_2.

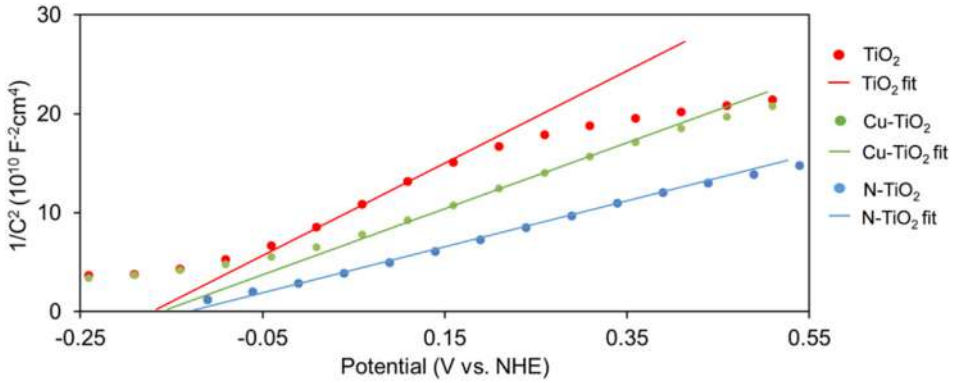

Figure 7.29
Mott–Schottky plots of TiO_2-based thin films in a Na_2SO_4 electrolyte. *Source: Reproduced from [58].*

7.8 UV–visible and photoluminescence spectroscopy

UV–Vis and photoluminescence (PL) spectroscopies are both based on the *interaction of light with matter in the UV–Vis range*. They can be considered complementary and they rely on two different phenomena. While UV–Vis measures the absorption of the light by the sample, PL spectroscopy measures the light at certain wavelengths emitted by a sample as the result of the absorption of light at a fixed wavelength.

7.8.1 UV–visible spectroscopy

A number of phenomena can take place when a beam of light comes into contact with a solid. The beam may be reflected, transmitted, scattered, or absorbed (Fig. 7.30). The attenuation of light traveling in a material can be obtained by the *Beer–Lambert law*, which states that the ratio between the transmitted intensity (I) and incident intensity (I_0), defined as *transmittance*, can be calculated as [24]:

$$T = \frac{I}{I_0} = e^{-k_\lambda l} \tag{7.15}$$

where k_λ is the attenuation coefficient characteristic of the medium through which the light is traveling and l is the path length of light through the sample.

The quantity of light absorbed (A) by a substance dissolved in a fully transparent solvent can be obtained from the opposite of the natural logarithm of T and Eq. (7.15) can be rearranged as follows:

$$A = k_\lambda l = \varepsilon c l = -\ln \frac{I}{I_0} \tag{7.16}$$

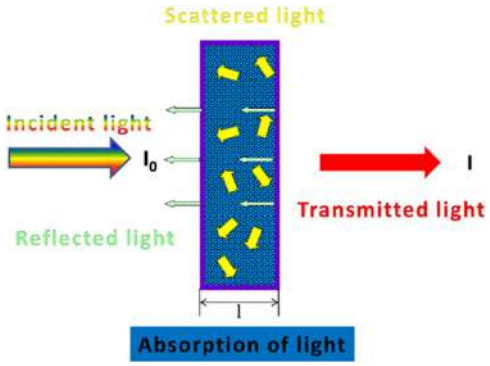

Figure 7.30
Different phenomena arising from the interaction between the light and the sample. *Source: Reproduced from [24].*

where ε and c are the molar extinction and the concentration of the absorbing species in the solvent.

UV−Vis analysis is performed in a spectrometer that measures I and compares it to I_0 in a wavelength range of typically 200−800 nm. The classical instrument consists of two light sources (one for the UV and one for the Vis range), a holder for the sample, a diffraction grating, or monochromator, consisting of one or more slits that allow selecting a narrow band of wavelengths from a polychromatic beam of light [65]. *Integrating spheres* are frequently used for the analysis of solid samples. The beam conveyed inside this accessory strikes the highly reflective walls, undergoing multiple diffuse reflections. The radiation is thus dispersed uniformly at the sphere walls after many reflections. The resulting integrated signal is directly proportional to the initial radiation level and can be easily measured by the detector [66].

In catalysis, UV−Vis spectroscopy can be used not only for *catalyst characterization* but also for ***monitoring the reaction trend*** over time through the acquisition of the absorption spectra of the target molecule dissolved in reaction media. Indeed, the variation in the absorption of the analyte arises from a change in its concentration during the catalytic reaction (Eq. 7.16).

From the point of view of material characterization, UV−Vis spectroscopy is mainly applied to the study of optical properties of semiconductor materials for photocatalytic applications. This technique enables to estimate the optical bandgap (E_g), which is the minimum energy required to excite an electron from the VB up to a state in the CB of the semiconductor, eventually triggering a redox process. The determination of E_g is a fundamental step in predicting photochemical properties of semiconductors, especially when applying these to technologies that rely on the conversion of solar to chemical energy or

electricity. Bandgaps can be of two types: direct and indirect. In a ***direct bandgap*** semiconductor, the top of the VB and the bottom of the CB are at the same value of momentum [67,68]. In this case the interaction of electrons in the sample with the photons in the incident beam is sufficient to produce the electronic transition, provided that the photons have higher energy than E_g. On the other hand, ***indirect bandgap*** semiconductors involve a third entity, namely, phonons, which are required for conservation of energy and momentum. In these materials the top of the VB is at a different value of momentum with respect to the minimum in the CB energy.

Tauc plots are commonly used to determine E_g in semiconductors. According to this model, the energy-dependent absorption coefficient α is expressed as follows:

$$(\alpha h\nu)^{1/n} = A(h\nu - E_g) \tag{7.17}$$

where h is the Planck constant, ν is the photon's frequency, and A is a constant. The factor n depends on the nature of the electron transition and is equal to 1/2 for direct allowed and 3/2 for direct forbidden transitions, 2 for indirect allowed, and 3 for indirect forbidden transitions [24].

In thin films materials the absorption coefficient can be determined from the transmittance and reflectance measurements, for instance by using the following equations [5]:

$$\alpha = \frac{1}{d}\ln\frac{(1-R)}{T} \tag{7.18}$$

where d is the thin-film thickness, while T and R are the measured transmittance and reflectance, respectively. After calculating α at different wavelengths, the Tauc plot can be constructed according to Eq. (7.17) and E_g obtained as the x-axis intersection point of the linear fit of the plot in the proximity of the absorption threshold.

In powder samples, E_g is usually determined by the *Kubelka–Munk method* from diffuse reflectance spectra. This model, based on the assumption of an infinitely thick sample, allows to convert the reflectance spectra to the function $F(R_\infty)$ [69]:

$$F(R_\infty) = \frac{\alpha}{S} = \frac{(1-R_\infty)^2}{2R_\infty} \tag{7.19}$$

where α is the absorption coefficient, S is the scattering coefficient, and R_∞ is the reflectance of an infinitely thick specimen obtained as the ratio of the intensity of light reflected from a sample to the intensity of the reflection from a standard. Introducing $F(R_\infty)$ in place of α into Eq. (7.17) yields the equation:

$$[F(R_\infty)]^{1/n} = A(h\nu - E_g) \tag{7.20}$$

Fig. 7.31 shows the optical characterization of Cu-doped TiO_2 NPs by using the Kubelka–Munk model [70]. From the reflectance spectra in (Fig. 7.31A), one can note that the Cu-doping produces a shift in the absorption edge of TiO_2 from the UV to the visible region, namely, the doped NPs start to absorb at higher/lower wavelengths/energies compared to pure TiO_2. Kubelka–Munk absorption curves (Fig. 7.31B) can be calculated from reflectance spectra and, finally, the bandgap can be computed from Eq. 7.20, keeping in mind that TiO_2 is indirect bandgap semiconductor ($n = 2$). The bandgap values, obtained from the x-intercept in the Tauc plots (Fig. 7.31C), confirm a red shift of the absorption edge and a narrowing in E_g with the doping.

UV/Vis spectroscopy can be also used to investigate the *surface plasmon resonance (SPR)* which may occur in Ag, Au, and Cu NPs. SPR is the manifestation of a resonance effect due to the interaction of electrons of metal NPs with incident photons [71]. This interaction depends on the size and shape of the metal NPs and on the nature and composition of the dispersion medium. The resonant excitation allows metallic NPs to collect the energy of photons to form a highly enhanced electromagnetic field that can be used to drive or accelerate chemical transformations [72]. SPR usually results in a broad peak in the visible region of the absorption spectrum, as displayed in Fig. 7.32A for a catalyst consisting of Au nanoparticles [73]. The resonance effect due to Au NP causes the appearance of an absorption peak at 500–600 nm, which becomes more prominent as the NPs grow during the synthesis process.

Another application of UV/Vis spectroscopy is the *identification of transition metal cations* in heterogeneous catalysts. Fig. 7.32B shows the adsorption spectra of mono- and bi-metallic catalysts for NO reduction [74]. Such catalysts consist of transition metal cations

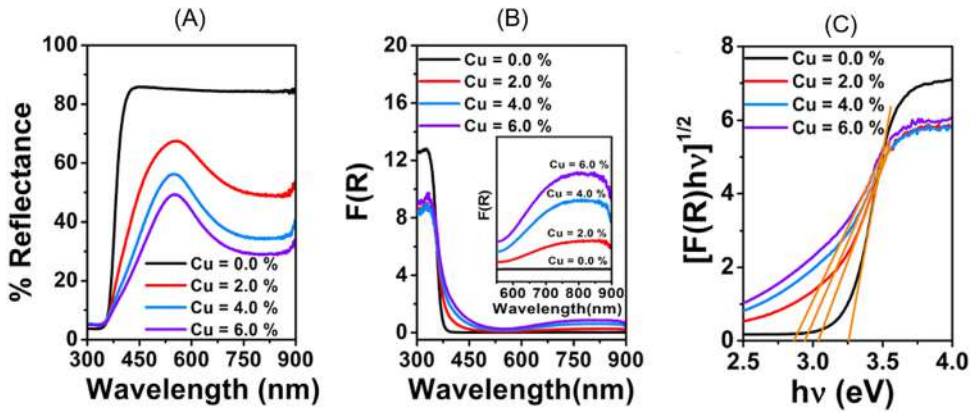

Figure 7.31

(A) Diffuse reflectance spectra, (B) Kubelka–Munk absorption curves, (C) bandgap determination for pure and Cu-doped TiO_2. *Source: (C) Reproduced from [70].*

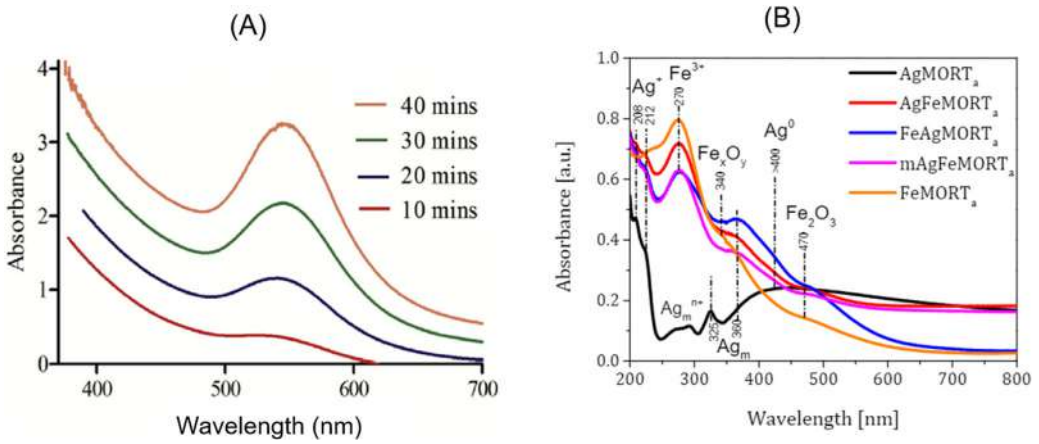

Figure 7.32

(A) Absorption spectra of Au NPs at different time during the synthesis process. (B) Absorption spectra of mono- and bimetallic catalysts consisting of metal cations Fe and Ag introduced in sodium mordenite zeolite. *SPR*, Surface plasmon resonance. *Source: (A) Reproduced from [73]. (B) Reproduced from [74].*

Fe and Ag introduced in sodium mordenite zeolite by (1) single-stage ion-exchange ($mAgFeMORT_a$ sample); (2) double-stage ion-exchange introducing iron first and silver later ($FeAgMORT_a$); and (3) double-stage ion-exchange introducing silver first and iron later ($AgFeMORT_a$). Monometallic samples ($AgMORT_a$ and $FeMORT_a$) were also tested. The sample $AgMORT_a$ shows the following signals ascribed to: ions (Ag^+); NPs (Ag^0) causing a broad absorption band above 370 nm; cationic clusters (Ag_m^{n+} with $3 < m < 5$) and metal clusters Ag_m ($m \leq 8$). On the other hand, $FeMORT_a$ exhibits the bands characteristic of oxygen-to-iron charge transfer of isolated Fe^{3+} ions in tetrahedral or higher coordination [$Fe^{3+}O_4$ and $Fe^{3+}O_{4+x}$ ($x = 1, 2$)]. Moreover, two more contributions stand out: octahedral Fe ions in oligomeric clusters of the Fe_xO_y type inside the mordenite channels and Fe_2O_3 particles on the external surface of mordenite particles. In bimetallic samples the main absorption band derives from oxygen-to-iron charge transfer of Fe^{3+} ions, while the intensity of the signal from Ag^+ decreases. This corroborates the reduction of Ag^+ ions in bimetallic samples, where silver is mostly present in the form of Ag^0.

7.8.2 Photoluminescence spectroscopy

PL is one of the most widely diffused experimental techniques for the characterization of semiconductor nanostructures. Photons are adsorbed to excite electrons in the semiconductor to a higher electronic excited state. Various relaxation processes take place following this excitation, leading to the emission of photons as the photoexcited electrons return to a lower energy state.

PL technique allows gaining a better insight into the electronic structure and optical properties of photocatalysts, providing valuable information on possible *defects* such as oxygen vacancies and interstitial atoms, which have a considerable impact on the *trapping and transfer of the photogenerated carriers*, and, in turn, on the photocatalytic performance.

In semiconductor materials, PL signal originates from the *recombination of photo-induced charge carriers* (e^-/h^+ pairs). Fig. 7.33A shows the typical excitation/

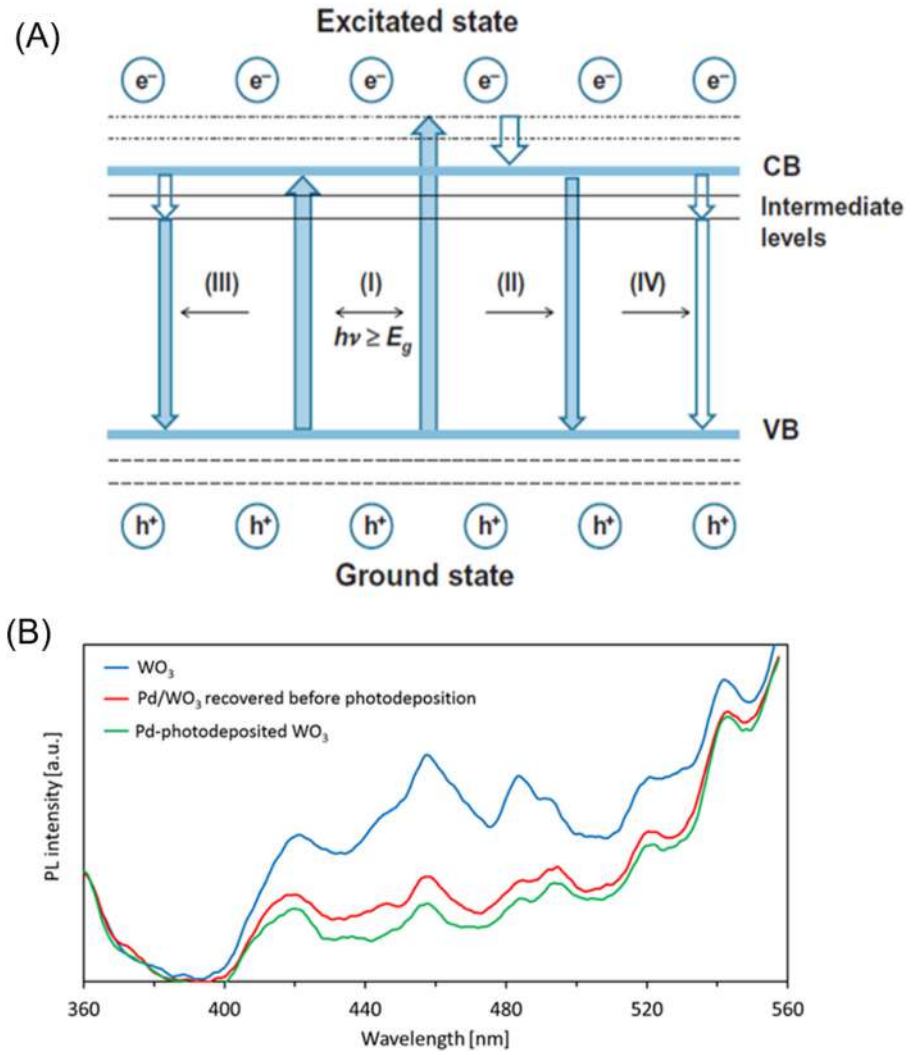

Figure 7.33

(A) Main photophysical processes in a semiconductor excited by photons of energy equal or higher to the bandgap. (B) PL spectra of WO_3 and Pd-loaded WO_3. *PL*, Photoluminescence. *Source: (A) Reproduced from [24]. (B) Reproduced from [76].*

relaxation processes occurring in a semiconductor following the absorption of photons with an energy higher than E_g [24,75]. Process I involves the excitation of electrons from VB to different levels of CB, leaving behind holes in the VB. The unstable photoexcited electrons can return to the VB, recombining with the holes and releasing chemical energy that can be transformed into heat or light. The emission of light energy gives rise to the PL phenomenon. The photoexcited electrons, which can occupy different energy levels in the CB, jump down to the bottom of the CB through nonradiative transition and then generate radiative phenomena as highlighted by processes II–IV in Fig. 7.33A. Process II involves a band–band transition, where electrons return to the top of VB with the emission of an energy equal to E_g. The remaining two processes first imply a nonradiative step, where the electrons are transferred to mid-gap states, and then a radiative transition (process III) or a further nonradiative transition (process IV) of these electrons to the top of VB. *Only processes II and III can thus give rises to PL.* Process II directly reflects the separation of e^-/h^+ pairs and, in general, the higher the intensity of the corresponding PL peak in the spectrum, the higher the extent of recombination of the photocarriers. The signals deriving from process III are more difficult to interpret and assign, as they do not reflect the separation of the photocarriers. Nevertheless, they can shed light on the presence of surface states and defects.

Fig. 7.33B shows the effect of metal loading by Pd on the PL emission of a WO_3 catalyst applied in fuel cells [76]. One can observe three different bands: (1) the peak at c. 460 nm can be ascribed to radiative recombination between CB and VB; (2) the two signals at c. 480 and 490 nm arise from the trapping of electrons in defects produced by unstable W^{5+} states; (3) the peak at c. 540 nm can be assigned to recombination of CB electrons downgraded to deep defects forming mid-gap states such as oxygen vacancy and interstitial tungsten. The lower emission in the samples decorated by Pd is indicative of a reduced recombination between the h^+/e^- pairs. This can be ascribed to the trapping effect of Pd toward the electrons which ensures a higher separation efficiency of the photocarriers.

Experimental techniques making use of pulsed lasers and a fast detector can be used to probe the transient dynamics of the photogenerated holes and electrons by determining the emission of a material as a function of time. In photocatalysis, these techniques mainly aim to measure the charge recombination lifetime (higher quality catalysts tend to have a longer emission time) [61,77].

PL is a useful tool to characterize the *coordination of transition metal cations and oxide anions* in order to get a better insight into acidic and basic features of the catalytic sites [78]. An example of application of PL in this area is the study of the surface basic sites in alkaline earth oxides. Here, the coordination of oxide anions in the bulk lattice can be defined by the number of nearest neighbor cations, which is six for octahedrally

coordinated oxides. The ions of lower coordination are designated by the subscript LC. The basicity of alkaline earth oxides such as MgO mainly depends on the hydroxyl coverage of the surface and distribution of oxide ions of low coordination $O^{2-}{}_{LC}$ (where LC = 3C, 4C, and 5C denote tri-, tetra-, and pentacoordinated oxide ions, respectively). PL is particularly sensitive to the coordination of such ions and the basicity of the surface can be evaluated by investigating the nature of the luminescent species generated following the interactions of $O^{2-}{}_{LC}$ with a polar molecule such as water and ethanol [79].

7.9 Solid-state nuclear magnetic resonance and electron paramagnetic resonance spectroscopies

7.9.1 Nuclear magnetic resonance

Nuclear magnetic resonance (NMR) spectroscopy allows to probe the *molecular structure of samples* by measuring the interaction among nuclear spins under the effect of a magnetic field. When subjected to a magnetic field, NMR active nuclei, such as ^{1}H and ^{13}C, absorb electromagnetic radiation at a frequency specific of the isotope. The resonant frequency, the amount of absorbed energy, and the intensity of the signal are proportional to the strength of the magnetic field. An NMR spectrum is a plot of the signal intensity versus the chemical shift δ, which is the resonant frequency of a nucleus relative to a standard in a magnetic field.

Solid-state NMR (SS-NMR) has become a valuable tool for the investigation of the surface of various heterogeneous catalysts such as zeolites, metal oxides, and solid heteropoly acids, which play a primary role in petrochemical industry [80]. Similarly to liquid-state NMR, SS-NMR probes molecular structure by relying on the alterations in the magnetic behavior of specific atomic nuclei deriving from the interaction with the surrounding electrons and atoms. However, while Brownian motion averages anisotropic effect to zero in the liquid state, most of the interactions are anisotropic in the solid state, that is, dependent on the orientation of the molecule with respect to the baseline NMR magnetic field. Anisotropic interactions cause broader spectral lines that are more difficult to resolve than the narrow signals obtained in the liquid state. Nevertheless, the occurrence of broad spectral lines, once considered a limitation, actually gives a lot of information on the chemistry, structure, and dynamics in the catalyst. The spectral resolution can, however, be improved by magic-angle spinning (MAS), a technique that involves the rotation of the sample at high rotation frequencies (up to 60,000 revolutions per second) around an axis tilted at 54.7 degrees to the direction of the NMR magnetic field. The high rotation speed of the sample aims to mimic the free tumbling of molecules in liquids, ensuring narrow spectral lines and thus high resolutions.

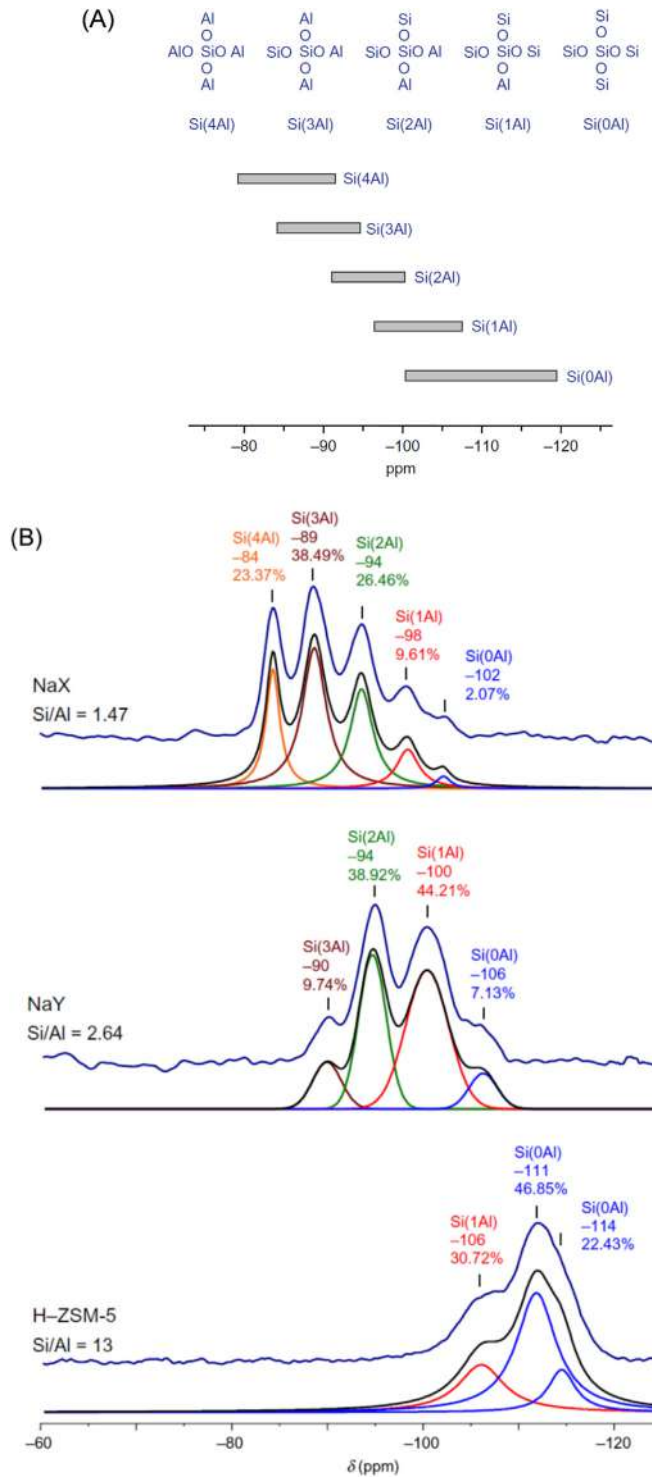

Figure 7.34

(A) ^{29}Si chemical shifts of Si(*n*Al) units in zeolite catalysts; (B) ^{29}Si MAS NMR spectra of NaX (Si/Al = 1.47), NaY (Si/Al = 2.64), HZSM-5 (Si/Al = 13). *Source: (B) Reproduced from [82].*
MAS, Magic-angle spinning; NMR, nuclear magnetic resonance.

In heterogeneous catalysis, SS-NMR can be used to get an insight into the constituent elements in the catalyst as well as of the species adsorbed on its surface. A typical application of NMR is *site identification* in catalytic materials. Nuclear spins of specific isotopes at atomic sites can produce NMR spectral lines at typical frequencies that are related to the atomic environments of the spins. The interactions that determine the NMR frequencies usually occur between the nuclear spins and electrons in the nearby localized orbitals (i.e., chemical shifts) or in metallic conduction bands (i.e., Knight shift) [81]. The NMR frequencies also depend on the interactions between nuclear spins and other spins present in surrounding atomic sites. Chemical and Knight shifts can be employed, for instance, to distinguish different Si and Al sites in zeolites. The basics unit of zeolite framework is TO_4 tetrahedra having Si atoms at the central T-position and ^{29}Si MAS NMR spectra of simple zeolites presents a maximum of five peaks deriving from five possible distribution of Si and Al atoms around the central silicon atom: Si(4Al), Si(3Al), Si(2Al), Si(1Al), and Si(0Al). As shown in Fig. 7.34A, each type of Si(nAl) ($n = 0$, 1, 2, 3, 4) produces a characteristic ^{29}Si MAS NMR signal within a well-defined range of chemical shift [82]. Fig. 7.34B shows the ^{29}Si MAS NMR spectra of three types of zeolite (i.e., NaX, NaY, and HZSM-5) characterized by different ratios among the various Si(nAl) units. Their relative concentration as well as the Si/Al ratio can be obtained from the deconvolution of the spectrum into separate lines and analysis of the relative intensities.

SS-NMR is a powerful technique for the determination of the *surface acidity of the catalysts* which can be described by three main properties: (1) the type of acid sites (Brønsted or Lewis sites); (2) the acid strength which depends, for the Brønsted site, on the ability of surface OH groups to protonate the adsorbed molecules; and (3) the concentration of the accessible acid sites. ^{1}H MAS NMR can detect OH groups which can act as proton donors, that is, Brønsted acid site, on the surface of the catalyst [80]. The advantage of ^{1}H MAS NMR compared to other techniques such as IR spectroscopy is the possibility to perform an accurate quantitative investigation of the concentration of OH groups, which can be determined from the measurement of the signal intensities [83].

SS-NMR is well suited for in situ studies on heterogeneous catalytic systems. The concentration of the active sites on the catalyst surface and absorbed species, including reactants, products, and intermediates, can be evaluated quantitatively during the reaction, which is very helpful for the determination of the reaction mechanism.

Fig. 7.35 shows the in situ ^{13}C MAS NMR measurements on ethylene-$^{13}C_2$ adsorbed on zeolite catalyst (HZSM-5) tested for the synthesis of toluene from ethylene [84]. The results proved that 1,3-dimethylcyclopentenyl carbenium ion is generated as intermediate, which, after 0.5 s of reaction, gives rise to peaks caused by isotropic resonances at 250 ppm (C1 and C2 of the allyl cationic moiety), 148 ppm (C2 of the allyl cationic moiety), 48 ppm

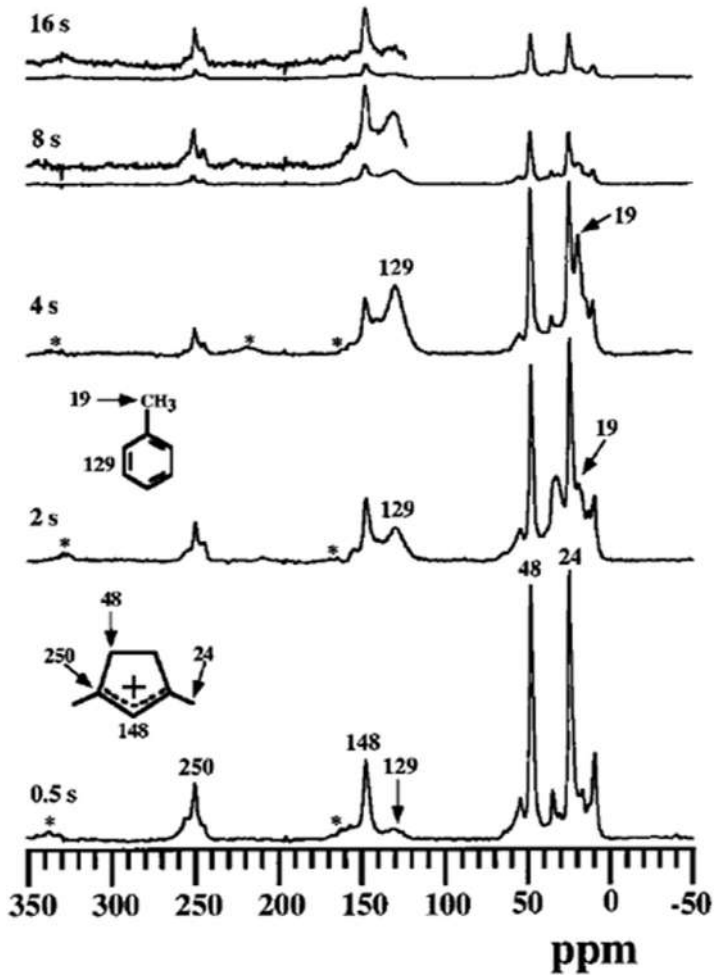

Figure 7.35
In situ ^{13}C MAS NMR of ethylene-$^{13}C_2$ adsorbed on HZSM-5 zeolite at a temperature of 623K for different reaction times. *Source: Reproduced from [84]. MAS,* Magic-angle spinning*; NMR,* nuclear magnetic resonance.

(CH_2 carbons), and 24 ppm (CH_3 carbons). The intensity of these peaks decreases after 2 s with a commensurate increase of the peaks characteristic of toluene at 20 ppm (methyl group) and 129 ppm (C in aromatic rings). After 16 s only, a modest amount of carbenium ion is present in the catalyst bed.

7.9.2 Electron paramagnetic resonance

The basic concepts of NMR are similar to those of electron paramagnetic resonance (EPR)—also known as electron spin resonance—a spectroscopic technique used to *probe*

the materials with unpaired electrons immersed in a strong magnetic field. However, unlike NMR, EPR relies on the magnetic excitation of electron spins rather than nuclear spins. EPR usually necessitates microwave-frequency radiation (GHz), while NMR is carried out at lower radio frequencies (MHz). Due to its detection principle, EPR technique can only analyze paramagnetic species with unpaired electrons. Therefore it is particularly suitable to probe free radicals, defects in materials and several transition metals, shedding light on the molecular structure in proximity of the unpaired electrons.

When a free electron is exposed to an external magnetic field with strength B_0, its angular momentum (spin) vector $\vec{S}$ aligns parallel or antiparallel to the z-direction of the field (Fig. 7.36A) [85]. According to the *Zeeman interaction*, the component of the spin vector along z, that is, S_z, is relevant for EPR. This situation creates two distinct energy levels for the unpaired electrons and each alignment has its specific energy E:

$$E = m_s g_e \beta B_0 \tag{7.21}$$

where $m_s = +\frac{1}{2}$ (parallel) or $-\frac{1}{2}$ (antiparallel); g_e is the electron g-factor, a dimensionless quantity that characterizes its magnetic moment ($g_e = 2.0023$ for the free electron); and β is a constant (i.e., Bohr magneton).

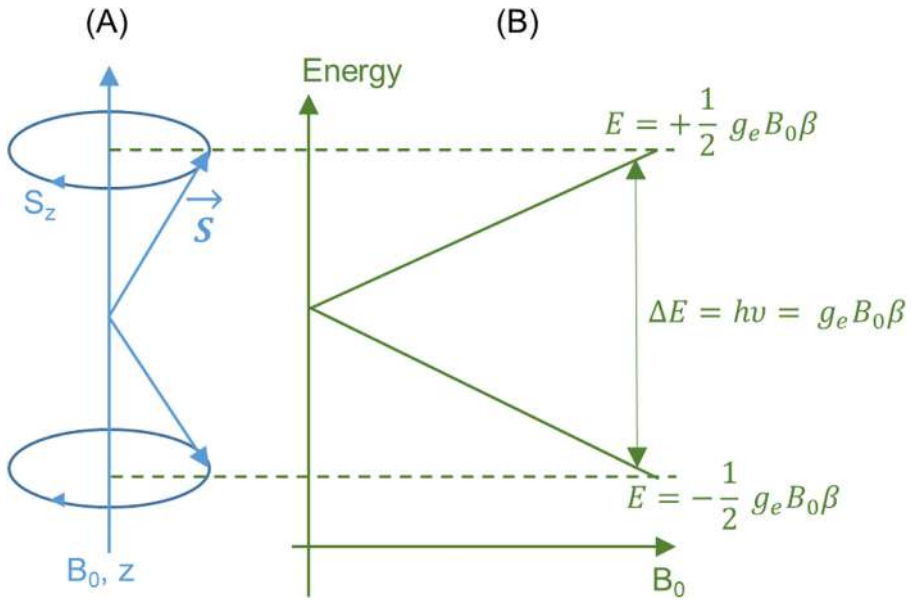

Figure 7.36

(A) Alignment of the spin vector of a free electron with the direction of the external magnetic field and (B) corresponding energy levels.

To attain a resonance condition, the sample is usually exposed to a fixed frequency of microwave irradiation while the strength of the magnetic field is increased until the separation between energy levels is equal to the energy of the microwave radiation [86]. The separation between the lower and the upper state ΔE can be obtained by the following equation:

$$\Delta E = h\nu = g_e \beta B_0 \tag{7.22}$$

where h is Planck's constant and ν is the frequency of microwave radiation. Since g_e and β are constant, the splitting of the energy levels is the function of only the magnetic field's strength, as shown in Fig. 7.36B. In real materials, atoms are surrounded by other atoms and additional interactions should be included in Eq. (7.22). The reader is referred to Refs. [85–87] for further information.

In heterogeneous catalysis, EPR spectroscopy is mainly applied to two areas, namely, the *detection of transition metal ions in paramagnetic valence states and radical ions formed on surfaces*.

Transition metal ions in paramagnetic valence states are incorporated in a wide range of oxide catalysts [88]. They play an important role in redox reactions, allowing the adsorption and stabilizations of different forms of oxygen as well as reducing agents on the catalyst surface. The aptitude of releasing or incorporating oxygen is a crucial asset for many catalytic processes. This ability is usually ensured by the presence of various structural defects in the catalyst which can significantly affect its activity and selectivity.

An example of EPR application in this area is provided in Fig. 7.37A, showing the EPR spectra of two TiO_2-based catalysts before and after a thermal annealing in medium vacuum (TAMV) [89]. The catalysts are bare TiO_2 and TiO_2 modified with nitrogen and grown on reduced graphene oxide (N-TiO_2/G); the detected paramagnetic species are Ti^{3+} and NO. The bare TiO_2 exhibits a small signal at g = 2.003 (blue bar in Fig. 7.37A) ascribed to Ti^{3+}/O^- centers. The intensity of this signal increases in N-TiO_2/G, indicating the formation of more defects following the introduction of N atoms in TiO_2 lattice. A further signal appears in these samples (red bar in Fig. 7.37A) which can be assigned to molecular NO permanently trapped in the structure. The intensity of the latter signal slightly decreases after TAMV due to the partial elimination of gaseous NO, while, on the other hand, the marked increase in the intensity of the signal at $g = 2.003$ denotes the formation of more lattice defects (i.e., oxygen vacancies) in annealed samples. These defects can facilitate water oxidation, increase the uptake of O_2, and, in turn, improve the photocatalytic activity of TiO_2.

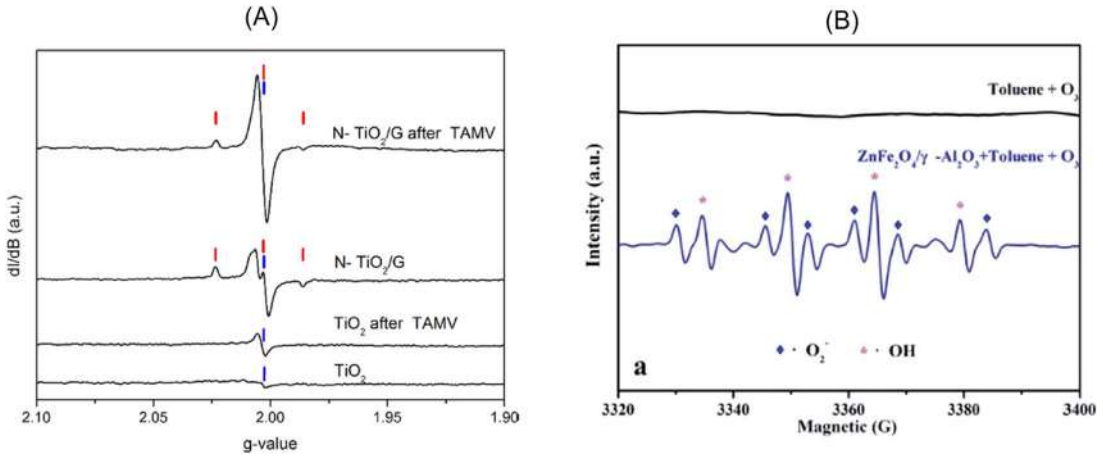

Figure 7.37

(A) EPR spectra of TiO_2 and N-TiO_2/G before and after TAMV. The N-TiO_2/G samples show the coexistence of two paramagnetic species denoted by blue and red bars. (B) EPR spectrum of superoxide radicals and hydroxyl radicals detected in the presence of a $ZnFe_2O_4/\gamma$-Al_2O_3 catalyst (bottom). The same radicals were not detect without catalyst as shown by the other EPR spectrum (up). *EPR*, Electron paramagnetic resonance; *TAMV*, thermal annealing in medium vacuum. *Source: (A) Reproduced from [89]. (B) Reproduced from [90].*

Radical neutral species and radical ions can derive from intrinsic constituents in the catalyst or from the conversion of reactant molecules. Some examples are the radical anions $O^{\bullet -}$ and $O_2^{\bullet -}$ anions that are recurrent intermediates in oxidation reactions as well as NO and $CO^{\bullet -}$ utilized to investigate special surface sites on the catalyst surface [85,91]. The detection of short-lived free radicals is usually carried out by the spin trapping technique, in which a nitrone spin trap reacts with the radical of interest to form a spin adduct, a nitroxide-based radical with sufficient long half-life to enable its detection by EPR spectroscopy. For instance, DMPO (5,5-dimethyl-1-pyrroline N-oxide) is an effective spin trap for superoxide ($O_2^{\bullet -}$) and hydroxyl radicals ($OH^{\bullet}$). An example of radical detection by EPR spectroscopy is shown in Fig. 7.37B, displaying the EPR spectra acquired in a mixed solution containing the target substrate (toluene), DMPO, and the catalyst, that is, nanoferrites supported on alumina ($ZnFe_2O_4/\gamma$-Al_2O_3) [90]. The addition of the catalyst implies the generation of $O_2^{\bullet -}$ and $OH^{\bullet}$ radicals, which can be easily detected by this method as shown by the EPR spectrum in the presence of the catalyst. These radicals ensure higher oxidation rates than ozone alone and, thus, an enhanced catalytic ozonation of toluene.

Focus 7.4: In situ NMR spectroscopy for the identification of the elementary steps in faujasite formation

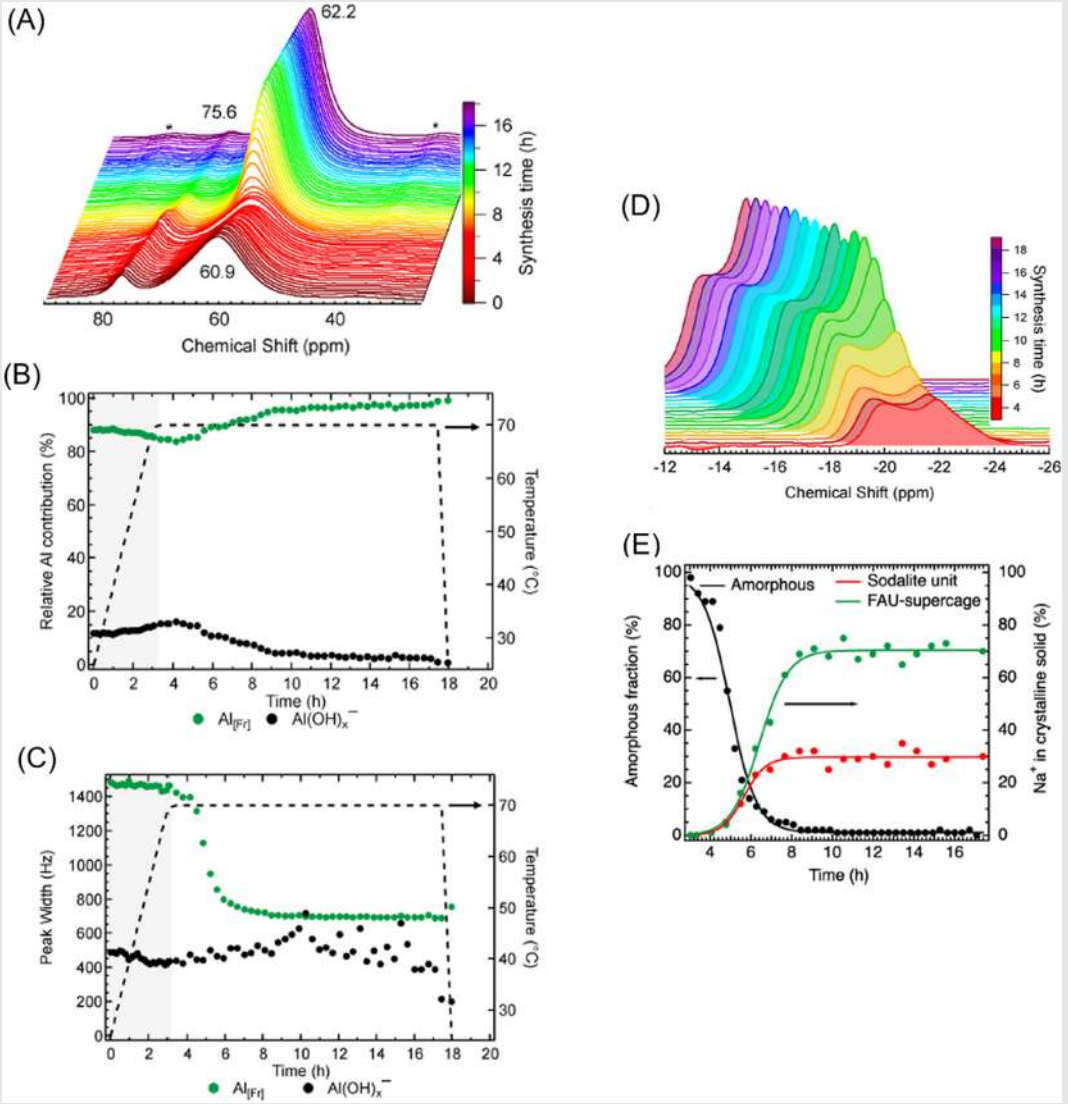

Figure 7.38

In situ ^{27}Al MAS NMR during the synthesis of faujasite and corresponding (B) peak area and (C) line width recorded for Al_{Ft} and $Al(OH)_x^-$. (D) Evolution of the spinning sidebands associated with solid Na^+ during the same reaction and (E) corresponding kinetic transformation of amorphous phase into crystalline faujasite associated with sodalite and supercage sites. *Source: (E) Reproduced from [93]. MAS,* Magic-angle spinning*; NMR,* nuclear magnetic resonance.

(*Continued*)

Focus 7.4: In situ NMR spectroscopy for the identification of the elementary steps in faujasite formation (Continued)

Recently, a great effort has been dedicated to developing a novel MAS NMR technology able to *investigate catalytic materials under working conditions*, which normally are very different from the standard spectroscopic environment of analysis. Advancement in technical capabilities has led to new rotors that can withstand high pressures and temperatures under fast spinning rates. This has led to the possibility to probe both structure and dynamics of the environments nearby a *multitude of nuclear constituents* (^{1}H, ^{13}C, ^{23}Na, ^{27}Al, etc.) and evaluate time-resolved interactions and transformations [92].

Fig. 7.38 shows an application of the MAS NMR technique to follow the reaction steps in the formation of zeolites at an atomistic level [93]. Advanced cutting-edge NMR tools have been developed in order to monitor the nucleation and crystallization steps at temperatures up to 250°C in a highly alkaline reaction medium [93,94]. In situ NMR spectra of the Al environment during the formation of faujasite from a hydrous gel are displayed in Fig. 7.38A. Two ^{27}Al species stand out: (1) solid tetrahedral aluminum from the framework, namely, Al_{Ft}, the peak of which shifts from 60.9 to 62.2 ppm; (2) tetrahedral Al in liquid phase, namely, $Al(OH)_x^-$, the peak of which shifts from 79.0 to 75.6 ppm due to hydroxyl replacement by siloxy groups. As the temperature increases and crystallization proceeds, the relative contribution of Al_{Ft} becomes more important than that of $Al(OH)_x^-$ (Fig. 7.38B). In parallel, the line width of Al_{Ft} decreases as a result of its improved crystallinity, while that of $Al(OH)_x^-$ remains almost unchanged (Fig. 7.38C).

The monitoring of the spinning sidebands of ^{23}Na during framework formation also provides relevant information (Fig. 7.38D). The spinning sidebands are spurious signals that result from the modulation of the magnetic field at the spinning frequency. The sidebands present at −20 and −22 ppm shift denote the presence of Na^+ in the sodalite unit and in the faujasite supercage, respectively, and derive from the corresponding isotropic chemical shifts at 2.8 and 0.8 ppm. Both species increase in abundance, with the sodalite population reaching a saturation earlier than the supercage (Fig. 7.38E). Moreover, the cationic sites fill the supercage and sodalite sites with a ratio of 70:30, providing a useful information on the confined environments experienced by reacting molecules and intermediates during a catalytic reaction.

7.10 Computational tools: density functional theory and molecular dynamic simulations

The synergy between experimental and theoretical studies in heterogeneous catalysis has become increasingly evident during the last decade. Density functional theory (DFT) and molecular dynamics (MD) simulations are the two computational methods widely used for heterogeneous catalysis modeling. Due to the complexity and extensive popularity of such methods, exhaustive coverage of this topic would be beyond the

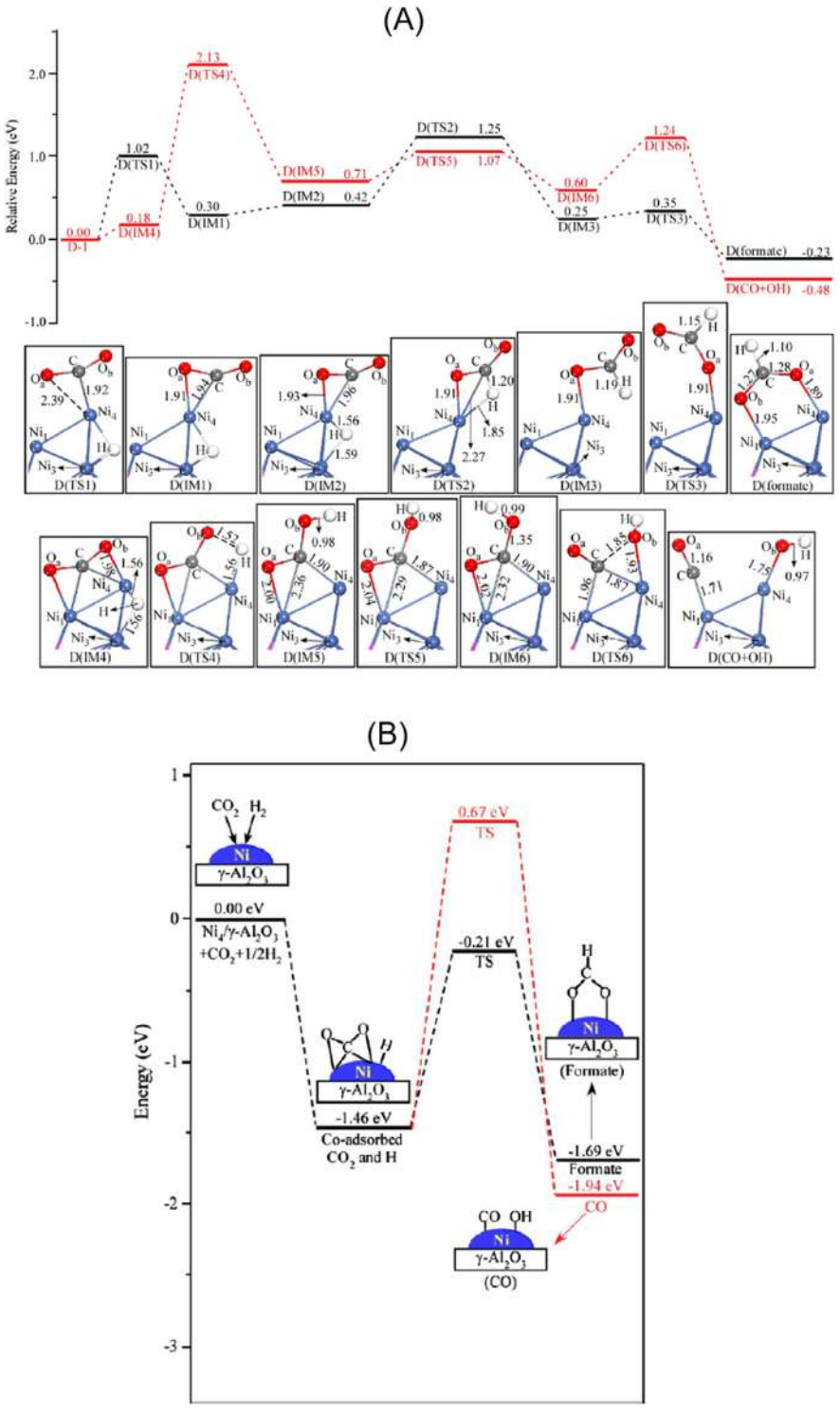

Figure 7.39

(A) Potential energy profiles for CO_2 hydrogenation to formate (black line) and to CO (red line) on D(Ni_4) catalyst. The structures of the intermediates (IM), transition states (TS), and products are also displayed. (B) Schematic potential energy diagrams for the same catalytic reaction, showing the transition states (TS) with the highest energy barriers for formate and CO formation.

Source: (B) Reproduced from [113].

scope of this section. As a consequence, only a flavor of the applications will be provided and the reader is referred to specialized reviews and textbooks [95–100] for further information.

The modeling of catalytic behavior at the molecular scale plays a primary role in ensuring a rational design of efficient catalysts. DFT is a valuable tool to facilitate the mechanistic understanding of catalysis through molecular and periodic simulations [95].

DFT is mainly used for two purposes: (1) *deriving descriptors of catalytic activity*, (2) *descriptor-based search for new catalysts* [101]. Adsorption energies are often employed as descriptors of the catalytic activity. As already discussed in chapter 1, Introduction, the volcano relationship is widely used in heterogeneous catalysis to identify the best catalysts for the target reaction, which are those materials with descriptors close to the peak of the volcano. The volcano plots for HER (Fig. 1.7B) are obtained from a combination of experimental data and DFT calculations. In such plots, the experimental HER exchange current densities achieved over different metal catalysts are plotted versus the free energy of hydrogen adsorption (ΔG_{H^*}), which is computed through DFT. The closer ΔG_{H^*} is to zero, the better the catalyst [102].

DFT is very helpful to *discern the elementary steps that characterize the pathway of a catalytic reaction* and assess the rate-determining step. In this regard, Fig. 7.39A shows the potential energy profiles for the catalytic hydrogenation of CO_2 to formate (black line) and CO (red line) [103]. The explored catalytic system is a Ni_4 cluster supported on the dry γ-Al_2O_3 (1 1 0) surface, named D(Ni_4). The intermediates and transition states along the reaction pathway are also presented in the figure. The starting structure for the reaction is D-1 (not shown here), which is the most stable configuration for the coadsorption of CO_2 and H on D(Ni_4) with an energy of −1.46 eV. The simplified potential diagrams showing only the transition states with the highest energy barrier are displayed in Fig. 7.39B. The reaction energy and the activation energies for formate generation, calculated with respect to the stable configuration with coadsorbed CO_2 and H, are −0.23 and 1.25 eV, respectively. On the other hand, the two same quantities for CO formation are −0.48 and 2.13 eV. This implies that formate formation is more favorable from the kinetic point of view, while CO formation is preferred thermodynamically.

The computational approach presents undoubted advantages over the experimental one as it requires only electricity and computers that are usually more economical and sustainable than preparing and testing candidate catalysts experimentally. Moreover, due to intrinsic limitations, experimental techniques often do not allow to manipulate the catalyst structure at the atomic scale, while, in computational methods, the nanoscopic properties of the catalyst can be varied and sampled throughout a wide range of potential candidates [104]. Yet, a close coupling between theory and experiments is essential to quantitatively describe a range of catalytic phenomena. Functional characterization and testing of catalysts allow to

corroborate the concepts developed by DFT calculations, which suffer from several limitations. For instance, the solvent effects in reactions taking place in liquid phase cannot be easily included in the modeling and, also, the effects of catalyst supports are often left out in DFT calculations. Moreover, the metal surfaces that can be modeled by DFT are crystalline, semiinfinite surfaces rather than an accurate representation of the actual catalyst particles. Also, the reaction rates calculated from DFT through transition state theory are not as accurate as those obtained experimentally. This is mainly due to the lack of accuracy in the absolute reaction rate computed by DFT since an error in activation energy, E_a, is magnified exponentially when E_a is used to derive the reaction rate constant through the Arrhenius equation. On the other hand, relative differences can be estimated from DFT with good accuracy. This implies that DFT is an excellent tool for reliably predicting which of the catalysts under investigation will ensure the highest performance, despite not providing an accurate estimation of their absolute reaction rates [105].

With increasing complexity of the reacting system, the description of this with few individual configurations may not be sufficiently accurate and one may adopt a statistical description over ensembles representative of reactants, products, and transition state configurations [100]. *MD simulations are employed to study the location of atoms in space*. Here, a single-point model is displaced by a dynamic model where the nuclear system is forced into motion. The simulation of the motion is conducted through the numerical solution of the classical Newtonian dynamic equations. The set of possible atom locations provides, for instance, a conformational ensemble profile for the target molecule. MD can also be used to probe the thermodynamic and dynamic properties of the molecules [106].

Fig. 7.40 shows an example of MD simulation on ammonia NH_3 synthesis from N_2 and H_2 over ruthenium NPs [107]. In the simulation model a Ru slab was introduced as support for spherical Ru NP under the assumption that the slab does not affect the reaction between the NPs and H_2/N_2. The simulations included a first step during which Ru NP is surrounded only by N_2 molecules at a given pressure (Fig. 7.40A) and, after that, N_2 molecules dissociate into N atoms on the NP surface. In the second step, all the remaining undissociated N_2 molecules are removed as they cannot contribute to the generation of NH_3. H_2 molecules are thus introduced in the system and dissociate on NP surface interacting with N atoms already present (Fig. 7.40B), leading to the formation of NH_3 and byproducts, mainly N_2H_2 (Fig. 7.40C). The activity and selectivity with varying NP sizes and H_2/N_2 pressures were obtained from a simulation. Fig. 7.40D and E show the effect of particle size. The dissociated number of N atoms was the lowest over the NPs with the largest diameter (i.e., 10 nm) due to the smallest surface area (Fig. 7.40D). After the N_2 dissociation, H_2 dissociation takes place with the subsequent generation of NH_3 and N_2H_2. The largest generation of NH_3 was found in the sample with 4 nm NPs followed by the 10 nm NPs, which showed a higher activity compared to 3 and 5 nm NPs

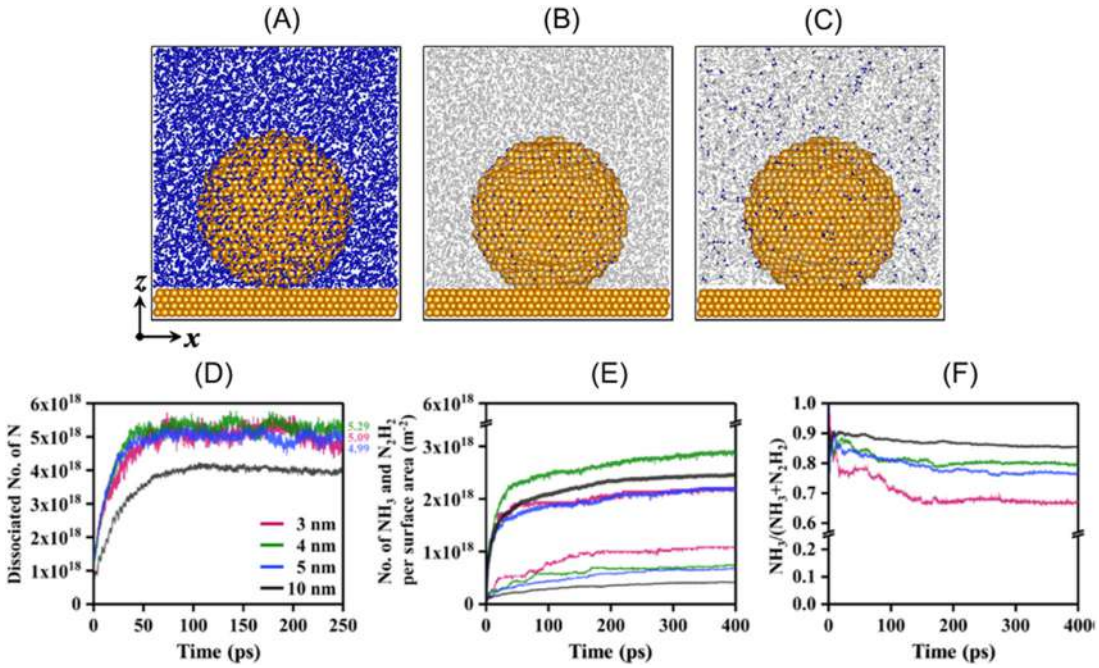

Figure 7.40

Simulation models for NH_3 generation over Ru NPs: (A) Initial atomic configuration for the dissociation of N_2; (B) initial atomic configuration for the dissociation of H_2; (C) MD snapshot after H_2 purging, resulting in NH_3 generation. (D) Number of dissociated N atoms and (E) generated NH_3 (thick line) and N_2H_2 (thin line) on NPs with different diameters; (F) selectivity toward NH_3. The color codes in (E) and (F) are the same as in (D). *MD*, Molecular dynamics; *NP*, nanoparticle. *Source: Reproduced from [107].*

(Fig. 7.40E) because of the higher concentration of face-centered-cubic sites, which are preferential H_2 dissociation sites. The 10 nm NPs also ensured the least byproduct N_2H_2, which was the main reason behind the highest selectivity of this catalyst toward NH_3 (Fig. 7.40F).

7.11 Questions and problems

1. You have to characterize a material made of a nanostructured catalyst supported on alumina. The catalyst is made of sulfated zirconia doped by nanoparticles of copper (with a size below 2 nm). The weight percentages of the components are 70% alumina; 29% sulfated zirconia; 1% copper. Which techniques would you recommend?

2. You have to characterize a catalyst consisting of manganese oxide supported on activated carbon. The catalyst is doped with nickel nanoparticles (average size 1.0 nm) and the weight percentages of the various components are 65% alumina, 34% manganese oxide, 1% nickel. Suggest the best techniques to evaluate crystal structure, morphology, oxidation states, surface area, pore size, and other relevant parameters.
3. After reading one of the studies reported in Refs. [89,108–115], answer the following questions.
   a. Which are the main conclusions derived from the research conducted in the study?
   b. If you are asked to select two of the most useful characterization techniques among the ones used by the authors enabling an understanding and correlation of activity results to catalyst's properties, which ones would you choose and why?
   c. Are the techniques you discussed in "b" surface sensitive or bulk sensitive? Explain the reasons behind this by discussing the working principles of the techniques and their applications.
   d. Which additional characterization would you suggest for a better understanding of the results and why?
   e. Are defective states of the catalyst relevant to understand its activity? If "yes," how have they been characterized?
4. Choose and discuss the most appropriate techniques to analyze the following properties of a catalyst: type and number of active centers; metal distribution on the porous surface of a support; bonding and oxidation states of the elements; crystal structure and crystallite size; exposed crystal facets.
5. The XRD pattern of monoclinic WO_3 thin film is acquired by using a diffractometer with monochromated Cu-$K\alpha$ radiation ($\lambda = 1.54178$ Å). Assuming a shape factor K of 0.9, use the Debye–Scherrer equation to estimate the crystallite size from the data obtained for the peak (2 0 0) at $2\theta = 24.4^\circ$.

2θ (°)	Intensity (counts)	2θ (°)	Intensity (counts)	2θ (°)	Intensity (counts)
23.868	1669.1	24.157	2237.7	24.446	3732.8
23.885	1660.2	24.174	2465.5	24.463	3375.7
23.902	1661.4	24.191	2583.7	24.48	3015.4
23.919	1634.9	24.208	2783	24.497	2666.7
23.936	1614.6	24.225	2951.3	24.514	2407.4
23.953	1605.1	24.242	3139.5	24.531	2104.4
23.97	1673.2	24.259	3399.5	24.548	1951.5
23.987	1730.7	24.276	3761.3	24.565	1855.9
24.004	1713.8	24.293	4146.4	24.582	1707.9
24.021	1740.6	24.31	4509	24.599	1666.9
24.038	1779.4	24.327	4768.6	24.616	1617.1
24.055	1792.5	24.344	5030.5	24.633	1533.9
24.072	1794.8	24.361	5158	24.65	1464.7
24.089	1862.3	24.378	5174.8	24.667	1424.5

(Continued)

(Continued)

2θ (°)	Intensity (counts)	2θ (°)	Intensity (counts)	2θ (°)	Intensity (counts)
24.106	1933.8	24.395	4968.7	24.684	1451.3
24.123	2048.4	24.412	4587.2	24.701	1417.5
24.14	2059.3	24.429	4193.5		

6. Carry out a literature review and write a report on the characterization of adsorbed CO through FTIR.
7. TPD measurements are conducted on Ni−Pd catalysts supported on alumina in order to determine the H_2 desorption energy. The table below reports the maximum peak temperature T_{max} recorded at increasing heating rate β. Use the Kissinger (Redhead) model (Eq. 7.6) to estimate the H_2 desorption energy.

T_{max} (K)	β (K/min)
493	10
501	12
504	13
509	15

8. Mott−Schottky analysis is carried out on an n-type semiconductor photocatalyst. The vacuum permittivity ε_0 is 8.854×10^{-14} F cm^{-1}, the Boltzmann constant k is 1.38×10^{-23} J K^{-1}, the temperature T is 298K, the electron charge e is 1.60×10^{-19} C and the dielectric constant of the material ε is 50. Estimate the flat band potential and the donor concentration using the data in the table below.

E versus Ag/AgCl (V)	C^{-2} (10^9 F^{-2} cm^4)
−0.7	0.030
− 0.65	0.042
− 0.6	0.088
− 0.55	0.186
− 0.5	0.360
− 0.45	0.625
− 0.4	0.834
− 0.35	0.958
− 0.3	1.021
− 0.25	1.089
− 0.2	1.142
− 0.15	1.207
− 0.1	1.259
− 0.05	1.322
0	1.404

9. By using the Kubelka–Munk method, estimate the bandgap of an indirect bandgap semiconductor from the following set of data obtained by UV–Vis diffuse reflectance measurements.

Wavelengths (nm)	Reflectance (%)
460	97.1
450	96.2
440	96.2
430	95.7
420	94.7
410	91.0
400	79.8
390	61.4
380	46.1
370	34.7
360	24.6
350	16.1
340	11.2
330	7.7
320	5.8
310	5.4
300	5.1
290	5.0
280	5.0

10. How can the extent of recombination of charges be assessed for a photocatalyst? Explain the meaning of the wavelengths at which emission and absorption bands appear.
11. Explain how EXAFS and HAXPES (which is a technique analog to XPS but more advanced given the possibility—for example—to tune the depth of measurements in the sample) have been conclusive in justifying the activity of the set of catalysts reported in Ref. [116]. Find analogous case studies in which these techniques have been also critical in the assessment of activity results.
12. Are the requirements for computational power greater for DFT or MD? Report a recent study on MD applied to CO_2 reduction.
13. Diffuse reflectance spectroscopy is the most common technique used to estimate the bandgap of a semiconductor. Can you mention how to estimate the absolute position of the valence/conduction bands by using the Mott–Schottky analysis and XPS? Carry out a literature survey to report few examples.
14. Mention a few paramagnetic species, which are relevant in catalytic processes, that can be studied by EPR. Can EPR be applied for (semi)quantitative assessments?
15. Analyze the analogies and dissimilarities between selected area electron diffraction (SAED) and X-ray diffraction (XRD).

References

[1] Y. Waseda, E. Matsubara, K. Shinoda, Scattering and diffraction, X-Ray Diffraction Crystallography, Springer, Berlin, Heidelberg, 2011, pp. 67–106.

[2] M. Birkholz, Principles of X-ray diffraction, Thin Film Analysis by X-Ray Scattering, Wiley-VCH Verlag GmbH & Co. KGaA, Weinheim, FRG, 2006, pp. 1–40.

[3] L. Guo, J. Sun, X. Ji, J. Wei, Z. Wen, R. Yao, et al., Directly converting carbon dioxide to linear α-olefins on bio-promoted catalysts, Commun. Chem. 1 (2018) 1–8.

[4] F. Tian, Y. Zhang, J. Zhang, C. Pan, Raman spectroscopy: a new approach to measure the percentage of anatase TiO_2 exposed (001) facets, J. Phys. Chem. C 116 (2012) 7515–7519.

[5] C. Garlisi, G. Scandura, J. Szlachetko, S. Ahmadi, J. Sa, G. Palmisano, E-beam evaporated TiO_2 and Cu-TiO_2 on glass: performance in the discoloration of methylene blue and 2-propanol oxidation, Appl. Catal. A Gen. 526 (2016) 191–199.

[6] Ou, Li, Lyu, Gui, Sun, Qian, et al., Facet-dependent interfacial charge transfer in TiO_2/nitrogen-doped graphene quantum dots heterojunctions for visible-light driven photocatalysis, Catalysts 9 (2019) 345.

[7] X. Wang, J.C. Hanson, A.I. Frenkel, J.Y. Kim, J.A. Rodriguez, Time-resolved studies for the mechanism of reduction of copper oxides with carbon monoxide: complex behavior of lattice oxygen and the formation of suboxides, J. Phys. Chem. B 108 (2004) 13667–13673.

[8] L. Wu, H. Lian, J.J. Willis, E.D. Goodman, I.S. McKay, J. Qin, et al., Tuning precursor reactivity toward nanometer-size control in palladium nanoparticles studied by in situ small angle X-ray scattering, Chem. Mater. 30 (2018) 1127–1135.

[9] P. van der Heide, Introduction, X-Ray Photoelectron Spectroscopy: An Introduction to Principles and Practices, John Wiley & Sons, Inc, Hoboken, NJ, 2011, pp. 1–12.

[10] A.M. Venezia, X-ray photoelectron spectroscopy (XPS) for catalysts characterization, Catal. Today 77 (2003) 359–370.

[11] J. Yuan, J.-J. Zhang, M.-P. Yang, W.-J. Meng, H. Wang, J.-X. Lu, CuO nanoparticles supported on TiO_2 with high efficiency for CO_2 electrochemical reduction to ethanol, Catalysts 8 (2018) 171.

[12] S. Rtimi, Indoor light enhanced photocatalytic ultra-thin films on flexible non-heat resistant substrates reducing bacterial infection risks, Catalysts 7 (2017) 57.

[13] Z. Liu, T. Duchoň, H. Wang, D.C Grinter, I. Waluyo, J. Zhou, Q. Liu, B. Jeong, E.J. Crumlin, V. Matolín, D.J. Stacchiola, J.A. Rodriguez, S.D. Senanayake, Ambient pressure XPS and IRRAS investigation of ethanol steam reforming on Ni-CeO_2(111) catalysts: An: in situ study of C-C and O-H bond scission, Phys. Chem. Chem. Phys. 18 (2016) 16621–16628.

[14] Y. Joly, S. Grenier, Theory of X-ray absorption near edge structure, X-Ray Absorption and X-Ray Emission Spectroscopy: Theory and Applications, John Wiley & Sons, Ltd, Chichester, 2016, pp. 73–97.

[15] J.J. Rehr, J.J. Kas, F.D. Vila, M. Newville, Theory and analysis of XAFS, XAFS Techniques for Catalysts, Nanomaterials, and Surfaces, Springer International Publishing, 2017, pp. 13–50.

[16] M. Wang, L. Árnadóttir, Z.J. Xu, Z. Feng, In situ X-ray absorption spectroscopy studies of nanoscale electrocatalysts, Nano-Micro Lett. 11 (2019) 1–18.

[17] A.M. Saib, A. Borgna, J. van de Loosdrecht, P.J. van Berge, J.W. Niemantsverdriet, XANES study of the susceptibility of nano-sized cobalt crystallites to oxidation during realistic Fischer-Tropsch synthesis, Appl. Catal. A Gen. 312 (2006) 12–19.

[18] M. Xu, S. He, H. Chen, G. Cui, L. Zheng, B. Wang, et al., TiO_{2-x}-modified Ni nanocatalyst with tunable metal-support interaction for water-gas shift reaction, ACS Catal. 7 (2017) 7600–7609.

[19] C.R.A. Catlow, P. Wells, D. Gianolio, Synchrotron radiation techniques in catalytic science, Phys. Chem. Chem. Phys. 22 (2020) 18745–18746.

[20] S. Bordiga, E. Groppo, G. Agostini, J.A. Van Bokhoven, C. Lamberti, Reactivity of surface species in heterogeneous catalysts probed by in situ X-ray absorption techniques, Chem. Rev. 113 (2013) 1736–1850.

[21] G. Margaritondo, Characteristics and properties of synchrotron radiation, Synchrotron Radiation: Basics, Methods and Applications, Springer, Berlin, Heidelberg, 2015, pp. 29–63.
[22] D.B. Williams, C.B. Carter, Transmission Electron Microscopy: A Textbook for Materials Science, Springer, United States, New York, 2009.
[23] B.J. Inkson, Scanning electron microscopy (SEM) and transmission electron microscopy (TEM) for materials characterization, Materials Characterization Using Nondestructive Evaluation (NDE) Methods, Elsevier Inc, 2016, pp. 17–43.
[24] S. Yurdakal, C. Garlisi, L. Özcan, M. Bellardita, G. Palmisano, (Photo)catalyst characterization techniques: adsorption isotherms and BET, SEM, FTIR, UV-Vis, photoluminescence, and electrochemical characterizations, Heterogeneous Photocatalysis: Relationships with Heterogeneous Catalysis and Perspectives, Elsevier, 2019, pp. 87–152.
[25] X. Zheng, Y. Li, L. Zhang, L. Shen, Y. Xiao, Y. Zhang, C. Au, L. Jiang, Insight into the effect of morphology on catalytic performance of porous CeO_2 nanocrystals for H_2S selective oxidation, Appl. Catal. B Environ. 252 (2019) 98–110.
[26] N.E. Salim, J. Jaafar, A.F. Ismail, M.H.D. Othman, M.A. Rahman, N. Yusof, et al., Preparation and characterization of hydrophilic surface modifier macromolecule modified poly (ether sulfone) photocatalytic membrane for phenol removal, Chem. Eng. J. 335 (2018) 236–247.
[27] G.M. Arzac, M. Paladini, V. Godinho, A.M. Beltrán, M.C. Jiménez De Haro, A. Fernández, Strong activation effect on a Ru-Co-C thin film catalyst for the hydrolysis of sodium borohydride, Sci. Rep. 8 (2018) 1–11.
[28] M. Park, J. Lee, K. Hembram, K.-R. Lee, S. Han, C. Yoon, et al., Oxygen reduction electrocatalysts based on coupled iron nitride nanoparticles with nitrogen-doped carbon, Catalysts 6 (2016) 86.
[29] B. He, Y. Zhang, X. Liu, L. Chen, In-situ transmission electron microscope techniques for heterogeneous catalysis, ChemCatChem 12 (2020) 1853–1872.
[30] T. Fujita, K. Higuchi, Y. Yamamoto, et al., TEM study of a nanoporous Ni–Co catalyst used for the dry reforming of methane, Metals (Basel) 7 (2017) 406.
[31] H. Feng, X. Xu, Y. Du, S.X. Dou, Application of scanning tunneling microscopy in electrocatalysis and electrochemistry, Electrochem. Energy Rev. 1 (2021) 3.
[32] M.C. Tanzi, S. Farè, G. Candiani, Techniques of analysis, Foundations of Biomaterials Engineering, Elsevier, 2019, pp. 393–469.
[33] F. Besenbacher, J.V. Lauritsen, S. Wendt, STM studies of model catalysts, Nano Today 2 (2007) 30–39.
[34] J.M. Chalmers, H.G.M. Edwards, M.D. Hargreaves, Vibrational spectroscopy techniques: basics and instrumentation, Infrared and Raman Spectroscopy in Forensic Science, John Wiley & Sons, Ltd, Chichester, 2012, pp. 9–44.
[35] P.J. Larkin, Basic principles, Infrared and Raman Spectroscopy: Principles and Spectral Interpretation, Elsevier, 2018, pp. 7–28.
[36] M.A. Bañares, I.E. Wachs, Raman spectroscopy of catalysts, Encyclopedia of Analytical Chemistry: Applications, Theory and Instrumentation, John Wiley & Sons, Ltd, Chichester, 2010.
[37] F. Zaera, New advances in the use of infrared absorption spectroscopy for the characterization of heterogeneous catalytic reactions, Chem. Soc. Rev. 43 (2014) 7624–7663.
[38] X. Song, L. Gao, Y. Li, W. Chen, L. Mao, J.H. Yang, Nickel phosphate-based materials with excellent durability for urea electro-oxidation, Electrochim. Acta 251 (2017) 284–292.
[39] H. Peng, Z. Mo, S. Liao, H. Liang, L. Yang, F. Luo, et al., High performance Fe- and N-doped carbon catalyst with graphene structure for oxygen reduction, Sci. Rep. 3 (2013) 1–7.
[40] Y. Stubrov, A. Nikolenko, V. Gubanov, V. Strelchuk, Manifestation of structure of electron bands in double-resonant Raman spectra of single-walled carbon nanotubes, Nanoscale Res. Lett. 11 (2016) 1–5.
[41] W. Lin, A.A. Herzing, C.J. Kiely, I.E. Wachs, Probing metal-support interactions under oxidizing and reducing conditions: in situ Raman and infrared spectroscopic and scanning transmission electron microscopic-X-ray energy-dispersive spectroscopic investigation of supported platinum catalysts, J. Phys. Chem. C 112 (2008) 5942–5951.

[42] M. Boaro, M. Vicario, C. De Leitenburg, G. Dolcetti, A. Trovarelli, The use of temperature-programmed and dynamic/transient methods in catalysis: characterization of ceria-based, model three-way catalysts, Catal. Today 77 (2003) 407–417.
[43] A. Gervasini, Temperature programmed reduction/oxidation (TPR/TPO) methods, in: Calorimetry and Thermal Methods in Catalysis, Springer, 2013, pp. 175–195.
[44] S. Besselmann, C. Freitag, O. Hinrichsen, M. Muhler, Temperature-programmed reduction and oxidation experiments with V_2O_5/TiO_2 catalysts, Phys. Chem. Chem. Phys. 3 (2001) 4633–4638.
[45] J. Yang, H. Yu, Y. Wang, F. Qi, H. Liu, L.L. Lou, et al., Effect of the oxygen coordination environment of Ca-Mn oxides on the catalytic performance of Pd supported catalysts for aerobic oxidation of 5-hydroxymethyl-2-furfural, Catal. Sci. Technol. 9 (2019) 6659–6668.
[46] A. Klinkova, P.V. Cherepanov, I.G. Ryabinkin, M. Ho, M. Ashokkumar, A.F. Izmaylov, et al., Shape-dependent interactions of palladium nanocrystals with hydrogen, Small 12 (2016) 2450–2458.
[47] J. Luo, F. Gao, K. Kamasamudram, N. Currier, C.H.F. Peden, A. Yezerets, New insights into Cu/SSZ-13 SCR catalyst acidity. Part I: Nature of acidic sites probed by NH_3 titration, J. Catal. 348 (2017) 291–299.
[48] S. Loganathan, R.B. Valapa, R.K. Mishra, G. Pugazhenthi, S. Thomas, Thermogravimetric analysis for characterization of nanomaterials, Thermal and Rheological Measurement Techniques for Nanomaterials Characterization: Micro and Nano Technologies, Elsevier, 2017, pp. 67–108.
[49] S. Ebnesajjad, Surface and material characterization techniques, Surface Treatment of Materials for Adhesive Bonding, Elsevier, 2014, pp. 39–75.
[50] P. Gill, T.T. Moghadam, B. Ranjbar, Differential scanning calorimetry techniques: Applications in biology and nanoscience, J. Biomol. Tech. 21 (2010) 167–193.
[51] O. Koshy, L. Subramanian, S. Thomas, Differential scanning calorimetry in nanoscience and nanotechnology, Thermal and Rheological Measurement Techniques for Nanomaterials Characterization: Micro and Nano Technologies, Elsevier, 2017, pp. 109–122.
[52] K.J. Lee, N. Elgrishi, B. Kandemir, J.L. Dempsey, Electrochemical and spectroscopic methods for evaluating molecular electrocatalysts, Nat. Rev. Chem. 1 (2017) 1–14.
[53] S. Chen, Practical electrochemical cells, Handbook of Electrochemistry, Elsevier, 2007, pp. 33–56.
[54] G. Inzelt, A. Lewenstam, F. Scholz, Handbook of Reference Electrodes, Springer, Berlin, Heidelberg, 2013.
[55] O. Fischer, E. Fischerová, Basic principles of voltammetry, Experimental Techniques in Bioelectrochemistry, Birkhäuser, Basel, 1995, pp. 41–157.
[56] R.G. Compton, C.E. Banks, Understanding Voltammetry, 2nd ed., Imperial College Press, 2010.
[57] J. Zhang, PEM Fuel Cell Electrocatalysts and Catalyst Layers: Fundamentals and Applications, Springer, London, 2008.
[58] C. Garlisi, C.-Y. Lai, L. George, M. Chiesa, G. Palmisano, Relating photoelectrochemistry and wettability of sputtered Cu- and N-doped TiO_2 thin films via an integrated approach, J. Phys. Chem. C 122 (2018) 12369–12376.
[59] K. Scott, Sustainable and Green Electrochemical Science and Technology, John Wiley & Sons, Ltd, Chichester, 2017.
[60] S. Sarker, A.J.S. Ahammad, H.W. Seo, D.M. Kim, Electrochemical impedance spectra of dye-sensitized solar cells: fundamentals and spreadsheet calculation, Int. J. Photoenergy 214 (2014) 17.
[61] C. Garlisi, J. Szlachetko, C. Aubry, D.L.A. Fernandes, Y. Hattori, C. Paun, et al., N-TiO_2/Cu-TiO_2 double-layer films: impact of stacking order on photocatalytic properties, J. Catal. 353 (2017) 116–122.
[62] M. Li, Z. Liu, Y. Hu, M. Wang, H. Li, Effect of doping elements on catalytic performance of CeO_2-ZrO_2 solid solutions, J. Rare Earths 26 (2008) 357–361.
[63] R. Beranek, (Photo)electrochemical methods for the determination of the band edge positions of TiO_2-based nanomaterials, Adv. Phys. Chem. 2011 (2011).
[64] Z. Zhang, J.T. Yates, Band bending in semiconductors: chemical and physical consequences at surfaces and interfaces, Chem. Rev. 112 (2012) 5520–5551.

[65] H.-H. Perkampus, Photometers and spectrophotometers, UV-VIS Spectroscopy and Its Applications, Springer, Berlin, Heidelberg, 1992, pp. 10–25.
[66] A.V. Arecchi, T. Messadi, R.J. Koshel, Field Guide to Illumination, SPIE, 2010.
[67] A. Rockett, The Materials Science of Semiconductors, Springer, United States, New York, 2008.
[68] R.W. Brander, A review of the merits of direct and indirect gap semiconductors for electroluminescence devices, Rev. Phys. Technol. 3 (1972) 145.
[69] P. Makuła, M. Pacia, W. Macyk, How to correctly determine the band gap energy of modified semiconductor photocatalysts based on UV-Vis spectra, J. Phys. Chem. Lett. 9 (2018) 6814–6817.
[70] B. Choudhury, M. Dey, A. Choudhury, Defect generation, d-d transition, and band gap reduction in Cu-doped TiO_2 nanoparticles, Int. Nano Lett. 3 (2013) 1–8.
[71] J. Jana, M. Ganguly, T. Pal, Enlightening surface plasmon resonance effect of metal nanoparticles for practical spectroscopic application, RSC Adv. 6 (2016) 86174–86211.
[72] Z. Zhang, C. Zhang, H. Zheng, H. Xu, Plasmon-driven catalysis on molecules and nanomaterials, Acc. Chem. Res. 52 (2019) 2506–2515.
[73] Z.U.H. Khan, A. Khan, Y. Chen, A. ullah Khan, N.S. Shah, N. Muhammad, B. Murtaza, K. Tahir, F.U. Khan, P. Wan, Photo catalytic applications of gold nanoparticles synthesized by green route and electrochemical degradation of phenolic Azo dyes using AuNPs/GC as modified paste electrode, J. Alloys Compd. 725 (2017) 869–876.
[74] P. Sánchez-López, Y. Kotolevich, S. Miridonov, F. Chávez-Rivas, S. Fuentes, V. Petranovskii, Bimetallic AgFe systems on mordenite: effect of cation deposition order in the NO reduction with C_3H_6/CO, Catalysts 9 (2019) 58.
[75] J. Liqiang, Q. Yichun, W. Baiqi, L. Shudan, J. Baojiang, Y. Libin, et al., Review of photoluminescence performance of nano-sized semiconductor materials and its relationships with photocatalytic activity, Sol. Energy Mater. Sol Cell 90 (2006) 1773–1787.
[76] D. Russo, M. Muscetta, L. Clarizia, et al., Fe(III)/Fe(II)/WO_3–Pd fuel cell for electricity generation using synthetic and real effluents under visible light, Renew. Energy 147 (2020) 1070–1081.
[77] R. Brüninghoff, K. Wenderich, J.P. Korterik, B.T. Mei, G. Mul, A. Huijser, Time-Dependent photoluminescence of nanostructured anatase TiO_2 and the role of bulk and surface processes, J. Phys. Chem. C 123 (2019) 26653–26661.
[78] M. Anpo, S. Dzwigaj, M. Che, Chapter 1: Applications of photoluminescence spectroscopy to the investigation of oxide-containing catalysts in the working state, Adv. Catal. 52 (2009) 1–42.
[79] M.-L. Bailly, G. Costentin, H. Lauron-Pernot, J.M. Krafft, M. Che, Physicochemical and in situ photoluminescence study of the reversible transformation of oxide ions of low coordination into hydroxyl groups upon interaction of water and methanol with MgO, J. Phys. Chem. B 109 (2005) 2404–2413.
[80] F. Deng, J. Yang, C. Ye, Solid state NMR characterization of solid surface of heterogeneous catalysts, Modern Magnetic Resonance, Springer, 2007, pp. 205–211.
[81] A.T. Bell, A. Pines, NMR Techniques in Catalysis, CRC Press, 1994.
[82] A.G. Stepanov, Basics of solid-state NMR for application in zeolite science: material and reaction characterization, Zeolites and Zeolite-Like Materials, Elsevier Inc, 2016, pp. 137–188.
[83] H. Pfeifer, H. Ernst, NMR studies of zeolites, Annu. Rep. NMR Spectrosc. 28 (1994) 91–187.
[84] J.F. Haw, J.B. Nicholas, W. Song, F. Deng, Z. Wang, T. Xu, et al., Roles for cyclopentenyl cations in the synthesis of hydrocarbons from methanol on zeolite catalyst HZSM-5, J. Am. Chem. Soc. 122 (2000) 4763–4775.
[85] A. Brückner, In situ electron paramagnetic resonance: a unique tool for analyzing structure–reactivity relationships in heterogeneous catalysis, Chem. Soc. Rev. 39 (2010) 4673–4684.
[86] J.H. Lunsford, EPR methods in heterogeneous catalysis, Catalysis, Springer, Berlin, Heidelberg, 1987, pp. 227–256.
[87] M. Brustolon, E. Giamello, Electron Paramagnetic Resonance: A Practitioner's Toolkit, John Wiley and Sons, Hoboken, NJ, 2008.

[88] M. Labanowska, EPR monitoring of redox processes in transition metal oxide catalysts, ChemPhysChem 2 (2001) 712–731.
[89] L.Y. Ozer, H. Apostoleris, F. Ravaux, S.I. Shylin, F. Mamedov, A. Lindblad, et al., Long-lasting non-hydrogenated dark titanium dioxide: medium vacuum anneal for enhanced visible activity of modified multiphase photocatalysts, ChemCatChem 10 (2018) 2949–2954.
[90] H. Jiang, X. Xu, R. Zhang, Y. Zhang, J. Chen, F. Yang, Nano ferrites (AFe_2O_4, A = Zn, Co, Mn, Cu) as efficient catalysts for catalytic ozonation of toluene, RSC Adv. 10 (2020) 5116–5128.
[91] M. Chiesa, E. Giamello, M. Che, EPR characterization and reactivity of surface-localized inorganic radicals and radical ions, Chem. Rev. 110 (2010) 1320–1347.
[92] N.R. Jaegers, K.T. Mueller, Y. Wang, J.Z. Hu, Variable temperature and pressure operando MAS NMR for catalysis science and related materials, Acc. Chem. Res. 53 (2020) 611–619.
[93] S. Prodinger, A. Vjunov, J.Z. Hu, J.L. Fulton, D.M. Camaioni, M.A. Derewinski, et al., Elementary steps of faujasite formation followed by in situ spectroscopy, Chem. Mater. 30 (2018) 888–897.
[94] I.I. Ivanova, Y.G. Kolyagin, I.A. Kasyanov, A.V. Yakimov, T.O. Bok, D.N. Zarubin, Time-resolved in situ MAS NMR monitoring of the nucleation and growth of zeolite BEA catalysts under hydrothermal conditions, Angew. Chem. Int. Ed. 56 (2017) 15344–15347.
[95] C.A. Gaggioli, S.J. Stoneburner, C.J. Cramer, L. Gagliardi, Beyond density functional theory: the multiconfigurational approach to model heterogeneous catalysis, ACS Catal. (2019).
[96] D.S. Sholl, J.A. Steckel, Density Functional Theory, John Wiley & Sons, Inc, Hoboken, NJ, 2009.
[97] W. Koch, M.C. Holthausen, A Chemist's Guide to Density Functional Theory, Wiley, 2001.
[98] C. Chizallet, P. Raybaud, Density functional theory simulations of complex catalytic materials in reactive environments: beyond the ideal surface at low coverage, Catal. Sci. Technol. 4 (2014) 2797–2813.
[99] A.P.J. Jansen, Molecular Dynamics for Reactions of Heterogeneous Catalysis, Springer, Boston, MA, 1991, pp. 133–144.
[100] L. Grajciar, C.J. Heard, A.A. Bondarenko, M.V. Polynski, J. Meeprasert, E.A. Pidko, et al., Towards operando computational modeling in heterogeneous catalysis, Chem. Soc. Rev. 47 (2018) 8307–8348.
[101] J.K. Nørskov, F. Abild-Pedersen, F. Studt, T. Bligaard, Density functional theory in surface chemistry and catalysis, Proc. Natl. Acad. Sci. U.S.A. 108 (2011) 937–943.
[102] J. Greeley, T.F. Jaramillo, J. Bonde, I. Chorkendorff, J.K. Nørskov, Computational high-throughput screening of electrocatalytic materials for hydrogen evolution, Nat. Mater. 5 (2006) 909–913.
[103] Y.X. Pan, C.J. Liu, Q. Ge, Effect of surface hydroxyls on selective CO_2 hydrogenation over Ni_4/γ-Al_2O_3: a density functional theory study, J. Catal. 272 (2010) 227–234.
[104] Y. Mao, H. Wang, P. Hu, Theory and applications of surface micro-kinetics in the rational design of catalysts using density functional theory calculations, WIREs Comput. Mol. Sci. 7 (2017).
[105] J. Yates, J.K. Johnson, Molecular Physical Chemistry for Engineers, University Science Books, Sausalito, CA, 2007.
[106] J. Polanski, Chemoinformatics, Comprehensive Chemometrics, Elsevier, 2009, pp. 459–506.
[107] S.Y. Kim, H.W. Lee, S.J. Pai, S.S. Han, Activity, selectivity, and durability of ruthenium nanoparticle catalysts for ammonia synthesis by reactive molecular dynamics simulation: the size effect, ACS Appl. Mater. Interfaces 10 (2018) 26188–26194.
[108] C. Garlisi, J. Szlachetko, C. Aubry, D.L.A. Fernandes, Y. Hattori, C. Paun, et al., N-TiO_2/Cu-TiO_2 double-layer films: impact of stacking order on photocatalytic properties, J. Catal. 353 (2017) 116–122.
[109] R. Ciriminna, G. Scandura, V. Pandarus, R. Delisi, A. Scurria, F. Béland, et al., Towards the broad utilization of gold nanoparticles entrapped in organosilica, ChemCatChem 9 (2017) 1322–1328.
[110] L.Y. Ozer, Y. Shin, A. Felten, H. Oladipo, O. Pikuda, C. Muryn, et al., Growing N-doped multiphase TiO_2 nanocomposites on reduced graphene oxide: characterization and activity under low energy visible radiation, J. Environ. Chem. Eng. 5 (2017) 5091–5098.
[111] M. Bellardita, C. Garlisi, L.Y. Ozer, A.M. Venezia, J. Sá, F. Mamedov, et al., Highly stable defective TiO_{2-x} with tuned exposed facets induced by fluorine: impact of surface and bulk properties on selective UV/visible alcohol photo-oxidation, Appl. Surf. Sci. 510 (2020) 145419.

[112] G. Scandura, J. Rodríguez, G. Palmisano, Hydrogen and propane production from butyric acid photoreforming over Pt-TiO_2, Front. Chem. 7 (2019) 563.
[113] M. Bellardita, C. Garlisi, A.M. Venezia, G. Palmisano, L. Palmisano, Influence of fluorine on the synthesis of anatase TiO_2 for photocatalytic partial oxidation: are exposed facets the main actors? Catal. Sci. Technol. 8 (2018) 1606–1620.
[114] M.J. Torralvo-Fernandez, E. Enciso, S. Martinez, I. Sobrados, J. Sanz, D. Tonti, et al., Influence of the preparation temperature on the photocatalytic activity of 3d-ordered macroporous anatase formed with an opal polymer template, ACS Appl. Nano Mater. 1 (2018) 2567–2578.
[115] O. Pikuda, C. Garlisi, G. Scandura, G. Palmisano, Micro-mesoporous N-doped brookite-rutile TiO_2 as efficient catalysts for water remediation under UV-free visible LED radiation, J. Catal. 346 (2017) 109–116.
[116] K. Asazawa, H. Kishi, H. Tanaka, D. Matsumura, K. Tamura, Y. Nishihata, et al., In situ XAFS and HAXPES analysis and theoretical study of cobalt polypyrrole incorporated on carbon (CoPPyC) oxygen reduction reaction catalysts for anion-exchange membrane fuel cells, J. Phys. Chem. C 118 (2014) 25480–25486.

Index

Note: Page numbers followed by "*b,*" "*f,*" and "*t*" refer to boxes, figures, and tables, respectively.

D

E

F

G

H

I